Structure and Reactivity of Aromatic Molecules on Metal Single-Crystal Surfaces and at Metal/Organic Interfaces

Kumulative Dissertationsschrift

zur Erlangung des
Doktorgrades der Naturwissenschaften
(Dr. rer. nat.)

dem Fachbereich Chemie
der Philipps-Universität Marburg

vorgelegt von
Claudio Kristoffer Krug, M.Sc.
aus Fritzlar

Marburg, 2020

Der praktische Teil der vorliegenden Arbeit wurde unter Leitung von Herrn Prof. Dr. J. Michael Gottfried in der Zeit von Januar 2016 bis Dezember 2019 am Fachbereich Chemie der Philipps-Universität Marburg angefertigt.

Vom Fachbereich Chemie der Philipps-Universität Marburg mit der Hochschulkennziffer 1180 als Dissertation am 09.07.2020 angenommen.

Tag der Einreichung: 29.06.2020

Tag der Disputation: 07.08.2020

Erstgutachter: Prof. Dr. J. Michael Gottfried

Zweitgutachter: Prof. Dr. Ralf Tonner (Universität Regensburg)

Lizenzierung

Für meine Mutter

Selbstständigkeitserklärung

gemäß § 10, Absatz 1 der Promotionsordnung der Mathematisch-Naturwissenschaftlichen Fachbereiche und des Medizinischen Fachbereichs für seine mathematisch-naturwissenschaftlichen Fächer der Philipps-Universität Marburg vom 15.07.2009.

Ich erkläre, dass eine Promotion noch an keiner anderen Hochschule als der Philipps-Universität Marburg, Fachbereich Chemie, von mir versucht wurde und versichere, dass ich meine vorgelegte Dissertation

Structure and Reactivity of Aromatic Molecules on Metal Single-Crystal Surfaces and at Metal/Organic Interfaces

selbst und ohne fremde Hilfe verfasst, nicht andere als die in ihr angegebenen Quellen oder Hilfsmittel benutzt, alle vollständig oder sinngemäß übernommenen Zitate als solche gekennzeichnet sowie die Dissertation in der vorliegenden oder einer ähnlichen Form noch bei keiner anderen in- oder ausländischen Hochschule anlässlich eines Promotionsgesuches oder zu anderen Prüfungszwecken eingereicht habe.

Marburg, _____

_____

Claudio K. Krug

Abstract

Low-dimensional carbon-based nanostructures are considered for the fabrication of modern electronic devices. For the realization of such devices, it is of utmost importance to achieve a high control over the structural quality. As a result, the field of on-surface synthesis, which aims at producing well-defined structures from tailor-made molecular precursors, has grown rapidly over the past decade. The reaction most frequently used to conduct on-surface synthesis is the Ullmann coupling reaction. Although a lot of work has already been invested, the fundamental principles determining the outcome of this reaction have not fully been understood to date. One prototypical case for such a situation is the product formation on the basis of precursor molecules that can either form long oligomer chains or macrocycles. This cumulative dissertation thesis contains a number of articles investigating the reaction products of different precursor molecules bearing these characteristics. They are investigated on metal single-crystal surfaces by scanning tunneling microscopy and complementary surface science techniques such as X-ray photoelectron spectroscopy or angle-resolved photoemission spectroscopy, accompanied by Monte Carlo simulations. The ring/chain ratio formed by the model system 1,3-dibromoazulene on Cu(111) was studied. By this means new insights on how the ring/chain ratio can be tuned by variation of coverage and temperature were gained based on fundamental physicochemical considerations. An alternative approach to steer the reaction outcome was used by applying a surface template, *i.e.*, a vicinal Ag surface, to exclusively form long, perfectly aligned oligomer chains from the 4,4''-dibromo-1,1':3',1''-terphenyl precursor. Furthermore, the 2,6-dibromoazulene precursor, which can exclusively form chains, was used to generate nanoribbons of the non-alternant graphene allotropes phagraphene and tetra-penta-hepta-graphene on Au(111). The structures of these species have been unambiguously elucidated by non-contact atomic force microscopy experiments carried out in a collaboration project. As a last project, the structural polymorphism of the pure self-assembly of 1,1':3',1'':4'',1'''-quaterphenyl-4,4'''-dicarbonitrile on the Ag(111) surface was investigated. This molecule shows an adsorbate structure containing flat-lying and upright-standing molecules. Such a structure had not been reported so

far. Along with the structures formed, the performance of organic-electronic devices is also crucially dependent on the interactions between the substrate and the organic layer itself. To contribute to this field of research, studies on different model systems, *i.e.*, porphyrins, corroles, and the non-alternant aromatic molecule azulene, have been performed in collaboration projects mostly involving synchrotron radiation beamtimes. In addition to the results already published in scientific journals, some unpublished results are part of this thesis. These are the investigation of the 1,3-dibromoazulene precursor on the Ag(111) surface with co-deposited Cu atoms and the successful initial operation of a commercially available atomic layer injection device. The experimental results are supplemented by the development and construction of technical instrumentation, which expands the capabilities of the measurement setup in the laboratory of the Gottfried group in Marburg.

Kurzzusammenfassung

Kohlenstoffbasierte Nanostrukturen bieten ein großes Potential für moderne elektronische Bauteile der Zukunft. Anwendungen dieser Art erfordern eine hohe Kontrolle über die strukturelle Qualität. Daher ist das Forschungsfeld der oberflächengestützten Synthese wohlbestimmter Strukturen aus maßgeschneiderten molekularen Präkursoren im letzten Jahrzehnt stark gewachsen. Die am häufigsten zur oberflächengestützten Synthese genutzte Reaktion ist die Ullmann-Kupplung. Trotz einer Vielzahl an Vorarbeiten sind die Grundlagen dieser Reaktion bisher noch nicht vollständig verstanden. Dies ist zum Beispiel bei der Produktverteilung von Präkursoren der Fall, die sowohl lange Oligomerketten als auch Makrocyclen bilden können. Diese kumulative Dissertationsschrift enthält einige Artikel, die die Reaktionsprodukte solcher Präkursoren auf Metall-Einkristall-Oberflächen mittels Rastertunnelmikroskopie untersuchen. Dabei wurden die Ergebnisse durch Methoden wie Röntgenphotoelektronenspektroskopie und winkelaufgelöste Ultraviolettphotoelektronenspektroskopie sowie Monte Carlo-Simulationen ergänzt. Auf diese Weise wurde der Einfluss von Bedeckungsgrad und Temperatur auf das Ring/Ketten-Verhältnis des Modellsystems 1,3-Dibromazulen auf Cu(111) grundlegend untersucht. Ein weiterer Ansatz, um das Reaktionsergebnis zu steuern, ist die Verwendung eines Oberflächen-Templats. Eine vicinale Ag-Oberfläche wurde genutzt, um lange, perfekt ausgerichtete Oligomerketten aus dem Präkursor 4,4''-Dibrom-1,1':3',1''-terphenyl zu bilden. Des Weiteren wurde 2,6-Dibromazulen genutzt, das aufgrund seiner molekularen Struktur ausschließlich Ketten bilden kann, um Nanobänder der nichtalternierenden Graphen-Allotrope Phagraphen und Tetra-Penta-Hepta-Graphen auf Au(111) zu erzeugen. Die Strukturen dieser Spezies wurden in einem Kooperationsprojekt eindeutig mittels *non-contact* Rasterkraftmikroskopie aufgeklärt. Als letztes Projekt wurde der strukturelle Polymorphismus von 1,1':3',1'':4'',1'''-Quaterphenyl-4,4'''-dicarbonitril auf der Ag(111)-Oberfläche untersucht. Dieses Molekül zeigt eine Adsorbatstruktur, die sowohl flach liegende als auch aufrecht stehende Moleküle beinhaltet. Eine solche Struktur war zuvor unbekannt. Zusätzlich zu den gebildeten Strukturen hängt die Leistung eines organischen elektronischen Bauteils entscheidend

von den Wechselwirkungen zwischen dem Substrat und der organischen Schicht selbst ab. Um etwas zu diesem Forschungsgebiet beizutragen, wurden Untersuchungen mit verschiedenen Modellsystemen wie Porphyrinen, Corrolen und dem nichtalternierenden Aromaten Azulen in Kooperationsprojekten im Rahmen von Synchrotron-Strahlzeiten durchgeführt. Neben den bereits in wissenschaftlichen Zeitschriften veröffentlichten Ergebnissen sind auch einige bisher unveröffentlichte Ergebnisse Teil dieser Arbeit. Hierbei handelt es sich um die Untersuchung des 1,3-Dibromazulen-Präkursors auf der Ag(111)-Oberfläche mit zusätzlich abgeschiedenen Cu-Atomen und die erfolgreiche Inbetriebnahme eines kommerziell erhältlichen *atomic layer injection*-Geräts. Die experimentellen Ergebnisse werden durch die Entwicklung und Konstruktion technischer Gerätschaften vervollständigt, die die Leistungsfähigkeit der Apparatur im Labor der AG Gottfried in Marburg erweitern.

Contents

Abbreviations

General Acronyms

0D	zero-dimensional
1D	one-dimensional
2D	two-dimensional
3D	three-dimensional
AEY	Auger electron yield
AFM	atomic force microscopy
ALI	atomic layer injection
ARPES	angle-resolved photoemission spectroscopy
ARUPS	angle-resolved ultraviolet photoelectron spectroscopy
CCD	charge-coupled device
DC	direct current
DFT	density functional theory
DOS	density of states
EELS	electron energy loss spectroscopy
EM	effective molarity
EPWE	electron plane wave expansion
ESCA	electron spectroscopy for chemical analysis
EY	electron yield
FM	frequency modulation
FY	fluorescence yield
GNR	graphene nanoribbon
HAXPES	hard X-ray photoelectron spectroscopy
HF	Hartree-Fock
HOMO	highest occupied molecular orbital
IMFP	inelastic mean free path
IPS	inverse photoemission spectroscopy
LDOS	local density of states
LEED	low-energy electron diffraction

LT	low temperature
LUMO	lowest unoccupied molecular orbital
MC	Monte Carlo
MCP	micro-channel plate
ML	monolayer
MO	molecular orbital
nc-AFM	non-contact atomic force microscopy
NEXAFS	near-edge X-ray absorption fine structure
NI-XSW	normal incidence X-ray standing wave
OFET	organic field-effect transistor
OFHC	oxygen-free high thermal conductivity
OLED	organic light-emitting diode
OPVC	organic photovoltaic cell
OTFT	organic thin film transistor
PAH	polycyclic aromatic hydrocarbon
PES	photoelectron spectroscopy
PEY	partial electron yield
PID	proportional-integral-derivative
QCM	quartz crystal microbalance
RT	room temperature
SECO	secondary electron cutoff
SPM	scanning probe microscopy
STM	scanning tunneling microscopy
STS	scanning tunneling spectroscopy
TEY	total electron yield
TMP	turbomolecular pump
TPD	temperature-programmed desorption
TZM	titanium-zirconium-molybdenum
UHV	ultra-high vacuum
UPS	ultraviolet photoelectron spectroscopy
UV	ultraviolet
VT	variable temperature
XPS	X-ray photoelectron spectroscopy

Chemical Compounds

2HOEP	octaethylporphyrin
2HTPP	*meso*-tetraphenylporphyrin
3HTpFPC	5,10,15-tris(pentafluorophenyl)-corrole
BIB	1,3-bis(*p*-bromophenyl)-5-(*p*-iodophenyl)benzene
CoTPP	Co tetraphenylporphyrin
DBAz	1,3-dibromoazulene
DBBA	10,10'-dibromo-9,9'-bianthryl
DBTP	4,4''-dibromo-1,1':4',1''-terphenyl
DCM	dichloromethane
DMQP	4,4''''-dibromo-1,1':4',1'':3'',1''':4''',1''''-quinquephenyl
DMTP	4,4''-dibromo-1,1':3',1''-terphenyl
FeHEDMC	Fe 2,3,8,12,17,18-hexaethyl-7,13-dimethylcorrole
FeOEP	Fe octaethylporphyrin
FeTPC	Fe 5,10,15-triphenylcorrole
LN_2	liquid nitrogen
***m*-4PDN**	1,1':3',1'':4'',1'''-quaterphenyl-4,4'''-dicarbonitrile
TPDCN	1,1':3',1''-terphenyl-4,4''-dicarbonitrile

1 Introduction

In our modern society mobile electronic devices play an outstanding role. To answer the ever-increasing demand for these devices available at low cost and to deal with the emerging quest for sustainability, organic electronics seem to be the inevitable solution.[1] While in some areas like display technology organic light-emitting diodes (OLEDs) are already state of the art,[2,3] the performance of other devices like, *e.g.*, organic photovoltaic cells (OPVCs)[4] or organic thin film transistors (OTFTs)[5] is still lacking far behind conventional solutions.[6–8]

To improve the performance of devices based on organic semiconductor molecules, a fundamental understanding of the processes involved is essential.[9,10] One way to increase this fundamental understanding is the study of basic model systems. This can be achieved by the investigation of organic molecules on metal single-crystal surfaces in ultra-high vacuum (UHV) environment.[11] Under these well-defined conditions the interactions between organic molecules and metal substrates can be studied without the impact of external influences.

Among these studies under UHV conditions several different approaches can be distinguished, which will be explained in the following sections. The first and probably most important one used in this thesis is the so-called bottom-up fabrication of carbon-based nanostructures. Secondly, the reactions of prototypical molecules with, *e.g.*, metal atoms, can be investigated in the monolayer (ML) or multilayer regime. Thirdly, the self-assembly of molecules on surfaces can be investigated using microscopic and spectroscopic methods.

1.1 On-Surface Synthesis

The main topic of this thesis is the bottom-up synthesis of carbon-based nanostructures on surfaces. There are several reactions that can be used for this purpose. These reactions, which are often similar to their equivalents known from solution chemistry, will be introduced in the following sections.[12–14] A big advantage of on-surface synthesis is that molecules that are not accessible by

solution chemistry due to bad solubility or instability can be realized. Furthermore, these new molecules can be unambiguously characterized with powerful surface science techniques.

Surface-Confined Ullmann Coupling

The most widely used reaction to achieve covalent C−C coupling between aryl compounds on surfaces is the Ullmann coupling reaction. This reaction was first described in solution for the coupling of two equivalents of 1-bromo-2-nitrobenzene to 2,2'-dinitrobiphenyl by Ullmann and Bielecki in 1901, using stoichiometric amounts of Cu.[15] Later on, the applicability of this reaction was also shown for iodinated aromatic molecules.[16] Today, Ullmann-type reactions can also be carried out with catalytic amounts of Cu.[17] The Ullmann coupling reaction of bromobenzene is schematically shown in Scheme 1.1a.

It took almost 90 years until this reaction was first realized on a surface in 1990 by Zhou, Castro, and White.[18] In that study the authors were able to show the formation of biphenyl from iodobenzene deposited on Ag(111) by means of temperature-programmed desorption (TPD). The first studies concerning the mechanism of this on-surface synthesis reaction were performed by Xi and Bent using iodobenzene on Cu(111).[19]

The first investigations on the surface-confined Ullmann coupling using scanning tunneling microscopy (STM) were made in the early 2000s.[20–23] It was shown that by applying thermal energy (or voltage pulses with the STM tip) the

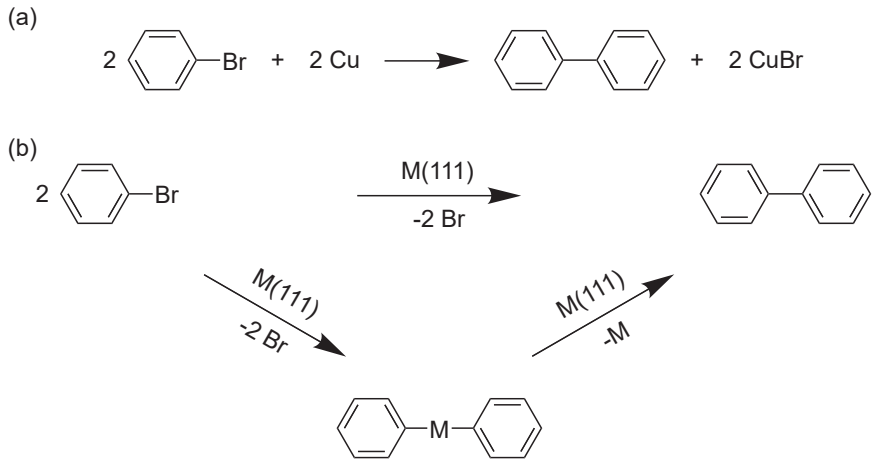

Scheme 1.1: (a) Conventional Ullmann coupling reaction of bromobenzene to biphenyl in solution with the use of stoichiometric amounts of Cu. (b) The Ullmann coupling reaction on coinage metal(111) surfaces. For M = Cu, Ag very often an organometallic intermediate species with a C−M−C bond is observed, whereas for M = Au this has only rarely been reported.

C−halogen bond can be cleaved and covalent C−C bonds are formed. However, it took until 2007, when Grill *et al.* reported on the fabrication of one-dimensional (1D) chains and two-dimensional (2D) networks formed after the coupling of brominated tetraphenylporphyrin molecules on Au(111) to realize that nanostructures can be synthesized in a controlled way by clever precursor design using this approach.[24] Since then the field of on-surface synthesis has grown rapidly. Although in the first place the reaction reported by Ullmann and named after him used Cu to couple brominated or iodinated aryl compounds, nowadays basically any coupling reaction of halogenated aryl compounds on coinage metal surfaces is considered as a surface-confined Ullmann coupling. Nevertheless, Br is the most commonly used halogen and while there are also many studies using iodinated molecules,[25–30] Cl is only of minor importance.[31–35]

The three coinage metal surfaces Cu, Ag, and Au differ in their reactivity towards dehalogenation. Cu is considered the most reactive surface, *i.e.*, the C−Br bond is usually already completely split at room temperature (RT).[36–42] In contrast, on the intermediate Ag surfaces only partial debromination takes place[43–48] and on the most inert Au surfaces the molecules usually remain intact at RT.[25,49–52] However, the reactivity towards dehalogenation is not the only difference between the different metal surfaces. Another very important point is that on Cu and Ag usually organometallic intermediates with C−M−C (M = Cu, Ag) bonds are observed,[30,35,38–40,42–44,46,47,53–64] which have only rarely been reported on Au surfaces (*cf.* Scheme 1.1b).[29,31,49,50,52,65–67] The existence of these organometallic intermediates can be very useful to control the final reaction outcome because of their reversibility.[25,45,68,69]

To date, numerous precursor molecules have been used to synthesize a wide range of nanostructures on surfaces.[26,41,70–72] One particularly interesting case is the investigation of molecules that can either form long chains, *i.e.*, 1D structures, or rings, which can be considered as zero-dimensional (0D). In a first study Fan *et al.* have shown that 4,4''-dibromo-1,1':3',1''-terphenyl (DMTP) on the Cu(111) surface can either form long zigzag chains or macrocycles called hyperbenzene ([18]-honeycombene).[36] Later, Chen *et al.* successfully synthesized the next larger macrocycle, *i.e.*, [30]-honeycombene, from the 4,4''''-dibromo-1,1':4',1'':3'',1''':4''',1''''-quinquephenyl (DMQP) precursor.[73] A first study how the ring/chain ratio formed by DMTP can be tuned showed that lowering the deposition rate, *i.e.*, applying pseudo-high-dilution conditions, increases the ring yield (*cf.* Figure 1.1).[45] The question how this reaction outcome, *i.e.*, whether rings or chains are formed, can be controlled has also inspired the work leading to this thesis.

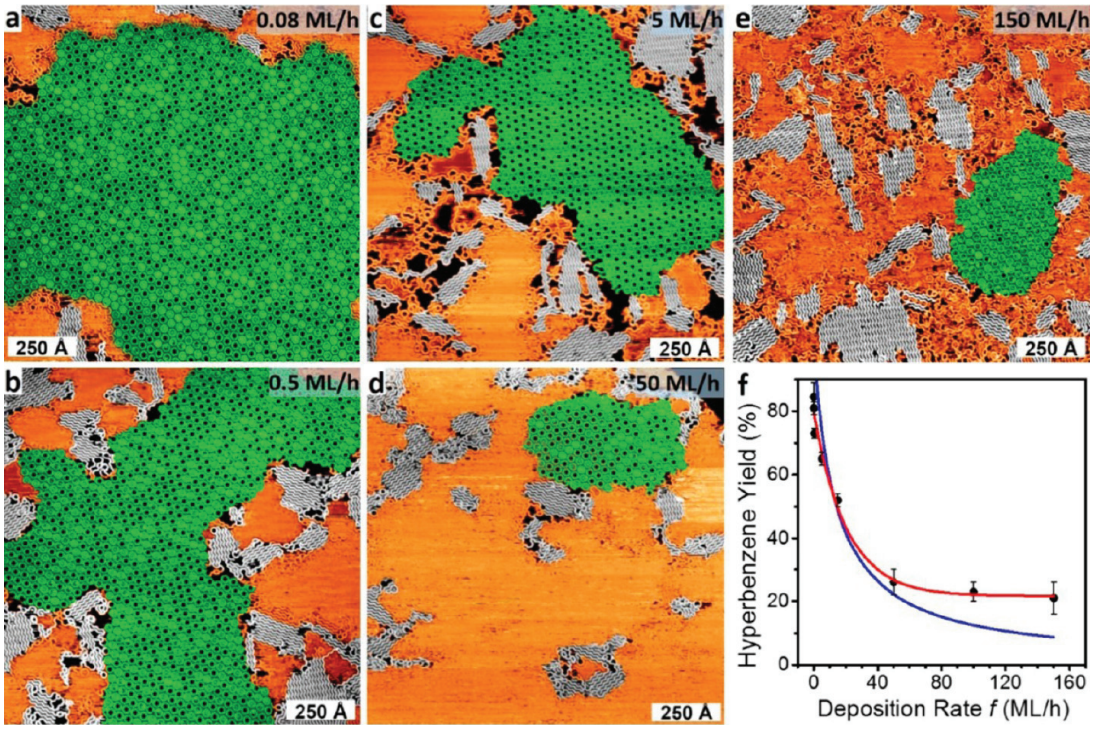

Figure 1.1: STM images showing the influence of the deposition rate of 4,4''-dibromo-1,1':3',1''-terphenyl (DMTP) on Ag(111) held at 463 K on the ring yield. According to the pseudo-high-dilution conditions a lower deposition rate leads to a higher ring yield. Rings are highlighted in green and chains in grey. Reprinted with permission from ref. [45]. © 2017 American Chemical Society.

Another way of controlling the reaction outcome is the application of surfaces that act as templates. So far, only the atomically flat M(111) surfaces (M = Cu, Ag, Au) have been considered. If, *e.g.*, vicinal surfaces are used, it is possible to achieve chains, which are aligned on the small terraces in the direction of the step edges.[74–77] Another way of using a surface as template was shown by Fan *et al.*, who used the Cu(110)-(2×1)O surface.[42] In this study the width of the bare Cu stripes determined whether rings or chains were formed.

Dehydrogenative Coupling

A material that has attracted tremendous interest since its discovery in 2004 is graphene.[78] This single-layer carbon allotrope is considered for many applications, *e.g.*, transistors, supercapacitors, or solar cells.[79–81] However, as a semimetal and thus without a band gap, it cannot be used for the fabrication of electronic devices, where semiconductors are needed.[78] One approach to make graphene a semiconductor is to cut it into small stripes, so-called graphene nanoribbons (GNRs).[82,83] This cutting can either be done in a top-down approach by lithography[84,85] or in a bottom-up approach. For the latter the first re-

action step is usually an Ullmann coupling reaction of brominated precursors. In the second step the oligomers formed in this way can be fully conjugated by splitting off hydrogen and forming new C−C bonds. This was first shown for the 10,10'-dibromo-9,9'-bianthryl (DBBA) precursor on the Au(111) surface (Scheme 1.2).[83]

Since this seminal work, a lot of precursor molecules have been used to synthesize GNRs on surfaces with different widths, edge structures and other elements as dopants.[86–114] The atomical precision, with which GNRs can be produced in this way, is illustrated by the non-contact atomic force microscopy (nc-AFM) images shown in Figure 1.2.[115]

In addition to the synthesis of GNRs, the dehydrogenation scheme has also been applied to synthesize molecular species, which are called nanographenes.[109,116–125] While GNRs are 1D cut-outs of graphene, which in principle are infinitely long in one dimension, the nanographenes can be considered as zero-dimensional.

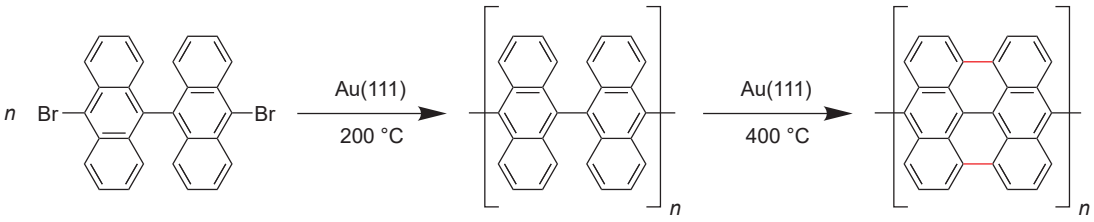

Scheme 1.2: Dehydrogenation reaction of 10,10'-dibromo-9,9'-bianthryl (DBBA) on Au(111) as described in ref. [83]. In the first step oligomers are formed by an Ullmann coupling reaction and in the second step the oligomers are fully conjugated by splitting off hydrogen. The newly formed C−C bonds due to this dehydrogenation reaction are shown in red.

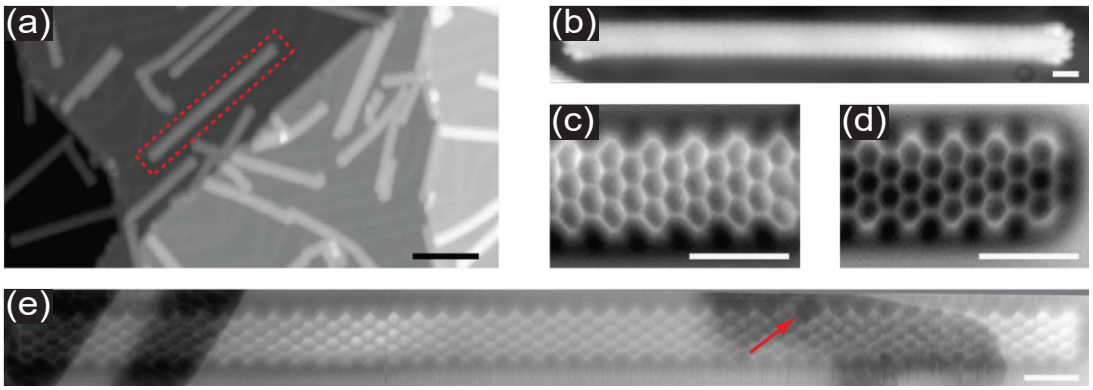

Figure 1.2: STM and nc-AFM images of DBBA on Au(111). (a) STM overview image. (b) STM image of a free GNR recorded with a CO-functionalized tip. (c), (d) Constant-height nc-AFM images of the middle and edge region of a GNR, respectively. (e) Constant-height nc-AFM image of a whole GNR. Adapted with permission from ref. [115]. © 2013 Springer Nature.

Other Reactions for Covalent C–C Coupling on Surfaces

Besides the Ullmann and dehydrogenative coupling reactions described in the previous sections, some other reactions known from solution chemistry have been applied to on-surface synthesis to form covalent C−C bonds on surfaces. These other reactions were not used in this thesis and have been reviewed extensively.[12,13,72,126–131] Thus, they will only briefly be introduced.

Some of the other reactions rely on halogenated precursor molecules like the Ullmann coupling reaction. One reaction known from solution chemistry is the Sonogashira coupling of terminal alkynes with halogenated aromatic compounds to link species containing C≡C triple bonds. The applicability of this reaction has been shown for iodinated[132] and brominated[133–135] precursor molecules. In a similar way, two brominated alkyne groups can be coupled directly to yield graphdiyne species.[67,136] However, it is also possible to generate C≡C triple bonds directly on a surface by coupling species carrying tribromo-[137,138] or trichloromethyl[139] substituents. Analogously, C=C double bonds can be generated by using dibromomethyl substituents[140] or alkenyl *gem*-dibromides, yielding cumulene species.[141,142] The same alkenyl *gem*-dibromide functionality can also form C≡C triple bonds.[143] Finally, C−C single bonds can be achieved by dehalogenative homocoupling of alkenyl bromides[144] or Wurtz reactions using alkyl bromides.[145] In addition, *ortho*-dihaloarenes can undergo [2+2] or [2+2+2] cycloaddition reactions.[64,146]

All the reactions mentioned this far have the disadvantage that the split-off halogen atoms remain adsorbed on the surface. To overcome this problem, some reactions that do not need halogen atoms have been introduced. The first one is the Glaser coupling, in which two terminal alkynes are linked.[147–150] Aryl alkynes can also undergo cyclotrimerization reactions.[151,152] Furthermore, the Bergmann cyclization utilizing two alkyne moieties within the same molecule has been successfully applied on a surface.[153] Using an appropriate surface as 1D template, linear alkane[154] or polyacetylene[155] chains can be realized on Au(110) or Cu(110), respectively.

For the realization of electronic devices metal surfaces cannot be used. In order to overcome this limitation, some of the reactions for covalent C−C couplings have also been successfully carried out on insulating substrates.[156–158]

1.2 Cyclic Tetrapyrrole Molecules

A different class of molecules that has been intensively studied on surfaces are cyclic tetrapyrrole molecules and their metal complexes. The surface chemistry of tetrapyrrole macrocycles has been extensively reviewed.[159] Thus, the present section will focus on the aspects relevant for this thesis. There are two classes of tetrapyrrole macrocycles that have been subject to investigations in this thesis, namely porphyrins and corroles. These two classes of molecules and their respective applications will be discussed in the following.

Porphyrins

Porphyrins are cyclic tetrapyrroles that are composed of the parent porphine macrocycle (Figure 1.3a) and a number of substituents. For example, substitution at the *meso* positions with phenyl groups leads to *meso*-tetraphenylporphyrin (2HTPP, Figure 1.3b).

All free-base porphyrins possess two pyrrolic (−NH−) and two iminic (−N=) nitrogen atoms. The pyrrolic nitrogen atoms are prone to deprotonation and thus the porphyrins can be used as ligands to stabilize metal dications forming metalloporphyrins. Accordingly, reaction of 2HTPP with a metal M leads to a metallotetraphenylporphyrin (MTPP, Figure 1.3c). This was, *e.g.*, shown for Co,[160,161] Zn,[162] or Fe.[163] Today, porphyrin complexes of many transition metals are known on surfaces.[159]

Whereas the pyrrolic and iminic nitrogen atoms can be distinguished in, *e.g.*, X-ray photoelectron spectroscopy (XPS) experiments, after metalation all four

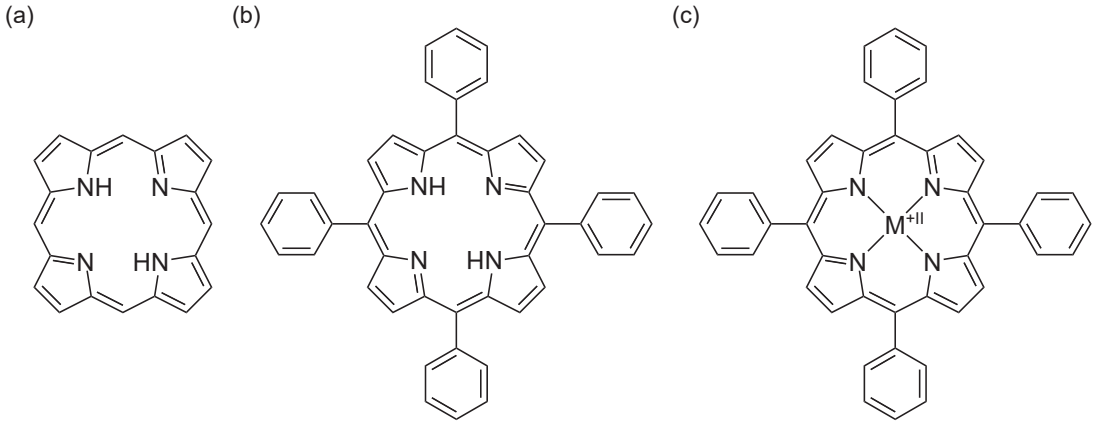

Figure 1.3: (a) Porphine, the parent macrocycle of all porphyrins. (b) *meso*-tetraphenylporphyrin (2HTPP), which is obtained by substitution of porphine with phenyl groups at the *meso* positions. (c) A metallotetraphenylporphyrin (MTPP) is formed by reaction of 2HTPP with a metal M, stabilizing a metal dication.

nitrogen atoms are chemically equivalent. Thus, the reaction between 2HTPP and a metal is a very subtle probe to monitor the diffusion of the metal into the organic layer, which is important for organic electronics.

Corroles

For the fabrication of electronic devices the stabilization of metal cations in high oxidation states might be required.[164,165] One way to stabilize higher oxidation states is a change in the ligand structure of the tetrapyrrole macrocycle. A class of molecules closely related to porphyrins are corroles. In these, there is one methine bridge (−CH=) less than in the porphyrins (marked in orange in Figure 1.4b), which leads to three pyrrolic (−NH−) and one iminic (−N=) nitrogen atoms and a smaller size of the macrocycle.

A free-base corrole that has been synthesized in solution is 2,3,8,12,17,18-hexaethyl-7,13-dimethylcorrole (3HHEDMC, Figure 1.4b), carrying six ethyl and two methyl substituents at the β positions of the pyrrole units.[166] This substitution pattern allows to distinguish 3HHEDMC from the similarly substituted octaethylporphyrin (2HOEP, Figure 1.4a) in STM experiments if a comparison of the two classes of tetrapyrrole macrocycles is needed.

The rather small change in the structure of the corroles compared with the porphyrins (*cf.* Figure 1.4a,b) can have a strong influence on its reactivity towards metal atoms. Because of their tribasic character and the contracted ring size corroles should be able to stabilize metal trications and also smaller metal ions in general (Figure 1.4c).[165] These properties make corroles interesting molecules not only for solution chemistry, but also for surface science studies.

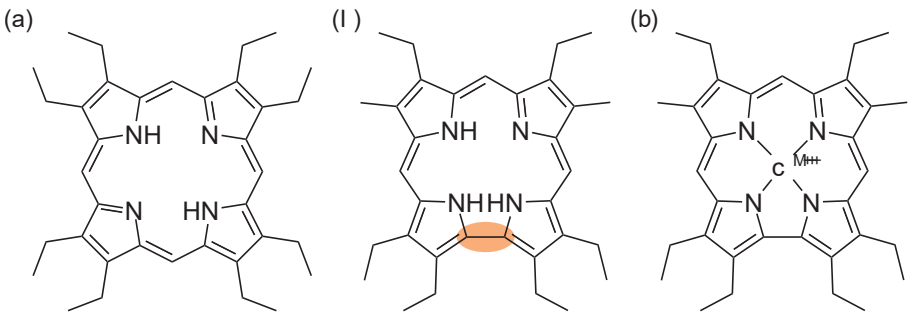

Figure 1.4: (a) Octaethylporphyrin (2HOEP), which is obtained by substitution of porphine with eight ethyl groups in the β positions of the pyrrole units. (b) 2,3,8,12,17,18-Hexaethyl-7,13-dimethylcorrole (3HHEDMC), which is obtained by substitution of the corrole core with six ethyl and two methyl groups in the β positions of the pyrrole units. (c) A metallo-2,3,8,12,17,18-hexaethyl-7,13-dimethylcorrole (MHEDMC) is formed by reaction of 3HHEDMC with a metal M, stabilizing a metal trication.

Nevertheless, studies of corroles on surfaces are scarce to date. The first investigations have been carried out on Fe 5,10,15-triphenylcorrole (FeTPC) on Cu(111), which was already metalated in solution.[167] Later on, 5,10,15-tris(pentafluorophenyl)-corrole (3HTpFPC), in which all phenyl substituents are perfluorinated, was investigated as the first free-base corrole on surfaces.[168–172] However, a direct metalation of a free-base corrole on a surface with post-deposited metal atoms, as it is well known for porphyrins, had not been reported before the beginning of this thesis.

1.3 Other Aromatic Molecules for Surface Chemistry Purposes

Besides the two big topics of brominated aromatic molecules and tetrapyrroles, some other molecules have been studied in the course of this thesis. These will be briefly introduced in the following sections.

Aromatic Dicarbonitriles

Aromatic dicarbonitriles are a class of molecules, which have attracted significant interest in surface science studies in the last decade. They are interesting because of their potential application in OTFTs[173] or OLEDs.[174,175]

The pure self-assembly of aromatic dicarbonitriles on coinage metal single-crystal surfaces has been intensively investigated. Linear oligophenylene-*para*-dicarbonitriles (NC−Ph_x−CN with x = 3, 4, 5, 6) show different adsorbate structures on the Ag(111) surface depending on their length (Figure 1.5). In these studies densely-packed chevron layers, open rhombic networks, and Kagome lat-

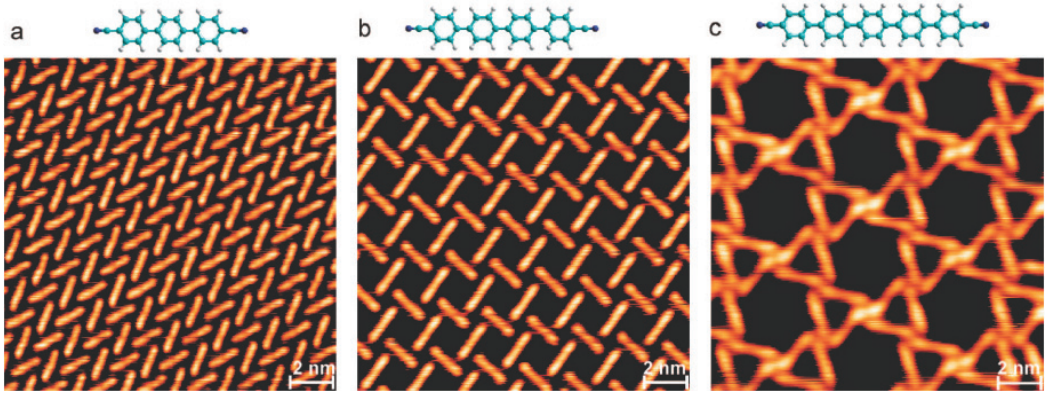

Figure 1.5: STM images of three linear oligophenylene-*para*-dicarbonitriles (NC−Ph_x−CN) with different lengths on Ag(111). (a) x = 3, (b) x = 4, (c) x = 5. The molecules show different adsorbate structures depending on their length. Reprinted with permission from ref. [176]. © 2008 American Chemical Society.

tices were observed.[176–180] Furthermore, non-linear molecules with *meta* linkings either in the oligophenylene backbone or of the carbonitrile groups show a wide variety of adsorbate structures, including upright-standing molecules.[181–185]

The complexity but also the quality of the adsorbate structures can even be increased by the co-deposition of metal atoms.[186–190] Co-deposition of NC−Ph_x−CN (x = 3, 4) with Ce atoms led to an unusual five-vertex Archimedean tiling on the Ag(111) surface[191] and with NC−Ph_4−CN and Eu on Au(111) even 2D quasicrystals could be realized.[192] Another very interesting case is the formation of metal-organic Sierpiński triangles, a fractal structure. They can be achieved by deposition of 1,1':3',1''-terphenyl-4,4''-dicarbonitrile (TPDCN) and Ni[193] (Figure 1.6) or Fe[194] on the Au(111) surface and with intrinsically present Cu adatoms on Cu(111).[185]

Azulene as a Prototype for Non-Alternant Aromatic Compounds

Another class of compounds that have recently attracted great interest in surface science are so-called non-alternant polycyclic aromatic hydrocarbons (PAHs).[195–200] The molecule that can be seen as the prototype of this class of compounds is azulene (Figure 1.7a).

Azulene and its alternant counterpart naphthalene (Figure 1.7b) are structural isomers. Yet, these two molecules differ strongly in some aspects. While naphthalene has no dipole moment due to symmetry reasons, azulene has a dipole

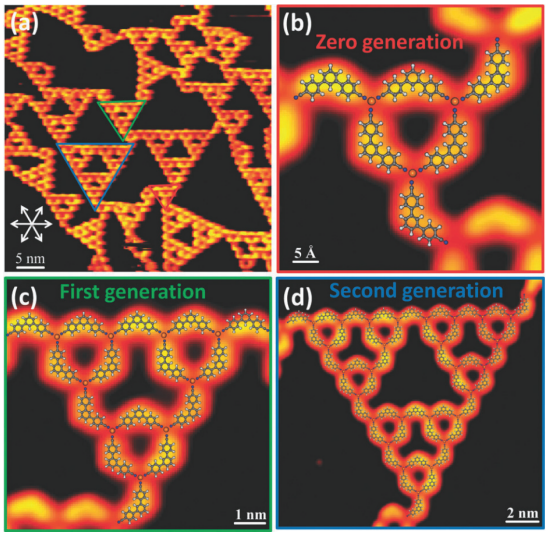

Figure 1.6: STM images of 1,1':3',1''-terphenyl-4,4''-dicarbonitrile (TPDCN) on Au(111). (a) Overview image. (b), (c), and (d) Sierpiński triangles of zeroth, first, and second generation, respectively. Reprinted with permission from ref. [193]. © 2015 Royal Society of Chemistry.

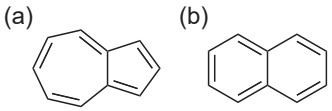

Figure 1.7: (a) The non-alternant PAH azulene. (b) Its alternant counterpart naphthalene.

moment of 0.8 D, which is quite large for a pure hydrocarbon.[201] Furthermore, the gap between highest occupied molecular orbital (HOMO) and lowest unoccupied molecular orbital (LUMO) can be expected to be smaller for azulene. Because of these unusual properties, azulene is an interesting candidate for organic field-effect transistors (OFETs) and OPVCs.[202,203] Moreover, five-seven ring structures – the structural motif of azulene – appear as defects in graphene and azulene can be considered as a model system for these defects.[204,205] All these reasons make azulene a very interesting molecule to study on surfaces.

2 Motivation

In order to build future electronic nanodevices based on structures realized using on-surface synthesis, a fundamental understanding of the processes determining the reaction products is crucial. Although many efforts have already been undertaken, these processes are not fully understood to date. One example of such a situation is the competition between ring and chain formation in the surface-confined Ullmann coupling reaction from precursor molecules that are able to form both these motifs due to their structure. Different approaches to steer the reaction outcome, *i.e.*, whether rings or chains are formed, were investigated within this cumulative dissertation thesis.

As a first project 1,3-dibromoazulene (DBAz, Figure 2.1a) on the Cu(111) surface was chosen as a model system. This molecular precursor for the surface-confined Ullmann coupling reaction is able to form either long oligomeric chains or macrocycles. On the stage of the organometallic intermediate of the Ullmann coupling, the concepts of kinetic and thermodynamic reaction control were applied to control the ring/chain ratio as monitored by scanning tunneling microscopy (STM). These findings based on first principles of reaction kinetics were substantiated by Monte Carlo (MC) simulations in a collaboration project. Due to these very basic considerations, the knowledge gained for this model system should be applicable to ring/chain competition in on-surface synthesis in general. This project resulted in two publications (P1 and P2).

In a second project, the 4,4''-dibromo-1,1':3',1''-terphenyl (DMTP) precursor (Figure 2.1c), which has been shown to form both rings and chains before, was used. Here, the control of chain over ring formation was achieved by using

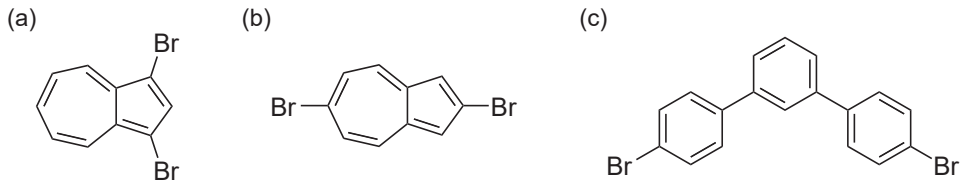

Figure 2.1: The molecular precursors for the surface-confined Ullmann coupling used within this thesis. (a) 1,3-Dibromoazulene (DBAz). (b) 2,6-dibromoazulene (2,6-DBAz). (c) 4,4''-dibromo-1,1':3',1''-terphenyl (DMTP).

a vicinal Ag surface as a template. In a collaboration project the exclusive formation of chains was shown by STM on a local scale and by low-energy electron diffraction (LEED) on a global scale, while angle-resolved photoemission spectroscopy (ARPES) was used to determine the electronic structure of these perfectly aligned chains. The results led to one publication (P3).

In a third project the 2,6-dibromoazulene (2,6-DBAz) precursor (Figure 2.1b) was investigated on the Au(111) surface. The substitution pattern of this structural isomer of DBAz is chosen in a way that it can exclusively form chains. However, it is not obvious whether bonds are exclusively formed between five-membered and seven-membered rings, in an alternating fashion, or completely random. While the connection pattern could already be assumed from STM images, it was unambiguously revealed by non-contact atomic force microscopy (nc-AFM) measurements conducted in a collaboration project. Furthermore, these measurements proved that fusion between the chains *via* dehydrogenative coupling is possible and revealed the products formed. These are nanoribbons of two new graphene allotropes, namely phagraphene and tetra-penta-heptagraphene. This project gave rise to publication P4.

In addition to the studies on the surface-confined Ullmann coupling reaction, further surface science studies are part of this cumulative dissertation thesis. The topic of the first one is the structural polymorphism of 1,1':3',1'':4'',1'''-quaterphenyl-4,4'''-dicarbonitrile (*m*-4PDN, Figure 2.2) on the Ag(111) surface. The structures formed by this molecule upon adsorption at different coverages were analyzed by STM, leading to one publication (P5).

Furthermore, the direct metalation of two tetrapyrrole macrocycles, *i.e.*, *meso*-tetraphenylporphyrin (2HTPP, *cf.* Figure 1.3b) and 2,3,8,12,17,18-hexaethyl-7,13-dimethylcorrole (3HHEDMC, *cf.* Figure 1.4b), was investigated using synchrotron radiation-based techniques in collaborative projects. For 2HTPP the reaction depth and interphase formation upon deposition of Co onto a 50 nm thick film were determined using hard X-ray photoelectron spectroscopy (HAXPES), which resulted in publication P6, while for 3HHEDMC the reaction with

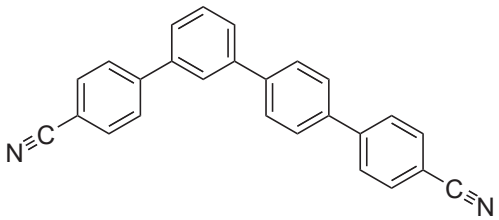

Figure 2.2: The polymorphism of the adsorbate structure of 1,1':3',1'':4'',1'''-quaterphenyl-4,4'''-dicarbonitrile (*m*-4PDN) was studied within this thesis.

Fe was studied using near-edge X-ray absorption fine structure (NEXAFS) spectroscopy and compared to the corresponding octaethylporphyrin (2HOEP, *cf.* Figure 1.4a) (P7).

At last, the interaction of the non-alternant polycyclic aromatic hydrocarbon (PAH) azulene (*cf.* Figure 1.7a) with the Cu(111) surface was studied in a collaborative project using a multi-technique approach. This study revealed fundamental differences in the interaction of azulene with Cu(111) compared with its alternant counterpart naphthalene (*cf.* Figure 1.7b) and led to publication P8.

The results already published in scientific journals are complemented by further unpublished results. First, the DBAz precursor is investigated on the Ag(111) surface using STM and XPS. Because of the insufficient reactivity of Ag(111) towards debromination, the ring/chain ratio formed on the stage of the organometallic intermediate of the surface-confined Ullmann coupling reaction is studied using co-deposited Cu atoms. Second, the successful initial operation of a commercially available atomic layer injection (ALI) device is shown by deposition of 2HTPP from a dichloromethane (DCM) solution using XPS and STM.

Besides the experimental studies, three construction projects are part of this thesis. The aim of these projects was to expand the capabilities of the combined STM and XPS setup in the laboratory of the Gottfried group in Marburg. First, the sputtering and annealing stage of the STM chamber was redesigned to establish a more accurate temperature control during annealing of the metal single-crystal samples. Second, the manipulator head of the custom-built preparation chamber was redesigned because the original design had several drawbacks, including the danger of breaking. Third, a line-of-sight evaporator was designed, which facilitates the deposition of medium-vapor pressure molecules like DBAz and 2,6-DBAz. It enabled the studies of these molecules presented in this thesis.

3 Experimental Techniques

A number of experimental techniques commonly used for surface characterization have been applied to obtain the results presented in this thesis. Most of all, these are surface sensitive microscopic and spectroscopic methods. In the following sections these techniques along with their physical background and instrumental realization will be introduced. The aim of this chapter is to provide the reader with the knowledge necessary to understand the presented data and not to give a complete discussion of the respective methods. For this purpose the reader is referred to the corresponding literature, on which this chapter is based.[206–211]

3.1 Scanning Probe Microscopy

The most important techniques used to gather the data within this thesis belong to the family of scanning probe microscopy (SPM). In an SPM experiment a sharp tip is raster-scanned across a surface. Different physical quantities are used as probe to give a microscopic image of the sample with a very high resolution. Two forms of SPM have been applied, namely scanning tunneling microscopy (STM) and atomic force microscopy (AFM), which will be introduced in the following.

3.1.1 Scanning Tunneling Microscopy

The first kind of SPM and also the method mainly used within this thesis is scanning tunneling microscopy (STM). It was invented in 1981 by Binnig and Rohrer,[212,213] who were awarded the Nobel Prize in Physics for this invention in 1986. This fact already highlights the high relevance of this experimental technique, which also laid the basis for all other SPMs. In the following the physical basics of STM will be explained.

In an STM experiment a very sharp metallic tip, which ideally has a single atom at its apex, is brought very close to the sample surface and scanned across it. The measured quantity is the tunneling current, which occurs if an external

potential is applied between sample and tip. In order to be able to measure a current this method is restricted to conducting samples.

The reason why the tunneling current occurs is the quantum mechanical tunneling effect (Figure 3.1). According to classical mechanics an electron cannot overcome a potential barrier if its energy ε is not sufficient. However, in quantum mechanics the electron is described by its wave function Ψ. If the wave function is incident on a potential barrier with thickness d, its value does not immediately drop to 0 but has a certain probability density $|\Psi|^2$ to be located inside the barrier. This means that an electron as a quantum mechanical particle also has a certain probability to reside inside the barrier and can thus overcome it. This effect is called tunneling. If an external potential V_t is applied between two potential wells with work functions Φ_i, the tunneling becomes directional. This directional flow of electrons results in a so-called tunneling current, which can be measured.

The Hamiltonian $\hat{\mathrm{H}}$ of the electron can be divided into three parts dependent on its location z. One before the barrier ($z < 0$)

$$\hat{\mathrm{H}} = -\frac{\hbar^2}{2m_\mathrm{e}}\frac{\mathrm{d}^2}{\mathrm{d}z^2} \ , \tag{3.1}$$

one inside the barrier ($0 < z < d$)

$$\hat{\mathrm{H}} = -\frac{\hbar^2}{2m_\mathrm{e}}\frac{\mathrm{d}^2}{\mathrm{d}z^2} + V \ , \tag{3.2}$$

and a third one after the barrier ($z > d$), which again has the form of Equa-

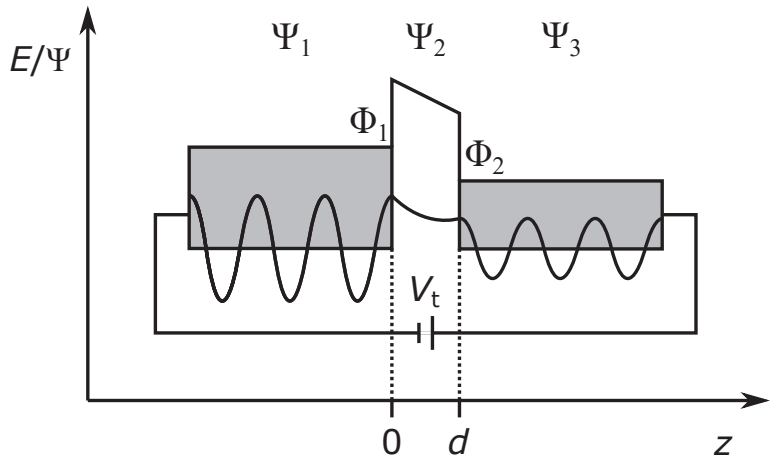

Figure 3.1: Tunneling of an electron with wave function Ψ_i through a barrier with finite thickness d. If an external potential V_t is applied between the two potential wells with work functions Φ_i, the tunneling preferably occurs in one direction and thus results in a tunneling current I_t.

tion (3.1). $\hbar$ is the reduced Planck constant $h/2\pi$ and m_e the electron mass. The wave functions of an electron outside and inside the barrier are given by Equations (3.3) and (3.4), respectively.

$$\Psi = A \cdot \mathrm{e}^{ikz} + B \cdot \mathrm{e}^{-ikz} \qquad \text{with} \qquad k = \sqrt{\frac{2m_\mathrm{e}E}{\hbar^2}} \tag{3.3}$$

$$\Psi = C \cdot \mathrm{e}^{ikz} + D \cdot \mathrm{e}^{-ikz} \qquad \text{with} \qquad k = \sqrt{\frac{2m_\mathrm{e}(E-V)}{\hbar^2}} \tag{3.4}$$

The wave functions before and after the barrier only differ by the two pre-exponential factors A and B, which are of course also different inside the barrier (C and D). The wave function in Equation (3.4) is the relevant one for STM. It has an imaginary part, which approaches infinity and is thus ignored, and a real part, which decreases exponentially with the distance d.[207] Thus, if the distance between tip and sample is small enough, a tunneling current can be measured depending on the local work function Φ_eff (Equation (3.5)).

$$I_\mathrm{t} \propto \mathrm{e}^{-2\kappa d} \qquad \text{with} \qquad \kappa = \sqrt{\frac{2m_\mathrm{e}\Phi_\mathrm{eff}}{\hbar^2}} \tag{3.5}$$

Because of this exponential dependence of the tunneling current on the distance between tip and sample, the largest amount of current flows between the tip apex and the topmost atoms of the surface.[214] This fact makes STM a suitable technique to image surface structures. If the tip is sharp enough resolution on the atomic or molecular scale can be achieved.

However, the tunneling current is determined not only by the topography of the sample, *i.e.*, the tip–sample distance, but also depends on the electronic structure of the sample and the tip. If, *e.g.*, a negative potential is applied, *i.e.*, tunneling takes place from the sample to the tip, those regions of the sample with a higher density of states (DOS) will contribute stronger to the tunneling current and thus appear higher in the STM images. This fact always needs to be kept in mind for the analysis of STM images.

The tunneling current can be calculated according to Equation (3.6) depending on the elementary charge e, the tunneling voltage, and the energy of an electron as well as the DOSs ρ_i and the Fermi energies $E_{\mathrm{F},i}$ of tip T and sample S.[206]

$$I_\mathrm{t} = \frac{4\pi e}{\hbar} \int_0^{eV_\mathrm{t}} \rho_\mathrm{T}(E_\mathrm{F,T} - eV_\mathrm{t} + \varepsilon) \cdot \rho_\mathrm{S}(E_\mathrm{F,S} + \varepsilon) \cdot \mathrm{e}^{-2\kappa d} \mathrm{d}\varepsilon \tag{3.6}$$

The critical dependence on the distance makes STM very sensitive to external vibrations. One way to overcome this problem is a compact design of the microscope. This was realized in the Aarhus-type STM invented by Lægsgaard, Besenbacher, and Stensgaard at the University of Aarhus, Denmark and offered by the company SPECS Surface Nano Analysis GmbH (Figure 3.2).[215]

In this setup the sample ① is rigidly mounted on a sample holder ②. The sample holder is pressed tightly to the top sample stage ④ by two clamps ③. The whole setup is housed in a gold coated copper block ⑤, which can be cooled with liquid nitrogen (LN_2). The sample is facing upside down and can be approached by the tip ⑥ from the bottom with an inchworm motor ⑨. This inchworm motor is a piezo tube consisting of three parts. The top and bottom part can clamp the approach motor rod ⑧ and by alternating contraction and expansion of the central part the tip is either approached to or retracted from the sample. The actual scanning is performed by another piezo tube ⑦, which controls the x, y, and z motion. Because these piezo elements are calibrated for operation at RT, the whole motor part can be counter-heated by a Zener diode ⑩ if the STM is cooled. To further reduce the influence of external vibrations, the block containing the STM is suspended on springs ⑪ and does not have any rigid contact to the STM chamber during scanning.

There are two scanning modes to actually record STM images. The first one is the constant height mode. In this mode the tip is scanned across the sample in a constant height and the resulting tunneling current is measured. This current in dependence of the x and y coordinates gives the STM image. The advantage of this mode is that scanning can be performed quickly. However, because the tip height is not adjusted there is the danger that the tip can collide with protruding

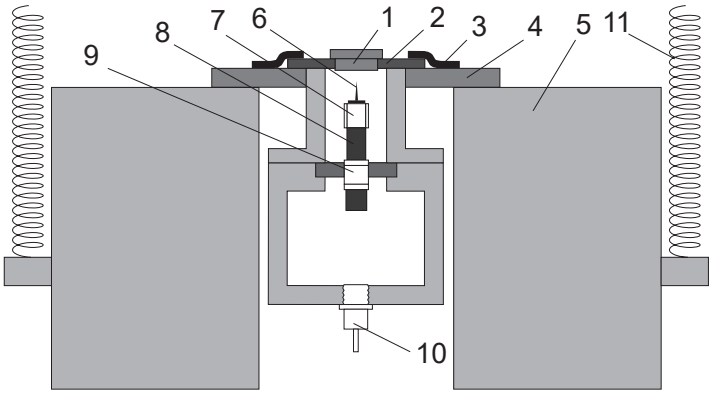

Figure 3.2: Cross-sectional sketch of the Aarhus-type STM offered by SPECS Surface Nano Analysis GmbH. ① Sample, ② sample holder, ③ sample holder clamp, ④ top sample stage, ⑤ gold coated copper block, ⑥ tip, ⑦ scanner piezo tube, ⑧ approach motor rod, ⑨ inchworm piezo tube, ⑩ Zener diode, ⑪ suspension springs. Adapted from refs. [216–218].

objects on the sample. These tip crashes can damage sample and tip and should thus be avoided, which limits the constant height mode to small and flat scanning areas.

In order to avoid tip crashes, the constant current mode can be used. In this mode the tunneling current is kept constant by adjusting the tip height with an external feedback loop. This is done by changing the voltage applied to the z component of the scanner piezo motor. Thus, the STM image is given by this voltage in dependence of the x and y coordinates. Although this operation mode is slower than the constant height mode, it is usually used in experiments.

Scanning Tunneling Spectroscopy

The fact that the tunneling current in STM depends not only on the tip–sample distance but also on the DOS can be used to obtain further information on the electronic structure of the sample. This method is called scanning tunneling spectroscopy (STS) and was first introduced by Hamers, Tromp, and Demuth in 1986.[219] In contrast to techniques like ultraviolet photoelectron spectroscopy (UPS, *cf.* Section 3.2.1), inverse photoemission spectroscopy (IPS), or electron energy loss spectroscopy (EELS), which average over a comparably large area of the surface, it can elucidate the electronic structure of single atoms or molecules. Furthermore, by changing the polarity of the potential between sample and tip it gives access to unoccupied states.

In STS the position of the tip is fixed on a certain point of the sample. Thus, the tunneling current depends on the applied bias voltage and the tip–sample distance. In all modes of STS the relation between two of these three quantities, I_t, V_t, and d, is measured, while the third one is kept constant. If the feedback regulating the tip height is switched off, *i.e.*, d remains constant, this is called $I_\mathrm{t}(V_\mathrm{t})$ spectroscopy, which is the most commonly used mode of STS. Simplified, the result of such a measurement can be regarded as the local density of states (LDOS) of the sample. An increase of the bias voltage will give rise to a higher tunneling current. If the voltage is high enough to access an electronic state of the sample, *e.g.*, a molecular orbital (MO), this leads to a steeper increase of the tunneling current.

However, the extraction of the LDOS from these $I_\mathrm{t}(V_\mathrm{t})$ curves can be difficult. Thus, the differential conductance $\mathrm{d}I_\mathrm{t}/\mathrm{d}V_\mathrm{t}$ is often considered. Since numerically differentiating the measured $I_\mathrm{t}(V_\mathrm{t})$ curve strongly amplifies the noise, directly measuring the $\mathrm{d}I_\mathrm{t}/\mathrm{d}V_\mathrm{t}$ curve is desirable. This can be achieved by using the lock-in technique. Here, the direct current (DC) bias voltage is modulated with

a high-frequency sinusoidal component $V_\mathrm{m} = V_0 \sin(\omega t + \varphi_0)$ with amplitude V_0, time t, frequency ω, and phase φ_0. If the amplitude of the modulation signal is small compared with V_t the tunneling current in Equation (3.6) can be expanded in a power series (3.7).

$$\begin{aligned} I_\mathrm{t}(V_\mathrm{t} + V_0(\omega t + \varphi_0)) =& I_\mathrm{t}(V_\mathrm{t}) + \frac{\mathrm{d}I_\mathrm{t}(V_\mathrm{t})}{\mathrm{d}V_\mathrm{t}} V_0 \sin(\omega t + \varphi_0) \\ &+ \frac{\mathrm{d}^2 I_\mathrm{t}(V_\mathrm{t})}{\mathrm{d}V_\mathrm{t}^2} \frac{V_0^2}{2} \sin^2(\omega t + \varphi_0) + ... \end{aligned} \tag{3.7}$$

In the lock-in amplifier the current is multiplied with a sinusoidal reference voltage V_ref and integrated over a time longer than its period. If the frequency of the reference voltage is the same as that of the modulation signal, all components except a signal proportional to the differential conductance in Equation (3.7) cancel and $(\mathrm{d}I_\mathrm{t}/\mathrm{d}V_\mathrm{t})\cos(\varphi - \varphi_0)$ remains. By adjusting the phase φ in a way that $\varphi - \varphi_0 = 0$ the signal is maximized and the differential conductance curve can be measured directly. In the same way, if V_ref has a frequency of 2ω, the second derivative can be measured.

3.1.2 Atomic Force Microscopy

The drawback of STM is its limitation to conducting samples because the measured quantity is the tunneling current. In order to facilitate an investigation of insulating samples, another physical quantity needs to be measured. Thus, atomic force microscopy (AFM) makes use of the forces acting between tip and sample. This technique was invented in 1986 by Binnig, who already invented the STM, Quate, and Gerber.[220]

The interactions $V(d)$ between atoms or molecules are described by the Lennard-Jones potential (3.8) with ϵ being the minimum interaction energy at equilibrium distance d_0 and σ the distance, at which $V(d) = 0$.

$$V(d) = 4\epsilon \left[\left(\frac{\sigma}{d}\right)^{12} - \left(\frac{\sigma}{d}\right)^{6} \right] \tag{3.8}$$

At larger distances attractive contributions such as electrostatic and van der Waals interactions prevail, which show a dependence on the distance with d^{-6}. The short-range interactions are mostly due to Pauli repulsion and show a much stronger variation with the distance of d^{-12}. The forces F acting between a

molecule and a planar surface can be described by Equation (3.9).

$$F = -\frac{\pi C \rho}{6d^3} \tag{3.9}$$

Here, C is a collection of constants and ρ the density of the material.[206] It becomes apparent that in this case the force varies with d^{-3} instead of d^{-6}. If the molecule is replaced by a hemisphere, which is a good approximation for an AFM tip, Equation (3.10) is derived, where A is the Hamaker constant and r the radius of the hemispherical tip.[207]

$$F = -\frac{Ar}{6d} \tag{3.10}$$

The inverse dependence of the force on the distance simplifies the actual measurement of the force.

In an AFM experiment a cantilever with a sharp tip is positioned parallel to the surface (Figure 3.3). The forces acting between tip and sample cause a displacement of the cantilever. This displacement can be measured, *e.g.*, by using a photodiode to record the intensity of a laser, which is reflected by the cantilever.

Just like in STM, where there are the constant current and the constant height mode, AFM can be conducted in constant force or in constant height mode. In constant height mode the variation of the cantilever deflection is measured as the tip is scanned across the surface, while in constant force mode the tip–sample distance is varied to keep the cantilever displacement constant.

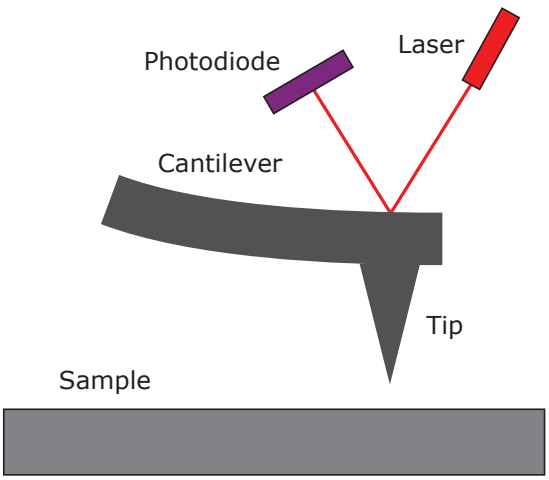

Figure 3.3: Schematic illustration of an AFM experiment. The cantilever is displaced due to the forces between tip and sample. This displacement is measured by a photodiode recording the intensity of a laser, which is reflected by the cantilever.

Non-Contact Mode

In the conventional mode of operation, the AFM tip is in mechanical contact with the sample. However, in this mode very high resolution up to the atomic scale cannot be achieved. This is mainly due to the fact that the tip always exerts a certain pressure on the sample and thus disrupts it. Additionally, the contact area is usually larger than one atom. In order to make atomic resolution possible, non-contact atomic force microscopy (nc-AFM) is conducted.

In the non-contact mode the cantilever is kept at a certain distance from the surface and oscillated at its resonance frequency f_0 with an amplitude A. Under UHV conditions usually the concept of frequency modulation (FM) is used.[221] Here, the cantilever is excited by a feedback loop. Interactions with the surface cause a frequency shift Δf. If the closest tip–surface distance d_{min} during the oscillation is larger than the amplitude of the cantilever oscillation, Equation (3.11) holds, where V_{TS} is the tip–surface potential and k is the spring constant of the cantilever.

$$\Delta f = \frac{f_0}{2k} \frac{\partial^2 V_{\mathrm{TS}}(d_{\mathrm{min}})}{\partial d^2} \tag{3.11}$$

In state-of-the-art nc-AFM experiments usually so-called qPlus sensors are used as cantilevers (Figure 3.4). They consist of a quartz tuning fork with Au electrodes placed on both tines. One of the tines is fixed and the other one is free to oscillate. A W tip is glued to the free tine.[222] Since the W tip is conducting it additionally allows STM measurements with the same setup.

To even further increase the resolution the tip can be functionalized, *e.g.*, with a CO molecule picked up from the surface.[223] By this means submolecular features can be visualized and structure elucidation with very high accuracy is possible.[224,225]

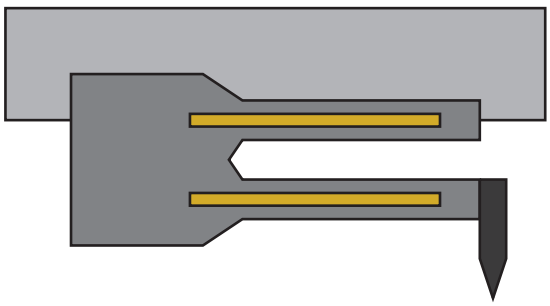

Figure 3.4: Schematic illustration of a qPlus sensor typically used for nc-AFM. The upper tine of the quartz tuning fork is fixed on a mount and the lower one is free to oscillate. A W tip is glued to the lower tine. The oscillation can be excited *via* the Au electrodes placed on the two tines.

3.2 Spectroscopic Methods

Besides the SPM techniques introduced in Section 3.1, a number of spectroscopic methods have been applied to complement the results. In contrast to the microscopic methods, the spectroscopic ones gather data on larger areas of the investigated samples. Among these spectroscopic methods are laboratory-based X-ray photoelectron spectroscopy (XPS) and ultraviolet photoelectron spectroscopy (UPS), as well as synchrotron radiation-based hard X-ray photoelectron spectroscopy (HAXPES) and near-edge X-ray absorption fine structure (NEXAFS) spectroscopy. These methods will be introduced in the following.

3.2.1 Photoelectron Spectroscopy

Photoelectron spectroscopy (PES) is based on the photoelectric effect, which was first discovered by Hertz in 1887[226] and later explained by Einstein in 1905.[227] Einstein was awarded the Nobel Prize in Physics in 1921 for this explanation.

The photoelectric effect describes the interaction of electromagnetic radiation with matter. If a material is irradiated with photons of energy $E = h\nu$, electrons are emitted only if a threshold energy is exceeded (Figure 3.5). The threshold is the material-specific work function Φ. A further increase of the energy leads to an increased kinetic energy E_{kin} of the emitted electrons (Equation (3.12)), while their amount does not change and only depends on the intensity of the exciting radiation with frequency ν.

$$E_{\mathrm{kin}} = h\nu - \Phi \tag{3.12}$$

The energy with which the electrons are bound to the atoms is characteristic for an element and is called binding energy E_{B}. If the excitation energy is known, the binding energy can be determined by measuring the kinetic energy of the emitted photoelectrons (Equation (3.13)) taking into account the work function.

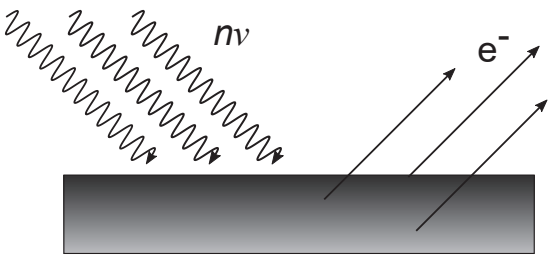

Figure 3.5: Schematic illustration of the photoelectric effect. A Sample is irradiated with photons of excitation energy $h\nu$, leading to the emission of photoelectrons.

$$E_{\mathrm{B}} = h\nu - E_{\mathrm{kin}} - \Phi \tag{3.13}$$

The binding energy does not only depend on the element itself but also on its surroundings. A simple way to calculate the binding energy of an electron is given by Koopmans' theorem (3.14).[228] According to this initial state approximation the binding energy is the negative orbital energy ε and can be calculated by quantum chemical methods like Hartree-Fock (HF).

$$E_{\mathrm{B}} = -\varepsilon \tag{3.14}$$

However, Koopmans' theorem neglects so-called final state effects, which occur in the generated ion after the photoionization process.

In a PES experiment the binding energy of the electron is not directly given by Equation (3.13) because the work function of the spectrometer Φ_{Sp} has to be taken into account, leading to a different measured kinetic energy $E_{\mathrm{kin,Sp}}$ (Equation (3.15)).

$$E_{\mathrm{B}} = h\nu - E_{\mathrm{kin,Sp}} - \Phi_{\mathrm{Sp}} \tag{3.15}$$

The energy levels in a photoelectron spectrometer are illustrated in Figure 3.6. The reason why the work function of the spectrometer needs to be known is because sample and spectrometer are usually both grounded to align their Fermi levels. The kinetic energy is measured relative to the vacuum energy E_{vac}, which

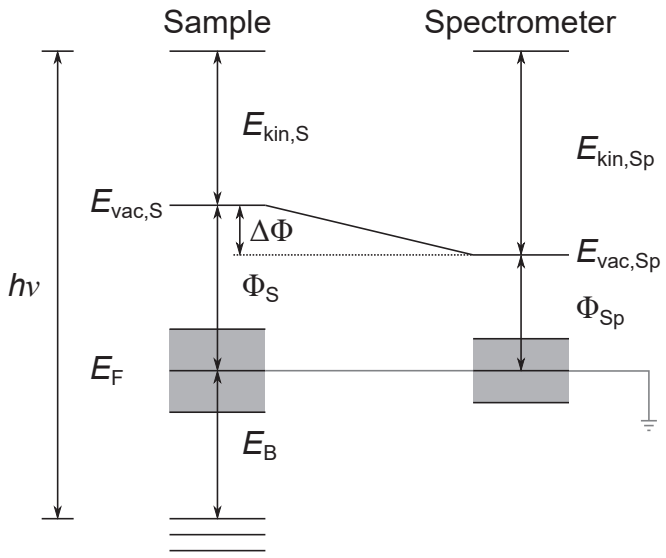

Figure 3.6: Schematic illustration of the energy levels in a photoelectron spectrometer. The Fermi levels of sample and spectrometer are aligned by connecting both to ground. In order to calculate the binding energy E_{B} from the measured kinetic energy $E_{\mathrm{kin,Sp}}$, the work function of the spectrometer Φ_{Sp} needs to be known.

is the difference between Fermi energy E_F and work function (Equation (3.16)).

$$\Phi = E_F - E_{vac} \tag{3.16}$$

Since the work functions of sample Φ_S and spectrometer are different, the measured kinetic energy $E_{kin,Sp}$ differs from the real one $E_{kin,S}$ by the work function difference $\Delta\Phi = \Phi_{Sp} - \Phi_S$. The work function of the spectrometer can be measured once with a calibration sample. Afterwards, all measured spectra can be corrected for this value and the work function of the sample does not need to be known.

To measure the kinetic energy of the photoelectrons and calculate their binding energy according to Equation (3.15), an electron energy analyzer system is needed. For this purpose usually hemispherical analyzers are used (Figure 3.7). As illustrated in Figure 3.5 photoelectrons are generated in the sample by an external radiation source. Those photoelectrons that are emitted under the right angle enter the lens system of the analyzer through the iris. In this lens system the electrons can be accelerated or decelerated by the applied voltages. The hemispherical analyzer itself consists of two hemispheres, between which a potential is applied. The outer hemisphere is on negative potential with respect to the inner one. Only electrons with a certain energy, the so-called pass energy E_{pass}, can travel through the hemispheres to reach the detector through the exit slit. The electrons with higher kinetic energy are not deflected strong enough and hit the outer hemisphere, while those with lower kinetic energy are deflected too strong and hit the inner one. To record a photoelectron spectrum

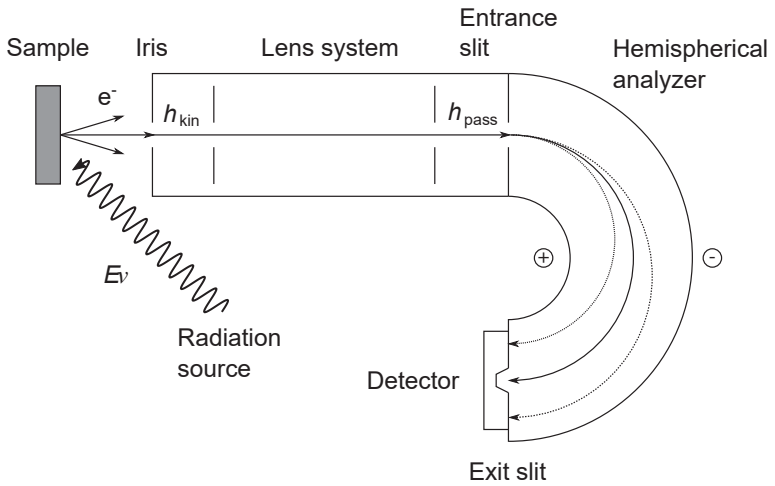

Figure 3.7: Schematic illustration of a hemispherical analyzer system used for PES. Photoelectrons enter the lens system, where they are accelerated or decelerated, through the iris and reach the hemispherical analyzer through the entrance slit. The electrons with the correct energy E_{pass} pass the analyzer and reach the detector through the exit slit.

the voltages in the lens system are varied systematically so that electrons with different original kinetic energies successively reach the detector. The detector counts the electrons and by knowing the applied voltages in the lens system the kinetic energy of those electrons that reached the detector can be calculated. Since all electrons counted by the detector have the same kinetic energy, *i.e.*, the pass energy, the same energy resolution for electrons of all different original kinetic energies is guaranteed. Usually electron-multiplying devices such as channeltrons are used as detectors. These increase the number of electrons by generating secondary electrons in a cascade, resulting in a measurable current as signal. This current is proportional to the original photoelectron intensity.

X-Ray Photoelectron Spectroscopy

As stated in Section 3.2.1 the binding energy of electrons is characteristic for the elements. Thus, by measuring the photoelectron intensity in the respective regions, information about the element composition of a sample can be obtained. The regions of interest here are the core levels. X-ray radiation is employed to excite these core-level electrons. Accordingly, the technique is called X-ray photoelectron spectroscopy (XPS).

In laboratory-based setups X-ray anodes are used to generate characteristic X-rays. However, due to the background caused by bremsstrahlung a monochromator is needed in order to obtain the exciting radiation with monochromatized energy and thus facilitate the calculation of the binding energy according to Equation (3.15). Typically, Al K_α or Mg K_α radiation is used but if higher excitation energies are needed other X-ray lines like, *e.g.*, Ga K_α can be applied. If energies that are not available from laboratory sources or a variation of the energy are needed, these energies can be provided by synchrotron radiation (*cf.* Section 3.2.2).

The binding energy of the core-level electrons is not only characteristic for a certain element but is additionally influenced by the surroundings of the atom in a sample. This is called chemical shift and was discovered by Siegbahn, who accordingly called the method electron spectroscopy for chemical analysis (ESCA) and was awarded the Nobel Prize in Physics in 1981 for its development. Due to this chemical shift the binding energy of electrons can differ by up to a few eV, depending on the chemical environment. This fact can be used, *e.g.*, to monitor chemical reactions taking place, which change the surroundings of a certain element.

If radiation of comparably low energy is used, the generated photoelectrons also have a relatively low kinetic energy. Because of this low energy they have a small escape depth from the sample (*cf.* Section 3.2.2), which makes XPS a surface-sensitive technique.

Ultraviolet Photoelectron Spectroscopy

In contrast to XPS, ultraviolet photoelectron spectroscopy (UPS) does not probe the core levels of a sample but the valence region. For this purpose ultraviolet (UV) radiation is applied because it has a large cross section for the ionization of valence orbitals. The valence region gives information, *e.g.*, about the chemical bonding in molecules. In order to provide the required UV radiation usually gas-discharge lamps are used, which provide spectral lines with high intensity. However, like in XPS a monochromator might be needed because of the coexistence of satellites or different spectral lines like, *e.g.*, He-I and He-II in He gas-discharge lamps. If energies that cannot be provided by laboratory-based radiation sources are needed, synchrotron radiation can also be used to perform UPS experiments (*cf.* Section 3.2.2).

Furthermore, UPS can be applied to determine the work function of a sample. This can be done by measuring the whole spectral range from the Fermi level to the secondary electron cutoff (SECO). While the electrons at the Fermi level have the highest kinetic energy $E_{\mathrm{kin,max}}$, those at the SECO can just escape the sample and have the lowest kinetic energy $E_{\mathrm{kin,min}}$. The difference of the excitation energy and the spectral range is the work function (Equation (3.17)).

$$\Phi = h\nu - (E_{\mathrm{kin,max}} - E_{\mathrm{kin,min}}) \tag{3.17}$$

Since the kinetic energy of the slowest electrons is basically 0, a bias voltage can be applied to the sample to accelerate the electrons so they can reach the detector.

Angle-Resolved Photoemission Spectroscopy

A special case of PES is angle-resolved photoemission spectroscopy (ARPES), also known as angle-resolved ultraviolet photoelectron spectroscopy (ARUPS) if UV radiation is used for the excitation of electrons. In ARPES not only information about the energy of the electrons but also about their momentum is gathered. This is achieved by variation of the polar ϑ and the azimuthal angle φ, under which the photoelectrons are detected. This method provides information about the band dispersion and the Fermi surface of the studied sample. The geometrical setup of an ARPES experiment is shown in Figure 3.8.

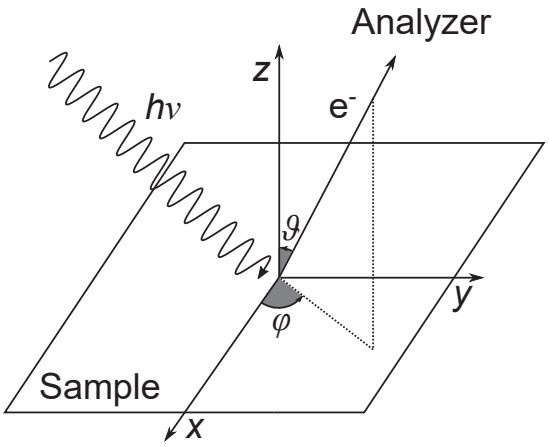

Figure 3.8: Schematic illustration of the geometrical setup in an ARPES experiment. The photoelectrons are detected in dependence of polar ϑ and azimuthal angle φ.

The momentum of an electron in reciprocal space is given by $k = p/\hbar$ with p being the momentum in real space. This momentum can be decomposed in the components of the three spatial directions x, y, and z (Equation (3.18)).

$$k = k_x + k_y + k_z \tag{3.18}$$

The single components are given by Equations (3.19) to (3.21).

$$k_x = \frac{1}{\hbar}\sqrt{2m_\mathrm{e}E_\mathrm{kin}}\sin(\vartheta)\cos(\varphi) \tag{3.19}$$

$$k_y = \frac{1}{\hbar}\sqrt{2m_\mathrm{e}E_\mathrm{kin}}\sin(\vartheta)\sin(\varphi) \tag{3.20}$$

$$k_z = \frac{1}{\hbar}\sqrt{2m_\mathrm{e}E_\mathrm{kin}}\cos(\vartheta) \tag{3.21}$$

If a surface is regarded, the momentum consists of a component parallel to the surface $k_\parallel$ and one perpendicular to the surface $k_\perp$ (Equations (3.22) and (3.23)).

$$k_\parallel = \sqrt{k_x^2 + k_y^2} = \frac{1}{\hbar}\sqrt{2m_\mathrm{e}E_\mathrm{kin}}\sin(\vartheta) \tag{3.22}$$

$$k_\perp = \frac{1}{\hbar}\sqrt{2m_\mathrm{e}E_\mathrm{kin}\cos^2(\vartheta) + V_0} \tag{3.23}$$

V_0 is the inner potential, which is the depth of the band from the vacuum energy to its bottom.

For the emission of an electron from the surface into the vacuum the momentum parallel to the surface is conserved because of the translational symmetry

of the surface. However, the perpendicular component is not conserved because of a sudden potential change. If 2D adsorbate structures on surfaces are investigated this is not a problem because their band dispersion along the z direction is negligible. Thus, it is sufficient to determine $k_{\parallel}$, which can be achieved by variation of the polar angle ϑ.

3.2.2 Synchrotron Radiation-Based Techniques

As stated in Section 3.2.1, some applications pose requirements on the excitation radiation that cannot be met by laboratory-based techniques. These requirements include special energies, which cannot be delivered by conventional X-ray or UV sources, as well as the variation of the excitation energy over a certain range. In order to overcome these limitations, synchrotron radiation sources can be used.

Synchrotron radiation is generated when relativistic charged particles, *e.g.*, electrons, are accelerated. In synchrotron radiation facilities electrons are first generated by thermionic emission and then accelerated close to the speed of light in a cyclic synchrotron. Afterwards, these electrons are injected into a storage ring in bunches, where they are kept on a circular path by bending magnets. Whenever the electrons are deflected by the bending magnets, which corresponds to a change of their velocity vector and thus an acceleration, they emit synchrotron radiation tangentially to their path. This radiation covers a wide range of the electromagnetic spectrum, delivering photons from near-UV to hard X-ray energies. The desired energy for a certain purpose can then be selected by a monochromator. Besides this broad spectral range, other advantages of synchrotron radiation are, *e.g.*, high intensity and brilliance as well as polarization.

To further increase the intensity of the radiation generated by a synchrotron, so-called wigglers have been invented. In these a number of alternatingly polarized dipole magnets are employed, yielding a similar but more intense spectrum as with simple bending magnets. Further improvement of the insertion devices is achieved in undulators. Here, the magnetic fields are smaller than in wigglers, resulting in smaller radiation lobes generated by the deflected electrons. As a consequence the radiation lobes can interfere, yielding a tunable line spectrum with high brilliance. In both wigglers and undulators the intensity depends on the number of deflection periods, but while in wigglers this dependence is linear it is quadratic in undulators.[229]

Hard X-Ray Photoelectron Spectroscopy

One variant of XPS that makes use of synchrotron radiation is hard X-ray photoelectron spectroscopy (HAXPES). Here, X-rays with high energy (typically ≥ 2 keV) are employed to probe deeper sample regions than in conventional XPS. Although these high energies can in principle also be generated using laboratory-based X-ray anodes such as Ga K_α (9.25 keV), depth profiling requires systematic variation of the excitation energy over a wide range, necessitating synchrotron radiation.

Depth profiling can be of interest, *e.g.*, if the diffusion-dependent chemical reaction of two species is investigated. The interaction of matter with X-rays is much smaller than with electrons. Thus, photoelectrons will always be generated in deeper sample regions but cannot escape the sample to reach the detector. The escape depth of photoelectrons is dependent on their kinetic energy. According to Equation (3.15) the kinetic energy increases with increasing excitation energy. The probability of electrons to interact with the atoms in a sample decreases with increasing speed. A measure for this interaction is the inelastic mean free path (IMFP), *i.e.*, the distance an electron travels on average between two inelastic scattering events. The dependence of the IMFP on the kinetic energy of electrons, often referred to as the universal curve, is shown in Figure 3.9. As can be seen the IMFP has a minimum in the region around 10 to 100 eV. In this region the interaction of the photoelectrons with the atoms in the sample is strongest. Towards lower energies the IMFP strongly increases, because there are simply fewer states available in the sample with which the photoelectrons could interact.

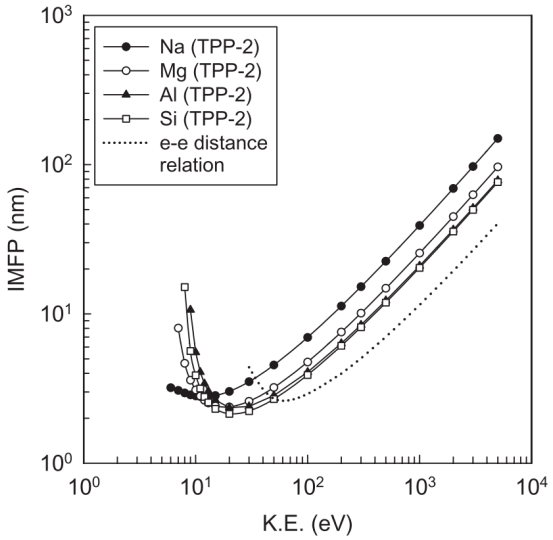

Figure 3.9: Dependence of the IMFP on the kinetic energy of electrons (K.E.). Reprinted with permission from ref. [208]. © 2012 John Wiley & Sons, Inc.

The region of interest for HAXPES is the high energy side. Here, the interaction probability decreases because the electrons become faster and might thus simply pass the atoms in the sample without interacting. It should be mentioned that the IMFP does not only depend on the kinetic energy itself but also on the sample material. Nevertheless, the general trend in the universal curve persists and can thus be used to gather information about different depths of a sample.

In a HAXPES experiment the photon energy is systematically varied. At higher photon energies more photoelectrons from deeper regions of the sample can escape and thus be detected. Accordingly, a depth profile of the investigated sample can be generated.

Near-Edge X-Ray Absorption Fine Structure Spectroscopy

The different PES techniques explained so far have in common that they probe occupied electronic states. In order to investigate unoccupied states, near-edge X-ray absorption fine structure (NEXAFS) spectroscopy can by carried out. In NEXAFS spectroscopy electrons from an occupied core level are excited into a formerly unoccupied state.

In general the photoemission cross section of a core level decreases with increasing excitation energy. However, if the photon energy exceeds the threshold for photoionization, this cross section is strongly increased, leading to an absorption edge. In a NEXAFS spectrum around this absorption edge a fine structure is visible, which arises due to the excitation of electrons into formerly unoccupied states and not into the continuum. Since the photon energy has to be varied in small steps around the absorption edge NEXAFS spectroscopy requires a synchrotron radiation source.

The intensity I of the transitions in the fine structure can be explained by Fermi's golden rule (3.24), which describes the probability P_{fi} of a dipole transition from an initial state i to a final state f.[230] It depends on the relative orientations of the electric field vector of the electromagnetic radiation $\vec{E}$ and the dipole transition operator $\hat{\mu}$ as well as on the electronic wave functions of initial ϕ_i and final state ϕ_f. A transition can only occur if there is DOS $\rho(E_f)$ at the final state.

$$I \propto P_{fi} = \frac{2\pi}{\hbar} \left| \langle \phi_f | \, \vec{E} \cdot \hat{\mu} \, | \phi_i \rangle \right|^2 \rho(E_f) \tag{3.24}$$

The transition is only allowed if the symmetries of the electric field vector, the dipole operator, and the wave functions produce a totally symmetrical representation. If linearly polarized light is used, which is the case for synchrotron radi-

ation, the electric field vector and the transition dipole moment $\vec{\mu}_{fi} = \langle\phi_f|\,\hat{\mu}\,|\phi_i\rangle$ can be separated (Equation (3.25)).[231]

$$I \propto \left|\vec{E}\cdot\langle\phi_f|\,\hat{\mu}\,|\phi_i\rangle\right|^2 \rho(E_f) \propto \left|\vec{E}\cdot\vec{\mu}_{fi}\right|^2 \rho(E_f) \tag{3.25}$$

For an excitation occurring from a spherically symmetric 1s orbital, as it is the case for organic molecules adsorbed on surfaces, the transition dipole moment for the K-edge directly depends on the orientation of the final state orbital. Only if the electric field vector and the transition dipole moment have the same direction the transition can be excited. This fact can be used to determine the orientation of molecules on surfaces by variation of the incidence angle α of the electric field vector of the electromagnetic radiation with respect to the surface normal $\vec{n}$ (Figure 3.10). If the molecule is adsorbed flat on the surface, *i.e.*, with the plane of its π orbitals parallel to the surface, the excitation into π^* orbitals can only take place for grazing incidence of the X-rays ($\alpha = 0°$, Figure 3.10a). On the contrary, excitation into a σ^* orbital is forbidden in this case and is only allowed for normal incidence ($\alpha = 90°$). If the molecule on the other hand is adsorbed upright on the surface, *i.e.*, with the plane of its π orbitals perpendicular to the surface, the situation is reversed (Figure 3.10b). Here, excitation into π^* orbitals is only possible under normal incidence, whereas grazing incidence is required for σ^* transitions. This effect is referred to as X-ray dichroism.

As the name already indicates, in NEXAFS spectroscopy the measured quantity is the absorption of X-ray photons. However, this cannot be measured directly in a transmission experiment because the samples are usually metal single crystals, which absorb all the photons in their bulk. Thus, indirect methods to measure the absorption need to be employed. The easiest way is to measure the sample current, which arises due to the emission of electrons. Furthermore,

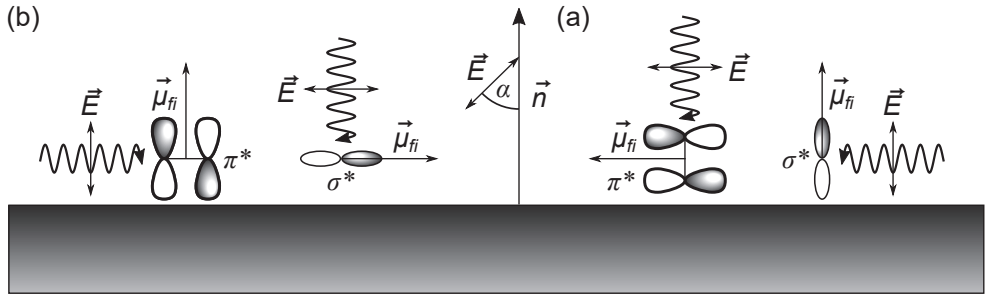

Figure 3.10: Schematic illustration of the X-ray dichroism occurring for organic molecules adsorbed on surfaces. (a) In molecules adsorbed flat on the surface, π^* and σ^* transitions are excited under grazing ($\alpha = 90°$) and normal incidence ($\alpha = 0°$), respectively. (b) For molecules adsorbed upright on the surface the situation is reversed.

the processes occurring in the sample after the excitation process can be used. These processes are illustrated in Figure 3.11. The excitation of a core-level electron by the X-ray photon creates a core hole, which will be filled by an electron from a higher occupied state (Figure 3.11a). The relaxation process creates excess energy, which can be released in two ways (Figure 3.11b). The first one is the emission of a fluorescence photon with energy $h\nu'$. In the second process the excess energy is transmitted to a third electron, which is then emitted as a so-called Auger electron. Both of these processes can be used to determine the X-ray absorption.

The emission of X-ray fluorescence photons is dominant for heavier elements. Thus, if samples containing heavier elements are investigated, the fluorescence yield (FY) mode of detection can be applied. Since X-rays have a longer mean free path in matter than electrons, the FY mode is considered as bulk sensitive.

For lighter elements, *e.g.*, present in organic molecules, the Auger process is preferred. Here, it is more suitable to detect electrons. This detection mode is called electron yield (EY). During the X-ray irradiation not only Auger electrons are generated but also photoelectrons from higher electronic states and other elements, which contribute to the background signal. Furthermore, all electrons, *i.e.*, photoelectrons and Auger electrons, generate secondary electrons. If all

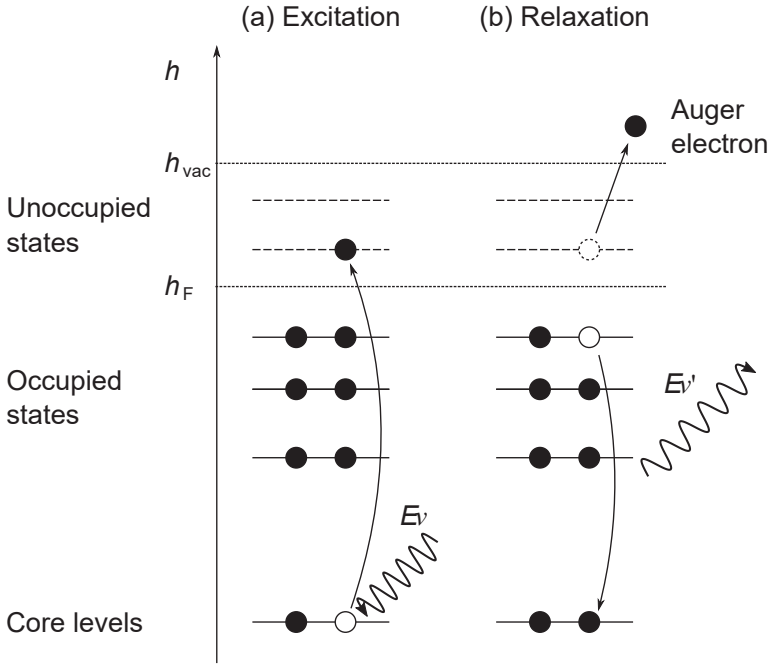

Figure 3.11: Schematic illustration of the processes occurring after the excitation of a transition in NEXAFS spectroscopy. (a) An electron is excited from a core level to a formerly unoccupied state, creating a core hole. (b) The excess energy during relaxation can either by released as a fluorescence photon with energy $h\nu'$ or by excitation of a third electron, a so-called Auger electron.

these electrons are included, the detection mode is called total electron yield (TEY). In order to prevent slow electrons to reach the detector and contribute to the signal, a bias voltage can be applied. This detection mode is called partial electron yield (PEY) and is more surface sensitive than the TEY mode since the probability of electrons generated deeper in the sample to reach the detector without losing some of their energy is small. The most surface sensitive detection mode is the Auger electron yield (AEY). Here, only Auger electrons with their characteristic energy are detected, which originate from regions close to the surface and have not been inelastically scattered. However, for this detection mode an electron energy analyzer is required, whereas TEY and PEY can be carried out in a simpler way with retardation grids, an electron multiplier, and a collector.[232]

3.3 Low-Energy Electron Diffraction

In addition to the microscopic and spectroscopic techniques discussed in Sections 3.1 and 3.2, low-energy electron diffraction (LEED) has been applied to supplement some of the results presented in this thesis. LEED is a technique for the investigation of periodic surface structures. It makes use of the wave properties of electrons described by the de Broglie relation (3.26), linking their wavelength λ_e and their momentum p_e.

$$\lambda_\mathrm{e} = \frac{h}{p_\mathrm{e}} = \frac{h}{\sqrt{2 m_\mathrm{e} E_\mathrm{kin}}} \tag{3.26}$$

In order to observe constructive interference when electrons are diffracted at a periodic surface, Bragg's law (3.27) has to be fulfilled, where n, d, and ϑ are the diffraction order, the lattice constant, and the diffraction angle, respectively.

$$n \cdot \lambda_\mathrm{e} = 2 \cdot d \cdot \sin(\vartheta) \tag{3.27}$$

In LEED electrons with comparably low energy (≤ 200 eV) are used. As discussed in Section 3.2.2 these electrons interact strongly with matter, restricting the interaction to the topmost layers of the sample and making LEED a surface sensitive technique. The setup of a LEED optics is shown schematically in Figure 3.12. The electrons are generated with an electron gun by thermionic emission and accelerated to the desired energy. When they hit the sample they are scattered. The electrons can either be scattered elastically or inelastically. The elastically scattered ones give rise to the diffraction pattern, whereas the inelas-

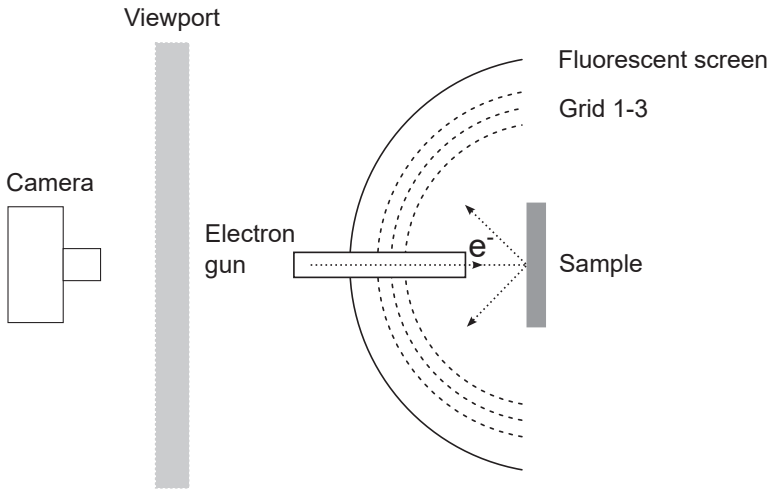

Figure 3.12: Schematic illustration of the setup for LEED experiments. Electrons are generated with an electron gun and accelerated towards the sample, where they are diffracted. The back-scattered electrons pass three grids and hit a fluorescent screen. The pattern on the screen can be recorded with a camera through a viewport.

tically scattered ones contribute to the background signal. The back-scattered electrons pass an array of three grids. The first one is on ground potential, while adjustable negative potentials are applied to the second and third one in order to suppress the background electrons. Detection of the electrons is achieved by means of a fluorescent screen, to which a high potential in the order of 5 keV is applied to accelerate the electrons and excite fluorescence. The diffraction pattern visible on the screen can be recorded with a camera through a viewport.

The diffraction pattern corresponds to the periodicity of the sample in reciprocal space. The width of the spots as well as the possible presence of other spots gives information about the structural quality of the sample. Furthermore, LEED can be used to obtain information about the lattice constants of adsorbate structures. The 2D lattice in real space is described by the lattice vectors $\vec{a}$ and $\vec{b}$, which span the unit cell of the surface. The lattice vectors in reciprocal space $\vec{a}^*$ and $\vec{b}^*$ can be calculated according to Equation (3.28), where $\vec{n}$ is a primitive vector orthogonal to the reciprocal lattice.

$$\vec{a}^* = \frac{\vec{b} \times \vec{n}}{|\vec{a} \times \vec{b}|} \; ; \quad \vec{b}^* = \frac{\vec{a} \times \vec{n}}{|\vec{a} \times \vec{b}|} \tag{3.28}$$

The points of the reciprocal lattice can be described by $\vec{G}_{hk}$ (Equation (3.29)), with h and k being the Miller indices in two dimensions.

$$\vec{G}_{hk} = h \cdot \vec{a}^* + k \cdot \vec{b}^* \tag{3.29}$$

The electrons incident on the sample are described by the wave vector $\vec{k}_0 = \vec{s}_0 \cdot 2\pi/\lambda$, while the back-scattered ones are described by $\vec{k} = \vec{s} \cdot 2\pi/\lambda$ with $\vec{s}_0$ and $\vec{s}$ being the unit vectors of the incident and the back-scattered electrons, respectively. Since only elastically scattered electrons are considered, energy conservation requires that Equation (3.30) is fulfilled.

$$|\vec{k}| = |\vec{k}_0| \tag{3.30}$$

Due to the fact that LEED is surface sensitive, only the components of the wave vectors parallel to the surface $\vec{k}^{\parallel}$ and $\vec{k}_0^{\parallel}$ matter. These are connected by $\vec{G}_{hk}$ (Equation (3.31)).

$$\vec{k}^{\parallel} - \vec{k}_0^{\parallel} = \vec{G}_{hk} \tag{3.31}$$

To visualize the appearance of the observed LEED spots the 2D Ewald's sphere construction can be used (Figure 3.13). At the intersection of the circle with the rods corresponding to the 2D lattice diffraction spots can be observed.

In addition to the determination of the lattice constants of the clean single crystal information of the periodic superstructures formed by adsorbed molecules can be obtained. In real space the lattice constants of the superstructures $\vec{a}_{\mathrm{S}}$ and $\vec{b}_{\mathrm{S}}$ are linked to the lattice constants of the substrate by the matrix $\mathbf{M} = \begin{pmatrix} M_{11} & M_{12} \\ M_{21} & M_{22} \end{pmatrix}$ (Equation (3.32)).

$$\vec{a}_{\mathrm{S}} = M_{11} \cdot \vec{a} + M_{12} \cdot \vec{b}_{\mathrm{S}} \; ; \quad \vec{b}_{\mathrm{S}} = M_{21} \cdot \vec{a} + M_{22} \cdot \vec{b}_{\mathrm{S}} \tag{3.32}$$

Analogously, the lattice constants of the superstructure in reciprocal space $\vec{a}_{\mathrm{S}}^{*}$

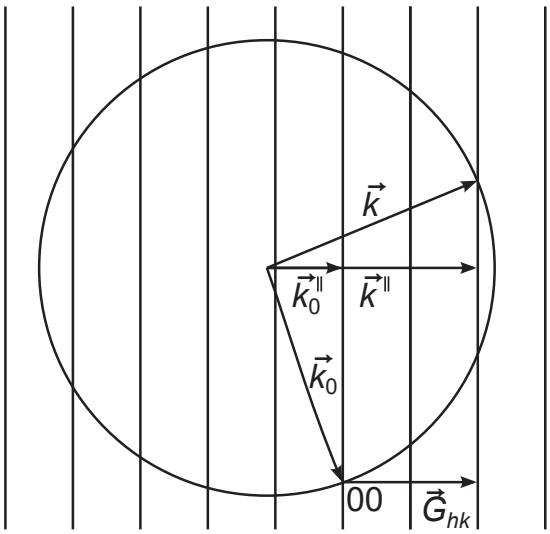

Figure 3.13: Ewald's sphere construction in two dimensions. The scattered wave vectors point to the intersections of the circle with the rods of the 2D lattice.

and $\vec{b}^*_S$ are linked to the lattice constants of the substrate in reciprocal space by the matrix $\mathbf{M}^* = (\mathbf{M}^{-1})^T = \begin{pmatrix} M_{22} & -M_{21} \\ -M_{12} & M_{11} \end{pmatrix}$ (Equation (3.33)).

$$\vec{a}^*_S = M^*_{11} \cdot \vec{a}^* + M^*_{12} \cdot \vec{b}^* \; ; \quad \vec{b}^*_S = M^*_{21} \cdot \vec{a}^* + M^*_{22} \cdot \vec{b}^* \tag{3.33}$$

While the lattice constants of the superstructure in real space are larger than those of the substrate, this is reversed in reciprocal space. Thus, the distance between the LEED spots of a superstructure is smaller than that of the substrate. The diffraction pattern of the superstructure can be observed around every spot of the substrate pattern.

3.4 Experimental Setups

The experiments leading to the results presented in this thesis were performed at several machines providing the possibility to carry out the different experimental methods described in the previous sections. These include two laboratory-based machines in Marburg and Donostia-San Sebastián as well as end-stations of three beamlines of the synchrotron radiation facility BESSY II in Berlin. In the following sections these machines will be described.

3.4.1 STM and XPS Setup in Marburg

The majority of the STM and XPS experiments presented in this thesis were carried out in the laboratory of the Gottfried group in Marburg. This laboratory hosts a setup for combined STM and PES studies, which was purchased from SPECS Surface Nano Analysis GmbH and augmented with further devices during the course of this thesis. A photograph of the machine is shown in Figure 3.14. The setup consists of three different chambers separated by gate valves and pumped by turbomolecular pumps (TMPs). Experiments were performed at a base pressure of $\leq 2 \cdot 10^{-10}$ mbar.

The STM chamber houses a SPECS STM 150 Aarhus as well as a sample storage and a stage for sputtering and annealing (*cf.* Section 4.1). For measurements at low temperature the STM can be cooled with LN_2.[233]

The analysis chamber is equipped with a SPECS XR50 M X-ray source, which contains two anodes for Al K_α and Ag L_α radiation. In this thesis only Al K_α radiation with an energy of 1486.7 eV was used. The X-ray radiation is monochromatized with a SPECS FOCUS 500 monochromator employing quartz single crystals in a Rowland circle geometry. The electron energy analyzer is

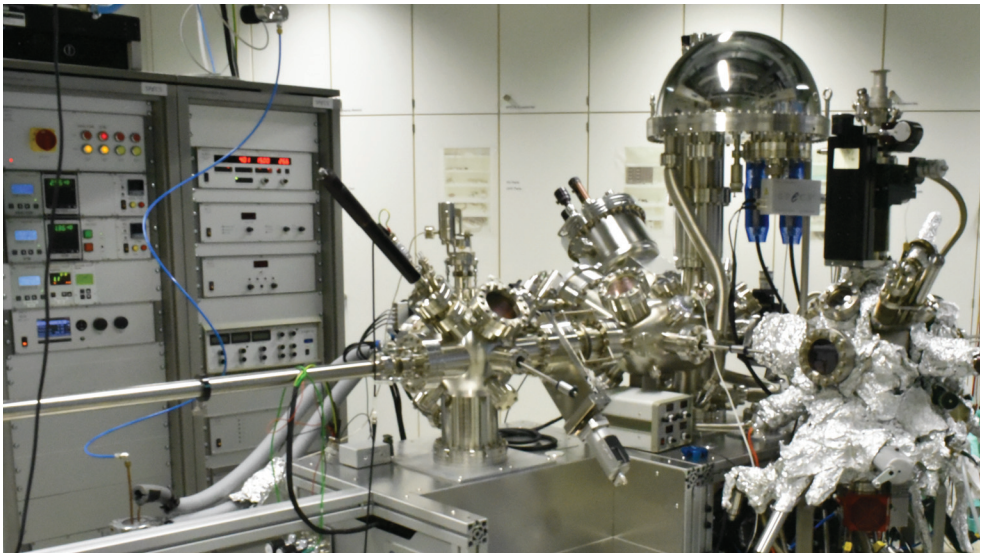

Figure 3.14: Photograph of the combined STM and XPS setup from SPECS Surface Nano Analysis GmbH in Marburg. The STM chamber is on the left, the analysis chamber with the hemispherical analyzer in the center and the preparation chamber on the right.

a hemispherical SPECS PHOIBOS 150 analyzer, which uses a SPECS MCD-9 multi channeltron as detector. In addition, the analysis chamber contains a SPECS UVS 10/35 He gas-discharge lamp, which can provide UV radiation for UPS experiments and a SPECS ErLEED 1000A LEED optics. The samples can be positioned *via* a manipulator with four degrees of freedom (x, y, z, and ϑ), which can be cooled with LN_2. Furthermore, the sample can be heated with an electron beam heating.

The preparation chamber is a custom-built chamber, which replaced the original one provided by SPECS during the course of this thesis. Its construction and installation are described in detail elsewhere.[234,235] The chamber has a manipulator with four degrees of freedom (x, y, z, and ϑ), which can be cooled with LN_2 and allows sample heating with an electron beam heating. The design of the sample stage was improved during this thesis and is described in Section 4.2. Furthermore, the chamber houses a sample storage, a quartz crystal microbalance (QCM), a SPECS IQE 11/35 sputter gun and a Hiden HALO 201-RC mass spectrometer for residual gas analysis. The chamber offers a lot of flanges, to which evaporators for organic molecules as well as metals can be mounted. One of these evaporators is a line-of-sight evaporator, which can be used for the deposition of medium-vapor pressure molecules. It was developed as a part of this thesis and is described in detail in Section 4.3. In addition, usually several evaporators for low-vapor pressure molecules, which consist of resistively heated stainless steel crucibles, and dosing valves for high-vapor pressure molecules are

mounted. To introduce new samples without venting the whole chamber, a load lock has been installed during the course of this thesis.

3.4.2 ARPES and STM Setup in Donostia-San Sebastián

The ARPES measurements presented in this thesis were carried out in a collaboration project in the laboratory of Prof. Dr. J. Enrique Ortega at Centro de Física de Materiales (Materials Physics Center) in Donostia-San Sebastián, Spain. Photographs of the ARPES setup are shown in Figure 3.15. The system consists of four chambers, which are separated by gate valves.

The core of the system is the analysis chamber, in which the ARPES measurements are performed. The analysis chamber typically has a base pressure of $8 \cdot 10^{-11}$ mbar. It is equipped with a vertical cryogenic manipulator employing a closed He cycle, which allows temperatures between 30 and 320 K controlled by a proportional-integral-derivative (PID) controller. For ARPES measurements on organic nanostructures it is kept at 150 K. The four degrees of freedom of the manipulator (x, y, z, and ϑ) are motorized and can be automatically adjusted during ARPES measurements. The UV radiation is generated by a monochromatized He gas-discharge lamp and usually the He-I_α line with an energy of 21.2 eV is used. The hemispherical electron energy analyzer is a SPECS PHOIBOS 150 analyzer, which can be seen wrapped in Al foil on the bottom right of Figure 3.15a. For the detection of the electrons a charge-coupled device (CCD) detector is used. This detector allows to measure 2D snapshots of energy *vs.* momentum and thus map the complete relevant k space in one di-

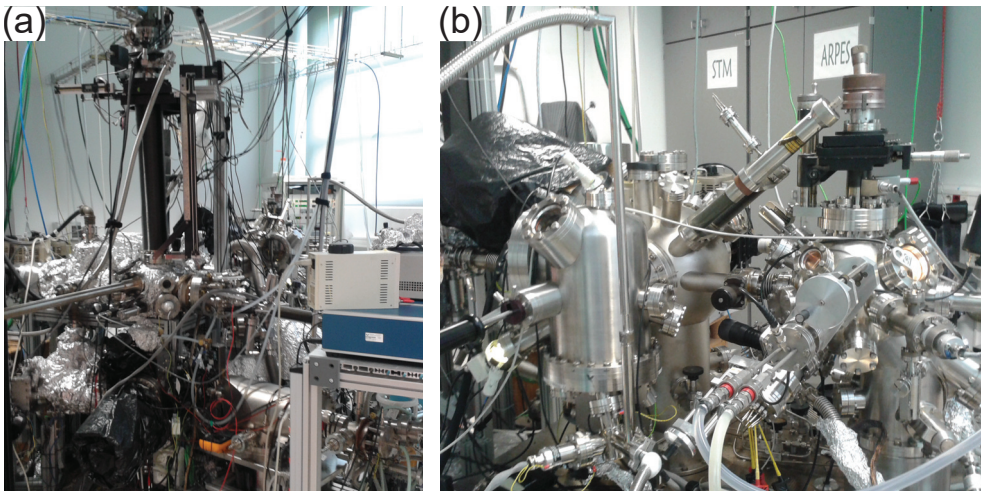

Figure 3.15: Photographs of the ARPES system in Donostia-San Sebastán. (a) View on the analysis chamber. The hemispherical analyzer is located on the bottom right. (b) View on the preparation and the STM and LEED chamber.

rection without sample rotation. In order to obtain Fermi surface mappings the sample needs to be rotated around the polar angle ϑ (*cf.* Figure 3.8). Directly connected to the analysis chamber is a preparation chamber (located in the center of Figure 3.15a), which was not used to obtain the results presented in this thesis.

Since the ARPES measurements are very time-consuming it is necessary to check the quality of the prepared organic nanostructures beforehand. This is done in the STM chamber, which can be seen on the left of Figure 3.15b. Its base pressure is typically $1 \cdot 10^{-10}$ mbar. It houses an Omicron variable temperature (VT)-STM, which is usually operated at RT but was cooled with LN_2 to 100 K to obtain the results presented in this thesis. To complement the local STM data on a more global scale (which is also relevant for ARPES), a LEED optics is available.

The preparation chamber is shown on the right of Figure 3.15b. Its base pressure is typically 3×10^{-10} mbar. The preparation chamber is equipped with a sputter gun and a sample manipulator, which can be resistively heated *via* a boron nitride plate. The chamber is used for sample cleaning as well as for the deposition of molecules. The deposition is done with a home-built evaporator mounted to an exchangeable port allowing the exchange of molecules without venting the preparation chamber. The evaporator houses two quartz crucibles resistively heated with W wires. The flux of the molecules can be monitored with a QCM. Furthermore, the chamber has a sample storage and a load lock is attached to introduce new samples without venting the chamber.

3.4.3 Synchrotron Beamlines at BESSY II in Berlin

The HAXPES, NEXAFS spectroscopy and some UPS measurements were performed at end-stations of three different beamlines of the synchrotron radiation facility BESSY II in Berlin. The respective beamlines and end-stations will be described in the following sections.

HIKE

The HIKE (high kinetic energy) end-station is located at the KMC-1 beamline of BESSY II in Berlin. The KMC-1 beamline is a bending magnet beamline with a double-crystal monochromator, which offers photon energies in the range from 2 to 12 keV. Depending on the used photon energy one of three pairs of Si single crystals can be used, namely Si(111), Si(311), and Si(422).[236]

The HIKE end-station is shown in Figure 3.16. It consists of three chambers. The core of the end-station is the analysis chamber, which can be seen in the front of Figure 3.16 with its VG Scienta R4000 hemispherical electron energy analyzer. The analyzer allows the detection of electrons with an energy range from 150 eV to 10 keV. A 2D CCD camera is used as detector. The X-rays are guided into the analysis chamber using a glass capillary. For the measurements the sample is positioned on a manipulator with five degrees of freedom, of which four (x, y, z, and ϑ) are motorized and controlled with a LabVIEW software. The manipulator can be cooled with LN_2 and heated. The HAXPES measurements presented in this thesis were usually carried out under grazing incidence and near-normal emission in order to maximize the information depth. In addition to the electron energy analyzer, the analysis chamber is equipped with a Bruker XFlash 4010 fluorescence detector, which allows the measurement of NEXAFS spectra in the FY mode. Measurements in the TEY mode *via* the sample current are also possible. Furthermore, the analysis chamber offers a sputter gun for sample cleaning and an electron flood gun to compensate sample charging.

Sample preparation was carried out in the preparation chamber (on the back of the end-station, not seen in Figure 3.16), which is equipped with a QCM. In addition, home-built evaporators for organic molecules as well as metals and a coolable sample manipulator described elsewhere[237] were mounted to the preparation chamber. The third chamber is a load lock with a sample storage.

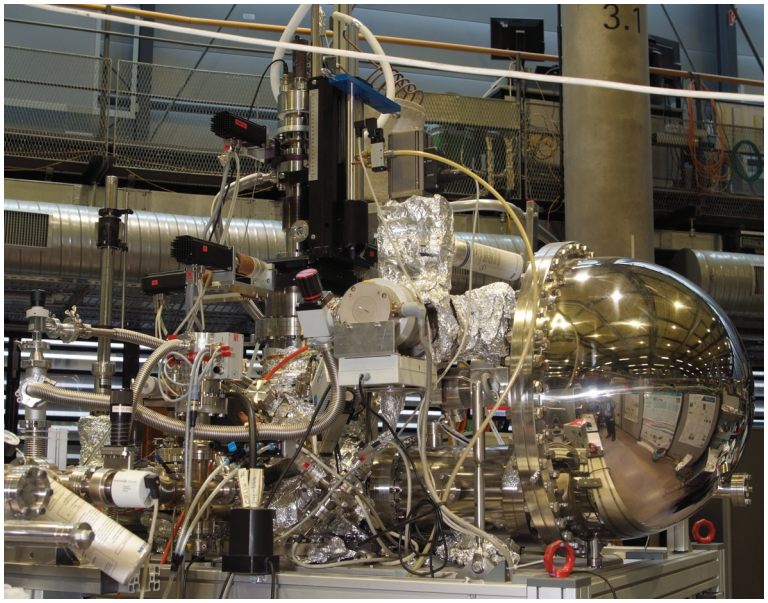

Figure 3.16: Photograph of the HIKE end-station located at the KMC-1 beamline at BESSY II in Berlin. The analysis chamber with the VG Scienta R4000 hemispherical electron energy analyzer is in the front, while the preparation chamber and the load lock are in the back.

HE-SGM

The end-station at the HE-SGM beamline of the synchrotron radiation facility BESSY II in Berlin is designed especially to meet the requirements for NEXAFS spectroscopy. The PREVAC UHV system is shown in Figure 3.17. It mainly consists of three chambers.

The analysis chamber (on the right in Figure 3.17) is directly connected to the bending magnet beamline, which delivers linearly polarized light with a polarization degree of $P = 0.91$. The photon energy can be selected in a range from 100 to 800 eV using three different gratings as monochromators. The detection of NEXAFS spectra can be performed with a channel plate detector allowing both the TEY and the PEY mode. Furthermore, a VG Scienta R3000 hemispherical electron energy analyzer is available, which allows the detection of NEXAFS spectra in the AEY mode as well as XPS experiments. The manipulator of the analysis chamber can be cooled with LN_2 and has five degrees of freedom (x, y, z, ϑ, and φ). The change of the polar angle ϑ allows the change of the photon incidence angle and thus the investigation of the X-ray dichroism. Sample heating is provided by the specially designed PREVAC sample holders, which can be equipped with an electron beam or a resistive heating.

The analysis and the preparation chamber (on the left in Figure 3.17) are connected by a transfer chamber, to which two additional sample storages are mounted. One of these can additionally be used as a load lock. The preparation chamber houses a sputter gun for sample cleaning and different ports to mount

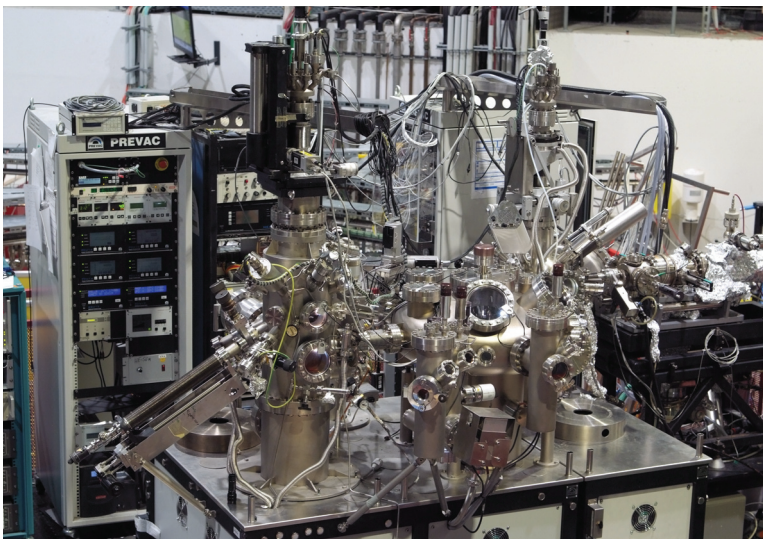

Figure 3.17: Photograph of the end-station located at the HE-SGM beamline at BESSY II in Berlin. The preparation chamber on the left and the analysis chamber on the right are connected by a transfer chamber.

evaporators for the deposition of molecules. The manipulator of the preparation chamber can be cooled during deposition with LN_2 and sample heating is provided by the sample holders.

LowDosePES

The LowDosePES end-station is located at the PM4 beamline of the synchrotron radiation facility BESSY II in Berlin. The PM4 is a bending magnet beamline with a photon energy range from 20 eV to 2 keV monochromatized with a plane grating monochromator. Thus, it facilitates XPS as well as UPS measurements with photon energies not available from laboratory-based sources. Photographs of the LowDosePES end-station are shown in Figure 3.18. The end-station consists of five chambers. The analysis chamber and two side preparation chambers are connected by a transfer chamber. A third preparation chamber is located on top of the analysis chamber.

The analysis chamber is directly connected to the beamline. It offers two different electron energy analyzers, a hemispherical VG Scienta SES100 analyzer (on the right in Figure 3.18b) and a VG Scienta ArTOF-10k analyzer (on the left in Figure 3.18a). The ArTOF (angle-resolved time of flight) analyzer simultaneously detects the kinetic energy and the emission angle of the photoelectrons, thus enabling ARPES measurements. The spectra are recorded as snapshots over a certain energy (corresponding to the time of flight) and angle range. However, for this purpose a pulsed source is required. This is achieved at the PM4 beamline with a MHz chopper system, which needs to be synchronized to the electron bunches in the storage ring. Conventional PE spectra can be obtained by integrating over all angles. The sample can be positioned with a manipulator with four degrees of freedom (x, y, z, and ϑ), which can be cooled with

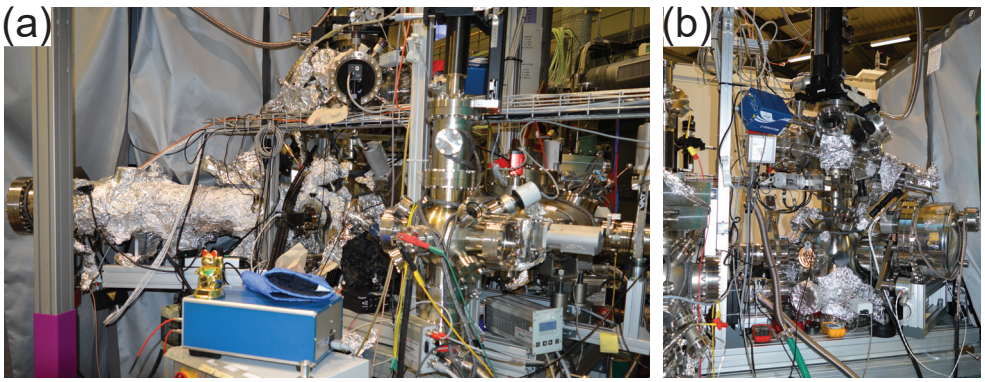

Figure 3.18: Photographs of the LowDosePES end-station located at the PM4 beamline at BESSY II in Berlin. (a) View showing the ArTOF analyzer. (b) View showing the SES100 hemispherical analyzer.

LN_2 and heated. On this manipulator the sample can be transferred to the top preparation chamber, which is located above the analysis chamber. This clean preparation chamber offers several free ports and is additionally equipped with a micro-channel plate (MCP) LEED optics (in the top center of Figure 3.18a) and a mass spectrometer (in the top left of Figure 3.18b).

The sample can be transferred to the two side preparation chambers *via* the transfer chamber. The first side preparation chamber (partly seen on the left of Figure 3.18b) is a clean preparation chamber for sample sputtering and annealing and the deposition of metals. It offers a sample storage with space for six samples and several ports for evaporators, *etc.* The second one (center of Figure 3.18a) is a preparation chamber intended for organic molecules. It also offers a sample storage with space for six samples and several ports. Furthermore, it can be used as a load lock. Both side preparations chambers can be equipped with a QCM.

4 Constructional Part

In order to improve the combined STM and XPS setup in the laboratory of the Gottfried group in Marburg described in Section 3.4.1, two parts have been redesigned. These are the stage for sputtering and annealing in the STM chamber to allow the use of the transferable thermocouple of the SPECS-type sample holder during annealing and the sample holder stage of the preparation chamber. Furthermore, a line-of-sight evaporator for the deposition of medium-vapor pressure molecules has been designed. The development of these three parts will be described in the following sections.

4.1 Sputtering and Annealing Stage for the STM Chamber

A photograph of the sputtering and annealing stage located at the bottom of the sample storage in the STM chamber provided by SPECS Surface Nano Analysis GmbH is shown in Figure 4.1a. The SPECS-type sample holders used in the setup in Marburg provide a transferable thermocouple, which is attached directly to the sample and allows a very accurate temperature measurement. However, the original sputtering and annealing stage was not equipped with the necessary contacts to use the transferable thermocouple and thus the temperature was

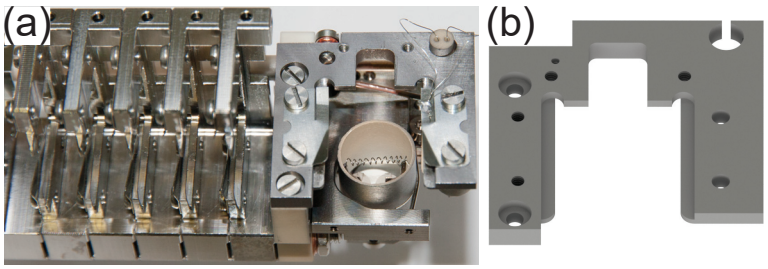

Figure 4.1: (a) Photograph of the sputtering and annealing stage provided by SPECS Surface Nano Analysis GmbH located at the bottom of the sample storage in the STM chamber. The original design did not allow the use of the transferable thermocouple of the SPECS-type sample holders. (b) Rendered image of the redesigned stage. The opening is widened compared with the original design to provide space for the transferable thermocouple and the contacts can be mounted to the two holes on both sides of the opening.

measured at the stage itself. It turned out that this measured temperature deviated strongly from the actual sample temperature, which was a high potential risk for the single crystal samples. Since the necessary contacts could not simply be installed on the original stage it had to be redesigned.

The redesigned sputtering and annealing stage is made of titanium-zirconium-molybdenum (TZM), an alloy mostly containing Mo. The reason to use TZM is that it possesses a high recrystallization temperature and reduced brittleness compared with pure Mo. A rendered image of the stage is shown in Figure 4.1b. Here, the opening in the top center of the stage is widened so that the contacts of the transferable thermocouple of the SPECS-type sample holder fit inside. Furthermore, two holes are located on both sides of it, where the springs establishing the thermocouple contact can be mounted. The constructional drawings used to manufacture the stage are shown in Appendix C.

An exploded view of the assembled redesigned sputtering and annealing stage is shown in Figure 4.2. The thermocouple springs, which serve to establish the contact with the transferable thermocouple of the SPECS-type sample holder, are mounted to the two holes. In order to insulate the springs from the sample holder stage itself as well as from the screws, ceramic washers are inserted. The sample holder is fixed in the stage with two sample holder plates. At last, a second thermocouple is directly attached to the sputtering and annealing stage with a screw to measure the temperature of the stage itself.

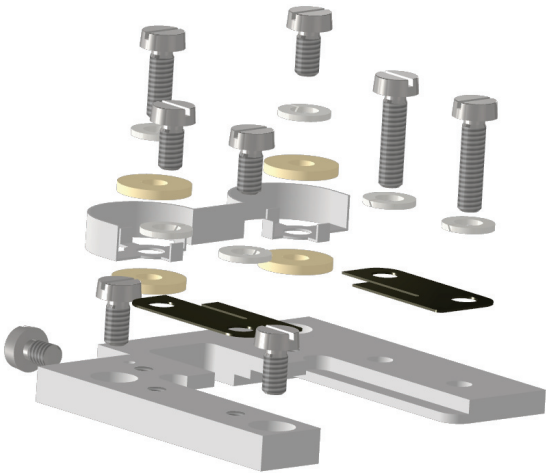

Figure 4.2: Exploded view of the redesigned sputtering and annealing stage. The springs establishing the contact to the transferable thermocouple of the SPECS-type sample holder can be mounted to two holes located on both sides of the widened opening.

4.2 Heatable and Coolable Sample Stage for the Preparation Chamber

In the course of this thesis the STM and XPS setup was equipped with a new custom-built preparation chamber, which replaced the original one provided by SPECS Surface Nano Analysis GmbH. This chamber was designed by Dr. B. P. Klein during his PhD stduies with the help of K. K. Greulich and installed by N. A. Wollscheid in his master's thesis.[234,235] One of the advantages of the new preparation chamber compared with the old one is that it possesses a manipulator with four degrees of freedom (x, y, z, and ϑ), which can be cooled with LN_2 and allows sample heating with an electron beam heating.

The manipulator head is made of oxygen-free high thermal conductivity (OFHC) Cu and can be filled with LN_2 guided through a cooling finger for cooling. However, it turned out that the walls of this head were too thin and that they might break after long-term use. Thus, the manipulator head was redesigned in the course of this thesis. The wall thickness was increased and some further drawbacks that became apparent after the initial use of the old one were improved. A cross-sectional view of the redesigned Cu manipulator head, which shows the thicker inner walls compared with the old one described in ref. [235], is shown in Figure 4.3a. Because some dimensions are changed in the redesigned manipulator head, several other parts necessary for the final

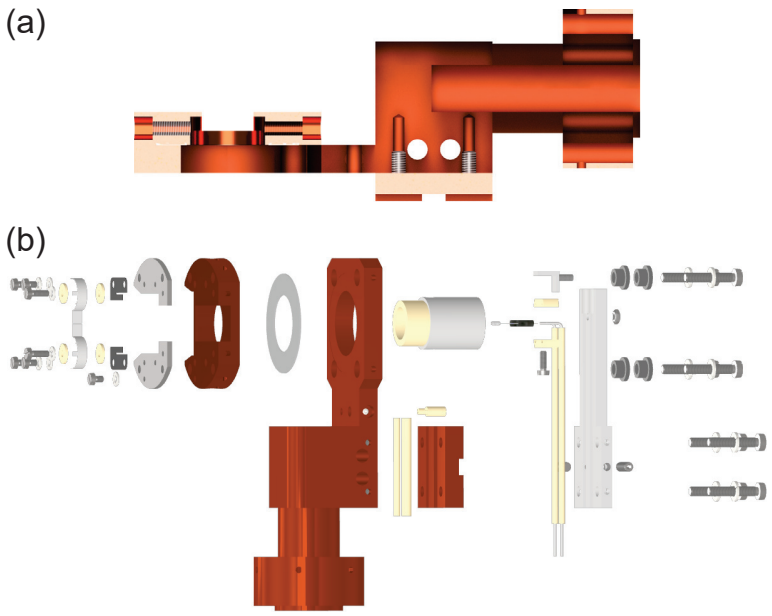

Figure 4.3: (a) Cross-sectional view of the redesigned manipulator head for the preparation chamber. The thickness of the inner walls is increased compared with the previous design. (b) Exploded view of the assembled manipulator head for the preparation chamber.

assembly also had to be changed. An exploded view showing the assembled manipulator head is shown in Figure 4.3b. The assembled manipulator head is mounted to a cooling finger. The cooling finger is connected to the PMM 12-100 manipulator equipped with a DDF 63 PL rotational feedthrough both purchased from VAb Vakuum-Anlagenbau GmbH *via* a CF63 cluster flange. A rendered image of the manipulator head and the cooling finger attached to the cluster flange is shown in Figure 4.4.

The manipulator head mainly consists of three Cu parts. The largest part has a CF16 knife edge so that it can be directly mounted to the cooling finger. The upper Cu part (left in Figure 4.3b) can host the sample. For this purpose two TZM plates are mounted on top of it, which guide the sample in its position. The sample is fixed in the position with two sample holder plates. Furthermore, thermocouple springs are mounted to the TZM plates to establish a connection to the transferable thermocouple of the SPECS-type sample holder in the same way already described for the STM sputtering and annealing stage (*cf.* Section 4.1). At last, a second thermocouple is directly attached to the lower TZM plate with a screw to measure the temperature of the manipulator head itself. The top Cu part is insulated from the main part with a sapphire disc.

The bottom Cu part has two furrows for ceramic tubes. One of these can host the four thermocouple wires and the other one the connection to the high voltage needed for the electron beam heating. The electron beam heating is mounted from the bottom (right in Figure 4.3b). It consists of a W filament, which is housed in a ceramic tube surrounded by a TZM cylinder. The connection to the Mo heating wires is made by small Ta tubes, which are pressed together by two ceramic pieces. Further details of the assembly of the manipulator head and the electronic connections can be found in ref. [235].

The constructional drawings used to manufacture all the changed parts are shown in Appendix C. For the top and central Cu parts no drawings were created since these very complex parts were given to the department's mechanical workshop as three-dimensional (3D) `*.stp` files. These files are available, like

Figure 4.4: Rendered image of the preparation chamber manipulator head attached to the cooling finger and the CF63 cluster flange. The whole part is mounted to the manipulator, which is equipped with a rotational feedthrough.

the files of all other designed parts, from the Inventor Database on the server of the Gottfried group.

4.3 Line-of-Sight Evaporator

To deposit molecules on surfaces under UHV conditions, usually two types of evaporation devices are used. Molecules with a low vapor pressure are filled into crucibles, which can be heated resistively. Due to the increased temperature the solid sublimes and the molecules fly towards the substrate surface where they resublime. On the other hand, for molecules with a high vapor pressure the low pressure in a UHV system is already sufficient to sublime a significant amount of molecules. These can be deposited on the sample *via* the background pressure with dosing valves. However, for molecules with a medium vapor pressure the situation is more complicated. If they were simply stored in open crucibles, the amount of molecules evaporating due to the low pressure in the UHV system would be too high. This would make a controlled deposition on the surface difficult and furthermore the crucible would empty quickly. Nevertheless, the vapor pressure is too low to use dosing valves, *i.e.*, it would take too long to get a sufficient amount of molecules into the gas phase and thus to adsorb on the sample.

Accordingly, if molecules with a medium vapor pressure shall be deposited another kind of evaporator is needed. For this purpose a line-of-sight evaporator can be used. Since the molecules DBAz and 2,6-DBAz investigated in this thesis are molecules with such a medium vapor pressure a line-of-sight evaporator, which can be mounted to the preparation chamber of the combined STM and XPS setup described in Section 3.4.1, has been designed and built. An exploded view of the line-of-sight-evaporator is shown in Figure 4.5.

The principle of the line-of-sight evaporator is to use a glass tube to guide the molecules in the gas phase directly to the sample. A glass tube with inner and

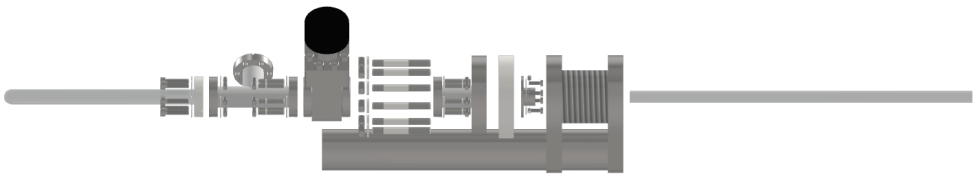

Figure 4.5: Exploded view of the line-of-sight evaporator used for the deposition of medium-vapor pressure molecules. The connection from the reservoir to the UHV system can be opened with a CF16 gate valve. The molecules are guided directly to the sample by a glass tube, which can be positioned *via* a linear motion.

outer diameter of 8 and 10 mm, respectively, was chosen to ideally fit the sample size (diameter 8 mm). Since the glass tube needs to be positioned as close to the sample as possible for deposition, the whole evaporator is mounted to the chamber with a linear motion. If the evaporator is not used, it can be retracted from the sample to ensure safe operation inside the chamber without touching the glass tube and breaking it or damaging the sample. In order to fix the glass tube, a mount fitting to its outer diameter was designed, which is mounted to a CF40 double flange with a hole also fitting the diameter of the tube. This double flange is connected to a CF16 gate valve *via* a CF16–CF40 adapter flange. The CF16 gate valve was chosen to prevent that a too high amount of molecules reaches the vacuum system. A CF16 T piece is used to connect the gate valve and the crucible. To this T piece a by-pass can be attached to pump down the crucible before the connection to the UHV system is opened. The crucible is a glass tube closed at one end and connected to the T piece with a glass-to-metal seal on the other end.

The use of a glass crucible for a UHV system is potentially dangerous because it can easily break. Thus, it needs to be protected from the outside, *e.g.*, with a stainless steel tube (not shown in Figure 4.5). Nevertheless, glass was chosen because it has some advantages over a metal crucible. First of all, through the glass tube it can always easily be checked whether the reservoir is empty and needs to be refilled. Furthermore, it offers the possibility to adjust the vapor pressure of the molecule by means of changing the temperature. Since the amount of molecules reaching the sample cannot reliably be controlled using the gate valve, it might be necessary to heat or cool the reservoir. This can be done by using a heating or cooling bath. Temperature equilibration is achieved quicker for the glass crucible than for a metal crucible, which is much heavier and thus has a higher heat capacity.

The constructional drawings used to manufacture all the custom-built parts are shown in Appendix C. The linear motion LDK 40-50, the CF16 gate valve and the glass-to-metal seal are commercially available and were purchased from VAb Vakuum-Anlagenbau GmbH, Kurt J. Lesker Company Ltd., and VACOM Vakuum Komponenten und Messtechnik GmbH, respectively.

5 Cumulative Part

At the time of writing, the research in the course of this PhD project has led to the publication of two articles, of which I am the first author. A third article with me as the first author was accepted for publication one day after handing in this thesis. Furthermore, this cumulative part contains five other publications with me as a co-author.

The cumulative part of this thesis is divided into two sections. The first one (Section 5.1) includes the on-surface synthesis of nanostructures from brominated precursor molecules and their characterization with various experimental techniques complemented by theoretical studies carried out by collaboration partners. This work, which investigates the ring/chain ratio in on-surface synthesis, can be considered the main topic of this thesis and has been introduced in Section 1.1. In the second section (Section 5.2) four other publications concerning surface and interface chemistry are summarized. The classes of molecules investigated in these publications have been introduced in Sections 1.2 and 1.3.

In this chapter each publication will be briefly summarized and my contribution will be explained. After this discussion the respective article along with its supporting material is appended. The permissions of use can be found in Appendix B.

Contents

5.1 Ring/Chain Competition in On-Surface Synthesis

This chapter contains four publications, which investigate carbon-based nanostructures generated by an on-surface synthesis approach. In all these studies brominated aromatic precursor molecules were investigated on coinage metal surfaces. Different strategies were applied to either maximize ring compared with chain formation or to exclusively form chains.

The two publications P1 and P2 investigate how the ring/chain ratio formed by the 1,3-dibromoazulene (DBAz) precursor on the Cu(111) surface can be steered. In P3 a surface template, *i.e.*, a vicinal Ag surface, is applied to exclusively form chains from the 4,4''-dibromo-1,1':3',1''-terphenyl (DMTP) precursor. Finally, in P4 the substitution pattern of the precursor molecule 2,6-dibromoazulene (2,6-DBAz) is varied compared with DBAz in order to only allow chain formation on Au(111).

I am the first author of publications P1 and P2, in which I share the first authorship with Dr. Qitang Fan and Dr. Damian Nieckarz, respectively. Publications P3 and P4 are collaboration projects, of which I am co-author. Here, I was mainly involved in the on-surface synthesis of the structures themselves, whereas their further characterization was mostly performed by the collaboration partners.

P1

P1 Organometallic ring *vs.* chain formation beyond kinetic control: steering their equilibrium in two-dimensional confinement

Citation: **C. K. Krug**‡, Q. Fan‡, F. Fillsack, J. Glowatzki, N. Trebel, L. J. Heuplick, T. Koehler, J. M. Gottfried, *Chem. Commun.* **2018**, *54*(70), 9741–9744, DOI 10.1039/c8cc05357j.

Summary

The topic of this communication is the competition of rings *vs.* chains as products in on-surface synthesis. For this purpose the 1,3-dibromoazulene (DBAz) precursor molecule is investigated on the Cu(111) surface with scanning tunneling microscopy (STM) accompanied by X-ray photoelectron spectroscopy (XPS). The study gives fundamental insight in how the ring/chain ratio can be influenced by reaction parameters such as temperature and coverage.

After deposition at 300 K the Br substituents of the DBAz precursor are split off and an organometallic intermediate of the surface-confined Ullmann coupling reaction is formed. While at 300 K almost exclusively long oligomeric chains are formed, annealing to 440 K leads to a strong increase of cyclic hexamers. This finding is investigated more closely for two different coverages of 0.1 and 1.0 ML. For the low coverage it is found that 88% of the monomers are incorporated in rings, whereas this yield decreases to 31% for the high coverage. The different ring/chain ratios are explained by fundamental physicochemical principles.

The preferred chain formation at 300 K can be explained by the concept of kinetic reaction control, which is associated with non-equilibrium conditions. The C−Cu−C bonds in the organometallic intermediate are irreversible on the time scale of the experiment and the connection of the monomer units in the oligomers is purely statistical. This statistics makes the formation of rings unlikely because all monomers would need to be connected in a *cis* orientation to their neighbors. The probability for a *cis* connection of two individual monomers is 1/2. For a cyclic hexamer this results in an overall probability of $0.5^5 = 1/32$ and thus they are only rarely observed. At 440 K the C−Cu−C bonds can be reversibly broken and reformed and accordingly thermodynamic reaction control prevails under these equilibrium conditions. Now the energetically favored product is preferably formed. This product is the ring because it has one more C−Cu−C bond compared with a chain consisting of the equal amount of monomer units.

‡These authors contributed equally to this study and share first authorship.

The influence of the coverage is explained by reaction kinetics. Chain formation is a second-order reaction because two molecules, *i.e.*, monomers or oligomers, need to react in an intermolecular reaction. On the contrary, ring closure is a first-order reaction because the two ends of an open chain react in an intramolecular reaction. For low concentrations, *i.e.*, low coverages, first-order reactions are preferred, whereas second-order reactions become more likely with higher concentrations. Thus, chain growth competes more strongly with ring closure at higher coverages, leading to a decreased ring yield. In addition to these very fundamental findings the structures of the organometallic rings and chains are elucidated by STM images with submolecular resolution.

Own Contribution

All measurements leading to this publication were performed with the combined STM and XPS setup in the laboratory of the Gottfried group in Marburg (*cf.* Section 3.4.1). Before these experiments could be performed I developed a new line-of-sight evaporator (*cf.* Section 4.3), which enables the preparation of samples with medium-vapor pressure molecules such as the commercially available DBAz. All samples were usually prepared by me in close collaboration with Dr. Qitang Fan and with the assistance of Florian Fillsack (in the course of his bachelor's thesis), Johannes Glowatzki, and Nicole Trebel (within research internship projects for their M.Sc. studies). All the measurements were performed by Dr. Qitang Fan and me. The data analysis was mostly performed by me with the help of Lukas J. Heuplick and Tabea Koehler (within research internship projects for their M.Sc. studies). The manuscript was written by me in close cooperation with Prof. Dr. J. Michael Gottfried and Dr. Qitang Fan and all authors were involved in the discussion.

ChemComm

COMMUNICATION

View Article Online
View Journal | View Issue

Cite this: *Chem. Commun.*, 2018, **54**, 9741

Received 4th July 2018,
Accepted 2nd August 2018

DOI: 10.1039/c8cc05357j

rsc.li/chemcomm

Organometallic ring *vs.* chain formation beyond kinetic control: steering their equilibrium in two-dimensional confinement†

Claudio K. Krug,‡ Qitang Fan,‡ Florian Fillsack, Johannes Glowatzki, Nicole Trebel, Lukas J. Heuplick, Tabea Koehler and J. Michael Gottfried *

Control over the competition between an organometallic hexamer macrocycle and oligomer chains formed from the non-alternant aromatic 1,3-dibromoazulene (DBAz) precursor has been achieved in surface-assisted synthesis on a copper(111) surface. In contrast to kinetic reaction control *via* the high-dilution principle, the ring formation is achieved here by thermodynamic control, which is based on two-dimensional (2D) confinement and reversible bonds.

Organometallic compounds formed from haloarenes are significant intermediates for the formation of covalently linked carbon-based nanostructures through the surface Ullmann coupling reaction.[1–9] The structure of the final covalent product is largely determined by the intermediate organometallic phase.[1] Therefore, the understanding of the linking and structure formation between haloarenes and metal atoms is of enormous significance for the fabrication of organometallic and covalent nanostructures. Recently, one-dimensional (1D) chains[2,6,10–12] and 2D networks[7,9,13] have been the most often reported organometallic structures formed from two-, three-, or four-fold halogenated aromatic monomers. In particular, when an angle other than 180° exists between the axes of two carbon–halogen (C–X) groups of a di-halogenated monomer, these monomers can couple forming either polymer chains or macrocycles due to the alternative *cis*- or *trans*-connection motifs. Since the properties of a linear open-chain oligomer and its cyclic counterpart can be substantially different,[14–21] the control over the formation of these two topologies is intriguing in the context of polymer science. Up to date, few approaches have been reported for the control of the ring-*vs.*-chain competition. One approach is using templates to guide the formation of macrocycles.[22] For instance, oligoporphyrin macrocycles have been synthesised in solution using a Vernier-template-directed method.[23–26] In the case of on-surface synthesis, grating templates on a Cu(110)–(1 × 2)O surface have been shown to provide control over the formation of organometallic rings with different sizes.[27] Another approach is the high-dilution principle, which relies on kinetic reaction control. It uses low concentrations to favour the unimolecular (first-order) ring closure process over the competing bimolecular (second-order) chain growth process.[16,17]

Here, we demonstrate that 2D confinement, combined with reversible bond formation, enables thermodynamic control over the competition between organometallic macrocycles and chains (Scheme 1). We show that the macrocycles and chains are the energetically and entropically favoured products, respectively. In contrast to rings and chains with covalent C–C bonds, which are irreversible under the experimental conditions, the organometallic macrocycles and chains can transform into each other and eventually establish an equilibrium. This equilibrium is coverage-dependent and shifts towards the formation of chains at high coverages.

The here reported organometallic hexamer macrocycle consists of six azulene units and six copper atoms. Compared to the much more frequently used benzenoid aromatic monomers, the azulene moiety in the precursor 1,3-dibromoazulene (DBAz) belongs to the non-alternant class of aromatic compounds. Its 5–7 topology also occurs in graphene defects[28–30] and has found attention in on-surface synthesis[31] and organic optoelectronics.[32]

Reaction of 1,3-dibromoazulene on Cu(111) at 300 K. Fig. 1a shows an STM image taken after the deposition of 0.24 ML

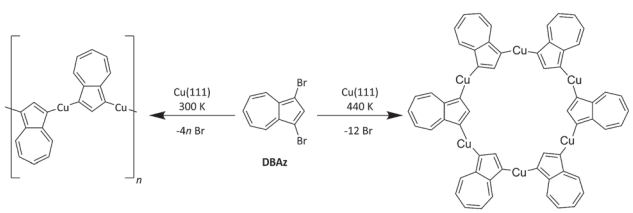

Scheme 1 Formation of an organometallic chain and a hexamer macrocycle with C–Cu–C bonds from 1,3-dibromoazulene (DBAz) on Cu(111).

Philipps-Universität Marburg, Fachbereich Chemie, Hans-Meerwein-Str. 4, 35032 Marburg, Germany. E-mail: michael.gottfried@chemie.uni-marburg.de

† Electronic supplementary information (ESI) available: Experimental details, product statistics, XPS data, additional STM images. See DOI: 10.1039/c8cc05357j

‡ These authors contributed equally to this study and share first authorship.

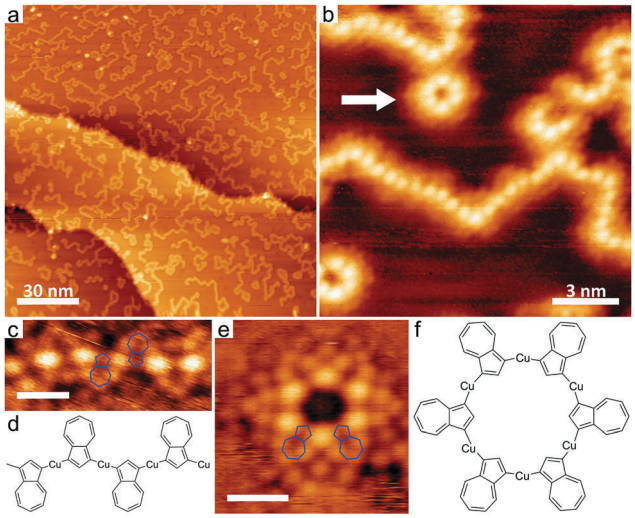

Fig. 1 STM images of DBAz deposited on Cu(111) at 300 K. (a) Large-scale image showing the formed organometallic chains. (b) Zoom-in image showing chains consisting of bright protrusions as well as a cyclic hexamer (marked with a white arrow) consisting of six bright protrusions. Panels (c) and (e) show submolecularly resolved images of a chain section and a hexamer macrocycle, respectively. Contours of the azulene moieties are overlaid with blue lines. Scale bars: 1 nm. Panels (d) and (f) show the chemical structures of the chain and macrocycle in panels (c) and (e), respectively. Tunneling parameters: (a) $U = -3.52$ V, $I = -0.09$ nA; (b) $U = -3.63$ V, $I = -0.08$ nA; (c) $U = 0.88$ V, $I = 0.18$ nA; (e) $U = 0.88$ V, $I = 0.19$ nA. All STM images in this work were processed with WSxM.[34]

DBAz onto Cu(111) held at 300 K with a flux of 0.05 ML min^{-1}. (See the ESI† for the definition of the monolayer.) As can be seen, chains with variable lengths and shapes are formed as the major species. The magnified view in Fig. 1b reveals evenly spaced protrusions in the chains. Occasionally, hexagonal macrocycles occur as marked by the white arrow in Fig. 1b. Considering that the C–Br bond scission on Cu(111) already occurs well below 300 K,[12] these chains and macrocycles are assigned to organometallic species with C–Cu–C bonds as confirmed by the Br 3p and C 1s XP spectra (see Fig. S1 in the ESI†).

The detailed structures of these organometallic species, *i.e.*, open chains and macrocycles, are revealed by submolecularly resolved STM images as shown in Fig. 1c and e. These images are obtained by using a low bias voltage, at which different orbitals of the species contribute to the STM contrast compared to Fig. 1b. The image of the chain in Fig. 1c reveals weak tri-lobed features between two bright protrusions as marked by the blue contours. These tri-lobed features, which appear alternatingly above and below two bright protrusions, resemble the LUMO at the tropylium ring of azulene.[33] Therefore, the weak tri-lobed feature and the bright protrusion are attributed to the azulene unit and the copper atom in the C–Cu–C bridge, respectively, as illustrated by the chemical structure in Fig. 1d. In line with this assignment, Fig. 1e shows the organometallic hexamer macrocycle with six azulene units and six copper atoms (Fig. 1f). The weak protrusions observed around the azulene units in the chain (Fig. 1c) and macrocyle (Fig. 1e) are assigned to Br adatoms from the debromination of DBAz,

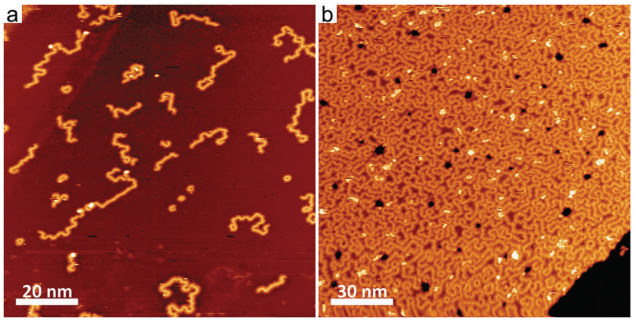

Fig. 2 Large-scale STM images taken after deposition of (a) 0.10 ML and (b) 1.00 ML DBAz onto Cu(111) at 300 K. The dark holes in panel (b) are attributed to vacancy islands on the Cu(111) surface.[12] Tunneling parameters: (a) $U = -3.52$ V, $I = -0.09$ nA; (b) $U = -1.85$ V, $I = -0.06$ nA.

in line with previous studies on bromoarenes on Cu(111).[2,4,7,11] In the hexagonal macrocycles, all azulene units are linked in *cis*-configuration, whereas the irregular shapes of the organometallic chains indicate random distribution of *cis*- and *trans*-connections. Noteworthy, the two C–Br bonds in DBAz enclose an angle of 144°, which would enable the formation of a ten-membered ring with straight, unstrained C–Cu–C bridges. The preferential formation of six-membered rings here is attributed to registry effects. An additional factor that favours the formation of small rings will be discussed later.

Reaction under non-equilibrium conditions (kinetic reaction control). Fig. 2a shows an STM image taken after the deposition of a low coverage (0.10 ML) of DBAz on Cu(111) at 300 K with a flux of 0.3 ML min^{-1}. Despite the high-dilution conditions, the fraction of rings is low, which makes it difficult to obtain reliable statistical data of the product distribution for comparison to other samples. Qualitatively, however, the yield of macrocycles is similarly low as in the medium-coverage sample (0.24 ML) in Fig. 1a. The chain length distribution for the sample in Fig. 2a is displayed in Fig. S2 in the ESI† and shows a typical step-polymerization behaviour, in agreement with previous work.[1] Deposition of a high coverage (1.00 ML) of DBAz onto Cu(111) at 300 K (flux: 3 ML min^{-1}) results again in the predominant formation of chains, which arrange in a disordered, densely packed phase together with Br adatoms between the chains (Fig. 2b). The maximum of the chain-length distribution is slightly shifted to shorter chains, compared to the low coverage case (see Fig. S2 in the ESI†), in line with the higher deposition rate.

The predominant formation of organometallic chains at 300 K can be understood considering that the scission and re-formation of C–Cu bonds at 300 K is very slow on the timescale of our experiment,[12] *i.e.*, the C–Cu bond formation is irreversible. Under these conditions, the formation of a hexamer macrocycle has a probability of $\frac{1}{2^5} = \frac{1}{32}$ among all the organometallic species containing six azulene units. This number arises from the fact that each of the five connections in a six-membered open-chain product has two possible (*trans*- or *cis*-) linking configurations.[1] The hexamer macrocycle represents the

P1

only case in which all connections are of the *cis* type. The actual probability of forming a hexamer macrocycle is even lower than $\frac{1}{32}$, because the six-membered chain only accounts for a fraction of all chains with different lengths. Thus, the chains are preferentially formed as the statistically favoured species, because they bear more possible configurational isomers than their macrocycle counterparts.

Reaction under equilibrium conditions (thermodynamic reaction control). At elevated temperatures, an equilibrium between chains and rings can be established, because the C–Cu bonds undergo frequent reversible dissociation and re-formation reactions.[11,12] We selected a temperature of 440 K because it is close to the highest temperature at which the C–Cu bonds exist in a reversible equilibrium situation with high rates of bond conversions. Temperatures higher than this initiate the irreversible C–C covalent coupling.[12,35] In a first experiment, we annealed the chain-rich sample from Fig. 2a to 440 K for 5 min and then cooled it rapidly. This treatment resulted in the formation of organometallic hexamer macrocycles with a high yield (Fig. 3a). To determine the ring to chain ratio, the area occupied by rings and chains in Fig. 3a has been analysed. 171 rings (1026 monomer units) occupy 88% of the covered surface, while 140 monomer units form twelve chains of different length.

In a second experiment, the high-coverage sample (1.00 ML) from Fig. 2b was treated in the same way. For this sample, we also found a substantial increase of the yield of the macrocycles, as shown by the well-ordered hexagonal close-packed islands in Fig. 3b. Fig. 3c shows the magnified view of an island of the macrocycles. Compared to the low-coverage sample in Fig. 3a, the yield of macrocycles is now lower (Fig. 3b), but still much higher than under kinetic control (Fig. 2b). 31% of the area in Fig. 3b is occupied by 1452 rings containing 8712 monomers as opposed to 19 391 monomers incorporated in chains. While Fig. 3b may not be entirely representative, large islands of rings can be found over the whole sample (*cf.* Fig. S3 in the ESI†).

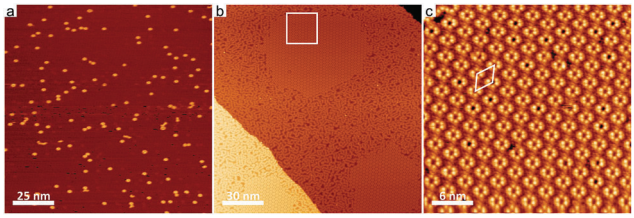

Fig. 3 STM images of DBAz on Cu(111) after annealing the samples from Fig. 2 to 440 K for 5 min and rapid cooling to 300 K; (a) 0.10 ML and (b) 1.00 ML. While at 0.10 ML cyclic hexamers are formed almost exclusively (88% of the visible azulene monomer units are contained in rings), their yield is decreased at saturation coverage (31% of the visible monomer units in rings). Note that (b) shows a selected area with a larger-than-average fraction of rings. (c) Enlarged image of the white-framed area in (b), showing the hexamer macrocycles. The indicated unit cell (a = 2.5 nm, b = 2.8 nm, γ = 122°) slightly deviates from the ideal hexagonal case, probably due to residual thermal drift. Tunneling parameters: (a) U = −2.59 V, I = −0.08 nA; (b) U = −3.31 V, I = −0.12 nA; (c) U = −2.51 V, I = −0.14 nA.

These observations can be interpreted as follows: the conversion of chains to rings during annealing indicates that the rings are thermodynamically more stable than the chains. This follows from the fact that the chains are statistically favoured, as was described above. If the macrocycles were not energetically favoured, they would not occur at all under equilibrium conditions. The higher stability of the macrocycles probably results from the additional C–Cu–C bond in a ring, compared to its open-chain counterpart. In addition, substrate registry effects may play a role. The rings are especially favoured under low-coverage equilibrium conditions (0.10 ML, Fig. 3a). This can be understood by considering the reactions that establish the equilibrium: both the ring opening and ring closure are unimolecular (first-order) reactions (Fig. 4a, left), which means that their rates are independent of the concentrations of other reactants (monomers, chains). In contrast, the chain extension, which competes with the ring closure, is a bimolecular (second-order) process (Fig. 4a, right). Its rate grows with increasing coverage of the reactants, as a result of the increased probability for intermolecular encounters. Therefore, the equilibrium between rings and chains is shifted towards the side of chains at high coverage (1.00 ML, Fig. 3b). Note that the barrier for the ring opening is higher than that for the ring closure, because the former includes the energy for breaking a C–Cu bond. This is equivalent to the statement that the rings are energetically favoured, as is illustrated in Fig. 4b (left).

Under equilibrium conditions, a "ring-like" chain initially formed by breaking a single C–Cu bond in a macrocycle (Fig. 4b, center) may undergo configurational changes into other chains as illustrated by Fig. 4b (right). The energy barriers for such changes ($E_s^{\neq}$) are likely higher than the barrier for the return to a closed ring, because the configurational change requires either the out-of-plane flipping of a chain segment

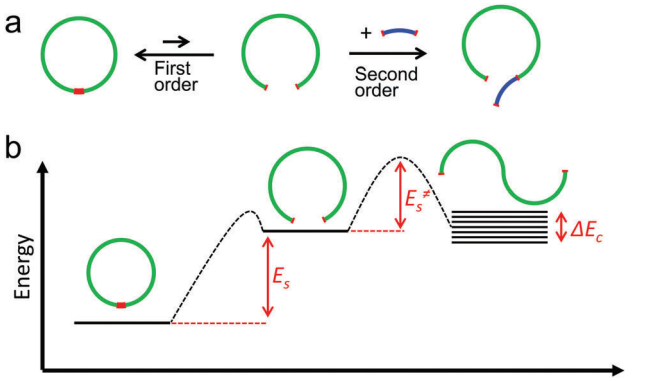

Fig. 4 (a) Reaction scheme for the ring-opening/ring-closure, which are first-order processes, and the extension of a chain, which is a second-order process. The latter becomes more likely at higher coverages. (b) Schematic energy diagram for the conversions between an organometallic macrocycle and its open-chain counterparts. E_s is the energy required for the dissociation of one C–Cu bond. $E_s^{\neq}$ represents the energy barrier for the conformational isomerisation of the open chain in 2D confinement through out-of-plane flipping or additional bond dissociation/re-formation. ΔE_c represents the possible different energies for the various chain conformations and corresponding registries to the surface.

(with simultaneous sliding movement of other parts of the chains) or the in-plane rotation of a chain segment after a second C–Cu bond cleavage.[1]

The effects described in this work largely result from the 2D confinement. In solution, chains have a much higher conformational flexibility and thus are even more entropically favoured than in 2D. Their equilibrium concentration in solution would therefore be much higher and the yield of rings correspondingly much lower. This is probably the reason why similar phenomena have not been reported for solution synthesis. In 2D confinement, the adsorbate–substrate interactions make the barriers for configurational changes ($E_S^{\neq}$) larger than in solution and dependent on the chain length. For a short ring-like chain as the initial ring-opening product of a small, stiff ring (like our hexamer), the barriers will be higher than for a long ring-like chain formed from a large ring, because the latter has an increased in-plane flexibility and its shape can change without flipping of chain segments or further C–Cu bond dissociation. In addition, the increased flexibility of longer chains will also make the reactive encounter of its two terminals less likely. This will reduce the rate of the back reaction (ring re-formation) in Fig. 4a. Both factors are closely related and disfavour larger macrocycles, in agreement with our finding of hexamers as the dominant ring size. As a rare example of a larger ring, octamer macrocycles with eight azulene monomer units and eight Cu adatoms are shown in Fig. S4 in the ESI.†

In conclusion, we have studied the formation of organometallic nanostructures from the non-alternant aromatic molecule 1,3-dibromoazulene on a Cu(111) surface. We have found that kinetic reaction control at 300 K results predominantly in the formation of oligomer chains. In contrast, high yields of mainly hexamer rings are obtained *via* thermodynamic reaction control at 440 K. A chemical equilibrium between rings and chains can exist because the rings are energetically more stable, while the chains are entropically favoured. This equilibrium is influenced by the coverage, with lower coverages resulting in higher yields of rings. Our study shows that 2D confinement, combined with reversible bond formation, is an important factor that enables thermodynamic reaction control of the competition between ring and chain formation.

Financial support by the Deutsche Forschungsgemeinschaft *via* the grant GO 1812/2-1 and the CRC 1083 is gratefully acknowledged. Q. T. F. thanks the Alexander von Humboldt-Foundation for a Research Fellowship for Postdoctoral Researchers.

Conflicts of interest

There are no conflicts to declare.

Notes and references

1 Q. Fan, T. Wang, J. Dai, J. Kuttner, G. Hilt, J. M. Gottfried and J. Zhu, *ACS Nano*, 2017, **11**, 5070–5079.
2 W. H. Wang, X. Q. Shi, S. Y. Wang, M. A. Van Hove and N. Lin, *J. Am. Chem. Soc.*, 2011, **133**, 13264–13267.
3 K.-H. Chung, B.-G. Koo, H. Kim, J. K. Yoon, J.-H. Kim, Y.-K. Kwon and S.-J. Kahng, *Phys. Chem. Chem. Phys.*, 2012, **14**, 7304–7308.
4 J. Park, K. Y. Kim, K.-H. Chung, J. K. Yoon, H. Kim, S. Han and S.-J. Kahng, *J. Phys. Chem. C*, 2011, **115**, 14834–14838.
5 E. A. Lewis, C. J. Murphy, M. L. Liriano and E. C. Sykes, *Chem. Commun.*, 2014, **50**, 1006–1008.
6 M. Di Giovannantonio, M. E. Garah, J. Lipton-Duffin, V. Meunier, L. Cardenas, Y. F. Revurat, A. Cossaro, A. Verdini, D. F. Perepichka, F. Rosei and G. Contini, *ACS Nano*, 2013, **7**, 8190–8198.
7 Q. Fan, C. Wang, L. Liu, Y. Han, J. Zhao, J. Zhu, J. Kuttner, G. Hilt and J. M. Gottfried, *J. Phys. Chem. C*, 2014, **118**, 13018–13025.
8 Q. Fan, J. M. Gottfried and J. Zhu, *Acc. Chem. Res.*, 2015, **48**, 2484–2494.
9 Q. Fan, T. Wang, L. Liu, J. Zhao, J. Zhu and J. M. Gottfried, *J. Chem. Phys.*, 2015, **142**, 101906.
10 D. Barton, H.-Y. Gao, P. A. Held, A. Studer, H. Fuchs, N. L. Doltsinis and J. Neugebauer, *Chem. – Eur. J.*, 2017, **23**, 6190–6197.
11 J. Dai, Q. Fan, T. Wang, J. Kuttner, G. Hilt, J. M. Gottfried and J. Zhu, *Phys. Chem. Chem. Phys.*, 2016, **18**, 20627–20634.
12 Q. Fan, C. Wang, Y. Han, J. Zhu, J. Kuttner, G. Hilt and J. M. Gottfried, *ACS Nano*, 2014, **8**, 709–718.
13 J. Eichhorn, T. Strunskus, A. Rastgoo-Lahrood, D. Samanta, M. Schmittel and M. Lackinger, *Chem. Commun.*, 2014, **50**, 7680–7682.
14 K. Endo, in *New Frontiers in Polymer Synthesis*, ed. S. Kobayashi, Springer, Berlin Heidelberg, 2nd edn, 2008, vol. 217, pp. 121–183.
15 Z. Jia and M. J. Monteiro, *J. Polym. Sci., Part A: Polym. Chem.*, 2012, **50**, 2085–2097.
16 Z. Jia and M. J. Monteiro, in *Hierarchical Macromolecular Structures: 60 Years after the Staudinger Nobel Prize II*, ed. V. Percec, Springer Publishing, Cham, 1st edn, 2013, vol. 262, pp. 295–327.
17 T. Josse, J. De Winter, P. Gerbaux and O. Coulembier, *Angew. Chem., Int. Ed.*, 2016, **55**, 13944–13958.
18 H. R. Kricheldorf, *J. Polym. Sci., Part A: Polym. Chem.*, 2010, **48**, 251–284.
19 B. A. Laurent and S. M. Grayson, *Chem. Soc. Rev.*, 2009, **38**, 2202–2213.
20 T. Yamamoto, *Polym. J.*, 2013, **45**, 711–717.
21 T. Yamamoto and Y. Tezuka, *Polym. Chem.*, 2011, **2**, 1930–1941.
22 V. Martí-Centelles, M. D. Pandey, M. I. Burguete and S. V. Luis, *Chem. Rev.*, 2015, **115**, 8736–8834.
23 D. V. Kondratuk, L. A. Perdigao, A. M. S. Esmail, J. N. O'Shea, P. H. Beton and H. L. Anderson, *Nat. Chem.*, 2015, **7**, 317–322.
24 M. Hoffmann, C. J. Wilson, B. Odell and H. L. Anderson, *Angew. Chem., Int. Ed.*, 2007, **46**, 3122–3125.
25 J. K. Sprafke, D. V. Kondratuk, M. Wykes, A. L. Thompson, M. Hoffmann, R. Drevinskas, W. H. Chen, C. K. Yong, J. Karnbratt, J. E. Bullock, M. Malfois, M. R. Wasielewski, B. Albinsson, L. M. Herz, D. Zigmantas, D. Beljonne and H. L. Anderson, *J. Am. Chem. Soc.*, 2011, **133**, 17262–17273.
26 S. A. Svatek, L. M. Perdigao, A. Stannard, M. B. Wieland, D. V. Kondratuk, H. L. Anderson, J. N. O'Shea and P. H. Beton, *Nano Lett.*, 2013, **13**, 3391–3395.
27 Q. Fan, J. Dai, T. Wang, J. Kuttner, G. Hilt, J. M. Gottfried and J. Zhu, *ACS Nano*, 2016, **10**, 3747–3754.
28 E. Cockayne, G. M. Rutter, N. P. Guisinger, J. N. Crain, P. N. First and J. A. Stroscio, *Phys. Rev. B: Condens. Matter Mater. Phys.*, 2011, **83**, 195425.
29 H. I. Rasool, E. B. Song, M. Mecklenburg, B. C. Regan, K. L. Wang, B. H. Weiller and J. K. Gimzewski, *J. Am. Chem. Soc.*, 2011, **133**, 12536–12543.
30 F. Banhart, J. Kotakoski and A. V. Krasheninnikov, *ACS Nano*, 2011, **5**, 26–41.
31 J. Hieulle, E. Carbonell-Sanromà, M. Vilas-Varela, A. Garcia-Lekue, E. Guitián, D. Peña and J. I. Pascual, *Nano Lett.*, 2018, **18**, 418–423.
32 H. Xin and X. Gao, *ChemPlusChem*, 2017, **82**, 945–956.
33 J. Xia, B. Capozzi, S. Wei, M. Strange, A. Batra, J. R. Moreno, R. J. Amir, E. Amir, G. C. Solomon, L. Venkataraman and L. M. Campos, *Nano Lett.*, 2014, **14**, 2941–2945.
34 I. Horcas, R. Fernández, J. M. Gómez-Rodríguez, J. Colchero, J. Gómez-Herrero and A. M. Baro, *Rev. Sci. Instrum.*, 2007, **78**, 013705.
35 Q. Fan, C. Wang, Y. Han, J. Zhu, W. Hieringer, J. Kuttner, G. Hilt and J. M. Gottfried, *Angew. Chem., Int. Ed.*, 2013, **52**, 4668–4672.

Electronic Supplementary Material (ESI) for Chemical Communications.

P1

Electronic Supplementary Information (ESI) for

Organometallic ring vs. chain formation beyond kinetic control: steering their equilibrium in two-dimensional confinement

Claudio K. Krug‡, Qitang Fan‡, Florian Fillsack, Johannes Glowatzki, Nicole Trebel, Lukas J. Heuplick, Tabea Koehler and J. Michael Gottfried*

Philipps-Universität Marburg, Fachbereich Chemie, Hans-Meerwein-Str. 4, 35032 Marburg, Germany

**michael.gottfried@chemie.uni-marburg.de*

‡ These authors contributed equally to this study and share first authorship.

1. Experimental details

The experiments were carried out in a UHV system consisting of three chambers, allowing complete microscopic and spectroscopic characterization of each individual sample. Deposition of DBAz was performed in a custom-built preparation chamber operated at a base pressure below 10^{-9} mbar**.** The DBAz molecules were deposited from a home-built line-of-sight evaporator consisting of a glass tube as a reservoir for the molecules, a CF16 gate valve and a glass tube, which can be positioned *via* a linear motion, guiding the molecules directly to the single crystal surface. Prior to deposition, the reservoir was cooled to 195 K with a mixture of acetone and dry ice and the gate valve was opened until the pressure in the chamber did not decrease any more to degas the reservoir. Afterwards the Cu(111) single crystal was positioned directly in front of the opening of the glass tube and the gate valve was opened until the desired coverage was reached. The monolayer phase (1.00 ML) is defined as the saturation coverage achieved at room temperature.

Prior to deposition of DBAz the Cu(111) single crystal (purity 99.9999%, roughness <0.01 µm, orientation accuracy <0.1°, from MaTecK/Germany) was prepared by iterated sputtering with Ar^+ ions (1 keV, 12 µA, 30 min) and annealing (800 to 820 K, 10 min) in the STM chamber. The temperatures were measured with a thermocouple directly mounted to the Cu(111) single crystal. Surface cleanliness was confirmed either by XPS or STM. The STM chamber is operated at a base pressure below 2×10^{-10} mbar and houses a SPECS Aarhus 150 STM, which was used for variable temperature STM (VT-STM). VT-STM measurements were performed using an electrochemically etched W tip. For the measurements, the STM was cooled to 100 K with liquid nitrogen and gradually warmed up during measuring. STM images were recorded in constant current mode and processed with WSxM 5.0 Develop 8.5.[1]

XPS experiments were carried out in a third chamber operated at a base pressure below 2×10^{-10} mbar with monochromatised Al Kα radiation using a SPECS XR 50 M X-ray anode, a SPECS FOCUS 500 monochromator and a SPECS PHOIBOS 150 electron energy analyzer equipped with an MCD-9 multi channeltron detector.

2. XPS data of 1,3-dibromoazulene on Cu(111)

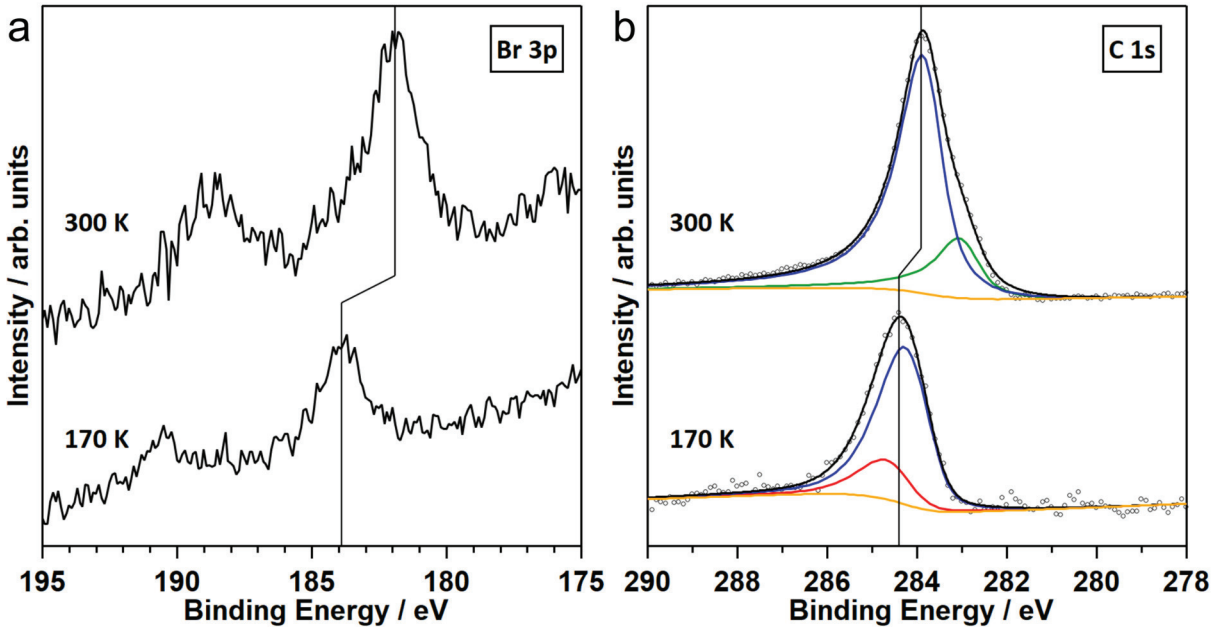

Fig. S1: (a) Br 3p and (b) C 1s XP spectra after deposition of DBAz on Cu(111) at 170 and 300 K, respectively. The shifts indicated by the lines show that the molecule stays intact at 170 K and becomes completely debrominated at 300 K. The C 1s spectra are fitted with two peaks in a 1:4 ratio; black dots: data points, red curve: Br-bonded C atoms, green curve: C-bonded C atoms, blue curves: all other C atoms, black curves: total fits, orange curves: background.

As shown by Fig. S1a, deposition of DBAz on Cu(111) at 170 K results in the Br $3p_{3/2}$ signal located at a binding energy (BE) of 183.9 eV, which is characteristic for the intact C-Br group on the Cu(111) surface.[2,3] The XP spectrum taken after deposition at 300 K exhibits a BE of 181.9 eV for the Br $3p_{3/2}$ peak, which is assigned to Br adatoms chemisorbed on Cu(111).[2,4,5] This shift in BE indicates the dissociation of the C-Br bonds. The formation of C-Cu organometallic bonds is confirmed by the C 1s XP spectra (Fig. S1b). The C 1s XP spectrum obtained at 170 K can be fitted with two species in a 1:4 ratio,[6 7] representing the carbon atoms in C-Br groups at a BE of 284.8 eV and the other carbon atoms at a BE of 284.3 eV, respectively. The C 1s spectrum acquired at 300 K can also be fitted with two components in a 1:4 ratio: the minor peak is located at a BE of 283.1 eV and the major peak at 284.0 eV. The minor peak with lower BE is assigned to carbon bound to copper adatoms, consistent with the formation of an organometallic species.[8] Noteworthy, the major peak of the C 1s spectrum obtained at 300 K is shifted by 0.3 eV towards lower BE relative to that of the C 1s spectrum at 170 K. This shift partly results from the work function increase caused by the chemisorbed Br atoms.[3,9]

3. Chain length distribution at 300 K for two different coverages

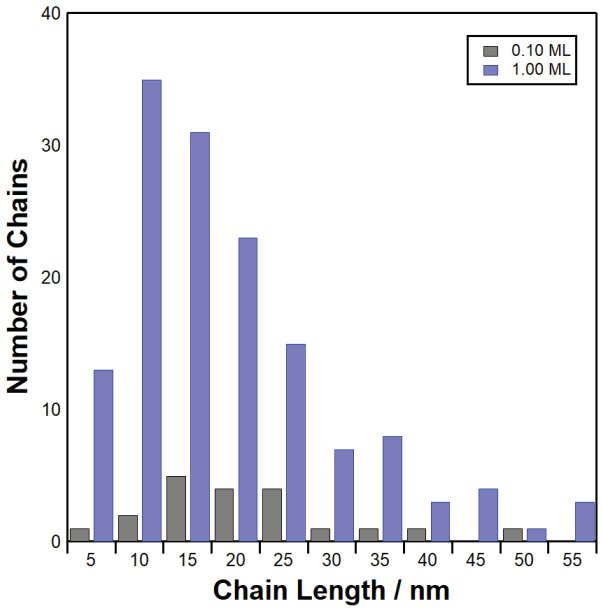

Fig. S2: Chain length distribution for the STM images in Fig. 2. The number on the vertical axis is the absolute number of chains in the image in the respective length interval. The length intervals are 5 nm wide, *i.e.*, the first interval includes all chains up to 5 nm length, while the second interval includes all chains from >5 nm up to 10 nm length.

4. Additional STM images

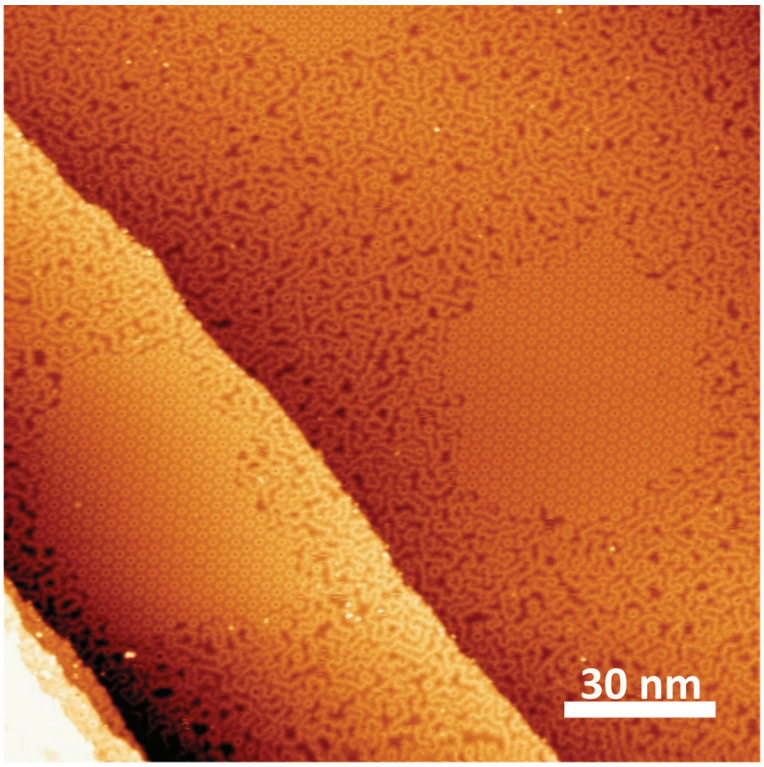

Fig. S3: STM image of the sample in Fig. 3b showing another area with different islands of cyclic hexamers. Tunneling parameters: U = -3.31 V, I = -0.11 nA.

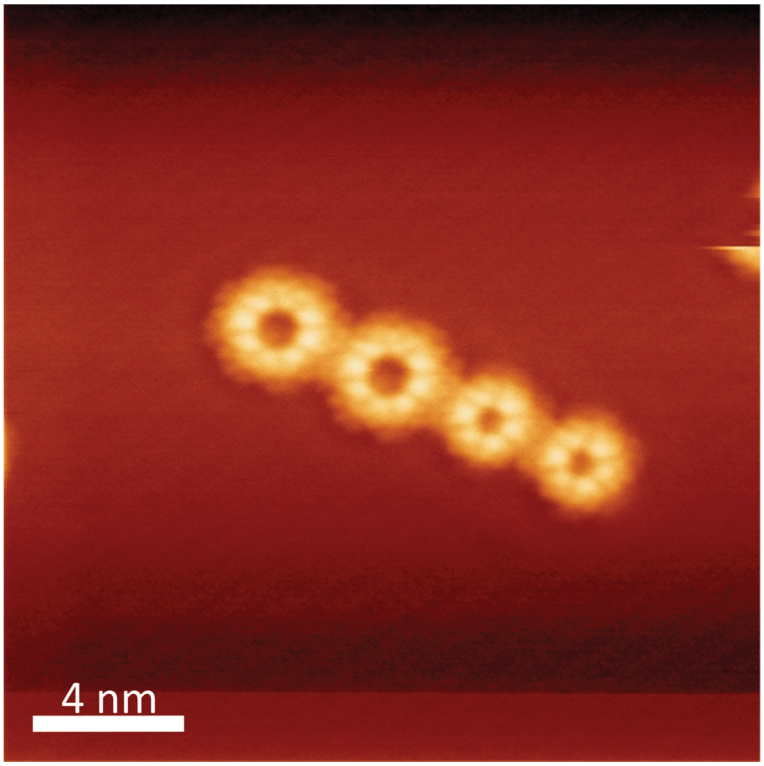

Fig. S4: STM image of the sample in Figure 3a showing two cyclic organometallic octamers (left) next to two hexamers. Tunneling parameters: *U* = -1.40 V, *I* = -0.16 nA.

References

1. I. Horcas, R. Fernández, J. M. Gómez-Rodríguez, J. Colchero, J. Gómez-Herrero and A. M. Baro, *Rev. Sci. Instrum.*, 2007, **78**, 013705.
2. Q. Fan, C. Wang, L. Liu, Y. Han, J. Zhao, J. Zhu, J. Kuttner, G. Hilt and J. M. Gottfried, *J. Phys. Chem. C*, 2014, **118**, 13018-13025.
3. M. Di Giovannantonio, M. E. Garah, J. Lipton-Duffin, V. Meunier, L. Cardenas, Y. F. Revurat, A. Cossaro, A. Verdini, D. F. Perepichka, F. Rosei and G. Contini, *ACS Nano*, 2013, **7**, 8190-8198.
4. M. Chen, X. Feng, L. Zhang, H. Ju, Q. Xu, J. Zhu, J. M. Gottfried, K. Ibrahim, H. Qian and J. Wang, *J. Phys. Chem. C*, 2010, **114**, 9908-9916.
5. Q. Fan, C. Wang, Y. Han, J. Zhu, J. Kuttner, G. Hilt and J. M. Gottfried, *ACS Nano*, 2014, **8**, 709-718.
6. M. Schmid, H.-P. Steinrück and J. M. Gottfried, *Surf. Interface Anal.*, 2014, **46**, 505-511.
7. M. Schmid, H.-P. Steinrück and J. M. Gottfried, *Surf. Interface Anal.*, 2015, **47**, 1080.
8. Q. Fan, L. Liu, J. Dai, T. Wang, H. Ju, J. Zhao, J. Kuttner, G. Hilt, J. M. Gottfried and J. Zhu, *ACS Nano*, 2018, **12**, 2267-2274.
9. M. Chen, J. Xiao, H.-P. Steinrück, S. Wang, W. Wang, N. Lin, W. Hieringer and J. M. Gottfried, *J. Phys. Chem. C*, 2014, **118**, 6820-6830.

P2 The Macrocycle versus Chain Competition in On-Surface Polymerization: Insights from Reactions of 1,3-Dibromoazulene on Cu(111)

Citation: **C. K. Krug**†, D. Nieckarz†, Q. Fan, P. Szabelski, J. M. Gottfried, *Chem. Eur. J.* **2020**, *26*(34), 7647–7656, DOI 10.1002/chem.202000486.

Summary

This full article is an expansion of the studies presented in the previously published communication (P1). The aim is to further broaden the fundamental understanding of the processes that determine the ring/chain ratio in on-surface synthesis. For this purpose the analysis is extended to more coverages and temperatures, the conclusions drawn from first principles are substantiated by Monte Carlo (MC) simulations, and further theoretical considerations are made.

While in P1 the ring/chain ratio has only been analyzed for two coverages, namely 0.1 and 1.0 ML, it is also carried out for intermediate coverages of 0.3 and 0.5 ML in this study. The analysis confirms the trend of decreasing ring yield with increasing coverage expected from the considerations based on reaction kinetics. To further test these considerations the principles of kinetic and thermodynamic reaction control are applied in MC simulations, in which the DBAz precursor molecule is represented by a very basic model system. A good qualitative agreement of the experimental and theoretical results proves the validity of the conclusions drawn from first principles. Furthermore, it shows their general applicability to on-surface oligomerization reactions because the specific properties of the DBAz molecule are neglected in the model system.

Moreover, an optimal reaction temperature to maximize the ring yield can be expected from the interplay of thermodynamic reaction control and simple thermodynamic considerations. Since the rings are preferably formed under thermodynamic reaction control they must be the energetically more stable product compared with the chains. However, this means that the chains are the entropically favored product and according to thermodynamics an increased temperature should favor their formation. Thus, a maximum in the ring yield can be expected for a certain temperature. This temperature needs to be just high enough to reach the regime of thermodynamic reaction control, while a further increase favors the chain formation again. The expected behavior is confirmed by stepwise annealing a sample with an intermediate coverage of 0.5 ML and an

†These authors contributed equally.

optimal temperature for ring formation of 430 K is found. The existence of such an optimal reaction temperature is again supported by the results of the MC simulations.

P2

As a last point, the concept of effective molarity (EM), which is well established for polymerization reactions in the gas phase or in solution, is applied to an on-surface synthesis case for the first time. The EM is a measure for the preference of ring over chain formation. A strong deviation from the expected behavior, *i.e.*, a constant value of the EM independent of the coverage, is found. The deviation is explained by the special conditions like 2D confinement, preferred adsorption sites, and high concentrations, which prevail in on-surface synthesis.

Own Contribution

As for the preceding communication (P1) most of the experimental work was performed by me in close collaboration with Dr. Qitang Fan and I performed all the data analysis. To get a deeper understanding of the phenomena observed experimentally, further insight from a theoretical point of view was necessary. Thus, we resorted to MC simulations, which were performed by Dr. Damian Nieckarz under the supervision of Dr. Paweł Szabelski at the Maria Curie-Skłodowska University in Lublin, Poland. Based on the experimental and theoretical results I wrote the manuscript in close cooperation with Prof. Dr. J. Michael Gottfried with some input by Dr. Damian Nieckarz and Dr. Paweł Szabelski concerning the MC simulations. All authors were involved in the discussion of the manuscript.

Surface Chemistry |Hot Paper|

The Macrocycle versus Chain Competition in On-Surface Polymerization: Insights from Reactions of 1,3-Dibromoazulene on Cu(111)

Claudio K. Krug[+],[a] Damian Nieckarz[+],[b] Qitang Fan,[a] Paweł Szabelski,[b] and J. Michael Gottfried*[a]

Abstract: Ring/chain competition in oligomerization reactions represents a long-standing topic of synthetic chemistry and was treated extensively for solution reactions but is not well-understood for the two-dimensional confinement of surface reactions. Here, the kinetic and thermodynamic principles of ring/chain competition in on-surface synthesis are addressed by scanning tunneling microscopy, X-ray photoelectron spectroscopy, and Monte Carlo simulations applied to azulene-based organometallic oligomers on Cu(111). Analysis of experiments and simulations reveals how the ring/chain ratio can be controlled through variation of coverage and temperature. At room temperature, non-equilibrium conditions prevail and kinetic control leads to preferential formation of the entropically favored chains. In contrast, high-temperature equilibrium conditions are associated with thermodynamic control, resulting in increased yields of the energetically favored rings. The optimum conditions for ring formation include the lowest possible temperature within the regime of thermodynamic control and a low coverage. The general implications are discussed and compared to the solution case.

Introduction

The competition between chain and ring formation in polymerization reactions has been a long-standing topic in synthetic chemistry[1–4] and has recently also found attention in on-surface synthesis.[5–9] The polymerizations can be performed under equilibrium or non-equilibrium conditions. Equilibrium implies that the decisive bonds are reversibly formed and dissociated during the reaction. These conditions lead to thermodynamic reaction control, which means that the product composition is determined by the relative thermodynamic stabilities, that is, by the standard free enthalpy of the reaction. In contrast, non-equilibrium conditions result in kinetic reaction control. In the limiting case that the rate of the backwards reaction is zero, the product composition is exclusively controlled by the relative rates of formation of the different products. The equilibrium case for oligomerization reactions in three-dimensional (3D) solution phases was first treated by Jacobson and Stockmayer using flight statistics,[1] an approach that was later refined.[10] In contrast, systems under kinetic control proved to be more difficult to describe.[2] Eventually, it was shown that the ring-size distribution under kinetic control is similar to that predicted for equilibrium conditions by the Jacobson–Stockmayer model.[3]

In on-surface polymerizations, the product composition is additionally influenced by the two-dimensional (2D) confinement and the specific interactions of the reactants with the surface. As a model reaction related to on-surface synthesis of carbon-based nanostructures,[11–22] we study here the formation of azulene-based organometallic oligo- and polymers from 1,3-dibromoazulene (DBAz, Figure 1). Such organometallic compounds of aromatic building blocks represent important and stable intermediates in the Ullmann-type on-surface synthesis of carbon-based nanostructures.[5,23] Previous work has shown that the linking pattern in the organometallic intermediates determines the structure of the covalent end product of the surface Ullmann coupling.[6] Therefore, it is important to control the structures of these intermediates.

Azulene is a building block with a prototypical non-alternant aromatic π-electron system, which has recently attracted attention in surface chemistry, organic electronics, and related areas.[24–35] Non-alternant aromatic π-electron systems typically

[a] C. K. Krug,[+] Dr. Q. Fan, Prof. Dr. J. M. Gottfried
Department of Chemistry, Philipps University Marburg
Hans-Meerwein-Straße 4, 35032 Marburg (Germany)
E-mail: michael.gottfried@chemie.uni-marburg.de

[b] Dr. D. Nieckarz,[+] Prof. Dr. P. Szabelski
Department of Theoretical Chemistry, Institute of Chemical Sciences
Faculty of Chemistry, Maria Curie-Skłodowska University in Lublin
Pl. M.C. Skłodowskiej 3, Lublin 20-031 (Poland)

[+] These authors contributed equally to this work.

Supporting information and the ORCID identification number(s) for the author(s) of this article can be found under: https://doi.org/10.1002/chem.202000486.

P2

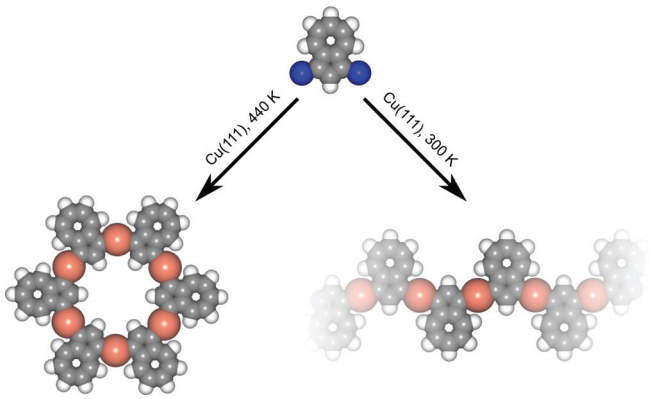

Figure 1. Space-filling model showing the possible cyclic (left) and open-chain (right) organometallic reaction products of 1,3-dibromoazulene (DBAz) on Cu(111). The ring/chain competition under kinetic and thermodynamic control is analyzed in this work. Color code: white, hydrogen; grey, carbon; red, copper; blue, bromine.

contain odd-numbered rings such as pentagons and heptagons. Their electronic properties differ strongly from those of their alternant isomers, resulting in stronger interactions with metal surfaces.[34] Non-alternant structural motifs also occur as defects in graphene and carbon nanotubes and influence their properties.[36–39]

In this work, we study the ring/chain competition in two-dimensional (2D) confinement using azulene-based organometallic oligomers. As was shown in a preliminary Communication,[9] the dominant cyclic product is the hexamer shown in Figure 1 (left) and the ring/chain competition can be influenced by reaction temperature and coverage. Here, we provide a comprehensive treatment of the observed phenomena in the context of thermodynamic and kinetic reaction control, using Monte Carlo (MC) simulations for the interpretation of the experimental data obtained by analysis of scanning tunneling microscopy (STM) images. In addition, we apply the concept of the effective molarity (EM) for the first time to on-surface chemistry.

Results and Discussion

Non-equilibrium conditions and kinetic reaction control

Figure 2 shows STM images taken after the deposition of 1,3-dibromoazulene (DBAz) on Cu(111) at 300 K, using four different coverages. At this temperature, the C–Br bonds dissociate, as was confirmed by XPS (see Figure S1 in the Supporting Information). The resulting debrominated azulene units form organometallic oligomers with C-Cu-C bonds, as shown in Figure 1.[9] According to previous work, the C–Cu bond is stable over the duration of the experiment at 300 K.[7,40–42] Therefore, we have a non-equilibrium situation of kinetic reaction control, which means that the initially formed product (i.e., the species that is produced with the fastest rate) prevails.

Statistically, the formation of chains is expected to be favored under these conditions, because there are more conformers (i.e., possible realizations) for an *n*-membered chain

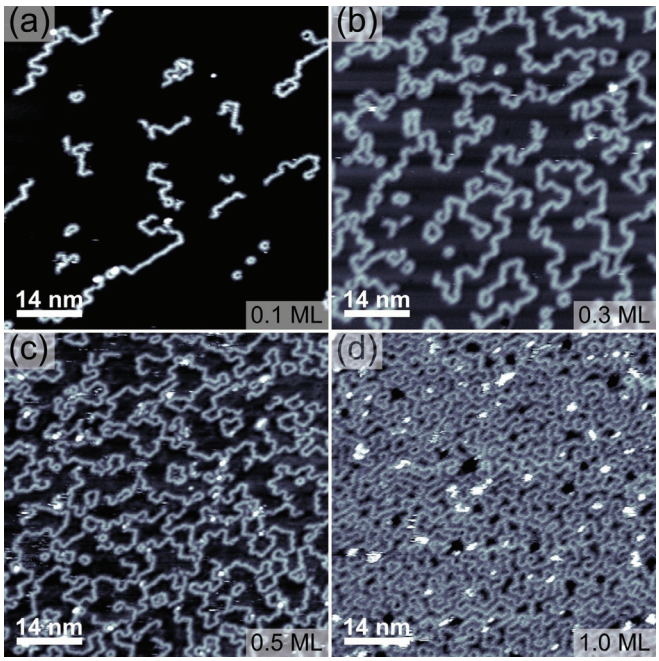

Figure 2. STM images of DBAz on Cu(111) after deposition at 300 K for four different coverages as indicated in the images. Tunneling parameters: (a) $U=-3.52$ V, $I=-0.09$ nA; (b) $U=-1.74$ V, $I=-0.15$ nA; (c) $U=-3.63$ V, $I=-0.16$ nA; (d) $U=-1.85$ V, $I=-0.11$ nA.

compared to an *n*-membered ring.[9] A small *n*-membered ring, such as the hexamer in Figure 1 with $n=6$, requires *cis*-configuration of all azulene units. Since an individual unit is *cis*-oriented relative to an existing segment with a probability of 0.5, the total probability for the formation of an *n*-membered ring is 0.5^{n-1}. All other, mixed *cis*/*trans* configurations with *n* segments can only form chains and therefore have a total combined probability of $1–0.5^{n-1}$. In the case of $n=6$, the probability for the formation of a hexamer under kinetic control is therefore only 1/32. Noteworthy, larger macrocycles may contain segments with *trans*-oriented units, which leads to a more complex situation.

Another important factor that controls the ring/chain ratio is the coverage, because the ring closure and the chain growth have different reaction orders and thus the ratio of their rates is coverage-dependent.[6,9] Generally, the intramolecular ring closure as a first-order reaction (Equation 1) with the rate constant k_{intra} prevails at low precursor coverage, while the chain growth as an intermolecular second-order reaction (Equation 2) with the rate constant k_{inter} will increasingly compete when the coverage is increased.[6]

$$M_6 \xrightarrow{k_{intra}} C_6 \quad (1)$$

$$M_i + M_1 \xrightarrow{k_{inter}} M_{i+1} \quad (2)$$

Based on these considerations, the STM data in Figure 2 can be understood qualitatively. In the following, we will discuss the relative yield of rings, especially of the dominant cyclic hexamers. This yield is defined as the percentage of monomer units incorporated in the cyclic hexamers.

Analysis for the sample with the lowest coverage (0.1 ML, Figure 2a) reveals that only 3% of the monomer units are incorporated in cyclic hexamers, close to the statistically expected value of $0.5^5 = 3.125\%$.[9] Increasing the coverage to 0.3 and 0.5 ML (Figure 2b,c) reduces the yield of rings to 2%. For the saturation coverage at 300 K (Figure 2d, coverage defined as 1.0 ML), the yield is even lower with 1%. Thus, the data show the expected trend of lower ring yields at higher coverages.

In homogeneous reactions (gas phase or solution), one advantage of ring closure over chain growth arises from the fact that the latter requires the bond formation between two reactants. As a result, three degrees of translational freedom and three degrees of rotational freedom of the two reactants are converted into six new degrees of vibrational freedom of the product, lowering its entropy content. Accordingly, ring formation can be entropically favored over chain formation.[43] In the adsorbed state, however, these translational and rotational degrees of freedom of the reactants are already mostly frustrated, that is, converted to vibrations. The loss of entropy content during chain formation is therefore expected to be much smaller. The situation may even be reversed, because the open radical ends of the reactants are expected to bind more strongly to the surface, and thus have less degrees of translational and rotational freedom than the product they form.

Equilibrium conditions and thermodynamic reaction control

The four different samples from Figure 2 were annealed to 440 K for 5 minutes and then cooled rapidly to the imaging temperature of 100 K. The temperature of 440 K was chosen to ensure chemical equilibrium, that is, fast reversible formation and dissociation of the organometallic C–Cu bonds. This reversible character of the C–Cu bonds at elevated temperatures at and above 440 K is well established.[5,44] Under these conditions, the product composition is given by the equilibrium constant and thus reflects the thermodynamic stability of the products. As shown by the STM images in Figure 3, now the cyclic hexamers are formed with much higher yields, indicating that they represent the thermodynamically more stable product.[9]

For the low-coverage sample (0.1 ML, Figure 3a), the ring yield is increased from 3% under kinetic control to 78% under thermodynamic control. For the samples with coverages of 0.3 and 0.5 ML (Figure 3b,c and Figure S2 in the Supporting Information) the ring yields are now 22 and 17%, respectively, which is also significantly increased compared to kinetic control. At 1.0 ML, large lateral fluctuations of the local concentration of rings are observed (Figures 3d and 3e). Apparently, the rings are sufficiently mobile at 440 K to aggregate into large islands, as shown in Figure 3e. These islands are stabilized by the interaction with the split-off Br atoms, which can be seen in Figure S3g,h in the Supporting Information.[5,45] In Figure 3f, the ring yields are plotted as functions of the coverage, illustrating that thermodynamic control leads to much higher ring yields than kinetic control.

Enlarged images of islands of hexamers are displayed in Figure 4 and Figures S3 and S4 in the Supporting Information. The images in Figures 4a and 4b were taken at different tunneling conditions. In Figure 4a, the Cu atoms appear as protrusions, whereas Figure 4b also shows the azulene units as bright uniform features. Related images of the chains at differ-

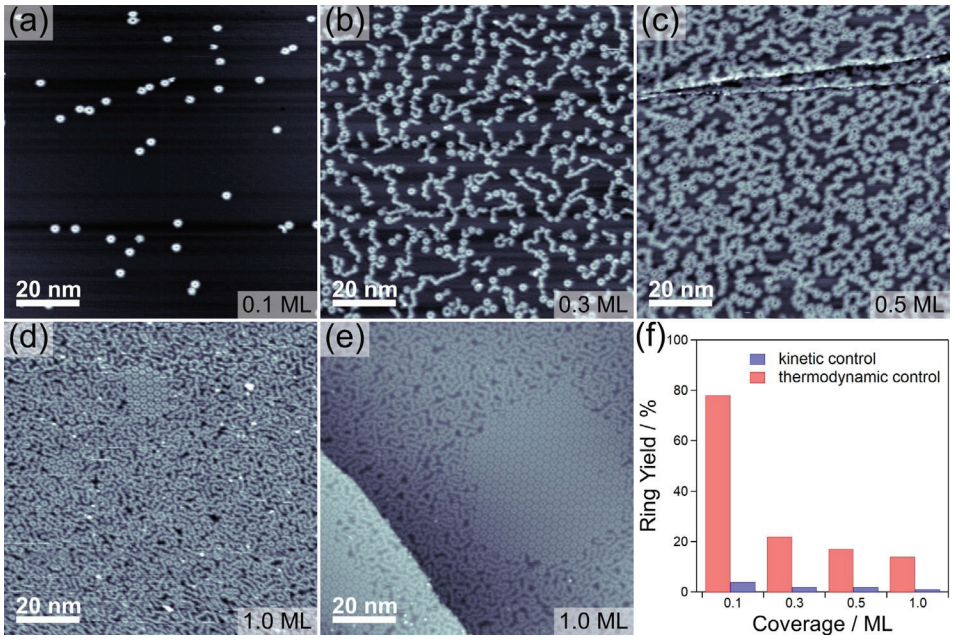

Figure 3. (a)–(e) STM images of DBAz on Cu(111) after annealing the four samples shown in Figure 2 to 440 K. Coverages as indicated in the images. For 1.0 ML, two different sample regions are shown. (f) Relative yield of hexamer rings as a function of the total coverage at 300 K (kinetic control) and 440 K (thermodynamic control). The percentage of rings (ring yield) is defined here as the total number of repeat units contained in cyclic hexamers divided by the total number of repeat units contained in chains and rings. Tunneling parameters: (a) $U = -2.84$ V, $I = -0.13$ nA; (b) $U = -1.10$ V, $I = -0.12$ nA; (c) $U = -3.52$ V, $I = -0.19$ nA; (d) $U = -3.63$ V, $I = -0.10$ nA; (e) $U = -3.31$ V, $I = -0.11$ nA.

P2

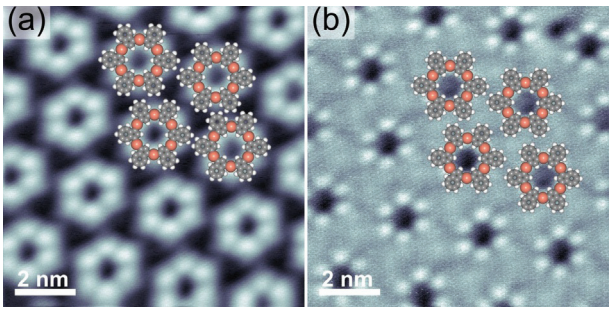

Figure 4. STM images of an island of the cyclic hexamer macrocycles, taken at different tunneling conditions, with overlaid molecular models. In image (a), the bridging Cu atoms are shown as bright protrusions, whereas (b) also shows the azulene units as bright features. Tunneling parameters: (a) $U=-0.94$ V, $I=-0.10$ nA; (b) $U=1.79$ V, $I=0.10$ nA.

ent tunneling conditions are shown in Figure S5 in the Supporting Information).

The formation of cyclic hexamers is remarkable, because they are strained, while the structure of the azulene molecule should enable the formation of strain-free cyclic decamers. The predominant formation of hexamers is attributed to registry effects. Azulene adsorbed on Cu(111) prefers adsorption sites on which the long molecular axis is aligned along a high-symmetry direction of the surface,[34] resulting in six possible preferential orientations. In the cyclic hexamer, all azulene units can assume their preferred orientation, while this is not the case for the cyclic decamer. The latter, although unstrained, is therefore energetically unfavorable. In rare cases, cyclic octamers were observed (see Figure S6 in the Supporting Information).

The variation of the ring yield with coverage (Figure 3 f) reflects the dynamic character of the chemical equilibrium between rings and chains. As mentioned above, the ring closure and chain growth have different reaction orders. With increasing coverage, the rate of the second-order chain growth increases faster than that of the first-order ring closure. As a result, the equilibrium is shifted towards the side of the chains as the coverage increases. (This trend is also reproduced by the MC simulations, as shown below and in Figure S10 in the Supporting Information)

The very high ring yield observed at the lowest coverage (see Figure 3 a and Figure S7 in the Supporting Information) is reminiscent of a specific result of the Jacobson–Stockmayer (J–S) theory. It predicts the existence of a critical concentration, below which the system consists entirely of rings.[1] However, the J–S theory was derived for rings that are sufficiently large to avoid short-range steric effects. Only then, the probability of the ring closure can be expressed as a well-defined function of the ring size. Here, we consider a 2D system, in which the molecules are confined to certain lattice sites. This confinement influences both the energy and the entropy term of the reaction free enthalpy (see below). The effects of the 2D confinement on the energy include the adsorbate–surface interaction energy and steric strain resulting from a forced planar geometry. The entropy term is influenced by excluding all non-planar conformations. Especially in the case of chains, which have a larger number of non-planar conformations than the rings, the 2D confinement should substantially reduce their entropy. The small size and the strained structure of the cyclic hexamers, along with effects of the 2D confinement, therefore limit the applicability of the J–S model for 2D systems, as was also previously observed.[6] As a consequence, we resorted to MC simulations to gain further insight into the different types of reaction control.

Monte Carlo simulations

In the MC model shown in Figure 5, the triangular lattice of equivalent adsorption sites represents a highly symmetric (111) surface, such as Cu(111). The azulene units are abstractly modelled as two planar, interconnected segments with an active part (red) and an inactive part (grey). One segment can occupy one adsorption site on the lattice, as is experimentally justified, because the azulene molecules show a strong adsorption site preference with alignment of the long molecular axis parallel to the high-symmetry directions of the Cu(111) surface.[34] The bonds between the model molecules are directional and limited to neighboring adsorption sites on the lattice. The molecules interact with the energy $\varepsilon=-1.0$. All remaining interactions, including the molecule-molecule and molecule-surface interactions, are neglected. The MC simulations were carried out in the canonical ensemble, where the number of molecules N, the size of the system L, and the temperature T were constant.[46,47] For further details, see the Experimental and Computational Details section.

Figure 6 shows the results of the MC simulations for low-temperature non-equilibrium conditions (Figures 6 a and 6 c, kinetic reaction control) in comparison with the high-temperature equilibrium conditions (Figures 6 b and 6 d, thermodynamic reaction control). The ratio of the two temperatures is the same as in the experiment (440 K, 300 K) with $T_{high}/T_{low}=1.47$. At low coverage under kinetic control (Figure 6 a), a considerable number of chains is formed, whereas cyclic hexamers dominate under thermodynamic control (Figure 6 b). Comparison of the simulated with the corresponding experimental

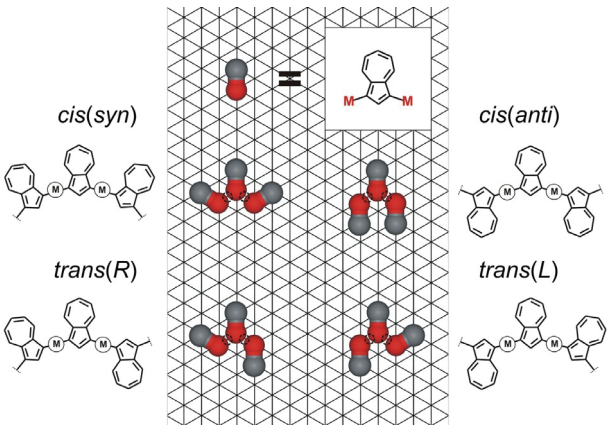

Figure 5. Model for the MC simulations. The azulene units are abstractly modeled as planar, interconnected segments with an active part (red) and an inactive part (grey). Four different connection motifs of three units are shown.

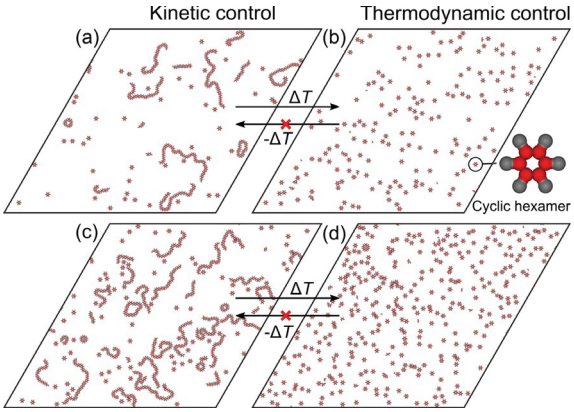

Figure 6. MC simulations with the model in Figure 5 for two different coverages ((a), (b) 0.05, and (c), (d) 0.1) and two different temperatures. The temperatures have a ratio of $T_{high}/T_{low} = 1.47$, which is identical to the experimental ratio. (a), (c) Low temperature, non-equilibrium conditions, kinetic control. (b), (d) High temperature, equilibrium conditions, thermodynamic control. The arrows between (a) and (b) as well as (c) and (d) express that it is possible to shift the systems from the non-equilibrium to the equilibrium state by increasing the temperature, whereas it is not possible to go the reverse way by lowering the temperature.

data (e.g., Figure 2a vs. Figure 6a and Figure 3a vs. Figure 6b) reveals a good qualitative agreement, which is quite remarkable considering the high degree of abstraction in the model system. It shows that the model captures important features of the system, in particular the transformation from kinetic to thermodynamic control, and that these features have a high degree of commonality.

Doubling the coverage (Figures 6c and 6d) leads to qualitatively similar results: At low temperature (Figure 6c), the formation of chains prevails, whereas high-temperature conditions lead to the formation of mostly hexamer macrocycles (Figure 6d). In the simulations, sometimes larger rings than cyclic hexamers are observed. An experimental example is shown in Figure S8 in the Supporting Information. Further MC simulations for two additional coverages are shown in the Supporting Information, Figures S11 and S12.

Figure 7 compares the relative abundances (fractions) of the four different main structural motifs, as defined in Figure 7a. The color code in Figure 7a corresponds to the colors in the bar graphs in Figures 7b–7g. The *cis*(*syn*) motif (red) is the only motif that occurs in the cyclic hexamers, while it rarely occurs in chains. All other motifs, that is, *cis*(*anti*), *trans*(*R*) and *trans*(*L*), occur only in chains. Therefore, the abundance of the *cis*(*syn*) (red), compared to the abundances of the other motifs, is a good approximation for the ratio of rings versus chains.

The data in Figure 7 reveal that the transition from kinetic to thermodynamic control leads to an increased formation of the *cis*(*syn*) motif. At the lowest coverage (Figures 7b and 7e), this change is very substantial, as the fraction of *cis*(*syn*) increases from 0.32 to 0.98.

The coverage-dependent changes in the regime of thermodynamic control (*cf.* Figures 7e–7g) reveal that the macrocycles are less favored at higher coverages. The same trend was observed experimentally (*cf.* Figure 3f) and was explained

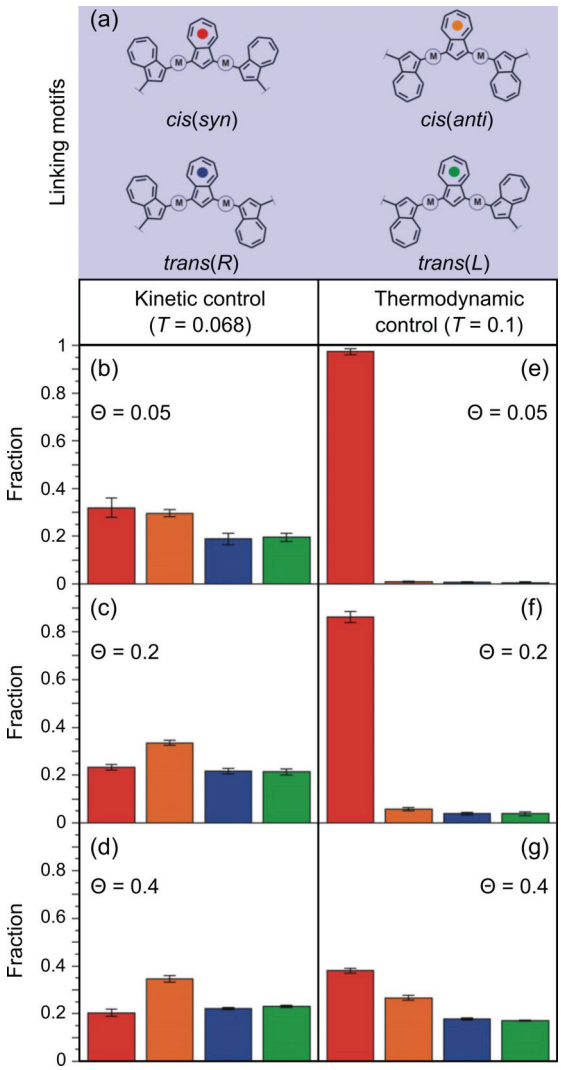

Figure 7. Relative abundances (fractions) of the main structural linking motifs defined in (a), obtained from the MC simulations for different coverages and temperatures. The presented results are averages from 10 independent systems. (b)–(d) Low temperature, kinetic control; (e)–(g) high temperature, thermodynamic control. The colors in the bar graphs correspond to the color scheme defined in (a).

above by the different reaction orders for ring and chain formation. The fact that the rather abstract MC model describes these trends correctly indicates that the ring/chain ratio is indeed largely controlled by fundamental principles, rather than specific properties of our system. Complete quantitative agreement for the abundances for the different structural motifs in experiment and simulation cannot be expected, because the equilibrium is additionally influenced by factors neglected in the MC simulations, especially molecular structure, specific interaction with the surface, or intermolecular interactions.

In the regime of kinetic control, similar coverage-dependent trends are observed (Figures 7b–7d). With increasing coverage, the fraction of the ring-related *cis*(*syn*) motif decreases. In contrast, the fractions of the other motifs increase, especially that of the *cis*(*anti*) motif (orange), which occurs in straight chain

segments. The same trend was observed in the experiment (*cf.* Figure 2 and Figure 3 f).

Optimal reaction temperature for ring formation

Above, we have shown by experiment and simulation that the ring yield under thermodynamic control depends on the coverage of azulene monomers. Now, we focus on the influence of the temperature and determine, whether there is an optimal temperature, at which the ring yield reaches its maximum. For this aim, an intermediate coverage of 0.5 ML of DBAz was deposited on Cu(111) at 300 K. Thereafter, the sample was stepwise annealed for 5 minutes, followed by rapid cooling to the imaging temperature of 100 K (Figure 8).

Deposition of DBAz at 300 K leads to predominant chain formation and a low ring yield (3%, Figure 8a), in agreement with the result discussed above for kinetic control. Annealing this sample to 350 K does not increase the ring yield (Figure 8b). Apparently, this temperature is still within the regime of kinetic control. It requires annealing to 390 K to observe a slight increase of the ring yield to 8% (Figure 8c). The maximum ring yield of 20% is obtained after annealing at 430 K (Figure 8d). This value is slightly higher than that obtained after annealing a different sample with the same coverage to 440 K (*cf.* Figure 3c, 17%). If the sample is annealed to 460 K (Figure 8e and Figure S9 in the Supporting Information), the trend is reversed and a decrease in the ring yield to 18% is observed. Further annealing to 470 K (Figure 8f) is accompanied by the onset of desorption. As a result, the residual coverage is reduced to 0.4 ML, while the ring yield remains at 18%. The temperature dependence of the ring yield is summarized in Figure 9a.

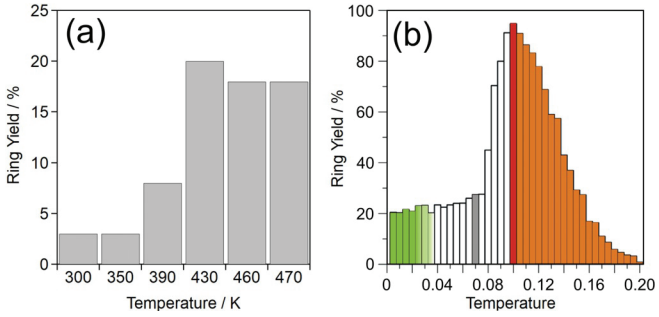

Figure 9. (a) Yield of hexamer rings as a function of temperature, as derived from the STM images in Figure 8. (b) Percentage of molecules contained in hexamer rings in the MC simulations as a function of temperature (for a coverage of 0.05). The green bars indicate temperatures at which on-surface diffusion of the molecules is very slow. Bars marked in orange correspond to high temperatures, at which competing processes such as desorption or degradation are significant in experimental systems.

Monte Carlo simulations

The MC simulations (Figure 9b) showed that the yield of hexagonal rings has a maximum at an intermediate temperature, in qualitative agreement with the experimental data. The existence of an optimal temperature for macrocycle formation can be understood based on the principles introduced above: At low temperatures, kinetic control favors chain formation at the expense of ring formation. This explains the low ring yields in the low-temperature range.

The decreasing ring yields at high temperatures, that is, under thermodynamic control, require a thermodynamic argument based on the standard free enthalpy $\Delta G^\circ = \Delta H^\circ - T\Delta S^\circ$, which determines the ring/chain equilibrium. (ΔH° *is* the stan-

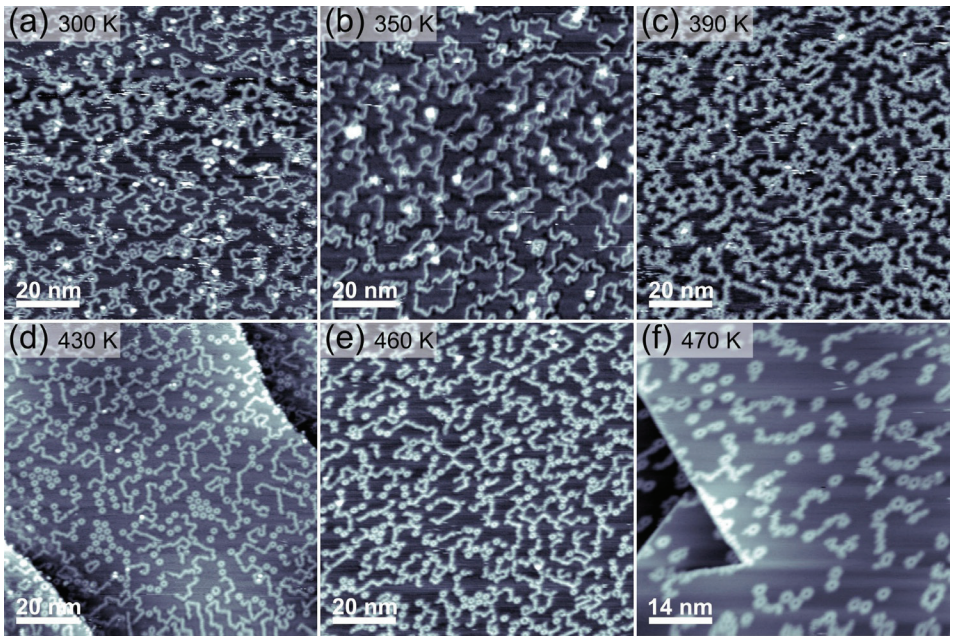

Figure 8. STM images of 0.5 ML DBAz on Cu(111) after deposition at 300 K and annealing (5 minutes) to the indicated temperatures, followed by rapid cooling to 100 K for imaging. Tunneling parameters: (a) $U=-3.63$ V, $I=-0.14$ nA; (b) $U=-3.63$ V, $I=-0.13$ nA; (c) $U=-3.63$ V, $I=-0.14$ nA; (d) $U=-3.63$ V, $I=-0.10$ nA; (e) $U=-3.63$ V, $I=-0.11$ nA; (f) $U=-3.63$ V, $I=-0.25$ nA.

dard enthalpy, ΔS° is the standard entropy, and T is the temperature.) The chains are entropically favored, because there are more possible conformers for an *n*-membered chain compared to an *n*-membered ring. Therefore, the rings must be energetically favored, because otherwise they would not exist at all in equilibrium. The ring closure of a chain therefore has a negative ΔH° and a negative ΔS°. With increasing temperature, the ΔH° term remains approximately constant, whereas the $T\Delta S^\circ$ term strongly increases and makes ΔG° for the ring closure reaction more positive. Since ΔG° is related to the equilibrium constant K^+ via $\Delta G^\circ = -RT\ln K^+$, a more positive ΔG° means that the equilibrium is shifted towards the chains with increasing temperature. In simpler terms, one can argue that the ring closure is an exothermic reaction, for which the equilibrium is shifted to the side of the reactant (i.e., the chain) with increasing temperature, according to the Le Châtelier–Braun principle. In conclusion, the optimum temperature for ring formation is just high enough to reach the regime of thermodynamic control, but not higher, because this reduces the ring yield.

Effective molarity

The concept of the effective molarity (EM) has been introduced for homogeneous (i.e., gas phase or solution) cyclization reactions as a measure for the preference of the intramolecular ring formation over the intermolecular chain growth.[48,49] To our knowledge, this concept has not yet been applied to surface reactions. For kinetic reaction control, the EM is defined as the ratio of the rate constant for the intramolecular over that for the intermolecular reaction k_{intra}/k_{inter}, whereas for thermodynamic control it is the ratio of the corresponding equilibrium constants K_{intra}/K_{inter} (*cf.* Scheme 1).[49]

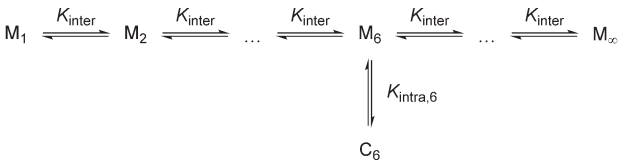

Scheme 1. Reaction Scheme of the equilibrium between the open-chain *i*-mers M_i (equilibrium constant K_{inter}) and the cyclic hexamer C_6 (intramolecular equilibrium constant $K_{intra,6}$).

For on-surface kinetic reaction control, it is not possible to determine the rate constants by real-time STM monitoring, because the reactions are too fast compared to the temporal resolution of the STM experiment. However, the post-reaction product composition can be analyzed with STM and be used to obtain the EM as the ratio of the rate constants. For this, we assume that each addition of a monomer unit to an existing chain corresponds to the intermolecular reaction taking place with the rate constant k_{inter}, whereas each ring closure of an open chain takes place with k_{intra}. For instance, the effective molarity for the cyclic hexamer $EM_6 = k_{intra,6}/k_{inter}$ (where $k_{intra,6}$ is the rate constant for the cyclization of a hexamer chain) can be calculated by dividing the number of cyclic hexamers (which is proportional to $k_{intra,6}$) by the total number of monomers minus the number of rings and chains (to take into account that formation of an oligomer takes one addition reaction less than the total number of monomers). The resulting values for the kinetic EM_6 are plotted as a function of the coverage in Figure 10b; the corresponding data are listed in Table S1 in the Supporting Information.

In the case of thermodynamic control, the determination of the equilibrium constants is in principle also possible by STM-based post-reaction product analysis. The equilibrium EM for a cyclic *i*-mer is defined as $EM_i = K_{intra,i}/K_{inter}$ with the equilibrium constant between an open chain M_i and the cyclic *i*-mer C_i according to $K_{intra,i} = [C_i]/[M_i]$. K_{inter} is the equilibrium constant for the intermolecular model reaction between monofunctional reactants.[50] In our case, this corresponds to the equilibrium constants between chains of different lengths, as shown in Scheme 1. While the concentration of cyclic hexamers can easily be obtained from the STM images by counting, this is not as trivial for the concentration of the corresponding hexamer chains, because the chain lengths are more difficult to measure. Furthermore, only a very small fraction of the chains are hexamers. Thus, a reasonably accurate determination of $K_{intra,i}$ from our experiments is not possible. Additionally, the value for K_{inter} cannot be obtained from the given experiments but would have to be known from literature data.

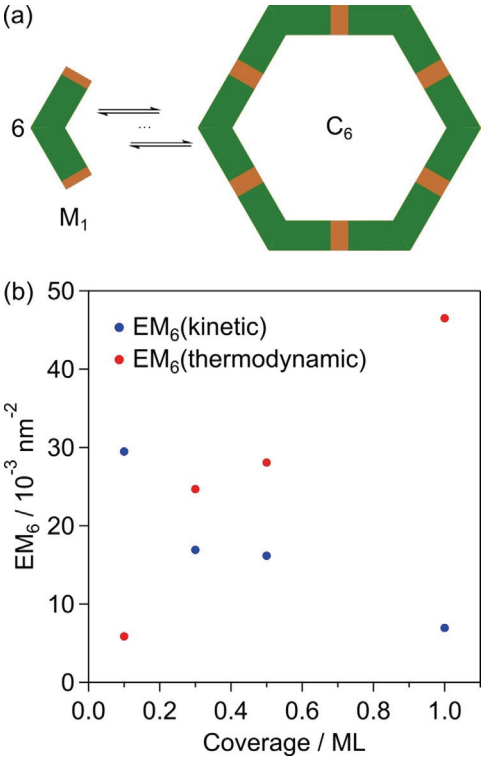

Figure 10. (a) Scheme illustrating the preferred formation of a cyclic hexamer C_6 from six monomers M_1 with two identical functionalities. (b) EM_6 values as a function of the coverage under kinetic reaction control for the four samples shown in Figure 2 and under thermodynamic reaction control as a function of the coverage for the four samples shown in Figure 3.

P2

However, we observe the strong preference of cyclic hexamers over all other ring sizes. This preferential formation of one ring size is known in solution chemistry as self-assembly macrocyclization[51] (which is not to be confused with the self-assembly on surfaces). As illustrated in Figure 10a, six monomers M_1 with two identical functionalities preferably form a cyclic hexamer C_6. The oligomerization proceeds successively starting from a single monomer M_1, which is in equilibrium to chains of different lengths M_i with the intermolecular equilibrium constant K_{inter} (Scheme 1). Only one macrocycle, here the hexamer C_6, is strongly preferred so that it can be formed from the open-chain hexamer M_6 with the respective intramolecular equilibrium constant $K_{intra,6}$. Under the assumption that K_{inter} is independent of the chain length, the concentration of the cyclic *i*-mer can be calculated by $[C_i] = EM_i x^i$, with x being the fraction of reacted end groups in the acyclic fraction of the product mixture.[50] This x can be determined by counting the number of chains and taking into account the total number of monomers (see Table S2 in the Supporting Information). The resulting thermodynamic EM_6 values are shown in Figure 10b. Comparison reveals that the kinetic EM decreases with increasing coverage, while the thermodynamic EM shows the opposite trend. The coverage-dependence of the EM is unexpected and requires interpretation. Both the kinetic and thermodynamic EM are exclusively composed of constants and thus should not depend on the coverage. Nevertheless, this behavior can be understood on a qualitative level. The increase of the thermodynamic EM towards higher coverages means that macrocyclization is overly favored in the high-coverage range. This can be explained by the formation of islands of the cyclic hexamer (*cf.* Figure 3e). The hexamers inside these islands are removed from the equilibrium, resulting in an additional equilibrium shift towards the macrocycle side, according to the Le Châtelier–Braun principle. The beginning of this island formation can already be observed for the coverages of 0.3 and 0.5 ML (*cf.* Figure 3c,d). In the case of kinetic control, it must be considered that the concentrations used here are very high compared to typical reactions in solution. At the highest coverage of 1 ML, the reactants completely fill the available space. For a reaction in the three-dimensional liquid phase, this would be equivalent to the complete absence of a solvent. Under these conditions, the mobility and flexibility of the reactants is strongly reduced. As the coverage increases, the ends of longer chains get increasingly immobile compared to monomers, lowering the probability for ring closure relative to that for the addition of monomers to existing chains. The observed substantial deviations from the expected ideal behavior show that the applicability of the EM concept to on-surface chemistry is limited due to substrate and high-concentration effects.

Conclusions

The ring/chain competition in on-surface organometallic oligomerization was studied in the regimes of kinetic and thermodynamic reaction control using STM and MC simulations. At room temperature, the oligomerization is kinetically controlled and results mainly in the formation of the entropically favored chains, which are formed with a higher statistical probability and thus with higher rates, as was confirmed by MC simulations. Rings prevail at higher temperatures, where the oligomerization is thermodynamically controlled and thus the energetically most stable product is preferentially formed. The ring/chain ratio is coverage-dependent, with higher coverages resulting in lower ring yields both in the experiment and the simulations. This observation can be explained by the different orders of the reactions competing in the dynamic equilibrium: With increasing coverage, the rate of the second-order chain growth increases faster than that of the first-order ring closure. The ring/chain equilibrium is also temperature-dependent and responds to increasing temperatures with lower ring yields, in line with the exothermic nature of the ring formation. Hence, there is a temperature optimum for the ring formation: It is sufficiently high to reach the regime of thermodynamic control, but otherwise as low as possible. Differences to macrocyclization in solution, as revealed by effective molarity considerations, are attributed to the 2D confinement, the preference of certain adsorption sites, and the high concentrations typically used in on-surface synthesis.

Experimental and Computational Details

The experiments were performed in an ultrahigh vacuum (UHV) system (base pressure 2×10^{-10} mbar) equipped with a SPECS Aarhus 150 variable-temperature STM, a SPECS Phoibos 150 electron energy analyzer, and a monochromatized Al Kα X-ray source (SPECS XR 50M, FOCUS 500). STM images were obtained with an electrochemically etched W tip at 100 K in constant current mode and processed with WSxM 5.0 Develop 8.5.[52] All voltages refer to the sample. Moderate filtering (Gaussian smooth, background subtraction) was applied for noise reduction. The Cu(111) single crystal (purity 99.9999%, roughness <0.01 μm, orientation accuracy $<0.1^\circ$, from MaTecK, Germany) was prepared by iterated sputtering with Ar^+ ions (1 keV, 12 μA, 30 min) and annealing (800 K, 10 min). Sample temperatures were measured with a thermocouple directly mounted to the Cu(111) crystal. DBAz (purity >98.0%) was purchased from TCI and deposited on the Cu(111) surface using a custom-built low-temperature Knudsen cell evaporator cooled to 195 K.

The simulations were performed on a rhombic fragment of the triangular lattice with linear size L equal to 200 adsorption sites. To eliminate edge effects, periodic boundary conditions in both directions were imposed. Intermolecular interactions were limited to nearest-neighbor sites on the lattice. The conventional MC method in the canonical ensemble with Metropolis sampling[46,47] was used as follows. In the first step, N molecules were randomly distributed on the surface and the temperature T was fixed. Next, a molecule was picked up at random and its potential energy U_0 was calculated by reckoning the interactions with neighboring molecules. Each of these interactions contributed with ε to U_0. The selected molecule was then moved to a new random position on the lattice and rotated by a multiple of ±60 degrees. If the insertion therein was successful, the potential energy in the new position U_n was obtained using the same procedure as for U_0; otherwise the simulation started from the beginning. To accept the new configuration, the probability factor $p = \min[1, \exp(-\Delta U/kT)]$, where $\Delta U = U_n - U_0$ and k is the Boltzmann factor, was calculated and compared with a

randomly generated number $r \in (0,1)$. If $r < p$, the new configuration was accepted, otherwise the molecule was left in the original (old) position. The above sequence, which constitutes one MC step, was repeated $N \times 10^6$ times to obtain the snapshots and statistics. The average values reported herein were taken over ten independent system replicas using 1% of the final MC steps of each simulation run. Energies and temperatures of our model are expressed in units of ε and $|\varepsilon|/k$, respectively. The surface coverage in the MC simulations was defined as the average number of molecular segments per lattice site, i.e., $2NL^{-2}$. The simulations were performed using 1000, 2000, 4000 and 8000 molecules, which corresponds to the MC surface coverages equal to 0.05, 0.1, 0.2 and 0.4, respectively. Note that the coverages in experiment and simulation have no direct correspondence. Comparison is only meaningful on a qualitative level (e.g., low vs. high coverage). The temperatures in the simulation have the same ratio (T_{high}/T_{low}) as in the experiment, while the absolute temperatures cannot be compared, because the temperature in the simulation is defined with respect to the arbitrary basic energy unit ε. Although we applied Metropolis sampling, which is aimed at reproducing Boltzmann statistics, i.e., the equilibrium case, metastable states can be trapped by immediate cooling directly after the first MC step. This procedure is equivalent to kinetic reaction control in the experiment.

Supporting Information available: X-ray photoelectron spectra, additional STM images, additional MC simulations, data for the effective molarity considerations.

Acknowledgements

Financial support by the Deutsche Forschungsgemeinschaft (DFG, German Research Foundation) through project number 223848855-SFB 1083 and GO1812/2-1 is gratefully acknowledged. Q.F. thanks the Alexander von Humboldt Foundation for a fellowship for postdoctoral researchers. We thank Florian Fillsack, Johannes Glowatzki und Nicole Trebel for support during the measurements.

Conflict of interest

The authors declare no conflict of interest.

Keywords: chain structures · macrocycles · metal–organic frameworks · polymerization · surface chemistry

[1] H. Jacobson, W. H. Stockmayer, *J. Chem. Phys.* **1950**, *18*, 1600 – 1606.
[2] M. Gordon, W. B. Temple, *Makromol. Chem.* **1972**, *152*, 277 – 289.
[3] X.-F. Yuan, A. J. Masters, C. V. Nicholas, C. Booth, *Makromol. Chem.* **1988**, *189*, 823 – 832.
[4] T. Josse, J. De Winter, P. Gerbaux, O. Coulembier, *Angew. Chem. Int. Ed.* **2016**, *55*, 13944 – 13958; *Angew. Chem.* **2016**, *128*, 14150 – 14164.
[5] Q. Fan, C. Wang, Y. Han, J. Zhu, J. Kuttner, G. Hilt, J. M. Gottfried, *ACS Nano* **2014**, *8*, 709 – 718.
[6] Q. Fan, T. Wang, J. Dai, J. Kuttner, G. Hilt, J. M. Gottfried, J. Zhu, *ACS Nano* **2017**, *11*, 5070 – 5079.
[7] Q. Fan, C. Wang, Y. Han, J. Zhu, W. Hieringer, J. Kuttner, G. Hilt, J. M. Gottfried, *Angew. Chem. Int. Ed.* **2013**, *52*, 4668 – 4672; *Angew. Chem.* **2013**, *125*, 4766 – 4770.
[8] Q. Fan, J. Dai, T. Wang, J. Kuttner, G. Hilt, J. M. Gottfried, J. Zhu, *ACS Nano* **2016**, *10*, 3747 – 3754.
[9] C. K. Krug, Q. Fan, F. Fillsack, J. Glowatzki, N. Trebel, L. J. Heuplick, T. Koehler, J. M. Gottfried, *Chem. Commun.* **2018**, *54*, 9741 – 9744.
[10] P. J. Flory, J. A. Semlyen, *J. Am. Chem. Soc.* **1966**, *88*, 3209 – 3212.
[11] G. Franc, A. Gourdon, *Phys. Chem. Chem. Phys.* **2011**, *13*, 14283 – 14292.
[12] J. Méndez, M. F. López, J. A. Martín-Gago, *Chem. Soc. Rev.* **2011**, *40*, 4578 – 4590.
[13] R. Lindner, A. Kühnle, *ChemPhysChem* **2015**, *16*, 1582 – 1592.
[14] Q. Fan, J. M. Gottfried, J. Zhu, *Acc. Chem. Res.* **2015**, *48*, 2484 – 2494.
[15] P. A. Held, H. Fuchs, A. Studer, *Chem. Eur. J.* **2017**, *23*, 5874 – 5892.
[16] M. Lackinger, *Chem. Commun.* **2017**, *53*, 7872 – 7885.
[17] Q. Sun, R. Zhang, J. Qiu, R. Liu, W. Xu, *Adv. Mater.* **2018**, *30*, 1705630.
[18] Q. Shen, H.-Y. Gao, H. Fuchs, *Nano Today* **2017**, *13*, 77 – 96.
[19] M. Chen, J. Shang, Y. Wang, K. Wu, J. Kuttner, G. Hilt, W. Hieringer, J. M. Gottfried, *ACS Nano* **2017**, *11*, 134 – 143.
[20] A. Gourdon in *On-Surface Synthesis*, Springer, Switzerland, **2016**.
[21] D. G. de Oteyza, C. Rogero in *On-Surface Synthesis II*, Springer, Switzerland, **2018**.
[22] S. Clair, D. G. de Oteyza, *Chem. Rev.* **2019**, *119*, 4717 – 4776.
[23] Q. Fan, J. Zhu, J. M. Gottfried in *Organometallic Structures and Intermediates in Surface Ullmann Coupling* (Ed.: K. Wandelt), Elsevier, Oxford, **2018**, pp. 343 – 353.
[24] J. Liu, T. Dienel, J. Liu, O. Groening, J. Cai, X. Feng, K. Müllen, P. Ruffieux, R. Fasel, *J. Phys. Chem. C* **2016**, *120*, 17588 – 17593.
[25] A. Shiotari, T. Nakae, K. Iwata, S. Mori, T. Okujima, H. Uno, H. Sakaguchi, Y. Sugimoto, *Nat. Commun.* **2017**, *8*, 16089.
[26] J. Hieulle, E. Carbonell-Sanromà, M. Vilas-Varela, A. Garcia-Lekue, E. Guitián, D. Peña, J. I. Pascual, *Nano Lett.* **2018**, *18*, 418 – 423.
[27] S. Mishra, M. Krzeszewski, C. A. Pignedoli, P. Ruffieux, R. Fasel, D. T. Gryko, *Nat. Commun.* **2018**, *9*, 1714.
[28] S. Mishra, T. G. Lohr, C. A. Pignedoli, J. Liu, R. Berger, J. I. Urgel, K. Müllen, X. Feng, P. Ruffieux, R. Fasel, *ACS Nano* **2018**, *12*, 11917 – 11927.
[29] D. Cui, M. Ebrahimi, J. M. Macleod, F. Rosei, *Nano Lett.* **2018**, *18*, 7570 – 7575.
[30] M. Liu, M. Liu, Z. Zha, J. Pan, X. Qiu, T. Li, J. Wang, Y. Zheng, D. Zhong, *J. Phys. Chem. C* **2018**, *122*, 9586 – 9592.
[31] H. Xin, X. Gao, *ChemPlusChem* **2017**, *82*, 945 – 956.
[32] Q. Sun, I. C.-Y. Hou, K. Eimre, C. A. Pignedoli, P. Ruffieux, A. Narita, R. Fasel, *Chem. Commun.* **2019**, *55*, 13466 – 13469.
[33] Q. Fan, D. Martin-Jimenez, D. Ebeling, C. K. Krug, L. Brechmann, C. Kohlmeyer, G. Hilt, W. Hieringer, A. Schirmeisen, J. M. Gottfried, *J. Am. Chem. Soc.* **2019**, *141*, 17713 – 17720.
[34] B. P. Klein, N. J. van der Heijden, S. R. Kachel, M. Franke, C. K. Krug, K. K. Greulich, L. Ruppenthal, P. Müller, P. Rosenow, S. Parhizkar, F. C. Bocquet, M. Schmid, W. Hieringer, R. J. Maurer, R. Tonner, C. Kumpf, I. Swart, J. M. Gottfried, *Phys. Rev. X* **2019**, *9*, 011030.
[35] X. Yang, F. Rominger, M. Mastalerz, *Angew. Chem. Int. Ed.* **2019**, *58*, 17577 – 17582; *Angew. Chem.* **2019**, *131*, 17741 – 17746.
[36] P. Y. Huang, C. S. Ruiz-Vargas, A. M. van der Zande, W. S. Whitney, M. P. Levendorf, J. W. Kevek, S. Garg, J. S. Alden, C. J. Hustedt, Y. Zhu, J. Park, P. L. McEuen, D. A. Muller, *Nature* **2011**, *469*, 389 – 392.
[37] F. Banhart, J. Kotakoski, A. V. Krasheninnikov, *ACS Nano* **2011**, *5*, 26 – 41.
[38] J.-C. Charlier, *Acc. Chem. Res.* **2002**, *35*, 1063 – 1069.
[39] K. Suenaga, H. Wakabayashi, M. Koshino, Y. Sato, K. Urita, S. Iijima, *Nat. Nanotechnol.* **2007**, *2*, 358 – 360.
[40] H. Walch, R. Gutzler, T. Sirtl, G. Eder, M. Lackinger, *J. Phys. Chem. C* **2010**, *114*, 12604 – 12609.
[41] M. Bieri, M.-T. Nguyen, O. Gröning, J. Cai, M. Treier, K. Aït-Mansour, P. Ruffieux, C. A. Pignedoli, D. Passerone, M. Kastler, K. Müllen, R. Fasel, *J. Am. Chem. Soc.* **2010**, *132*, 16669 – 16676.
[42] M. Di Giovannantonio, M. Tomellini, J. Lipton-Duffin, G. Galeotti, M. Ebrahimi, A. Cossaro, A. Verdini, N. Kharche, V. Meunier, G. Vasseur, Y. Fagot-Revurat, D. F. Perepichka, F. Rosei, G. Contini, *J. Am. Chem. Soc.* **2016**, *138*, 16696 – 16702.
[43] M. I. Page, W. P. Jencks, *Proc. Natl. Acad. Sci. USA* **1971**, *68*, 1678 – 1683.
[44] C.-X. Wang, J.-L. Chen, C.-H. Shu, K.-J. Shi, P.-N. Liu, *Phys. Chem. Chem. Phys.* **2019**, *21*, 13222 – 13229.
[45] J. Dai, Q. Fan, T. Wang, J. Kuttner, G. Hilt, J. M. Gottfried, J. Zhu, *Phys. Chem. Chem. Phys.* **2016**, *18*, 20627 – 20634.
[46] D. Nieckarz, P. Szabelski, *Chem. Commun.* **2014**, *50*, 6843 – 6845.
[47] P. Szabelski, W. Rżysko, D. Nieckarz, *J. Phys. Chem. C* **2016**, *120*, 13139 – 13147.

[48] R. Cacciapaglia, S. D. Stefano, L. Mandolini, *Acc. Chem. Res.* **2004**, *37*, 113 – 122.
[49] S. Di Stefano, L. Mandolini, *Phys. Chem. Chem. Phys.* **2019**, *21*, 955 – 987.
[50] G. Ercolani, L. Mandolini, P. Mencarelli, S. Roelens, *J. Am. Chem. Soc.* **1993**, *115*, 3901 – 3908.
[51] G. Ercolani, *J. Phys. Chem. B* **1998**, *102*, 5699 – 5703.
[52] I. Horcas, R. Fernández, J. M. Gómez-Rodríguez, J. Colchero, J. Gómez-Herrero, A. M. Baro, *Rev. Sci. Instrum.* **2007**, *78*, 013705.

Manuscript received: January 28, 2020
Accepted manuscript online: February 7, 2020
Version of record online: June 5, 2020

P2

Chemistry–A European Journal

Supporting Information

The Macrocycle versus Chain Competition in On-Surface Polymerization: Insights from Reactions of 1,3-Dibromoazulene on Cu(111)

Claudio K. Krug[+],[a] Damian Nieckarz[+],[b] Qitang Fan,[a] Paweł Szabelski,[b] and J. Michael Gottfried*[a]

1. X-ray photoelectron spectra

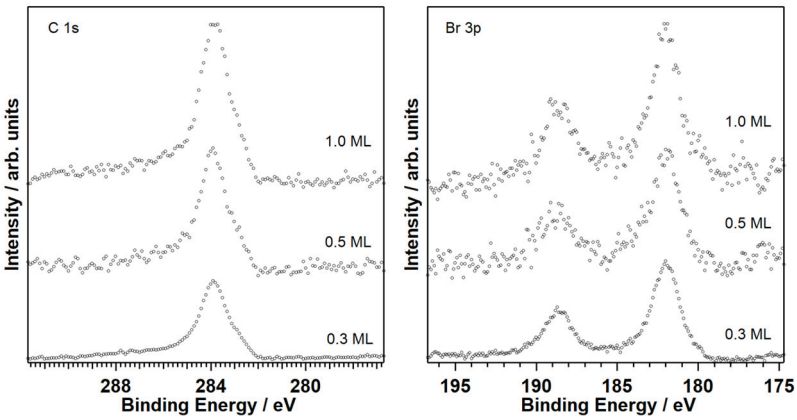

Figure S1. Normalized C 1s (left) and Br 3p (right) XP spectra for the three samples from Figure 2b-d of the main text. The C 1s spectra indicate the amount of deposited molecules, while the peak positions in the Br 3p spectra prove that scission of the C–Br bond is complete after deposition at 300 K.

2. Additional STM images

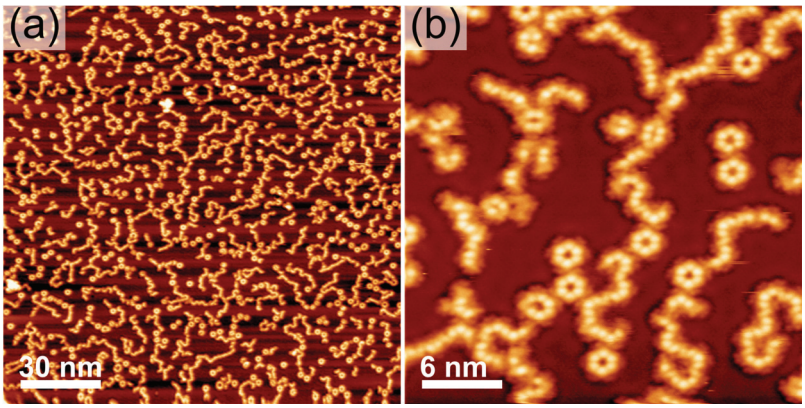

Figure S2. Additional STM images of the sample shown in Figure 3b of the main text. The images show a mixture of rings and chains. Coverage: 0.3 ML, tunneling parameters: (a) U = -1.10 V, I = -0.12 nA; (b) U = -1.10 V, I = -0.13 nA.

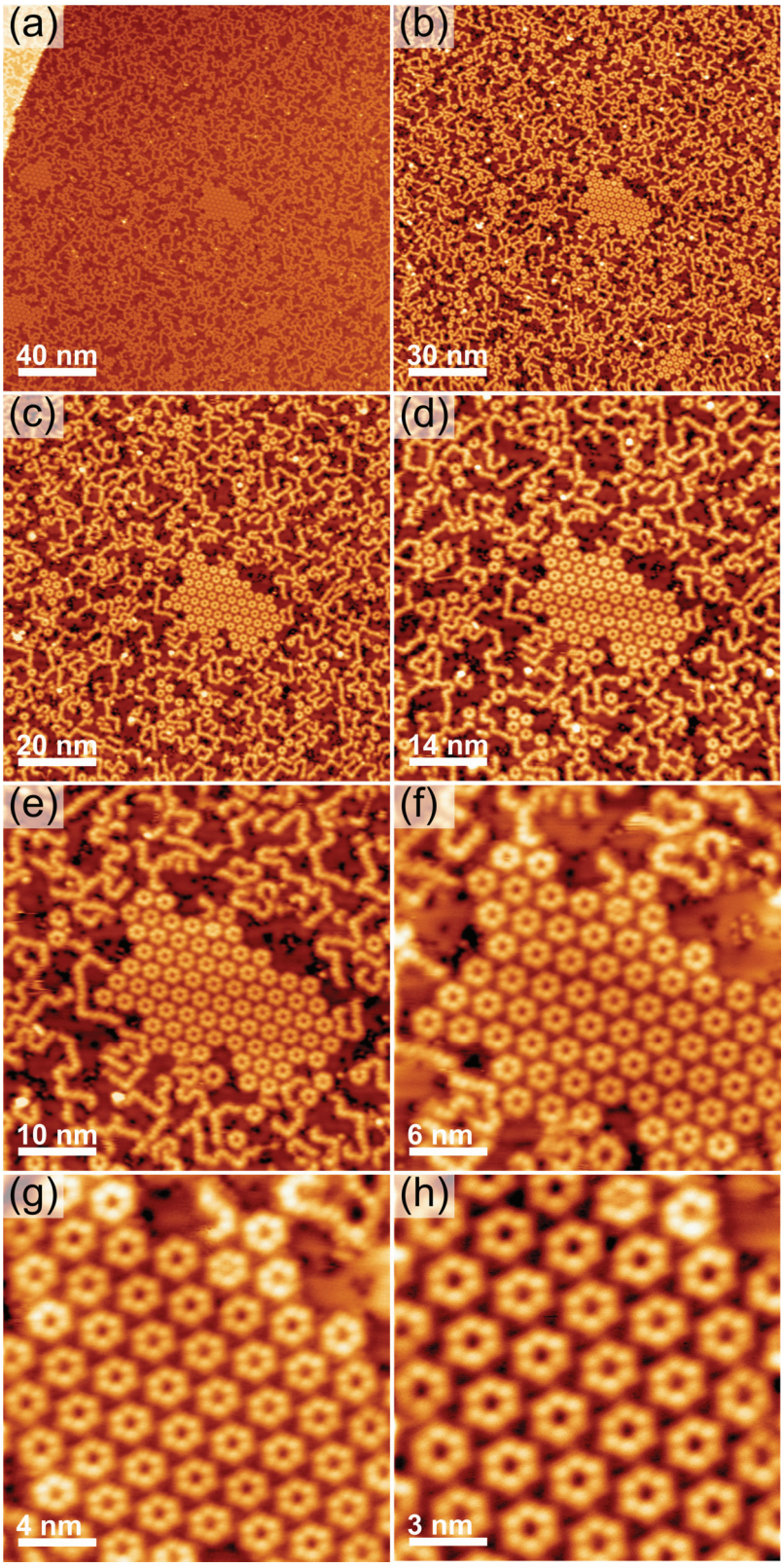

Figure S3. Series of STM images showing the zoom-in on an island of cyclic hexamers after annealing the sample shown in Figure 3c of the main text to 460 K. Coverage: 0.5 ML; tunneling parameters: (a) U = -1.03 V, I = -0.10 nA; (b) - (d) U = -1.03 V, I = -0.11 nA; (e) - (h) U = -1.03 V, I = -0.12 nA.

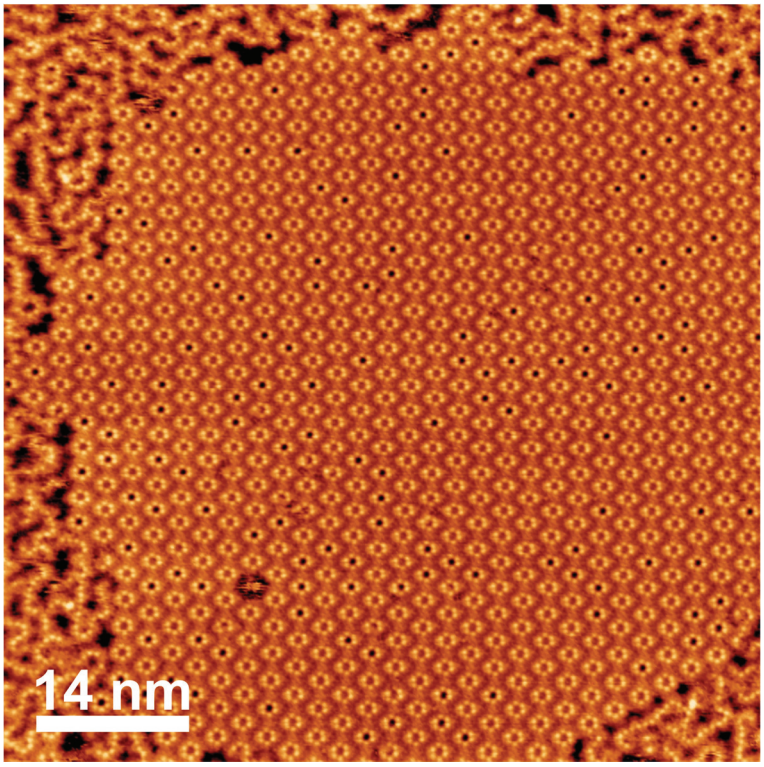

Figure S4. STM image of a large island of cyclic hexamers from the sample shown in Figure 3d,e of the main text. Coverage: 1.0 ML, tunneling parameters: U = -3.31 V, I = -0.18 nA.

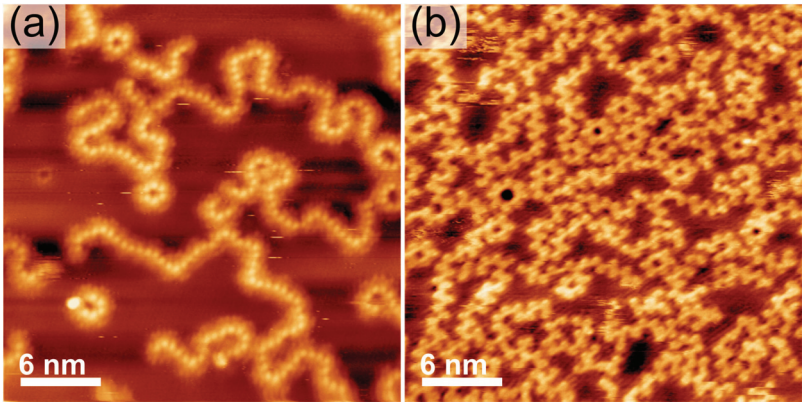

Figure S5. STM images showing mostly organometallic chains and some cyclic hexamers. Due to different tip states, (a) shows mainly the bridging Cu atoms, whereas (b) also shows the azulene building blocks. Coverage: (a) 0.3 ML, (b) 0.5 ML, tunneling parameters: (a) U = -2.67 V, I = -0.24 nA; (b) U = -1.85 V, I = -0.10 nA.

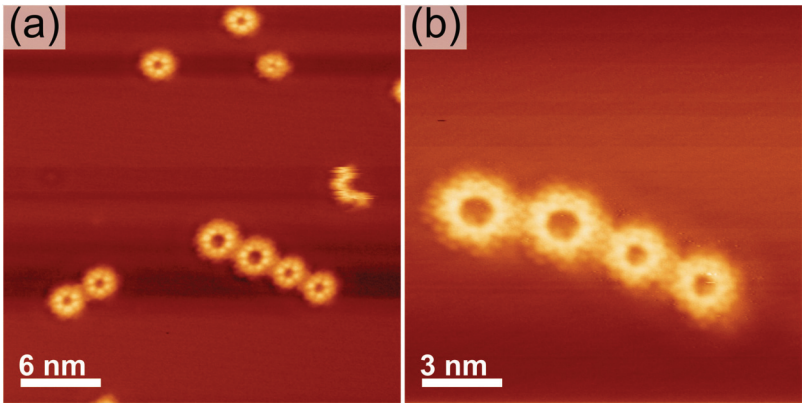

Figure S6. STM images showing cyclic organometallic octamers along with hexamers. (a) Two octamers next to some hexamers. (b) Zoom-in of two octamers (left) and two hexamers (right) with the azulene building blocks visible. The images were taken after annealing the sample from Figure 3a of the main text to 470 K. Coverage: 0.1 ML, tunneling parameters: (a) U = -1.40 V, I = -0.15 nA; (b) U = -0.37 V, I = -0.73 nA.

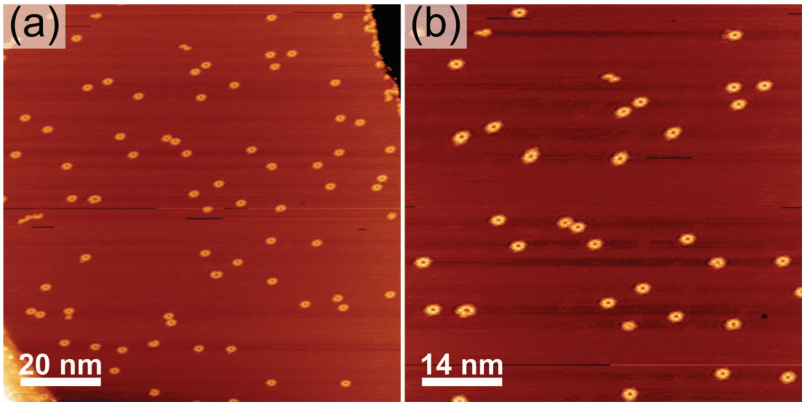

Figure S7. Additional STM images of the sample from Figure 3a of the main text. Besides the high ring yield, no long chains are found. Coverage: 0.1 ML, tunneling parameters: (a) U = -2.51 V, I = -0.15 nA; (b) U = -2.51 V, I = -0.19 nA.

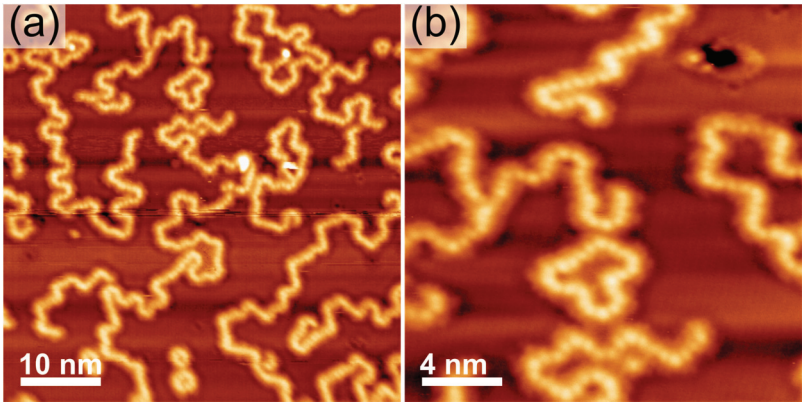

Figure S8. Additional STM images showing a larger ring than a cyclic hexamer as observed in the MC simulations in Figure 6 of the main text. Panel (b) is a zoom-in image of panel (a). The sample is the same as in Figure 2b of the main text. Coverage: 0.3 ML, tunneling parameters: (a) U = -2.84 V, I = -0.14 nA; (b) U = -2.84 V, I = -0.15 nA.

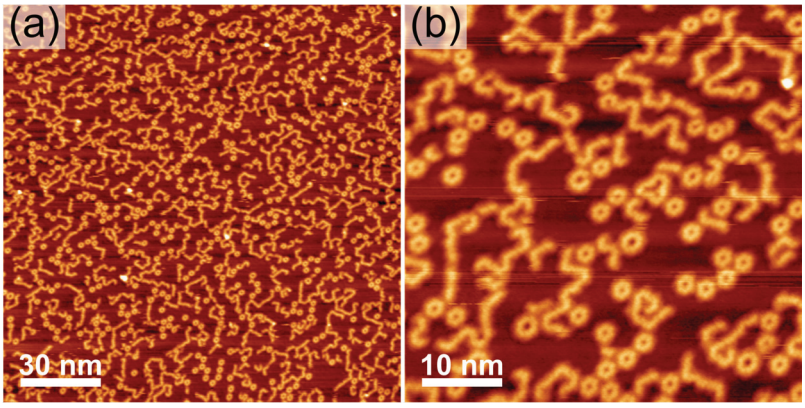

Figure S9. Additional STM images of the sample shown in Figure 8e of the main text. The images show a mixture of rings and chains. Coverage: 0.5 ML, tunneling parameters: (a) U = -3.63 V, I = -0.21 nA; (b) U = -3.63 V, I = -0.10 nA.

3. Additional Monte Carlo simulations

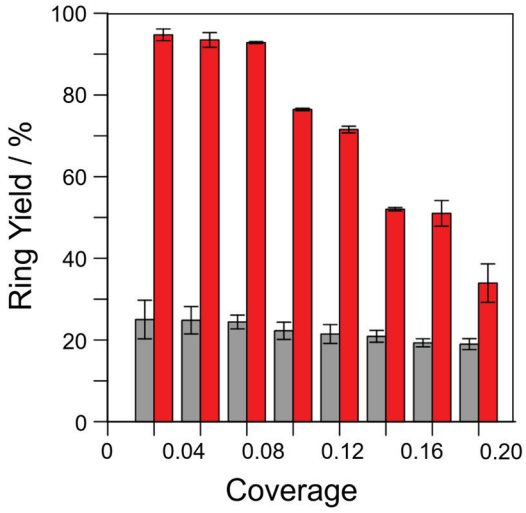

Figure S10. Yield of cyclic hexamers as a function of the coverage for two temperatures (grey, $T = 0.068$ and red, $T = 0.1$). The results are averages from 10 independent systems.

The ring yield as a function of coverage for two different temperatures is shown in Figure S10. The grey bars represent the low-temperature conditions with kinetic control, whereas the red bars indicate the yields at high temperature and thermodynamic control. As expected on the basis of the data from Figure 7 of the main text, the ring yields decrease towards higher coverages in both cases, but the changes are more pronounced in the case of thermodynamic control. The trends are the same as in the corresponding experimental data (Figure 3f of the main text).

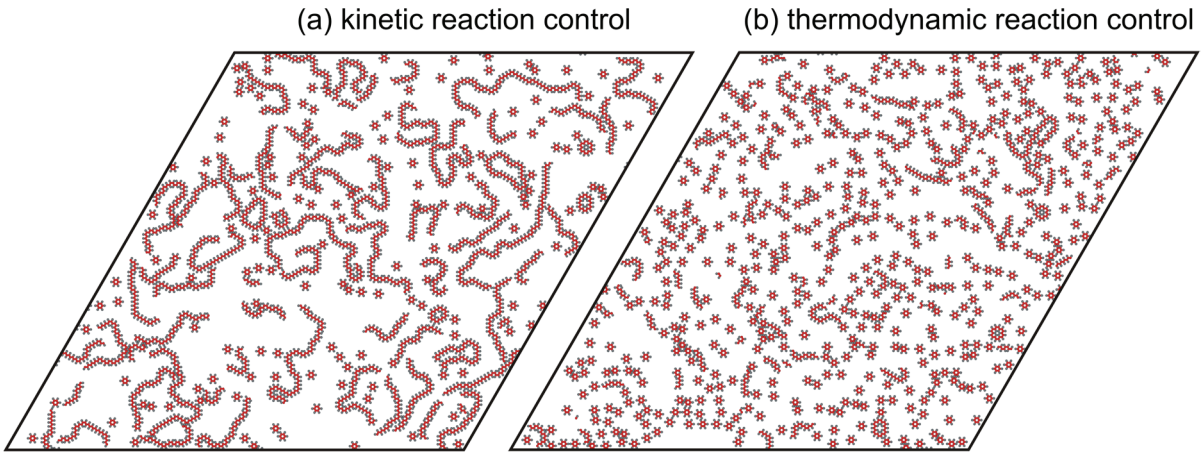

Figure S11. MC simulations for a coverage of 0.2 at two different temperatures with a ratio of T_{high}/T_{low} = 1.47, corresponding to the ratio of 440 K / 300 K = 1.47. (a) Low temperature, non-equilibrium conditions, kinetic control. (b) High temperature, equilibrium conditions, thermodynamic control.

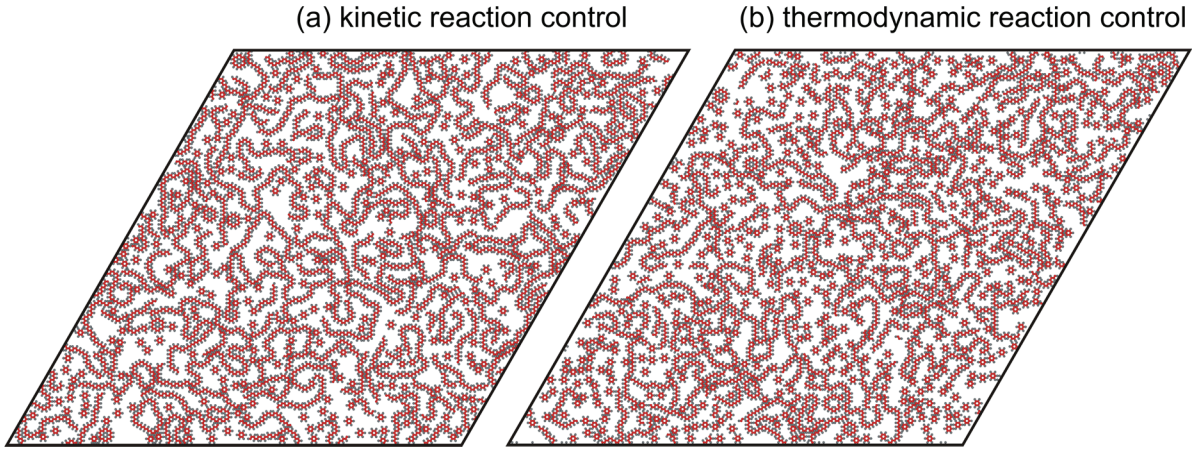

Figure S12. MC simulations for a coverage of 0.4 at two different temperatures with a ratio of T_{high}/T_{low} = 1.47, corresponding to the ratio of 440 K / 300 K = 1.47. (a) Low temperature, non-equilibrium conditions, kinetic control. (b) High temperature, equilibrium conditions, thermodynamic control.

4. Data needed to calculate the effective molarities

P2

Table S1. Number of cyclic hexamers C_6, other macrocycles C_n, surface concentration of cyclic hexamers $[C_6]$, number of monomers M_1, number of chains M_n, and effective molarity for the cyclic hexamer EM_6 under kinetic reaction control for the samples shown in Figure 2 of the main text.

Coverage / ML	# C_6	# C_n	$[C_6]$ / nm^{-2}	# M_1	# M_n	EM_6 / nm^{-2}
0.1	3	2	0.0006	637	21	0.0295
0.3	6	18	0.0012	2205	36	0.0169
0.5	9	8	0.0018	3466	54	0.0162
1.0	8	7	0.0016	7162	48	0.0069

Table S2. Number of cyclic hexamers C_6, other macrocycles C_n, surface concentration of cyclic hexamers $[C_6]$, number of monomers M_1, number of chains M_n, fraction of reacted end groups in chains x, and effective molarity for the cyclic hexamer EM_6 under thermodynamic reaction control for the samples shown in Figure 3 of the main text.

Coverage / ML	# C_6	# C_n	$[C_6]$ / nm^{-2}	# M_1	# M_n	x	EM_6 / nm^{-2}
0.1	33	3	0.0033	255	3	0.908	0.0059
0.3	145	21	0.0145	4032	254	0.915	0.0247
0.5	237	17	0.0237	8187	184	0.972	0.0281
1.0	726	34	0.0363	31897	1102	0.960	0.0465

P3 Electronic Structure Tunability by Periodic *meta*-Ligand Spacing in One-Dimensional Organic Semiconductors

Citation: I. Piquero-Zulaica, A. Garcia-Lekue, L. Colazzo, **C. K. Krug**, M. S. G. Mohammed, Z. M. Abd El-Fattah, J. M. Gottfried, D. G. de Oteyza, J. E. Ortega, J. Lobo-Checa, *ACS Nano* **2018**, *12*(10), 10537–10544, DOI 10.1021/acsnano.8b06536.

Summary

The study presented in this article aims at the exclusive formation of chains in the surface-confined Ullmann coupling reaction, while a maximization of the ring yield was the topic of P1 and P2. For this purpose the 4,4''-dibromo-1,1':3',1''-terphenyl (DMTP) precursor is chosen, which can either form rings or chains. The exclusive formation of chains is achieved by applying a vicinal surface as a template. The perfect alignment of the chains with the steps of the substrate allows to investigate their electronic structure with angle-resolved photoemission spectroscopy (ARPES) as a space-averaging technique. The results are complemented by scanning tunneling spectroscopy (STS) and theoretical studies.

In previous investigations it had been shown that the DMTP precursor can form rings as well as chains and the maximization of the ring yield had already been studied applying pseudo-high-dilution conditions. Here, a curved Ag(645) single crystal is used as surface template. This crystal has equally-spaced (111) terraces with different widths depending on its curvature. The terraces are separated by kinked monoatomic steps running along the $[1\,1\,\overline{2}]$ direction. At a position 3.6° off the (111) plane the terrace width is 3.8 nm on average. This terrace width and the kinked steps, which can reconstruct in order to match the zigzag structure of the chains, enable the exclusive formation of chains. The chains are perfectly aligned in the direction of the step edges as shown by scanning tunneling microscopy (STM) on a local and low-energy electron diffraction (LEED) on a global scale with a commensurate $\left(\begin{smallmatrix} 9 & 5 \\ 0 & 4 \end{smallmatrix}\right)$ superstructure.

The very high structural quality allows the investigation of the band structure with ARPES. The spectra reveal two weakly dispersive bands along the direction of the zigzag chains (E *vs.* k_y), which show a periodicity corresponding to the size of the phenyl units. In the direction perpendicular to the chains (E *vs.* k_x) no dispersion is visible. The molecular origin of the observed bands and their intensity in the ARPES measurements are confirmed by electron plane wave expansion (EPWE) simulations. A comparison with poly-(*para*-phenylene) fur-

thermore shows the strong influence of the *meta* junctions on the band structure of the polymer. The band gap of the zigzag chains is determined to be 3.7 eV by STS.

At last, the influence of the distance between the single *meta* junctions on the band gap is investigated. For this purpose 4,4''-dibromo-1,1':4',1''-terphenyl (DBTP) was co-deposited with DMTP to synthesize zigzag chains with longer straight segments. The band gaps determined by STS show a decrease with increasing length of the linear segment, in accordance with density functional theory (DFT) calculations.

P3

Own Contribution

The project leading to this publication was conceived by Dr. Ignacio Piquero-Zulaica, Dr. Jorge Lobo-Checa, Prof. Dr. J. Enrique Ortega, and Prof. Dr. J. Michael Gottfried. Preceding to the actual experiments discussed in the article I performed preparative experiments with the combined STM and XPS setup in the laboratory of the Gottfried group in Marburg (*cf.* Section 3.4.1) together with Dr. Qitang Fan. The purpose of these was to find out whether already known zigzag chains formed by DMTP could be aligned along the step edges in order to be able to perform ARPES measurements. Afterwards, I instructed Dr. Ignacio Piquero-Zulaica and Dr. Jorge Lobo-Checa in the laboratory of Prof. Dr. J. Enrique Ortega in Donostia-San Sebastián, Spain (*cf.* Section 3.4.2) how to prepare samples of DMTP zigzag chains with high yield and structural quality. We were able to achieve the desired result on vicinal surfaces. On these samples we performed the first STM, LEED, and ARPES measurements and after my stay in Donostia-San Sebastián was over Dr. Ignacio Piquero-Zulaica and Dr. Jorge Lobo-Checa finished these experiments. Later on, the data were complemented by low temperature (LT)-STM and STS experiments, DFT calculations and EPWE simulations. I was closely involved in the data analysis and writing of the manuscript at all times, which was mainly done by Dr. Ignacio Piquero-Zulaica and Dr. Jorge Lobo-Checa. All co-authors contributed to the final discussion of the manuscript.

ACS NANO
Cite This: ACS Nano 2018, 12, 10537−10544
www.acsnano.org

ARTICLE P3

Electronic Structure Tunability by Periodic *meta*-Ligand Spacing in One-Dimensional Organic Semiconductors

Ignacio Piquero-Zulaica,[*,†] Aran Garcia-Lekue,[‡,§] Luciano Colazzo,[‡] Claudio K. Krug,[∥] Mohammed S. G. Mohammed,[‡,†] Zakaria M. Abd El-Fattah,[⊥,#] J. Michael Gottfried,[∥] Dimas G. de Oteyza,[†,‡,§] J. Enrique Ortega,[†,‡,▽] and Jorge Lobo-Checa[*,○,◆]

[†]Centro de Física de Materiales CSIC/UPV-EHU-Materials Physics Center, Paseo Manuel de Lardizabal 5, E-20018 San Sebastián, Spain
[‡]Donostia International Physics Center (DIPC), Paseo Manuel de Lardizabal 4, E-20018 Donostia-San Sebastián, Spain
[§]Ikerbasque, Basque Foundation for Science, 48011 Bilbao, Spain
[∥]Fachbereich Chemie, Philipps-Universität Marburg, Hans-Meerwein-Str. 4, 35032 Marburg, Germany
[⊥]ICFO-Institut de Ciencies Fotoniques, The Barcelona Institute of Science and Technology, 08860 Castelldefels, Barcelona, Spain
[#]Physics Department, Faculty of Science, Al-Azhar University, Nasr City, E-11884 Cairo, Egypt
[▽]Dpto. Física Aplicada I, Universidad del País Vasco, E-20018 San Sebastián, Spain
[○]Instituto de Ciencia de Materiales de Aragón (ICMA), CSIC-Universidad de Zaragoza, E-50009 Zaragoza, Spain
[◆]Departamento de Física de la Materia Condensada, Universidad de Zaragoza, E-50009 Zaragoza, Spain

Supporting Information

ABSTRACT: **Designing molecular organic semiconductors with distinct frontier orbitals is key for the development of devices with desirable properties. Generating defined organic nanostructures with atomic precision can be accomplished by on-surface synthesis. We use this "dry" chemistry to introduce topological variations in a conjugated poly(*para*-phenylene) chain in the form of *meta*-junctions. As evidenced by STM and LEED, we produce a macroscopically ordered, monolayer thin zigzag chain film on a vicinal silver crystal. These cross-conjugated nanostructures are expected to display altered electronic properties, which are now unraveled by highly complementary experimental techniques (ARPES and STS) and theoretical calculations (DFT and EPWE). We find that *meta*-junctions dominate the weakly dispersive band structure, while the band gap is tunable by altering the linear segment's length. These periodic topology effects induce significant loss of the electronic coupling between neighboring linear segments leading to partial electron confinement in the form of weakly coupled quantum dots. Such periodic quantum interference effects determine the overall semiconducting character and functionality of the chains.**

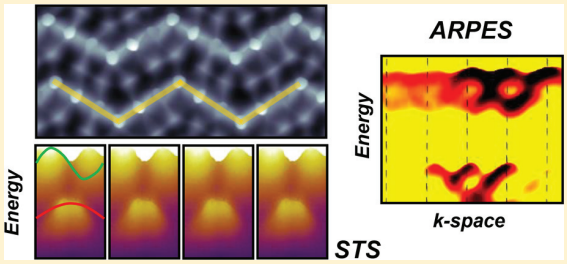

KEYWORDS: *on-surface synthesis, cross-conjugated polymers, ultrathin organic films, vicinal surfaces, electronic structure, electron confinement*

Conjugated polymers in the form of molecular chains are extensively used in industry as light emitting materials, photocatalysts, solar cells and biosensors due to their large and tunable band gaps.[1−4] Control over their electronic properties is accomplished through topological functionalization of these π-conjugated oligophenylene chains, *i.e.*, modification of their conductive pathways. In particular, changes of conjugation (from linear to cross-conjugation) by precise transitions from *para*- to *meta*-ligand substitutions[5,6] weaken the electronic communication between the repeating units of the polymer.[7] Such modifications have also been described as quantum interference electron pathways,[8−10] and bear predicted effects such as scarcely dispersive bands,[5] wider band gap,[11] distinct optical properties,[4] electronic switching capabilites[12] and low conductance properties.[8−10,13,14] However, periodic *meta*-junction zigzag chains may also show enhanced charge

Received: August 27, 2018
Accepted: October 8, 2018
Published: October 8, 2018

DOI: 10.1021/acsnano.8b06536
ACS Nano 2018, 12, 10537−10544

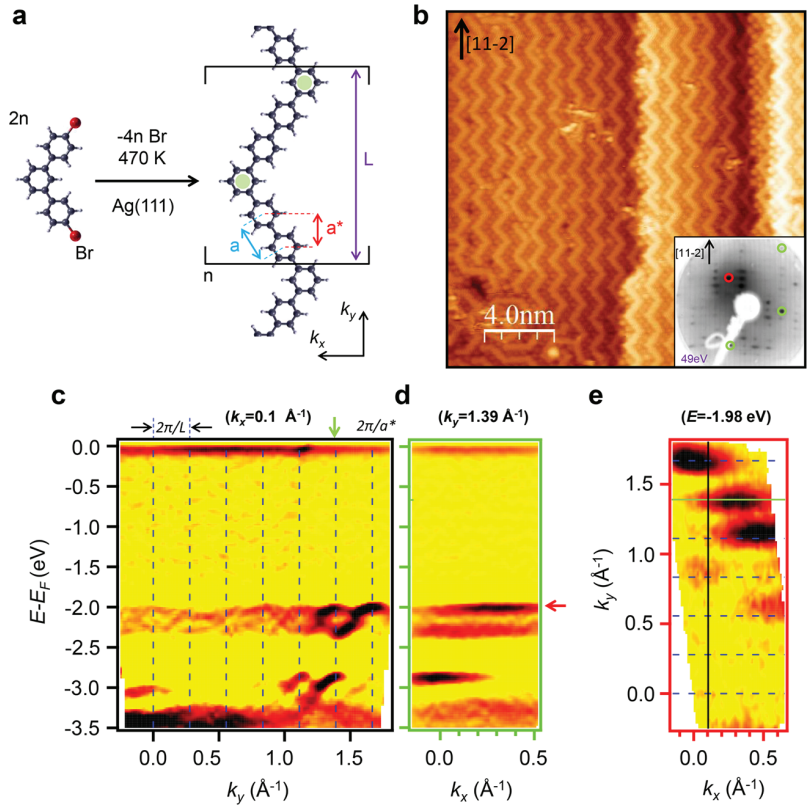

Figure 1. Structural arrangement and ARPES electronic band structure of the zigzag chain film grown on a vicinal Ag(111) surface. (a) Schematic representation of the DMTP precursor and the resulting zigzag covalent chain, showing its characteristic lengths: phenyl−phenyl distance (a) and its projection along the chain's average direction (a*), and polymer superperiodicity (L). (b) High resolution STM image after chain synthesis on a vicinal plane ∼3.6° off from the (111) crystal position. The zigzag chains are separated by Br atoms and preferentially follow the step parallel direction ([11−2]). (STM parameters: V = −394 mV, I = 234 pA, T_{sample} = 100 K). Inset shows the LEED pattern after chain formation that exhibits single-domain, well-aligned arrangement. The superstructure spots are in registry with the circled main spots (in red the (0,0) and in green the substrate's first order diffractions), implying commensurability with the terrace atoms (LEED parameters: E_{kin} = 49 eV, T_{sample} = 300 K). (c) ARPES experimental band structure of *meta*-junctioned cross-conjugated zigzag chains parallel to the average direction of chains and steps (E vs k_y with k_x = 0.1 Å^{-1}). (d) Experimental band structure perpendicular to the chain average axis (E vs k_x, with k_y = 1.39 Å^{-1} indicated by green arrow in (c)). (e) Isoenergetic cut (k_x vs k_y) at the top of the valence molecular band (E = −1.98 eV, marked by red arrow in (d)). The second derivative of the intensity is shown in a linear color scale (highest being black). (ARPES parameters: $h\nu$ = 21.2 eV, T_{sample} = 150 K).

mobility as compared to their poly(*para*-phenylene) counterparts, reaching values comparable to those of amorphous silicon.[15]

Despite this wealth of industrially attractive properties of cross-conjugated polymers, key fundamental information, such as the predicted electronic structure, awaits experimental validation. Such deficiency of fundamental knowledge limits the confidence in the existing predictions, according to which topology is expected to affect the electronic properties of the polymer. Several obstacles are responsible for the lack of the aforementioned experimental confirmation: (i) the need of generating atomically identical chains exhibiting repeated *para*- to *meta*-ligand substituted units, (ii) the synthesis of well-aligned chains, to be probed by nonlocal, averaging spectroscopies, (iii) the minimization of lateral interactions, prone to affect their intrinsic band structure, and (iv) the right choice of a support that sufficiently decouples the electronic signal from the investigated oligophenylene chains.

To overcome such obstacles, solutions can be found within the context of Surface Science. Particularly, the first prerequisite for obtaining perfectly reproducible cross-conjugated zigzag polymers can be accomplished by bottom-up on-surface synthesis. Surface-assisted C−C coupling processes have been recently applied to generate graphene nanoribbons (GNRs) with different edge terminations and widths,[16−21] and other types of oligophenylene chains.[22−25] Second, the chain alignment for nonlocal characterization can be achieved by the use of nanotemplated substrates, such as vicinal surfaces.[26−29] These special surfaces have been successfully used for the macroscopic alignment of carbon-based chains, a fundamental requirement for angle resolved photoemission (ARPES) experiments.[23,24,30,31] With respect to the minimization of lateral interchain coupling, this is an inherent feature of the Ullmann-type surface reactions[22] since the halogens are cleaved during the synthesis positioning themselves between neighboring chains.[23,24,32] These adatoms are reported to laterally decouple adjoining chains, without affecting the polymer's band structure, except for a minimal rigid energy shift similar to doping effects.[24,33] Finally, the substrate plays a fundamental role as a catalyst of the Ullmann reaction, making its choice crucial for a successful oligomer coupling. Good candidates that present excellent yields, control and reproducibility are the closed packed surfaces of coinage metals, which are extensively used for Ullmann-type surface

DOI: 10.1021/acsnano.8b06536
ACS Nano 2018, 12, 10537−10544

reactions. Among these, silver stands out as a promising substrate, since it weakly interacts with the products while exhibiting large adsorbate diffusion rates.[34] Moreover, its *d*-bands are furthest from the Fermi level (below −3 eV), allowing a wide energy range for the study of the chain's band structure (see Figure S1 in the Supporting Information (SI)).

In this work, we have overcome all the aforementioned obstacles and have generated an extended film of atomically precise zigzag chains on a vicinal Ag(111) surface, as evidenced by scanning tunneling microscopy (STM) and low energy electron diffraction (LEED). The electronic band structure of such films has been unraveled by means of ARPES and complemented by scanning tunneling spectroscopy (STS) measurements on Ag(111). In this way, we determine the experimental energy gap and visualize the spatial distribution of the frontier orbitals. Such wealth of experimental information has been clarified and expanded by a comprehensive set of density functional theory (DFT) calculations and electron plane wave expansion (EPWE) simulations.

RESULTS AND DISCUSSION

We have produced a monolayer film of cross-conjugated zigzag chains from the surface polymerization of the 4,4″-dibromo-*meta* terphenyl (DMTP) molecular aromatic precursors via C−C coupling (see Figure 1a and Methods section). The template of choice is a vicinal Ag(111) crystal surface with linear, monoatomic steps running parallel to the [11−2] direction[29] that corresponds to the so-called fully kinked (100% kinked) configuration of the step-edge. We used this particular substrate since it provides a higher flexibility to reconstruct and therefore accommodate the produced zigzag structures more efficiently (cf. Methods section and Figure S1 in the SI). Indeed, we can already disclose that we achieved an excellent film featuring a high yield of well-ordered and aligned zigzag chains.

The formed zigzag chains appear practically planar on the surface (Figure 1b) and are covalently bonded, displaying the characteristic phenyl−phenyl distance of $a \sim 4.3$ Å along the straight segments and a superperiodicity of $L \sim 2.24$ nm between equivalent elbows.[22,35] The unit cell of the chain features two straight subunits made up of two phenyl rings (in *para*-positions) linked to two edge rings acting as *meta*-junctions (Figure 1a). Note that in the STM image these chains are separated by spherical features attributed to Br atoms split off from the precursor molecules at the initial step of the on-surface reaction.[36−43] The LEED pattern reveals that the organic chains are aligned parallel to the steps and show long-range order as they are commensurate with the underlying substrate (Figures 1b and S2). Particularly, the main silver diffraction spots (red and green circles) are surrounded by a set of spots aligned along the average step direction yielding a (9, 5; 0, 4) superstructure.

Our STM and LEED structural results contain the required ingredients (atomic precision of the structure, defined alignment, long-range order and minimization of lateral interactions by Br adatom presence) to expect the existence of a defined and coherent electronic band structure from these chains. Figure 1c−e shows the second derivative (to enhance the details) of the ARPES spectral weight obtained from such a film saturating the surface (raw data is shown in Figure S3 in the SI). The resulting electronic structure in the direction parallel to the average step direction and the main axis of the zigzag chains (E vs k_y with $k_x = 0.1$ Å^{-1}) exhibits weakly dispersive bands between −1.8 and −3.5 eV, separated by an ∼0.6 eV gap (cf. Figure 1c). None of these ARPES features are observable on the pristine substrate (cf. Figure S1 in the SI). A closer inspection reveals that each one of them consists of a pair of antiphase oscillatory bands (Figures S3 and S4 in the SI). The spectral intensity peaks around $2\pi/a^*$, where a^* represents the projected phenyl−phenyl distance along the average chain direction (Figure 1a), assuring its molecular origin.[44] The faint replicas with $2\pi/L$ periodicity (vertical dashed blue lines) stem from the zigzag chain superperiodicity L (Figure 1a), in agreement with the STM data set.

The 1D nature of these zigzag chains is demonstrated by the lack of dispersion perpendicular to the average chain axis. Figure 1d shows a representative cut (E vs k_x) across the center of the sixth Brillouin zone (green arrow at $k_y = 1.39$ Å^{-1} in Figure 1c), where discrete flat bands can be observed. This confirms that they stem from different molecular orbitals of the zigzag polymer.[45] The nondispersive character at the top of the valence band (red arrow at −1.98 eV) can also be traced from the isoenergetic cut (k_x vs k_y) shown in Figure 1e, where 1D polymer bands replicate at each Brillouin zone center, gaining intensity for the larger k_y values. These photoemission intensity modulations have been simulated with the EPWE method,[46,47] which confirms that these features are neither affected by the templating Ag surface nor by the presence of Br atoms intercalated between the chains (see Methods section and Figure S4 in the SI). Indeed, we experimentally find that the presence of Br embedded in between the zigzag chains only causes a rigid shift of the molecular band structure by 200 ± 50 meV to higher energy, according to Figure S5 in the SI and in agreement with previous work.[24,33]

Our ARPES results suggest that the zigzag chains are largely decoupled from the metallic substrate since the observed molecular bands do not show signs of hybridization with the substrate in that energy window. Besides, the chains are semiconducting in nature with a band gap certainly larger than 2 eV, since no other bands closer to the Fermi energy are observed in the occupied region. The band structure strongly contrasts with that of the poly(*para*-phenylene) (called PPP hereafter) chains, which exhibits a single, highly dispersive molecular band across the entire Brillouin zone[23−25] (Figure S6 in the SI). Instead, it closely resembles the one predicted for poly(*meta*-phenylene) (called PMP hereafter) chains,[5] implying that the presence of *meta*-junctions strongly modifies the electronic structure of a polymeric chain[13] (cf. Figure S7 in the SI).

The weak interaction observed between the zigzag chain film and the substrate is a favorable playground for a systematic theoretical analysis. As a first approximation, we consider the polymers as free-standing and planar. On this basis, we use DFT calculations to corroborate the weakly dispersive band structure observed experimentally. The calculated electronic structure shown in Figure 2a exhibits convincing qualitative agreement with the experimental data. In particular, the dispersive character of the first four valence bands (VBs) of the zigzag chain (between −1 and −2.5 eV) is consistent with that in Figure 1c. The energy mismatch can be attributed to the absence of a substrate in the calculations, as well as to the well-known limitation of DFT to accurately predict HOMO−LUMO gaps. Note that the calculated bands span from the $\bar{\Gamma}$ point to the Brillouin zone boundary (π/L), which in the experiment appears 12 times replicated until $2\pi/a^*$. For comparison, the calculations are extended to straight PPP chains (Figure 2b) which strongly differ in the electronic structure by exhibiting a highly dispersive single VB in the same energy window.

DOI: 10.1021/acsnano.8b06536
ACS Nano 2018, 12, 10537−10544

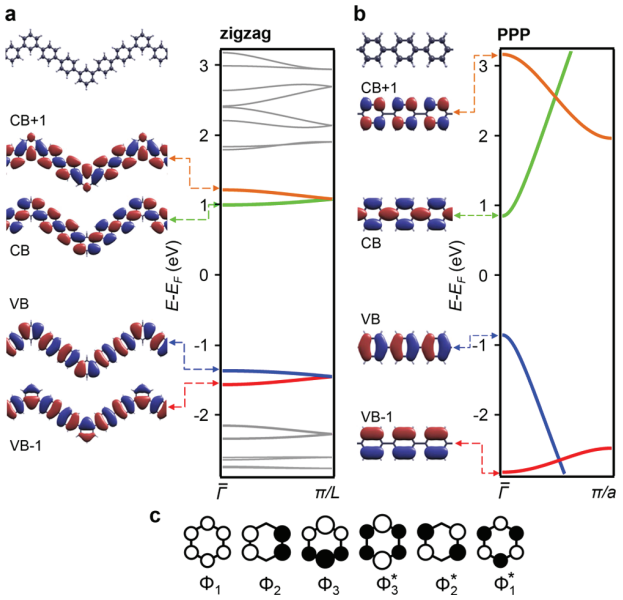

Figure 2. Comparison of molecular orbital shape and band structure between zigzag chains and straight PPP chains, as obtained from DFT calculations. The right plots in (a) and (b) show the calculated electronic band structure, where (a) corresponds to the zigzag polymer and (b) to PPP. The highly dispersive character of the PPP bands contrasts with the practically flat bands of the zigzag chains, accompanied by a notable difference in the frontier orbital band gap. Left panels in (a) and (b) show the spatially resolved molecular orbitals at $\bar{\Gamma}$ for each band. In a simplistic view, they are constructed by overlapping different benzene molecular orbitals, which are schematically shown in (c).

Moreover, the zigzag chain exhibits a greater band gap than its straight counterpart, confirming the enhanced semiconductive character of the former (see Figure S7 in the SI).

The experimental value of the frontier orbital band gap of the zigzag chains can be obtained by low-temperature (4 K) STS. For such measurements, we deposit a submonolayer coverage of DMTP molecules on Ag(111) so that small zigzag island patches are formed on the surface while still allowing access to the bare substrate for tip calibration and treatment (Figures 3 and S5). Figure 3a shows the dI/dV spectra at the center (red) of a straight arm of a zigzag chain (see figure inset) and the Ag substrate (gray). The VB onset is detected close to −2.1 V (coinciding with the ARPES value in Figure 1d) while the conduction band (CB) edge is around 1.6 V resulting in an overall band gap of ∼3.7 V. Therefore, this value is larger than the 3.2 V reported for PPP chains grown on Au(111)[42] and confirms the enhanced semiconducting character of the zigzag chains.

DFT calculations can also shed light onto the effect that the periodically spaced *meta*-junctions have on the overall electronic structure by comparing the spatially resolved molecular orbitals at the $\bar{\Gamma}$ point with the π molecular orbitals of benzene (Figure 2c). In the PPP case (Figure 2b), VB and CB are constructed by the overlap of Φ_3 and Φ_3^* benzene molecular orbitals, respectively. These orbitals present a large electronic weight on the carbon atoms linking the phenyl rings (*para*-positions), giving rise to highly dispersive valence and conduction bands. Likewise, the less dispersive character of the VB-1 and CB+1 bands can be attributed to the orbital set that exhibits a nodal plane through the *para* carbon atoms (Φ_2 and Φ_2^* orbitals). Contrarily, for the zigzag chains (Figure 2a) the VB and CB are a combination of two degenerate orbitals.[7] In particular, the VB is made up of Φ_3 (straight sections) and Φ_2 (elbows) orbitals, which is mirrored in the CB by Φ_3^* (straight sections) and Φ_2^* (elbows). This orbital mixing, along with the reduced orbital amplitude at the *meta*-positions and expected phase shifts induced by momentum steering at the elbows, results in a diminished orbital interaction (overlap) that leads to a severe weakening of the electron coupling between adjacent straight segments. Indeed, the flat band character is also exhibited by the VB-1 and CB+1, even though they mostly arise from a single type of benzene molecular orbital coupling (Φ_3 and Φ_3^*, respectively). This strong electronic effect governed by the *meta*-junction is generally referred to as cross-conjugation[5,6] or destructive quantum interference.[8−10,14]

The reduced electronic coupling between neighboring linear segments causes electron localization, an effect that can be adequately addressed with STS. Figure 3b presents a color plot representing stacked dI/dV point spectra measured along a single straight segment (black dashed line in the inset of Figure 3a). Aside from clearly visualizing an overall band gap of 3.7 eV, we observe confinement in the CB within such segments where the spatial modulations in the local density of states (LDOS) are consistent with the first two stationary states of a particle in a box. In particular, their amplitudes die away at the edges of the linear segments (elbow positions of the zigzag chains) but the lower state at 1.9 V features an antinode at the segment's center (the peak in the red spectrum of Figure 3a), whereas the second state at 2.5 V oppositely exhibits a node at that position. Such electron confinement effects have also been observed in related structures, as in the case of finite size PPP chains featuring a single elbow (in *meta*-junction)[13] or in closed-cycle geometries of honeycombenes.[48] In essence, we can conclude that *meta*-junctions act as scattering barriers for the polymer electrons regardless of the overall geometry, *i.e.*, as closed structures[48] or as edged (nonlinear) chains.[13]

Once we have verified that each straight segment of our zigzag chains acts as a confining unit, reminiscent of a 1D array of weakly interacting Quantum Dots (QDs),[49] it should be possible to tune their electronic properties by modulating the straight segment's length. Varying the 1D QD length should affect the energy levels as well as the corresponding frontier orbital band gap. To do so, we coevaporated on Ag(111) linear precursors (DBTP molecules[24]) together with the previously used ones to generate the zigzag chains, as shown in Figure 1a. The Ullmann coupling reaction is likewise activated by postannealing to 470 K, resulting in linear segments of phenyl length configurations of $N = 4 + 3n$ (with N being the total phenyl number and n the amount of DBTP precursors embedded in the straight segment). Figure 4b shows color plots of the dI/dV linescan for $N = 7$ (bottom) and $N = 10$ (top) QDs, which evidence the expected squared wave function intensity variations in the CBs for the same energy range as Figure 3b. Most importantly, by comparison to the dashed white lines corresponding to the $N = 4$ segment, we observe that the band gap shrinks as the size of the segment increases (dashed blue lines). A quantitative analysis of the experimentally determined band gap is shown in Figure 4c, revealing a $1/N$ behavior in agreement with previous work for similar chains.[13] Such behavior matches our DFT calculations for planar, free-standing, periodic zigzag chains of different straight segment length, which

DOI: 10.1021/acsnano.8b06536
ACS Nano 2018, 12, 10537−10544

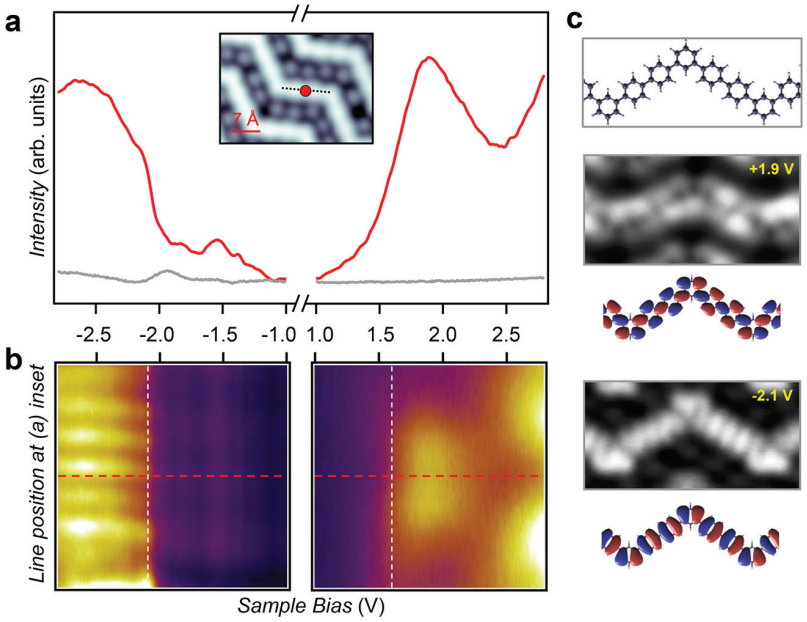

Figure 3. STS experimental determination of the zigzag chain's frontier orbitals on Ag(111). (a) Constant-height dI/dV spectra acquired at the center of a zigzag straight arm (red point in STM image inset) and substrate (gray) (STM imaging parameters: 50 mV, 100 pA; frame: 3.6 × 2.5 nm^2). (b) Constant-height dI/dV linescan spectra along the zigzag arm (indicated by a dotted line in the STM topography inset) for the same bias range of panel (a). The onsets of the VB and CB are clearly defined (vertical dashed white lines), yielding a band gap of ∼3.7 eV (STS bias voltage modulation for (a) and (b): 10 mV$_{rms}$ at 341 Hz. Close-feedback parameters: −350 mV, 150 pA and 1200 mV, 100 pA for the negative and positive resonances regions, respectively). (c) From top to bottom: ball and stick model of the zigzag chain. High-resolution dI/dV maps acquired at constant-height with a CO functionalized STM tip at 1.9 and −2.1 V, *i.e.*, close to the CB and VB onsets (frames: 3.0 × 1.5 nm^2; bias voltage modulation 10 mV$_{rms}$ at 341 Hz). Underneath each map, the corresponding DFT gas phase molecular frontier orbitals are shown for comparison.

confirm not only that the band gap of the cross-conjugated zigzag chains is larger than the one of its linear PPP counterpart, but it is also tunable as 1/N (cf. Figures S7 and S8 in the SI).

Finally, we should discuss an additional property of this system that may affect the frontier orbital band gap: the relative twisting of the phenyl rings (nonplanar chain morphology). Figure 3c shows high-resolution constant height dI/dV maps close to the valence and conduction band onsets, namely, at −2.1 and 1.9 eV, respectively. Both maps replicate well the molecular orbital simulations of Figure 2a, which are calculated for planar structures and are depicted below for direct comparison. While the slight discrepancies in nodal positions are attributed to the CO probe functionalization,[50] the intensity variations are in turn ascribed to the twisting of the phenyl rings.[42] The phenyl twisting is confirmed from constant height bond resolution imaging with a CO functionalized tip,[51] on which we find subtle intensity modulations on the external parts of the phenyl rings (see Figure S9 in the SI) indicative of such phenyl twisting. This is in agreement with previous work that found ∼20° phenyl twisting on PPP chains with respect to the surface plane.[24] To determine the effect of the twisting on the frontier orbital band gap, we have performed DFT calculations for free-standing zigzag chains and obtained an energy minimum close to 30° phenyl twisting of the zigzag chain. However, the calculations show that the electronic band gap is scarcely increased compared to the planar configuration. Given that the underlying substrate is known to decrease the phenyl twisting by flattening the chains, we expect this effect to be smaller than ∼200 meV (cf. Figure S10 in the SI), validating the use of free-standing, planar configuration geometries in the DFT calculations that support our findings.

CONCLUSIONS

We have been able to synthesize and macroscopically align a saturated film of cross-conjugated oligophenylene zigzag chains on a vicinal Ag(111) surface. We find that these atomically precise chains remain sufficiently decoupled from each other and from the substrate to probe their elusive band structure with ARPES, revealing weakly dispersing one-dimensional electronic bands along the chain direction. DFT band structure calculations and EPWE photoemission intensity simulations satisfactorily reproduce our experimental findings. By means of STS, we find that the zigzag chain has a larger frontier orbital band gap than its straight counterpart (PPP) and observe electronic confinement in each straight segment of the zigzag chains, reminiscent of 1D arrays of weakly interacting QDs. Such states can be tuned by changing the length of the straight segments, affecting the frontier orbital band gap, which follows a 1/N dependency. Indeed, our molecular orbital simulations confirm that the periodically spaced *meta*-junctions at the elbows of the zigzag chain are the main structural feature responsible for the reduction of electronic coupling between adjacent linear segments. These findings corroborate the important effects that the conductive path topology of a molecular wire has on its frontier orbitals, which are responsible for defining its chemical, optical and electronic properties. Recent advances in transfer techniques ensure that on-surface synthesized and well-aligned organic nanostructures can be collectively transferred onto insulating substrates maintaining their relative arrangement,[52−54] which opens the path to further study the transport and optical properties of these cross-conjugated oligophenylene zigzag chains.

DOI: 10.1021/acsnano.8b06536
ACS Nano 2018, 12, 10537−10544

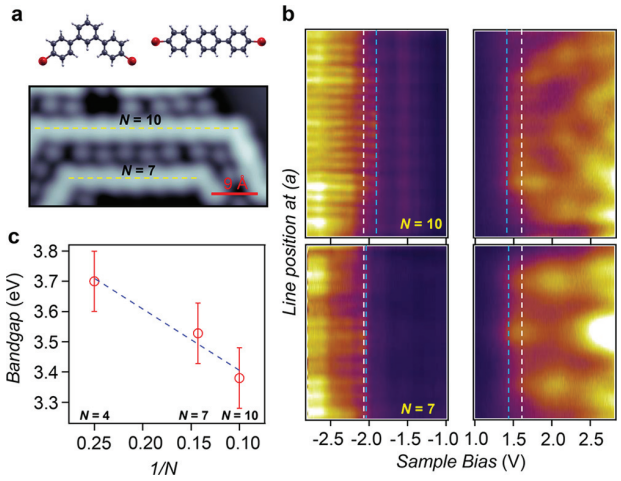

Figure 4. Tuning the electronic confined states through the linear segment's length (QD size). (a) Schematic representation of the coevaporated molecular precursors (DMTP and DBTP) that generate longer straight segments between the *meta*-coordinating phenyls. The STM image shows two longer linear segments of 7 and 10 phenyl rings between elbows (Imaging parameters: 50 mV, 100 pA; frame: 4.5 × 2.3 nm^2). (b) Constant-height dI/dV line profiles close to the VB and CB onsets along the two segments following the dashed lines in (a). The intensity modulation of the CB confirms the confinement nature of the *meta*-junction termination. Furthermore, the frontier orbital band gap (vertical dashed blue lines) is reduced compared to the N = 4 case, which is indicated by the two vertical dashed white lines. (STS parameters: bias voltage modulation of 10 mV$_{rms}$ at 341 Hz; close-feedback at −350 mV, 150 pA and 1200 mV, 120 pA for the negative and positive resonances regions, respectively). (c) Experimental band gap extracted from the STS line profiles revealing a 1/N behavior (compare to Figure S8 in the SI).

METHODS

A silver crystal surface curved around the (645) direction was used as tunable vicinal substrate for chain formation and alignment.[29] This curved sample exhibits (111) terraces of variable size (position dependent on its curvature) separated by monoatomic steps oriented along the [11−2] direction. The steps are of fully kinked type, in which out-protruding atoms have no side neighbors (Figure S1 in the SI). Notably, periodic roughening of such step-edges bears negligible energy cost, and hence can readily accommodate to the zigzag structure of the chains.[29] The saturated zigzag film that presents best order was observed at the vicinal plane ∼ 3.6° from the (111) region, corresponding to an average terrace size of 3.8 nm. The ARPES data shown in Figures 1, S1, S3, S4, and S6 corresponds to this position of the substrate. The sample was cleaned by repeated cycles of Ar^+ sputtering at energies of 1.0 keV, followed by annealing at 700 K. This produced clean and well-ordered surface step arrays as verified by the splitting of the LEED spots along the surface curvature.

The *meta*-junctioned haloaromatic compound, DMTP, was sublimated from a Knudsen cell at 360 K at a low flux (1 ML/hour) while the sample was held at 470 K.[22,48,55] Covalently bonded zigzag chains appeared separated by Br adatoms, suggesting some influence from the latter in steering chain growth and alignment. The step flexibility promoted the chain formation while keeping other irregular structures or hyperbenzene macrocycles to a minimum.[41] The structures remained densely packed up to high temperatures (∼600 K), beyond which halogen desorption starts, accompanied by chain misalignment.[18,56]

ARPES measurements were performed with a lab-based experimental setup using a display-type hemispherical electron analyzer (SPECS Phoibos 150, energy/angle resolution of 40 meV/0.1°) combined with a monochromatized Helium I ($h\nu$ = 21.2 eV) source. Measurements were acquired with the sample at 150 K by moving the polar angle, which is set to be parallel to the average step direction.

The STM measurements on the curved Ag(111) crystal were carried out at 100 K using a variable temperature Omicron STM instrument with a Nanonis SPM control system. The bias voltages given in the paper refer to a grounded tip. STM data were acquired in constant current mode and were processed with the WSxM software.[57]

LT-STM/STS measurements were performed with a commercial Scienta-Omicron low temperature system, operating in ultrahigh vacuum (UHV) at 4.3 K. For the measurement, the bias voltage was applied to the tip while the sample was electronically grounded. The STM tip was prepared *ex situ* by clipping a Pt/Ir wire (0.25 mm) and sharpened *in situ* by repeatedly indenting the tip a few nanometers (1−4 nm) into the Ag surface while applying bias voltages from 2 to 4 V between tip and sample. In order to perform bond-resolved STM imaging, the tip apex was terminated with a CO molecule, directly picked up from the surface, by positioning the sharp metal tip on top of it and applying a 500 ms bias pulse at −2 V. The imaging was performed by measuring at constant height while applying a bias voltage to the tip within the range of 2.0 and 3.5 mV. For spectroscopic point spectra and conductance maps, the dI/dV signals were measured by a digital lock-in amplifier (Nanonis). STM images were analyzed by using the WSxM software.[57]

Ab initio calculations were carried out using density functional theory, as implemented in the SIESTA code.[58] The optB88-vdW functional,[59] which accounts for nonlocal corrections, was adopted for the exchange and correlation potential. For each organic nanostructure, we considered a supercell consisting of a chain infinite along the x axis, with vacuum gaps of 15 Å in y and z directions in order to avoid interactions between chains in adjacent cells. A Monkhorst−Pack k-point grid with 20 × 1 × 1 k-points was used for the Brillouin zone sampling and the mesh cutoff for real space integrations was set to 300 Ry. We employed a double-ξ plus polarization (DZP) basis set, and a mesh-cutoff of 300 Ry for the real-space integrations. All structures were fully relaxed until residual forces were less than 0.01 eV/Å.

The electron plane wave expansion method, which was recently used to describe the electronic properties of graphene nanostructures,[47] is employed to simulate ARPES data. Within the EPWE approach, the photoemission intensity for a given binding energy and photoelectron wave vector is obtained from Fermi's golden rule applied to the in-plane wave function (an initial state) and a normalized plane wave (a final state) for the parallel component of the photoelectron wave function, as detailed in ref. 47. In this semiempirical method, zigzag chains are considered free-standing and planar, which implies that the simulated bands are substrate independent and free of Br interactions.

ASSOCIATED CONTENT

Supporting Information

The Supporting Information is available free of charge on the ACS Publications website at DOI: 10.1021/acsnano.8b06536.

This file contains: Growth details and zigzag chain alignment on a Ag(111) curved vicinal crystal; ARPES band structure and photoemission intensity simulations using the EPWE method; Br effect on the electronic structure of zigzag chains studied by STM/STS; ARPES band structure comparison of zigzag chains vs PPP chains; band structure variations with straight segment length of the zigzag chains from DFT calculations; phenyl twisting considerations of zigzag chains by STM/STS and DFT (PDF)

AUTHOR INFORMATION

Corresponding Authors

*E-mail: ipiquerozulaica@gmail.com.

*E-mail: jorge.lobo@csic.es.

DOI: 10.1021/acsnano.8b06536
ACS Nano 2018, 12, 10537−10544

ORCID

Ignacio Piquero-Zulaica: 0000-0002-4296-0961
J. Michael Gottfried: 0000-0001-5579-2568
Dimas G. de Oteyza: 0000-0001-8060-6819
J. Enrique Ortega: 0000-0002-6643-806X
Jorge Lobo-Checa: 0000-0003-2698-2543

Author Contributions

I.P-Z., J.L-C., and C.K.K. conducted the experimental measurements of the saturated film (ARPES, STM, and LEED) and corresponding data analysis; L.C., I.P-Z., M.S., and D.G.O. performed LT-STM/STS measurements of the partially covered surface; A.G-L. performed the DFT calculations, and Z.M.A. performed EPWE simulations; I.P-Z. and J.L-C. wrote the manuscript. All authors contributed to the revision and final discussion of the manuscript. I.P-Z., J.L-C., J.E.O., and J.M.G. conceived this project.

Notes

The authors declare no competing financial interest.

ACKNOWLEDGMENTS

I.P.-Z. thanks Dr. Jens Brede for fruitful discussion. Z.M.A. thanks Prof. F. J. García de Abajo for providing the EPWE code. We acknowledge the financial support from the Spanish Ministry of Economy, Industry and Competitiveness (MINECO, Grant No. MAT2016-78293-C6), from the Basque Government (Grant No. IT-621-13), from the regional Government of Aragon (RASMIA project), from the European Regional Development Fund (ERDF) under the program Interreg V-A España-Francia-Andorra (Contract No. EFA 194/16 TNSI), from the German Science Foundation (DFG) through the CRC 1083 and Grant No. GO 1812/2 and funding from the European Research Council (ERC) under the European Union's Horizon 2020 research and innovation programme (grant agreement no. 635919).

REFERENCES

(1) Günes, S.; Neugebauer, H.; Sariciftci, N. S. Conjugated Polymer-Based Organic Solar Cells. *Chem. Rev.* **2007**, *107*, 1324−1338.
(2) Li, G.; Chang, W.-H.; Yang, Y. Low-Bandgap Conjugated Polymers Enabling Solution Processable Tandem Solar Cells. *Nat. Rev. Mater.* **2017**, *2*, 17043.
(3) Masai, H.; Terao, J. Stimuli-Responsive Functionalized Insulated Conjugated Polymers. *Polym. J.* **2017**, *49*, 805−814.
(4) Guiglion, P.; Zwijnenburg, M. A. Contrasting the Optical Properties of the Different Isomers of Oligophenylene. *Phys. Chem. Chem. Phys.* **2015**, *17*, 17854−17863.
(5) Hong, S. Y.; Kim, D. Y.; Kim, C. Y.; Hoffmann, R. Origin of the Broken Conjugation in m-Phenylene Linked Conjugated Polymers. *Macromolecules* **2001**, *34*, 6474−6481.
(6) van der Veen, M.; Rispens, M.; Jonkman, H.; Hummelen, J. Molecules with Linear π- Conjugated Pathways between All Substituents: Omniconjugation. *Adv. Funct. Mater.* **2004**, *14*, 215−223.
(7) Kocherzhenko, A. A.; Grozema, F. C.; Siebbeles, L. D. A. Single Molecule Charge Transport: From a Quantum Mechanical to a Classical Description. *Phys. Chem. Chem. Phys.* **2011**, *13*, 2096−2110.
(8) Manrique, D. Z.; Huang, C.; Baghernejad, M.; Zhao, X.; Al-Owaedi, O. A.; Sadeghi, H.; Kaliginedi, V.; Hong, W.; Gulcur, M.; Wandlowski, T.; Bryce, M. R.; Lambert, C. J. A Quantum Circuit Rule for Interference Effects in Single-Molecule Electrical Junctions. *Nat. Commun.* **2015**, *6*, 6389.
(9) Guédon, C. M.; Valkenier, H.; Markussen, T.; Thygesen, K. S.; Hummelen, J. C.; van der Molen, S. J. Observation of Quantum Interference in Molecular Charge Transport. *Nat. Nanotechnol.* **2012**, *7*, 305−309.
(10) Markussen, T.; Stadler, R.; Thygesen, K. S. The Relation between Structure and Quantum Interference in Single Molecule Junctions. *Nano Lett.* **2010**, *10*, 4260−4265.
(11) Limacher, P. A.; Lüthi, H. P. Cross-Conjugation. *Wiley Interdiscip. Rev. Comput. Mol. Sci.* **2011**, *1*, 477−486.
(12) Thompson, A. L.; Ahn, T.-S.; Thomas, K. R. J.; Thayumanavan, S.; Martínez, T. J.; Bardeen, C. J. Using Meta Conjugation To Enhance Charge Separation versus Charge Recombination in Phenylacetylene Donor-Bridge-Acceptor Complexes. *J. Am. Chem. Soc.* **2005**, *127*, 16348−16349.
(13) Wang, S.; Wang, W.; Lin, N. Resolving Band-Structure Evolution and Defect-Induced States of Single Conjugated Oligomers by Scanning Tunneling Microscopy and Tight-Binding Calculations. *Phys. Rev. Lett.* **2011**, *106*, 206803.
(14) Tada, T.; Yoshizawa, K. Molecular Design of Electron Transport with Orbital Rule: Toward Conductance-Decay Free Molecular Junctions. *Phys. Chem. Chem. Phys.* **2015**, *17*, 32099−32110.
(15) Terao, J.; Wadahama, A.; Matono, A.; Tada, T.; Watanabe, S.; Seki, S.; Fujihara, T.; Tsuji, Y. Design Principle for Increasing Charge Mobility of π-Conjugated Polymers Using Regularly Localized Molecular Orbitals. *Nat. Commun.* **2013**, *4*, 1691.
(16) Cai, J.; Ruffieux, P.; Jaafar, R.; Bieri, M.; Braun, T.; Blankenburg, S.; Muoth, M.; Seitsonen, A. P.; Saleh, M.; Feng, X.; Müllen, K.; Fasel, R. Atomically Precise Bottom-Up Fabrication of Graphene Nanoribbons. *Nature* **2010**, *466*, 470−473.
(17) Talirz, L.; Ruffieux, P.; Fasel, R. On-Surface Synthesis of Atomically Precise Graphene Nanoribbons. *Adv. Mater.* **2016**, *28*, 6222−6231.
(18) de Oteyza, D. G.; Garcia-Lekue, A.; Vilas-Varela, M.; Merino-Díez, N.; Carbonell-Sanromà, E.; Corso, M.; Vasseur, G.; Rogero, C.; Guitián, E.; Pascual, J. I.; Ortega, J. E.; Wakayama, Y.; Peña, D. Substrate-Independent Growth of Atomically Precise Chiral Graphene Nanoribbons. *ACS Nano* **2016**, *10*, 9000−9008.
(19) Corso, M.; Carbonell-Sanromà, E.; de Oteyza, D. G. In *On-Surface Synthesis II*; de Oteyza, D. G., Rogero, C., Eds.; Springer International Publishing: Cham, 2018; pp 113−152.
(20) Gröning, O.; Wang, S.; Yao, X.; Pignedoli, C. A.; Borin Barin, G.; Daniels, C.; Cupo, A.; Meunier, V.; Feng, X.; Narita, A.; Müllen, K.; Ruffieux, P.; Fasel, R. Engineering of Robust Topological Quantum Phases in Graphene Nanoribbons. *Nature* **2018**, *560*, 209−213.
(21) Rizzo, D. J.; Veber, G.; Cao, T.; Bronner, C.; Chen, T.; Zhao, F.; Rodriguez, H.; Louie, S. G.; Crommie, M. F.; Fischer, F. R. Topological Band Engineering of Graphene Nanoribbons. *Nature* **2018**, *560*, 204−208.
(22) Fan, Q.; Wang, C.; Han, Y.; Zhu, J.; Hieringer, W.; Kuttner, J.; Hilt, G.; Gottfried, J. M. Surface-Assisted Organic Synthesis of Hyperbenzene Nanotroughs. *Angew. Chem., Int. Ed.* **2013**, *52*, 4668−4672.
(23) Vasseur, G.; Fagot-Revurat, Y.; Sicot, M.; Kierren, B.; Moreau, L.; Malterre, D.; Cardenas, L.; Galeotti, G.; Lipton-Duffin, J.; Rosei, F.; Di Giovannantonio, M.; Contini, G.; Le Fèvre, P.; Bertran, F.; Liang, L.; Meunier, V.; Perepichka, D. F. Quasi One-Dimensional Band Dispersion and Surface Metallization in Long-Range Ordered Polymeric Wires. *Nat. Commun.* **2016**, *7*, 10235.
(24) Basagni, A.; Vasseur, G.; Pignedoli, C. A.; Vilas-Varela, M.; Peña, D.; Nicolas, L.; Vitali, L.; Lobo-Checa, J.; de Oteyza, D. G.; Sedona, F.; Casarin, M.; Ortega, J. E.; Sambi, M. Tunable Band Alignment with Unperturbed Carrier Mobility of On-Surface Synthesized Organic Semiconducting Wires. *ACS Nano* **2016**, *10*, 2644−2651.
(25) Abadía, M.; Ilyn, M.; Piquero-Zulaica, I.; Gargiani, P.; Rogero, C.; Ortega, J. E.; Brede, J. Polymerization of Well-Aligned Organic Nanowires on a Ferromagnetic Rare-Earth Surface Alloy. *ACS Nano* **2017**, *11*, 12392−12401.

DOI: 10.1021/acsnano.8b06536
ACS Nano 2018, 12, 10537−10544

(26) Ortega, J. E.; Mugarza, A.; Repain, V.; Rousset, S.; Pérez-Dieste, V.; Mascaraque, A. One-Dimensional versus Two-Dimensional Surface States on Stepped Au(111). *Phys. Rev. B: Condens. Matter Mater. Phys.* **2002**, *65*, 165413.
(27) Mugarza, A.; Schiller, F.; Kuntze, J.; Cordón, J.; Ruiz-Osés, M.; Ortega, J. E. Modelling Nanostructures with Vicinal Surfaces. *J. Phys.: Condens. Matter* **2006**, *18*, S27.
(28) Corso, M.; Schiller, F.; Fernández, L.; Cordón, J.; Ortega, J. E. Electronic States in Faceted Au(111) Studied with Curved Crystal Surfaces. *J. Phys.: Condens. Matter* **2009**, *21*, 353001.
(29) Ortega, J. E.; Vasseur, G.; Piquero-Zulaica, I.; Matencio, S.; Valbuena, M. A.; Rault, J. E.; Schiller, F.; Corso, M.; Mugarza, A.; Lobo-Checa, J. Structure and Electronic States of Vicinal Ag(111) Surfaces with Densely Kinked Steps. *New J. Phys.* **2018**, *20*, 073010.
(30) Ruffieux, P.; Cai, J.; Plumb, N. C.; Patthey, L.; Prezzi, D.; Ferretti, A.; Molinari, E.; Feng, X.; Müllen, K.; Pignedoli, C. A.; Fasel, R. Electronic Structure of Atomically Precise Graphene Nanoribbons. *ACS Nano* **2012**, *6*, 6930−6935.
(31) Senkovskiy, B. V.; Usachov, D. Y.; Fedorov, A. V.; Haberer, D.; Ehlen, N.; Fischer, F. R.; Grüneis, A. Finding the Hidden Valence Band of N = 7 Armchair Graphene Nanoribbons with Angle-Resolved Photoemission Spectroscopy. *2D Mater.* **2018**, *5*, 035007.
(32) Cai, L.; Yu, X.; Liu, M.; Sun, Q.; Bao, M.; Zha, Z.; Pan, J.; Ma, H.; Ju, H.; Hu, S.; Xu, L.; Zou, J.; Yuan, C.; Jacob, T.; Björk, J.; Zhu, J.; Qiu, X.; Xu, W. Direct Formation of C−C Double-Bonded Structural Motifs by On-Surface Dehalogenative Homocoupling of *gem* -Dibromomethyl Molecules. *ACS Nano* **2018**, *12*, 7959−7966.
(33) Merino-Díez, N.; Lobo-Checa, J.; Nita, P.; Garcia-Lekue, A.; Basagni, A.; Vasseur, G.; Tiso, F.; Sedona, F.; Das, P. K.; Fujii, J.; Vobornik, I.; Sambi, M.; Pascual, J. I.; Ortega, J. E.; de Oteyza, D. G. Switching from Reactant to Substrate Engineering in the Selective Synthesis of Graphene Nanoribbons. *J. Phys. Chem. Lett.* **2018**, *9*, 2510−2517.
(34) Bieri, M.; Nguyen, M.-T.; Gröning, O.; Cai, J.; Treier, M.; Aït-Mansour, K.; Ruffieux, P.; Pignedoli, C. A.; Passerone, D.; Kastler, M.; Müllen, K.; Fasel, R. Two-Dimensional Polymer Formation on Surfaces: Insight into the Roles of Precursor Mobility and Reactivity. *J. Am. Chem. Soc.* **2010**, *132*, 16669−16676.
(35) Judd, C. J.; Haddow, S. L.; Champness, N. R.; Saywell, A. Ullmann Coupling Reactions on Ag(111) and Ag(110); Substrate Inuence on the Formation of Covalently Coupled Products and Intermediate Metal-Organic Structures. *Sci. Rep.* **2017**, *7*, 14541.
(36) Wang, W.; Shi, X.; Wang, S.; Van Hove, M. A.; Lin, N. Single-Molecule Resolution of an Organometallic Intermediate in a Surface-Supported Ullmann Coupling Reaction. *J. Am. Chem. Soc.* **2011**, *133*, 13264−13267.
(37) Di Giovannantonio, M.; El Garah, M.; Lipton-Duffin, J.; Meunier, V.; Cardenas, L.; Fagot Revurat, Y.; Cossaro, A.; Verdini, A.; Perepichka, D. F.; Rosei, F.; Contini, G. Insight into Organometallic Intermediate and Its Evolution to Covalent Bonding in Surface-Confined Ullmann Polymerization. *ACS Nano* **2013**, *7*, 8190−8198.
(38) Fan, Q.; Wang, C.; Han, Y.; Zhu, J.; Kuttner, J.; Hilt, G.; Gottfried, J. M. Surface Assisted Formation, Assembly, and Dynamics of Planar Organometallic Macrocycles and Zigzag Shaped Polymer Chains with C-Cu-C Bonds. *ACS Nano* **2014**, *8*, 709−718.
(39) Koch, M.; Gille, M.; Viertel, A.; Hecht, S.; Grill, L. Substrate-Controlled Linking of Molecular Building Blocks: Au(111) vs. Cu(111). *Surf. Sci.* **2014**, *627*, 70−74.
(40) Chen, M.; Shang, J.; Wang, Y.; Wu, K.; Kuttner, J.; Hilt, G.; Hieringer, W.; Gottfried, J. M. On-Surface Synthesis and Characterization of Honeycombene Oligophenylene Macrocycles. *ACS Nano* **2017**, *11*, 134−143.
(41) Fan, Q.; Wang, T.; Dai, J.; Kuttner, J.; Hilt, G.; Gottfried, J. M.; Zhu, J. On-Surface Pseudo-High-Dilution Synthesis of Macrocycles: Principle and Mechanism. *ACS Nano* **2017**, *11*, 5070−5079.
(42) Merino-Díez, N.; Garcia-Lekue, A.; Carbonell-Sanromà, E.; Li, J.; Corso, M.; Colazzo, L.; Sedona, F.; Sánchez-Portal, D.; Pascual, J. I.; de Oteyza, D. G. Width Dependent Band Gap in Armchair Graphene Nanoribbons Reveals Fermi Level Pinning on Au(111). *ACS Nano* **2017**, *11*, 11661−11668.
(43) Fan, Q.; Liu, L.; Dai, J.; Wang, T.; Ju, H.; Zhao, J.; Kuttner, J.; Hilt, G.; Gottfried, J. M.; Zhu, J. Surface Adatom Mediated Structural Transformation in Bromoarene Monolayers: Precursor Phases in Surface Ullmann Reaction. *ACS Nano* **2018**, *12*, 2267−2274.
(44) Offenbacher, H.; Lüftner, D.; Ules, T.; Reinisch, E. M.; Koller, G.; Puschnig, P.; Ramsey, M. G. Orbital Tomography: Molecular Band Maps, Momentum Maps and the Imaging of Real Space Orbitals of Adsorbed Molecules. *J. Electron Spectrosc. Relat. Phenom.* **2015**, *204*, 92−101.
(45) Koller, G.; Berkebile, S.; Oehzelt, M.; Puschnig, P.; Ambrosch-Draxl, C.; Netzer, F. P.; Ramsey, M. G. Intra- and Intermolecular Band Dispersion in an Organic Crystal. *Science* **2007**, *317*, 351−355.
(46) Mugarza, A.; Mascaraque, A.; Pérez-Dieste, V.; Repain, V.; Rousset, S.; García de Abajo, F. J.; Ortega, J. E. Electron Connement in Surface States on a Stepped Gold Surface Revealed by Angle-Resolved Photoemission. *Phys. Rev. Lett.* **2001**, *87*, 107601.
(47) Abd El-Fattah, Z. M.; Kher-Elden, M. A.; Piquero-Zulaica, I.; García de Abajo, F. J.; Ortega, J. E. Graphene: Free Electron Scattering Within an Inverted Honeycomb Lattice. arXiv:1808.06034.
(48) Fan, Q.; Dai, J.; Wang, T.; Kuttner, J.; Hilt, G.; Gottfried, J. M.; Zhu, J. Confined Synthesis of Organometallic Chains and Macrocycles by Cu-O Surface Templating. *ACS Nano* **2016**, *10*, 3747−3754.
(49) Piquero-Zulaica, I.; Lobo-Checa, J.; Sadeghi, A.; Abd El-Fattah, Z. M.; Mitsui, C.; Okamoto, T.; Pawlak, R.; Meier, T.; Arnau, A.; Ortega, J. E.; Takeya, J.; Goedecker, S.; Meyer, E.; Kawai, S. Precise Engineering of Quantum Dot Array Coupling Through Their Barrier Widths. *Nat. Commun.* **2017**, *8*, 787.
(50) Gross, L.; Moll, N.; Mohn, F.; Curioni, A.; Meyer, G.; Hanke, F.; Persson, M. High-Resolution Molecular Orbital Imaging Using a p-Wave STM Tip. *Phys. Rev. Lett.* **2011**, *107*, No. 086101, DOI: 10.1103/PhysRevLett.107.086101.
(51) Hieulle, J.; Carbonell-Sanromà, E.; Vilas-Varela, M.; Garcia-Lekue, A.; Guitián, E.; Peña, D.; Pascual, J. I. On-Surface Route for Producing Planar Nanographenes with Azulene Moieties. *Nano Lett.* **2018**, *18*, 418−423.
(52) Ohtomo, M.; Sekine, Y.; Hibino, H.; Yamamoto, H. Graphene Nanoribbon Field-Effect Transistors Fabricated by Etchant-Free Transfer from Au(788). *Appl. Phys. Lett.* **2018**, *112*, 021602.
(53) Llinas, J. P.; et al. Short-Channel Field-Effect Transistors with 9-Atom and 13-Atom Wide Graphene Nanoribbons. *Nat. Commun.* **2017**, *8*, 633.
(54) Moreno, C.; Vilas-Varela, M.; Kretz, B.; Garcia-Lekue, A.; Costache, M. V.; Paradinas, M.; Panighel, M.; Ceballos, G.; Valenzuela, S. O.; Peña, D.; Mugarza, A. Bottom Up Synthesis of Multifunctional Nanoporous Graphene. *Science* **2018**, *360*, 199−203.
(55) Fan, Q.; Gottfried, J. M.; Zhu, J. Surface-Catalyzed C-C Covalent Coupling Strategies toward the Synthesis of Low-Dimensional Carbon-Based Nanostructures. *Acc. Chem. Res.* **2015**, *48*, 2484−2494.
(56) Goddard, P.; Schwaha, K.; Lambert, R. Adsorption-Desorption Properties and Surface Structural Chemistry of Bromineon Clean and Sodium-Dosed Ag(111). *Surf. Sci.* **1978**, *71*, 351−363.
(57) Horcas, I.; Fernández, R.; Gómez-Rodríguez, J. M.; Colchero, J.; Gómez-Herrero, J.; Baro, A. M. WSXM: A Software for Scanning Probe Microscopy and a Tool for Nan otechnology. *Rev. Sci. Instrum.* **2007**, *78*, 013705.
(58) Soler, J. M.; Artacho, E.; Gale, J. D.; García, A.; Junquera, J.; Ordejón, P.; Sánchez Portal, D. The SIESTA Method for *Ab Initio* Order-*N* Materials Simulation. *J. Phys.: Condens. Matter* **2002**, *14*, 2745−2779.
(59) Klimes, J.; Bowler, D. R.; Michaelides, A. Chemical Accuracy for the Van Der Waals Density Functional. *J. Phys.: Condens. Matter* **2010**, *22*, 022201.

DOI: 10.1021/acsnano.8b06536
ACS Nano 2018, 12, 10537−10544

Supplementary Information of:

Electronic Structure Tunability by Periodic *meta*-Ligand Spacing in One-Dimensional Organic Semiconductors

Ignacio Piquero-Zulaica[*,1], Aran Garcia-Lekue[2,3], Luciano Colazzo[2], Claudio K. Krug[4], Mohammed S. G. Mohammed[1,2], Zakaria M. Abd El-Fattah[5,6], J. Michael Gottfried[4], Dimas G. de Oteyza[1,2,3], J. Enrique Ortega[1,2,7], Jorge Lobo-Checa[*,8,9]

[1]Centro de Física de Materiales CSIC/UPV-EHU-Materials Physics Center, Paseo Manuel de Lardizabal 5, E-20018 San Sebastián, Spain
[2]Donostia International Physics Center (DIPC), Paseo Manuel de Lardizabal 4, E-20018 Donostia-San Sebastián, Spain
[3]Ikerbasque, Basque Foundation for Science, 48011 Bilbao, Spain
[4]Fachbereich Chemie, Philipps-Universität Marburg, Hans-Meerwein-Str. 4, 35032 Marburg, Germany
[5] ICFO-Institut de Ciencies Fotoniques, The Barcelona Institute of Science and Technology, 08860 Castelldefels, Barcelona, Spain
[6] Physics Department, Faculty of Science, Al-Azhar University, Nasr City, E-11884 Cairo, Egypt
[7]Dpto. Física Aplicada I, Universidad del País Vasco, E-20018 San Sebastián, Spain
[8]Instituto de Ciencia de Materiales de Aragón (ICMA), CSIC-Universidad de Zaragoza, E-50009 Zaragoza, Spain
[9]Departamento de Física de la Materia Condensada, Universidad de Zaragoza, E-50009 Zaragoza, Spain

This file discussess the following topics related to the main manuscript:

1. Growth Details and Zigzag Chain Alignment on a Ag(111) Curved Vicinal Crystal.
2. ARPES Band Structure and Photoemission Intensity Simulations Using the Electron Plane Wave Expansion (EPWE) Method.
3. Br Effect on the Electronic Structure of Zigzag Chains Studied by STM/STS.
4. ARPES Band Structure Comparison of Zigzag Chains vs Poly(*para*-Phenylene) (PPP) Chains.
5. Band Structure Variations with Straight Segment's Length of the Zigzag Chains from DFT Calculations.
6. Phenyl Twisting Considerations of Zigzag Chains by STM/STS and DFT.

It contains 10 supporting figures and its corresponding references.

I. Growth Details and Zigzag Chain Alignment on a Ag(111) Curved Vicinal Crystal

We have used a curved vicinal Ag(111) crystal[1] featuring 100% kinked steps running along the [11-2] direction (Fig. S1a, b). These steps promote the long-range zigzag chain ordering, an essential requirement to obtain properly defined band structures. The substrate's band structure has the *d*-bands' onset below -3 eV, which provides a large energy window for the zigzag chain bands undisrupted observation (Fig. S1c, d).

Zigzag chains grow into a long-range ordered polymer film parallel to the steps at the sample position of ~3.6º off from the (111) region, yielding a (9, 5; 0, 4) matrix superstructure in LEED (Figure S2 (a-c)). However, in the (111) region, the chains condense into multidomains, as extracted from STM topography images and macroscopically by LEED (Figure S2 (d-f)).

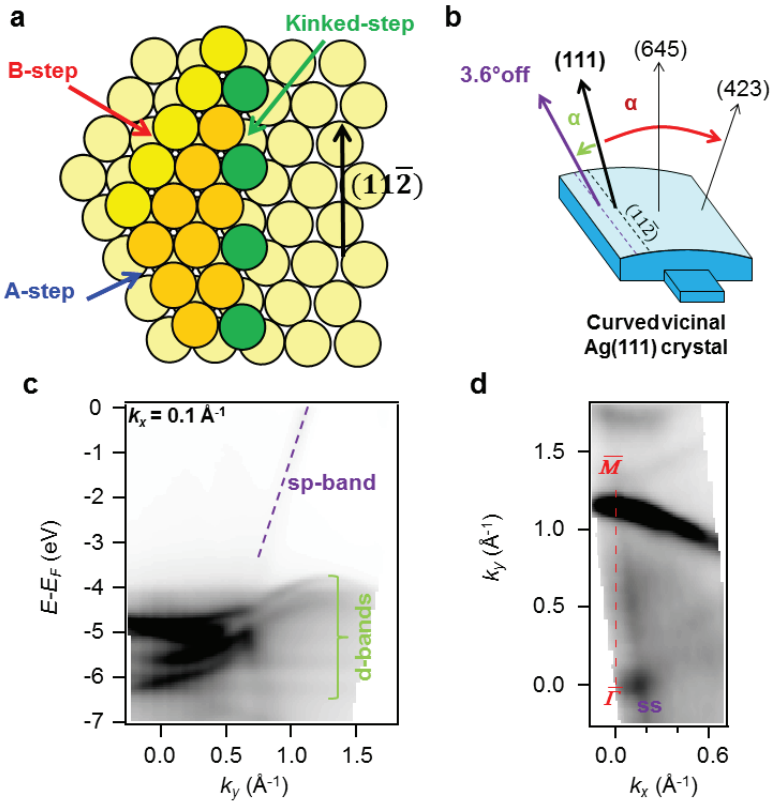

Figure S1 *Atomic and macroscopic geometry of the 100% kinked curved Ag(111) crystal and its electronic structure ~3.6° off the (111) plane.* ***(a)*** *Schematic drawing highlighting the three step types present on close-packed vicinal surfaces. In our case, the step termination corresponds to the one ending in the green spheres (100% kinked) that runs along the [11-2] direction. (**b**) Schematic drawing of the curved Ag(111) substrate. The crystal was polished so that the (111) region is away from the center of the crystal by 9.27°. Zigzag chain films showed best alignment at the position with a local vicinal plane of ~3.6° off from the (111) region, where kinked steps are 3.8 nm separated in average from*

*each other. (**c**) The ARPES band structure (E vs k_y) at k_x = 0.1 Å^{-1} corresponds to the direction parallel to the [11-2]. The characteristic silver d-bands exist below -3 eV and the sp-band shows a large dispersive character as it raises and crosses the Fermi level (highlighted by a side dashed purple line). (**d**) Fermi Surface Map (k_x vs k_y at E = 0), exhibiting the characteristic Shockley state (surface state) close to the $\bar{\Gamma}$ point and the dispersive dominant sp-bulk bands closer to the $\bar{M}$ point.*

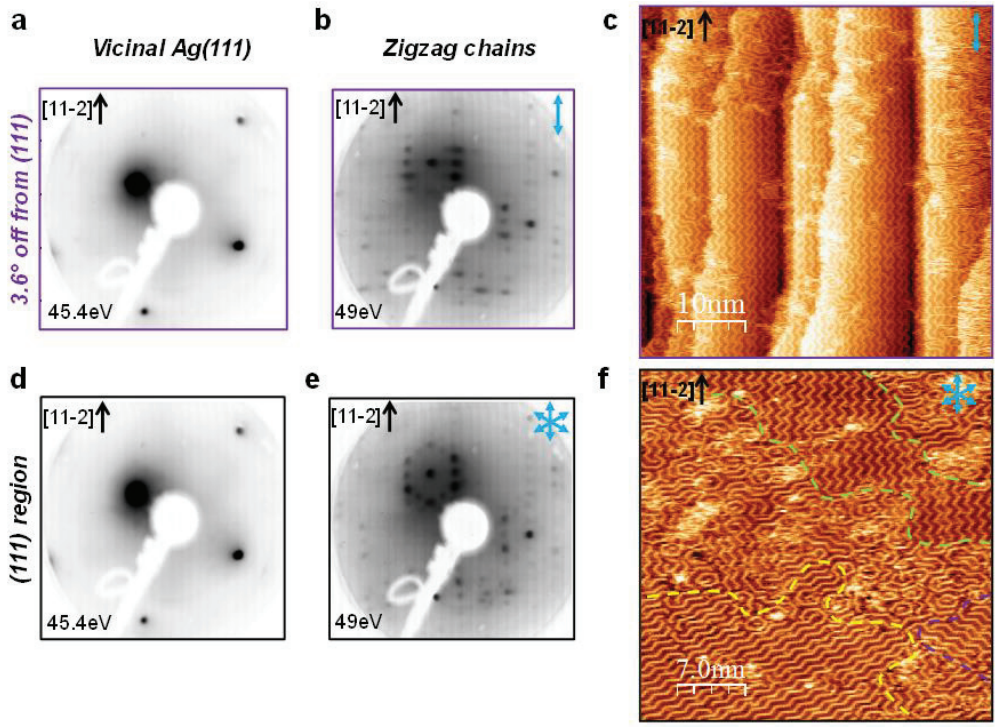

Figure S2 | Uniaxial zigzag chain ordering vs multi-domain structures determined by LEED and STM. *Experimental LEED patterns of the silver substrate before **(a)** and after **(b)** the formation of the zigzag chain film at the ~3.6° position off from the (111). This pattern agrees with a (9, 5; 0, 4) matrix, which corresponds to an elbow-elbow distance of 9 atomic spacings of the Ag substrate. (**c**) Corresponding STM image showing macroscopic preferential uniaxial alignment of the zigzag chains parallel to the step direction (STM parameters: size = 50 x 50 nm^2, V = -393.7 mV; I = 234 pA). Panels (**d**) and (**e**) show respectively the LEED patterns of the pristine silver substrate before and after forming zigzag chains at the (111) region. At this position, a hexagonal pattern around the (0,0) spot is observed which evidences that the chains primarily follow three main directions. This is accordingly observed in the corresponding STM image in (**f**), where 120° rotated patches co-exist as highlighted in green, yellow and purple. (STM parameters: size = 35 x 35 nm^2, V = 425.2 mV; I = 254 pA).*

II. ARPES Band Structure and Photoemission Intensity Simulations Using the Electron Plane Wave Expansion (EPWE) Method

The ARPES band structure for the zigzag chains presented in Fig.1 of the main manuscript, corresponds to the second derivative treatment of the photoemission intensity. Such data treatment is used to enhance weak photoemission features. For completeness, the raw data is included in Fig. S3.

To capture the photoemission intensity modulations observed in ARPES, we perform photoemission intensity simulations using the EPWE method[3]. These simulations (excluding the substrate and Br atoms presence) match the experimental data in Fig. S4 and support the argument of the scarce effects that the underlying Ag substrate and Br atoms have on the electronic properties of the zigzag chains.

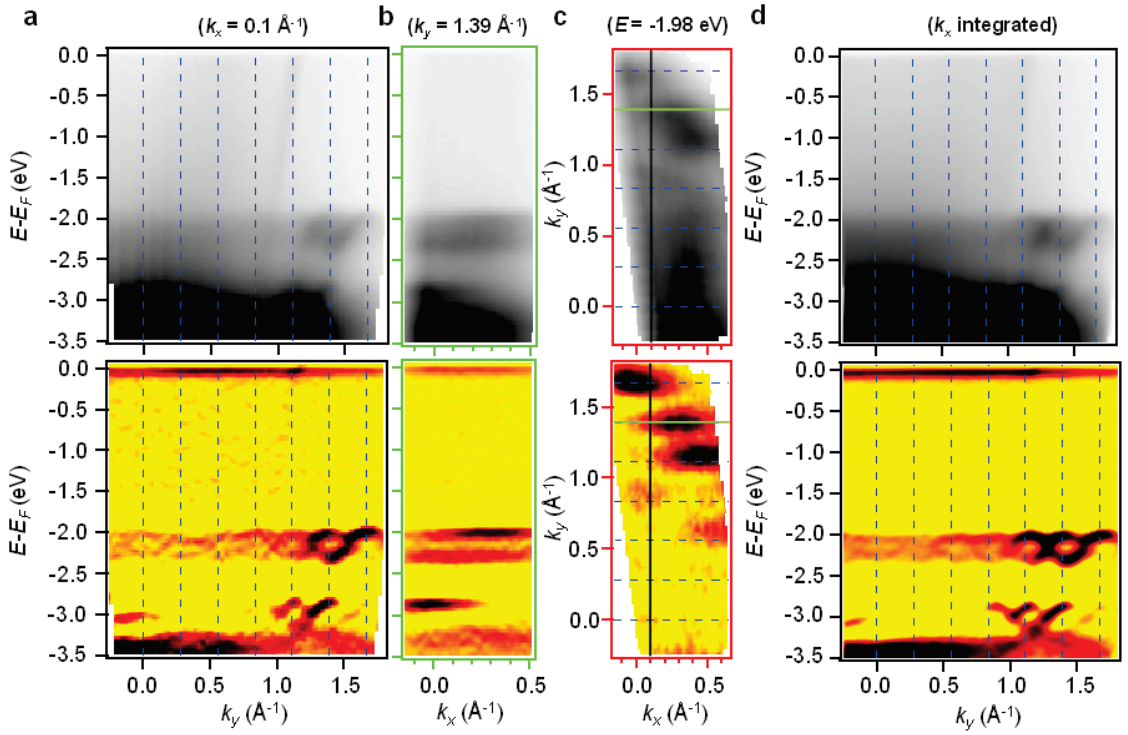

Figure S3 | Raw data comparison to the 2nd derivative treatment for the electronic band structure of zigzag chains at the vicinal plane ~3.6° off the (111) region. *The ARPES spectral intensity raw data is shown on the top row and the 2nd derivative in the bottom row. (**a**) ARPES band maps (E vs k_y) for k_x = 0.1 Å^{-1}. (**b**) Band structure perpendicular to the chains average axis (E vs k_x with k_y = 1.39 Å^{-1}). (**c**) Isoenergetic cut (k_x vs k_y) at the top of the VB (E = -1.98 eV). The photoemission intensity presented in (a) has been obtained by following the direction highlighted by the vertical black line. The band structure perpendicular to the main zigzag chain axis shown in (b) is shown as a horizontal green line. **(d)** The k_x integrated ARPES spectral intensity is shown to better*

capture all the replicating bands, which follow the periodicity of the zigzag chain unit cell (2π/L) marked with vertical dashed blue lines.

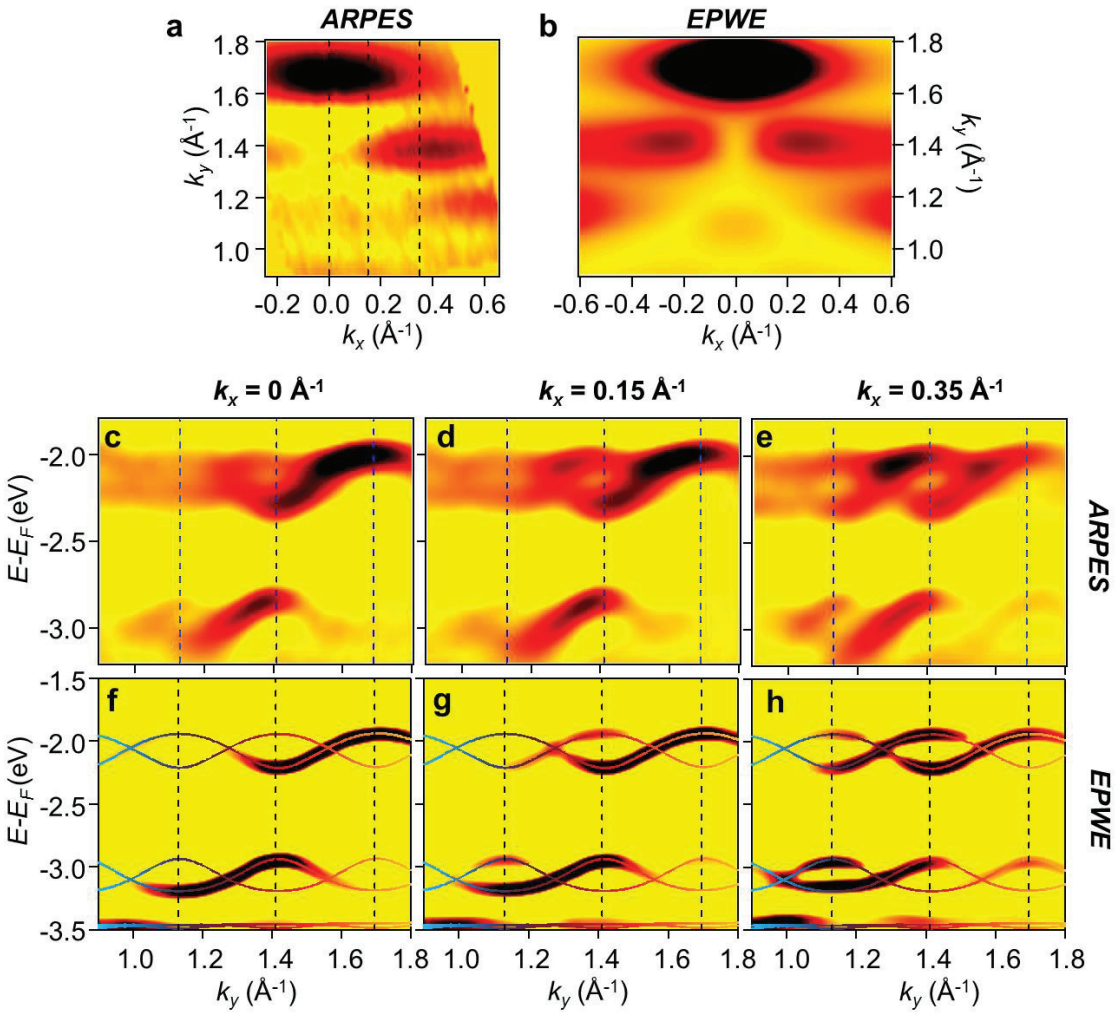

Figure S4 | Experimental ARPES data comparison to EPWE photoemission intensity simulations. *The top row (**a, b**) shows the 2nd derivative of the ARPES and EPWE isoenergetic cuts (k_x vs k_y) performed at the top of the VB (E=-1.98 eV in ARPES). The middle row **(c-e)** corresponds to the 2nd derivative of the experimental ARPES spectral intensities (E vs k_y) at different k_x values (indicated as dashed lines in (a)). The bottom row **(f-h)** shows the equivalent photoemission intensity simulations performed with the EPWE code. Their match is exceptional, supporting the idea of weak electronic interactions between the zigzag chains with the substrate and surrounding Br atoms.*

III. Br Effect on the Electronic Structure of Zigzag Chains Studied by STM/STS

After the Ullmann coupling reaction takes place, zigzag chains condense into islands. The cleaved Br atoms accumulate between the chains (Fig.1 in the main manuscript and Fig. S5). These observations have been already reported for zigzag chains grown on Cu(111), hyperbenzene and honeycombene closed rings on Ag(111) and other covalent nanostructures such as PPP chains[4,5,6,7]. The Br atoms remain on the Ag(111) up to ~600 K and can likely stabilize the long-range ordered zigzag structures observed in the present work. According to Merino and co-workers[7] the desorption of Br atoms intercalated in between the chains produces a lowering of the work function and a shift of the electronic states to higher binding energies without affecting their effective mass. We obtain similar results when we compare dI/dV spectra of tip manipulated isolated chains with island condensed ones (Fig. S5). In particular, we observe a rigid shift of the frontier orbitals to higher energies by 200 ± 50 mV, implying that the *N*=4 zigzag chain energy gap (~3.7 eV) is unchanged. This evidences the limited effect of the halogen atoms on the electronic properties of the polymers.

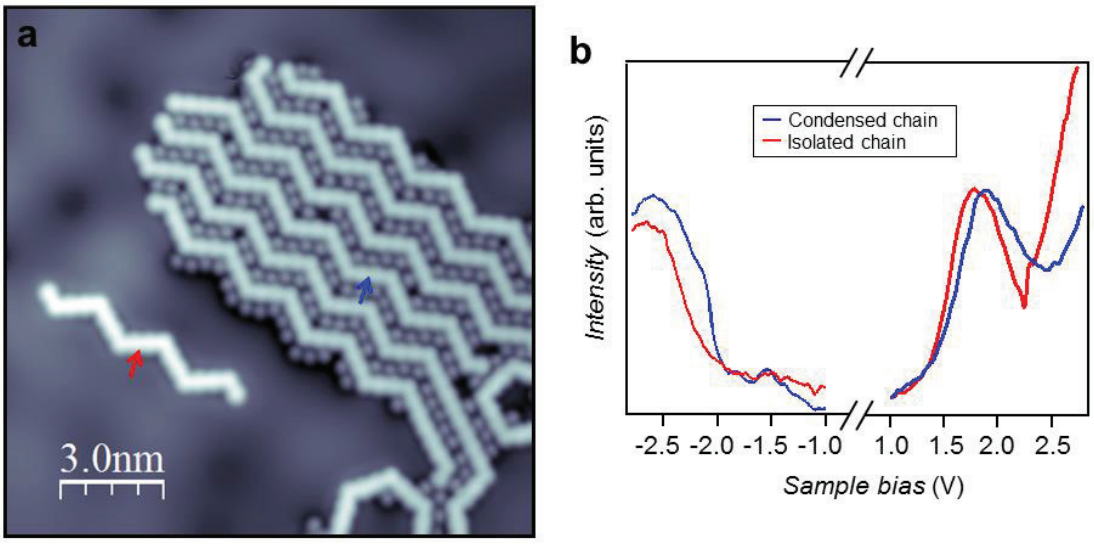

Figure S5 | Effect of Br adatoms on the electronic structure of isolated and condensed chains. ***(a)*** *STM image of a Br stabilized zigzag chain island (condensed chains) and an isolated, Br-free zigzag chain obtained via tip manipulation (Imaging parameters: 50 mV, 100 pA; frame: 15 x 15 nm²).* ***(b)*** *Corresponding constant-height dI/dV spectra for the VB and CB at selected positions. The presence of Br rigidly shifts the VB and CB onsets by 200 ± 50 mV to higher energies (STS parameters: Bias voltage modulation of 10 mV_{rms} at 341 Hz. Close-feedback parameters: -350 mV, 150 pA and 1200 mV, 100 pA for the negative and positive resonances regions, respectively).*

IV. ARPES Band Structure Comparison of Zigzag Chains vs Poly-(*Para*-Phenylene) (PPP) Chains.

The occupied experimental band structure of the zigzag chains is compared to the straight PPP chains in Figure S6. The PPP polymer film has likewise been grown using a vicinal Ag substrate with (544) orientation and featuring an average terrace width of 2.4 nm terminated by straight steps rotated 30º from the fully kinked curved Ag(111) (see Figure S1). Indeed, the step direction of Ag(544) follows the [1-10] direction and the terraces are slightly smaller than the one used for the zigzag, but can still host in average 3-4 parallel chains. The difference in the electronic nature between both chain types is evident from the dataset and closely follows the DFT calculations reported in Fig. 2 of the main text.

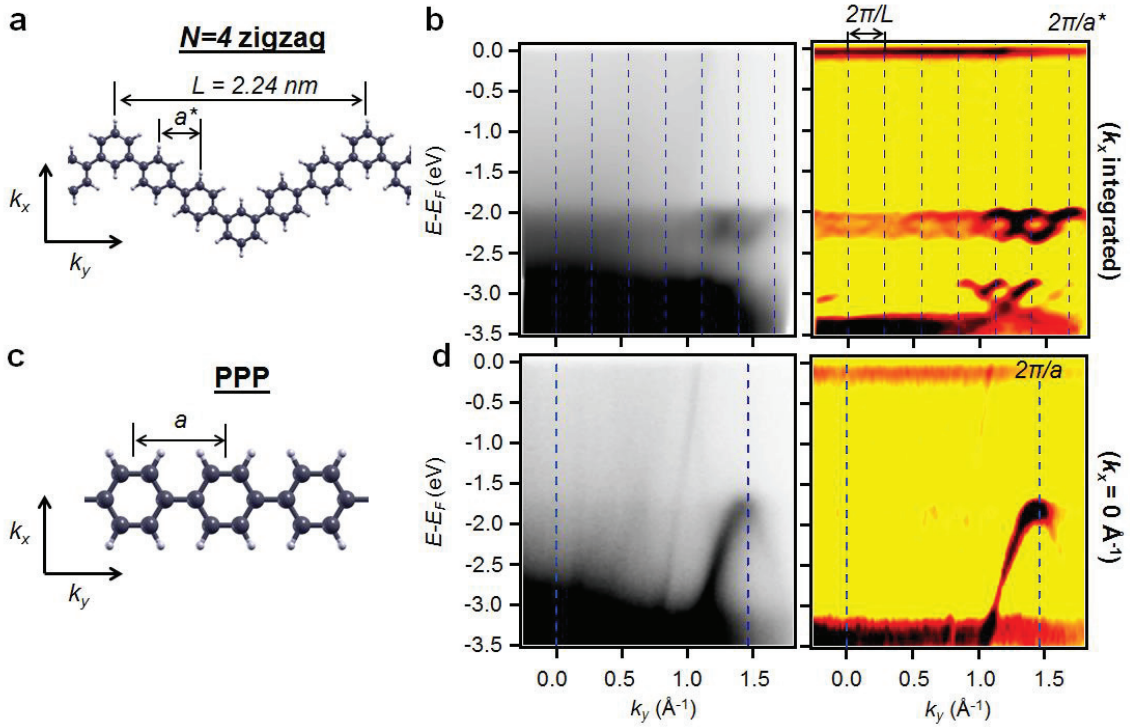

Figure S6 | N=4 zigzag chain ARPES band structure comparison with that of PPP chains. *Schematic representations of the N=4 zigzag chains* ***(a)*** *and the poly(para-phenylene) (PPP) chains* ***(c)****.* ***(b)*** *and* ***(d)*** *show in the same row their respective raw (left) and second derivative (right) of the* k_x *integrated ARPES spectral intensity (E vs* k_y*) along the chain axis. These plots follow the periodicity of the chain unit cells (2π/L) marked with vertical dashed blue lines. For the PPP polymer film the substrate used is a Ag(544) vicinal crystal (see text for details).*

V. Band Structure Variations with Straight Segment's Length of the Zigzag Chains from DFT Calculations

To further investigate the evolution of the frontier orbital bandgap and electronic structure with the straight segment's length, we perform additional DFT calculations. As indicated in the main manuscript and depicted in Figure S7, zigzag chains with *N*=4 bear a closer resemblance to poly(*meta*-phenylene) (PMP) rather than to the straight, highly dispersive polymer poly(*para*-phenylene) (PPP) counterpart. Moreover, a gradual reduction of the electronic bandgap of the frontier orbitals is already observed (PMP > zigzag *N*= 4 > zigzag *N*= 7 > PPP) as the straight segments are enlarged. Such an evolution is clearly shown in Fig. S8 for a varying number of phenyl rings from 4 up to 11 in a planar, free-standing configuration. In agreement with previous work[9], we find that the band gap shrinks linearly as 1/*N* as the size of the straight segment is increased. This also agrees with our experimental results of Fig. 4c of the main manuscript, which are represented on the right axis of the graph. This evidences that while the electronic band dispersion is governed by the periodically spaced *meta*-junctions, the bandgap varies with the size of the straight segments.

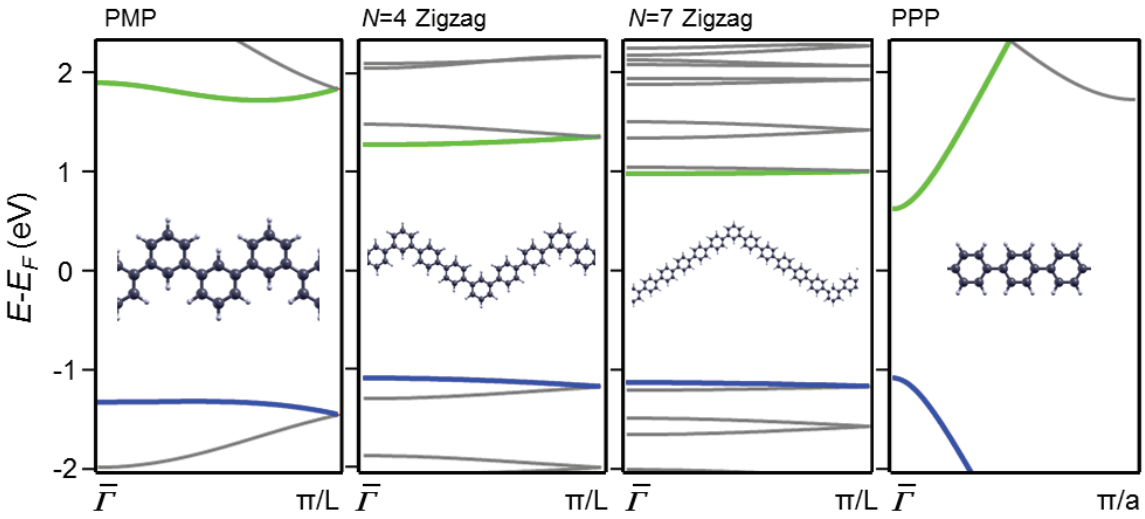

Figure S7 | Band structure comparison between PMP, zigzag and PPP chains, as obtained by DFT calculations. *The highly dispersive band structure of PPP chains (on the right) clearly shows a different behavior to the other three cases. These plots show a progressive reduction of the electronic bandgap as the meta-junctions (elbows) are separated further. We attribute this to the cross-conjugated nature of the polymers hosting periodically spaced meta-junctions.*

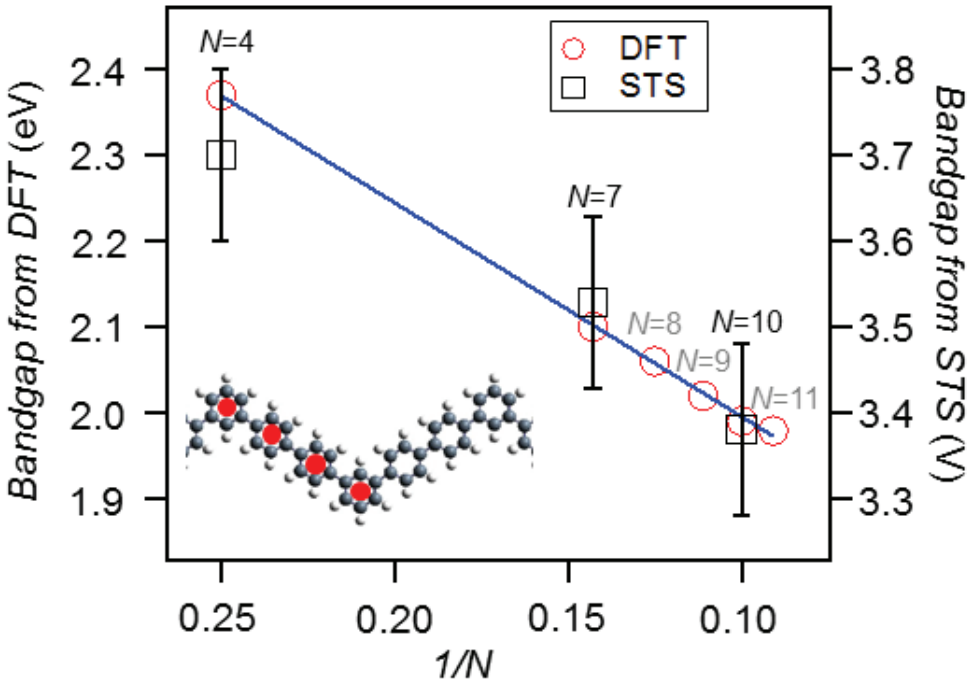

Figure S8 | Evolution of the zigzag chain frontier orbital bandgap with increasing number of phenyl rings at the straight segments. *Both DFT (theory) and STS (experimental) show a clear 1/N dependency of the bandgap with increasing number of phenyl rings inside the straight segments.*

VI. Phenyl Twisting Considerations of Zigzag Chains by STM/STS and DFT

Finally, it is worth considering the electronic effects that phenyl-phenyl twisting has on the on-surface zigzag chains. In order to reveal whether such morphological effects are present, we acquired constant height STM images with bond resolution on condensed zigzag chains (surrounded by Br atoms) that are compared with an isolated chain obtained after tip manipulation (Fig. S9). Both types of 1D structures show some very weak intensity variations at the phenyl rings, which suggest that there are slight twists in the configurations. This would agree with the observations for poly(*para*-phenylene) PPP chains where a phenyl twisting of 20 ± 5 degrees was observed with respect to the planar configuration[8]. Indeed, the surrounding morphological conditions are determinant, since the twisting is different when the zigzag chains are condensed into islands (asymmetric arms) or are isolated (symmetric twisting of consecutive arms). Such subtle variations could be caused by the hindrance of Br or by a different matching to the underlying substrate.

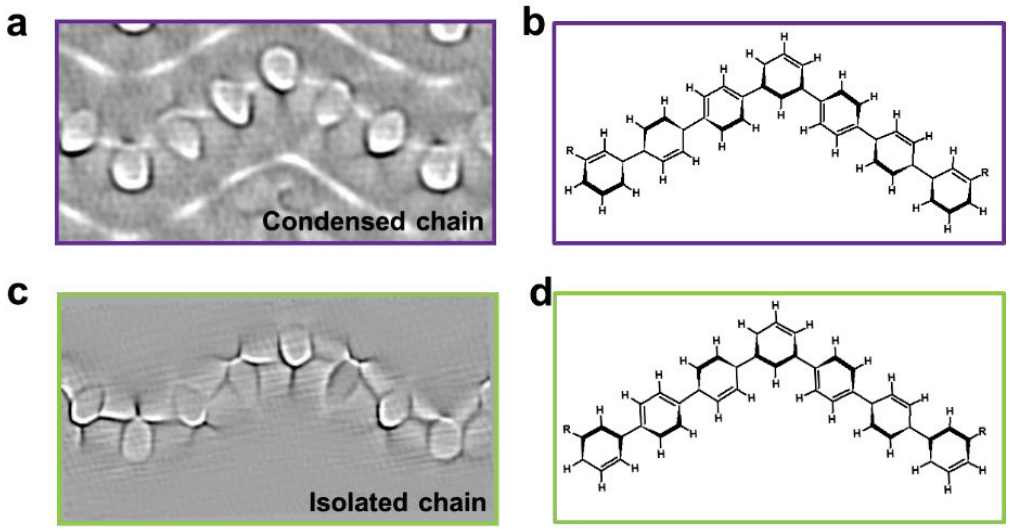

Figure S9 | Phenyl-phenyl twisting of condensed and isolated zigzag chains. *Bond-resolution STM images (current signal, post-processed with a Laplace filter) acquired at constant height with a CO-functionalized STM tip (frames: 3.0 x 1.5 nm^2, V_{tip} = 2 mV) of zigzag chains condensed within an island* ***(a)*** *and an isolated chain obtained by tip manipulation* ***(c).*** *These images suggest a slight phenyl twisting, which for the condensed chain is asymmetric with respect to the central meta-junction of both straight segments (left ascending and right descending), as shown in* ***(b)****, whereas it is symmetric with respect to the central meta-junction for both straight arms for the isolated chain, as shown in* ***(d).***

The effect that the phenyl twisting has on the electronic structure can be clarified by DFT calculations. We focus on the *N*=4 zigzag chain and we consider three phenyl twisting configurations: a single phenyl twisting, twisting of two phenyls with the same orientation, and twisting of two phenyls with opposite orientation (see Fig. S10). As shown in Fig. S10d, in all three cases the energy minimum is found for twisting angles of approximately 20 to 35 degrees with respect to the planar configuration. However, according to the results in Figure S10e, such deviations from planarity would only induce a slight increase (by about 7%) of the frontier orbital bandgap. Upon adsorption on the substrate, the polymers are known to flatten (phenyl twist of approx. 20 degrees or less), resulting in even smaller variations of the bandgap.

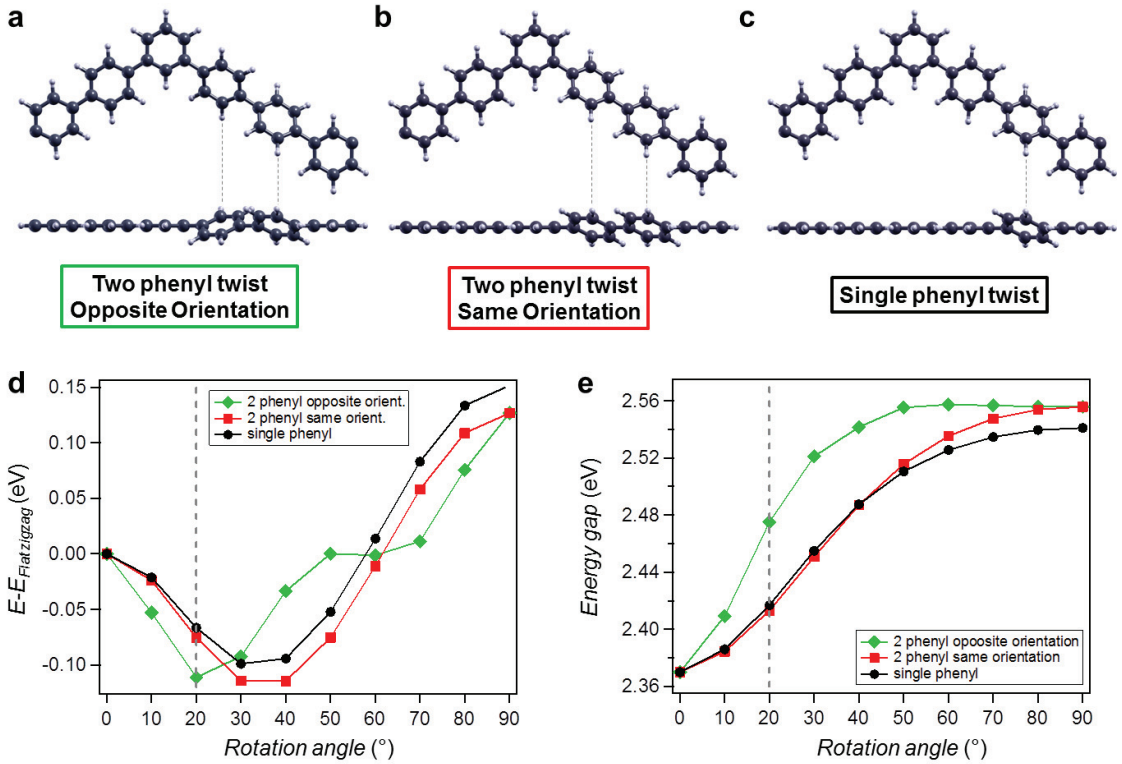

Figure S10 | Influence of phenyl-phenyl twisting on the stability of the zigzag chains and their electronic bandgap. *Three different phenyl twisting configurations have been considered: two-phenyl twist (opposite orientation)* ***(a)****, two-phenyl twist (same orientation)* ***(b)*** *and single phenyl twist* ***(c)****.* ***(d)*** *Energy of the three twisting configurations with respect to the fully planar configuration (zero energy).* ***(e)*** *Evolution of the electronic bandgap with respect to the phenyl rotation angle, for the three different configurations.*

References

(1) Ortega, J.E.; Vasseur, G.; Piquero-Zulaica, I.; Matencio, S.; Valbuena, M.; Rault, J.E.; Schiller, F.; Corso, M.; Mugarza, A.; Lobo-Checa, J. Structure and Electronic States of Vicinal Ag(111) Surfaces with Densely Kinked Steps. *New J. Phys.* **2018**, 20, 073010.

(2) Hieulle, J.; Carbonell-Sanromà, E.; Vilas-Varela, M.; Garcia-Lekue, A.; Guitián, E.; Peña, D.; Pascual, J.I. On-Surface Route for Producing Planar Nanographenes with Azulene Moieties. *Nano Lett.* **2018**, 18, 418–423.

(3) Abd El-Fattah, Z. M.; Kher-Elden, M. A.; Piquero-Zulaica, I.; García de Abajo, F. J.; Ortega, J. E. Graphene: Free Electron Scattering Within an Inverted Honeycomb Lattice. *arXiv:1808.06034*

(4) Koch, M.; Gille, M.; Viertel, A.; Hecht, S.; Grill, L. Substrate-Controlled Linking of Molecular Building Blocks: Au(111) vs. Cu(111). *Surf. Sci.* **2014**, 627, 70–74.

(5) Fan, Q.; Wang, C.; Han, Y.; Zhu, J.; Kuttner, J.; Hilt, G.; Gottfried, J.M. Surface-Assisted Formation, Assembly, and Dynamics of Planar Organometallic Macrocycles and Zigzag Shaped Polymer Chains with C–Cu–C Bonds. *ACS Nano* **2014**, 8, 709–718.

(6) Chen, M.; Shang, J.; Wang, Y.; Wu, K.; Kuttner, J.; Hilt, G.; Hieringer, W.; Gottfried, J.M. On-Surface Synthesis and Characterization of Honeycombene Oligophenylene Macrocycles. *ACS Nano* **2017**, 11, 134–143.

(7) Merino-Díez, N.; Lobo-Checa, J.; Nita, P.; Garcia-Lekue, A.; Basagni, A.; Vasseur, G.; Tiso, F.; Sedona, F.; Das, P.K.; Fujii, J.; Vobornik, I.; Sambi, M.; Pascual, J.I.; Ortega, J.E.; de Oteyza, D.G. Switching from Reactant to Substrate Engineering in the Selective Synthesis of Graphene Nanoribbons. *J. Phys. Chem. Lett.* **2018**, 9, 2510–2517.

(8) Basagni, A.; Vasseur, G.; Pignedoli, C.A.; Vilas-Varela, M.; Peña, D.; Nicolas, L.; Vitali, L.; Lobo-Checa, J.; de Oteyza, D.G.; Sedona, F.; Casarin, M.; Ortega, J.E., Sambi, M. Tunable Band Alignment with Unperturbed Carrier Mobility of On-Surface Synthesized Organic Semiconducting Wires. *ACS Nano* **2016,** 10, 2644–2651.

(9) Wang, S.; Wang, W.; Lin, N. Resolving Band-Structure Evolution and Defect-Induced States of Single Conjugated Oligomers by Scanning Tunneling Microscopy and Tight-Binding Calculations. *Phys. Rev. Lett.* **2011**, 106.

P4 Nanoribbons with Nonalternant Topology from Fusion of Polyazulene: Carbon Allotropes Beyond Graphene

Citation: Q. Fan*, D. Martin-Jimenez*, D. Ebeling, **C. K. Krug**, L. Brechmann, C. Kohlmeyer, G. Hilt, W. Hieringer, A. Schirmeisen, J. M. Gottfried, *J. Am. Chem. Soc.* **2019**, *141*(44), 17713–17720, DOI 10.1021/jacs.9b08060.

Summary

The goal of this study is to synthesize long covalent oligomeric chains from the 2,6-dibromoazulene (2,6-DBAz) precursor on Au(111). Furthermore, these chains shall be fused by dehydrogenative coupling to yield graphene nanoribbons (GNRs) with non-alternant topology. The structures formed are unraveled by scanning tunneling microscopy (STM) and non-contact atomic force microscopy (nc-AFM), accompanied by density functional theory (DFT) calculations.

The substitution pattern of the 2,6-DBAz precursor compared with its structural isomer 1,3-dibromoazulene (DBAz, *cf.* P1 and P2) is chosen in a way that only chains can be formed as products of the surface-confined Ullmann coupling reaction. However, the connection pattern of the single monomer units cannot be predicted. STM images prove that indeed long oligomeric chains are formed if 2,6-DBAz on the Au(111) surface is annealed to 690 K for 20 min. The STM images show some bright protrusions in the chains, which are attributed to the connection of two seven-membered rings, since here the steric hindrance is largest and forces the molecular backbone to rotate out of the surface plane. nc-AFM images with a CO-functionalized tip and submolecular resolution prove this hypothesis and furthermore elucidate the complete connection pattern of the chains. No preferred connection motif is found, *i.e.*, connections between two seven-membered rings are found as well as connections between two five-membered rings and connections between five- and seven-membered rings.

Annealing the oligomer chains on Au(111) to 730 K for 30 min induces the fusion of neighboring chains by dehydrogenative coupling. Depending on the chain connectivity different GNRs with non-alternant topologies can be formed. nc-AFM images with submolecular resolution show that these can be considered as nanoribbons of the two non-alternant carbon allotropes phagraphene and tetra-penta-hepta-graphene, which were theoretically predicted but had not been synthesized before. The electronic structure of these nanoribbons is investigated with DFT, suggesting lower band gaps than in their alternant counterparts.

*Q.F. and D.M.-J. contributed equally.

Own Contribution

The project leading to this publication investigating the reactions of 2,6-DBAz on Au(111) is based on the preceding investigations of the structural isomer DBAz (*cf.* P1 and P2). Since the strong steric hindrance between the H atoms at the 1- and 3-positions of DBAz made a covalent coupling between the monomers in the surface-confined Ullmann coupling impossible another substitution pattern of the interesting azulene molecule (*cf.* P8) seemed promising to synthesize polyazulene species on a surface. Thus, 2,6-DBAz was synthesized by Lea Brechmann and Corinna Kohlmeyer under the supervision of Prof. Dr. Gerhard Hilt at the Carl von Ossietzky University Oldenburg. The first experiments of 2,6-DBAz on the Au(111) surface were performed by Dr. Qitang Fan and me at the combined STM and XPS setup in the laboratory of the Gottfried group in Marburg (*cf.* Section 3.4.1). The 2,6-DBAz molecules were deposited using the line-of-sight evaporator developed and built by me (*cf.* Section 4.3). After the first very promising results it became apparent that these STM experiments needed to be complemented by nc-AFM measurements to further elucidate the structure of the reaction products. The nc-AFM measurements were performed by Dr. Qitang Fan, Dr. Daniel Martin-Jimenez and Dr. Daniel Ebeling in the laboratory of Prof. Dr. André Schirmeisen at the Justus Liebig University Gießen. Finally, the experimental results were complemented by DFT calculations by PD Dr. Wolfgang Hieringer. Dr. Qitang Fan wrote the manuscript and I contributed to its discussion along with all other co-authors.

JACS
JOURNAL OF THE AMERICAN CHEMICAL SOCIETY
Article
Cite This: J. Am. Chem. Soc. 2019, 141, 17713−17720
pubs.acs.org/JACS

Nanoribbons with Nonalternant Topology from Fusion of Polyazulene: Carbon Allotropes beyond Graphene

Qitang Fan,[†,#] Daniel Martin-Jimenez,[‡,§,#] Daniel Ebeling,[*,‡,§] Claudio K. Krug,[†] Lea Brechmann,[†] Corinna Kohlmeyer,[∥] Gerhard Hilt,[*,∥] Wolfgang Hieringer,[*,⊥] André Schirmeisen,[‡,§] and J. Michael Gottfried[*,†]

[†]Department of Chemistry, Philipps University Marburg, Hans-Meerwein-Straße 4, Marburg 35032, Germany
[‡]Institute of Applied Physics (IAP), and [§]Center for Materials Research (LaMa), Justus Liebig University Gießen, Heinrich-Buff-Ring 16, Gießen 35392, Germany
[∥]Institute of Chemistry, Carl von Ossietzky University Oldenburg, Carl-von-Ossietzky-Straße 9-11, Oldenburg 26111, Germany
[⊥]Theoretical Chemistry and Interdisciplinary Center for Molecular Materials (ICMM), Department of Chemistry and Pharmacy, Friedrich-Alexander-Universität Erlangen-Nürnberg, Egerlandstraße 3, Erlangen 91058, Germany

P4

Supporting Information

ABSTRACT: Various two-dimensional (2D) carbon allotropes with nonalternant topologies, such as pentaheptites and phagraphene, have been proposed. Predictions indicate that these metastable carbon polymorphs, which contain odd-numbered rings, possess unusual (opto)electronic properties. However, none of these materials has been achieved experimentally due to synthetic challenges. In this work, by using on-surface synthesis, nanoribbons of the nonalternant graphene allotropes, phagraphene and tetra-penta-hepta(TPH)-graphene, have been obtained by dehydrogenative C−C coupling of 2,6-polyazulene chains. These chains were formed in a preceding reaction step via on-surface Ullmann coupling of 2,6-dibromoazulene. Low-temperature scanning probe microscopies with CO-functionalized tips and density functional theory calculations have been used to elucidate their structural properties. The proposed synthesis of nonalternant carbon nanoribbons from the fusion of synthetic line-defects may pave the way for large-area preparation of novel 2D carbon allotropes.

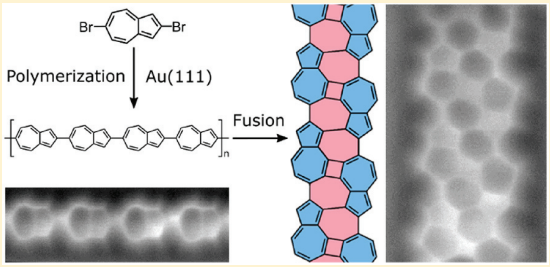

INTRODUCTION

Modifying the topology of pristine graphene with atomic precision has attracted tremendous attention in recent years, because it serves as a versatile route to novel graphene-related materials with exotic (opto)electronic properties.[1−3] Examples include graphene nanoribbons,[4−8] porous graphene,[9−11] and nanographenes,[12−16] which have been successfully prepared through various bottom-up approaches. The majority of these materials are cut-outs of graphene; that is, they are composed of sp^2 carbon atoms arranged to form benzenoid hexagonal rings. The electronic properties of these so-called alternant π-electron systems[17] are determined by factors such as size, shape, and edge structure. An alternative and not yet well-developed method to modify graphene is to change the connectivity pattern of the sp^2 carbon atoms in a nonhexagonal (nonbenzenoid) manner. Theoretical considerations have predicted the existence of numerous planar nonbenzenoid carbon allotropes,[18−20] including pentaheptites (**1**, Figure 1a),[21−23] haeckelites,[24] T-graphene,[25] octa-penta graphene,[26] pentahexoctites,[27] and phagraphene **2**.[28] These 2D carbon allotropes are expected to show dramatically different (opto)-electronic properties,[29,30] electron transportation,[31,32] magnetism,[33] chemical reactivity,[34] and mechanical stability.[33,35,36] However, the experimental realization of these materials lags far behind the theoretical studies. This problem is mainly caused by the enormous challenges that lie in the atomically precise control over the growth of extended nonbenzenoid carbon structures. Although nonbenzenoid structural motifs, such as the Stone−Wales (5−7−7−5) and 5−8−5 defects, can be randomly introduced into graphene by moderate electron beam bombardment, irradiation, or chemical treatment,[37,38] the periodic arrangement of these structural elements is so far difficult to achieve.

Very recently, the on-surface synthetic approach has demonstrated its potential for the growth of nonbenzenoid 2D carbon allotropes in a more controlled way. Through cyclodehydrogenative C−C coupling of specially designed benzenoid organic molecules, it was possible to make nanographenes with embedded 5−7 ring pairs[14,39−41] and graphene-like carbon nanoribbons with periodically arranged 4−8−4 motifs.[42,43] The growth of polymers with periodically arranged odd-numbered polygon motifs, for example, the 5−7 ring pairs, is intriguing because the connectivity pattern of

Received: July 27, 2019
Published: October 16, 2019

DOI: 10.1021/jacs.9b08060
J. Am. Chem. Soc. 2019, 141, 17713−17720

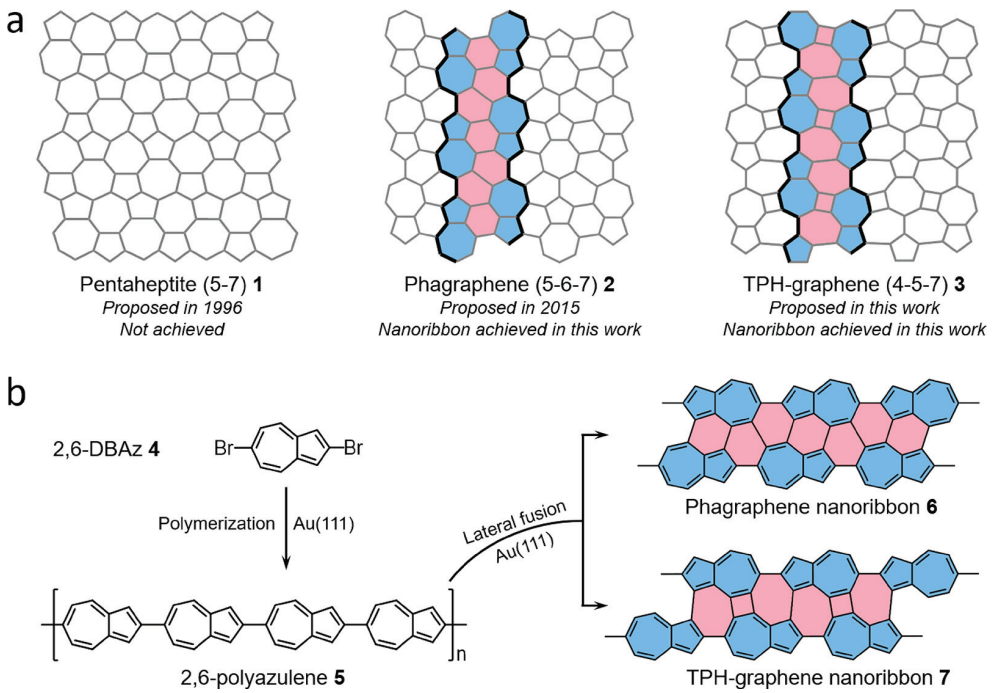

Figure 1. Reaction scheme for the synthesis of nanoribbons of nonalternant 2D carbon allotropes. (a) Skeletons of three proposed 2D carbon allotropes, that is, pentaheptite **1**, phagraphene **2**, and THP-graphene **3**, all consisting of sp^2 carbon atoms. The colored stripes denote the nanoribbons achieved in this work. (b) Ullmann C−C coupling of 2,6-dibromoazulene (2,6-DBAz) **4** into 2,6-polyazulene **5** chains and their fusion into carbon nanoribbons rich with nonhexagonal rings, including phagraphene nanoribbon **6** and TPH-graphene nanoribbon **7**. These two carbon nanoribbons correspond to the stripes cut out from the proposed 2D carbon allotropes in panel (a).

carbon atoms alters from alternant (hexagons) into nonalternant.[17] In contrast, the 4−8 structural motif is nonhexagonal, but remains alternant. The former case is especially interesting, because molecular π-electron systems with nonalternant topology have drastically different electronic properties as compared to their alternant counterparts.[17,44] All of the above-mentioned examples of growing 5−7 motifs represent only embedded point defects. Up to now, the embedment of a continuous one-dimensional (1D) arrangement of pentagon-heptagon (5−7) motifs is still lacking.

Here, by employing 2,6-dibromoazulene (**4**, Figure 1b) as a nonalternant nonbenzenoid precursor consisting of annulated five- and seven-membered rings, we have successfully obtained the 2,6-polyazulene chains **5** via on-surface Ullmann coupling. The 2,6-polyazulene chain could be reckoned as 1D line defect with fused pentagons and heptagons (5−7 motif). Subsequently, the lateral dehydrogenative coupling (fusion) of two 2,6-polyazulene chains results in the formation of carbon nanoribbons that are rich in 5−7 defects and locally resemble the phagraphene nanoribbon **6** or the TPH-graphene nanoribbon **7**. The two different carbon nanoribbons are formed due to the different relative positions of the two fused 2,6-polyazulene chains. These two carbon nanoribbons represent the stripes (colored) cut out from two yet unachieved 2D carbon allotropes, phagraphene **2** and TPH-graphene **3**. The structures of these two nanoribbons are elucidated unambiguously by scanning tunneling microscopy (STM), noncontact atomic force microscopy (AFM) in ultrahigh vacuum environment at low temperature (5.2 K) by using CO-functionalized tuning-fork sensors, and density functional theory (DFT) calculations.[45] The synthetic strategy used in this work may pave the way for the synthesis of other extended carbon allotropes with nonbenzenoid and nonalternant character.

RESULTS

On-Surface Synthesis of Polyazulene Chains. In the first step, polyazulene chains have been prepared on a Au(111) surface by Ullmann coupling. As shown by Figure 2a, deposition of a submonolayer of 2,6-DBAz onto Au(111) at 300 K followed by two annealing steps at 480 and 690 K leads to ordered domains of chains. The detailed structure of these chains is revealed by a combination of high-resolution STM (Figure 2b) and constant-height AFM (Figure 2c) images of a section of the domain (red-framed region in Figure 2a), using a CO-functionalized tip.[46] As can been seen in Figure 2b, weak protrusions are observed between the chains, which are assigned as bromine adatoms formed by C−Br bond scission. The resulting Br···H hydrogen bonds are the driving force for the parallel arrangement of the polyazulene chains, similar to previous findings for polyphenylene chains.[47] The AFM image enables the visualization of the C−C bonds in the azulene units, revealing the feature of annulated five- and seven-membered rings, in agreement with previous AFM images of single azulene molecules.[17] Therefore, the molecular structures of these polyazulene chains can be assigned unambiguously, as is exemplified for the left-most chain in the red frame in Figure 2c. The corresponding chemical structure is given in Figure 2d. As can be seen, the azulene units in this chain are not uniformly oriented. The irregularities result from the three different possible types of C−C coupling. A uniform, regular orientation would require that the five-membered ring of one azulene unit binds to the seven-membered ring of its neighbor (5−7 coupling). However, 5−5 and 7−7 coupling motifs also

DOI: 10.1021/jacs.9b08060
J. Am. Chem. Soc. 2019, 141, 17713−17720

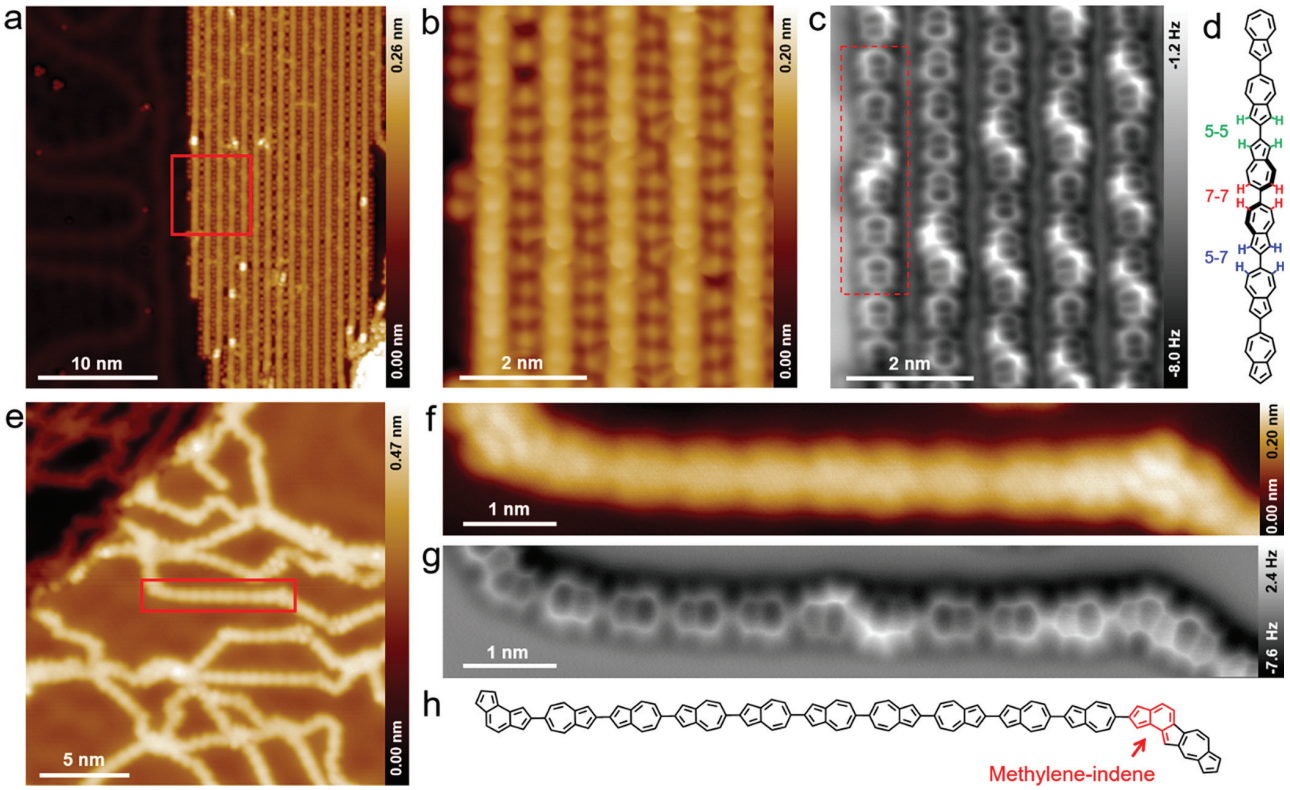

Figure 2. STM and nc-AFM images of polyazulene chains on Au(111). (a,e) Overview STM images of polyazulene chains formed after deposition of a submonolayer of 2,6-DBAz onto Au(111) at 300 K followed by successive annealing to 480 K for 30 min and 690 K for 20 min (a), and 730 K for 30 min (e). (b,c) Zoom-in STM (b) and constant-height AFM (c) images of the red-framed region in panel (a). (d) The chemical structure of the chain marked by the red frame in panel (c) highlights the different types of C−C coupling (5−7, 5−5, and 7−7). (f−h) Zoom-in STM (f), constant-height AFM (g) images, and chemical structure (h) of the curved chain in the red-framed region of panel (e). The methylene-indene units formed by isomerization of azulene units have been colored red in (h). Image parameters: (a,f) U = 10 mV, I = 10 pA; (b) U = 10 mV, I = 70 pA; (e) U = 100 mV, I = 10 pA. Tip distances for the constant-height AFM images: (c) z = 50 pm, and (f) z = 25 pm with respect to the tunneling gap at an STM set point of I = 10 pA and U = 10 mV above the Au(111) substrate. All of the STM and AFM images were measured with a CO-functionalized tip and an oscillation amplitude of 70 pm.

occur, as indicated by the labels in Figure 2d. The 7−7 coupling type is associated with characteristic bright features, which can be explained by a nonplanar adsorption conformation due to in-plane steric repulsion between C−H bonds of two neighboring azulene units (highlighted with red color). Similar features have been observed previously in AFM images of twisted phenyl units or aliphatic hydrocarbons.[48−51] In contrast, for the 5−7 and 5−5 coupling motifs, the involved azulene units exhibit almost planar adsorption configurations, indicating reduced repulsion due to the larger distances between the C−H bonds (Figure 2d, colored blue and green). The relative yields for these three types of coupling amount to 21.2% (5−5), 54.6% (5−7), and 24.2% (7−7) (see Figure S1 for details). These ratios are close to the expected random distribution of 1:2:1, indicating trivial selectivity among these three coupling types.

Further annealing of the sample in Figure 2a to 730 K results in the separation and occasional bending of the polyazulene chains, as shown by the STM image in Figure 2e. In addition, a certain amount of single chains cross-link at their terminals. These structural changes can be interpreted as follows. Annealing to 730 K desorbs the bromine adatoms from Au(111). This is evidenced by the absence of the weak protrusions around the chains. As a result, the chains have an increased probability to encounter and react through dehydrogenative coupling. Note that the C−H bond scission is expected to occur on the Au(111) surface at 730 K, according to previous work.[13,52,53] The occasional bending of the polyazulene chains is caused by rearrangements in the carbon framework, as is demonstrated for a typical single chain with two bends (red-framed region in Figure 2e). Its structure has been scrutinized by detailed STM (Figure 2f) and AFM (Figure 2g) measurements and is shown in Figure 2h. The straight part of this chain consists entirely of azulene units, whereas the bend bears a methylene-indene moiety, as marked by red color. Because methylene-indene is an isomer of azulene, it is likely that an azulene moiety undergoes C−C bond rearrangement (or isomerization) into the methylene-indene moiety on Au(111) already at 730 K. Besides the methylene-indene motif, naphthalene as another isomer of azulene has occasionally been observed as a structural motif at the corners of a single curved chain, as shown by Figure S4e−g in the SI. Related carbon−carbon (C−C) bond rearrangements have been reported for a polycyclic aromatic hydrocarbon with azulene moieties on a Cu(001) surface.[39] Interestingly, the 5−6−5−7−5 fused-ring moieties at the two terminals of the chain in Figure 2f show a prominent electronic state, which is not present at the azulene moieties. This feature may be related to the antiaromatic character of the 20 π-electron system, which may be in resonance with an open-shell

DOI: 10.1021/jacs.9b08060
J. Am. Chem. Soc. 2019, 141, 17713−17720

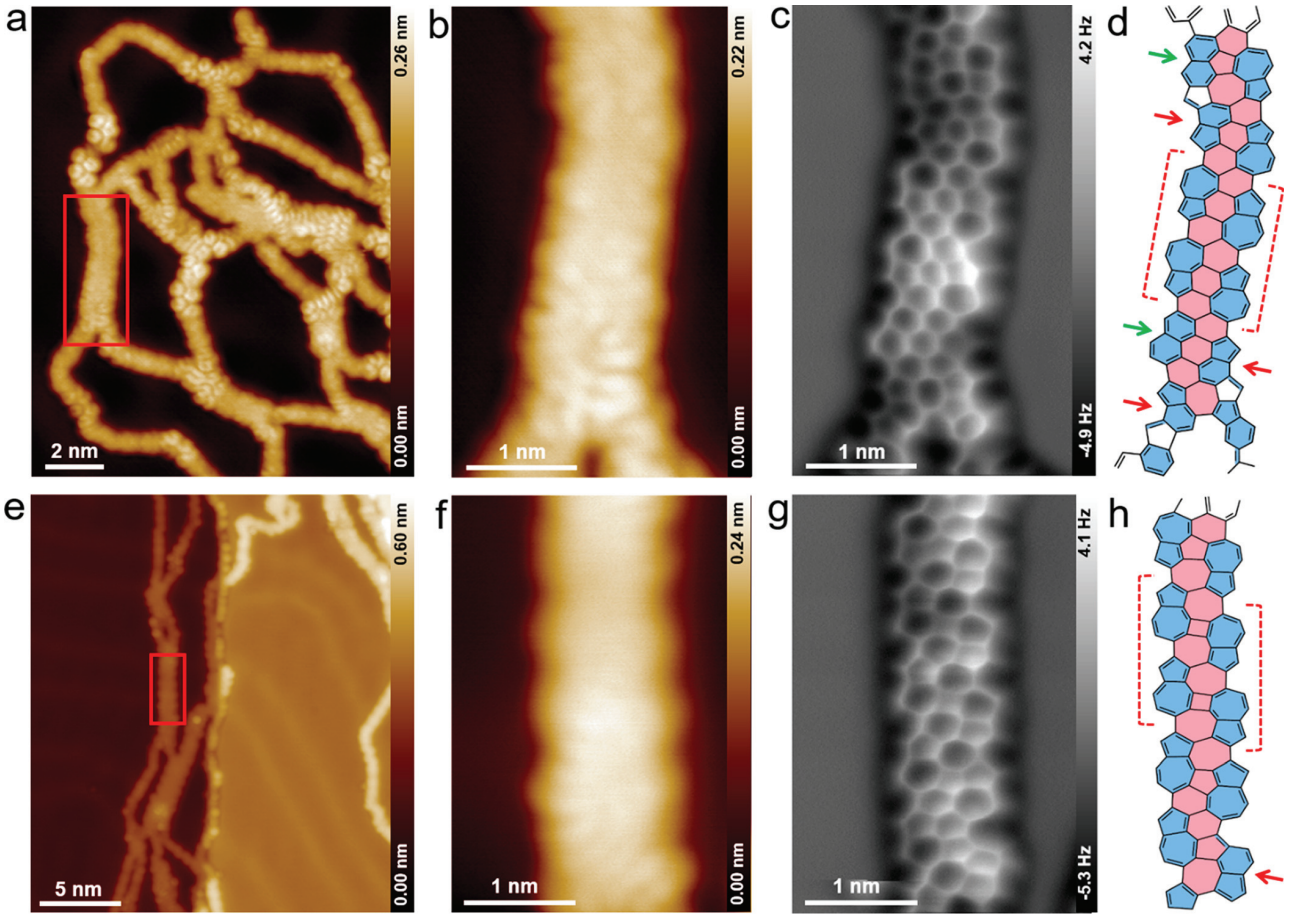

Figure 3. STM and nc-AFM images of carbon nanoribbons on Au(111). (a,e) Overview STM images of different regions of the sample (same as in Figure 2e), showing wider nanoribbons with different structures. (b–d) High-resolution STM (b), constant-height AFM (c) images, and chemical structure (d) of the nanoribbon in the red-framed region in panel (a). (f–h) High-resolution STM (f), constant-height AFM (g) images, and chemical structure (h) of the nanoribbon in the red-framed region in panel (e). In (d) and (h), the blue color marks the two chains fused into the nanoribbon by forming polygons marked by red color. Green and red arrows point out the naphthalene and methylene-indene moieties, respectively, formed by isomerization of azulene moieties. Image parameters: (a,b) U = 10 mV, I = 10 pA; (e,f) U = 100 mV, I = 10 pA. Tip distances for the AFM images: (c) z = 120 pm, and (g) z = 80 pm with respect to the STM set point of I = 10 pA and U = 10 mV above the Au(111) substrate. All of the STM and AFM images are measured with a CO-functionalized tip and an oscillation amplitude of 70 pm.

diradical structure (Figure S3, right), similar to what was reported in previous work.[54−56] Charging such moieties by electron transfer from the surface (and the surrounding π-electron system) may lead to stabilization due to increased aromatic character.

Lateral Fusion of Polyazulene Chains into Non-alternant Carbon Nanoribbons. At this stage (after heating to 730 K, see Figure 2e) also pairwise lateral dehydrogenative fusion of the polyazulene chains is induced, leading to the formation of wider nanoribbons as presented by Figure 3a and e showing different sample regions. Two representative nanoribbons are selected for detailed structural analysis. The structure of the nanoribbon in the red-framed region in Figure 3a is revealed by the zoom-in STM (Figure 3b) and the corresponding bond-resolving AFM (Figure 3c) images. As illustrated in Figure 3d, the nanoribbon contains two chains (blue colored) that are fully fused forming polygons (red colored) in the interspace. The major structural motif in the chains (blue) is azulene. Minority structural motifs are naphthalene (marked by green arrows) and methylene-indene moieties (marked by red arrows), which originate from the isomerization of the azulene moieties in the polyazulene chains as discussed above. A short section of the nanoribbons marked by the red bracket in Figure 3d represents the perfect lateral fusion of two oppositely oriented, regular 2,6-polyazulene chains. As can be seen, hexagons are formed exclusively between the two chains. Therefore, this structure can be considered as a stripe cut out from the carbon-allotrope phagraphene (**6**, Figure 1b) proposed in previous theoretical work.[28] Another nanoribbon with different structure is marked by the red frame in Figure 3e; its enlargement is shown in Figure 3f. The detailed structure of this ribbon, as derived from the AFM image in Figure 3g, is displayed in Figure 3h. As can be seen, this nanoribbon is again based on two single chains consisting of C−C bonded azulene (and methylene-indene) moieties. Similar to the first nanoribbon (Figure 3c), the section marked by the red bracket shows a periodic structure derived from two oppositely oriented regular 2,6-polyazulene chains. As compared to the first case (Figure 3d), the two chains have a shifted relative position, such that a carbon nanoribbon with four-, five-, and seven-membered rings is obtained. Thus, this nanoribbon represents a stripe of the

DOI: 10.1021/jacs.9b08060
J. Am. Chem. Soc. 2019, 141, 17713−17720

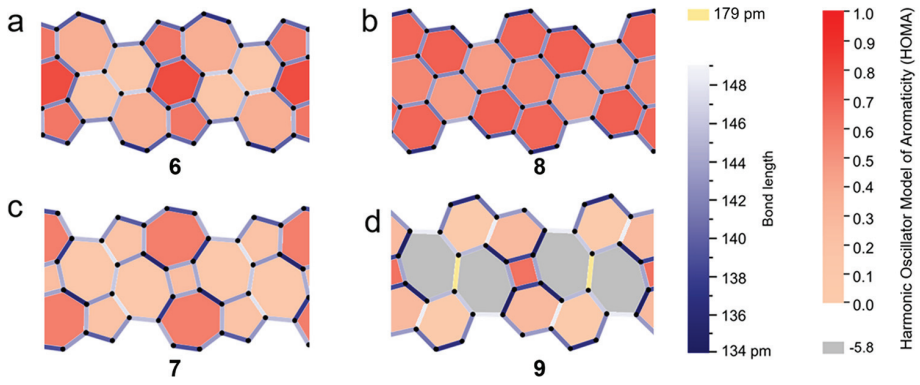

Figure 4. DFT-calculated C−C bond lengths of planar carbon nanoribbons. (a,c) Optimized gas-phase chemical structure of the nonalternant phagraphene nanoribbon **6** (a) and TPH-graphene nanoribbon **7** (c). (b,d) GNR counterparts of phagraphene and TPH-graphene nanoribbons obtained by isomerization of azulene moieties into naphthalene in these two types of nanoribbons (**8** and **9**). The bond lengths and harmonic oscillator model of aromaticity (HOMA) values of each polygon are presented with gradient colors as illustrated by the color scales at the right part of the figure. The average HOMA values are (a) 0.426, (b) 0.614, (c) 0.282, and (d) −1.48.

TPH-graphene **7** in Figure 1b. Additional examples of these two types of nonalternant carbon nanoribbons are shown in Figure S2.

DISCUSSION

The high-yield formation of longer phagraphene **6** and TPH-graphene **7** nanoribbons is still challenging, mainly because of two issues: First, carbon allotropes with nonalternant structural elements may isomerize to their corresponding alternant structures, which are usually more stable. In particular, isomerization of the azulene units in **6** and **7** to naphthalene units is expected to be energetically favorable, considering that naphthalene is 1.62 eV more stable than azulene.[57] If C−C bond rearrangements are kinetically possible under the reaction conditions, these transformations are likely to occur, as shown in Figure S4. The stability of the nonalternant structures is therefore an important aspect of their on-surface synthesis. Indeed, the present periodic DFT calculations for the electrically neutral free-standing, planar nanoribbons (cf., Figure 4) suggest that **6** (Figure 4a) is thermodynamically less stable by 2.7 eV per $C_{20}H_6$ formula unit than its alternant counterpart **8** shown in Figure 4b. Both structures enclosing four-membered rings (**7** and **9**, Figure 4c,d) are even more destabilized by 5.2 and 7.2 eV, respectively, as compared to the low-energy structure **8**. This may be rationalized on the basis of the high ring tension within the four-membered rings in **7** and **9**. The hypothetical naphthalene-based nanoribbon **9** also features an exceptionally long C−C bond of 179 pm, indicating a highly strained structure.

In the following, we discuss that the relative stabilities of the different structures are also consistent with qualitative aromaticity considerations. The color code of the bonds in Figure 4 shows the calculated C−C bond lengths for the two nanoribbons **6** and **7** (Figure 4a,c) and for the corresponding hypothetical structures **8** and **9** formed by isomerization of their azulene units to naphthalene units (Figure 4b,d). On the basis of the C−C bond lengths, the aromatic character of the rings can be assessed using the harmonic oscillator model of aromaticity (HOMA).[58] A higher HOMA value is generally associated with increased aromatic stabilization.[58] The HOMA values of the rings are illustrated by the different shades of orange color in Figure 4. Comparison of the phagraphene ribbon **6** with its alternant isomer **8** reveals that the latter has considerably higher HOMA values and thus experiences increased aromatic stabilization. Therefore, isomerization of **6** to its alternant counterpart **8** [(2,1)-GNR] should be energetically favored, in agreement with the experimental observations (Figure S4) and the DFT energies (ΔE_{8-6} = −2.7 eV). In contrast, the HOMA values indicate that the TPH-graphene nanoribbon **7** is more stable than its hypothetical isomerization product **9**, again in line with the DFT results (ΔE_{9-7} = +2.0 eV). Comparison of the HOMA data for the two experimental nanoribbons **6** and **7** reveals a slight advantage in aromatic stabilization for **6**, in agreement with the difference of their DFT energies (ΔE_{7-6} = +2.5 eV). According to these considerations, **7** may be more resistant to isomerization of azulene to naphthalene units than **6**. Furthermore, a preliminary theoretical analysis of the electronic structures at the DFT-GGA level suggests smaller band gaps of the nonalternant phagraphene **6** (Figure S5a, cf. also ref 28) and THP-graphene **7** (Figure S5b) nanoribbons as compared to their alternant counterparts **8** (Figure S5c) and **9** (Figure S5d), respectively. This is in analogy to the lower HOMO−LUMO gap of azulene as compared to naphthalene.[17]

The second challenge in the synthesis of phagraphene and TPH-graphene nanoribbons arises from the requirements of structural homogeneity and alignment of the 2,6-polyazulene chains. These chains should exclusively contain 5−7 connections and have opposite orientations. The first condition is demanding considering that the polyazulene chains are formed with randomly orientated azulene units at the first Ullmann coupling step. The second requirement is the reason why wider nanoribbons with more than two fused chains have only rarely been observed: They require alternating orientations of the 2,6-polyazulene chains, which is of diminishing probability with the increasing width of the ribbon.

CONCLUSION

Carbon allotrope nanoribbons with nonalternant topologies of their π-electron systems have been achieved by the lateral dehydrogenative coupling of polyazulene chains formed in a preceding step via surface Ullmann coupling of the 2,6-dibromoazulene precursor on Au(111). The distinctive phagraphene nanoribbon **6** and the THP-graphene nanoribbon

DOI: 10.1021/jacs.9b08060
J. Am. Chem. Soc. 2019, 141, 17713−17720

7 sections are frequent structural elements observed in these carbon allotrope nanoribbons. The different structures of these nanoribbons are determined by the relative positions of the fused polyazulene chains. Their yields are limited by the mixed connection types and isomerization of the azulene units in the polyazulene chains. DFT calculations suggest that the nonalternant phagraphene and THP-graphene nanoribbons exhibit lower band gaps than their alternant counterparts. These nonalternant carbon nanoribbons may represent promising candidates for the search of new carbon-based quantum materials with exotic properties. Moreover, the hierarchical coupling of nonalternant and nonbenzoid conjugated rings of carbon atoms opens possibilities for the synthesis of novel 2D carbon allotropes.

P4

METHODS

Synthesis. 2,6-Dibromoazulene was prepared by using a published procedure as described in Supporting Information part 3. The details of the synthesis and characterization of 2,6-dibromoazulene are also included in Supporting Information part 3.

Sample Preparation. The Au(111) crystal (MaTecK, Germany) was cleaned by multiple cycles of Ar^+ sputtering (E = 1.5 kV, I = 3.6 μA, $p = 6 \times 10^{-6}$ mbar for initial cycles and E = 0.8 kV, I = 1.1 μA, $p = 3 \times 10^{-6}$ mbar for final cycles) and annealing (1000 K for initial cycles and 730 K for final cycles). The 2,6-DBAz molecules were evaporated on the Au(111) surface by using a home-built evaporation device held at room temperature.[59] To induce chemical reactions on the surface, the sample was placed in a heating station (Scienta Omicron, Germany) where it was heated by thermal radiation of a tungsten filament. The sample temperatures were deduced from the heating power of the filament and a thermocouple that is attached to the heating station close to the sample plate. The heating station was previously calibrated by using a second thermocouple that was spot-welded to the center of an empty sample plate.

STM/AFM. STM and AFM images were obtained at 5.2 K and a pressure below 1×10^{-10} mbar with a low-temperature AFM/STM (Scienta Omicron, Germany). A Q-plus tuning fork sensor with a tungsten tip was used. The tip was sharpened by voltage pulses and indentations into the Au(111) surface. The AFM tip was functionalized with a CO molecule using standard procedures described in the literature.[60] The resonance frequency and quality factor of the sensor (f_r = 25.866 kHz, Q = 18 000−25 000) were determined by acoustic tunes with a tip−sample separation of about 10 nm. The Q-plus sensor was driven in frequency modulation mode using an external phase-locked loop electronics (MFLI, Zürich Instruments, Switzerland) for obtaining both STM and AFM images.[51] The oscillation amplitude of the sensor was kept constant at 70 pm. AFM images were taken in constant-height and constant-current scanning modes.[51]

Computational Details. Periodic density functional-theory calculations of free-standing carbon nanoribbons were performed with the Vienna Ab Initio Simulation Package (VASP)[61] using the PBE functional[62] and the D3(BJ) dispersion correction.[63,64] Please see the Supporting Information for further details.

ASSOCIATED CONTENT

Supporting Information

The Supporting Information is available free of charge on the ACS Publications website at DOI: 10.1021/jacs.9b08060.

Precursor synthesis and characterization, additional STM and AFM images, and details of the DFT calculations (PDF)

AUTHOR INFORMATION

Corresponding Authors

*daniel.ebeling@ap.physik.uni-giessen.de
*gerhard.hilt@uni-oldenburg.de
*wolfgang.hieringer@fau.de
*michael.gottfried@chemie.uni-marburg.de

ORCID

Daniel Ebeling: 0000-0001-5829-170X
Gerhard Hilt: 0000-0002-5279-3378
J. Michael Gottfried: 0000-0001-5579-2568

Author Contributions

#Q.F. and D.M.-J. contributed equally.

Notes

The authors declare no competing financial interest.

ACKNOWLEDGMENTS

Financial support by the Deutsche Forschungsgemeinschaft via grants 223848855-SFB 1083, GO 1812/2-1, HI 655/18-1, EB 535/1-1, and SCHI 619/13, the Cluster of Excellence EXC 315 "Engineering of Advanced Materials", and the GRK 2204 "Substitute Materials for Sustainable Energy Technologies" is gratefully acknowledged. The RRZE of the University of Erlangen-Nürnberg is acknowledged for computational resources. Q.F. thanks the Alexander von Humboldt-Foundation for a Research Fellowship for Postdoctoral Researchers.

REFERENCES

(1) Wu, J.; Pisula, W.; Müllen, K. Graphenes as Potential Material for Electronics. *Chem. Rev.* **2007**, *107*, 718−747.
(2) Yuan, W.; Chen, J.; Shi, G. Nanoporous Graphene Materials. *Mater. Today* **2014**, *17*, 77−85.
(3) Celis, A.; Nair, M. N.; Taleb-Ibrahimi, A.; Conrad, E. H.; Berger, C.; de Heer, W. A.; Tejeda, A. Graphene Nanoribbons: Fabrication, Properties and Devices. *J. Phys. D: Appl. Phys.* **2016**, *49*, 143001.
(4) Talirz, L.; Ruffieux, P.; Fasel, R. On-Surface Synthesis of Atomically Precise Graphene Nanoribbons. *Adv. Mater.* **2016**, *28*, 6222−31.
(5) Ruffieux, P.; Wang, S.; Yang, B.; Sánchez-Sánchez, C.; Liu, J.; Dienel, T.; Talirz, L.; Shinde, P.; Pignedoli, C. A.; Passerone, D.; Dumslaff, T.; Feng, X.; Müllen, K.; Fasel, R. On-Surface Synthesis of Graphene Nanoribbons with Zigzag Edge Topology. *Nature* **2016**, *531*, 489−492.
(6) Rizzo, D. J.; Veber, G.; Cao, T.; Bronner, C.; Chen, T.; Zhao, F.; Rodriguez, H.; Louie, S. G.; Crommie, M. F.; Fischer, F. R. Topological Band Engineering of Graphene Nanoribbons. *Nature* **2018**, *560*, 204−208.
(7) Gröning, O.; Wang, S.; Yao, X.; Pignedoli, C. A.; Borin Barin, G.; Daniels, C.; Cupo, A.; Meunier, V.; Feng, X.; Narita, A.; Müllen, K.; Ruffieux, P.; Fasel, R. Engineering of Robust Topological Quantum Phases in Graphene Nanoribbons. *Nature* **2018**, *560*, 209−213.
(8) Cai, J.; Ruffieux, P.; Jaafar, R.; Bieri, M.; Braun, T.; Blankenburg, S.; Muoth, M.; Seitsonen, A. P.; Saleh, M.; Feng, X.; Müllen, K.; Fasel, R. Atomically Precise Bottom-up Fabrication of Graphene Nanoribbons. *Nature* **2010**, *466*, 470−473.
(9) Moreno, C.; Vilas-Varela, M.; Kretz, B.; Garcia-Lekue, A.; Costache, M. V.; Paradinas, M.; Panighel, M.; Ceballos, G.; Valenzuela, S. O.; Peña, D.; Mugarza, A. Bottom-Up Synthesis of Multifunctional Nanoporous Graphene. *Science* **2018**, *360*, 199.
(10) Bieri, M.; Treier, M.; Cai, J.; Aït-Mansour, K.; Ruffieux, P.; Gröning, O.; Gröning, P.; Kastler, M.; Rieger, R.; Feng, X.; Müllen, K.; Fasel, R. Porous Graphenes: Two-Dimensional Polymer Synthesis with Atomic Precision. *Chem. Commun.* **2009**, 6919−6921.
(11) Fan, Q.; Wang, C.; Liu, L.; Han, Y.; Zhao, J.; Zhu, J.; Kuttner, J.; Hilt, G.; Gottfried, J. M. Covalent, Organometallic, and Halogen-Bonded Nanomeshes from Tetrabromo-Terphenyl by Surface-Assisted Synthesis on Cu(111). *J. Phys. Chem. C* **2014**, *118*, 13018−13025.
(12) Kolmer, M.; Zuzak, R.; Steiner, A. K.; Zajac, L.; Engelund, M.; Godlewski, S.; Szymonski, M.; Amsharov, K. Fluorine-Programmed

DOI: 10.1021/jacs.9b08060
J. Am. Chem. Soc. 2019, 141, 17713−17720

Nanozipping to Tailored Nanographenes on Rutile TiO_2 Surfaces. *Science* **2019**, *363*, 57−60.
(13) Treier, M.; Pignedoli, C. A.; Laino, T.; Rieger, R.; Müllen, K.; Passerone, D.; Fasel, R. Surface-Assisted Cyclodehydrogenation Provides a Synthetic Route Towards Easily Processable and Chemically Tailored Nanographenes. *Nat. Chem.* **2011**, *3*, 61−67.
(14) Hieulle, J.; Carbonell-Sanroma, E.; Vilas-Varela, M.; Garcia-Lekue, A.; Guitian, E.; Pena, D.; Pascual, J. I. On-Surface Route for Producing Planar Nanographenes with Azulene Moieties. *Nano Lett.* **2018**, *18*, 418−423.
(15) Beser, U.; Kastler, M.; Maghsoumi, A.; Wagner, M.; Castiglioni, C.; Tommasini, M.; Narita, A.; Feng, X.; Müllen, K. A C216-Nanographene Molecule with Defined Cavity as Extended Coronoid. *J. Am. Chem. Soc.* **2016**, *138*, 4322−4325.
(16) Zhong, Q.; Hu, Y.; Niu, K.; Zhang, H.; Yang, B.; Ebeling, D.; Tschakert, J.; Cheng, T.; Schirmeisen, A.; Narita, A.; Müllen, K.; Chi, L. Benzo-Fused Periacenes or Double Helicenes? Different Cyclodehydrogenation Pathways on Surface and in Solution. *J. Am. Chem. Soc.* **2019**, *141*, 7399−7406.
(17) Klein, B. P.; van der Heijden, N. J.; Kachel, S. R.; Franke, M.; Krug, C. K.; Greulich, K. K.; Ruppenthal, L.; Müller, P.; Rosenow, P.; Parhizkar, S.; Bocquet, F. C.; Schmid, M.; Hieringer, W.; Maurer, R. J.; Tonner, R.; Kumpf, C.; Swart, I.; Gottfried, J. M. Molecular Topology and the Surface Chemical Bond: Alternant Versus Nonalternant Aromatic Systems as Functional Structural Elements. *Phys. Rev. X* **2019**, *9*, 011030.
(18) Georgakilas, V.; Perman, J. A.; Tucek, J.; Zboril, R. Broad Family of Carbon Nanoallotropes: Classification, Chemistry, and Applications of Fullerenes, Carbon Dots, Nanotubes, Graphene, Nanodiamonds, and Combined Superstructures. *Chem. Rev.* **2015**, *115*, 4744−4822.
(19) Sui, C.; Zhao, Y.; Zhang, Z.; He, J.; Zhang, Z.; He, X.; Wang, C.; Wu, J. Morphology-Controlled Tensile Mechanical Characteristics in Graphene Allotropes. *ACS Omega* **2017**, *2*, 3977−3988.
(20) Enyashin, A. N.; Ivanovskii, A. L. Graphene Allotropes. *Phys. Status Solidi B* **2011**, *248*, 1879−1883.
(21) Molepo, M. P.; Mapasha, R. E.; Obodo, K. O.; Chetty, N. First Principles Calculations of Pentaheptite Graphene and Boronitrene Derivatives. *Comput. Mater. Sci.* **2014**, *92*, 395−400.
(22) Fthenakis, Z. G.; Lathiotakis, N. N. Graphene Allotropes Under Extreme Uniaxial Strain: An *ab initio* Theoretical Study. *Phys. Chem. Chem. Phys.* **2015**, *17*, 16418−16427.
(23) Crespi, V. H.; Benedict, L. X.; Cohen, M. L.; Louie, S. G. Prediction of a Pure-Carbon Planar Covalent Metal. *Phys. Rev. B: Condens. Matter Mater. Phys.* **1996**, *53*, 13303−13305.
(24) Terrones, H.; Terrones, M.; Hernández, E.; Grobert, N.; Charlier, J. C.; Ajayan, P. M. New Metallic Allotropes of Planar and Tubular Carbon. *Phys. Rev. Lett.* **2000**, *84*, 1716−1719.
(25) Liu, Y.; Wang, G.; Huang, Q.; Guo, L.; Chen, X. Structural and Electronic Properties of T Graphene: A Two-Dimensional Carbon Allotrope with Tetrarings. *Phys. Rev. Lett.* **2012**, *108*, 225505.
(26) Su, C.; Jiang, H.; Feng, J. Two-Dimensional Carbon Allotrope with Strong Electronic Anisotropy. *Phys. Rev. B: Condens. Matter Mater. Phys.* **2013**, *87*, 075453.
(27) Sharma, B. R.; Manjanath, A.; Singh, A. K. Pentahexoctite: A New Two-Dimensional Allotrope of Carbon. *Sci. Rep.* **2015**, *4*, 7164.
(28) Wang, Z.; Zhou, X. F.; Zhang, X.; Zhu, Q.; Dong, H.; Zhao, M.; Oganov, A. R. Phagraphene: A Low-Energy Graphene Allotrope Composed of 5−6-7 Carbon Rings with Distorted Dirac Cones. *Nano Lett.* **2015**, *15*, 6182−6186.
(29) Bravo, S.; Correa, J.; Chico, L.; Pacheco, M. Tight-Binding Model for Opto-Electronic Properties of Penta-Graphene Nanostructures. *Sci. Rep.* **2018**, *8*, 11070.
(30) Xin, H.; Gao, X. Application of Azulene in Constructing Organic Optoelectronic Materials: New Tricks for an Old Dog. *ChemPlusChem* **2017**, *82*, 945−956.
(31) Cervenka, J.; Flipse, C. F. J. Structural and Electronic Properties of Grain Boundaries in Graphite: Planes of Periodically Distributed Point Defects. *Phys. Rev. B: Condens. Matter Mater. Phys.* **2009**, *79*, 195429.
(32) Peres, N. M. R.; Guinea, F.; Castro Neto, A. H. Electronic Properties of Disordered Two-Dimensional Carbon. *Phys. Rev. B: Condens. Matter Mater. Phys.* **2006**, *73*, 125411.
(33) Cervenka, J.; Katsnelson, M. I.; Flipse, C. F. J. Room-Temperature Ferromagnetism in Graphite Driven by Two-Dimensional Networks of Point Defects. *Nat. Phys.* **2009**, *5*, 840.
(34) Malola, S.; Häkkinen, H.; Koskinen, P. Structural, Chemical, and Dynamical Trends in Graphene Grain Boundaries. *Phys. Rev. B: Condens. Matter Mater. Phys.* **2010**, *81*, 165447.
(35) Grantab, R.; Shenoy, V. B.; Ruoff, R. S. Anomalous Strength Characteristics of Tilt Grain Boundaries in Graphene. *Science* **2010**, *330*, 946−948.
(36) Wei, Y.; Wu, J.; Yin, H.; Shi, X.; Yang, R.; Dresselhaus, M. The Nature of Strength Enhancement and Weakening by Pentagon−Heptagon Defects in Graphene. *Nat. Mater.* **2012**, *11*, 759.
(37) Banhart, F.; Kotakoski, J.; Krasheninnikov, A. V. Structural Defects in Graphene. *ACS Nano* **2011**, *5*, 26−41.
(38) Cockayne, E.; Rutter, G. M.; Guisinger, N. P.; Crain, J. N.; First, P. N.; Stroscio, J. A. Grain Boundary Loops in Graphene. *Phys. Rev. B: Condens. Matter Mater. Phys.* **2011**, *83*, 195425.
(39) Shiotari, A.; Nakae, T.; Iwata, K.; Mori, S.; Okujima, T.; Uno, H.; Sakaguchi, H.; Sugimoto, Y. Strain-Induced Skeletal Rearrangement of a Polycyclic Aromatic Hydrocarbon on a Copper Surface. *Nat. Commun.* **2017**, *8*, 16089.
(40) Mishra, S.; Krzeszewski, M.; Pignedoli, C. A.; Ruffieux, P.; Fasel, R.; Gryko, D. T. On-Surface Synthesis of a Nitrogen-Embedded Buckybowl with Inverse Stone−Thrower−Wales Topology. *Nat. Commun.* **2018**, *9*, 1714.
(41) Mishra, S.; Lohr, T. G.; Pignedoli, C. A.; Liu, J.; Berger, R.; Urgel, J. I.; Müllen, K.; Feng, X.; Ruffieux, P.; Fasel, R. Tailoring Bond Topologies in Open-Shell Graphene Nanostructures. *ACS Nano* **2018**, *12*, 11917−11927.
(42) Liu, M.; Liu, M.; She, L.; Zha, Z.; Pan, J.; Li, S.; Li, T.; He, Y.; Cai, Z.; Wang, J.; Zheng, Y.; Qiu, X.; Zhong, D. Graphene-Like Nanoribbons Periodically Embedded with Four- and Eight-Membered Rings. *Nat. Commun.* **2017**, *8*, 14924.
(43) Liu, M.; Liu, M.; Zha, Z.; Pan, J.; Qiu, X.; Li, T.; Wang, J.; Zheng, Y.; Zhong, D. Thermally Induced Transformation of Nonhexagonal Carbon Rings in Graphene-like Nanoribbons. *J. Phys. Chem. C* **2018**, *34*, 1884−1891.
(44) Ruedenberg, K. Quantum Mechanics of Mobile Electrons in Conjugated Bond Systems. III. Topological Matrix as Generatrix of Bond Orders. *J. Chem. Phys.* **1961**, *34*, 1884−1891.
(45) Fan, Q.; Martin-Jimenez, D.; Ebeling, D.; Krug, C. K.; Brechmann, L.; Kohlmeyer, C.; Hilt, G.; Hieringer, W.; Schirmeisen, A.; Gottfried, J. M. Nanoribbons with Non-Alternant Topology from Fusion of Polyazulene: Carbon Allotropes Beyond Graphene. *J. Am. Chem. Soc.* **2019**, 1 DOI: 10.1021/jacs.9b08060.
(46) Gross, L.; Mohn, F.; Moll, N.; Liljeroth, P.; Meyer, G. The Chemical Structure of a Molecule Resolved by Atomic Force Microscopy. *Science* **2009**, *325*, 1110.
(47) Wang, W. H.; Shi, X. Q.; Wang, S. Y.; Van Hove, M. A.; Lin, N. Single-Molecule Resolution of an Organometallic Intermediate in a Surface-Supported Ullmann Coupling Reaction. *J. Am. Chem. Soc.* **2011**, *133*, 13264−13267.
(48) Ebeling, D.; Sekutor, M.; Stiefermann, M.; Tschakert, J.; Dahl, J. E. P.; Carlson, R. M. K.; Schirmeisen, A.; Schreiner, P. R. Assigning the Absolute Configuration of Single Aliphatic Molecules by Visual Inspection. *Nat. Commun.* **2018**, *9*, 2420.
(49) Ebeling, D.; Sekutor, M.; Stiefermann, M.; Tschakert, J.; Dahl, J. E. P.; Carlson, R. M. K.; Schirmeisen, A.; Schreiner, P. R. London Dispersion Directs On-Surface Self-Assembly of [121]Tetramantane Molecules. *ACS Nano* **2017**, *11*, 9459−9466.
(50) Ebeling, D.; Zhong, Q.; Schloder, T.; Tschakert, J.; Henkel, P.; Ahles, S.; Chi, L.; Mollenhauer, D.; Wegner, H. A.; Schirmeisen, A. Adsorption Structure of Mono- and Diradicals on a Cu(111) Surface:

DOI: 10.1021/jacs.9b08060
J. Am. Chem. Soc. 2019, 141, 17713−17720

Chemoselective Dehalogenation of 4-Bromo-3′′-iodo-*p*-terphenyl. *ACS Nano* **2019**, *13*, 324−336.
(51) Martin-Jimenez, D.; Ahles, S.; Mollenhauer, D.; Wegner, H. A.; Schirmeisen, A.; Ebeling, D. Bond-Level Imaging of the 3D Conformation of Adsorbed Organic Molecules Using Atomic Force Microscopy with Simultaneous Tunneling Feedback. *Phys. Rev. Lett.* **2019**, *122*, 196101.
(52) Basagni, A.; Sedona, F.; Pignedoli, C. A.; Cattelan, M.; Nicolas, L.; Casarin, M.; Sambi, M. Molecules−Oligomers−Nanowires−Graphene Nanoribbons: A Bottom-Up Stepwise On-Surface Covalent Synthesis Preserving Long-Range Order. *J. Am. Chem. Soc.* **2015**, *137*, 1802−1808.
(53) Soe, W.-H.; Wong, H. S.; Manzano, C.; Grisolia, M.; Hliwa, M.; Feng, X.; Müllen, K.; Joachim, C. Mapping the Excited States of Single Hexa-peri-benzocoronene Oligomers. *ACS Nano* **2012**, *6*, 3230−3235.
(54) Majzik, Z.; Pavlicek, N.; Vilas-Varela, M.; Perez, D.; Moll, N.; Guitian, E.; Meyer, G.; Pena, D.; Gross, L. Studying an Antiaromatic Polycyclic Hydrocarbon Adsorbed on Different Surfaces. *Nat. Commun.* **2018**, *9*, 1198.
(55) Di Giovannantonio, M.; Eimre, K.; Yakutovich, A. V.; Chen, Q.; Mishra, S.; Urgel, J. I.; Pignedoli, C. A.; Ruffieux, P.; Müllen, K.; Narita, A.; Fasel, R. On-Surface Synthesis of Antiaromatic and Open-Shell Indeno[2,1-b]fluorene Polymers and Their Lateral Fusion into Porous Ribbons. *J. Am. Chem. Soc.* **2019**, *141*, 12346−12354.
(56) Di Giovannantonio, M.; Urgel, J. I.; Beser, U.; Yakutovich, A. V.; Wilhelm, J.; Pignedoli, C. A.; Ruffieux, P.; Narita, A.; Müllen, K.; Fasel, R. On-Surface Synthesis of Indenofluorene Polymers by Oxidative Five-Membered Ring Formation. *J. Am. Chem. Soc.* **2018**, *140*, 3532−3536.
(57) Roth, W. R.; Böhm, M.; Lennartz, H.-W.; Vogel, E. Resonance Energy of Bridged [10]Annulenes. *Angew. Chem., Int. Ed. Engl.* **1983**, *22*, 1007−1008.
(58) Setiawan, D.; Kraka, E.; Cremer, D. Quantitative Assessment of Aromaticity and Antiaromaticity Utilizing Vibrational Spectroscopy. *J. Org. Chem.* **2016**, *81*, 9669−9686.
(59) Zint, S.; Ebeling, D.; Ahles, S.; Wegner, H. A.; Schirmeisen, A. Subsurface-Controlled Angular Rotation: Triphenylene Molecules on Au(111) Substrates. *J. Phys. Chem. C* **2016**, *120*, 1615−1622.
(60) Bartels, L.; Meyer, G.; Rieder, K. H. Controlled Vertical Manipulation of Single CO Molecules with the Scanning Tunneling Microscope: A Route to Chemical Contrast. *Appl. Phys. Lett.* **1997**, *71*, 213−215.
(61) Kresse, G.; Hafner, J. *Vienna Ab Initio Simulation Package (VASP), version 5.2*; Institut für Materialphysik, Universität Wien: Vienna, 1991; www.vasp.at.
(62) Perdew, J. P.; Burke, K.; Ernzerhof, M. Generalized Gradient Approximation Made Simple. *Phys. Rev. Lett.* **1996**, *77*, 3865−3868.
(63) Grimme, S.; Antony, J.; Ehrlich, S.; Krieg, H. A Consistent and Accurate *ab initio* Parametrization of Density Functional Dispersion Correction (DFT-D) for the 94 Elements H-Pu. *J. Chem. Phys.* **2010**, *132*, 154104.
(64) Grimme, S.; Ehrlich, S.; Goerigk, L. Effect of the Damping Function in Dispersion Corrected Density Functional Theory. *J. Comput. Chem.* **2011**, *32*, 1456−1465.

DOI: 10.1021/jacs.9b08060
J. Am. Chem. Soc. 2019, 141, 17713−17720

Supplementary Information

for

Nanoribbons with Non-Alternant Topology from Fusion of Polyazulene: Carbon Allotropes Beyond Graphene

Qitang Fan[1‡], Daniel Martin-Jimenez[2,3‡], Daniel Ebeling[2,3], Claudio K. Krug[1], Lea Brechmann[1], Corinna Kohlmeyer[4], Gerhard Hilt[4], Wolfgang Hieringer[5], André Schirmeisen[2,3], J. Michael Gottfried[1]

[1]Department of Chemistry, Philipps University Marburg, Hans-Meerwein-Straße 4, 35032 Marburg, Germany

[2]Institute of Applied Physics (IAP), Justus Liebig University Gießen, Heinrich-Buff-Ring 16, 35392 Gießen, Germany

[3]Center for Materials Research (LaMa), Justus Liebig University Giessen, Heinrich-Buff-Ring 16, 35392 Giessen, Germany

[4]Institute of Chemistry, Carl von Ossietzky University Oldenburg, Carl-von-Ossietzky-Straße 9-11, 26111 Oldenburg, Germany

[5]Theoretical Chemistry and Interdisciplinary Center for Molecular Materials (ICMM), Department of Chemistry and Pharmacy, Friedrich-Alexander-Universität Erlangen-Nürnberg, Egerlandstraße 3, 91058 Erlangen, Germany

1. Additional STM and AFM images.

(a) Fig. S1a,b and S1d,e show the STM and nc-AFM images of other phagraphene and TPH-graphene nanoribbons on the same sample as that in Fig. 3a of the main text, respectively. Their chemical structures are derived as shown by Fig. S1c and Fig. S1f, respectively.

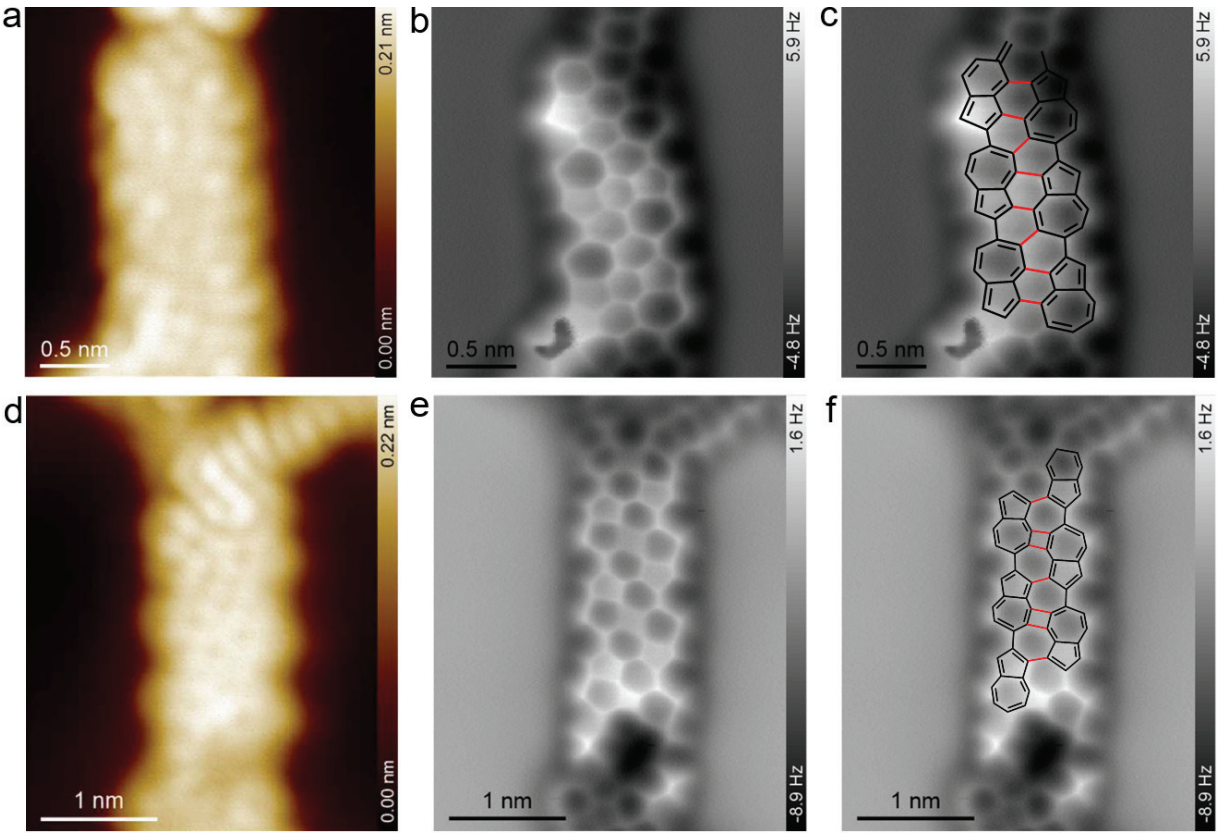

Fig. S1 | Additional STM and nc-AFM images of phagraphene and TPH-graphene nanoribbons on Au(111). a-c, High resolution STM (**a**), nc-AFM (**b**) images and the overlaid chemical structure (**c**) of another short phagraphene nanoribbon from the sample in Fig. 3a of the main text. **d-f,** High resolution STM (**d**), nc-AFM (**e**) images and overlaid chemical structure (**f**) of another short TPH-graphene nanoribbon from the sample in Fig. 3a of the main text. Tunneling parameters for the STM images: (**a**),(**d**) U = 10 mV, I = 10 pA. Tip distances for the constant-height AFM images: (**b**) z = 100 pm, and (**e**) z = 50 pm with respect to the STM set point of I = 10 pA and U = 10 mV above Au(111) substrate.

(b) Annealing of the sample to 780 K leads to extensive rearrangement resulting in the formation of hexagonal rings. As shown by Fig. S2a and 2b, the wide carbon nanoribbons are more curved than that in Fig. 3a. This is due mainly to the formation of a high percentage of hexagonal rings as demonstrated by the zoom-in nc-AFM image in Fig. S2c. The derived carbon skeleton of this carbon nanoribbon section is displayed in Fig. S2d. Only two azulene moieties (red colored) are left in the structure indicating that carbon hexagonal rings are more stable than the five- and seven-membered rings.

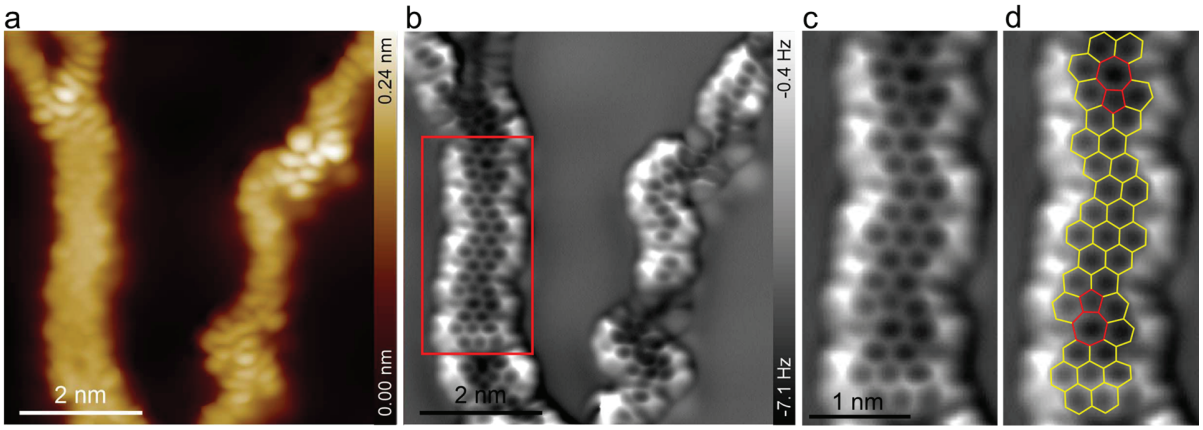

Fig. S2 | STM and nc-AFM images of the carbon nanoribbons on Au(111) at 780 K. a,b, Constant-current nc-AFM images showing the topographical (**a**) and frequency shift (**b**) channels of carbon nanoribbons obtained by directly annealing the sample to 793 K for 30 minutes. **c,d,** Zoom-in constant-current frequency shift image (**c**) and the derived carbon skeleton (**d**) of the section of carbon nanoribbon in the red-framed region in panel (**b**). The frequency shift image in constant current mode are measured with topographical STM image feedback at U = 10 mV and I = 100 pA.[1]

2. Computational details

Periodic density-functional theory calculations of the planar, free-standing (i. e., without the Au(111) substrate) one-dimensional nanoribbons (cf. Figure 4 of the main paper) were performed with the Vienna Ab Initio Simulation Package (VASP).[2] The PBE functional[3] was used in combination with the third-generation van der Waals dispersion correction due to Grimme (DFT-D3(BJ))[4,5] and the projector-augmented wave (PAW) ansatz[6,7] for the atomic cores. A plane-wave cutoff energy of 520 eV was employed. The orthorhombic unit cells contained a $C_{20}H_6$ formula unit for each system, which was periodically repeated in one dimension. The distance to the periodic images in each of the other two directions (i. e., perpendicular to the direction of propagation of the nanoribbon) was about 10 Å to separate the ribbons from their periodic images. The cell dimensions as well as the atomic positions were optimized using a force convergence criterion of $5 \cdot 10^{-3}$ eV/Å or better. Note that the atoms were strictly kept in a perfect plane, i. e., no out-of-plane distortions were possible; the resulting free-standing structures hence do not necessarily represent local minima on the energy hypersurface in the absence of the Au(111) substrate. A 32×1×1 Monkhorst-Pack k-point mesh was used. The resulting geometries are provided in VASP POSCAR format at the end of this file.

3. Synthesis of 2,6-dibromoazulene

General Information

All reactions with air or water sensitive starting materials were carried out under nitrogen atmosphere in heat-gun-dried glassware using schlenk techniques. Benzene and ethanol were stored over molecular sieves (3 Å) under nitrogen atmosphere. Column chromatography was carried out on Macherey-Nagel silica gel 60 (230–400 mesh). For thin layer chromatography Merck TLC plates (Silica 60, F254 with fluorescence indicator) were used. ^{1}H and ^{13}C NMR spectra were either recorded on a Bruker Avance 300 (^{1}H NMR: 300 MHz, ^{13}C NMR: 75 MHz) or Avance III (^{1}H NMR: 500 MHz, ^{13}C NMR: 125 MHz). For EI and EI-HRMS a *Finnigan MAT 95* or a *DFS High Resolution Magnetic Sector MS* (*Thermo Scientific*) with an energy of 70 eV and for ESI-HRMS a *Q-TOF Premier* (*Waters*) were used. IR spectra were recorded on a Bruker Tensor 27 (FTIR) spectrometer.

Synthesis of 2,6-dibromoazulene

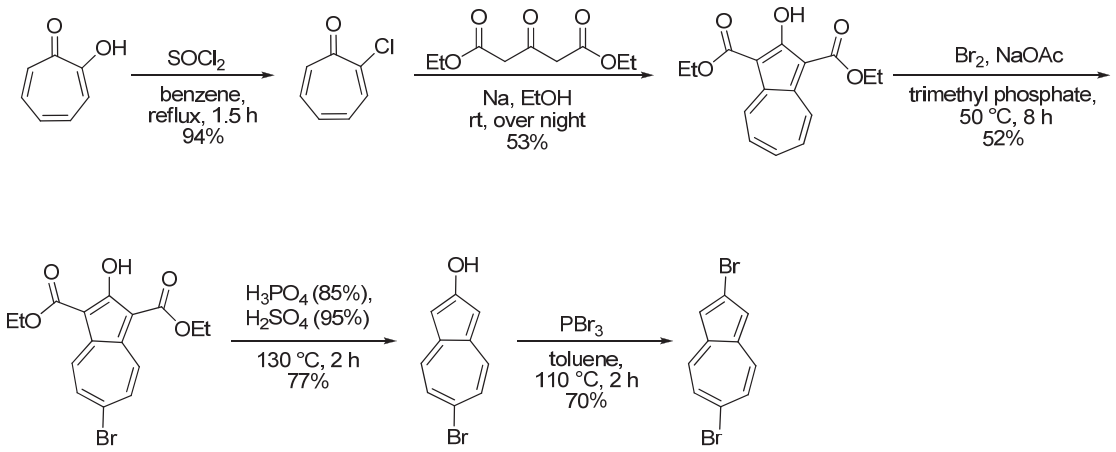

2-Chlorocyclohepta-2,4,6-trien-1-one

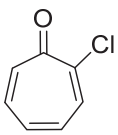

According to a procedure of Marson[8] under nitrogen atmosphere α-tropolone (2.20 g, 18.0 mmol, 1.00 equiv.) was dissolved in anhydrous benzene (55 mL). $SOCl_2$ (1.7 mL, 23.4 mmol, 1.30 equiv.) was added dropwise and the mixture was stirred for 2.5 h at 95 °C. The solvent was removed under vacuum and the crude product was purified by column chromatography (CH_2Cl_2:methanol = 40:1). The product was obtained in 94% yield (2.37 g, 16.9 mmol) as brown solid.

^{1}H NMR (300 MHz, $CDCl_3$, ppm): δ = 7.79 (dd, *J* = 9.3, 0.9 Hz, 1H), 7.25–7.19 (m, 2H), 7.12–7.02 (m, 1H), 6.93 (ddt, *J* = 10.6, 9.4, 1.0 Hz, 1H).

^{13}C NMR (75 MHz, $CDCl_3$, ppm): δ = 180.2, 149.0, 138.6, 135.9, 135.7, 134.2, 131.6.

HRMS (ESI, +): calcd for C_7H_5ONaCl: 162.9927, found 162.9921.

IR (film, cm^{-1}): 3032, 2360, 2159, 2029, 1957, 1626, 1575, 1504, 1457, 1372, 1270, 1243, 1213, 1064, 975, 902, 865, 777, 669, 631.

The analytical data for the ^{1}H NMR spectra is in accordance with the literature.[9]

P4

Diethyl 2-hydroxyazulene-1,3-dicarboxylate

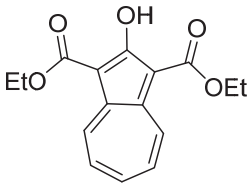

According to a procedure of Marson[8] under nitrogen atmosphere sodium (1.44 g, 62.4 mmol, 26.8 equiv.) was added in portions to anhydrous EtOH (32 mL). Diethyl 3-oxopentanedionate (1.46 g, 4.24 mmol, 3.08 equiv.) was added dropwise and the reaction mixture turned yellow. After adding a solution of 2-chlorocyclohepta-2,4,6-trien-1-one (660 mg, 4.70 mmol, 2.00 equiv.) in anhydrous EtOH (16 mL) the reaction mixture turned dark red and was stirred at ambient temperature overnight. Then, water (50 mL) was added and the reaction mixture was filtered. The solid was dissolved in glacial acetic acid, carefully diluted with water and the aqueous phase was extracted with CH_2Cl_2. The combined organic phase was dried ($MgSO_4$), filtered and concentrated under reduced pressure. The crude product was recrystallized (EtOH) to afford 53% (751 mg, 2.50 mmol) as brown solid.

^{1}H NMR (300 MHz, $CDCl_3$, ppm): δ = 11.75 (s, 1H), 9.30 (s, 2H), 7.66 (s, 3H), 4.49 (q, *J* = 7.2 Hz, 4H), 1.48 (t, *J* = 7.2 Hz, 6H).

^{13}C NMR (75 MHz, $CDCl_3$, ppm): δ = 172.3, 143.4, 136.2, 134.8, 132.5, 101.4, 60.6, 14.7.

The analytical data are in accordance with the literature.[10]

Diethyl 6-bromo-2-hydroxyazulene-1,3-dicarboxylate

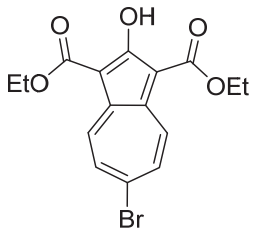

According to a procedure of Tajiri[11] under nitrogen atmosphere diethyl 2-hydroxyazulene-1,3-dicarboxylate (144 mg, 0.50 mmol, 1.00 equiv.) was dissolved in trimethyl phosphate (3.5 mL) and NaOAc (41.0 mg, 0.05 mmol, 1.00 equiv.) was added. Then, bromine (0.05 mL, 1.00 mmol, 2.00 equiv.) was added dropwise and the reaction mixture was stirred 8 h at 50 °C. The mixture was quenched with saturated NH_4Cl solution (10%) and the phases were separated. The aqueous phase was extracted with CH_2Cl_2 and the combined organic phase was dried ($MgSO_4$) and filtered. The solvent was removed under reduced pressure and the crude product was purified by column chromatography (CH_2Cl_2:MeOH = 40:1). The product was obtained in 52% yield (96 mg, 0.26 mmol) as pale yellow solid.

^{1}H NMR (300 MHz, $CDCl_3$, ppm): δ = 11.68 (s, 1H), 8.94 (d, *J* = 11.3 Hz, 2H), 7.93–7.85 (m, 2H), 4.48 (q, *J* = 7.1 Hz, 4H), 1.47 (t, *J* = 7.1 Hz, 6H).

^{13}C NMR (75 MHz, $CDCl_3$, ppm): δ = 172.3, 166.4, 141.5, 135.3, 132.8, 132.7, 102.7, 60.8, 14.6. $C_{q,Br}$ is not detectable.

HRMS (ESI, +): calcd for $C_{16}H_{14}O_5Br$: 365.0025, found 365.0023.

IR (film, cm^{-1}): 2922, 2354, 2196, 1957, 1660, 1583, 1523, 1471, 1439, 1382, 1331, 1252, 1166, 1021, 999, 929, 859, 831, 790, 693, 680, 627.

The analytical data for the ^{1}H NMR spectra are in accordance with the literature.[11]

6-Bromoazulen-2-ol

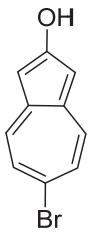

According to a procedure of Lörtscher[12] diethyl 6-bromo-2-hydroxyazulene-1,3-dicarboxylate (150 mg, 0.40 mmol, 1.00 equiv.) was dissolved in 95% H_2SO_4 (15 mL). Carefully 85% H_3PO_4 (75 mL) was added and the reaction mixture was stirred 2 h at 130 °C. After cooling down to ambient temperature the reaction mixture was poured into ice water. The aqueous phase was extracted with Et_2O, dried ($MgSO_4$) and filtered. After removal of solvent the crude product was purified by column chromatography (CH_2Cl_2:Et_2O = 9:1). The product was obtained in 77% yield (70.0 mg, 0.30 mmol) as dark red solid.

^{1}H NMR (300 MHz, DMSO-d_6, ppm): δ = 11.22 (s, 1H), 7.81 (d, *J* = 10.9 Hz, 2H), 7.48 (d, *J* = 10.9 Hz, 2H), 6.81 (s, 2H).

^{13}C NMR (75 MHz, DMSO-d_6, ppm): δ = 168.7, 138.7, 128.7, 126.8, 126.2, 105.5.

The analytical data are in accordance with the literature.[12]

2,6-Dibromoazulene

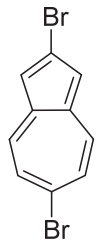

According to a procedure of Lörtscher[12] 6-bromoazulen-2-ol (100 mg, 0.45 mmol, 1.00 equiv.) was dissolved in toluene (60 mL). Then PBr_3 (0.13 mL, 1.36 mmol, 3.00 equiv.) was added dropwise and the reaction mixture was stirred 2 h at 110 °C. After cooling down to ambient temperature the reaction mixture was poured into ice water. The phases were separated and the aqueous phase was extracted with toluene. The combined organic phase was washed with water, dried ($MgSO_4$) and filtered. The solvent was removed under reduced pressure and the crude product was purified by column chromatography (*n*-pentane:CH_2Cl_2 = 9:1). The product was obtained in 70% yield (90.0 mg, 0.31 mmol) as purple solid.

^{1}H NMR (300 MHz, DMSO-d_6, ppm): δ = 8.20 (d, *J* = 10.4 Hz, 2H), 7.70 (d, *J* = 10.1 Hz, 2H), 7.54 (s, 2H).

^{13}C NMR (75 MHz, DMSO-d_6, ppm): δ = 139.0, 135.0, 133.8, 128.6, 128.6, 121.2.

MS (EI) *m*/*z* (%): 286 (33, [M^+]), 284 (17), 208 (1), 205 (9), 204 (1), 143 (3), 127 (9), 126 (100), 125(7), 104 (1), 100 (5), 99 (9), 87 (6), 76 (9), 74 (15), 63 (28), 62 (9), 50 (11).

HRMS (EI, *m*/*z*): calcd for $C_{10}H_6Br_2$: 283.8831, found 283.8827.

IR (film, cm^{-1}): 2928, 2209, 2148, 1917, 1573, 1521, 1466, 1435, 1389, 1283, 1215, 1072, 1011, 971, 853, 832, 815, 786, 723, 701, 608.

The analytical data are in accordance with the literature.[12]

NMR Spectra

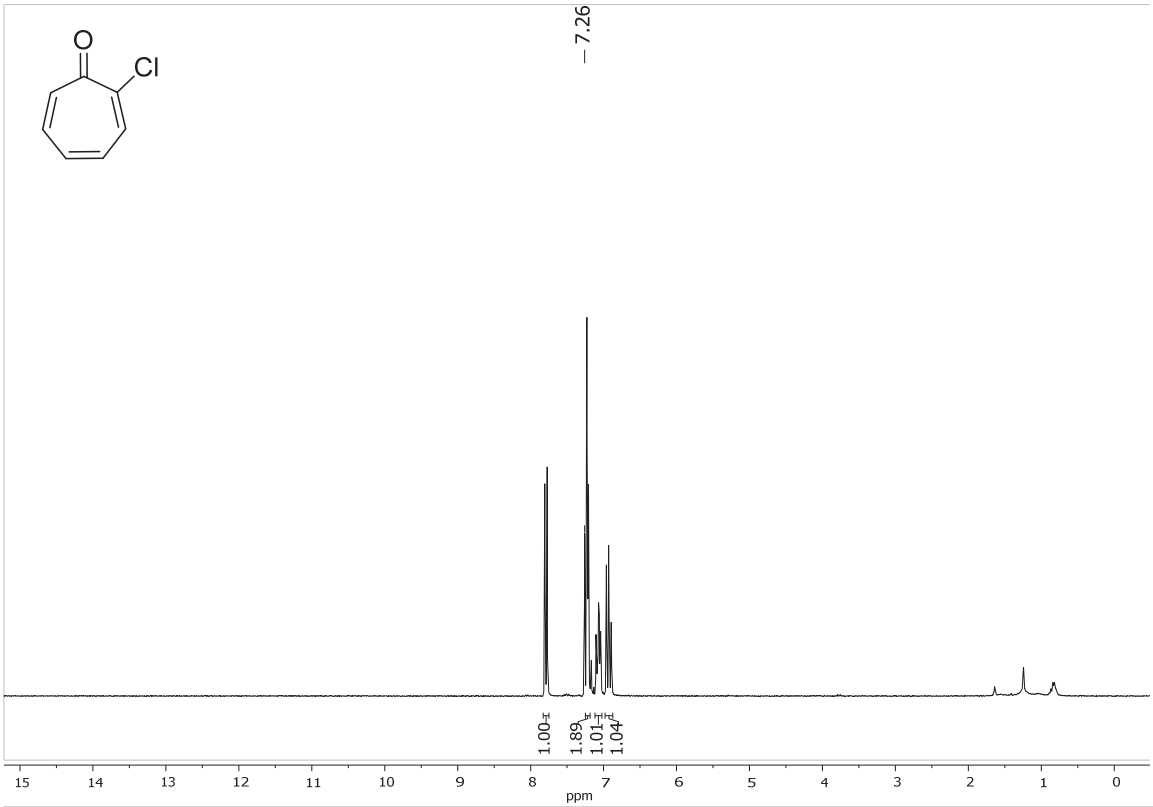
O
Cl
7.26
1.00
1.89
1.01
1.04
15 14 13 12 11 10 9 8 7 6 5 4 3 2 1 0
ppm

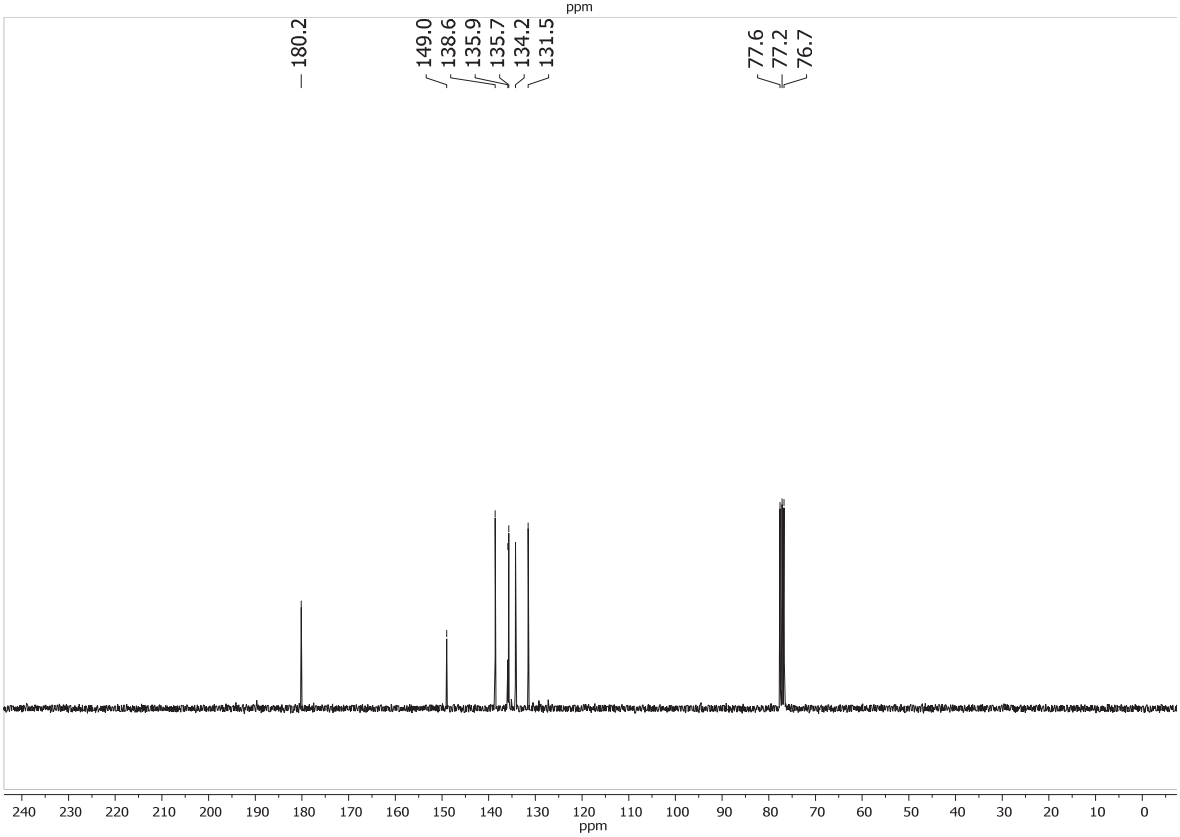
180.2
149.0
138.6
135.9
135.7
134.2
131.5
77.6
77.2
76.7
240 230 220 210 200 190 180 170 160 150 140 130 120 110 100 90 80 70 60 50 40 30 20 10 0
ppm

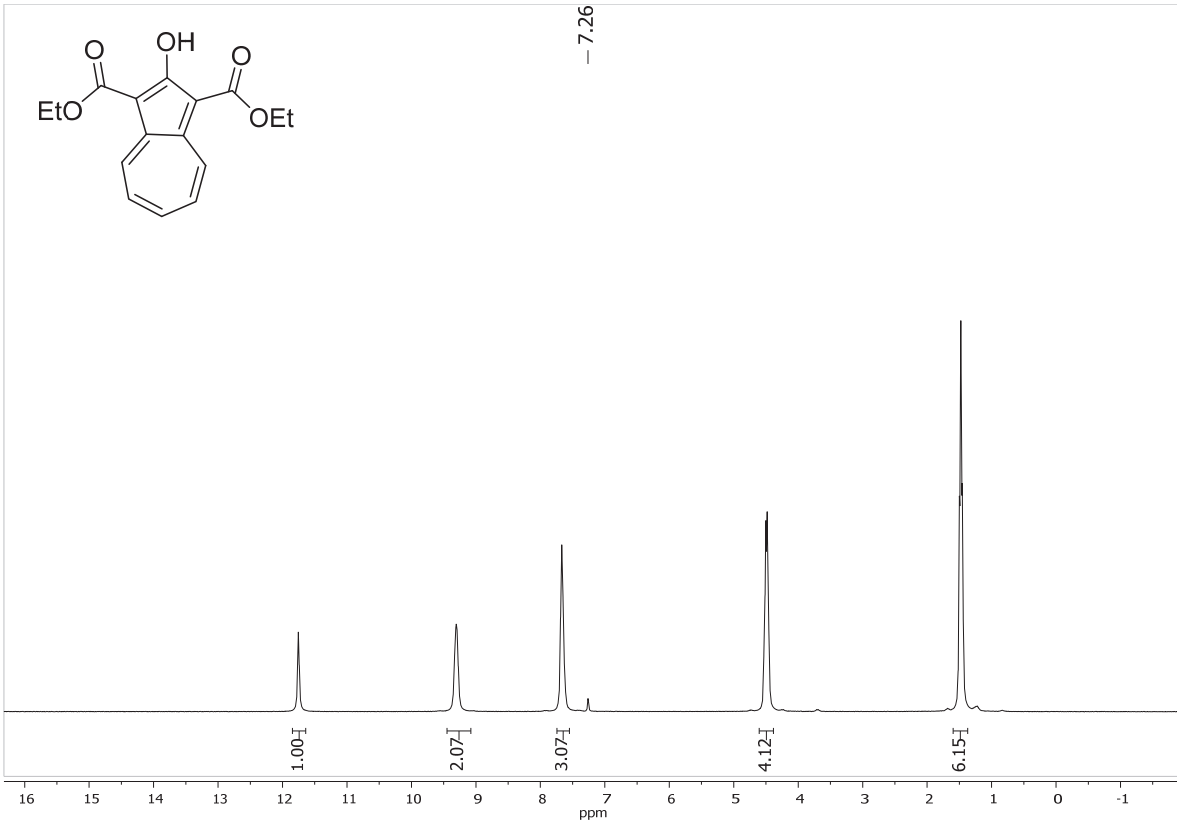
OH
O
O
EtO
OEt
7.26
1.00
2.07
3.07
4.12
6.15
ppm

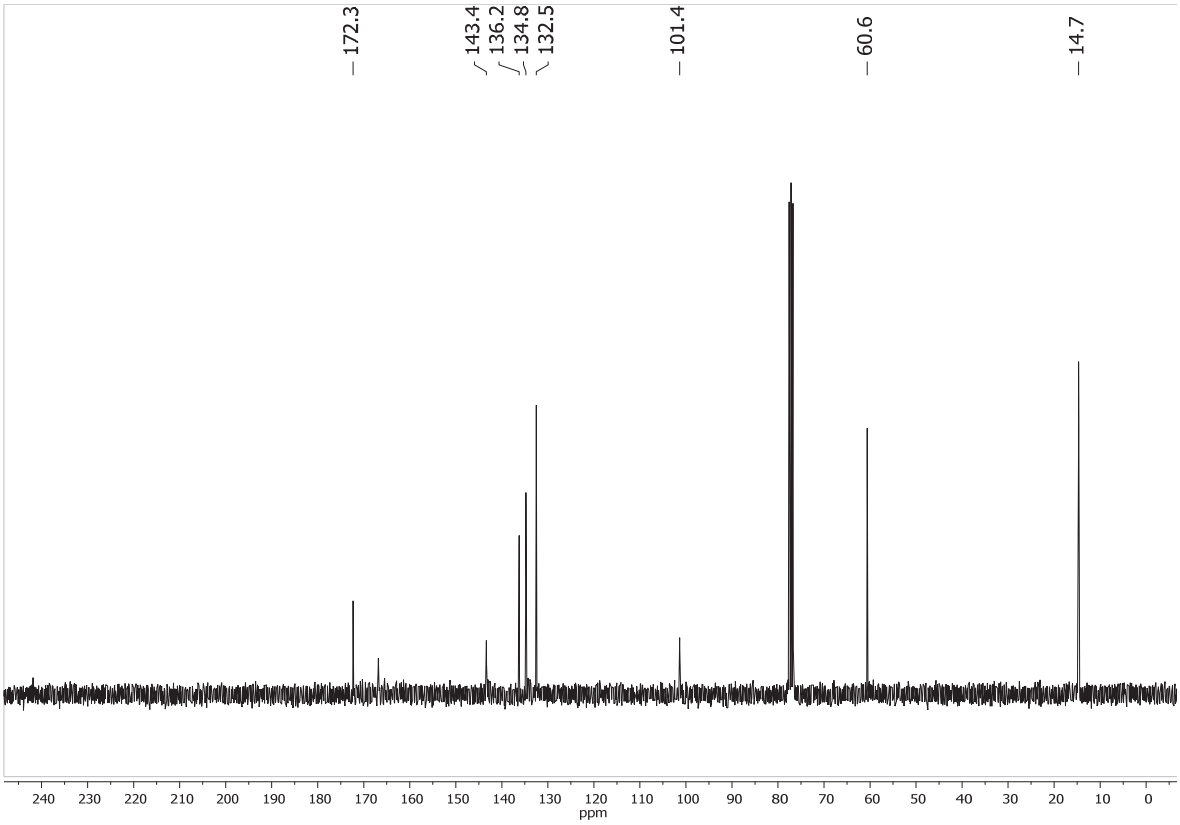
172.3
143.4
136.2
134.8
132.5
101.4
60.6
14.7
ppm

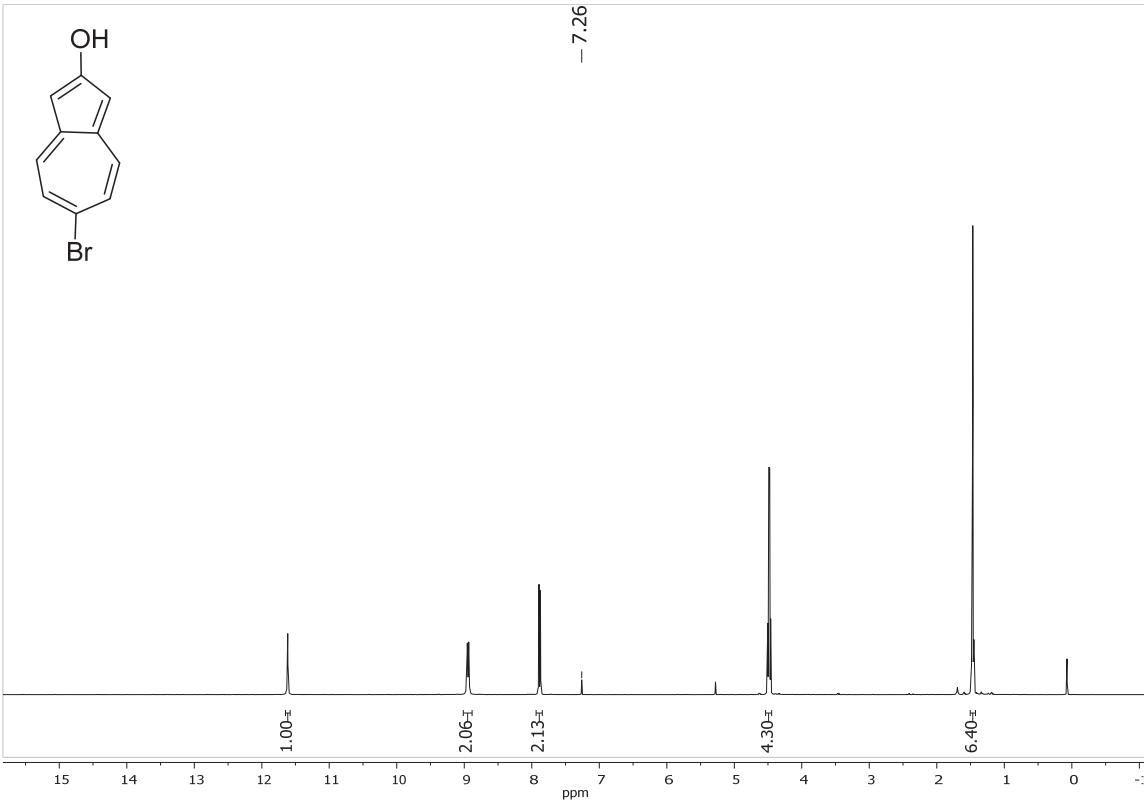
OH
Br
7.26
1.00
2.06
2.13
4.30
6.40
ppm

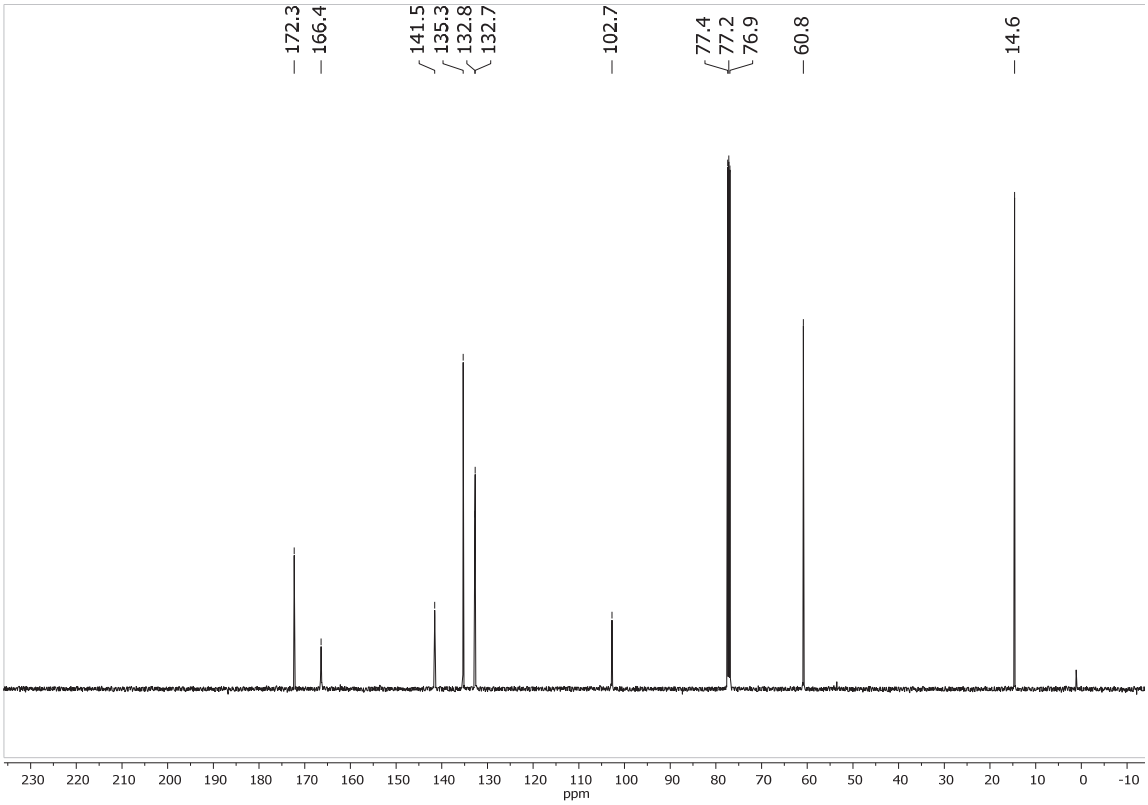
172.3
166.4
141.5
135.3
132.8
132.7
102.7
77.4
77.2
76.9
60.8
14.6
ppm

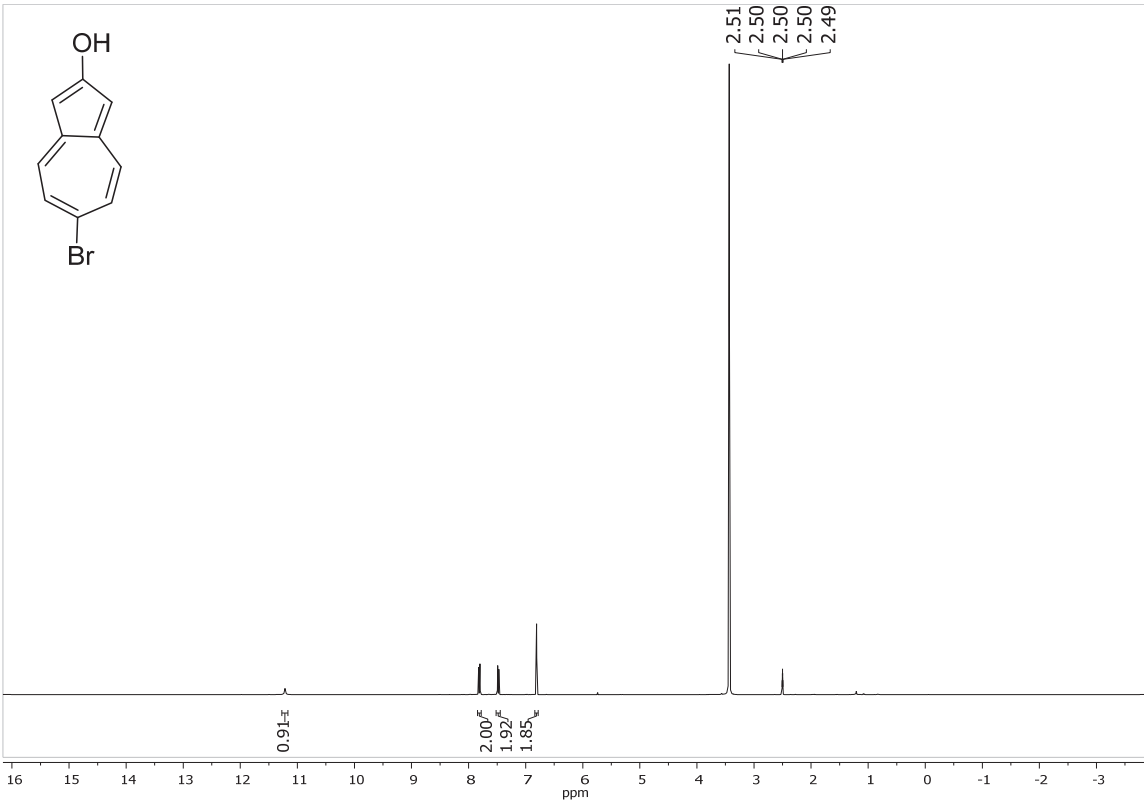
OH
Br
2.51
2.50
2.50
2.50
2.49
0.91
2.00
1.92
1.85
ppm

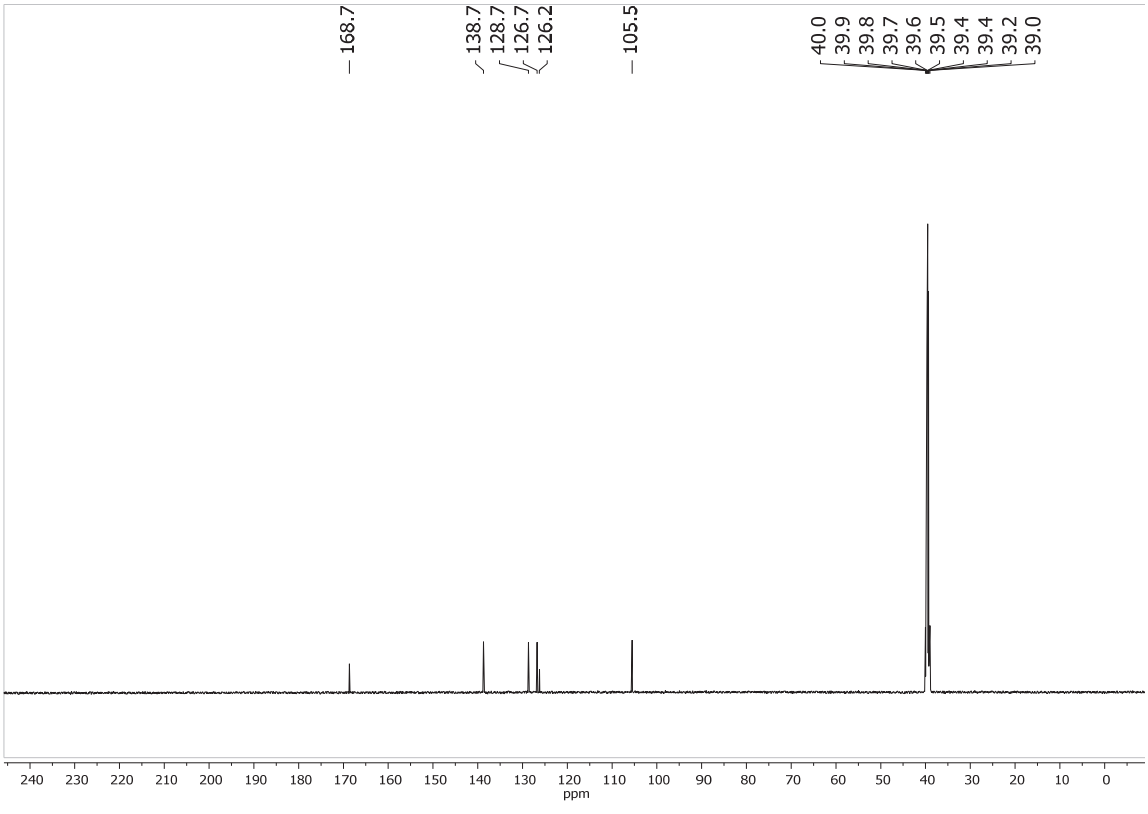
168.7
138.7
128.7
126.7
126.2
105.5
40.0
39.9
39.8
39.7
39.6
39.5
39.4
39.4
39.2
39.0
ppm

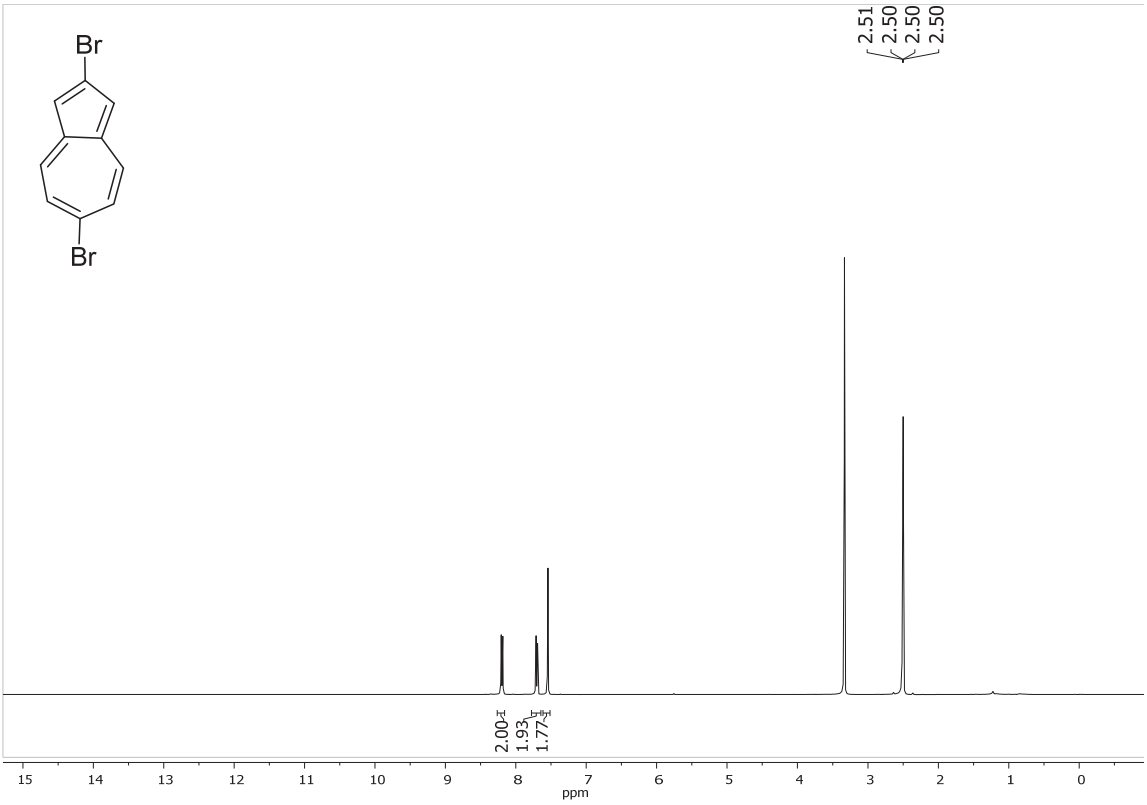
Br
Br
2.51
2.50
2.50
2.50
2.00
1.93
1.77
ppm

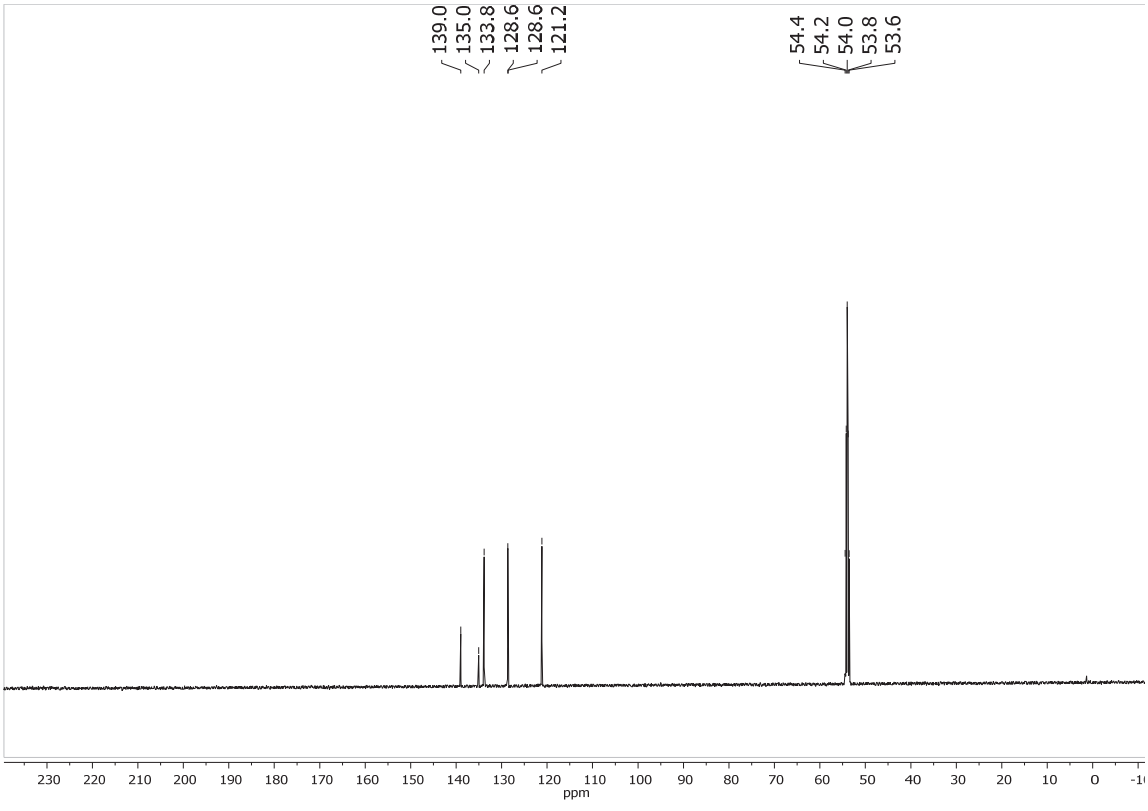
139.0
135.0
133.8
128.6
128.6
121.2
54.4
54.2
54.0
53.8
53.6
ppm

4. DFT-optimized geometries (VASP POSCAR format):

Phagraphene, cf. Figure 4a

1.00000000000000

6.6933222301648030 0.0000000000000000 0.0000000000000000

0.0000000000000000 19.9945370318452902 0.0000000000000000

0.0000000000000000 0.0000000000000000 9.9972685159226451

C H

20 6

Direct

0.9305023410464344 0.3394975141631420 0.5000000000000000

0.0290385604536638 0.4031389438167139 0.5000000000000000

0.9456387273584070 0.4702014666864542 0.5000000000000000

0.7351179547437212 0.3188885303525808 0.5000000000000000

0.7803135639196412 0.6033104957089392 0.5000000000000000

0.7285108422307900 0.4800266830727509 0.5000000000000000

0.6543585396131277 0.5460251343961318 0.5000000000000000

0.6555661236073220 0.6605905892804387 0.5000000000000000

0.5663321908942223 0.3601968541395237 0.5000000000000000

0.5711595917440775 0.4327139251851833 0.5000000000000000

0.4506922372100277 0.5667533743363649 0.5000000000000000

0.4555288328989349 0.6392688257777976 0.5000000000000000

0.3662827196248344 0.3388920803383328 0.5000000000000000

0.3674883650829770 0.4534474021106618 0.5000000000000000

0.2933226376518192 0.5194430165521453 0.5000000000000000

0.2415149782669914 0.3961740352515761 0.5000000000000000

0.2867073612571289 0.6805651728391595 0.5000000000000000

0.0761856021821927 0.5292722275961950 0.5000000000000000

0.0912908199085720 0.6599714333525029 0.5000000000000000

0.9928061539280719 0.5963320207166944 0.5000000000000000

0.0361576307303793 0.2981237171173845 0.5000000000000000

0.9856650579254662 0.7013576983531635 0.5000000000000000

0.7090710385150913 0.2649022718186416 0.5000000000000000

0.6993319232195176 0.7129130763694604 0.5000000000000000

0.3224626099758936 0.2865767022266468 0.5000000000000000

0.3127314594225936 0.7345570152564846 0.5000000000000000

Naphthalene analogue of phagraphene, cf. Figure 4b

1.00000000000000

6.5528376349350159 0.0000000000000000 0.0000000000000000

0.0000000000000000 19.5748763094411302 0.0000000000000000

0.0000000000000000 0.0000000000000000 9.7874381546716300

C H

20 6

Direct

0.8653258480143720 0.3492306889336945 0.5000000000050022

0.0094001328428419 0.4018121695727856 0.5000000000050022

0.9379851982139016 0.4712251848127238 0.5000000000050022

0.6548350100065221 0.3618272947835450 0.5000000000050022

0.7914764955701372 0.6095119748314985 0.5000000000050022

0.7245780322489139 0.4850542230804891 0.5000000000050022

0.6521716144290437 0.5543453669559639 0.5000000000050022

0.7130562993056060 0.6774008751433485 0.5000000000050022

0.5107689254690726 0.3074410383642956 0.5000000000050022

0.5814366686987142 0.4306170157789211 0.5000000000050022

0.4369921213446091 0.5670574275602149 0.5000000000050022

0.5076626711675232 0.6902119722268054 0.5000000000050022

0.3053483058644986 0.3202527729239222 0.5000000000050022

0.3663056051860494 0.4433245139469477 0.5000000000050022

0.2938543541446634 0.5126085816878998 0.5000000000050022

0.2269389071126540 0.3881655107484292 0.5000000000050022

0.3635895656498889 0.6358327493337299 0.5000000000050022

0.0804341532854949 0.5264479760825083 0.5000000000050022

0.1530944470044062 0.6484408763329341 0.5000000000050022

0.0090259306777440 0.5958807664944743 0.5000000000050022

0.9139417094045257 0.2960202405113677 0.5000000000050022

0.1044575666305576 0.7016456882573010 0.5000000000050022

0.5671465671890417 0.2549604210370688 0.5000000000050022

0.8178592296189180 0.7205279770812325 0.5000000000050022

0.2005335542879223 0.2771225269064956 0.5000000000050022

0.4512174879421593 0.7426806795184930 0.5000000000050022

TPH-graphene, cf. Figure 4c

1.00000000000000

6.9002423548684684 0.0000000000000000 0.0000000000000000

0.0000000000000000 20.2189499257740728 0.0000000000000000

0.0000000000000000 0.0000000000000000 10.1094749628870364

C H

20 6

Direct

0.0815348043163553 0.5357428678466292 0.5000000000000000

0.0812551038581120 0.6521626007503940 0.5000000000000000

0.2052645485360571 0.5954048356667627 0.5000000000000000

0.8890435965752346 0.5622063650214173 0.5000000000000000

0.8859744874933781 0.6338727711893171 0.5000000000000000

0.7828407082244908 0.3988456907530491 0.5000000000000000

0.6784469975878551 0.3367440191434170 0.5000000000000000

0.7235724052107173 0.5261467923466228 0.5000000000000000

0.7182647490882772 0.6757182047884811 0.5000000000000000

0.6769982158039909 0.4565504186474740 0.5000000000000000

0.4800879416911101 0.3243766453062733 0.5000000000000000

0.5211388607940322 0.5435722799038558 0.5000000000000000

0.5198855621450917 0.6633737938843751 0.5000000000000000

0.4745588698611201 0.4739692575093528 0.5000000000000000

0.4153819916186734 0.6012967452841167 0.5000000000000000

0.3122899657209572 0.3662238455282605 0.5000000000000000

0.3091299497072484 0.4379048229710136 0.5000000000000000

0.1169648306246742 0.3479596964627518 0.5000000000000000

0.1166743771283336 0.4643901847573488 0.5000000000000000

0.9929480698412334 0.4047396342213219 0.5000000000000000

0.1329869986440997 0.7029749828361957 0.5000000000000000

0.7674892941215177 0.2921784018458808 0.5000000000000000

0.7547277330022482 0.7284194544792157 0.5000000000000000

0.4436625591963974 0.2716718774199265 0.5000000000000000

0.4309041287440039 0.7079529558257818 0.5000000000000000

0.0652197660563374 0.2971475846256482 0.5000000000000000

Naphthalene analogue of TPH-graphene, cf. Figure 4d

1.00000000000000

6.7287360850331259 0.0000000000000000 0.0000000000000000

0.0000000000000000 19.7164057390543164 0.0000000000000000

0.0000000000000000 0.0000000000000000 9.8582028695758837

C H

20 6

Direct

0.0829007128662931 0.5450467719134585 0.5000000000000000

0.1402261862356685 0.6715111026105045 0.5000000000000000

0.2178411374127576 0.6033316109000877 0.5000000000000000

0.8797140138362507 0.5699085636642205 0.5000000000000000

0.9453774310170878 0.6910643943978845 0.5000000000000000

0.7540202183910338 0.3945621529443262 0.5000000000000000

0.6014618444719868 0.3437431171797558 0.5000000000000000

P4

0.7238275792198747 0.5267021540632593 0.5000000000000000

0.7988059615934551 0.6399713963658200 0.5000000000000000

0.6679565588877067 0.4561249391842058 0.5000000000000000

0.3933958336708990 0.3599858770747774 0.5000000000000000

0.5243226899776794 0.5438183644564124 0.5000000000000000

0.5907636580511260 0.6562105405810650 0.5000000000000000

0.4684696626523568 0.4732453709747688 0.5000000000000000

0.4382219299771296 0.6053855337490107 0.5000000000000000

0.2468775411450346 0.3088793919018351 0.5000000000000000

0.3125716228959664 0.4300474242726509 0.5000000000000000

0.0520292056255809 0.3284317986983409 0.5000000000000000

0.1093526585314196 0.4548937164121816 0.5000000000000000

0.9743985438061279 0.3966114797991578 0.5000000000000000

0.2525485012942588 0.7113052536379276 0.5000000000000000

0.6357243590975168 0.2896145389556261 0.5000000000000000

0.9048986387146201 0.7446689191078132 0.5000000000000000

0.2874086917371503 0.2552835510013876 0.5000000000000000

0.5565038567264934 0.7103425576711522 0.5000000000000000

0.9396879064718606 0.2886472246150026 0.5000000000000000

References:

1. Martin-Jimenez, D.; Ahles, S.; Mollenhauer, D.; Wegner, H. A.; Schirmeisen, A.; Ebeling, D. Bond-Level Imaging of the 3D Conformation of Adsorbed Organic Molecules Using Atomic Force Microscopy with Simultaneous Tunneling Feedback. *Phys. Rev. Lett.* **2019,** *122,* 196101.

2. Kresse, G.; Hafner, J. Vienna *Ab Initio* Simulation Package (VASP), version 5.2. *Institut für Materialphysik, Universität Wien, Vienna, since* **1991,** *www.vasp.at*.

3. Perdew, J. P.; Burke, K.; Ernzerhof, M. Generalized Gradient Approximation Made Simple. *Phys. Rev. Lett.* **1996,** *77,* 3865-3868.

4. Grimme, S.; Antony, J.; Ehrlich, S.; Krieg, H. A Consistent and Accurate *ab initio* Parametrization of Density Functional Dispersion Correction (DFT-D) for the 94 Elements H-Pu. *J. Chem. Phys.* **2010,** *132,* 154104.

5. Grimme, S.; Ehrlich, S.; Goerigk, L. Effect of the Damping Function in Dispersion Corrected Density Functional Theory. *J. Comput. Chem.* **2011,** *32,* 1456-1465.

6. Blochl, P. E. Projector Augmented-Wave Method. *Phys. Rev. B* **1994,** *50,* 17953-17979.

7. Kresse, G.; Joubert, D. From Ultrasoft Pseudopotentials to the Projector Augmented-Wave Method. *Phys. Rev. B* **1999,** *59,* 1758-1775.

8. Brettle, R.; Dunmur, D. A.; Estdale, S.; Marson, C. M. Synthesis, Linear Dichroism and Mesogenic Properties of Substituted Azulenes. *J. Mater. Chem.* **1993,** *3,* 327-331.

9. Zhang, J.; Petoud, S. Azulene-Moiety-Based Ligand for the Efficient Sensitization of Four Near-Infrared Luminescent Lanthanide Cations: Nd3+, Er3+, Tm3+, and Yb3+. *Chem. Eur. J.* **2008,** *14,* 1264-1272.

10. Chen, A.-H. Electrochemical Methoxylation of 1,2,3-Trisubstituted Azulenes. *J. Chin. Chem. Soc.* **1999,** *46,* 35-39.

11. Ito, S.; Ando, M.; Nomura, A.; Morita, N.; Kabuto, C.; Mukai, H.; Ohta, K.; Kawakami, J.; Yoshizawa, A.; Tajiri, A. Synthesis and Properties of Hexakis(6-octyl-2-azulenyl)benzene as a Multielectron Redox System with Liquid Crystalline Behavior. *J. Org. Chem.* **2005,** *70,* 3939-3949.

12. Schwarz, F.; Koch, M.; Kastlunger, G.; Berke, H.; Stadler, R.; Venkatesan, K.; Lörtscher, E. Charge Transport and Conductance Switching of Redox-Active Azulene Derivatives. *Angew. Chem. Int. Ed.* **2016,** *55,* 11781-11786.

5.2 Surface and Interface Chemistry of Other Aromatic Molecules

This chapter is composed of four publications that study different aspects of surface and interface chemistry of aromatic molecules. They cover the broad range of topics investigated in the Gottfried group. In general, they focus on understanding the fundamental interactions of organic molecules with surfaces as well as co-deposited metal atoms.

The publication P5 deals with the self-assembly of the aromatic dicarbonitrile 1,1':3',1'':4'',1'''-quaterphenyl-4,4'''-dicarbonitrile (*m*-4PDN) and investigates the different adsorbate structures formed by this molecule on the Ag(111) surface. The publications P6 and P7 study metalation reactions of the two tetrapyrroles *meso*-tetraphenylporphyrin (2HTPP) and 2,3,8,12,17,18-hexaethyl-7,13-dimethylcorrole (3HHEDMC). P8 characterizes the interaction of the non-alternant aromatic compound azulene with the Cu(111) surface compared with its alternant counterpart naphthalene.

I am the first author of publication P5. The publications P6 to P8, of which I am co-author, are concerned with other research projects of the Gottfried group. I contributed to them mostly with measurements at the synchrotron radiation facility BESSY II in Berlin but also in the laboratory in Marburg.

P5 Polymorphism at the Metal/Organic Interface: Hybrid Phase with Alternating Coplanar and Vertical Adsorption Geometry

Citation: **C. K. Krug**, M. Zugermeier, J. Kuttner, M. Schmid, G. Hilt, J. M. Gottfried, **2020**, *J. Phys. Chem. C 124*(29), 15928–15934, DOI 10.1021/acs.jpcc.0c03601.

Summary

In this article, which was accepted for publication one day after handing in this thesis, the polymorphism of 1,1':3',1'':4'',1'''-quaterphenyl-4,4'''-dicarbonitrile (*m*-4PDN) on the Ag(111) surface is studied with scanning tunneling microscopy (STM) accompanied by X-ray photoelectron spectroscopy (XPS). At saturation coverage it is shown that the *m*-4PDN molecules form a densely packed phase, while the coexistence of two different ordered phases and a dilute phase is observed at a low coverage.

The *m*-4PDN molecule, which is investigated in this study, is chiral in the adsorbed state. When it is deposited on the Ag(111) surface two different enantiomers (denoted as R_p and S_p) are observed. At saturation coverage (1.0 ML) a close-packed layer is formed, which consists of both enantiomers. The molecules arrange in pairs exclusively consisting of one enantiomer. The pairs of one enantiomer arrange in rows, which are surrounded by rows of pairs of the other enantiomer. Stabilization of this adsorbate structure is achieved by intermolecular H···NC hydrogen bonds between the nitrile groups of one molecule and the phenyl H atoms of its neighbors.

A reduction of the coverage to 0.1 ML (determined by XPS) leads to the formation of two polymorphic adsorbate structures. The first one is a quasi-Kagome structure, which consists of six nodes formed by three molecules each. All molecules in a domain of this adsorbate structure belong to the same enantiomer *i.e.*, R_p or S_p, and it is observed for both enantiomers on different regions of the sample. The second adsorbate structure is a mixed phase of flat-lying and upright-standing molecules. The nitrile groups of the standing molecules coordinate to Ag atoms of the substrate and the standing molecules are enclosed by rows of lying molecules, which are arranged similar to the pairs observed in the close-packed layer. Such a phase with coexisting lying and standing molecules had not been reported before. Both low-coverage structures are stabilized by intermolecular H···NC hydrogen bonds similar to those observed in the close-packed layer.

Own Contribution

All the experiments leading to this publication were performed with the combined STM and XPS setup in the laboratory of the Gottfried group in Marburg (*cf.* Section 3.4.1) by Dr. Malte Zugermeier and me with additional help by Dr. Martin Schmid. The *m*-4PDN molecule was synthesized by Dr. Julian Kuttner under the supervision of Prof. Dr. Gerhard Hilt based on the idea of Prof. Dr. J. Michael Gottfried. I performed the data analysis and wrote the manuscript in cooperation with Prof. Dr. J. Michael Gottfried and all authors were involved in its discussion.

THE JOURNAL OF PHYSICAL CHEMISTRY C

pubs.acs.org/JPCC Article

Polymorphism at the Metal/Organic Interface: Hybrid Phase with Alternating Coplanar and Vertical Adsorption Geometry

Claudio K. Krug, Malte Zugermeier, Julian Kuttner, Martin Schmid, Gerhard Hilt,* and J. Michael Gottfried*

Cite This: *J. Phys. Chem. C* 2020, 124, 15928−15934 Read Online

ACCESS | Metrics & More | Article Recommendations | Supporting Information

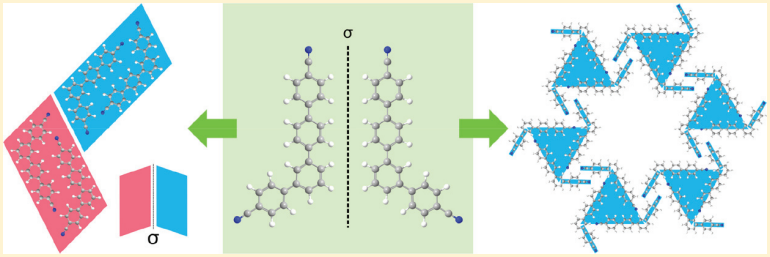

ABSTRACT: Polymorphism of organic molecular materials plays a prominent role in organic (opto)electronic devices, where the structural properties of metal/organic interfaces determine performance-critical parameters such as charge carrier injection rates. Here, we show that (sub)monolayers of a 2D-prochiral aromatic dinitrile with a bent quaterphenyl backbone engage in pronounced polymorphism on a Ag(111) surface and form a unique phase with alternating polar orientation of the molecules. In the saturated monolayer, the molecules are nearly coplanar with the substrate (flat-lying) and form an ordered racemic structure consisting of chiral dimers stabilized by H···NC hydrogen bonds. At submonolayer coverages, two ordered phases coexist with a dilute mobile phase. One phase forms homochiral domains with a quasi-Kagome structure. The other phase has a unique structure consisting of alternating rows of flat-lying and upright-standing molecules. The two different polar orientations can be distinguished by scanning tunneling microscopy. The upright-standing molecules have a straight and brighter shape and show increased packing density compared to their flat-lying counterparts. These results reveal the great local variability of molecular arrangements at metal/organic interfaces, even for fixed global parameters such as temperature and coverage.

INTRODUCTION

Polymorphism, i.e., the existence of a chemical compound in different crystal structures, is a phenomenon that plays a prominent role in organic molecular solids because the different polymorphic forms can differ strongly in their physical and chemical properties.[1−3] One particularly important case is the polymorphism of pharmaceuticals, where polymorphs may show different pharmacological activity and a new polymorph of a patented substance may not be subject to patent protection.[4,5] Thus, understanding what determines the formation of different polymorphs is of great importance in the context of crystal engineering.[6]

Structure formation at metal/organic interfaces is another area where polymorphism comes into play. The electronic properties of organic semiconductors and their interfaces with metals in organic (opto)electronic devices also vary between different polymorphs.[7,8] Especially important is the structure of the first adsorbed layer, which determines the interface properties and can also control the structure of further molecular layers during deposition.[9,10] Related previous work was mainly performed at the solid/liquid interface, where the solvent was shown to strongly influence the interface structure.[11−23] Examples for molecular polymorphism at the solid/vacuum interface include self-assembled monolayers,[24,25] halogenated polyphenylenes,[26−29] porphyrins,[30] subphthalocyanines,[31] amino acids such as alanine,[32] and squaric acid.[33]

Arene dicarbonitriles constitute a class of organic molecules that are well-studied with respect to their adsorbate structures on metal single-crystal surfaces. This holds especially for the linear oligophenylene *para*-dicarbonitriles (Figure 1a), which show pronounced size and substrate dependence of their (sub)monolayer structures.[34−40] All these linear molecules adsorb in a nearly coplanar (flat-lying) geometry on the different surfaces, and their observed adsorbate structures are stabilized by H···NC hydrogen bonds between the nitrile groups and H atoms at the phenylene groups of neighboring

Received: April 23, 2020
Revised: June 16, 2020
Published: June 30, 2020

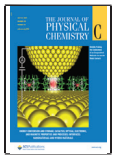

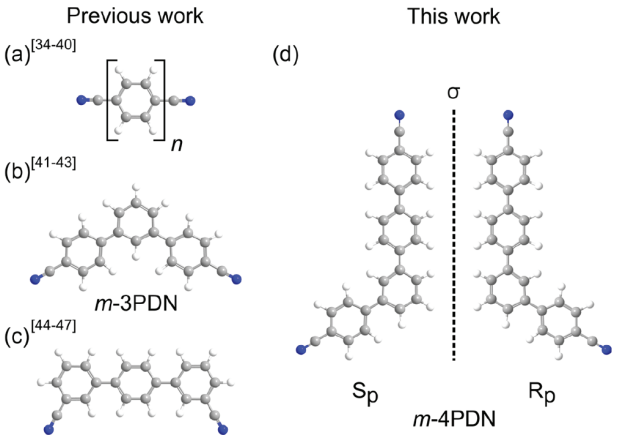

Figure 1. Balls-and-sticks models showing (a) linear oligophenylene *para*-dicarbonitriles, (b) 1,1′:3′,1″-terphenyl-4,4″-dicarbonitrile (*m*-3PDN), (c) 1,1′;4′,1″-terphenyl-3,3″-dicarbonitrile, and (d) 1,1′:3′1″:4″,1‴-quaterphenyl-4,4‴-dicarbonitrile (*m*-4PDN). In the adsorbed state, *m*-4PDN shows two-dimensional (2D) chirality. The two 2D enantiomers are here denoted S_p and R_p, where the lower index p refers to the planar chirality. Color code: white, hydrogen; gray, carbon; blue, nitrogen. The dotted line marks the position of the mirror plane σ.

P5

molecules. Other, closely related dicarbonitriles have oligophenylene backbones with a *meta*-substituted phenylene ring, resulting in a 120° angle between the terminal nitrile groups. A prominent example is 1,1′:3′,1″-terphenyl-4,4″-dicarbonitrile (*m*-3PDN, Figure 1b), which can form metal−organic Sierpiński triangles with codeposited metal atoms.[41,42] The adsorbate structure of *m*-3PDN on Cu(111) is strongly coverage-dependent and comprises either hydrogen bonds, coordination bonds to Cu adatoms, or a combination of both.[43] A 120° angle between the terminal CN groups is also possible with a linear oligophenylene backbone when the CN groups are placed in *meta*-positions, as in 1,1′;4′,1″-terphenyl-3,3″-dicarbonitrile (Figure 1c).[44−46] This molecule was shown to adsorb in an upright-standing manner in densely packed layers on Cu(111) and with codeposited Co atoms also on Ag(111).[47]

In this study, we focus on another dicarbonitrile with a 120° angle, namely 1,1′:3′1″:4″,1‴-quaterphenyl-4,4‴-dicarbonitrile (*m*-4PDN, Figure 1d). Like *m*-3PDN, this molecule has a *meta*-substituted phenylene ring in its backbone, but its reduced symmetry makes it chiral in the adsorbed state. Using scanning tunneling microscopy (STM) and X-ray photoelectron spectroscopy (XPS), we show here that (sub)monolayers of *m*-4PDN on Ag(111) form different polymorphs. One of these polymorphs has a unique structure, consisting of flat-lying and upright-standing molecules in an ordered arrangement. Another polymorph forms homochiral domains with a porous quasi-Kagome structure.

METHODS

The experiments were performed in an ultrahigh-vacuum (UHV) system (base pressure 2×10^{-10} mbar) equipped with a SPECS Aarhus 150 variable-temperature STM (scan range 1.5 μm × 1.5 μm), a SPECS Phoibos 150 electron energy analyzer, a monochromatized Al Kα X-ray source (SPECS XR 50 M, FOCUS 500), and other instruments. STM images were obtained with an electrochemically etched W tip at 170 K in constant current mode and processed with WSxM 5.0 Develop 9.4.[48] All voltages refer to the sample. Moderate filtering (Gaussian smooth, background subtraction) was applied for noise reduction. The Ag(111) single crystal (purity 99.999%, roughness <0.01 μm, orientation accuracy <0.1°, from MaTecK, Germany) was prepared by iterated sputtering with Ar^+ ions (0.5 keV, 12 μA, 30 min) and annealing (800−820 K, 10 min). The purity and structure of the sample were checked by XPS and low-energy electron diffraction (LEED), respectively. Sample temperatures were measured with a thermocouple mounted to the sample holder of the Ag(111) crystal. The *m*-4PDN molecules were synthesized as described in the Supporting Information and evaporated from a home-built stainless steel Knudsen cell evaporator that was resistively heated to 420 K. The Ag(111) substrate was kept at 300 K during deposition. The molecular flux was monitored during deposition by a quartz crystal microbalance (QCM), and the thickness was checked with XPS afterward. Monolayer coverage (1.0 ML) is defined as the densely packed layer shown in the STM images in Figure 2. All other global coverages are determined by XPS and referenced to this phase (see Figure S1 in the Supporting Information).

RESULTS AND DISCUSSION

Adsorbate Structure I. Deposition of a saturated monolayer of *m*-4PDN onto Ag(111) at 300 K leads to the

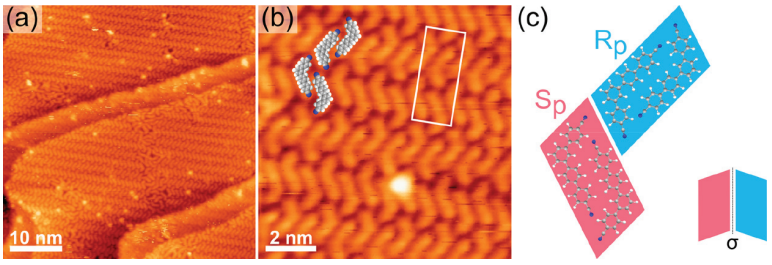

Figure 2. Adsorbate structure I: STM images of 1.0 ML of *m*-4PDN on Ag(111) after deposition at 300 K, showing the close-packed adsorbate structure consisting of two different enantiomers of pairwise arranged molecules. (a) Large-scale image showing the extension of the adsorbate structure over several terraces (with some defects). (b) Zoom-in image with superimposed 1.53(±0.10) nm × 3.74(±0.10) nm, 90°(±5°) unit cell and space-filling models representing pairs of S_p and R_p enantiomers. Tunneling parameters for (a) and (b): $U = -1.24$ V and $I = -0.69$ nA. (c) Structural model of the pairwise arrangement of the enantiomers S_p and R_p in two homochiral dimers, as indicated by the red (S_p) and blue (R_p) areas. The small lower inset symbolizes the enantiomeric nature of the red and blue areas. Color code of the molecular models: white, hydrogen; gray, carbon; blue, nitrogen.

https://dx.doi.org/10.1021/acs.jpcc.0c03601
J. Phys. Chem. C 2020, 124, 15928−15934

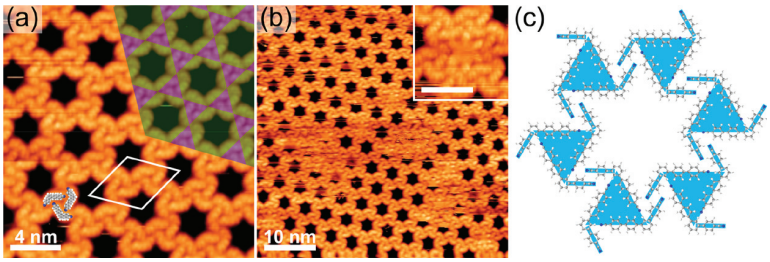

Figure 3. Adsorbate structure II: STM images taken after deposition of 0.1 ML of *m*-4PDN on Ag(111) at 300 K show a quasi-Kagome adsorbate structure consisting exclusively of the R_p enantiomer. (a) Zoom-in image with 4.20(±0.10) nm × 4.29(±0.10) nm, 118°(±5°) unit cell, space-filling model showing a trimer node, and ideal Kagome network superimposed. (b) Large-scale image showing the long-range order of the adsorbate structure and some streaky features attributed to mobile molecules. The inset shows a filled pore; the scale bar corresponds to 4 nm. Tunneling parameters: (a) U = 1.74 V, I = 0.56 nA; (b) U = 1.79 V, I = 0.54 nA. (c) Structural model of six chiral trimer nodes enclosing one void. Color code of the molecular models: white, hydrogen; gray, carbon; blue, nitrogen.

formation of a close-packed, well-ordered self-assembled structure, which covers large areas of the surface with only a few defects (Figure 2a). The rectangular 1.53(±0.10) nm × 3.74(±0.10) nm, 90°(±5°) unit cell of this adsorbate structure contains four molecules, corresponding to a molecular density of 0.65 nm^{-2} (Figure 2b). The pairwise interaction of the molecules is attributed to H···NC hydrogen bonds between the nitrile group at the long arm of one molecule and the hydrogen atoms at the short arm of the other molecule in the pair (see the space-filling models superimposed to the STM image in Figure 2b and the structural model in Figure 2c). The resulting chiral pairs consist only of either S_p or R_p enantiomers. The two neighboring pairs of molecules in the unit cell are formed by the two different enantiomers. The interaction between neighboring pairs (i.e., red and blue pair in Figure 2c) is attributed to H···NC hydrogen bonds between the nitrile group at the short arm of one molecule (e.g., in the red pair in Figure 2c) and the hydrogen atom on the outer part of the 120° angle of another one (e.g., the blue pair in Figure 2c). A similar pairwise packing motif has been reported for another aromatic dicarbonitrile molecule on the Ag(111) surface.[49] At a global coverage of 1.0 ML, no other adsorbate structure has been observed on the sample. However, we cannot fully exclude that other structures coexist with adsorbate structure I at this coverage due to the limited scan range of our Aarhus-type STM (see the Methods section).

Adsorbate Structure II. If the total coverage is reduced to 0.1 ML (as determined by XPS; see Figure S1), two different local adsorbate structures are observed. One of them shows large areas of hexagonally arranged voids (Figure 3). Each void is enclosed by six nodes consisting of three molecules each. The near-hexagonal 4.20(±0.10) nm × 4.29(±0.10) nm, 118°(±5°) unit cell of this phase contains six molecules (two nodes with three molecules each, Figure 3a). The corresponding local molecular density is 0.38 nm^{-2}, which is equivalent to 58% of the close-packed layer (i.e., to 0.58 ML) and is thus substantially higher than the global coverage of 0.1 ML as determined by XPS. The deviation between the coverages determined by XPS and STM will be discussed later.

The hexagonal adsorbate structure resembles the Kagome network (superimposed to the STM image in Figure 3a), which is a frequently observed structure formed by organic molecules on single crystal surfaces.[35,36,50−52] However, a closer look reveals deviations from the ideal Kagome case because the trimer nodes and the overall network are chiral. While the ideal Kagome lattice (wallpaper group *p6m*) has mirror planes, these are absent in the present adsorbate structure (wallpaper group *p6*) due to the chirality of the nodes (see space-filling models superimposed to the STM image in Figure 3a and the structural model in Figure 3c). The trimer nodes appear to be stabilized by H···NC hydrogen bonds between the nitrile group of the long arm of one molecule and H atoms in the 120° angle of another one (illustrated by the space-filling models superimposed to the STM image in Figure 3a and the structural model in Figure 3c). The interaction between different trimer nodes is caused by H···NC hydrogen bonds between the nitrile group of the short arm and H atoms at neighboring trimer nodes. The adsorbate structure consists exclusively of one enantiomer (R_p in the case of Figure 3). An STM image of the enantiomeric structure consisting entirely of S_p can be found in Figure S2.

Defect-free areas of the quasi-Kagome structure are observed only on small scales (Figure 3a). On a larger scale, streaky features attributed to mobile molecules as well as structural defects occur (Figure 3b and Figure S3). Some of the pores of the quasi-Kagome network are not empty. As illustrated in Figures S6 and S7, a filled pore can host one or two additional *m*-4PDN molecules. These molecules are not clearly resolved, probably because they are partially mobile and rotate inside the pore at the measurement temperature of 170 K. This is in agreement with size considerations: the pore diameter is 2.15 nm, while the length of the molecule along its long axis is only 1.85 nm. Thus, a single molecule (and less so also a pair of molecules) has space for rotation inside a pore (Figures S6c,d and S7b). Because the pores are chiral, one of the two enantiomers may be preferentially trapped (chiral recognition). However, the chirality of the inside of the pore is not very pronounced because it deviates only slightly from the D_{6h} symmetry, as can be seen in the models in Figure S6a,b. In addition, none of the nitrile groups, which are more strongly interacting and thus could increase the chiral bias, point toward the inside of the pore. Therefore, we do not expect pronounced enantioselectivity of the pore. The trapping of additional molecules shows the suitability of the quasi-Kagome structure as a host for guest species, as has also been discussed in the literature.[52]

Adsorbate Structure III. Another adsorbate structure observed at a total coverage (XPS) of 0.1 ML is presented in Figure 4. The overview image in Figure 4a shows alternating rows of darker and brighter appearance, surrounded by disordered areas. In the zoom-in image (Figure 4b), the typical bent shape of flat-lying *m*-4PDN molecules can clearly

P5

https://dx.doi.org/10.1021/acs.jpcc.0c03601
J. Phys. Chem. C 2020, 124, 15928−15934

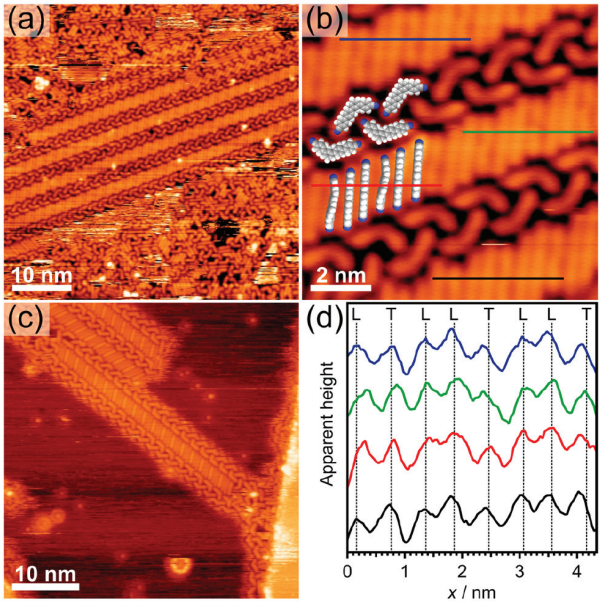

Figure 4. Adsorbate structure III: STM investigation after deposition of 0.1 ML of *m*-4PDN on Ag(111) at 300 K. (a) Large-scale image showing four rows of upright-standing molecules enclosed by flat-lying ones, surrounded by a disordered phase. (b) Zoom-in image on three rows of standing molecules with space-filling models superimposed to illustrate the twisted shape of every third standing molecule. (c) Large-scale image showing the starting of the rows close to a step edge (lower right) and away from a step edge (center top). The ordered domain is surrounded by an area with streaky features, which are attributed to a dilute phase of mobile molecules. Tunneling parameters: (a) U = 1.68 V, I = 0.29 nA; (b) U = 1.68 V, I = 0.32 nA; (c) U = −1.58 V, I = −0.76 nA. (d) Height profiles taken along the (randomly chosen) lines in (b). The colors of the lines correspond to the colors of the height profiles. Linear and twisted molecules are indicted by L and T, respectively. The distances between the vertical dashed lines correspond to the average distances between two linear molecules (L−L) or between a linear and a twisted molecule (L−T). For further details, see the text. Color code of the molecular models: white, hydrogen; gray, carbon; blue, nitrogen.

be distinguished within the darker rows. The brighter rows consist of parallel linear features, which we assign to upright-standing molecules. For the dinitrile molecules shown in Figure 1c, Marschall et al. have previously observed a coverage-driven transition from nearly coplanar with the Ag(111) substrate to upright-standing.[47] In this case, however, the adsorption structure uniformly consisted of upright-standing molecules. A mixed phase with alternating flat-lying and upright-standing molecules, as observed here, appears to be unprecedented.

The flat-lying molecules form a zipper-like structure. Similar to adsorbate structure II, this structure is stabilized by H···NC hydrogen bonds between the nitrile groups of the long molecular arm and hydrogen atoms of the phenylene rings in the 120° angle of another one. One row of the flat-lying molecules is exclusively formed by one enantiomer of *m*-4PDN. In Figure 4b, both rows consist of the S_p enantiomer, although they run in opposite directions. A row consisting of R_p molecules can be seen in Figure 4a. In line with previous work,[47] we propose that the nitrile groups of the upright-standing molecules point toward the Ag(111) surface because of their pronounced tendency to from coordination bonds to metals.[34,41,42,47] Within a row of upright-standing molecules, every third molecule appears shorter and slightly twisted, whereas the other two molecules are always completely straight. This twisting of the backbone has also been observed in bulk crystal structures of other polyphenylene molecules.[38,53] We tentatively suggest that the twisting occurs to optimize registry with the Ag(111) surface.

The upright-standing geometry is further supported by the following observations: (a) The respective rows appear brighter than those of the flat-lying molecules, as expected for an increased geometric height. (b) The line scans in Figure 4d indicate that the lateral distance between two straight, upright-standing molecules is only 0.49(±0.05) nm (averaged over 23 pairs of linear molecules), while that between a straight and a twisted molecule is 0.60(±0.06) nm (averaged over 43 pairs of linear and twisted molecules). These distances are considerably smaller than the minimum lateral distance of 0.75 nm between close-packed linear, flat-lying *p*-quaterphenyl dicarbonitrile molecules on Ag(111).[38] In fact, the distance between two straight molecules (0.49 nm) is closer to the typical π-stacking distance between two coplanar benzene molecules (0.41 nm).[54]

On the basis of these geometry considerations, it can be excluded that the straight features stem from impurities of other molecules, especially linear *p*-oligophenylene dicarbonitriles. Besides the geometric argument, the presence of impurities with linear shape can also be ruled out on the basis of careful investigation of our *m*-4PDN sample by NMR spectroscopy and other methods (see the Supporting Information). Furthermore, linear *p*-oligophenylene dicarbonitriles form submonolayer structures that are very different from the structures we observe here.[35,38]

The molecular density of the adsorbate structure III shown in Figure 4a is 0.68 nm^{-2}. This is almost twice the density of the quasi-Kagome structure (cf. Figure 3) and is much higher than the global coverage of 0.1 ML (0.065 nm^{-2}) as determined by XPS. In fact, the local molecular density of adsorbate structure III even slightly exceeds that of the monolayer structure of flat-lying molecules (Figure 2, 0.65 nm^{-2}). This is only possible if other areas of the surface are covered with a more dilute phase, i.e., if there are lateral variations of the local coverage. Indeed, Figure 4c shows that the ordered domains are surrounded by areas with streaky features, which can be attributed to mobile molecules in a dilute phase. Similar observations were made for another oligophenylene dicarbonitrile on Ag(111).[44,47] The coexistence with a disordered mobile phase was also observed for the quasi-Kagome structure (adsorbate structure II), as can be seen in Figure S4. The adsorbate structures II and III can also coexist in close proximity, as shown in Figure S5.

It is interesting to note that the densely packed mixed structure III is not observed when a full monolayer of *m*-4PDN is deposited, even though the local coverages of structures I and III are very similar (0.65 and 0.68 nm^{-2}, respectively). A possible reason for this is that only the monolayer structure I is thermodynamically stable, whereas the structures II and III are metastable. In fact, the observation that both structures II and III coexist with each other (see Figure S5 showing the structures in close proximity) and with a dilute phase reveals that the system is not in thermodynamic equilibrium. Otherwise, there should be only one, the most stable, ordered phase in coexistence with a dilute phase. (The alternative explanation that II and III coexist, because they have

https://dx.doi.org/10.1021/acs.jpcc.0c03601
J. Phys. Chem. C 2020, 124, 15928−15934

coincidentally the same free energy, would imply that the system is at a triple point. This is very unlikely, especially as the temperature (~170 K) is not completely constant during the measurements. This means that a possible triple point would be left.) The formation of the unusual metastable structure III may be kinetically driven and may require a lower average molecular density and the presence of a dilute phase to permit a suitable low-energy path. Such dynamic considerations, however, cannot be further pursued with our current methodology but should be addressed in the future by multiscale molecular dynamics simulations.

CONCLUSIONS

(Sub)monolayer phases of the quaterphenyl dicarbonitrile *m*-4PDN on Ag(111) form several polymorphs, including one with an unprecedented arrangement of flat-lying and upright-standing molecules. At saturation coverage (1.0 ML), a close-packed structure is formed, in which the molecules are nearly coplanar with the surface (flat-lying) and form chiral dimers stabilized by H···NC hydrogen bonds. Each dimer contains only one of the two possible 2D enantiomers of *m*-4PDN. The two types of enantiomeric dimers are arranged alternatingly, forming a lattice with a nonprimitive rectangular unit cell. At low coverage (0.1 ML), two well-ordered phases with higher local coverages coexist with a mobile dilute phase. One of the ordered phases has a chiral quasi-Kagome structure with a hexagonal unit cell containing six molecules. Its hexagram-shaped pores are surrounded by six chiral trimer nodes and sometimes host additional molecules. This phase forms two enantiomeric domains, which are homochiral, i.e., contain only one of the two 2D enantiomers of *m*-4PDN. The other ordered phase consists of alternating rows of flat-lying and upright-standing molecules. The upright-standing molecules are identified by their straight shape, brighter appearance in STM, and denser packing. Because of the latter, this adsorbate structure has a higher local coverage than the saturated monolayer of flat-lying molecules. The observed morphological variability is attributed to the terminal −CN groups, which can not only engage in various intermolecular hydrogen bonds but also bind to the metal surface, and to the 2D chirality of the molecule.

ASSOCIATED CONTENT

Supporting Information

The Supporting Information is available free of charge at https://pubs.acs.org/doi/10.1021/acs.jpcc.0c03601.

Coverage determination from X-ray photoelectron spectra, additional STM images, structural models of the filled quasi-Kagome pores, and details of the synthesis and spectroscopic characterization of *m*-4PDN (PDF)

AUTHOR INFORMATION

Corresponding Authors

Gerhard Hilt − *Institute of Chemistry, Carl von Ossietzky University Oldenburg, Oldenburg 26111, Germany;* orcid.org/0000-0002-5279-3378; Email: gerhard.hilt@uni-oldenburg.de

J. Michael Gottfried − *Department of Chemistry, Philipps University Marburg, 35032 Marburg, Germany;* orcid.org/0000-0001-5579-2568; Email: michael.gottfried@chemie.uni-marburg.de

Authors

Claudio K. Krug − *Department of Chemistry, Philipps University Marburg, 35032 Marburg, Germany*

Malte Zugermeier − *Department of Chemistry, Philipps University Marburg, 35032 Marburg, Germany*

Julian Kuttner − *Department of Chemistry, Philipps University Marburg, 35032 Marburg, Germany*

Martin Schmid − *Department of Chemistry, Philipps University Marburg, 35032 Marburg, Germany;* orcid.org/0000-0002-1686-241X

Complete contact information is available at: https://pubs.acs.org/10.1021/acs.jpcc.0c03601

Notes

The authors declare no competing financial interest.

ACKNOWLEDGMENTS

Financial support by the Deutsche Forschungsgemeinschaft (DFG, German Research Foundation) through project numbers 223848855-SFB 1083 and GO1812/2-1 is gratefully acknowledged.

REFERENCES

(1) Bernstein, J.; Davey, R. J.; Henck, J.-O. Concomitant Polymorphs. *Angew. Chem., Int. Ed.* **1999**, *38*, 3440−3461.

(2) Moulton, B.; Zaworotko, M. J. From Molecules to Crystal Engineering: Supramolecular Isomerism and Polymorphism in Network Solids. *Chem. Rev.* **2001**, *101*, 1629−1658.

(3) Erdemir, D.; Lee, A. Y.; Myerson, A. S. Nucleation of Crystals from Solution: Classical and Two-Step Models. *Acc. Chem. Res.* **2009**, *42*, 621−629.

(4) Yu, L.; Reutzel, S. M.; Stephenson, G. A. Physical Characterization of Polymorphic Drugs: An Integrated Characterization Strategy. *Pharm. Sci. Technol. Today* **1998**, *1*, 118−127.

(5) Saifee, M.; Inamda, N.; Dhamecha, D.; Rathi, A. Drug Polymorphism: A Review. *Int. J. Health Res.* **2010**, DOI: 10.4314/ijhr.v2i4.55423.

(6) Desiraju, G. R. Crystal Engineering: From Molecule to Crystal. *J. Am. Chem. Soc.* **2013**, *135*, 9952−9967.

(7) Jurchescu, O. D.; Mourey, D. A.; Subramanian, S.; Parkin, S. R.; Vogel, B. M.; Anthony, J. E.; Jackson, T. N.; Gundlach, D. J. Effects of Polymorphism on Charge Transport in Organic Semiconductors. *Phys. Rev. B: Condens. Matter Mater. Phys.* **2009**, *80*, 085201.

(8) Diao, Y.; Lenn, K. M.; Lee, W.-Y.; Blood-Forsythe, M. A.; Xu, J.; Mao, Y.; Kim, Y.; Reinspach, J. A.; Park, S.; Aspuru-Guzik, A.; et al. Understanding Polymorphism in Organic Semiconductor Thin Films through Nanoconfinement. *J. Am. Chem. Soc.* **2014**, *136*, 17046−17057.

(9) Meyer zu Heringdorf, F.-J.; Reuter, M. C.; Tromp, R. M. Growth Dynamics of Pentacene Thin Films. *Nature* **2001**, *412*, 517−520.

(10) Zhang, Y.; Li, D.; Jiang, C. Influence of Grain Size at First Monolayer on Bias-Stress Effect in Pentacene-Based Thin Film Transistors. *Appl. Phys. Lett.* **2013**, *103*, 213304.

(11) De Feyter, S.; De Schryver, F. C. Two-Dimensional Supramolecular Self-Assembly Probed by Scanning Tunneling Microscopy. *Chem. Soc. Rev.* **2003**, *32*, 139−150.

(12) Plass, K. E.; Grzesiak, A. L.; Matzger, A. J. Molecular Packing and Symmetry of Two-Dimensional Crystals. *Acc. Chem. Res.* **2007**, *40*, 287−293.

(13) Brown, R. D.; Corcelli, S. A.; Kandel, S. A. Structural Polymorphism as the Result of Kinetically Controlled Self-Assembly. *Acc. Chem. Res.* **2018**, *51*, 465−474.

(14) Furukawa, S.; Uji-i, H.; Tahara, K.; Ichikawa, T.; Sonoda, M.; De Schryver, F. C.; Tobe, Y.; De Feyter, S. Molecular Geometry Directed Kagome and Honeycomb Networks: Toward Two-Dimensional Crystal Engineering. *J. Am. Chem. Soc.* **2006**, *128*, 3502−3503.

(15) Kampschulte, L.; Lackinger, M.; Maier, A.-K.; Kishore, R. S. K.; Griessl, S.; Schmittel, M.; Heckl, W. M. Solvent Induced Polymorphism in Supramolecular 1,3,5-Benzenetribenzoic Acid Monolayers. *J. Phys. Chem. B* **2006**, *110*, 10829−10836.
(16) Zhou, H.; Dang, H.; Yi, J.-H.; Nanci, A.; Rochefort, A.; Wuest, J. D. Frustrated 2D Molecular Crystallization. *J. Am. Chem. Soc.* **2007**, *129*, 13774−13775.
(17) Yang, Y.; Wang, C. Solvent Effects on Two-Dimensional Molecular Self-Assemblies Investigated by Using Scanning Tunneling Microscopy. *Curr. Opin. Colloid Interface Sci.* **2009**, *14*, 135−147.
(18) Zhang, X.; Chen, T.; Chen, Q.; Deng, G.-J.; Fan, Q.-H.; Wan, L.-J. One Solvent Induces a Series of Structural Transitions in Monodendron Molecular Self-Assembly from Lamellar to Quadrangular to Hexagonal. *Chem. - Eur. J.* **2009**, *15*, 9669−9673.
(19) Ahn, S.; Matzger, A. J. Six Different Assemblies from One Building Block: Two-Dimensional Crystallization of an Amide Amphiphile. *J. Am. Chem. Soc.* **2010**, *132*, 11364−11371.
(20) Adisoejoso, J.; Tahara, K.; Lei, S.; Szabelski, P.; Rżysko, W.; Inukai, K.; Blunt, M. O.; Tobe, Y.; De Feyter, S. One Building Block, Two Different Nanoporous Self-Assembled Monolayers: A Combined STM and Monte Carlo Study. *ACS Nano* **2012**, *6*, 897−903.
(21) Coenen, M. J. J.; den Boer, D.; van den Bruele, F. J.; Habets, T.; Timmers, K. A. A. M.; van der Maas, M.; Khoury, T.; Panduwinata, D.; Crossley, M. J.; Reimers, J. R.; et al. Polymorphism in Porphyrin Monolayers: The Relation Between Adsorption Configuration and Molecular Conformation. *Phys. Chem. Chem. Phys.* **2013**, *15*, 12451−12458.
(22) Sirtl, T.; Song, W.; Eder, G.; Neogi, S.; Schmittel, M.; Heckl, W. M.; Lackinger, M. Solvent-Dependent Stabilization of Metastable Monolayer Polymorphs at the Liquid-Solid Interface. *ACS Nano* **2013**, *7*, 6711−6718.
(23) Lee, S.-L.; Yuan, Z.; Chen, L.; Mali, K. S.; Müllen, K.; De Feyter, S. Flow-Assisted 2D Polymorph Selection: Stabilizing Metastable Monolayers at the Liquid-Solid Interface. *J. Am. Chem. Soc.* **2014**, *136*, 7595−7598.
(24) Cyganik, P.; Buck, M. Polymorphism in Biphenyl-Based Self-Assembled Monolayers of Thiols. *J. Am. Chem. Soc.* **2004**, *126*, 5960−5961.
(25) Jiang, P.; Nion, A.; Marchenko, A.; Piot, L.; Fichou, D. Rotational Polymorphism in 2-Naphthalenethiol SAMs on Au(111). *J. Am. Chem. Soc.* **2006**, *128*, 12390−12391.
(26) Chung, K.-H.; Park, J.; Kim, K. Y.; Yoon, J. K.; Kim, H.; Han, S.; Kahng, S.-J. Polymorphic Porous Supramolecular Networks Mediated by Halogen Bonds on Ag (111). *Chem. Commun.* **2011**, *47*, 11492−11494.
(27) Sicot, M.; Tristant, D.; Gerber, I. C.; Kierren, B.; Chérioux, F.; Fagot-Revurat, Y.; Moreau, L.; Granet, J.; Malterre, D. Polymorphism of Two-Dimensional Halogen Bonded Supramolecular Networks on a Graphene/Iridium(111) Surface. *J. Phys. Chem. C* **2017**, *121*, 2201−2210.
(28) Shang, J.; Wang, Y.; Chen, M.; Dai, J.; Zhou, X.; Kuttner, J.; Hilt, G.; Shao, X.; Gottfried, J. M.; Wu, K. Assembling Molecular Sierpinski Triangle Fractals. *Nat. Chem.* **2015**, *7*, 389−393.
(29) Fan, Q.; Liu, L.; Dai, J.; Wang, T.; Ju, H.; Zhao, J.; Kuttner, J.; Hilt, G.; Gottfried, J. M.; Zhu, J. Surface Adatom Mediated Structural Transformation in Bromoarene Monolayers: Precursor Phases in Surface Ullmann Reaction. *ACS Nano* **2018**, *12*, 2267−2274.
(30) Gottfried, J. M. Surface Chemistry of Porphyrins and Phthalocyanines. *Surf. Sci. Rep.* **2015**, *70*, 259−379.
(31) Jiang, N.; Wang, Y.; Liu, Q.; Zhang, Y.; Deng, Z.; Ernst, K.-H.; Gao, H.-J. Polymorphism and Chiral Expression in Two-Dimensional Subphthalocyanine Crystals on Au (111). *Phys. Chem. Chem. Phys.* **2010**, *12*, 1318−1322.
(32) Barlow, S. M.; Louafi, S.; Le Roux, D.; Williams, J.; Muryn, C.; Haq, S.; Raval, R. Polymorphism in Supramolecular Chiral Structures of R- and S-Alanine on Cu(110). *Surf. Sci.* **2005**, *590*, 243−263.
(33) Ueji, K.; Jung, J.; Oh, J.; Miyamura, K.; Kim, Y. Thermally Activated Polymorphic Transition from a 1D Ribbon to a 2D Carpet: Squaric Acid on Au(111). *Chem. Commun.* **2014**, *50*, 11230−11233.
(34) Klyatskaya, S.; Klappenberger, F.; Schlickum, U.; Kühne, D.; Marschall, M.; Reichert, J.; Decker, R.; Krenner, W.; Zoppellaro, G.; Brune, H.; et al. Surface-Confined Self-Assembly of Di-carbonitrile Polyphenyls. *Adv. Funct. Mater.* **2011**, *21*, 1230−1240.
(35) Schlickum, U.; Decker, R.; Klappenberger, F.; Zoppellaro, G.; Klyatskaya, S.; Auwärter, W.; Neppl, S.; Kern, K.; Brune, H.; Ruben, M.; et al. Chiral Kagomé Lattice from Simple Ditopic Molecular Bricks. *J. Am. Chem. Soc.* **2008**, *130*, 11778−11782.
(36) Klappenberger, F.; Kühne, D.; Krenner, W.; Silanes, I.; Arnau, A.; García de Abajo, F. J.; Klyatskaya, S.; Ruben, M.; Barth, J. V. Dichotomous Array of Chiral Quantum Corrals by a Self-Assembled Nanoporous Kagomé Network. *Nano Lett.* **2009**, *9*, 3509−3514.
(37) Kühne, D.; Klappenberger, F.; Decker, R.; Schlickum, U.; Brune, H.; Klyatskaya, S.; Ruben, M.; Barth, J. V. Self-Assembly of Nanoporous Chiral Networks with Varying Symmetry from Sexiphenyl-Dicarbonitrile on Ag (111). *J. Phys. Chem. C* **2009**, *113*, 17851−17859.
(38) Klappenberger, F.; Kühne, D.; Marschall, M.; Neppl, S.; Krenner, W.; Nefedov, A.; Strunskus, T.; Fink, K.; Wöll, C.; Klyatskaya, S.; et al. Uniform π-System Alignment in Thin Films of Template-Grown Dicarbonitrile-Oligophenyls. *Adv. Funct. Mater.* **2011**, *21*, 1631−1642.
(39) Pivetta, M.; Pacchioni, G. E.; Fernandes, E.; Brune, H. Temperature-Dependent Self-Assembly of NC-Ph_5-CN Molecules on Cu(111). *J. Chem. Phys.* **2015**, *142*, 101928.
(40) Pacchioni, G. E.; Pivetta, M.; Brune, H. Competing Interactions in the Self-Assembly of NC-Ph_3-CN Molecules on Cu(111). *J. Phys. Chem. C* **2015**, *119*, 25442−25448.
(41) Sun, Q.; Cai, L.; Ma, H.; Yuan, C.; Xu, W. On-Surface Construction of a Metal-Organic Sierpiński Triangle. *Chem. Commun.* **2015**, *51*, 14164−14166.
(42) Li, N.; Zhang, X.; Gu, G.-C.; Wang, H.; Nieckarz, D.; Szabelski, P. l.; He, Y.; Wang, Y.; Lü, J.-T.; Tang, H.; et al. Sierpiński-Triangle Fractal Crystals with the C_{3v} Point Group. *Chin. Chem. Lett.* **2015**, *26*, 1198−1202.
(43) Cai, L.; Sun, Q.; Bao, M.; Ma, H.; Yuan, C.; Xu, W. Competition between Hydrogen Bonds and Coordination Bonds Steered by the Surface Molecular Coverage. *ACS Nano* **2017**, *11*, 3727−3732.
(44) Marschall, M.; Reichert, J.; Seufert, K.; Auwärter, W.; Klappenberger, F.; Weber-Bargioni, A.; Klyatskaya, S.; Zoppellaro, G.; Nefedov, A.; Strunskus, T.; et al. Supramolecular Organization and Chiral Resolution of *p*-Terphenyl-*m*-Dicarbonitrile on the Ag(111) Surface. *ChemPhysChem* **2010**, *11*, 1446−1451.
(45) Abbasi-Pérez, D.; Recio, J. M.; Kantorovich, L. Building Motifs during Self-Assembly of *para*-Terphenyl-*meta*-dicarbonitrile on a Metal Surface: A Gas-Phase Study. *J. Phys. Chem. C* **2014**, *118*, 10358−10365.
(46) Abbasi-Pérez, D.; Manuel Recio, J.; Kantorovich, L. The Role of Isomerization in the Kinetics of Self-Assembly: *p*-Terphenyl-*m*-dicarbonitrile on the Ag(111) Surface. *Phys. Chem. Chem. Phys.* **2015**, *17*, 11182−11192.
(47) Marschall, M.; Reichert, J.; Diller, K.; Klyatskaya, S.; Ruben, M.; Nefedov, A.; Wöll, C.; Kantorovich, L. N.; Klappenberger, F.; Barth, J. V. Meta-Positioning of Carbonitrile Functional Groups Induces Interfacial Edge-On Phase of Oligophenyl Derivatives. *J. Phys. Chem. C* **2014**, *118*, 2622−2633.
(48) Horcas, I.; Fernández, R.; Gómez-Rodríguez, J. M.; Colchero, J.; Gómez-Herrero, J.; Baro, A. M. WSXM: A Software for Scanning Probe Microscopy and a Tool for Nanotechnology. *Rev. Sci. Instrum.* **2007**, *78*, 013705.
(49) Reichert, J.; Marschall, M.; Seufert, K.; Ecija, D.; Auwärter, W.; Arras, E.; Klyatskaya, S.; Ruben, M.; Barth, J. V. Competing Interactions in Surface Reticulation with a Prochiral Dicarbonitrile Linker. *J. Phys. Chem. C* **2013**, *117*, 12858−12863.
(50) Shi, Z.; Lin, N. Structural and Chemical Control in Assembly of Multicomponent Metal-Organic Coordination Networks on a Surface. *J. Am. Chem. Soc.* **2010**, *132*, 10756−10761.

https://dx.doi.org/10.1021/acs.jpcc.0c03601
J. Phys. Chem. C 2020, 124, 15928−15934

(51) Kaposi, T.; Joshi, S.; Hoh, T.; Wiengarten, A.; Seufert, K.; Paszkiewicz, M.; Klappenberger, F.; Ecija, D.; Đorđević, L.; Marangoni, T.; et al. Supramolecular Spangling, Crocheting, and Knitting of Functionalized Pyrene Molecules on a Silver Surface. *ACS Nano* **2016**, *10*, 7665−7674.
(52) Wang, T.; Fan, Q.; Feng, L.; Tao, Z.; Huang, J.; Ju, H.; Xu, Q.; Hu, S.; Zhu, J. Chiral Kagome Lattices from On-Surface Synthesized Molecules. *ChemPhysChem* **2017**, *18*, 3329−3333.
(53) Baudour, J.-L.; Délugeard, Y.; Rivet, P. Structural Phase Transition in Polyphenyls. VI. Crystal Structure of the Low-Temperature Ordered Phase of *p*-Quaterphenyl at 110 K. *Acta Crystallogr., Sect. B: Struct. Crystallogr. Cryst. Chem.* **1978**, *34*, 625−628.
(54) Hobza, P.; Selzle, H. L.; Schlag, E. W. Potential Energy Surface for the Benzene Dimer. Results of ab Initio CCSD(T) Calculations Show Two Nearly Isoenergetic Structures: T-Shaped and Parallel-Displaced. *J. Phys. Chem.* **1996**, *100*, 18790−18794.

https://dx.doi.org/10.1021/acs.jpcc.0c03601
J. Phys. Chem. C 2020, 124, 15928−15934

Supporting Information for

Polymorphism at the Metal/Organic Interface: Hybrid Phase with Alternating Coplanar and Vertical Adsorption Geometry

Claudio K. Krug[a], Malte Zugermeier[a], Julian Kuttner[a], Martin Schmid[a], Gerhard Hilt[b*], J. Michael Gottfried[a*]

[a] *Department of Chemistry, Philipps University Marburg, Hans-Meerwein-Straße 4, 35032 Marburg, Germany, michael.gottfried@chemie.uni-marburg.de*

[b] *Institute of Chemistry, Carl von Ossietzky University Oldenburg, Carl-von-Ossietzky-Straße 9-11, Oldenburg 26111, Germany, gerhard.hilt@uni-oldenburg.de*

1. Coverage determination by X-ray photoelectron spectroscopy

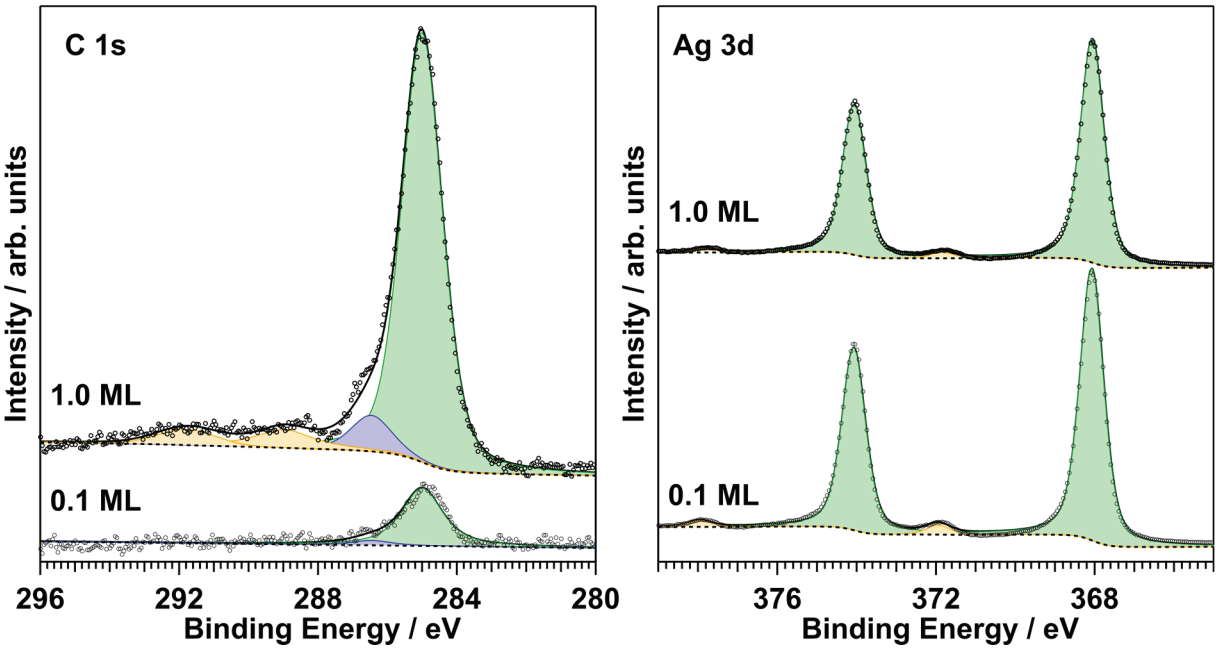

Figure S1. C 1s (left) and Ag 3d (right) XP spectra of *m*-4PDN on Ag(111). The coverage was determined by the C 1s/Ag 3d intensity ratios. The intensity ratio of the sample with 1.0 ML coverage was used as reference for a close-packed layer according to the STM results (*cf*. Figure 2 of the main text). Circles: experimental data points; black solid line: total fit; colored solid lines: single fitted peaks; dashed black line: background. The C 1s signal of the sample with 1.0 ML coverage was fitted with four peaks (green: aromatic C atoms; blue: nitrile C atoms; orange: satellite peaks). For the spectrum with 0.1 ML coverage the satellite peaks are not visible and thus omitted in the fit. The ratio between the nitrile and the aromatic C atoms was fixed to 2/24 according to the expected stoichiometry in the molecule. The Ag 3d signal was fitted with two doublet peaks (green: main peak; orange: satellites).

2. Additional STM images

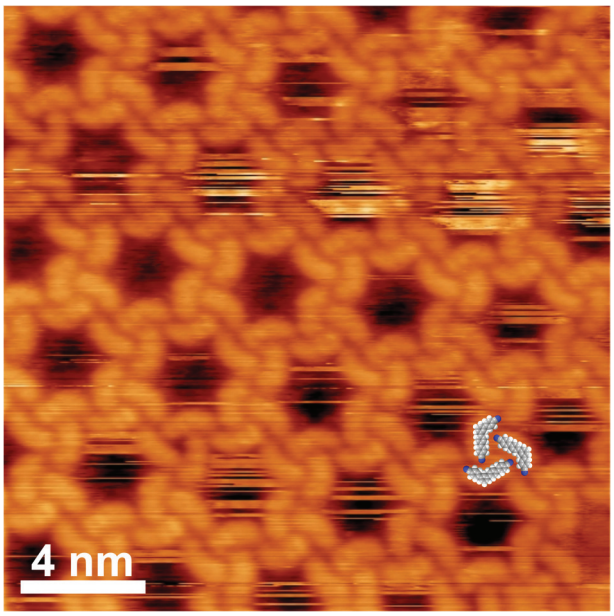

Figure S2. Additional STM image of adsorbate structure II formed by 0.1 ML of *m*-4PDN on Ag(111) consisting exclusively of the S_p enantiomer with space-filling models of the molecule superimposed. Tunneling parameters: $U = 1.74$ V, $I = 0.29$ nA.

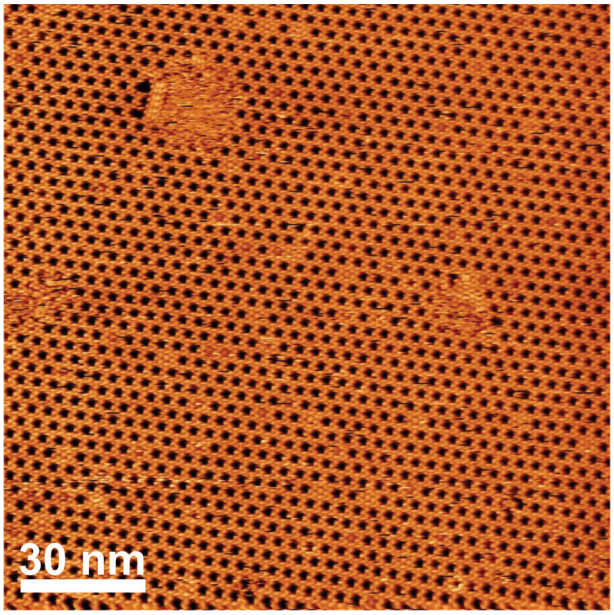

Figure S3. Additional STM image of adsorbate structure II formed by 0.1 ML of *m*-4PDN on Ag(111) showing the extension over a terrace with a size of at least 150 nm × 150 nm. Tunneling parameters: $U = 1.44$ V, $I = 0.20$ nA.

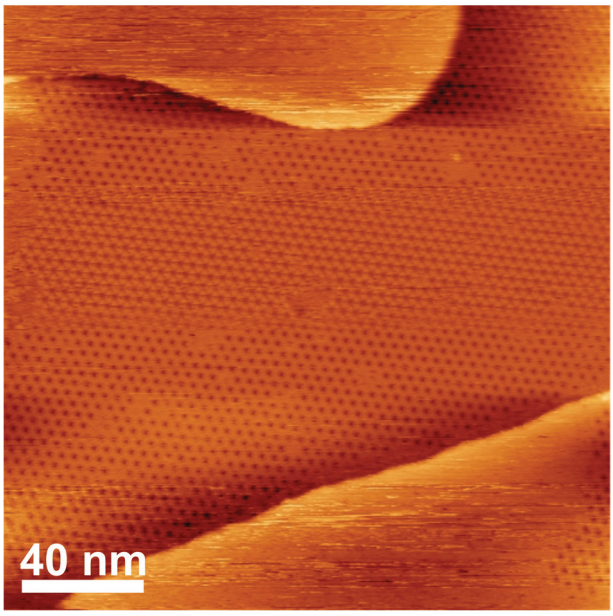

Figure S4. Additional STM image of adsorbate structure II formed by 0.1 ML of *m*-4PDN on Ag(111) coexisting with a dilute phase of mobile molecules. This coexistence explains the deviations between local coverages determined by STM and global coverages determined by XPS. Tunneling parameters: $U = 1.74$ V, $I = 0.31$ nA.

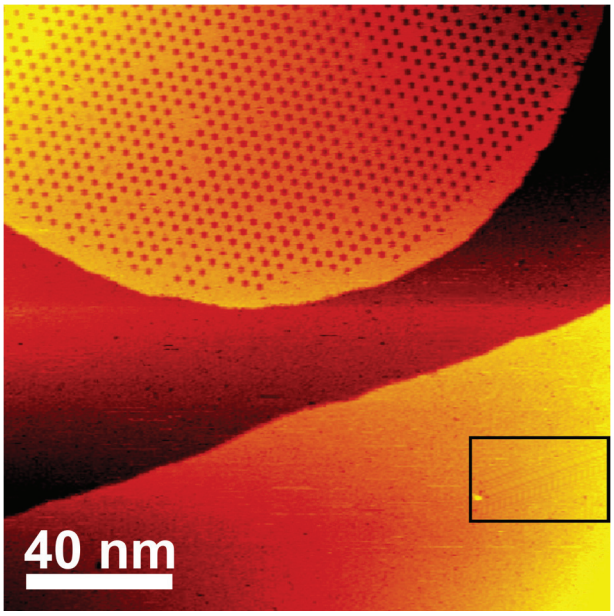

Figure S5. Additional STM image of 0.1 ML of *m*-4PDN on Ag(111) showing the coexistence of adsorbate structure II (quasi-Kagome, center-top) and adsorbate structure III (mixed phase, black frame, lower-right). Tunneling parameters: $U = 1.74$ V, $I = 0.45$ nA.

3. Trapped molecules in porous adsorbate structure II

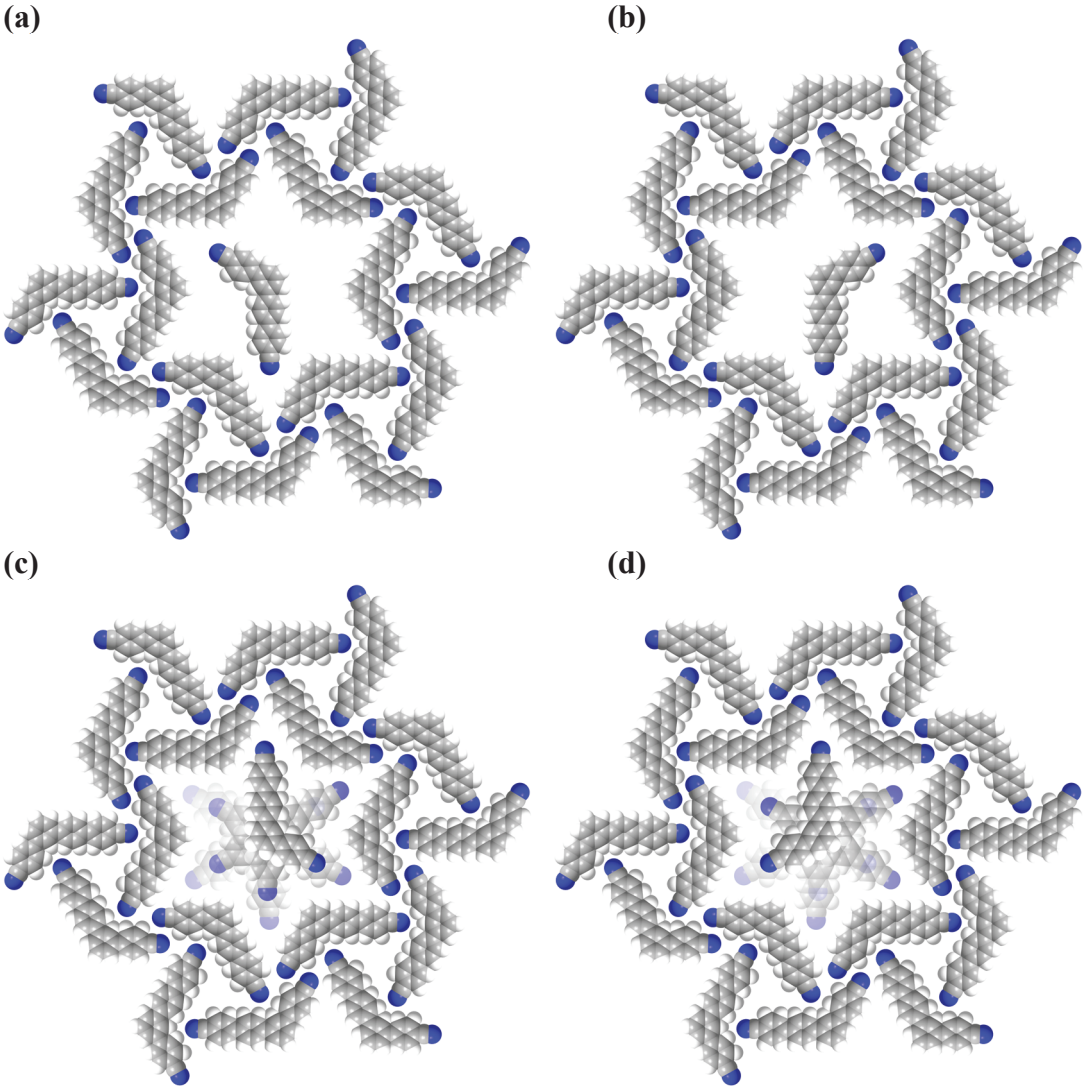

Figure S6. Molecular model depicting a pore of adsorbate structure II (exclusively consisting of the R_p enantiomer) with one molecules inside. (a) R_p enantiomer, (b) S_p enantiomer. (c, d) Overlay of the trapped molecules in 6 different orientations (each rotated by 60°), illustrating that rotation faster than the scanning speed of the STM imaging could produce the image presented in Figure 3b (inset) of the main text.

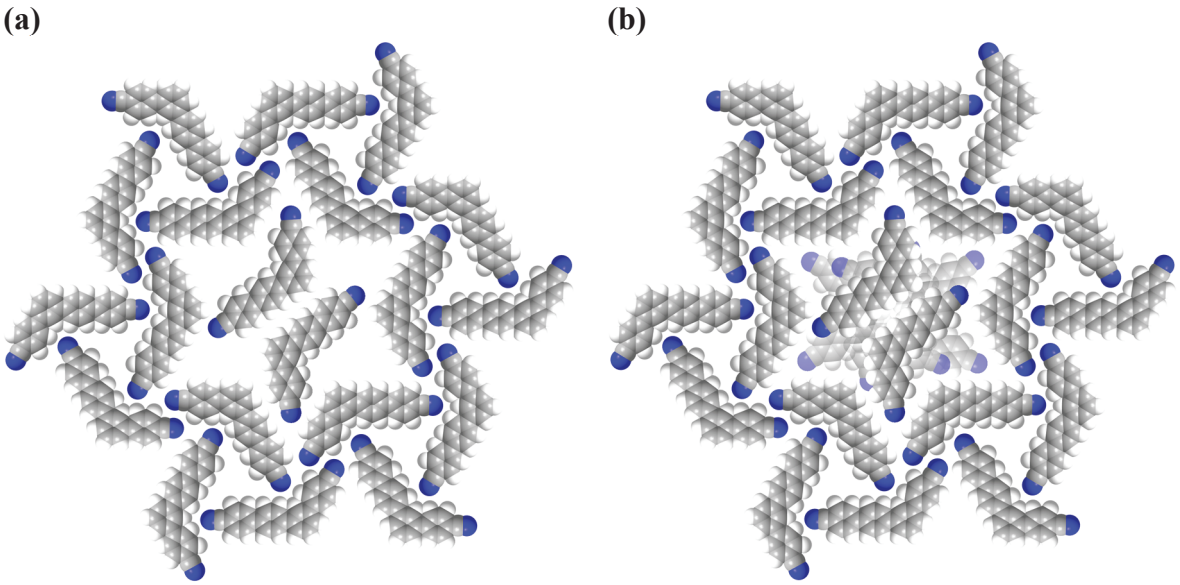

Figure S7. (a) Molecular model depicting a pore of adsorbate structure II (exclusively consisting of the R_p enantiomer) with a pair of trapped molecules (R_p enantiomer). (b) Overlay of three pairs of trapped R_p enantiomers, each rotated by 120°. The model illustrates that rotation of the pair faster than the scanning speed of the STM imaging could produce the image presented in Figure 3b (inset) of the main text.

4. Synthesis of 1,1′:3′1′′:4′′,1′′′-quaterphenyl-4,4′′′-dicarbonitrile (*m*-4PDN)

4.1. Overview

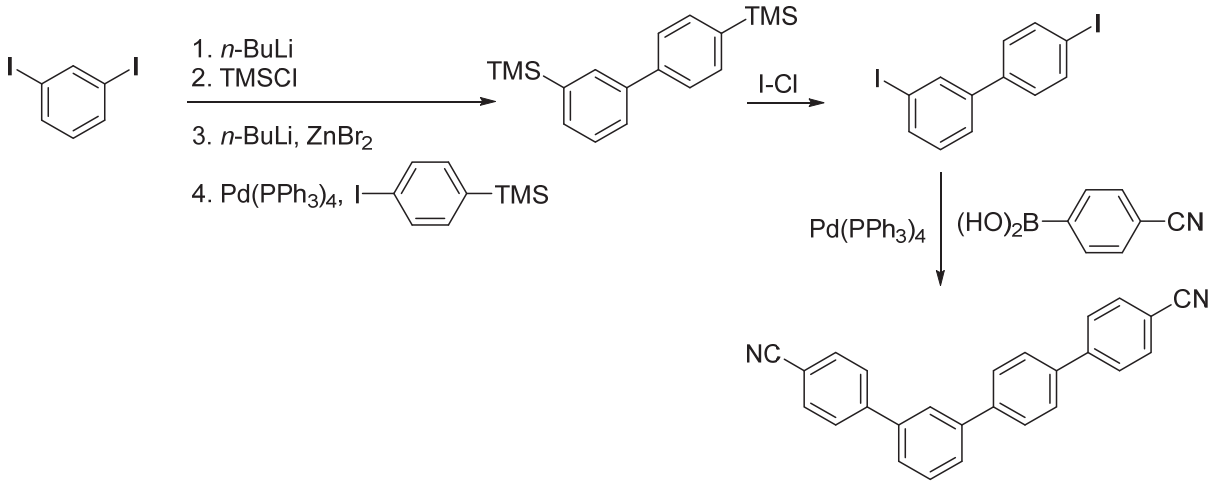

4.2. Synthesis of biphenyl-3,4'-diylbis(trimethylsilane)

1,3-Diiodobenzene (1.32 g, 4.0 mmol, 1.3 equiv.) was dissolved in diethyl ether (25 mL) under inert atmosphere and cooled to −78 °C. First, *n*-butyl lithium (2.5 M in hexane, 1.6 mL, 4.0 mmol, 1.3 equiv.) was added dropwise and after 30 min chlorotrimethylsilane (0.5 mL, 3.9 mmol, 1.3 equiv.) was added. The mixture was warmed to room temperature and stirred for an additional 30 min. Thereafter, the solution was cooled to −78 °C and *n*-butyl lithium (2.5 M in hexane, 1.6 mL, 4.0 mmol, 1.3 equiv.) was added dropwise. Then, the solution was warmed to −40 °C and $ZnBr_2$ (1.30 g, 5.8 mmol, 1.9 equiv.) was added. Then the mixture was warmed slowly to 0 °C and diluted with cold THF (25 mL) and (4-iodophenyl)trimethylsilane (850 mg, 3.08 mmol, 1.0 equiv.) as well as $Pd(PPh_3)_4$ (175 mg, 0.15 mmol, 4.9 mol%) were added. The mixture was stirred at ambient temperature for 15 h before filtration through a small plug of silica gel (eluent: pentane:diethyl ether = 10:1). The solvent was removed under reduced pressure and the residue was purified by column chromatography (eluent: pentane) giving biphenyl-3,4'-diylbis(trimethylsilane) (822 mg, 2.75 mmol, 89%) as colorless solid.

^{1}H NMR (300 MHz, $CDCl_3$): δ = 7.74 (s, 1H), 7.67-7.50 (m, 6H), 7.45 (t, *J* = 7.4 Hz, 1H), 0.37-0.25 (m, 18H) ppm.

^{13}C NMR (75 MHz, $CDCl_3$): δ = 142.1, 141.0, 140.5, 139.1, 133.8, 132.3, 132.2, 128.1, 127.7, 126.7, -1.1 ppm.

IR (Film): $\bar{\nu}$ = 3054, 3017, 2953, 2894, 1594, 1465, 1404, 1375, 1314, 1247, 1113, 1038, 829, 789, 751, 696, 652, 620, 573, 521, 435, 408 cm^{-1}.

4.3. Synthesis of 3,4'-diiodobiphenyl

Biphenyl-3,4‘-diylbis(trimethylsilane) (190 mg, 0.54 mmol, 1.0 equiv.) was dissolved in dichloromethane (2.0 mL) and cooled to −78 °C. Then a solution of iodine monochloride (1 M in dichloromethane, 1.2 mL, 1.2 mmol, 2.2 equiv.) was added. After 1 h, the reaction mixture was filtered over a small plug of silica gel (eluent: pentane). The filtrate was washed with saturated aqueous Na_2SO_3 solution, dried over $MgSO_4$, filtered and the solvent was removed under reduced pressure. 3,4'-Diiodobiphenyl (220 mg, 0.54 mmol, 100%) was obtained as colorless solid, which was used in the synthesis of 1,1‘:3‘,1‘‘:4‘‘,1‘‘‘-quaterphenyl-4,4‘‘‘-dicarbonitrile without further purification.

4.4. Synthesis of 1,1‘:3‘,1‘‘:4‘‘,1‘‘‘-quaterphenyl-4,4‘‘‘-dicarbonitrile

3,4’-Diiodobiphenyl (220 mg, 0.54 mmol, 1.0 equiv.), 4-cyanophenylboronic acid (195 mg, 1.33 mmol, 2.5 equiv.), $K_3PO_4 \cdot H_2O$ (945 mg, 4.10 mmol, 7.6 equiv.) and $Pd(PPh_3)_4$ (30 mg, 26 µmol, 4.8 mol%) were dissolved in anhydrous THF (10 mL) under inert atmosphere. The mixture was stirred at 65 °C for 20 h, then filtered over a small plug of silica gel (eluent: chloroform:ethyl acetate = 10:1) and the solvent was removed under reduced pressure. The residue was purified by column chromatography (eluent: pentane:ethyl acetate = 5:1 → 4:1 + 10% dichloromethane) giving 1,1‘:3‘,1‘‘:4‘‘,1‘‘‘-quaterphenyl-4,4‘‘‘-dicarbonitrile (106 mg, 0.30 mmol, 55%) as colorless solid.

^{1}H NMR (300 MHz, $CDCl_3$): δ = 7.85-7.82 (m, 1H), 7.81-7.66 (m, 13H), 7.63-7.58 (m, 2H) ppm.

^{13}C NMR (75 MHz, $CDCl_3$): δ = 145.4, 144.9, 141.2, 140.9, 139.9, 138.4, 132.6 (2C), 129.7, 127.9, 127.8, 127.7, 127.6, 127.3, 126.5, 126.0, 118.83, 118.80, 111.2, 111.1 ppm

IR (film, CH_2Cl_2): $\bar{\nu}$ = 3056, 2223, 1601, 1475, 1390, 1310, 1254, 1179, 1116, 1005, 908, 827, 794, 734, 698, 652, 610, 557, 476 cm^{-1}.

HRMS (EI): m/z $[M]^+$ calculated for $C_{26}H_{16}N_2$: 356.1313; found: 356.1308.

4.5. NMR Spectra

Biphenyl-3,4'-diylbis(trimethylsilane):

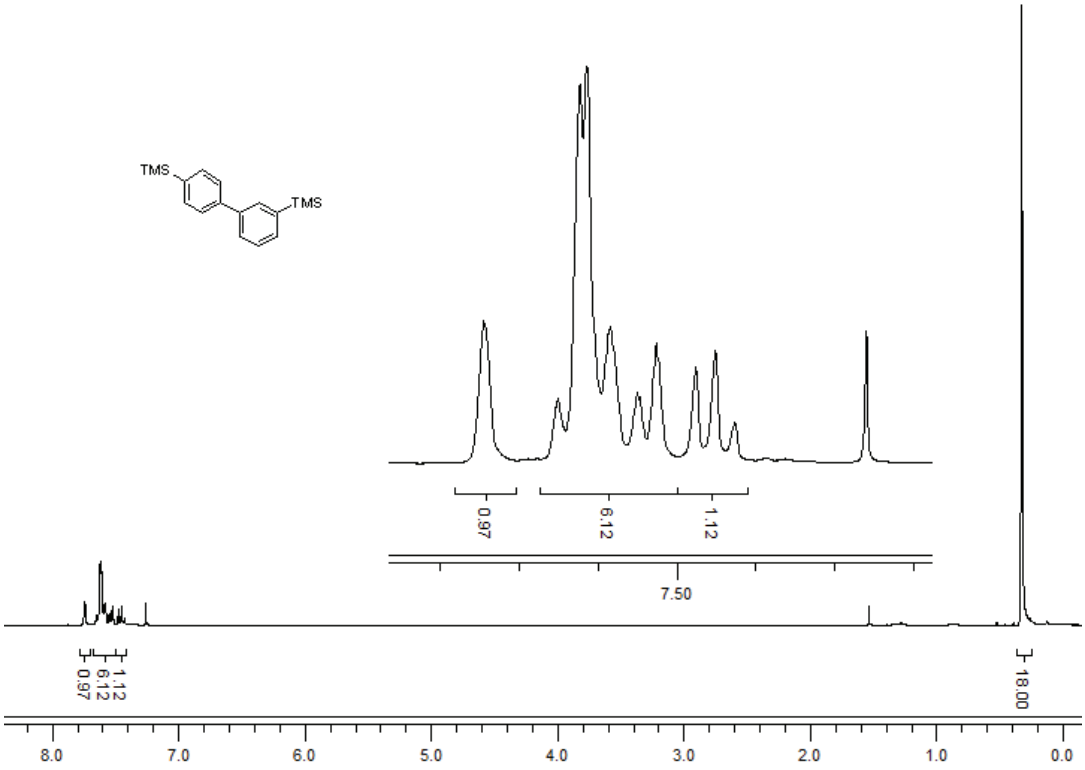

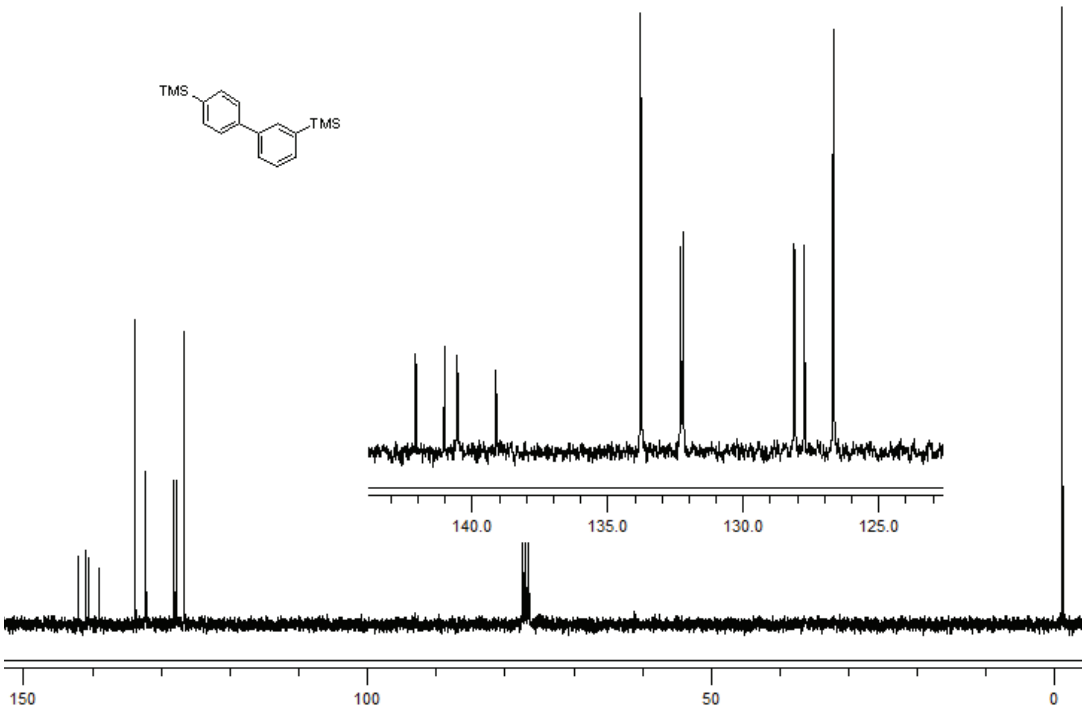

1,1‘:3‘,1‘‘:4‘‘-1‘‘‘-Quaterphenyl-4,4‘‘‘-dicarbonitrile:

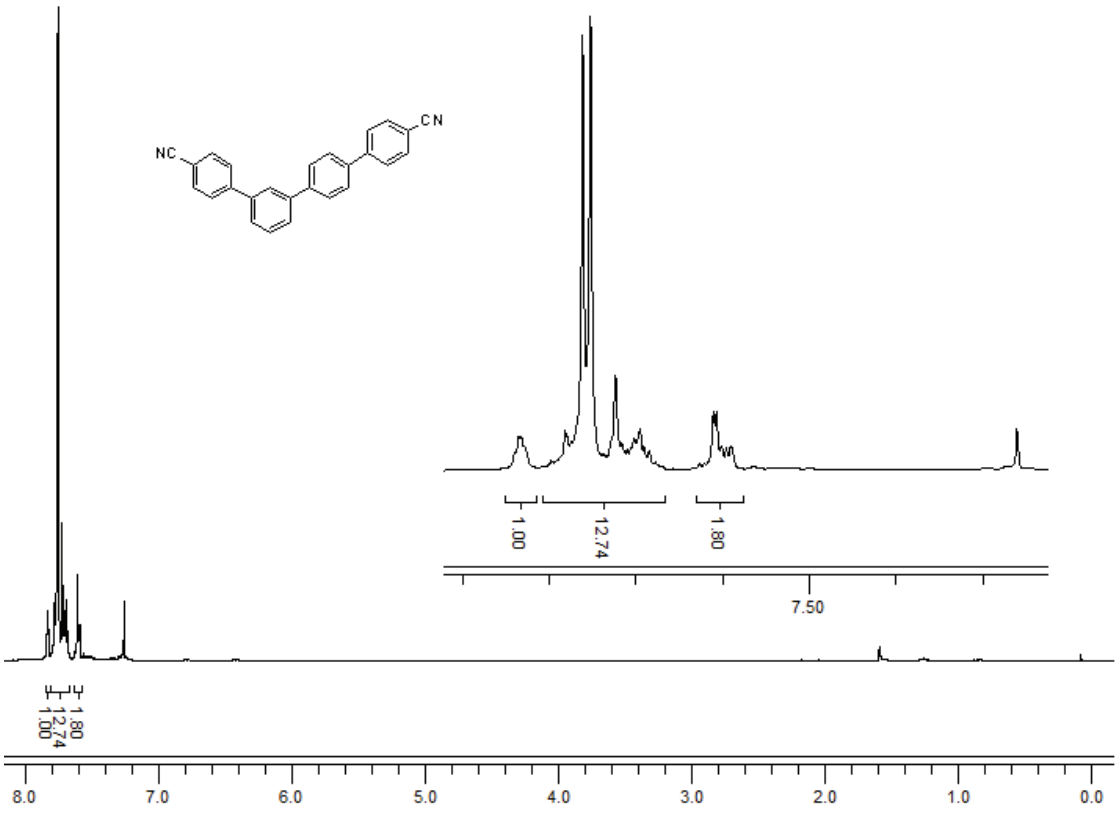

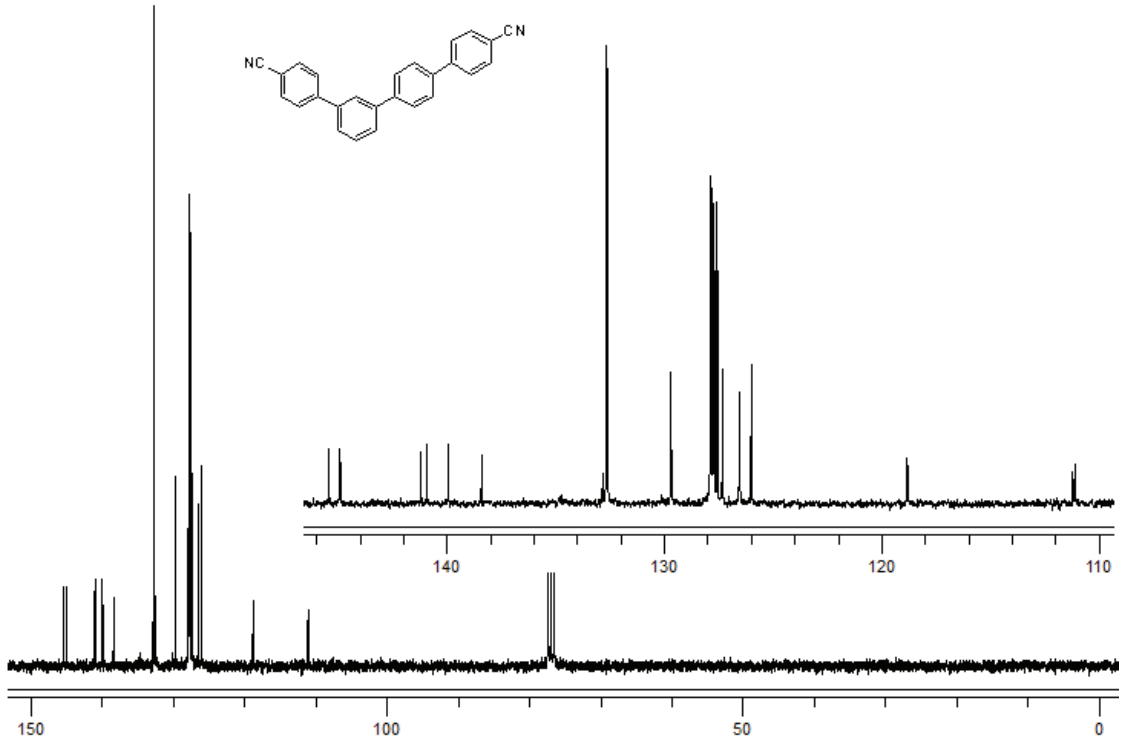

P5

P6 Formation of an interphase layer during deposition of cobalt onto tetraphenylporphyrin: a hard X-ray photoelectron spectroscopy (HAXPES) study

Citation: M. Chen, H. Zhou, B. P. Klein, M. Zugermeier, **C. K. Krug**, H.-J. Drescher, M. Gorgoi, M. Schmid, J. M. Gottfried, *Phys. Chem. Chem. Phys.* **2016**, *18*(44), 30643–30651, DOI 10.1039/c6cp05894a.

Summary

In this publication the interphase formation between *meso*-tetraphenylporphyrin (2HTPP) and Co is studied using hard X-ray photoelectron spectroscopy (HAXPES). For this purpose Co is deposited onto multilayers of 2HTPP and the reaction depth is monitored by using different X-ray excitation energies.

If Co is deposited on a multilayer film of 2HTPP Co tetraphenylporphyrin (CoTPP) is formed as the reaction product. However, this reaction does not lead to an abrupt interface but rather to an interphase, in which reacted CoTPP and 2HTPP coexist. Under the assumption of three distinct layers (*i.e.* Co/CoTPP/2HTPP) analysis of the N 1s XP spectra yields a thickness of the CoTPP layer of 1.6 nm. This result is confirmed by numerical simulations of the N 1s intensities. In addition, the more complex concentration profile in the interphase is modeled using a genetic algorithm.

Own Contribution

For this publication I was part of the experimentalist team, who performed the HAXPES experiments at the HIKE end-station of the KMC-1 beamline (*cf.* Section 3.4.3) at the synchrotron radiation facility BESSY II in Berlin during two beamtimes. The sample preparations and measurements were carried out together with Dr. Min Chen, Dr. Han Zhou, Dr. Benedikt P. Klein, Dr. Malte Zugermeier, Dr. Hans-Jörg Drescher, and Dr. Martin Schmid. Dr. Min Chen and Dr. Martin Schmid performed the data analysis and wrote the manuscript. I contributed to its discussion together with all other co-authors.

PCCP

PAPER

View Article Online
View Journal | View Issue

Cite this: *Phys. Chem. Chem. Phys.*, 2016, **18**, 30643

Formation of an interphase layer during deposition of cobalt onto tetraphenylporphyrin: a hard X-ray photoelectron spectroscopy (HAXPES) study†

Min Chen,[a] Han Zhou,[a] Benedikt P. Klein,[a] Malte Zugermeier,[a] Claudio K. Krug,[a] Hans-Jörg Drescher,[a] Mihaela Gorgoi,[b] Martin Schmid[a] and J. Michael Gottfried*[a]

Received 25th August 2016,
Accepted 17th October 2016

DOI: 10.1039/c6cp05894a

www.rsc.org/pccp

The interface formation upon vapor deposition of a metal onto a molecular organic semiconductor was studied using a well-defined complexation reaction between a metal and a porphyrin. Specifically, metallic cobalt (Co) was vapor deposited onto a thin film of 2*H*-tetraphenylporphyrin (2HTPP) at room temperature. The resulting interface was probed with Hard X-ray Photoelectron Spectroscopy (HAXPES) using photon energies between 2 and 6 keV to obtain a detailed depth profile of the chemical composition. Characteristic changes in the N 1s core level signals reveal the formation of a cobalt tetraphenylporphyrin (CoTPP) layer between the Co and 2HTPP layers. Assuming an abrupt interface between CoTPP and 2HTPP (layer-by-layer model), analysis of the XPS data results in a thickness of the CoTPP reaction layer of 1.6 nm. However, a more advanced numerical analysis allowed us to reconstruct details of the actual depth distribution of the CoTPP interphase layer: up to a depth of 1.5 nm, all 2HTPP molecules were converted into CoTPP. Beyond this depth, the CoTPP concentration decreases sharply within 0.15 nm to zero.

P6

1. Introduction

The performance of organic-electronic devices, such as organic light emitting diodes (OLED),[1,2] organic thin film transistors (OTFT),[3] and organic photovoltaic (OPV) devices[4] depends on the electronic, chemical, and geometric structure of interfaces between metals and organic semiconductors.[5,6] The alignment of the frontier molecular orbitals of a molecular semiconductor with respect to the Fermi level of the adjacent metal determines the energy barrier for electron (hole) injection at the cathode (anode), which is among the key factors influencing charge injection efficiency and ultimately device performance.[7,8] Possible diffusion processes and chemical reactions at the metal/organic contact (interface) are very important, because the resulting reacted interphase layer (Fig. 1) will separate the metal from the pristine organic semiconductor and therefore influence wave function overlap, charge injection rates, and energy level alignment.

Most previous model studies of metal/organic interfaces focused on well-controlled systems involving abrupt, non-reactive interfaces, such as monolayers of organic molecules on (mostly inert) single-crystal surfaces. In contrast, interfaces in real devices are typically buried interfaces and may involve reactive low-work function metals, which are often directly deposited onto the organic layer. As a consequence, the electron-injecting electrode partially reacts with the organic substrate, forming a chemically complex interface structure. The organometallic compounds formed at such reactive metal/organic interfaces have received increasing interest in the recent years. Despite the fact

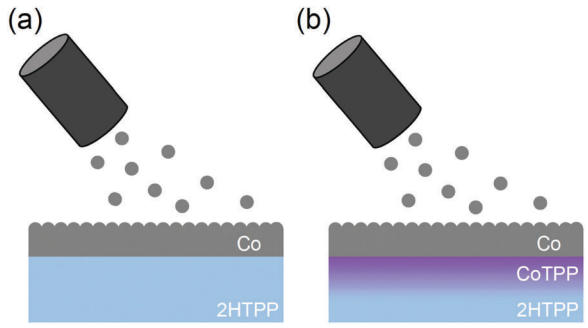

Fig. 1 Physical vapor deposition of metals onto molecular organic solids. Formation of (a) an abrupt interface and (b) a diffuse reaction zone (interphase). Here, deposition of cobalt (Co) onto tetraphenylporphyrin (2HTPP) leads to the formation of an interphase layer consisting of cobalt(II)tetraphenylporphyrin (CoTPP), as shown in (b).

[a] *Fachbereich Chemie, Philipps-Universität Marburg, Hans-Meerwein-Straße 4, 35032 Marburg, Germany. E-mail: michael.gottfried@chemie.uni-marburg.de*
[b] *Helmholtz Zentrum Berlin für Materialien und Energie GmbH, Albert-Einstein Str. 15, 12489 Berlin, Germany*

† Electronic supplementary information (ESI) available. See DOI: 10.1039/c6cp05894a

that a detailed chemical and structural understanding of this contact could be beneficial for the rational design of organic electronic devices, systematic investigations of reactive buried interfaces between metals and molecular organic semiconductors are rather rare.[9–13] More related studies were performed with interfaces between metals and polymer semiconductors, but in most cases, no detailed depth profiling of the extended interphase layer was performed.[14–21]

In this work, we intend to study the diffusion and reaction of a metal during its deposition onto a molecular organic semiconductor. As a suitable model process, we chose the deposition of cobalt onto 2*H*-tetraphenylporphyrin, because these reactants are known to undergo a well-defined redox reaction forming the complex cobalt-tetraphenylporphyrin (CoTPP).[22,23]

$$2\mathrm{HTPP} + \mathrm{Co}^0 \rightarrow \mathrm{Co}^{\mathrm{II}}\mathrm{TPP} + \mathrm{H}_2\uparrow \qquad (1)$$

This reaction is suitable for monitoring the diffusion of the metal into the organic material for the following reasons: (a) the reactant 2HTPP and the product CoTPP can easily be distinguished by photoelectron spectroscopy, (b) there are no side reactions between the metal and the porphyrin molecules, and (c) the reaction has a very low barrier and thus is fast at room temperature.[23] It is advantageous as well that the metalation of porphyrins and other tetrapyrroles is a very well understood reaction type and has been studied in detail for a wide range of systems.[24–27] Most metalation studies were performed with porphyrin monolayers. However, there are also studies in which metalation was achieved by vapor deposition of metal atoms onto porphyrin multilayers, *i.e.*, in the absence of a metal surface.[28] Specifically, it has been confirmed that 2HTPP monolayers readily react with Co at room temperature to form CoTPP.[22,23] Fast room-temperature reaction was also reported for the deposition of Fe onto 2HTPP multilayers, resulting in the formation of FeTPP.[28]

In the following, we will introduce the depth profiling by hard X-ray photoelectron spectroscopy (HAXPES) and describe several approaches for data analysis, before we apply them to variable-energy HAXPES data for the Co/2HTPP system. Using a genetic algorithm, a detailed concentration *vs.* depth profile for the interphase species, CoTPP, is obtained.

2. Methods

2.1. Depth profiling with hard X-ray photoelectron spectroscopy (HAXPES)

There are various complementary approaches for depth profiling with X-ray photoelectron spectroscopy (XPS): incremental ion bombardment is used to successively expose the deeper layers of the sample for XPS analysis, which is then performed in the surface-sensitive kinetic energy regime. While this method provides a potentially very large information depth, it is destructive and alters the composition of the sample because of element-specific sputtering probabilities. Another approach uses the variation of the information depth with the electron collection angle. As typically performed with laboratory X-ray sources, this method has only a small maximum information depth of few nanometers. The third approach extends the information depth by increasing the kinetic energy of the photoelectrons through the usage of hard X-rays and is therefore termed Hard X-ray Photoelectron Spectroscopy (HAXPES).[29–32] HAXPES is typically performed with synchrotron radiation, which allows for depth profiling by variation of the photon energy. The key to this method is that the information depth of XPS is determined by the photoelectrons' escape depth, which is a direct function of their kinetic energy. Due to energy conservation, the kinetic energy E_{kin} depends linearly on the applied photon energy $h\nu$ according to $E_{\mathrm{kin}} = h\nu - E_{\mathrm{b}}$, in which E_{b} is the electron binding energy. The distance over which the photoelectrons can, on average, travel through a solid material without losing energy is referred to as inelastic mean free path (IMFP) λ, which is a function of E_{kin}. The probability that a photoelectron, created at a depth z below the solid/vacuum interface, actually reaches this interface without being subject to energy loss decreases exponentially. The ratio between the initial flux of photoelectrons at a depth $z(I_0)$ and the flux measured at the solid/vacuum interface (I) is given by:

$$\frac{I}{I_0} = \mathrm{e}^{-z/\lambda\cos\theta} \qquad (2)$$

This equation, in which θ is the angle between the electron trajectory and the surface normal, also provides the precise definition of λ. Because of the exponential dampening of the signal with increasing z, approximately 95% of the total signal of a given photoelectron line emerge from a near-surface layer with a thickness of $3\lambda\cdot\cos\theta$. This value is typically referred to as information depth. For most materials, λ increases monotonically with the kinetic energy for energies above 100 eV.[33,34] As a consequence, the relative contribution of the electrons originating from deeper layers to the total signal increases for larger photon energies, as illustrated in Fig. 2.

In this study, HAXPES depth profiling was performed in normal-emission geometry by variation of the photon energy, rather than by variation of the detection angle at constant photon energy.

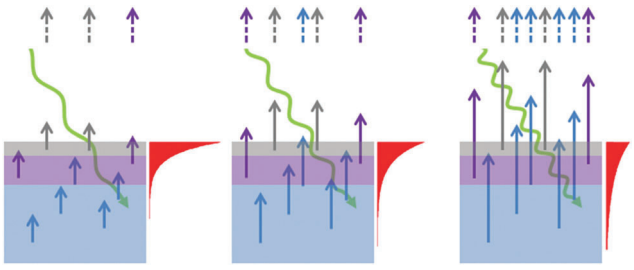

Fig. 2 Relation between photon energy, information depth and relative contributions of the different layers. The photon energy (green wave) increases from left to right. The photoelectron escape probability from different layers (gray, purple, blue) is indicated by arrows, the length of which correlates with the IMFP. The contribution to the XPS signal, normalized to total area, as a function of vertical position, is given as the width of the red areas. Note that this scheme assumes constant photoelectron production rate (number of arrows) and hence is not taking changes of photon flux and cross sections into account. Especially the reduced photoemission cross sections at higher photon energies would typically lead to a global decrease of the signal intensity from left to right.

This approach has the advantage that effects of the surface roughness on the depth coordinate are minimized.[35] For example, even if the local surface inclination (due to roughness) would be as large as 10° relative to the surface normal, the path length of the photoelectrons (and thus the apparent thickness) increases by only a factor of 1.015, *i.e.*, by 1.5%. The actual magnitude of the local surface inclination of the 2HTPP film is expected to be much lower than this: according to a previous study for 50 nm 2HTPP films on polycrystalline Au, an arithmetic roughness of R_a = 18.2 nm was reported,[36] while the protrusions had a mean perimeter of around 4 μm. From these values, one can geometrically estimate a typical local inclination of the 2HTPP surface of the order of 1°. For a global normal-emission geometry, this increases the path length by a negligible factor of 1.0002.

Previous studies suggest that preferential orientation of the molecules in the film is possible. For a 2HTPP film with a thickness of 7 nm on Au(111), a preferential orientation of the molecules with an angle of 24° between molecular plane and surface was reported.[37] A similar value of 28° was reported for 20 nm thick ZnTPP films on Ag(poly).[38] High degrees of geometric order are not unique to porphyrin films, but have also been found for thin films of other tetrapyrrole compounds such as phthalocyanines.[39,40]

The HAXPES technique is also suitable for inspecting the interface between two different bulk phases, *e.g.*, between a metal and an organic material, provided that the interface-related signals are not obscured by signals from the bulk phase above. In recent related work, the characterization of the electronic states in buried layers using bias voltage dependent HAXPES has been proposed.[41,42] By analyzing the HAXPES data taken with changing detection angles, Shibuta *et al.* have unveiled the depth profile of specific chemical states at the buried hetero-interface of organic/organic ($CuPc/C_{60}$) and metal/organic (Au/C_{60}) systems.[43] In our study, we take advantage of chemical depth profiling with HAXPES to investigate the model system Co/2HTPP. The photon energy dependent intensities of individual features in the recorded XP spectra are used to determine the vertical extension of the CoTPP interphase layer formed by the reaction between the pure metal (Co) and the pristine organic phase (2HTPP).

3. Experimental

3.1. Hard X-ray photoelectron spectroscopy (HAXPES)

The photoemission measurements were carried out at the synchrotron radiation source BESSY II (Helmholtz-Zentrum Berlin) using the HIKE end-station located at the beamline KMC-1.[44,45] The HIKE system is designed for hard X-ray, high kinetic energy photoelectron spectroscopy (HAXPES) experiments in the excitation energy range from 2 keV to 12 keV. A Scienta R4000 hemispherical electron analyzer, which is suitable for electron kinetic energies of up to 10 keV, is installed in the experimental setup. Photoelectron spectra were recorded for each sample, tuning the photon energy from 2 keV up to 6 keV in steps of 1 keV. In all measurements, photoelectrons were detected along the surface normal (0°). The photon incidence angle was 80° relative to the surface normal. Reduced photon flux of the beam line at high photon energies was partially compensated by increased measurement time. To minimize potential beam damage, the position of the incident beam on the sample was shifted for each recorded spectrum. The reported binding energies were referenced to the Au 4f peak of a clean Au surface mounted in close vicinity to the sample. Since only the relative intensities of the individual features are necessary for the discussion, all spectra were normalized to the total area for enhanced comparability. The intrinsic band width of the monochromator in the beam line changes with energy, as can be seen in Fig. 3, and increasingly reduces the energy resolution as the photon energy increases. For comparison, the full width at half maximum (FWHM) of the Au $4f_{7/2}$ peaks from the reference spectra are listed in Table 1.

3.2. Sample preparation

2*H*-Tetraphenylporphyrin (2HTPP, purity >98%, Porphyrin Systems GbR) was degassed in vacuum for 24 h at 420 K prior to deposition. Naturally oxidized Al foil was cleaned by Ar ion sputtering (1 keV, 5.3 μA) for 10 minutes such that the oxide layer is partially preserved and an inert yet sufficiently conductive substrate is obtained. 2HTPP multilayers were prepared by vapor deposition from a home-built Knudsen cell evaporator onto the cleaned Al foil held at 300 K. The vapor deposition of cobalt was carried out with an Omicron e-beam evaporator (FOCUS EFM 4). A cobalt rod with a diameter of 2 mm and purity of 99.99% purchased from Mateck was used as evaporant. For preparation of the layered sample, 18 nm 2HTPP were deposited first onto a cleaned aluminum foil, whereafter 1.8 nm Co were deposited onto the 2HTPP layer with a flux of 0.03 nm per minute. The sample was strictly held at room temperature during the deposition steps. Flux and thickness measurements were performed with a quartz crystal microbalance (QCM).

3.3. Monte-Carlo simulation of the photoelectron spectra with SESSA

Simulation of the XP spectra of the layered system was performed with the National Institute of Standards and Technology (NIST) Database for the Simulation of Electron Spectra for Surface Analysis (SESSA).[46,47] This very versatile database and simulation package employs the partial-intensity approach for the electron–solid interaction.[48,49] This approach breaks down the total emitted yield of photoelectrons into groups, which are characterized by the number of elastic or inelastic collisions that the electrons have experienced on their path through the solid. Simulation of the electron trajectories is performed by a Monte-Carlo method. The energy distribution after a certain number of collisions is obtained by taking the probability of an inelastic loss into account for each collision. A more detailed description of the approach is given elsewhere.[46–49]

3.4. Numerical extraction of the concentration profile

To extract the depth profile of the reaction zone beyond the approximation of layers with abrupt interfaces, a genetic algorithm was used to 'breed' the CoTPP concentration profile that is in best agreement to the experimental values.

P6

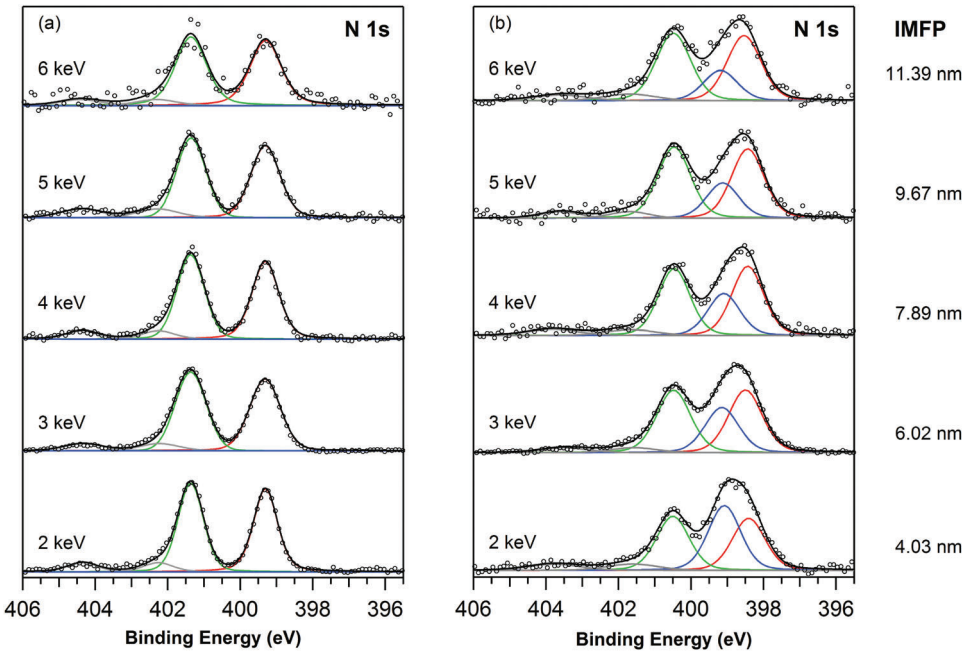

P6

Fig. 3 N 1s spectra of an 18 nm 2HTPP layer, taken (a) before and (b) after vapor deposition of 1.8 nm Co. The photon energies increase from bottom to top as indicated. This leads to related change of the inelastic mean free path (IMFP) λ, as shown on the right. The IMFP values were taken from the work of Ashley *et al.*[51] The two peaks (green, red) in the left panel correspond to the two nitrogen species in pristine 2HTPP (green, –NH– and red, –N═); the additional peak in the right panel corresponds to CoTPP formed by the interface reaction according to eqn (1).

Table 1 Photon energies and related widths of the Au $4f_{7/2}$ signal as a measure of the overall energy resolution

Photon energy (keV)	Au $4f_{7/2}$ FWHM	Monochromator crystal
2	0.61	Si(111)
3	0.70	Si(111)
4	0.57	Si(311)
5	0.70	Si(311)
6	0.87	Si(311)

Genetic algorithms are frequently used when an optimization/minimization problem cannot be solved by conventional methods, which rely on a gradual improvement of a certain optimization criterion. For an overview, see for instance Mühlenbein *et al.*[50]

4. Results

To obtain reference spectra of the initial pristine 2HTPP layer, 18 nm of the metal-free ligand tetraphenylporphyrin (2HTPP) were vapor deposited onto the cleaned aluminum foil at room temperature. Afterwards, photoemission measurements were performed on this sample. Fig. 3a displays the resulting N 1s XP spectra for photon energies from 2 to 6 keV. The two peaks represent the two chemically different nitrogen species (–NH– at 401.4 eV, green; –N═ at 399.3 eV, red). The peak separation of 2.1 eV and the peak shape remain almost unchanged in all spectra, except for the resolution-dependent Gaussian peak broadening. Furthermore, the intensity ratio of the two peaks is close to the stoichiometric 1 : 1 value.

After deposition of 1.8 nm Co onto the 2HTPP layer at room temperature with a Co flux of 0.03 nm per minute, HAXPES measurements with identical settings were performed (Fig. 3b). A new feature (blue peak, 399.1 eV) appears between the original N 1s peaks related to 2HTPP. By comparison with the literature, the new feature is unambiguously assigned to CoTPP as the product of the direct metalation of the porphyrin.[24–27] As can be seen, the intensity of the new feature is highest at 2 keV and decreases with increasing photon energy.

Note that a complete metalation of an 18 nm thick 2HTPP layer requires a stoichiometric amount of Co that is equivalent to a Co layer of 0.3 nm thickness. Despite the excess of Co used in the experiment (1.8 nm), the 2HTPP film is still only partially metalated. This behavior is expected for a layered structure in which most of the Co is contained in a metal layer on top of the organic phase. Furthermore, after deposition of Co, the peak positions corresponding to the original N species as well as the features in the C 1s spectra (see the ESI†) shift by 0.9 eV towards lower binding energies. This shift is most likely due to electron injection from the Co layer to the porphyrin layer, introducing band-bending at the metal/semiconductor interface.[7] Metal-induced lifting of residual charging could also contribute to this shift.

5. Analysis and discussion

5.1. Co/CoTPP/2HTPP layered system (abrupt interface approximation)

The photoelectron intensity originating from an energy level of an atomic species, which is embedded in a homogeneous material, is given by

$$I = \int_0^\infty F\sigma D k \mathrm{e}^{-z/\lambda\cos\theta}\mathrm{d}z \qquad (3)$$

where F represents the X-ray flux, σ the cross section for photoionization for a given atom within a given shell and given photon excitation energy, D the number density, *i.e.*, atoms per volume, of the given species, k the spectrometer factor (which depends on the analyzer), λ the inelastic mean free path of electrons with a certain kinetic energy in a given material, and z is the distance that photoelectrons must travel through the material to escape into the vacuum. The exponential term in eqn (3) is the Beer–Lambert law.

For the layered, reactive system in this study, the intensity ratio between N 1s signals of the pristine, unreacted species (2HTPP, index ur) and the reacted species (CoTPP, index r) is given by eqn (4a). The conditions of our experiment imply $\lambda_r = \lambda_{ur}$, $\sigma_r = \sigma_{ur}$, F = const., k = const. and $\theta = 90°$, which leads to eqn (4b):

$$\left(\frac{I_r}{I_{ur}}\right) = \frac{F\sigma_r k}{F\sigma_{ur} k} \cdot \frac{\int_0^\infty D_{r(z)} \exp\left(-\frac{z}{\lambda_r \cos\theta}\right) dz}{\int_0^\infty D_{ur(z)} \exp\left(-\frac{z}{\lambda_{ur} \cos\theta}\right) dz} \quad (4a)$$

$$= \frac{\int_0^\infty c_{r(z)} \exp\left(-\frac{z}{\lambda}\right) dz}{\int_0^\infty \left(1 - c_{r(z)}\right) \exp\left(-\frac{z}{\lambda}\right) dz} \quad (4b)$$

In eqn (4a) and (4b), the number density $D_{r(z)}$ of the reacted species at a given depth z is the product of the (constant) number density of the porphyrin moiety ρ and the probability $c_{r(z)}$ that a given molecule at a depth z belongs to the reacted species. In eqn (4b), the eqn (5b) for $D_{ur(z)}$ was applied:

$$D_{r(z)} = \rho \cdot c_{r(z)} \quad (5a)$$

$$D_{ur(z)} = \rho \cdot c_{ur(z)} = \rho \cdot (1 - c_{r(z)}) \quad (5b)$$

The usage of a constant density ρ is justified, because the unit cell volumes for 2HTPP and CoTPP are very similar.[52,53] For the tetragonal crystal structure, the atomic densities of N atoms in 2HTPP layers ($\rho_{2HTPP} = 5.02 \times 10^{27}$ atoms per m^3) and CoTPP layers ($\rho_{CoTPP} = 5.05 \times 10^{27}$ atoms per m^3) can be considered identical for our purposes.

First, we consider the approximation of an abrupt CoTPP/2HTPP interface at a depth d, with an *infinitely* thick unreacted 2HTPP layer underneath: for this system, eqn (4b) can be simplified such that the value of d can be extracted from the measured intensity ratio I_r/I_{ur}. The abrupt interface assumption is mathematically expressed as

$$c_{r(z)} = \begin{cases} 1 & z \le d \\ 0 & z > d \end{cases} \quad (6a)$$

$$c_{ur(z)} = \begin{cases} 0 & z \le d \\ 1 & z > d \end{cases} \quad (6b)$$

With eqn (6a) and (6b), eqn (4b) simplifies to:

$$\left(\frac{I_r}{I_{ur}}\right) = \frac{\int_0^d \exp\left(-\frac{z}{\lambda}\right) dz}{\int_d^\infty \exp\left(-\frac{z}{\lambda}\right) dz} \quad (7)$$

Which leads to:

$$d = \lambda \ln\left[\frac{I_r}{I_{ur}} + 1\right] \quad (8)$$

The derivation of eqn (8) requires the approximation that I_{ur} corresponds to a saturated signal from the unreacted layer, *i.e.*, the unreacted layer must be infinitively thick ('infinitely' in a sense that the layer is thick enough to exceed by far the information depth of XPS).[18,54,55] However, depending on the experimental conditions, this approximation is not necessarily true. In particular, the organic films in this study are not thick enough to be considered as bulk-like substrates in the regime of high photon energies. (Note that thicker film were not used because otherwise charging problems could occur during the XPS experiment.) Therefore, eqn (8) has to be modified, as will be described in the following section.

For an abrupt CoTPP/2HTPP interface at a depth d with an unreacted layer of *finite* thickness l underneath, there is only a limited probability of finding an unreacted molecule. This is described by the following relation:

$$c_{ur(z)} = \begin{cases} 0 & 0 < z \le d \\ 1 & d < z \le l \\ 0 & z > l \end{cases} \quad (9)$$

Applied to eqn (4b), this leads to:

$$\left(\frac{I_r}{I_{ur}}\right) = \frac{\int_0^d \exp\left(-\frac{z}{\lambda}\right) dz}{\int_d^l \exp\left(-\frac{z}{\lambda}\right) dz} \quad (10)$$

which can be solved and re-arranged to calculate the layer thickness by the relation:

$$d = \lambda \ln\left(\frac{\frac{I_r}{I_{ur}} + 1}{1 + \frac{I_r}{I_{ur}} \cdot e^{-\frac{l}{\lambda}}}\right) \quad (11)$$

If eqn (11) is employed to calculate the thickness d of the CoTPP layer from the ratios I_r/I_{ur} at different photon energies, an average value of 1.62 nm is obtained. The required values for the inelastic mean free paths have been obtained from the work of Ashley *et al.*[51] In agreement with the considerations above, the usage of eqn (8) did not result in a consistent reaction depth (due to the limited thickness of the 2HTPP layers in our study). Table 2 summarizes the results.

Table 2 Energy-dependent inelastic mean free path[51] of N 1s electrons, together with the intensity ratios I_r/I_{ur} and the therefrom calculated reaction depths d, without (eqn (8)) and with (eqn (11)) taking the finite thickness of the organic substrate into account

			Reaction depth (nm)	
Photon energy (keV)	IMFP (nm)	I_r/I_{ur}	Eqn (8)	Eqn (11)
2	4.03	0.51	1.66	1.64
3	6.02	0.32	1.67	1.58
4	7.89	0.27	1.88	1.67
5	9.67	0.22	1.92	1.60
6	11.39	0.20	2.08	1.62

P6

The presented arguments are also valid in the presence of an additional, *e.g.*, metallic, cover layer. Both XPS signals, either from the reacted or the unreacted layer, will be attenuated in the same way, *i.e.*, the intensity is reduced by a common factor. Since the calculation uses the ratio of the signal intensities, this factor cancels out and the influence of the top layer can be ignored in this approach.

5.2. Simulation by SESSA for the abrupt interface approximation

In the treatment in Section 5.1, elastic scattering of the electrons was not taken into account. In reality, however, elastic scattering has the effect of lengthening the average path for a photoelectron emerging from a solid, a process that should ideally be treated as a diffusion problem.[56] As described in Section 3.3, the database and program package SESSA (Simulation of Electron Spectra for Surface Analysis),[46–49] which was used here for this treatment, performs Monte Carlo simulations of the energy and angular distribution of photoelectrons for signal generation in XPS. Both multiple inelastic and elastic scattering of photoelectrons are included to achieve a more realistic analysis.

P6

The geometries, especially the polarization and gracing incidence (80°) of the photon beam with variable energy, are set to match the experimental conditions. The photoelectrons are collected perpendicular to the sample's surface using a field of view of 15°. The substrate is approximated by an Al substrate covered by a 4 nm aluminum oxide (Al_2O_3, E_{gap} = 7 eV, ρ = 4 g cm^{-3}) layer[57,58] followed by a 2HTPP ($C_{44}H_{30}N_4$, E_{gap} = 2.2 eV, ρ = 1.22 g cm^{-3}) layer[59–61] and a CoTPP ($C_{44}H_{28}N_4Co$, E_{gap} = 2.5 eV, ρ = 1.42 g cm^{-3}) layer[53,62] of variable thicknesses. Furthermore, samples are capped by a cover layer of metallic Co. Parameters for the individual peaks were taken from the fitting results of the experimental data (N 1s) or from tabulated values (C 1s, N 2s, Al 2s, Al 2p, Co 2p, Co 3s). Abrupt Co/CoTPP and CoTPP/2HTPP interfaces were assumed.

As shown in Fig. 4, after suitable settings for the experimental geometry and the employed excitation source (photon energy, polarization state and direction), the simulation was achieved diligently by adjusting compositions and sublevel peak parameters, until maximum consistency between simulated (red, solid lines) and measured spectra (black, round circles) was achieved. In the region of the N 1s main peaks, the simulated curves reproduce experimental spectra quite well. The simulated spectra show a slightly higher background, which probably arises from the large amount of scattered electrons from abundant metallic cobalt. Other models with different sample compositions were also evaluated. Specifically, additional simulations with 1.3 nm CoTPP or 1.9 nm CoTPP at the excitation energy of 2 keV were performed. The resulting spectra, which are displayed at the bottom of Fig. 4 for comparison, show that the total simulated N 1s peak shape varies substantially with the thickness of the CoTPP layer. The comparison presented in Fig. 4 predicts a thickness of 1.6 nm CoTPP with satisfactory accuracy. This agrees well with our calculation by signal damping in Section 5.1, where we obtained an average thickness of the CoTPP layer 1.62 nm.

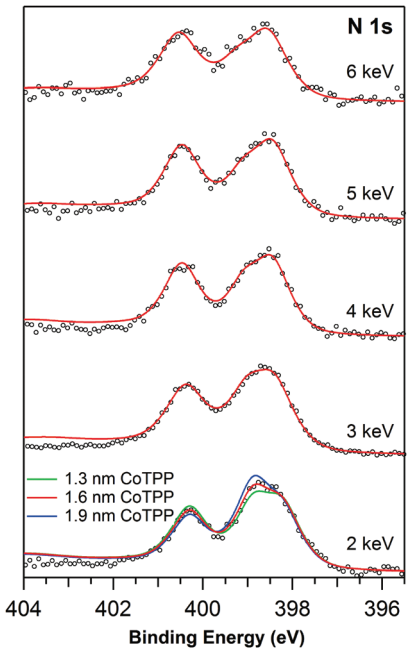

Fig. 4 Simulation of the photoemission spectra of 18 nm 2HTPP on a Al_2O_3/Al substrate with post-deposition of 1.8 nm Co on top. The spectra were simulated by SESSA[46–48] using the partial-intensity approach for the electron–solid interaction. The simulations (red lines) predict the measured intensities (black circles) well for the spectral features but slightly overestimate the background at higher binding energies. The blue and green lines illustrate typical deviations between experiment and simulation that occur for other than the optimal thickness of the interphase CoTPP layer.

5.3. Analysis beyond the abrupt-interface approximation

Up to this point, it was assumed that the reacted interphase layer (CoTPP) and the unreacted organic material (2HTPP) below are separated by an abrupt interface. However, since the migration and distribution of Co atoms in the organic material is driven by diffusion, such an abrupt interface can only be an approximation. Since it is known that in a related two-dimensional system the diffusion of metal atoms (Fe) in a layer of 2HTPP is faster than the metalation reaction,[28] it is possible that individual Co atoms migrate into the 2HTPP layer without reacting immediately, in particular since the activation barrier for metalation is higher for Co compared to Fe.[23] This scenario would give rise to a CoTPP concentration profile $c_{r(z)}$, which will decrease continuously (and monotonically) into the 2HTPP bulk. However, if $c_{r(z)}$ does not have the simple shape according to eqn (6) or eqn (9), a numerical solution of eqn (4b) is not feasible any longer, therefore one cannot extract $c_{r(z)}$ directly from eqn (4b). Nevertheless, it is possible to find $c_{r(z)}$ numerically by analyzing how the ratio I_r/I_{ur} changes with photon energy. (Note that the photon energy enters eqn (4b) indirectly *via* the inelastic mean free paths λ.)

The task to find the optimal concentration profile – *i.e.*, the profile that best reproduces the measured dependency between the intensity ratio I_r/I_{ur} and the photon energy – was accomplished by an optimization procedure based on a genetic algorithm. In brief, the genetic algorithm that was used for the analysis of the energy dependence of I_r/I_{ur} produced a large number of test

concentration profiles ($\sim 10^5$) in a random way and calculated the intensity ratio for each according to the following equation, which takes the finite thickness l of the organic layer into account:

$$\left(\frac{I_r}{I_{ur}}\right) = \frac{\int_0^l c_{r(z)} \exp\left(-\frac{z}{\lambda}\right) dz}{\int_0^l \left(1 - c_{r(z)}\right) \exp\left(-\frac{z}{\lambda}\right) dz} \quad (12)$$

The test profiles were constrained such that the concentration of CoTPP could only stay constant or monotonically decrease with increasing depth z.

For genetic optimization, the test profiles that gave the best agreement to the variation of I_r/I_{ur} with photon energy were kept and a new 'generation' of test profiles was created based on the parameters of the previous 'generation'. Again, the agreement of each test profile in this new generation to the energy dependence of I_r/I_{ur} was evaluated with eqn (12) and the procedure of selection and re-generation was continually repeated until an optimal reproduction of the experimental data was achieved (Fig. 5a). In addition, the inelastic mean free path, which is an important energy-dependent variable in eqn (12), was allowed to vary slightly around its literature values (to account for inaccuracies in those values, Fig. 5b). Eventually the best test profiles converged toward the sigmoidal shape shown in Fig. 5c. Notably, the ensemble of test profiles also contained curves representing an abrupt interface (as assumed in Sections 5.1 and 5.2) or curves with a non-zero concentration of 2HTPP at $z = 0$. However, those profile shapes showed lower agreement with the experimental data and did not prevail in the genetic optimization routine.

The calculated concentration profile shows complete conversion of 2HTPP into CoTPP up to a depth of 1.5 nm below the Co layer. Beyond this depth, the CoTPP concentration decreases within 0.15 nm to zero. The optimized inelastic mean free paths show only slight deviations from the NIST literature values by at most 9%.

The rather abrupt interface between CoTPP and the pristine 2HTPP phase shown in Fig. 5c indicates that the reaction of the Co atoms with the 2HTPP molecules is faster than their

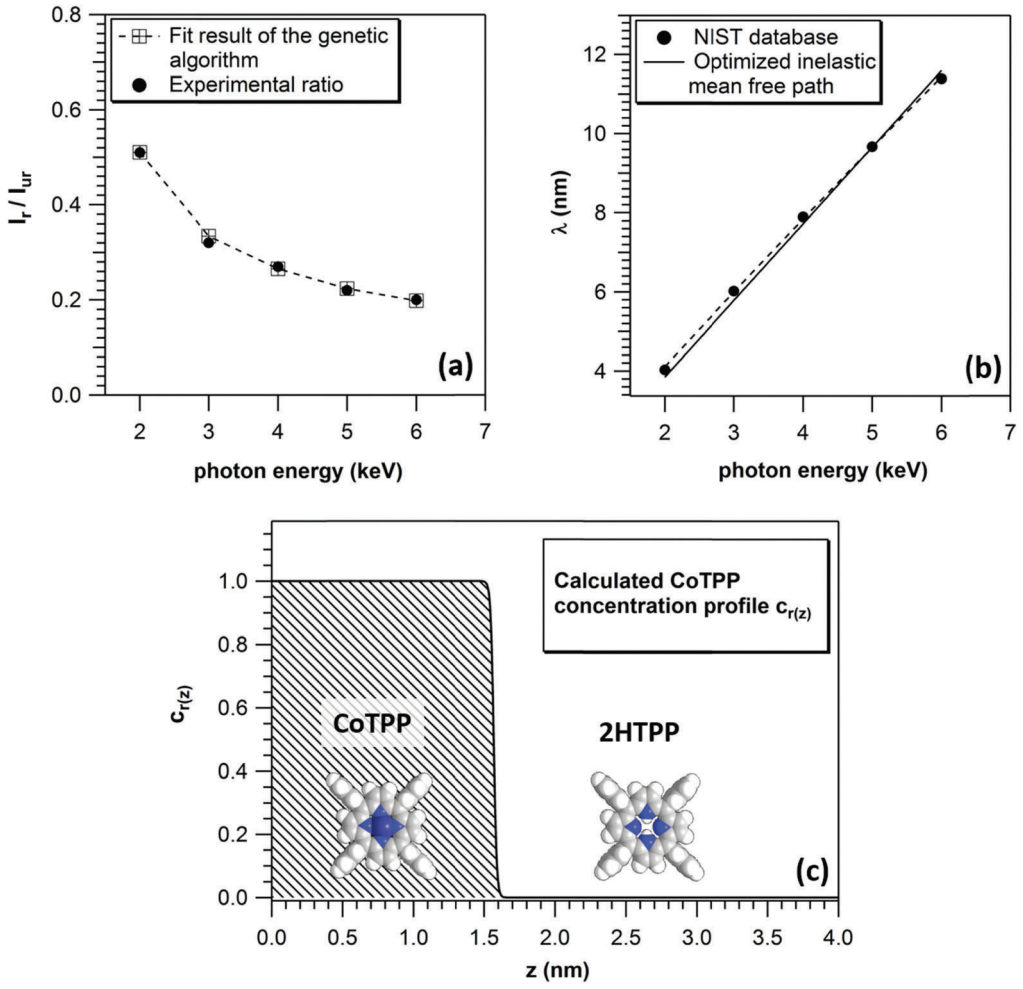

Fig. 5 Data analysis and determination of the CoTPP concentration *vs.* depth profile using a genetic algorithm. (a) Measured and calculated ratio I_r/I_{ur} as a function of the photon energy. (b) Literature values[51] and optimized values of the inelastic mean free paths as a function of the photon energy. (c) Concentration *vs.* depth profile $c_{r(z)}$ for the interphase layer that leads to the best agreement between the measured and calculated curve I_r/I_{ur} values in panel (a).

diffusion, because otherwise the CoTPP concentration would decrease more slowly over a wider depth range. This contrasts findings for the metalation of 2HTPP monolayers on Ag(111) with Fe, where the diffusion was the faster process. In addition, the abrupt decrease of the CoTPP concentration also confirms that the sample is strictly layered and that the roughness is low enough to justify the usage of a laterally integrating spectroscopic technique (see also Fig. S2 in the ESI† and the related text).

6. Summary

The interface reaction between a metallic cobalt layer and a free-base tetraphenylporphyrin (2HTPP) film was examined with Hard X-ray Photoelectron Spectroscopy (HAXPES). Diffusion of the Co atoms into the 2HTPP layer and a coordination reaction result in the formation of an interphase layer consisting of cobalt(II)-tetraphenylporphyrin (CoTPP). A main objective of the experiments was to obtain a depth profile of this CoTPP interphase layer. If a simple layer-by-layer configuration of CoTPP/2HTPP is assumed (abrupt interface), the HAXPES data are consistent with a thickness of the CoTPP layer of 1.6 nm. A refined data analysis was achieved with the aid of a genetic optimization routine, which allowed us to extract a concentration *vs.* depths profile of the CoTPP interphase layer: up to a depth of approximately 1.5 nm below the Co layer, virtually all 2HTPP was converted into CoTPP. Beyond this saturated layer, the CoTPP concentration decreases within 0.15 nm to zero. The rather abrupt CoTPP/2HTPP interface also indicates that the whole system is laterally uniform.

P6

Acknowledgements

This work was supported by the Deutsche Forschungsgemeinschaft through SFB 1083. We thank the Helmholtz-Zentrum Berlin (BESSY II) for the allocation of synchrotron radiation beamtime. H. Z. thanks the China Scholarship Council for a PhD fellowship. M. S. gratefully acknowledges funding by the Fonds der Chemischen Industrie through a Liebig Fellowship.

References

1 J. H. Burroughes, D. D. C. Bradley, A. R. Brown, R. N. Marks, K. Mackay, R. H. Friend, P. L. Burns and A. B. Holmes, *Nature*, 1990, **347**, 539–541.
2 C. W. Tang and S. A. Vanslyke, *Appl. Phys. Lett.*, 1987, **51**, 913–915.
3 C. D. Dimitrakopoulos and P. R. L. Malenfant, *Adv. Mater.*, 2002, **14**, 99–117.
4 C. W. Tang, *Appl. Phys. Lett.*, 1986, **48**, 183–185.
5 *Organic electronics*, ed. H. Klauk, Wiley-VCH, Weinheim, 2006.
6 *Organic electronics: materials, processing, devices and applications*, ed. F. So, CRC Press, 2009.
7 H. Ishii, K. Sugiyama, E. Ito and K. Seki, *Adv. Mater.*, 1999, **11**, 605–625.
8 X. Y. Zhu, *Surf. Sci. Rep.*, 2004, **56**, 1–83.
9 V. E. Choong, M. G. Mason, C. W. Tang and Y. G. Gao, *Appl. Phys. Lett.*, 1998, **72**, 2689–2691.
10 G. Gavrila, D. R. T. Zahn and W. Braun, *Appl. Phys. Lett.*, 2006, **89**, 162102.
11 Y. Hirose, A. Kahn, V. Aristov and P. Soukiassian, *Appl. Phys. Lett.*, 1996, **68**, 217–219.
12 Q. T. Le, L. Yan, Y. Gao, M. G. Mason, D. J. Giesen and C. W. Tang, *J. Appl. Phys.*, 2000, **87**, 375–379.
13 H. Yoshida and N. Sato, *Chem. Phys. Lett.*, 2011, **511**, 146–150.
14 F. Bebensee, M. Schmid, H.-P. Steinrück, C. T. Campbell and J. M. Gottfried, *J. Am. Chem. Soc.*, 2010, **132**, 12163–12165.
15 F. Bebensee, J. F. Zhu, J. H. Baricuatro, J. A. Farmer, Y. Bai, H.-P. Steinrück, C. T. Campbell and J. M. Gottfried, *Langmuir*, 2010, **26**, 9632–9639.
16 J. C. Sharp, F. Bebensee, J. H. Baricuatro, H.-P. Steinrück, J. M. Gottfried and C. T. Campbell, *J. Phys. Chem. C*, 2013, **117**, 23781–23789.
17 J. C. Sharp, X. F. Feng, J. A. Farrner, Y. X. Guo, F. Bebensee, J. H. Baricuatro, E. Zillner, J. F. Zhu, H.-P. Steinrück, J. M. Gottfried and C. T. Campbell, *J. Phys. Chem. C*, 2014, **118**, 2953–2962.
18 J. Zhu, F. Bebensee, W. Hieringer, W. Zhao, J. H. Baricuatro, J. A. Farmer, Y. Bai, H.-P. Steinrück, J. M. Gottfried and C. T. Campbell, *J. Am. Chem. Soc.*, 2009, **131**, 13498–13507.
19 X. F. Feng, W. Zhao, H. X. Ju, L. Zhang, Y. F. Ye, W. H. Zhang and J. F. Zhu, *Org. Electron.*, 2012, **13**, 1060–1067.
20 H. X. Ju, K. M. Knesting, W. Zhang, X. Pan, C. H. Wang, Y. W. Yang, D. S. Ginger and J. F. Zhu, *ACS Appl. Mater. Interfaces*, 2016, **8**, 2125–2131.
21 X. Pan, H. X. Ju, X. F. Feng, Q. T. Fan, C. H. Wang, Y. W. Yang and J. F. Zhu, *Acta Phys. Sin.*, 2015, **64**, 077304.
22 J. M. Gottfried, K. Flechtner, A. Kretschmann, T. Lukasczyk and H. P. Steinrück, *J. Am. Chem. Soc.*, 2006, **128**, 5644–5645.
23 T. E. Shubina, H. Marbach, K. Flechtner, A. Kretschmann, N. Jux, F. Buchner, H.-P. Steinrück, T. Clark and J. M. Gottfried, *J. Am. Chem. Soc.*, 2007, **129**, 9476–9483.
24 W. Auwärter, D. Ecija, F. Klappenberger and J. V. Barth, *Nat. Chem.*, 2015, **7**, 105–120.
25 J. M. Gottfried, *Surf. Sci. Rep.*, 2015, **70**, 259–379.
26 H. Marbach, *Acc. Chem. Res.*, 2015, **48**, 2649–2658.
27 K. Diller, A. C. Papageorgiou, F. Klappenberger, F. Allegretti, J. V. Barth and W. Auwärter, *Chem. Soc. Rev.*, 2016, **45**, 1629–1656.
28 F. Buchner, K. Flechtner, Y. Bai, E. Zillner, I. Kellner, H. P. Steinrück, H. Marbach and J. M. Gottfried, *J. Phys. Chem. C*, 2008, **112**, 15458–15465.
29 K. Siegbahn, *Nucl. Instrum. Methods Phys. Res., Sect. A*, 2005, **547**, 1–7.
30 R. Knut, R. Lindblad, M. Gorgoi, H. Rensmo and O. Karis, *J. Electron Spectrosc. Relat. Phenom.*, 2013, **190**, 278–288.
31 G. Panaccione and K. Kobayashi, *Surf. Sci.*, 2012, **606**, 125–129.
32 R. Claessen, M. Sing, M. Paul, G. Berner, A. Wetscherek, A. Müller and W. Drube, *New J. Phys.*, 2009, **11**, 125007.
33 C. B. Duke, *Proc. Natl. Acad. Sci. U. S. A.*, 2003, **100**, 3858–3864.

34 M. P. Seah and W. A. Dench, *Surf. Interface Anal.*, 1979, **1**, 2–11.
35 S. V. Merzlikin, N. N. Tolkachev, T. Strunskus, G. Witte, T. Glogowski, C. Wöll and W. Grünert, *Surf. Sci.*, 2008, **602**, 755–767.
36 Y. Kalachyova, O. Lyutakov, A. Solovyev, P. Slepička and V. Švorčík, *Nanoscale Res. Lett.*, 2013, **8**, 547.
37 M. Chen, X. F. Feng, L. Zhang, H. X. Ju, Q. Xu, J. F. Zhu, J. M. Gottfried, K. Ibrahim, H. J. Qian and J. O. Wang, *J. Phys. Chem. C*, 2010, **114**, 9908–9916.
38 S. Narioka, H. Ishii, Y. Ouchi, T. Yokoyama, T. Ohta and K. Seki, *J. Phys. Chem.*, 1995, **99**, 1332–1337.
39 H. Peisert, I. Biswas, M. Knupfer and T. Chassé, *Phys. Status Solidi B*, 2009, **246**, 1529–1545.
40 H. Peisert, T. Schwieger, J. M. Auerhammer, M. Knupfer, M. S. Golden, J. Fink, P. R. Bressler and M. Mast, *J. Appl. Phys.*, 2001, **90**, 466–469.
41 T. Nagata, M. Haemori, Y. Yamashita, H. Yoshikawa, Y. Iwashita, K. Kobayashi and T. Chikyow, *Appl. Phys. Lett.*, 2011, **99**, 223517.
42 Y. Yamashita, H. Yoshikawa, T. Chikyow and K. Kobayashi, *J. Appl. Phys.*, 2013, **113**, 163707.
43 M. Shibuta, T. Eguchi, Y. Watanabe, J.-Y. Son, H. Oji and A. Nakajima, *Appl. Phys. Lett.*, 2012, **101**, 221603.
44 M. Gorgoi, S. Svensson, F. Schäfers, G. Öhrwall, M. Mertin, P. Bressler, O. Karis, H. Siegbahn, A. Sandell, H. Rensmo, W. Doherty, C. Jung, W. Braun and W. Eberhardt, *Nucl. Instrum. Methods Phys. Res., Sect. A*, 2009, **601**, 48–53.
45 F. Schaefers, M. Mertin and M. Gorgoi, *Rev. Sci. Instrum.*, 2007, **78**, 123102.
46 W. Smekal, W. S. M. Werner and C. J. Powell, *Surf. Interface Anal.*, 2005, **37**, 1059–1067.
47 W. S. M. Werner, W. Smekal, T. Hisch, J. Himmelsbach and C. J. Powell, *J. Electron Spectrosc. Relat. Phenom.*, 2013, **190**, 137–143.
48 W. S. M. Werner, *Surf. Interface Anal.*, 2001, **31**, 141–176.
49 W. S. M. Werner, *Surf. Interface Anal.*, 2005, **37**, 846–860.
50 H. Mühlenbein and D. Schlierkamp-Voosen, *Evolut. Comput.*, 1993, **1**, 25–49.
51 J. C. Ashley, C. J. Tung and R. H. Ritchie, *IEEE Trans. Nucl. Sci.*, 1978, **25**, 1566–1570.
52 M. J. Hamor, T. A. Hamor and J. L. Hoard, *J. Am. Chem. Soc.*, 1964, **86**, 1938–1942.
53 P. Madura and W. R. Scheidt, *Inorg. Chem.*, 1976, **15**, 3182–3184.
54 E. McCafferty and J. P. Wightman, *Surf. Interface Anal.*, 1998, **26**, 549–564.
55 P. J. Cumpson and M. P. Seah, *Surf. Interface Anal.*, 1997, **25**, 430–446.
56 T. A. Carlson and G. E. McGuire, *J. Electron Spectrosc. Relat. Phenom.*, 1972, **1**, 161–168.
57 F. C. Walsh, D. V. Bavykin, L. Torrente-Murciano, A. A. Lapkin and B. A. Cressey, *Trans. Inst. Met. Finish.*, 2006, **84**, 293–299.
58 E. O. Filatova and A. S. Konashuk, *J. Phys. Chem. C*, 2015, **119**, 20755–20761.
59 M. Ashida, H. Yanagi, S. Hayashi and K. Takemoto, *Acta Crystallogr., Sect. B: Struct. Sci.*, 1991, **47**, 87–91.
60 K. M. Kadish, K. M. Smith and R. Guilard, Electron transfer, *The Porphyrin Handbook*, Academic Press, vol. 8, 2000.
61 M. Zerner and M. Gouterma, *Theor. Chim. Acta*, 1966, **4**, 44–63.
62 M. S. Liao and S. Scheiner, *J. Chem. Phys.*, 2002, **117**, 205–219.

Electronic supplementary information (ESI) for

Formation of an Extended Interphase Layer During Deposition of Cobalt onto Tetraphenylporphyrin: A Hard X-Ray Photoelectron Spectroscopy (HAXPES) Study

Min Chen[1], Han Zhou[1], Malte Zugermeier[1], Benedikt Klein[1], Claudio Krug[1], Hans-Jörg Drescher[1], Mihaela Gorgoi[2], Martin Schmid[1], J. Michael Gottfried[1]*

[1]Fachbereich Chemie, Philipps-Universität Marburg, Hans-Meerwein-Straße 4, 35032 Marburg, Germany, michael.gottfried@chemie.uni-marburg.de

[2]Helmholtz Zentrum Berlin für Materialien und Energie GmbH, Albert-Einstein Str. 15, 12489 Berlin, Germany

1. C 1s X-ray photoelectron spectra

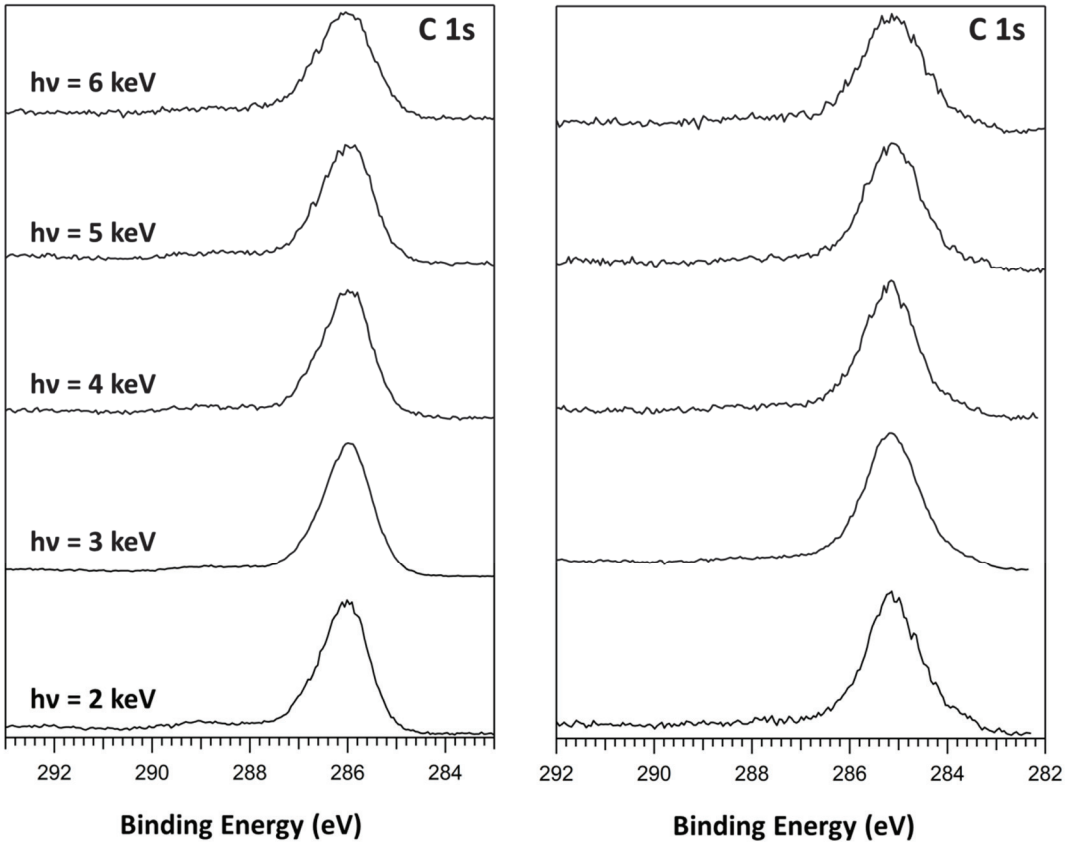

Figure S1. C 1s XP spectra of a pristine 18 nm 2HTPP layer, taken before (left panel) and after (right panel) vapor deposition of 1.8 nm Co. From bottom to up, spectra were taken with different photon energies as indicated. Electrons were collected at 0° relative to the surface normal.

2. Interface roughness

Derivation of the depth distribution of the reacted interphase layer (here CoTPP) is straightforward only for a flat interface (Figure S2a). In this case, the concentration vs. depth profile $c_r(z)$ derived from HAXPES (red line) correctly shows the abrupt interface between the interphase layer (CoTPP) and the underlying pristine 2HTPP.

For a rough, buckled interface, the situation is more complicated. In the simple model shown in Figure S2b, a HAXPES experiment in normal emission geometry would detect two different thicknesses, as visualized by the black arrows representing the electron trajectories. As a result, the concentration *vs.* depth profile $c_r(z)$ would show two steps (red line). In the case of a real rough interface with a distribution of different angles between the emission direction (black arrows) and the orientation of the reacted layer, a gradual decrease of $c_r(z)$ would result (green dotted line). Therefore, even if the CoTPP/2HTPP interface is locally abrupt (as in Figure S2b), the experiment would yield a concentration profile that is identical to one of a diffuse interface (with partial intermixing of CoTPP and 2HTPP).

P6

Conversely, if the HAXPES analysis shows an abrupt interface, then the interface is not only abrupt, it is also laterally sufficiently uniform for the application of a spatially integrating spectroscopic technique.

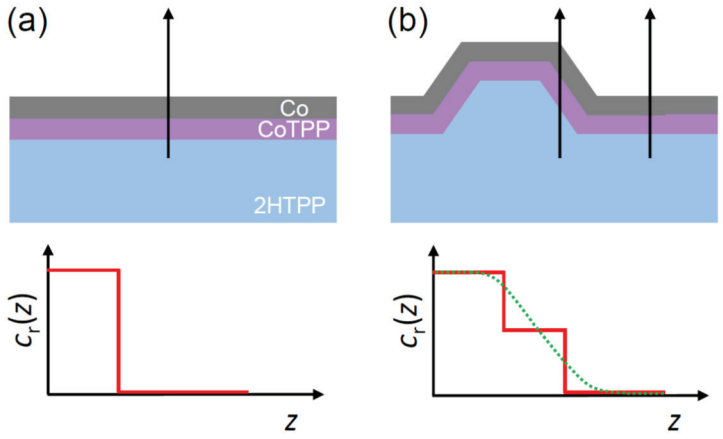

Figure S2. (a) HAXPES on a flat layer-by-layer interface in normal emission geometry (as indicated by the black arrow). The concentration *vs.* depth profile, $c_r(z)$, of the reacted component, CoTPP, is shown below (red line). (b) Corresponding model for a buckled layer-by-layer interface. The concentration *vs.* depth profile (red line) now has two steps because there are two apparent thicknesses of the reacted layer (CoTPP). For a real buckled interface with a distribution of different angles between the emission direction and orientation of the reacted layer, a gradual decrease of the apparent concentration would result (green dotted line).

However, it should be noted that the sensitivity of the normal-emission HAXPES experiment to surface roughness is rather moderate. The reason for this is that any inclination of the actual surface (due to roughness) by an angle $\Delta\theta$ relative to the normal emission direction will increase the path length of the photoelectrons by the factor of $1/(\cos\Delta\theta)$. Outside normal emission geometry, this effect is larger due to the shape of the cos function. This has also been experimentally verified in previous work.[1] Calculation for the roughness induced increase of the photoelectron path lengths are given in Section 2.1 of the paper.

References

1. S. V. Merzlikin, N. N. Tolkachev, T. Strunskus, G. Witte, T. Glogowski, C. Wöll and W. Grünert, *Surf. Sci.*, 2008, **602**, 755-767.

P7 On-Surface Synthesis and Characterization of an Iron Corrole

Citation: M. Schmid, M. Zugermeier, J. Herritsch, B. P. Klein, **C. K. Krug**, L. Ruppenthal, P. Müller, M. Kothe, P. Schweyen, M. Bröring, J. M. Gottfried, *J. Phys. Chem. C* **2018**, *122*(19), 10392–10399 DOI 10.1021/acs.jpcc.8b00067.

Summary

This publication investigates the metalation reaction of 2,3,8,12,17,18-hexaethyl-7,13-dimethylcorrole (3HHEDMC) with Fe and compares it with the closely related octaethylporphyrin (2HOEP) in the monolayer and in the multilayer. The electronic structure of the two reaction products Fe 2,3,8,12,17,18-hexaethyl-7,13-dimethylcorrole (FeHEDMC) and Fe octaethylporphyrin (FeOEP) is investigated using X-ray photoelectron spectroscopy (XPS), ultraviolet photoelectron spectroscopy (UPS), Fe L-edge near-edge X-ray absorption fine structure (NEXAFS) spectroscopy, and scanning tunneling microscopy (STM).

The partial metalation of 3HHEDMC with Fe in the multilayer is proven by XPS. A direct metalation of a corrole on a surface had not been reported before. An oxidation state of Fe(+III) is found for FeHEDMC, whereas it is Fe(+II) in FeOEP. This finding is supported by the Fe L-edge NEXAFS spectra. The influence of the Ag(111) substrate in the monolayer is investigated with XPS, NEXAFS spectroscopy, and UPS. A distinct difference between FeHEDMC and FeOEP is revealed, which can also be seen in STM images.

Own Contribution

For this publication I was part of the experimentalist team, who performed the NEXAFS spectroscopy experiments at the HE-SGM beamline (*cf.* Section 3.4.3) of the synchrotron radiation facility BESSY II in Berlin. The measurements were performed during a beamtime together with Dr. Martin Schmid, Dr. Malte Zugermeier, Dr. Benedikt P. Klein, Lukas Ruppenthal, and Philipp Müller. Dr. Martin Schmid, Dr. Malte Zugermeier and Jan Herritsch performed the data analysis and wrote the manuscript. I contributed to its discussion together with all other co-authors.

THE JOURNAL OF PHYSICAL CHEMISTRY C

Article

Cite This: J. Phys. Chem. C 2018, 122, 10392−10399

pubs.acs.org/JPCC

On-Surface Synthesis and Characterization of an Iron Corrole

Martin Schmid,*[,†] Malte Zugermeier,[†] Jan Herritsch,[†] Benedikt P. Klein,[†] Claudio K. Krug,[†] Lukas Ruppenthal,[†] Philipp Müller,[†] Michael Kothe,[‡] Peter Schweyen,[§] Martin Bröring,[§] and J. Michael Gottfried[†]

[†]Fachbereich Chemie, Philipps-Universität Marburg, Hans-Meerwein-Str. 4, 35032 Marburg, Germany

[‡]Fachbereich Physik, Philipps-Universität Marburg, Renthof 7, 35032 Marburg, Germany

[§]Institut für Anorganische und Analytische Chemie, Technische Universität Braunschweig, Hagenring 30, 38106 Braunschweig, Germany

Supporting Information

ABSTRACT: To explore the possibility of tuning the oxidation state of a coordinated metal ion in an adsorbed tetrapyrrole complex by a minor modification of the ligand structure, multilayers and monolayers of 3H-hexaethyl-dimethyl-corrole (3H-HEDMC) on Ag(111) were in situ metalated under ultrahigh vacuum (UHV) conditions and subsequently analyzed with spectroscopic and microscopic methods. The metalation reaction leads to the formation of Fe(III)-hexaethyl-dimethyl-corrole (Fe-HEDMC). The results were compared with those for Fe-octaethyl-porphyrin (Fe-OEP), in which the Fe metal center has a formal Fe(+II) character. The analysis of the nearly unperturbed iron-corrole in the multilayer regime with X-ray photoelectron spectroscopy (XPS) and near edge X-ray absorption fine structure (NEXAFS) spectroscopy shows that the electronic structure of the corrole-coordinated iron is consistent with an Fe(+III) state in Fe-HEDMC. In the monolayers, the Fe centers in Fe-HEDMC and Fe-OEP interact similarly with the Ag(111) surface, as indicated by contributions to the Fe 2p signals at a typical Fe(0) position. Nevertheless, a closer investigation of the Fe-HEDMC and Fe-OEP monolayers with NEXAFS, UV photoelectron spectroscopy (UPS), and scanning tunneling microscopy (STM) reveal significant differences between electronic states of the Fe centers, depending on the type of ligand. Apparently, the interfacial interactions between the coordinated metal centers and the surface modify the electronic state of Fe but do not fully equalize the differences induced by the corrole and porphyrin ligand structures. Thus, the experiments show that it is not only possible to perform a direct in situ metalation of corroles with iron atoms under UHV conditions but also that the differences in the electronic structures between Fe-corroles and Fe-porphyrins persist even in the presence of interfacial interactions with Ag(111). Especially, the differences in the Fe-related density of states around the Fermi energy are expected to result in different chemical reactivities and potential catalytic activities of the two supported Fe complexes.

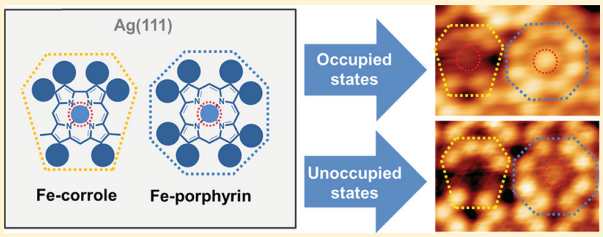

P7

1. INTRODUCTION

The surface-assisted synthesis of coordination compounds provides a promising approach for the design of novel catalytically active materials, which combine the primary advantage of homogeneous catalysts—uniform active sites—with the simplicity of product/catalyst separation known from heterogeneous catalysts. The major directions that have been pursued in this field include the formation of 2D metal−organic coordination networks[1,2] and, more recently, the direct metalation[3,4] of adsorbed phthalocyanines and porphyrins under ultrahigh vacuum (UHV) conditions.[5−7] These highly stable and planar tetrapyrrole derivatives readily self-assemble to form well-ordered monolayers on many metals, oxides, and other substrates such as monolayer graphene.[8−10] In the adsorbed state, they can oxidize co-adsorbed metal atoms M to the corresponding dications M(II) and form M(II)−phthalocyanine or M(II)−porphyrin complexes with them. This redox reaction is completed by the release of the pyrrolic hydrogen atoms (−NH−) in the form of molecular hydrogen (H_2). Because the molecules contain only two acidic −NH− groups, the metal center is typically oxidized to a +II oxidation state.[6] This metalation reaction has been used for the on-surface synthesis of many porphyrin and phthalocyanine complexes, including those in which the M(II) ion is highly reactive such as in Fe(II)- and Ti(II)-tetraphenylporphyrins[11−14] or V(II)-phthalocyanine.[15] The phthalocyanine ligand can also show non-innocent behavior in the on-surface metalation, as was shown with the on-surface synthesis of AlPc, which contains Al(III) while the excess electron is delocalized on the phthalocyanine ring.[16]

In the monolayer, one of the two vacant axial coordination sites of a free tetrapyrrole complex is blocked by the surface. Furthermore, the surface may also influence the oxidation state and reactivity of the metal centers.[17,18] In many cases, a partial

Received: January 8, 2018
Revised: February 20, 2018
Published: March 21, 2018

DOI: 10.1021/acs.jpcc.8b00067
J. Phys. Chem. C 2018, 122, 10392−10399

reduction by electron transfer from the substrate was observed. For example, Fe(II) in Fe-TPP[11,12] or Fe-Pc[19] on Ag(111) was partially reduced to a lower oxidation state, according to X-ray and electron spectroscopies. How can the oxidation state be *increased*? A possible approach is the attachment of an additional axial ligand, such as NO, which counteracts the substrate influence (surface trans effect[17]). However, this would block the remaining vacant coordination site and make the complex unsuitable as a catalyst or sensor. Therefore, we pursue a different approach in this work: by a minor modification of the ligand structure, we attempt to force the metal ion to the M(III) state. Specifically, we modified the structure of porphin (Figure 1a), which is the parent macrocycle of all porphyrins.

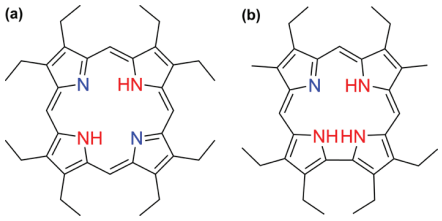

Figure 1. (a) 2H-octaethyl-porphyrin (2H-OEP) and (b) 3H-2,3,8,12,17,18-hexaethyl-7,13-dimethyl-corrole (3H-HEDMC).

By formally removing one of the four methine-bridges we arrive at the corresponding corrole (Figure 1b). The smaller corrole macrocycle provides a tighter coordination environment and thus stabilizes high-valent transition state metal ions with smaller ionic radii, whereas low-valent metal complexes are highly reactive.[20−23] In nature, the partially hydrogenated corroles, the corrins, play an important role as active centers of biomolecules; an example is the Co corrin in cobalamin (vitamin B_{12}). Furthermore, Fe-corroles are utilized, for example, in the contexts of catalysis[24,25] or diabetes treatment.[26] The aromatic free-base corrole macrocycle contains three pyrrolic hydrogen atoms (−NH−) and thus, formally, should be able to oxidize suitable metal atoms to their +III oxidation state. The removal of the third pyrrolic H atom is compatible with a mechanism proposed for the direct metalation of tetrapyrroles which involves hydrogen transfer to a metal surface.[27] In addition, there are examples from classical coordination chemistry in solution, where one or two inner hydrogen atoms actually remain in the complex and the corrole acts as a dianionic or monoanionic ligand, respectively.[23,28] The direct oxidation of a metal atom to its trication by an adsorbed corrole is therefore by no means trivial, in particular because tetrapyrroles can act as non-innocent ligands[16] and influence the oxidation state of the central metal ion.

In our study, we examine—to the best of our knowledge for the first time—feasibility and outcome of a direct metalation of a free-base corrole molecule, 3H-HEDMC (Figure 1), with iron atoms in a UHV environment. In general, the in situ metalation approach allows to produce tetrapyrrole complexes which are potentially chemically unstable under ambient conditions and to design (two-dimensional) chemical systems in a bottom-up approach. Here, the specific goals are: (a) to confirm the expected Fe(III) oxidation state in metalated corrole multilayers with X-ray photoelectron spectroscopy (XPS) and near edge X-ray absorption fine structure (NEXAFS) and (b) to clarify in the monolayer regime whether or not the metal centers in Fe-OEP and Fe-HEDMC remain electronically different, despite their direct contact to the Ag(111) surface.

2. EXPERIMENTAL SECTION

The Ag(111) sample was prepared by repeated cycles of Ar^+ ion bombardment (500 eV) and annealing (800 K). Surface cleanliness was confirmed in all experiments by XPS. 3H-HEDMC was synthesized from the respective didesoxybiladiene by oxidative ring closure (see the Supporting Information).

During sample preparation in the UHV environment, all fluxes were measured with a quartz crystal microbalance. The term *monolayer* is used for a complete, monomolecular layer that uniformly covers the substrate. In contrast, the unit ML refers to the number of objects (atoms or molecules) per Ag surface atom. Considering the size of the porphyrin and corrole molecules, it is estimated that 0.03 ML of iron are sufficient to metalate one monolayer (flat lying configuration) of 2H-OEP or 3H-HEDMC.

3H-HEDMC was vapor-deposited under UHV conditions onto the Ag(111) surface from a home-built Knudsen cell evaporator operated at ∼470 K. For multilayer preparation, typical fluxes were in the range of 0.4 nm/min. For synchrotron experiments (N 1s XPS, Fe L-edge NEXAFS), corrole monolayers were prepared by multilayer desorption by flash annealing of the multilayer to 515 K. In this case, the monolayer comprised 2H-HEDMC molecules because of temperature-induced loss of one hydrogen atom from the central pocket.[29] For monolayer preparations in the laboratory setup, the sample was cooled to 125 K to avoid the initial onset of the surface-induced partial dehydrogenation of the 3H-HEDMC molecules. The molecular fluxes were in the range of 0.04 nm/min. However, for all monolayer metalation experiments the sample was allowed to reach room temperature before Fe deposition. Thus, the reaction partners were always 2H-HEDMC/Ag(111) and Fe.

2H-OEP was deposited in an identical manner with a Knudsen cell, at an operation temperature of approximately 545 K. Typical fluxes for multilayer preparation varied between 0.1 and 0.3 nm/min. 2H-OEP monolayers were routinely prepared by multilayer desorption (flash annealing to 515 K). This procedure yields chemically intact and well-ordered 2H-OEP monolayers.[3,4,8]

An electron beam evaporator (FOCUS EFM-4) was used for the vapor deposition of Fe and was typically operated at iron fluxes of 0.01 ML/min. To facilitate the metalation reactions, the samples were annealed to 400 K during or after the deposition of Fe onto the molecular layers.

NEXAFS and XPS data were acquired at the HE-SGM endstation of the BESSY II synchrotron radiation facility in Berlin, Germany. This dipole beamline has a photon energy range of 100−700 eV, the photon incidence angle during measurements was 53°. NEXAFS data were recorded with a channel plate detector, which was operated in partial electron yield mode with a bias voltage of −150 V. For XPS measurements, a Scienta R4000 analyzer was used. The sample preparation chamber of the HE-SGM endstation was used to prepare the porphyrin and corrole samples as described above. The NEXAFS spectra were treated according to standard procedures.[30] Specifically, the spectra were normalized in the pre-edge region (700 and 705 eV for multilayer and monolayer measurements, respectively). For background correction, spectra of the clean Ag(111) substrate were interpolated with

DOI: 10.1021/acs.jpcc.8b00067
J. Phys. Chem. C 2018, 122, 10392−10399

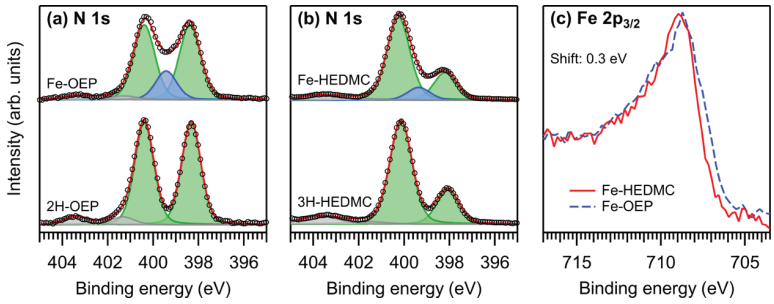

Figure 2. (a) N 1s XP spectra recorded before (bottom) and after (top) the partial metalation of a 2H-OEP multilayer with Fe. (b) N 1s XP spectra recorded before (bottom) and after (top) the partial metalation of a 3H-HEDMC multilayer with Fe. The components at 399.4 and 399.3 eV (blue) are associated with the metalation products, i.e., Fe-OEP in (a) and Fe-HEDMC in (b). (c) Related Fe $2p_{3/2}$ XP spectra taken after partial metalation of 2H-OEP and 3H-HEDMC multilayers with Fe. The spectra were recorded with a photon energy of 1486.7 eV. Full metalation of the multilayers was not attempted to prevent the competing formation of metallic Fe clusters, which would lead to an additional Fe(0) signal in the Fe $2p_{3/2}$ XP spectrum.

a smoothing spline and then subtracted from the sample spectra.

UV photoelectron spectroscopy (UPS) and further XPS data were recorded in a multichamber UHV laboratory setup (base pressure in the low 10^{-10} mbar range), equipped with a gas-discharge UV source, a monochromated Al Kα X-ray source (1486.7 eV), a SPECS Phoibos 150 electron spectrometer, an MCD-9 multichanneltron detector, and a preparation chamber, which was used for the deposition of 3H-HEDMC, 2H-OEP, and Fe onto the Ag(111) crystal surface.

Scanning tunneling microscopy (STM) images were acquired with a SPECS SPM 150 Aarhus, which was attached to the same multichamber setup. All STM measurements were conducted at 100−160 K in constant-current mode. The images were processed with WSxM v5.0 Develop 8.4[31] by carefully using flatten and plane tools, scale adjustment, and slightly filtering with a Gaussian filter. The reported bias voltages refer to the sample.

3. RESULTS AND DISCUSSION

3.1. Multilayer: Metalation and Oxidation State. To establish a porphyrin-based reference system for the corrole experiments, a multilayer of 2H-OEP with a thickness of approximately 5.5 nm was partially metalated with Fe atoms that were directly vapor-deposited onto this multilayer. Such metalation reactions are in multilayer systems limited to the first molecular layers.[32] Before and after deposition of 0.09 ML iron (sufficient to metalate approximately three molecular layers of 2H-OEP), N 1s core level spectra were recorded ($h\nu$ = 1486.7 eV) from the multilayers to confirm a reaction between the iron atoms and 2H-OEP, as shown in Figure 2a. The reaction is expected to proceed at room temperature because of the absence of a reaction barrier.[6] The spectrum of the pristine 2H-OEP multilayer (bottom) consists of two main components at 400.4 and 398.3 eV, corresponding to −NH− and =N− groups, respectively. The peak intensities slightly deviate from the expected ideal 1:1 ratio. This is a well-known phenomenon and is in general associated with a satellite from the iminic nitrogen species (=N−) peak overlapping with the pyrrolic species (−NH−) signal.[33] Deposition of 0.09 ML of iron gives rise to an additional component at 399.4 eV in the N 1s signal. In line with the literature, this feature is attributed to the reaction between iron and the porphyrin resulting in the formation of Fe-OEP.[8,34]

The next experimental step addresses the core question of this study: can corroles be metalated by an on-surface reaction, similar to porphyrins and phthalocyanines? To answer this question, a 3H-HEDMC multilayer (thickness approximately 8 nm) was prepared and examined with XPS. As shown in Figure 2b, the XP spectrum of pristine 3H-HEDMC shows two distinct peaks in the N 1s region: one at 398.1 eV (=N−) and the second at 400.1 eV (−NH−). This is similar to the case of 2H-OEP, except for the intensity ratio of 3:1, which reflects the correct stoichiometric ratio of −NH− and =N− groups in 3H-HEDMC. Noteworthy, the slight deviation from the ideal = N− to −NH− ratio observed for 2H-OEP does not occur here. After deposition of 0.09 ML iron, an additional peak appears at 399.3 eV, indicating that 3H-HEDMC engages in a reaction with iron, similar to 2H-OEP.

The N 1s spectrum taken after Fe deposition (Figure 2b, top) can be fitted with three peaks: a single peak for the newly formed iron complex and a doublet with a 3:1 ratio for 3H-HEDMC. This finding indicates that the metalation reaction does remove all three hydrogen atoms from the central cavity of the molecules and thus leads to the formation of Fe-HEDMC. If FeH-HEDMC or FeH_2-HEDMC species were present in the multilayer, the simple fit approach in Figure 2b would not be sufficient to describe the experimental data. This result is also consistent with the known stabilization of high oxidation states by corrole ligands.[35,36]

The N 1s spectra analyzed so far show that a corrole can be metalated similar to its porphyrin counterpart; however, the N 1s spectra do not provide direct information about the chemical state of the iron metal centers. For further insight into the differences in the electronic structures of Fe-OEP and Fe-HEDMC, Fe $2p_{3/2}$ core level signals were recorded. In open-shell iron complexes, such as Fe-tetrapyrroles, the Fe $2p_{3/2}$ peak is generally broadened because of spin−spin coupling in the corresponding photoions, giving rise to multiplet effects.[37,38] This broadening effect is present in the spectra in Figure 2c, where the signal from Fe-OEP has a broad and asymmetric shape, a result in full agreement with previous studies.[38] The Fe $2p_{3/2}$ signal from the Fe-HEDMC appears similar, yet by 0.4 eV more narrow, its peak maximum is shifted by 0.3 eV toward higher binding energies relative to the corresponding Fe-OEP signal. This finding can be interpreted as an indication for a higher oxidation state of iron in the corrole ligand. The peak shift is rather small compared to the total width of the signal but in agreement with previous studies.[39] To corroborate our

DOI: 10.1021/acs.jpcc.8b00067
J. Phys. Chem. C 2018, 122, 10392−10399

XPS results, we conducted further NEXAFS measurements of Fe L-edges of Fe-OEP and Fe-HEDMC multilayers.

In particular, Fe L-edge NEXAFS measurements for mixed multilayers of Fe-OEP/2H-OEP and Fe-HEDM/3H-HEDMC were performed. As shown in Figure 3, the direct comparison

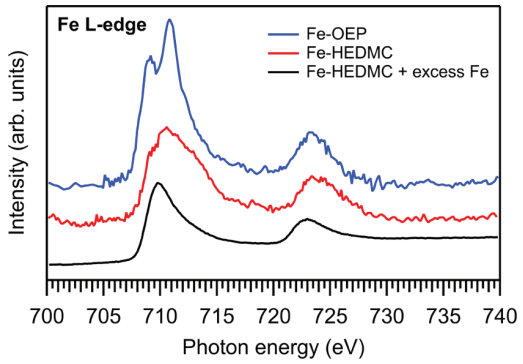

Figure 3. Fe L-edge NEXAFS spectra of Fe-HEDMC (red curve), Fe-OEP (blue curve), and excess Fe + Fe-HEDMC (black curve). The Fe complexes were obtained by vapor deposition of Fe onto multilayers of the respective free-base ligands.

of the L-edges of both samples reveals marked differences in the spectral patterns. While the L_3-edge of Fe-OEP has a two-peak structure (as one would expect based on the Fe L-edges of Fe-phthalocyanine[19]), Fe-HEDMC only shows a broad structure without a distinct splitting into subpeaks. Noteworthy, the spectrum resembles the L-edge of the Fe(III) species in Fe-TPP-Cl.[40] In fact, the L-edge of the Fe in Fe-HEDMC shows also a significant resemblance to the L-edge of MnPc[41]—an interesting result considering that Mn(II) and Fe(III) are isoelectronic. For further comparison with metallic Fe(0), additional NEXAFS data with an excess of iron on the 3H-HEDMC layer were recorded, showing a simpler yet asymmetric peak shape of the Fe-L2/L3 edges.

3.2. Monolayer: Metalation and Molecule−Surface Interaction. The Fe L-edge NEXAFS spectra indicate that the electronic structures of Fe-OEP and Fe-HEDMC differ significantly in the multilayer. However, it is not clear whether these differences persist for Fe-OEP and Fe-HEDMC molecules with a direct contact to a Ag(111) surface. Recent studies show that the coupling between metal centers of tetrapyrroles and surfaces can be influenced even by changes on the molecular periphery of the tetrapyrrole ligands.[42] On the other hand, it is known that metal substrates, and in particular Ag(111), can have a very substantial influence on the oxidation state of coordinated metal centers such as Fe(II) or Co(II) in adsorbed tetrapyrrole complexes.[17,43] To clarify whether Fe-HEDMC molecules interact in a similar way with the Ag(111) surface as Fe-OEP molecules, further XPS, NEXAFS, UPS, and STM experiments were performed; these methods give insight into the electronic interaction between the metal centers and the Ag(111) surface.

As a first step, we performed monolayer metalation experiments with both molecules. For this purpose, monolayers of the free-base ligands were produced by thermal desorption of thin multilayers and then partially metalated by vapor deposition of Fe. Understoichiometric amounts of Fe (35−40% of the stoichiometric amount, corresponding to an Fe coverage of approximately 0.01 ML) were used to strictly avoid the presence of unreacted Fe, which would affect the Fe-related signals in the XPS and NEXAFS data. Additionally, the sample was annealed to 400 K after the deposition of Fe to accelerate the reaction, although at least porphyrins are known to react rapidly with Fe atoms already at room temperature.[12,38]

The N 1s XP spectra taken before and after partial metalation of the monolayers are shown in Figure 4. The 2H-OEP

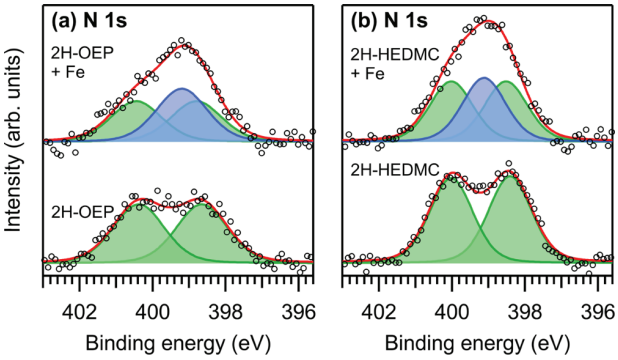

Figure 4. N 1s core level spectra of (a) porphyrin (OEP) and (b) corrole (HEDMC) monolayers on Ag(111) before (bottom) and after (top) metalation. Green, signals related to the free-base ligands; blue, signals related to the Fe complexes. The amount of deposited Fe and thus the degree of metalation was limited to at most 40% of the stoichiometric amount to avoid residual unreacted Fe that would interfere with the XPS and NEXAFS measurements of Fe. The spectra were recorded with a photon energy of 600 eV.

monolayer spectrum in Figure 4a (bottom) comprises the two signals related to =N− and −NH− (398.7 and 400.4 eV, respectively), similar as in the related multilayer spectrum (Figure 2a). The surface-induced broadening and small shifts of the peaks are in agreement with the literature.[44,45] After deposition of Fe, a new peak (blue) related to Fe-OEP arises at 399.2 eV. The final degree of metalation is 40%, according to the relative intensities of reacted and unreacted signal contributions.

The monolayer N 1s XP spectrum of the corrole in Figure 4b (bottom) shows a 1:1 peak ratio because of a surface-induced loss of one of the three −NH− hydrogen atoms. This surface reaction of free-base corroles has previously been observed[29] and is in agreement with the fact that free-base corroles show a much higher acidity (pK_a = 5.2) for the first deprotonation than related porphyrins (pK_a = 32.8).[46] The corrole monolayer is therefore described as 2H-HEDMC with two iminic (=N−, 398.4 eV) and two pyrrolic (−NH−, 400.0 eV) groups. Deposition of substoichiometric amounts of Fe (enough to achieve a metalation degree of 35%) results in the formation of a new peak (blue) at 399.1 eV, which is attributed to Fe-HEDMC formed in the monolayer. Apparently, the metalation does also proceed in the monolayer regime, similar to what has been observed in the multilayer.

To clarify the electronic state of the Fe centers in the monolayers of Fe-OEP and Fe-HEDMC, XPS measurements were performed. Analysis of the resulting Fe $2p_{3/2}$ spectra is, however, even more difficult than in the multilayer regime. As can be seen in Figure 5, the Fe 2p signal overlaps with the intense Ag 3s signal of the substrate, necessitating background subtraction that might induce systematic errors. The background-corrected spectra in Figure 5b reveal that the Fe $2p_{3/2}$ signals contain considerable contributions at a typical Fe(0) position, which is in contrast to the nominal +II or +III

DOI: 10.1021/acs.jpcc.8b00067
J. Phys. Chem. C 2018, 122, 10392−10399

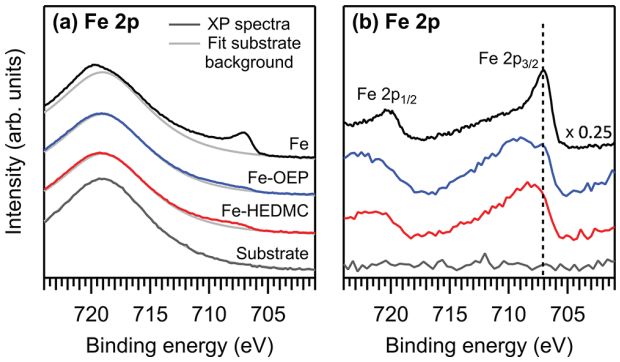

Figure 5. Fe 2p XP spectra ($h\nu$ = 1486.7 eV) of Fe-OEP and Fe-HEDMC submonolayers on Ag(111), obtained by partial metalation of the corresponding free-base monolayers. (a) Original spectra with fits of the substrate-related background (light gray lines), which is dominated by the Ag 3s signal, (b) background-corrected spectra in the same order. The differences between the Fe-OEP and Fe-HEDMC signals are not conclusive and require further measurements.

oxidation states. Similar shifts toward lower binding energies in the monolayer range have previously been reported for various transition-metal complexes of porphyrins and phthalocyanines on metal substrates. They are attributed to electron transfer from the substrate to the metal centers.[8,17,18] However, the differences between the spectra for Fe-OEP and Fe-HEDMC are *not* distinct enough to conclusively answer whether or not the metal centers in Fe-HEDMC are equally influenced by the Ag(111) substrate as in Fe-OEP.[34] To resolve this ambiguous situation, we employed NEXAFS (XANES), UPS, and STM. These methods reveal more distinct differences in the Fe electronic structure between Fe-OEP/Ag(111) and Fe-HEDMC/Ag(111).

To obtain more reliable information about the electronic states of iron in Fe-OEP and Fe-HEDMC molecules in the monolayer regime, Fe L-edges were recorded and analyzed (Figure 6). The degree of metalation was 40% for the porphyrin and 35% for the corrole. The curves show clear differences between Fe-OEP and Fe-HEDMC. They are particularly obvious in the background-corrected spectra, where Fe-HEDMC has a double-peak structure, with one peak at 709 eV and the other at 712 eV. Interestingly, such a double-peak structure has been observed for CH_2Cl_2···Fe(III)-

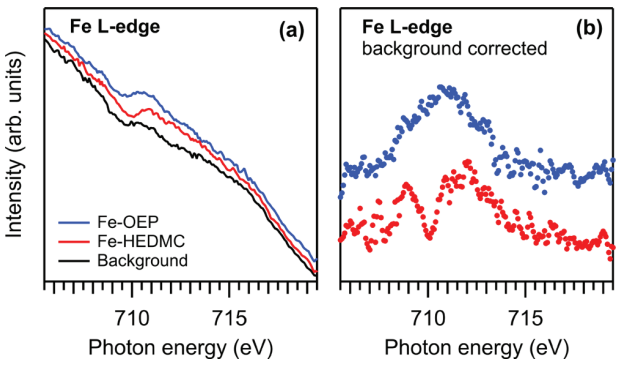

Figure 6. Fe L-edge NEXAFS spectra of Fe-OEP and Fe-HEDMC obtained by partial metalation of the corresponding free-base monolayers. (a) Original NEXAFS spectra, (b) after background correction.

OEP-Cl, i.e., for an Fe(III) porphyrin with a weakly bound ligand (CH_2Cl_2) at the Fe center.[40] Apparently, the Ag(111) surface has a similarly weak influence on the Fe center as the CH_2Cl_2 ligand. In contrast to Fe-HEDMC, the Fe-OEP monolayer does not show any fine structure in the L_3 absorption edge, a result in agreement to literature data from Fe-phthalocyanine monolayers on Ag(111).[19]

Further indications for differences in the electronic states of iron in Fe-OEP and Fe-HEDMC monolayers were found in the valence photoelectron spectra of the partially (30%) metalated layers, as shown in Figure 7. The Fe-OEP spectrum shows an

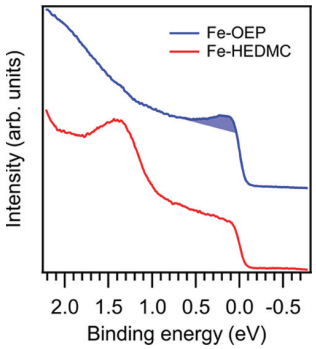

Figure 7. Normalized UPS spectra ($h\nu$ = 21.2 eV) of the valence region of the Fe-HEDMC (bottom) and Fe-OEP (top) monolayers on Ag(111). The additional intensity due to the interaction of the Fe(II) center in Fe-OEP with the Ag(111) substrate is highlighted. The peak at 1.4 eV in the spectrum of Fe-HEDMC is associated with the ligand but not with the metal center. See the text for details.

enhanced intensity in the vicinity of the Fermi edge, in agreement with previous work,[8,17,18] where this signal is associated with the electronic interaction between the formerly unoccupied Fe d-orbitals and the Ag(111) substrate.[47] In contrast, the valence spectrum of Fe-HEDMC on Ag(111) does not show the additional intensity near the Fermi edge. Instead, there is a signal at 1.4 eV binding energy, which is associated with the highest occupied molecular orbitals of the corrole ligand and is equally present in the spectrum of the unmetalated corrole, as shown in Figure S1 in the Supporting Information. Apparently, the iron-related valence electronic structure is significantly different in the Fe-OEP/Ag(111) and Fe-HEDMC/Ag(111) systems, and only the spectrum of Fe-OEP/Ag(111) shows clear evidence for a molecule−surface interaction.

Considering that Fe-OEP and Fe-HEDMC differ in the electronic valence states close to the Fermi energy (E_F), it appears likely that these molecules show different contrasts in STM images because the electronic states near E_F contribute significantly to tunneling probabilities.[48] For a direct comparison of the STM features, mixed submonolayers of free-base 2H-OEP and 3H-HEDMC were prepared and subsequently exposed to Fe.

Co-deposited OEP and HEDMC form (almost) homomolecular submonolayer domains, which are shown in Figure 8a. There are only small amounts of the respective other molecule in a domain. Subsequently deposited iron (0.06 ML, representing an excess of Fe with two times the stoichiometric amount for the metalation of one monolayer) either metalates the molecules in the monolayer or forms iron clusters, which are visible as bright spots in Figure 8a.

DOI: 10.1021/acs.jpcc.8b00067
J. Phys. Chem. C 2018, 122, 10392−10399

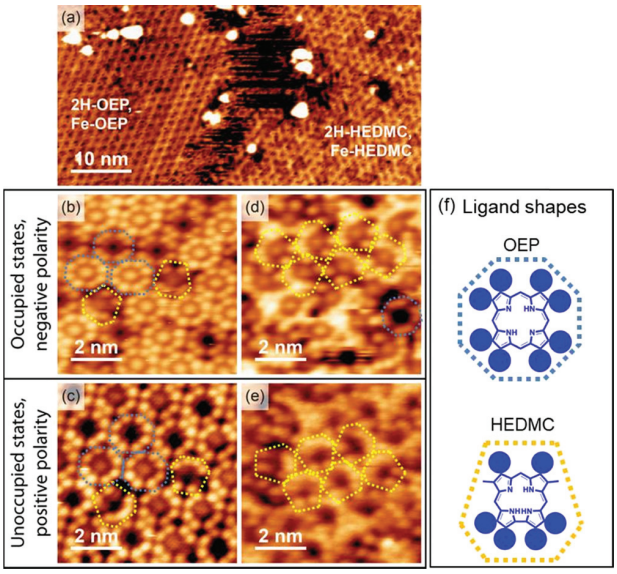

Figure 8. Overview STM image of a co-deposition experiment with (a) partially Fe-metalated OEP-rich (left side of image) and HEDMC-rich domains. The bright spots are Fe clusters which form on the surface. Details of OEP-rich (b,c) and HEDMC-rich domains (d,e) reveal rotational disorder in the HEDMC-rich domains, as well as the coexistence of metalated and unmetalated molecules. Imaging parameters: (a) 1.63 V, 0.08 nA; (b) −1.06 V, −0.05 nA; (c) 1.06 V, 0.10 nA; (d) −1.49 V, −0.07 nA; (e) 1.74 V, 0.11 nA. Dotted contour lines are added to help identify some of the individual molecules (blue lines for OEP and yellow lines for HEDMC). (f) Molecular models in which the ethyl groups are represented by blue spheres.

Both ligands, OEP and HEDMC, can easily be distinguished in the STM images by the number of ethyl groups, which appear as bright protrusions. OEP molecules exhibit eight ethyl groups which form a ringlike structure around the molecular center (Figure 8b,c). The HEDMC ligand (Figure 8d,e) contains six ethyl groups, of which four form an elongated group on one side of the molecule, while the other two appear as single protrusions on the other side. The rotational disorder of the HEDMC phase makes it difficult to identify individual molecules; one can, however, easily recognize individual HEDMC molecules within OEP domains, for example, the HEDMC molecules in the third and fourth molecular row in Figure 8b,c.

Metalated and unmetalated OEP molecules can easily be distinguished, because the iron atom in Fe-OEP leads to an additional bright protrusion in the center of the molecule for images taken at positive as well as negative polarities. In the case of negative polarity, this central protrusion is equally bright as the ethyl groups on the periphery of the molecule. In images at positive polarity, the central protrusion appears less bright than the ethyl groups.

Metalation influences the brightness of OEP molecules in an additional way: in images taken with negative polarity, the total brightness of Fe-OEP molecules is significantly larger than the brightness of 2H-OEP molecules. A similar phenomenon has been observed by Comanici and co-workers[48] for mixed monolayers of 2H-tetraphenylporphyrin (2H-TPP) and Co-tetraphenylporphyrin (Co-TPP). This effect was explained with differences in the occupied density of states (DOS) between 2H-TPP and Co-TPP. Noteworthy, metalated and unmetalated corroles show the same molecular brightness (in particular of the ethyl groups) as *unmetalated* porphyrins, if the occupied states close to the Fermi edge are probed in the STM images (Figure 8a). In strong contrast to the porphyrins, the effects described by Comanici and co-workers[48] do not appear for the corroles. This is further evidence that the electronic structures of the iron-corroles and iron-porphyrins are substantially different despite the proximity of the Ag(111) surface.

If recorded with a negative bias voltage (probing occupied states), metalated HEDMC and OEP ligands exhibit a bright metal center, as evident from a comparison of Figure 9a,c to

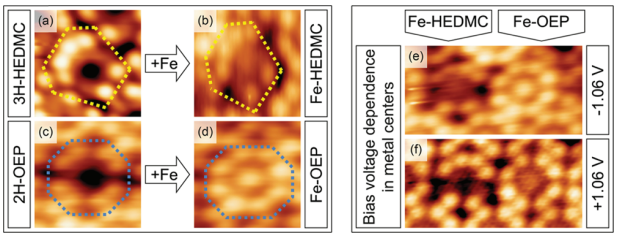

Figure 9. STM images of (a,c) unmetalated and (b,d,e,f) metalated HEDMC and OEP molecules. The molecules are indicated by dashed lines. The bias voltage dependence is shown in a co-deposition metalation experiment of Fe-HEDMC and Fe-OEP (e,f). Imaging parameters: (a) −1.58 V, −0.99 nA; (b) −1.06 V, −0.05 nA; (c) −1.06 V, −0.04 nA; (d) −1.06 V, −0.04 nA; (e) −1.06 V, −0.04 nA; (f) +1.06 V, +0.10 nA.

9b,d, respectively. However, changing the tunneling voltage to positive values influences the contrasts in Fe-OEP and Fe-HEDMC in a different manner. While the formal Fe(II) metal centers of the porphyrins turn darker, but remain visible, the formal Fe(III) metal centers of the corroles disappear. This is illustrated in Figure 9e,f, which show two neighboring Fe-HEDMC and Fe-OEP molecules imaged with negative and positive tunneling voltage. The contrast difference between Fe-HEDMC and Fe-OEP not only is specific for the selected pair of molecules but also occurs for the other metalated species in the layer, as can be seen in further overview images in the Supporting Information (Figure S2) and Figure 8.

The fact that the metal centers apparently disappear in images of the Fe-HEDMC molecules at positive tunneling voltages, but remain visible in Fe-OEP, may be directly explained by the valence electronic structure which is displayed in Figure 7. There, Fe-OEP does have an enhanced DOS right at the Fermi edge. Specifically, it appears that the Fermi edge intersects the peak that is associated with the molecule/surface interaction, dividing it into a part which is occupied by electrons and a part which remains unoccupied. Both occupied and unoccupied parts are visible in STM images with negative and positive tunneling voltages, respectively. In the case of Fe-HEDMC, there is no equivalent phenomenon; there is neither enhanced occupied DOS at E_F (Figure 7) nor is there DOS right above E_F contributing to tunneling at a positive bias. Apart from the invisible metal centers in Fe-HEDMC molecules, images based on tunneling into unoccupied states (positive polarity) show identical submolecular contrasts and apparent heights for all investigated systems (Figures 8c and 9f).

The STM images of mixed phases of metalated and unmetalated corroles and porphyrins confirm that the metalation reaction proceeds, as expected, also in the monolayer regime. They also provide evidence for significantly different

DOI: 10.1021/acs.jpcc.8b00067
J. Phys. Chem. C 2018, 122, 10392−10399

electronic structures of the Fe metal centers in corrole and porphyrin ligands around the Fermi edge. This agrees with the results from UPS, which show that the two Fe complexes differ in the Fe-related contributions to the DOS around the Fermi energy. Considering that the DOS of the d-electrons around the Fermi energy is known to correlate with the chemical reactivity and the catalytic activity of a surface,[49,50] it is expected that the observed differences in the electronic structure also lead to different chemical properties of the corresponding monolayers.

4. SUMMARY

Multilayers and monolayers of 3H-HEDMC on Ag(111) were metalated at room temperature by vapor-deposition of Fe atoms under UHV conditions. For comparison, analogous metalation experiments were performed with 2H-OEP. Investigations with photoelectron and X-ray absorption spectroscopies reveal that the reaction leads to the related metal complexes Fe-HEDMC and Fe-OEP. Detailed analysis of the spectroscopic data for the multilayer reveals that the Fe center in Fe-HEDMC has a formal Fe(III) oxidation state, which is different from the +II oxidation state of Fe in Fe-OEP. In the monolayers, differences in the electronic structures of the Fe centers persist, despite the interactions with the Ag(111) substrate. Analysis of Fe 2p XP spectra shows that for both complexes, Fe-HEDMC and Fe-OEP, the Fe $2p_{3/2}$ signals have contributions at an Fe(0) position. However, this does not mean that the electronic states of iron in Fe-HEDMC and Fe-OEP are equalized by the interaction with the substrate. Complementary UPS, NEXAFS, and STM measurements reveal that the electronic structures of iron differ significantly between Fe-HEDMC and Fe-OEP monolayers on Ag(111). The UPS spectra of Fe-OEP/Ag(111) show additional intensity, related to the presence of the formal Fe(II) center, around the Fermi energy (E_F). In contrast, the formal Fe(III) center of Fe-HEDMC/Ag(111) does not lead to enhanced intensity around E_F. Analysis of STM images of mixed monolayers of 2H-OEP, Fe-OEP, 2H-HEDMC, and Fe-HEDMC confirms that the coupling between the iron metal centers and the Ag(111) substrate strongly depends on the type of ligand. Related differences can be seen in the Fe L-edge NEXAFS spectra. Because the d-electron DOS around E_F correlates with the chemical reactivity of a surface, it is likely that monolayers of Fe-HEDMC and Fe-OEP on Ag(111) also differ significantly with respect to their chemical properties.

■ ASSOCIATED CONTENT

Supporting Information

The Supporting Information is available free of charge on the ACS Publications website at DOI: 10.1021/acs.jpcc.8b00067.

N 1s XPS binding energies of metalated and unmetalated corrole and porphyrin multilayers and monolayers; UPS spectra of metalated and unmetalated porphyrin and corrole monolayers; STM images of a mixed 2H-OEP, Fe-OEP, 2H-HEDMC, and Fe-HEDMC monolayer with an overlaid grid (to illustrate the adsorption sites within the monolayer); and synthesis of the 3H-HEDMC ligand (PDF)

■ AUTHOR INFORMATION

Corresponding Author

*E-mail: schmidm5@staff.uni-marburg.de. Phone: (+49) 6421-2822543.

ORCID

Martin Schmid: 0000-0002-1686-241X

J. Michael Gottfried: 0000-0001-5579-2568

Notes

The authors declare no competing financial interest.

■ ACKNOWLEDGMENTS

Financial support by the Deutsche Forschungsgemeinschaft (DFG) through the SFB 1083 "Structure and Dynamics of Internal Interfaces" and grant INST 160/606-1 FUGG is gratefully acknowledged. We thank the Helmholtz-Zentrum Berlin for allocation of synchrotron radiation beamtime at BESSY II. M.S. thanks the Stiftung Stipendien-Fonds des Verbandes der Chemischen Industrie for funding.

■ REFERENCES

(1) Barth, J. V. Molecular Architectonic on Metal Surfaces. *Annu. Rev. Phys. Chem.* **2007**, *58*, 375−407.

(2) Barth, J. V. Fresh Perspectives for Surface Coordination Chemistry. *Surf. Sci.* **2009**, *603*, 1533−1541.

(3) Marbach, H. Surface-Mediated in Situ Metalation of Porphyrins at the Solid-Vacuum Interface. *Acc. Chem. Res.* **2015**, *48*, 2649−2658.

(4) Diller, K.; Papageorgiou, A. C.; Klappenberger, F.; Allegretti, F.; Barth, J. V.; Auwärter, W. In Vacuo Interfacial Tetrapyrrole Metallation. *Chem. Soc. Rev.* **2016**, *45*, 1629−1656.

(5) Gottfried, J. M.; Flechtner, K.; Kretschmann, A.; Lukasczyk, T.; Steinrück, H.-P. Direct Synthesis of a Metalloporphyrin Complex on a Surface. *J. Am. Chem. Soc.* **2006**, *128*, 5644−5645.

(6) Shubina, T. E.; Marbach, H.; Flechtner, K.; Kretschmann, A.; Jux, N.; Buchner, F.; Steinrück, H.-P.; Clark, T.; Gottfried, J. M. Principle and Mechanism of Direct Porphyrin Metalation: Joint Experimental and Theoretical Investigation. *J. Am. Chem. Soc.* **2007**, *129*, 9476−9483.

(7) Gottfried, M.; Marbach, H. Surface-Confined Coordination Chemistry with Porphyrins and Phthalocyanines: Aspects of Formation, Electronic Structure, and Reactivity. *Z. Phys. Chem.* **2009**, *223*, 53−74.

(8) Gottfried, J. M. Surface Chemistry of Porphyrins and Phthalocyanines. *Surf. Sci. Rep.* **2015**, *70*, 259−379.

(9) Auwärter, W.; Écija, D.; Klappenberger, F.; Barth, J. V. Porphyrins at Interfaces. *Nat. Chem.* **2015**, *7*, 105−120.

(10) Bhattarai, A.; Marchbanks-Owens, K.; Mazur, U.; Hipps, K. W. Influence of the Central Metal Ion on the Desorption Kinetics of a Porphyrin from the Solution/HOPG Interface. *J. Phys. Chem. C* **2016**, *120*, 18140−18150.

(11) Buchner, F.; Schwald, V.; Comanici, K.; Steinrück, H.-P.; Marbach, H. Microscopic Evidence of the Metalation of a Free-Base Porphyrin Monolayer with Iron. *ChemPhysChem* **2007**, *8*, 241−243.

(12) Buchner, F.; Flechtner, K.; Bai, Y.; Zillner, E.; Kellner, I.; Steinrück, H.-P.; Marbach, H.; Gottfried, J. M. Coordination of Iron Atoms by Tetraphenylporphyrin Monolayers and Multilayers on Ag(111) and Formation of Iron-Tetraphenylporphyrin. *J. Phys. Chem. C* **2008**, *112*, 15458−15465.

(13) Duncan, D. A.; Deimel, P. S.; Wiengarten, A.; Han, R.; Acres, R. G.; Auwärter, W.; Feulner, P.; Papageorgiou, A. C.; Allegretti, F.; Barth, J. V. Immobilised Molecular Catalysts and the Role of the Supporting Metal Substrate. *Chem. Commun.* **2015**, *51*, 9483−9486.

(14) Goldoni, A.; Pignedoli, C. A.; Di Santo, G.; Castellarin-Cudia, C.; Magnano, E.; Bondino, F.; Verdini, A.; Passerone, D. Room Temperature Metalation of 2H-TPP Monolayer on Iron and Nickel Surfaces by Picking up Substrate Metal Atoms. *ACS Nano* **2012**, *6*, 10800−10807.

(15) Eguchi, K.; Nakagawa, T.; Takagi, Y.; Yokoyama, T. Direct Synthesis of Vanadium Phthalocyanine and Its Electronic and Magnetic States in Monolayers and Multilayers on Ag(111). *J. Phys. Chem. C* **2015**, *119*, 9805−9815.
(16) Hong, I.-P.; Li, N.; Zhang, Y.-J.; Wang, H.; Song, H.-J.; Bai, M.-L.; Zhou, X.; Li, J.-L.; Gu, G.-C.; Zhang, X.; et al. Vacuum Synthesis of Magnetic Aluminum Phthalocyanine on Au(111). *Chem. Commun.* **2016**, *52*, 10338−10341.
(17) Hieringer, W.; Flechtner, K.; Kretschmann, A.; Seufert, K.; Auwärter, W.; Barth, J. V.; Görling, A.; Steinrück, H.-P.; Gottfried, J. M. The Surface Trans Effect: Influence of Axial Ligands on the Surface Chemical Bonds of Adsorbed Metalloporphyrins. *J. Am. Chem. Soc.* **2011**, *133*, 6206−6222.
(18) Peisert, H.; Uihlein, J.; Petraki, F.; Chassé, T. Charge Transfer between Transition Metal Phthalocyanines and Metal Substrates: The Role of the Transition Metal. *J. Electron Spectrosc. Relat. Phenom.* **2015**, *204*, 49−60.
(19) Petraki, F.; Peisert, H.; Aygül, U.; Latteyer, F.; Uihlein, J.; Vollmer, A.; Chassé, T. Electronic Structure of FePc and Interface Properties on Ag(111) and Au(100). *J. Phys. Chem. C* **2012**, *116*, 11110−11116.
(20) Erben, C.; Will, S.; Kadish, K. M. Metallocorroles: Molecular Structure, Spectroscopy and Electronic States. In *The Porphyrin Handbook Vol. 2*; Kadish, K. M., Smith, K. M., Guilard, R., Eds.; Academic Press: San Diego, 2000; Vol. 7, pp 235−300.
(21) Aviv, I.; Gross, Z. Corrole-Based Applications. *Chem. Commun.* **2007**, 1987−1999.
(22) Aviv-Harel, I.; Gross, Z. Coordination Chemistry of Corroles with Focus on Main Group Elements. *Coord. Chem. Rev.* **2011**, *255*, 717−736.
(23) Aviv-Harel, I.; Gross, Z. Aura of Corroles. *Chem.—Eur. J.* **2009**, *15*, 8382−8394.
(24) Aviv, I.; Gross, Z. Iron(III) Corroles and Porphyrins as Superior Catalysts for the Reactions of Diazoacetates with Nitrogen- or Sulfur-Containing Nucleophilic Substrates: Synthetic Uses and Mechanistic Insights. *Chem.—Eur. J.* **2008**, *14*, 3995−4005.
(25) Mahammed, A.; Gross, Z. Iron and Manganese Corroles Are Potent Catalysts for the Decomposition of Peroxynitrite. *Angew. Chem., Int. Ed.* **2006**, *45*, 6544−6547.
(26) Haber, A.; Angel, I.; Mahammed, A.; Gross, Z. Combating Diabetes Complications by 1-Fe, a Corrole-Based Catalytic Antioxidant. *J. Diabetes Complicat.* **2013**, *27*, 316−321.
(27) Röckert, M.; Franke, M.; Tariq, Q.; Lungerich, D.; Jux, N.; Stark, M.; Kaftan, A.; Ditze, S.; Marbach, H.; Laurin, M.; et al. Insights in Reaction Mechanistics: Isotopic Exchange During the Metalation of Deuterated Tetraphenyl-21,23D-Porphyrin on Cu(111). *J. Phys. Chem. C* **2014**, *118*, 26729−26736.
(28) Rabinovich, E.; Goldberg, I.; Gross, Z. Gold(I) and Gold(III) Corroles. *Chem.—Eur. J.* **2011**, *17*, 12294−12301.
(29) Tebi, S.; Paszkiewicz, M.; Aldahhak, H.; Allegretti, F.; Gonglach, S.; Haas, M.; Waser, M.; Deimel, P. S.; Aguilar, P. C.; Zhang, Y.-Q.; et al. On-Surface Site-Selective Cyclization of Corrole Radicals. *ACS Nano* **2017**, *11*, 3383−3391.
(30) Stöhr, J. *NEXAFS Spectroscopy*; Springer-Verlag Berlin Heidelberg, 1996.
(31) Horcas, I.; Fernández, R.; Gómez-Rodríguez, J. M.; Colchero, J.; Gómez-Herrero, J.; Baro, A. M. WSxM: A Software for Scanning Probe Microscopy and a Tool for Nanotechnology. *Rev. Sci. Instrum.* **2007**, *78*, 013705.
(32) Chen, M.; Zhou, H.; Klein, B. P.; Zugermeier, M.; Krug, C. K.; Drescher, H. J.; Gorgoi, M.; Schmid, M.; Gottfried, J. M. Formation of an Interphase Layer During Deposition of Cobalt onto Tetraphenylporphyrin: A Hard X-Ray Photoelectron Spectroscopy (HAXPES) Study. *Phys. Chem. Chem. Phys.* **2016**, *18*, 30643−30651.
(33) Karweik, D. H.; Winograd, N. Nitrogen Charge-Distributions in Free-Base Porphyrins, Metalloporphyrins, and Their Reduced Analogs Observed by X-Ray Photoelectron-Spectroscopy. *Inorg. Chem.* **1976**, *15*, 2336−2342.
(34) Borghetti, P.; Di Santo, G.; Castellarin-Cudia, C.; Fanetti, M.; Sangaletti, L.; Magnano, E.; Bondino, F.; Goldoni, A. Adsorption Geometry, Conformation, and Electronic Structure of 2H-Octaethylporphyrin on Ag(111) and Fe Metalation in Ultra High Vacuum. *J. Chem. Phys.* **2013**, *138*, 144702.
(35) Gross, Z. High-Valent Corrole Metal Complexes. *J. Biol. Inorg Chem.* **2001**, *6*, 733−738.
(36) Meier-Callahan, A. E.; Gray, H. B.; Gross, Z. Stabilization of High-Valent Metals by Corroles: Oxo[Tris(Pentafluorophenyl)-Corrolato]Chromium(V). *Inorg. Chem.* **2000**, *39*, 3605−3607.
(37) Ivanova, T.; Naumkin, A.; Sidorov, A.; Eremenko, I.; Kiskin, M. X-Ray Photoelectron Spectra and Electron Structure of Polynuclear Cobalt Complexes. *J. Electron Spectrosc. Relat. Phenom.* **2007**, *156−158*, 200−203.
(38) Schmid, M.; Zirzlmeier, J.; Steinrück, H.-P.; Gottfried, J. M. Interfacial Interactions of Iron(II) Tetrapyrrole Complexes on Au(111). *J. Phys. Chem. C* **2011**, *115*, 17028−17035.
(39) Dees, A.; Jux, N.; Tröppner, O.; Dürr, K.; Lippert, R.; Schmid, M.; Küstner, B.; Schlücker, S.; Steinrück, H.-P.; Gottfried, J. M.; et al. Reactions of Superoxide with Iron Porphyrins in the Bulk and the Near-Surface Region of Ionic Liquids. *Inorg. Chem.* **2015**, *54*, 6862−6872.
(40) Xiao, J.; Golnak, R.; Atak, K.; Pflüger, M.; Pohl, M.; Suljoti, E.; Winter, B.; Aziz, E. F. Assistance of the Iron Porphyrin Ligands to the Binding Interaction between the Fe Center and Small Molecules in Solution. *J. Phys. Chem. B* **2014**, *118*, 9371−9377.
(41) Petraki, F.; Peisert, H.; Latteyer, F.; Aygül, U.; Vollmer, A.; Chassé, T. Impact of the 3d Electronic States of Cobalt and Manganese Phthalocyanines on the Electronic Structure at the Interface to Ag(111). *J. Phys. Chem. C* **2011**, *115*, 21334−21340.
(42) Balle, D.; Adler, H.; Grüninger, P.; Karstens, R.; Ovsyannikov, R.; Giangrisostomi, E.; Chassé, T.; Peisert, H. Influence of the Fluorination of CoPc on the Interfacial Electronic Structure of the Coordinated Metal Ion. *J. Phys. Chem. C* **2017**, *121*, 18564−18574.
(43) Deimel, P. S.; Bababrik, R. M.; Wang, B.; Blowey, P. J.; Rochford, L. A.; Thakur, P. K.; Lee, T.-L.; Bocquet, M.-L.; Barth, J. V.; Woodruff, D. P.; et al. Direct Quantitative Identification of the "Surface Trans-Effect". *Chem. Sci.* **2016**, *7*, 5647−5656.
(44) Bai, Y.; Buchner, F.; Kellner, I.; Schmid, M.; Vollnhals, F.; Steinrück, H.-P.; Marbach, H.; Gottfried, J. M. Adsorption of Cobalt (II) Octaethylporphyrin and 2H-Octaethylporphyrin on Ag(111): New Insight into the Surface Coordinative Bond. *New J. Phys.* **2009**, *11*, 125004.
(45) Bai, Y. *Photoelectron Spectroscopic Investigations of Porphyrins and Phthalocyanines on Ag(111) and Au(111): Adsorption and Reactivity*; Friedrich-Alexander Universität Erlangen-Nürnberg, 2010.
(46) Mahammed, A.; Weaver, J. J.; Gray, H. B.; Abdelas, M.; Gross, Z. How Acidic Are Corroles and Why? *Tetrahedron Lett.* **2003**, *44*, 2077−2079.
(47) Buchner, F.; Warnick, K.-G.; Wölfle, T.; Görling, A.; Steinrück, H.-P.; Hieringer, W.; Marbach, H. Chemical Fingerprints of Large Organic Molecules in Scanning Tunneling Microscopy: Imaging Adsorbate-Substrate Coupling of Metalloporphyrins. *J. Phys. Chem. C* **2009**, *113*, 16450−16457.
(48) Comanici, K.; Buchner, F.; Flechtner, K.; Lukasczyk, T.; Gottfried, J. M.; Steinrück, H.-P.; Marbach, H. Understanding the Contrast Mechanism in Scanning Tunneling Microscopy (STM) Images of an Intermixed Tetraphenylporphyrin Layer on Ag(111). *Langmuir* **2008**, *24*, 1897−1901.
(49) Hammer, B.; Norskov, J. K. Why Gold Is the Noblest of All the Metals. *Nature* **1995**, *376*, 238−240.
(50) Tong, Y. Y.; Renouprez, A. J.; Martin, G. A.; van der Klink, J. J. Electron Availability and the Surface Fermi Level Local Density of States: An Alternative Way to See Catalytic Activity of Metals. *Stud. Surf. Sci. Catal.* **1996**, *101*, 901−910.

P7

DOI: 10.1021/acs.jpcc.8b00067
J. Phys. Chem. C 2018, 122, 10392−10399

Supporting Information for:

On-Surface Synthesis and Characterization of an Iron Corrole

Martin Schmid[a], Malte Zugermeier[a], Jan Herritsch[a], Benedikt P. Klein[a], Claudio K. Krug[a], Lukas Ruppenthal[a], Philipp Müller[a], Michael Kothe[b], Peter Schweyen[c], Martin Bröring[c], J. Michael Gottfried[a]

[a] Philipps-Universität Marburg, Fachbereich Chemie, Hans-Meerwein-Str. 4, 35032 Marburg
[b] Philipps-Universität Marburg, Fachbereich Physik, Renthof 7, 35032 Marburg
[c] Technische Universität Braunschweig, Institut für Anorganische und Analytische Chemie, Hagenring 30, 38106 Braunschweig

P7

Corresponding author:

Dr. Martin Schmid

E-Mail: schmidm5@staff.uni-marburg.de
Tel.: (+49) 6421 – 2822543

1. Synthesis of 3H-HEDMC

1,19-Didesoxy-2,3,8,12,17,18-hexaethyl-9,13-dimethylbiladiene dihydrobromide[S1] (2.00 g, 3.03 mmol) and tetrachloro-*p*-benzoquinone (1.12 g, 4.55 mmol) are stirred in methanol (650 mL) for 5 min. Potassium bicarbonate (2.28 g, 22.7 mmol) is then added in one portion, and the mixture is stirred until the color changes to blue-violet and a solid forms. Hydrazine hydrate (1.5 mL) is added to quench the reaction, and the dark precipitate is then filtered and washed with methanol and water. Recrystallization of the dark residue from dichloromethane/methanol 1:1 yields the corrole as a pink, crystalline solid, in a yield of 76% (1.14 g, 2.31 mmol).

^{1}H-NMR (300 MHz, CD_2Cl_2): δ = 9.35 (*s*, 2H, *meso-H*), 9.13 (*s*, 1H, *meso-H*), 4.00 (*q*, *J* = 7.57 Hz, 4H, 2 x C*H*$_2$CH$_3$), 3.90-3.83 (*m*, 8H, C*H*$_2$CH$_3$), 3.42 (*s*, 6H, C*H*$_3$), 1.80-1.72 (*m*, 18H, CH$_2$C*H*$_3$).

^{13}C-NMR (75 MHz, CD_2Cl_2)*:* δ = 142.9, 140.4, 138.4, 134.3, 133.4, 130.4, 129.3, 124.0, 93.1, 88.2, 20.7, 19.9, 19.6, 18.2, 17.8, 17.2, 11.2.

P7

UV/VIS (CH_2Cl_2) λ_{max} (ε): 593 (23600), 549 (18500), 536 (18700), 396 (127100), 282, (20100), 227 (32100).

MS (EI): *m/z* = 494 [M^+].

HRMS (EI): calc. for $C_{33}H_{42}N_4$ ([M^+]): 494.3410; found: 494.3416.

[S1] Johnson, A. W.; Kay, I. T., Corroles. Part I. Synthesis. *J. Chem. Soc. C* **1965**, 1620-1629.

2. X-ray Photoelectron Spectroscopy

	N 1s (-NH-)	N 1s (=N-)	N 1s (Fe-N)
2H-OEP (multilayer)	400.4	398.3	-
Fe-OEP (multilayer)	400.4	398.4	399.4
2H-OEP (monolayer)	400.4	398.7	-
Fe-OEP (monolayer)	400.5	398.8	399.2
3H-HEDMC (multilayer)	400.1	398.1	-
Fe-HEDMC (multilayer)	400.3	398.2	399.3
2H-HEDMC (monolayer)	400.0	398.4	-
Fe-HEDMC (monolayer)	400.0	398.5	399.1

Table S1. XPS binding energies of 2H-OEP, Fe-OEP, 3H-HEDMC, and Fe-HEDMC multilayers as well as 2H-OEP, Fe-OEP, 2H-HEDMC, and Fe-HEDMC monolayers. The binding energy scale was calibrated with the C1s binding energy at 285.4 eV.

3. UV Photoelectron Spectroscopy

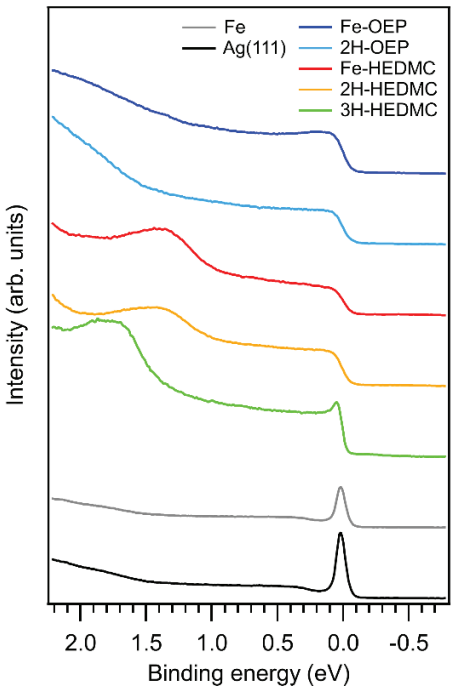

Figure S1. Normalized UV photoelectron spectra (hν = 21.2 eV) of the valence region of the free-base and iron metalated corrole and porphyrin layers on Ag(111). Spectra of the clean Ag(111) and Fe on the substrate are shown for comparison.

4. Scanning Tunneling Microscopy

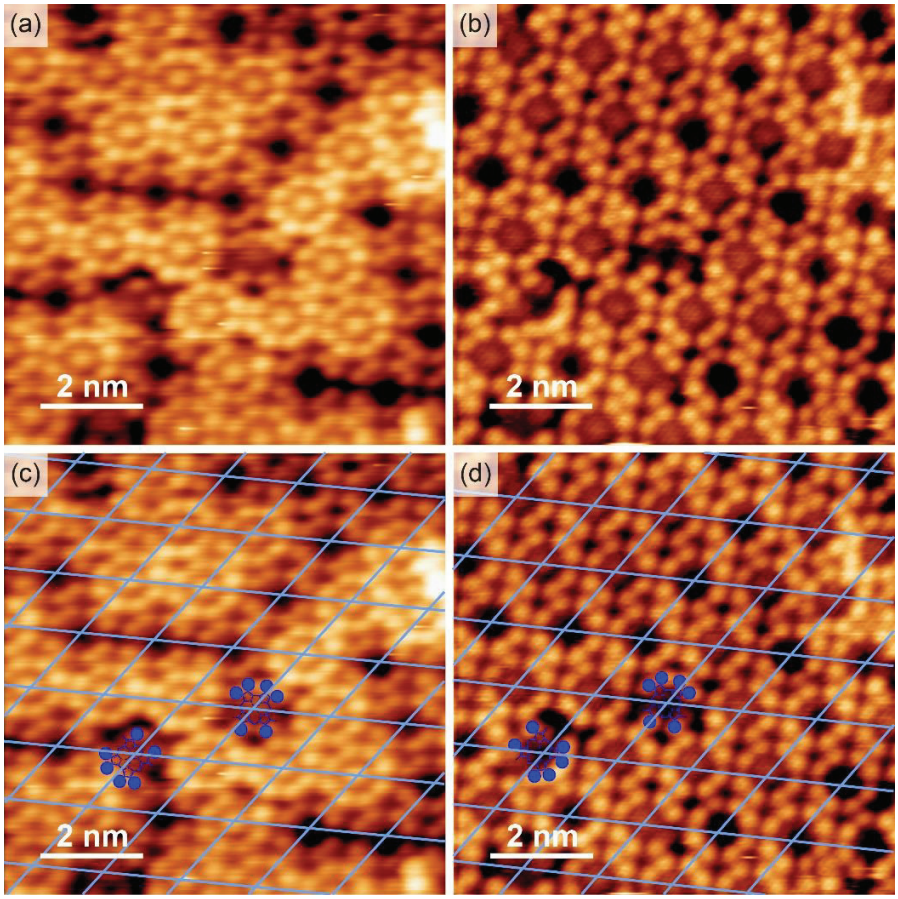

Figure S2. STM image of a mixed layer of iron metalated OEP and HEDMC molecules at (a) negative and (b) positive tunneling voltage. The two Fe-HEDMC molecules show protrusions at negative voltage and dark centers at positive voltage. Imaging parameters (a) -1.06 V, -0.04 nA; (b) +1.06 V, +0.10 nA. (c) and (d) show the same images with molecular models of Fe-HEDMC and an overlaid grid to illustrate the regularity of the adsorption sites.

P8 Molecular Topology and the Surface Chemical Bond: Alternant Versus Nonalternant Aromatic Systems as Functional Structural Elements

Citation: B. P. Klein, N. J. van der Heijden, S. R. Kachel, M. Franke, **C. K. Krug**, K. K. Greulich, L. Ruppenthal, P. Müller, P. Rosenow, S. Parhizkar, F. C. Bocquet, M. Schmid, W. Hieringer, R. J. Maurer, R. Tonner, C. Kumpf, I. Swart, J. M. Gottfried, *Phys. Rev. X* **2019**, *9*(1), 011030, DOI 10.1103/physrevx.9.011030.

Summary

In this publication the adsorption and desorption of the non-alternant polycyclic aromatic hydrocarbon (PAH) azulene on Cu(111) is compared with its alternant counterpart naphthalene. For this purpose a multi-technique approach is used. It is found that azulene interacts much more strongly with Cu(111) than naphthalene.

The adsorption heights of the two molecules are determined by the normal incidence X-ray standing wave (NI-XSW) technique and azulene is found to adsorb with a distance of 2.30 Å to Cu(111), whereas this value is 3.04 Å for naphthalene. The difference in the adsorption height can be seen as an indication for a stronger interaction of azulene with the surface than for naphthalene. This finding is substantiated by temperature-programmed desorption (TPD) experiments, which show a higher desorption temperature for azulene than for naphthalene. The zero-coverage desorption energy for azulene of 179 kJ/mol is also much higher than for naphthalene with 103 kJ/mol.

The electronic structure of azulene and naphthalene on Cu(111) in the multilayer and in the monolayer is investigated with X-ray photoelectron spectroscopy (XPS), ultraviolet photoelectron spectroscopy (UPS), and near-edge X-ray absorption fine structure (NEXAFS) spectroscopy. XPS and NEXAFS spectroscopy show much stronger differences in the monolayer spectra compared with the multilayer spectra for azulene than for naphthalene. This is further substantiated by the UPS data, which show a higher intensity between the Cu d band and the Fermi edge for azulene.

The adsorbate structure of azulene on Cu(111) is investigated using scanning tunneling microscopy (STM) and non-contact atomic force microscopy (nc-AFM). A commensurate $(2\sqrt{3} \times 2\sqrt{3})$-R30° superstructure is found. Furthermore, STM images at negative bias voltage strongly resemble the LUMO of

azulene, indicating electron transfer from the substrate to the molecule. The adsorption height and molecular deformation are determined using nc-AFM. Here, azulene is found to adsorb closer to the surface and to show a stronger deformation than naphthalene.

All the data are accompanied by extensive theoretical studies, which are in line with the experimental findings and further prove the much stronger interaction of azulene with the Cu(111) surface compared with naphthalene. While naphthalene can be considered as purely physisorbed the strong interactions of azulene can be attributed to the formation of a chemical bond. As a last point, azulene is used as a molecular model system for 5-7 defects in graphene. Periodic density functional theory (DFT) calculations of the defect structure show charge accumulation at the five-membered and depletion at the seven-membered ring, and new electronic states in the density of states (DOS) arise near the Fermi edge due to the presence of the defect.

Own Contribution

The project leading to this publication was conceived by Prof. Dr. J. Michael Gottfried and started by Dr. Benedikt P. Klein and me with DFT calculations of azulene and naphthalene on the Ag(111) surface under the supervision of Prof. Dr. Ralf Tonner (not included in the article). Regarding the data shown in the publication I performed the STM measurements with the combined STM and XPS setup in the laboratory of the Gottfried group in Marburg (*cf.* Section 3.4.1). Furthermore, I was part of the experimentalist team, who performed UPS experiments at the LowDosePES end-station of the PM4 beamline (*cf.* Section 3.4.3) at the synchrotron radiation facility BESSY II in Berlin during a beamtime together with Dr. Benedikt P. Klein, Katharina K. Greulich and Lukas Ruppenthal. Dr. Benedikt P. Klein wrote the manuscript and all co-authors contributed to its discussion.

Molecular Topology and the Surface Chemical Bond: Alternant Versus Nonalternant Aromatic Systems as Functional Structural Elements

Benedikt P. Klein,[1] Nadine J. van der Heijden,[2] Stefan R. Kachel,[1] Markus Franke,[3] Claudio K. Krug,[1] Katharina K. Greulich,[1] Lukas Ruppenthal,[1] Philipp Müller,[1] Phil Rosenow,[1] Shayan Parhizkar,[3] François C. Bocquet,[3] Martin Schmid,[1] Wolfgang Hieringer,[4] Reinhard J. Maurer,[5] Ralf Tonner,[1] Christian Kumpf,[3] Ingmar Swart,[2] and J. Michael Gottfried[1,*]

[1]*Philipps-Universität Marburg, Fachbereich Chemie, Hans-Meerwein-Straße 4, 35032 Marburg, Germany*
[2]*Condensed Matter and Interfaces, Debye Institute for Nanomaterials Science, Utrecht University, P.O. Box 80000, 3508 TA Utrecht, The Netherlands*
[3]*Peter Grünberg Institut (PGI-3), Forschungszentrum Jülich, 52425 Jülich, Germany and Jülich Aachen Research Alliance (JARA), Fundamentals of Future Information Technology, 52425 Jülich, Germany*
[4]*Lehrstuhl für Theoretische Chemie, Universität Erlangen-Nürnberg, Egerlandstraße 3, 91058 Erlangen, Germany*
[5]*Department of Chemistry and Centre for Scientific Computing, University of Warwick, Gibbet Hill Road, Coventry, CV4 7AL, United Kingdom*

(Received 15 August 2018; revised manuscript received 22 November 2018; published 13 February 2019)

The interaction of carbon-based aromatic molecules and nanostructures with metals can strongly depend on the topology of their π-electron systems. This is shown with a model system using the isomers azulene, which has a nonalternant π system with a 5-7 ring structure, and naphthalene, which has an alternant π system with a 6-6 ring structure. We found that azulene can interact much more strongly with metal surfaces. On copper (111), its zero-coverage desorption energy is 1.86 eV, compared to 1.07 eV for naphthalene. The different bond strengths are reflected in the adsorption heights, which are 2.30 Å for azulene and 3.04 Å for naphthalene, as measured by the normal incidence x-ray standing wave technique. These differences in the surface chemical bond are related to the electronic structure of the molecular π systems. Azulene has a low-lying LUMO that is close to the Fermi energy of Cu and strongly hybridizes with electronic states of the surface, as is shown by photoemission, near-edge x-ray absorption fine-structure, and scanning tunneling microscopy data in combination with theoretical analysis. According to density functional theory calculations, electron donation from the surface into the molecular LUMO leads to negative charging and deformation of the adsorbed azulene. Noncontact atomic force microscopy confirms the deformation, while Kelvin probe force microscopy maps show that adsorbed azulene partially retains its in-plane dipole. In contrast, naphthalene experiences only minor adsorption-induced changes of its electronic and geometric structure. Our results indicate that the electronic properties of metal-organic interfaces, as they occur in organic (opto)electronic devices, can be tuned through modifications of the π topology of the molecular organic semiconductor, especially by introducing 5-7 ring pairs as functional structural elements.

DOI: 10.1103/PhysRevX.9.011030

Subject Areas: Chemical Physics, Condensed Matter Physics, Materials Science

P8

I. INTRODUCTION

Carbon-based materials with aromatic π-electron systems, such as π-conjugated molecular solids [1,2], polymers [3,4], and low-dimensional nanostructures [5,6], have attracted considerable attention as organic semiconductors [7–9]. A crucial aspect for the application of these materials in (opto) electronic devices is their interface formation with metal surfaces at the contacting electrodes. The electronic properties of the resulting metal-organic interfaces determine important performance parameters such as charge carrier injection rates [10,11]. Precise control over various interface properties, especially the wave-function overlap and the energy-level alignment, is therefore critical for the rational improvement of organic electronic devices [12].

*michael.gottfried@chemie.uni-marburg.de

The properties of a π-electron system are largely determined by its topology, i.e., the connectivity pattern as expressed through the topological matrix in the Hückel molecular orbital (HMO) theory [13]. Most organic semiconductors have carbon backbones with alternant topology because they consists of six-membered rings [1,7]. Only very recently has increased interest in so-called *nonalternant* aromatic structures [14] arisen in the field of graphene nanoribbons [15], nanographenes [16], and polycyclic aromatic hydrocarbons [17,18]. These nonalternant structures often contain linked 5- and 7-membered rings. It has been recognized that their unique electronic structure makes nonalternant aromatic systems highly interesting as novel (opto)electronic semiconductor materials for organic field-effect transistors (OFET) and photovoltaic cells (OPVC) [19,20]. Nonalternant structural elements also occur in graphene in the form of 5-7 defects [21,22]. Theoretical studies have predicted that various properties of graphene depend on the presence of these nonalternant structural elements, including electron transport properties [23,24], mechanical stability [25,26], magnetism [27], and chemical reactivity [28].

While interfaces between metals and alternant organic semiconductor materials have been widely studied [29–33], up until now it has not been known how the surface chemical bond is influenced by nonalternant structural elements. To address this fundamental question, we perform a direct comparison between two isomeric aromatic molecules on a Cu(111) surface. One of these isomers, azulene, is a prototypical nonalternant aromatic system with a 5-7 ring structure, while naphthalene, with its 6-6 ring structure, serves as its alternant counterpart (Fig. 1). Some previous work exists for naphthalene on Cu(111) [34–38] but not for azulene. Copper was chosen as a model substrate because of its frequent use for the epitaxial growth of graphene [39–41] or the on-surface synthesis of carbon-based nanostructures [42].

Below, we show that the topology of the molecular π system drastically influences its electronic interaction with a metal surface. It is therefore proposed that the incorporation of nonalternant structural elements in molecular semiconductors can be used to control and to optimize performance-related properties of functional metal-organic interfaces. Recent achievements in the synthesis on novel, structurally complex, nonalternant, aromatic molecules [16,19,20,43] show that this is a feasible and promising approach.

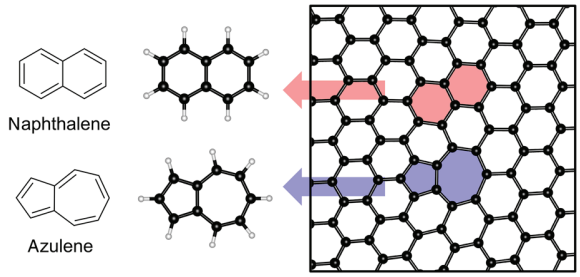

FIG. 1. Right, graphene lattice with an embedded nonalternant 5-7 defect, highlighted in blue. If this structural element is cut out of graphene and terminated with hydrogen atoms, the resulting molecule is azulene, shown on the left. Its isomer naphthalene serves as the complementary model system for the regular, alternant 6-6 structure, highlighted in red.

For a quantitative comparison of the adsorbate-metal bonds of aromatic 5-7 and 6-6 carbon skeletons, we determine the adsorbate-substrate bond distances with the normal incidence x-ray standing wave (NIXSW) technique and noncontact atomic force microscopy (nc-AFM), while adsorbate-substrate bond energies are measured by temperature-programmed desorption (TPD). The electronic structures are analyzed by x-ray and UV photoelectron spectroscopy (XPS/UPS) in combination with near-edge x-ray absorption fine-structure (NEXAFS) measurements. Complemented by dispersion-corrected density functional theory (DFT) calculations, our results provide a detailed understanding of the surface chemical bond and its dependence on the π topology.

II. METHODS

A. Experimental methods

The interaction of azulene and naphthalene with Cu(111) was studied under ultrahigh vacuum (UHV) conditions. Azulene (Sigma-Aldrich, purity $> 99.0\%$) and naphthalene (Sigma-Aldrich, purity $> 99.7\%$) were introduced into the vacuum systems through leak valves after initial pump-freeze-thaw cycles of the reservoirs. A polished Cu(111) single-crystal surface (purity $> 99.9999\%$, roughness < 0.03 μm, orientation accuracy $< 0.1°$, from MaTecK/Germany) was prepared by iterated sputtering with Ar^+ ions (0.5–1 keV, 5–15 μA, 30 min) and annealing (800–830 K, 15 min). Surface cleanliness and structure were confirmed by XPS, low energy electron diffraction, and scanning tunneling microscopy (STM). Sample temperatures were measured with a type K thermocouple directly mounted to the Cu single crystal. Coverages are given in monolayers (ML). The coverage was determined by a consistent routine using XPS, nc-AFM, and TPD measurements. For a detailed description, see the Supplemental Material [44].

NIXSW measurements were performed at the undulator beam line I-09 at Diamond Light Source in Didcot, UK, using a VG Scienta EW4000 HAXPES hemispherical electron analyzer for photoelectron detection, which is mounted at 90° with respect to the incident x-ray beam. Nondipolar effects were neglected in the data analysis, which was performed using the software package Torricelli [45]. The sample temperature was approximately 150 K, which led to a Bragg energy of 2980 eV for the Cu(111) lattice planes.

TPD measurements were carried out with a HIDEN EPIC 1000 mass spectrometer mounted inside a differentially pumped cryoshroud cooled to 80 K with l-N_2. This

P8

setup is a variant of line-of-sight mass spectrometry [46] and ensures that molecules hitting the inner wall of the cryoshroud stick there, such that the mass spectrometer detects only molecules with a straight trajectory between sample and detector. This leads to improved quality of the TPD traces and is the basis for their quantitative analysis.

XPS was performed with monochromatic Al-K_α radiation using a SPECS XR 50 M x-ray anode, a FOCUS 500 monochromator, and a PHOIBOS 150 electron energy analyzer equipped with an MCD-9 multichanneltron detector. Work functions were measured with He-I radiation from a UVS 10/35 gas discharge lamp. UPS was performed at the PM4 dipole beam line with the LowDosePES end station at the synchrotron radiation facility BESSY II (Helmholtz-Zentrum Berlin) using a Scienta ArTOF angle-resolved time-of-flight spectrometer. A photon energy of 16.5 eV was used.

NEXAFS spectroscopy was also performed at BESSY II using the HE-SGM dipole beam line, which provides linearly polarized radiation with a polarization factor of 0.91 and an energy resolution of 300 meV at the carbon K-edge. The partial electron-yield (PEY) mode was used with a retarding field of −150 V and a channeltron detector voltage of 2.2 keV. Further information on the data treatment can be found in the Supplemental Material [44].

For variable-temperature scanning tunneling microscopy (VT-STM), a SPECS 150 Aarhus STM with SPC 260 electronics was used. VT-STM measurements were performed at a sample temperature of 150 K using an etched tungsten tip conditioned by initial Ar^+ sputtering and pulsing. The reported bias voltages refer to the sample. The STM images were recorded in constant-current mode and were processed with WSxM v5.0 D8.4 [47] by carefully using flatten and plane tools, scale adjustment, and slightly filtering with a Gaussian filter.

The nc-AFM images were taken with an Omicron NanoTechnology LT-STM/AFM with a commercially available qPlus sensor, operating at approximately 4.6 K in UHV with an average pressure of 5×10^{-10} mbar. The baked qPlus sensor (3 h at 120 °C) had a quality factor of $Q \approx 30\,000$, a resonance frequency of $f_0 = 21\,922$ Hz, and a peak-to-peak oscillation amplitude of less than 1 Å. Tip conditioning was accomplished with controlled crashes into the copper surface and bias pulses until the STM resolution was satisfactory. The tip apex was functionalized with a CO molecule. The AFM was operated in constant-height mode, and AFM images show the frequency shift (Δf) with respect to the resonance frequency. During the AFM scan, the tunneling current was also measured, which gives a constant-height STM scan.

B. Density functional theory calculations

Periodic density functional theory calculations of azulene and naphthalene on Cu(111) were performed with the Vienna *Ab Initio* Simulation Package (VASP) [48–51]. The PBE functional [52] was used in combination with the third-generation van der Waals dispersion correction by Grimme (DFT-D3) [53] and the projector-augmented wave (PAW) ansatz [54,55] for the atomic cores. Further details can be found in the Supplemental Material [44].

XP and x-ray absorption spectra were calculated using the pseudopotential plane-wave code CASTEP-17.1 [56]. For the XPS chemical shifts, the delta self-consistent field (DeltaSCF) method of constraining electronic occupations to resemble full core-hole excitations was used. NEXAFS simulations were performed using on-the-fly generated USPPs and the CASTEP module ELNES [57] and the transition-potential approach [58,59]. For more details on the computational settings, analysis, and implementation, see the Supplemental Material [44] and Diller *et al.* [60] as well as Maurer and Reuter [61]. Furthermore, the Supplemental Material [44] contains additional NEXAFS simulations obtained by a more approximate method.

III. RESULTS

A. Adsorbate-substrate bond distances (adsorption heights)

The vertical distance of an adsorbed molecule from the surface is an important parameter for the quantitative characterization of the adsorbate-substrate bond. To measure the adsorption heights of azulene and naphthalene over the Cu(111) surface [Fig. 2(a)], we used the NIXSW technique. This method utilizes the standing x-ray wave field generated by a crystalline substrate when near-normal incidence x rays undergo Bragg diffraction on a set of lattice planes $H = (hkl)$ with a distance of d^H [62]. The standing wave field can be vertically shifted by $d^H/2$ by scanning the photon energy E through the Bragg energy [62].

At any certain adsorption height, the photon field intensity will therefore change in a characteristic way during such a scan. Hence, one expects characteristic x-ray absorption profiles for different adsorption heights since the atomic absorption is proportional to the local photon intensity. By recording the photoelectron yield of any core level of this species, which is (within the dipole approximation) proportional to the atomic absorption, one can measure the x-ray absorption profile at the position of the adsorbate atom and obtain the height D^H of this atomic species relative to the substrate diffraction plane locations. The variation of the atomic absorption $I(E)$ can be calculated with dynamical diffraction theory and follows the equation

$$I(E) = 1 + R + 2\sqrt{R} \cdot F^H \cdot \cos(\Phi + 2\pi \cdot P^H), \quad (1)$$

where $R = R(E)$ is the reflectivity and $\Phi = \Phi(E)$ is the phase of the standing wave field [63,64].

Data analysis on the basis of Eq. (1) provides the coherent position P^H and the coherent fraction F^H. The coherent position P^H equals D^H modulo d^H, i.e., $D^H/d^H = n + P^H$ ($n = 0, 1, 2\ldots$) In the case of single-site adsorption,

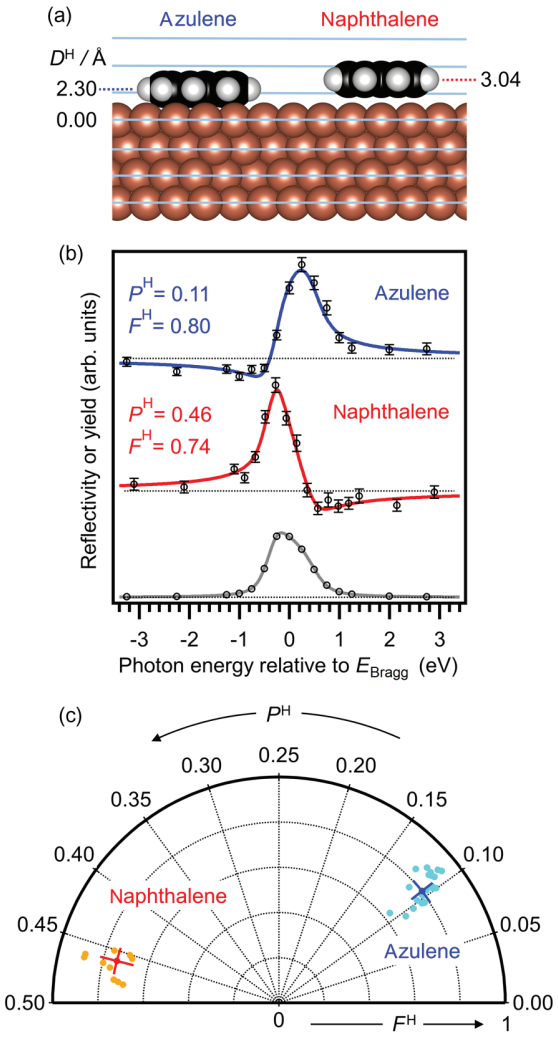

FIG. 2. Adsorption heights from NIXSW measurements for azulene and naphthalene on Cu(111), coverage 1 ML. (a) Space-filling adsorbate models with the heights true to scale as obtained from NIXSW. (b) C 1s photoelectron yields for azulene (top) and naphthalene (center) along with the x-ray reflectivity $R(E)$ (bottom) as a function of the photon energy around the Bragg energy E_{Bragg}. The yield data are shown as open circles (with error bars); the solid blue and red lines are fits with Eq. (1). (c) Argand diagram with the results of the individual measurements in light colors and the averaged value in bold colors, with error bars.

i.e., when each atomic species occupies only one adsorption height (this is the relevant case for the systems discussed here), F^H is a measure for the scattering of the real heights around the coherent position. A coherent fraction of $F^H = 1$ means that all contributing atoms have exactly the same height D^H, whereas a fraction of $F^H = 0$ means that they have a random height distribution. Note that the latter is not necessarily true if (at least) two clearly different adsorption heights occur. In this case, averaging of coherent positions and fractions has to be performed in an Argand vector diagram [62–65].

For our systems, we used the background corrected total intensity of the C 1s spectral region to obtain the photoelectron yield curve for each individual NIXSW scan. A typical yield curve is shown in Fig. 2(b). A distinction between the different carbon atoms within one molecule was not possible because the core level shifts were too small compared to the available energy resolution. Note that we have not performed any correction for nondipolar parameters in our analysis since the NIXSW data were recorded close to grazing emission geometry (90° between incident x-ray beam and the analyzer). In this geometry, nondipolar effects are minimal.

The results of the analysis are summarized in the Argand diagram in Fig. 2(c). The coherent position for azulene at monolayer coverage is $P^H = 0.11 \pm 0.01$, which yields an adsorption height of $D^H = 2.30 \pm 0.03$ Å. This number was derived using $d^H = 2.08$ Å for the Cu(111) surface at the measurement temperature of 150 K. The corresponding coherent fraction of $F^H = 0.80 \pm 0.06$ is in a typical range for a rather homogeneous contribution of the adsorption heights. For the naphthalene monolayer, the analysis gives a coherent position of $P^H = 0.46 \pm 0.01$, from which an adsorption height of 3.04 ± 0.03 Å is obtained. The coherent fraction is similar, with $F^H = 0.74 \pm 0.08$.

Comparison of these values [see also Fig. 2(a)] reveals a much lower adsorption height for azulene. A shorter adsorbate-substrate bond distance typically indicates a stronger bond [66], which agrees with the higher desorption energy of azulene as discussed below. The adsorption height for naphthalene is quite similar to the sum of the van der Waals radii of a carbon and a copper atom (3.10 Å) [67]. In contrast, the adsorption height of azulene, 2.30 Å, is closer to known organometallic carbon-copper bond lengths of approximately 2.10 Å [67]. All these considerations lead to the conclusion that naphthalene engages only in dispersive interaction with the Cu(111) surface, whereas azulene forms a chemical bond.

NIXSW as a laterally integrating technique averages over a large number of molecules. Later, we present nc-AFM data that qualitatively confirm the height difference between azulene and naphthalene on the single-molecule level.

B. Adsorbate-substrate bond energies

Another quantitative parameter describing the strength of the adsorbate-substrate interactions is the activation energy for desorption, which can be derived from temperature-programmed desorption (TPD) data [68–70]. At low submonolayer coverages, the TPD traces of both molecules are governed by first-order desorption kinetics [Figs. 3(a) and 3(b)]. As can be seen, the low-coverage desorption maxima occur at 520 K for azulene and at 340 K for naphthalene. Qualitatively, this large temperature difference shows that the adsorbate-substrate interaction is substantially higher for the 5-7 isomer.

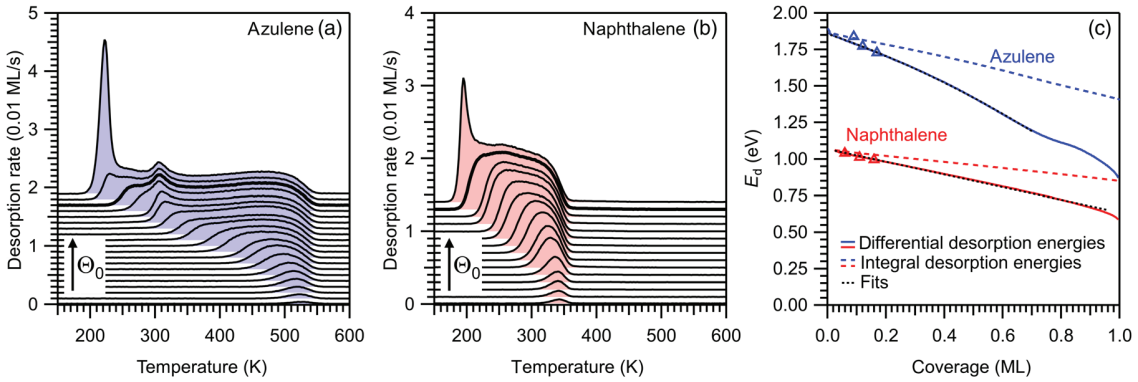

FIG. 3. TPD traces of (a) azulene and (b) naphthalene on Cu(111), with a heating rate 1.0 K/s. Curves with different initial coverage Θ_0 are shifted along the vertical axis for clarity, but we start with a zero desorption rate in each case. The monolayer coverages are marked by bold lines. The other initial coverages are listed in Tables S II in the Supplemental Material [44]. (c) Desorption activation energies as a function of coverage for azulene (blue) and naphthalene (red). Solid lines: Differential desorption energies. Dashed lines: Integral energies for comparison with DFT calculations. Black dotted lines: Fits of the differential desorption energies with the equations mentioned in the text. Triangles: Energies from HRV analysis. Note that HRV is only possible at low coverages, where the peaks have a regular first-order shape.

With increasing coverage, the TPD traces of both molecules broaden towards lower temperatures. The effect, which is attributed to lateral intermolecular repulsion, is more pronounced for azulene. Its monolayer TPD trace reaches a width of 330 K, compared to 180 K for naphthalene (bold lines). Lateral intermolecular repulsion in adsorbates on metal surfaces is usually dominated by a dipole-dipole interaction between vertical dipoles created by electron transfer between molecules and surface, as well as by the pillow (or pushback) effect. This effect is caused by Pauli repulsion between the electrons in the molecule and those in the metal [71–74]. Apparently, these effects play a larger role for azulene than for naphthalene. The vertical dipole moments are also related to the adsorbate-induced work-function change. We show below that azulene causes a larger work-function change than naphthalene, in line with the stronger lateral repulsion of the former.

The high-coverage TPD traces of azulene show an additional desorption maximum at 300 K, which is attributed to a compressed phase occurring close to monolayer saturation (above 0.7 ML). This phase can also be observed in the nc-AFM images discussed below. Above monolayer coverage, narrow second-layer peaks occur at 220 K (azulene) and 190 K (naphthalene).

Quantitative analysis of the TPD spectra gives access to the desorption activation energy E_d as a measure of the adsorbate-substrate bond energy [68–70]. The most rigorous analyses, the so-called complete methods [75,76], are not suitable here because of the strong lateral repulsion [70]. Instead, we use an alternative approach, which provides the coverage-dependent desorption energy from a single TPD trace [70,77]. The resulting curves for azulene and naphthalene are shown in Fig. 3(c) (solid lines). The desorption energies in the zero-coverage limit, E_d^0, are 1.86 eV for azulene and 1.07 eV for naphthalene. This confirms that azulene forms a much stronger bond to the metal surface than naphthalene. While both curves show a substantial decrease of E_d with increasing coverage as a result of the lateral repulsion, the effect is more pronounced for azulene. In the case of naphthalene, E_d decreases nearly linearly with coverage following the equation $E_d = (1.07 - 0.44\Theta)$ eV, where Θ is in units of monolayers. In contrast, the desorption energy of azulene is well described by the second-order polynomial $E_d = (1.86 - 0.67\Theta - 0.40\Theta^2)$ eV for coverages up to 0.75 ML. Figure 3(c) also shows the integral desorption energies necessary for comparison with DFT results (dashed lines).

The desorption prefactors used for the analysis are determined by heating rate variation (HRV) analysis [68], which is only meaningful for the regular first-order peaks in the low-coverage range. The related data are presented in the Supplemental Material [44]. For the respective coverages, the HRV analysis also provides the desorption energies [triangles in Fig. 3(c)], which agree well with the other data.

C. Occupied electronic states: Photoelectron spectroscopy

The very different adsorption energies and heights of azulene and naphthalene are expected to correspond to characteristic differences in the electronic structure. First, we focus on the molecules in a thick multilayer, i.e., without the influence of the metal surface. The multilayer C 1s XP spectra of azulene and naphthalene are compared in Fig. 4(a). The C 1s signal of azulene has a broader shape with a distinct shoulder at the low binding energy side. This shape can be understood by theoretical modeling. For this aim, we calculate the relative peak positions for the different carbon atoms in the molecule by DFT. The details of the calculation and the theoretical modeling can be found in the Supplemental Material [44]. The results are in agreement with previously reported values [78]. While these calculations are performed for the isolated molecules, this

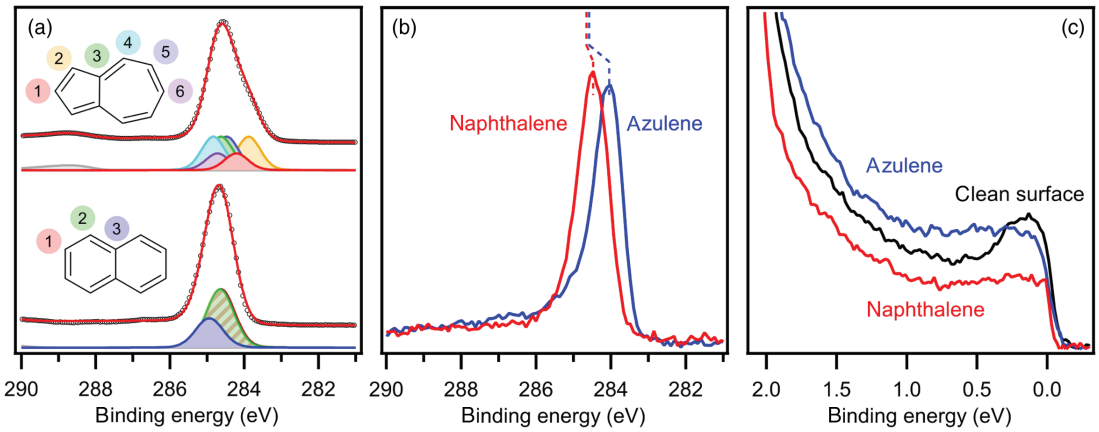

FIG. 4. Photoelectron spectra: (a) Multilayer C 1s XP spectra of azulene and naphthalene, compared with a theoretical model based on DFT calculations. Black circles are experimental data; red lines are fitted results from DFT-based model calculations. The colors of the component peaks correspond to the colors of the labels on the molecular formulas. The shake-up satellite of azulene is shown in grey. (b) C 1s XP spectra of monolayers of azulene and naphthalene on Cu(111). The dotted lines indicate the shifts relative to the multilayer peak positions. (c) UP spectra of azulene and naphthalene monolayers and of the clean Cu(111) surface, taken with a photon energy of 16.5 eV.

simplification appears to be justified considering that the intermolecular interactions in the multilayer are relatively weak and thus have only little influence on the electronic energies and transitions. The resulting theoretical model agrees well with the experimental data for azulene. It further reveals that the shoulder at low binding energies is associated with the five-membered ring. For naphthalene, the calculations of the C 1s spectrum are performed in the same way and confirm the narrower peak shape of the experimental spectrum. In the azulene multilayer spectrum [Fig. 4(a)], a shake-up satellite at 289 eV is shown in grey. The corresponding satellite for naphthalene appears above 290 eV and is thus not visible in this plot. However, it can be seen in an extended plot in Fig. S3 of the Supplemental Material [44].

In the monolayer, the differences between the XP spectra of azulene and naphthalene are even more pronounced. As can be seen in Fig. 4(b), the naphthalene signal is shifted by only −0.2 eV relative to its multilayer position and is only slightly asymmetric. In contrast, the azulene peak shifts by −0.5 eV and develops a strong asymmetry. The asymmetric peak shape is attributed to the interaction of the C 1s core hole with electron density close to the Fermi edge [79]. This is an indication for a distinctly different electronic valence structure of azulene compared to naphthalene when adsorbed on Cu(111). In an initial-state picture, the shift of the C 1s signal of azulene towards lower binding energies suggests a transfer of negative charge from the surface to the molecule. Further evidence for a negative charging of the molecule will be presented below. In addition, the closer distance of the azulene molecule to the surface will likely cause increased final-state screening, which would also lead to a shift to lower binding energy.

Synchrotron-based valence photoelectron spectroscopy (PES) was used for the direct probing of the occupied valence electronic structure. In the PE spectra, the molecular states already occupied in the free molecules cannot be identified because they have binding energies above 2 eV and thus are obscured by the d-band of the substrate. Nevertheless, the important changes in the valence electronic structure close to the Fermi edge are quite visible [Fig. 4(c)]. For azulene/Cu(111), the entire range between the Cu d-band and the Fermi edge experiences a massive rise in intensity with a broad maximum around 0.3–0.4 eV. In contrast, naphthalene only causes attenuation of the region between 0 and 2 eV, including the surface state. The occurrence of broad, adsorbate-related features for azulene, but not for naphthalene, is consistent with the calculated densities of states, as will be discussed later.

Adsorbate-induced work-function changes were extracted from He-I UPS data and show that both azulene and naphthalene lower the work function of the Cu(111) surface. The change is larger for azulene with −1.07 eV than for naphthalene with −0.73 eV, both at full monolayer coverage. Apparently, azulene causes a larger vertical surface dipole upon adsorption than naphthalene, in agreement with the stronger intermolecular repulsion of azulene observed in TPD. The negative sign of the work-function change indicates that the pillow effect is dominant and overcompensates for any contributions by the charge transfer from the surface to the molecule.

D. Unoccupied electronic states: NEXAFS

Information about the unoccupied valence electronic structure of the adsorbed molecules is obtained from carbon K-edge NEXAFS spectra. Multilayers of both molecules show a distinct set of π^* and σ^* resonances, which are well reproduced by the theoretical calculations, as shown in Fig. 5.

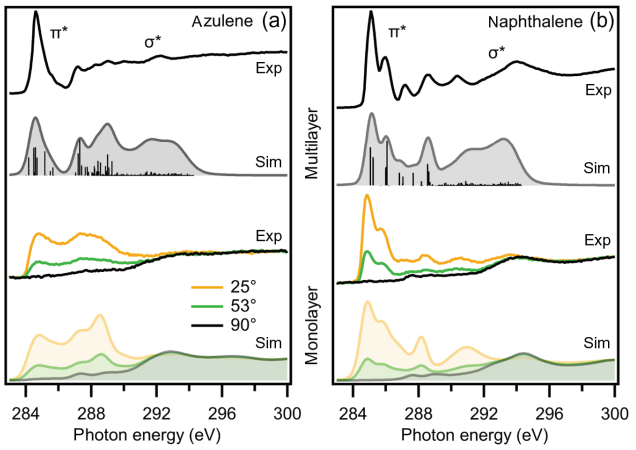

FIG. 5. Experimental carbon K-edge NEXAFS spectra and corresponding DFT simulations for (a) azulene and (b) naphthalene. Upper part: Multilayer spectra and simulations for the free molecule. The multilayer spectra were taken with the electric field vector oriented 90° relative to the surface normal. Lower part: Monolayer spectra and simulations for different angles of the electric field vector relative to the surface normal as indicated. The simulations for the free molecules are displayed both as isolated excitations and after broadening; the simulations for the monolayers are only shown in broadened form. For the broadening, each excitation is represented by a pseudo-Voigt peak with an increasing width and Lorentzian contribution at higher photon energies. The simulated spectra were shifted by −6.1 eV to match the experimental data.

In the monolayer spectra, the π^* resonances disappear when the electric field vector of the incident x rays is parallel to the surface (i.e., 90° relative to the surface normal). This shows that the molecular planes are parallel to the surface for both azulene and naphthalene.

In the case of naphthalene, the monolayer spectrum taken with the electric field vector oriented 25° relative to the surface normal closely resembles the multilayer spectrum; only a slight signal broadening is visible. This result confirms that the unoccupied valence electronic states of naphthalene are only weakly influenced by the metal surface.

For azulene, however, the shape of the π^* resonance is very different in the monolayer and multilayer spectra. The narrow π^* peak in the multilayer spectrum, resulting from the excitation into the LUMO and LUMO+1 of the azulene molecule, turns into a very broad monolayer feature, which is lower in intensity and covers a broad range of 5 eV. For both systems, the NEXAFS spectra are correctly reproduced by DFT-based transition potential simulations, which are discussed in detail later. A simpler approach for simulating NEXAFS spectra based only on ground-state properties can be found in the Supplemental Material [44].

E. Geometric structure: Scanning probe microscopies

Local information about the bonding situation of azulene as the model 5-7 structural element is obtained by scanning probe microscopies. These methods also provide valuable input for the DFT calculations discussed further below because there is no information in the literature about the adsorbate structure of azulene on Cu(111), in stark contrast to naphthalene [34–36,38,80]. In the low submonolayer range, azulene avoids the formation of ordered islands, in line with the strong lateral repulsion seen in TPD. Corresponding submonolayer STM and nc-AFM images are shown in Fig. S4 of the Supplemental Material [44]. When the coverage is increased, azulene eventually forms a long-range-ordered, commensurate $(2\sqrt{3}\times 2\sqrt{3})$-R30° superstructure [Fig. 6(a)]. This structure does not represent the saturated monolayer but has a coverage of only 0.65 ML. (Note that 1 ML is defined here as the coverage in the saturated monolayer as determined by TPD.) Upon deposition of additional molecules onto this commensurate structure, the molecules are even more closely packed but lose the long-range order. This case is illustrated in the nc-AFM image in Fig. 6(b), which still shows one unit cell of the commensurate $(2\sqrt{3}\times 2\sqrt{3})$-R30° structure in the image center. The molecules surrounding this unit cell, however, are more densely packed and break the translational symmetry.

Formation of a commensurate phase, which is followed by a more densely packed, incommensurate phase without long-range order at full monolayer coverage, has previously been found for other organic molecules with lateral intermolecular repulsion and preference of a certain adsorption

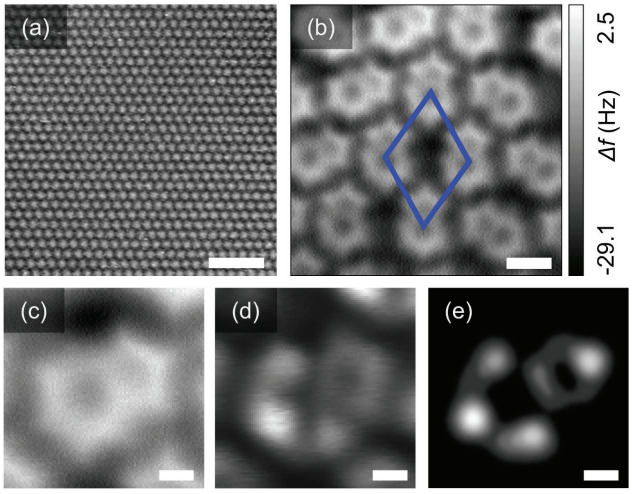

FIG. 6. STM and nc-AFM images of azulene on Cu(111). (a) Large-scale STM image of azulene on Cu(111), commensurate $(2\sqrt{3}\times 2\sqrt{3})$-R30° structure (0.65 ML), $I_t = -0.06$ nA $U_t = -1.28$ V, scale bar = 5 nm. (b) nc-AFM image of azulene on Cu(111), partially compressed phase (total coverage 0.78 ML), with an overlaid unit cell of the $(2\sqrt{3}\times 2\sqrt{3})$-R30° structure, scale bar = 0.5 nm. Note the disordered structure with higher density around the central unit cell of the commensurate structure. (c) nc-AFM image of an azulene molecule, (d) corresponding STM constant-height image, (e) DFT Tersoff-Hamann simulation of azulene adsorbed on Cu(111) within an energy range of 0 to 0.1 V below E_F. Scale bar for (c-e) = 0.1 nm.

site, such as porphine on Ag(111) [81]. The transition from the compressed quasidisordered phase to the commensurate $(2\sqrt{3} \times 2\sqrt{3})$-R30° phase during desorption is associated with the small maximum around 300 K in the TPD curve [Fig. 3(a)].

In the nc-AFM images, the two rings of the azulene molecule can clearly be distinguished, and thus its azimuthal orientation on the surface can be determined. In the $(2\sqrt{3} \times 2\sqrt{3})$-R30° unit cell, all molecules point along the $[1\bar{1}0]$ direction (and symmetry equivalent directions) of the substrate.

During the nc-AFM scans, naphthalene showed a higher tendency for tip-induced lateral displacements, whereas azulene was more resistant to accidental manipulation and only occasionally showed rotation by a 60° angle. Example images for both phenomena are shown in Figs. S5 and S6 of the Supplemental Material [44]. The reduced susceptibility of azulene for tip-induced displacement probably also means that it has a higher barrier for spontaneous diffusion.

In Figs. 6(c)–6(e), we compare an nc-AFM image of an adsorbed azulene molecule with the corresponding constant-height STM scan and with a DFT Tersoff-Hamann simulation [82]. The nc-AFM image in Fig. 6(c) shows the molecular structure with the five- and seven-membered rings. The STM current map in Fig. 6(d) was taken during the nc-AFM scan with negative sample bias (i.e., with electrons flowing from the sample to the tip) and shows well-defined features with lobes and nodes. Considering the bias voltage, these features must be attributed to an occupied state of the adsorbed azulene. They are well reproduced by a Tersoff-Hamann simulation using the DFT density of states (DOS) in the energy range from 0 to 0.1 eV below the Fermi energy [Fig. 6(e)]. The shape of this occupied state closely resembles that of the LUMO of the free molecule, as will be discussed in more detail below.

The difference in adsorption height between azulene and naphthalene as found by NIXSW was also measured on the single-molecule level by comparing the positions of the minima of frequency shift distance, i.e., $\Delta f(z)$ curves [83]. The inset of Fig. 7(a) shows a STM image of codeposited azulene and naphthalene molecules. Naphthalene appears as a single bright white feature, whereas azulene is imaged as a two-segmented grey shape. The vertical and lateral position at which the feedback loop was interrupted is the same for both molecules (above the metal, the STM set point of $V = 100$ mV and $I = 10$ pA corresponds to $z = 0$ Å). The minimum z_{min} in the $\Delta f(z)$ curve for azulene occurs 0.92 ± 0.08 Å closer to the substrate than for naphthalene. This difference is highly reproducible for different tip terminations and molecules. Considering the margins of error, this value is only slightly larger than the difference in the NIXSW heights of 0.74 ± 0.06 Å. The deviation between NIXSW and AFM values is possibly a temperature-related effect or due to small influences of the AFM tip.

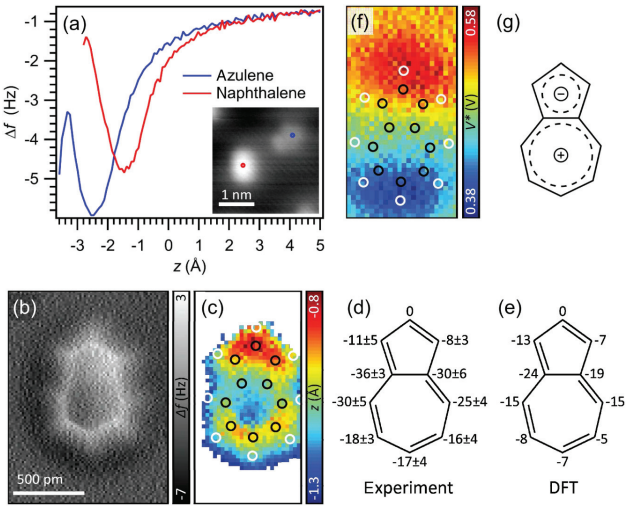

FIG. 7. (a) $\Delta f(z)$ spectra over azulene and naphthalene molecules illustrating the difference in z_{min}, which is indicative of the difference in adsorption height. The inset is an STM image, where the blue and red dots indicate the positions at which the $\Delta f(z)$ spectra were taken. The STM image was acquired with $I_t = 10$ pA at $U_t = 100$ mV. (b) Constant-height nc-AFM image of a single azulene molecule at −180 pm w.r.t. an STM set-point of 10 pA at 100 mV. (c) z_{min} map of azulene, overlaid with carbon (black) and hydrogen (white) atom positions. (d) Experimentally obtained z_{min} height of all C atoms with respect to the C atom at the apex of the 5-membered ring, in pm. (e) z_{min} heights of all C atoms with respect to the nose-C atom calculated by DFT, in pm. (f) KPFM map of a single azulene molecule, overlaid with carbon (black) and hydrogen (white) atom positions. (g) Model of the azulene molecule indicating the direction of the dipole moment.

The AFM-based height measurements also reveal a substantial adsorption-induced deformation of the azulene molecule. Figure 7(b) shows a constant-height nc-AFM image of azulene, in which the 5-7-ring structure is clearly resolved. The corresponding Fig. 7(c) shows a map with the lateral variation of z_{min}, indicating that the apices of the 5- and 7-membered rings are located farther away from the surface than the C—C bond that joins the two rings. This V-shaped adsorption geometry is later confirmed by DFT calculations [Figs. 7(e) and 8]. A detailed comparison of the relative heights as extracted from the AFM experiments and DFT calculations is given in Figs. 7(d) and 7(e). The value for the atom with the highest position is set to zero. Both in the experiment and in theory, one long side of the molecule is located somewhat closer to the surface than the other. These results demonstrate that AFM can be used to detect vertical relaxations in single molecules in the range of a few pm.

The free azulene molecule has a considerable in-plane dipole moment of 0.8 D [67]. To establish whether azulene adsorbed on Cu(111) still has an in-plane dipole moment, we performed Kelvin probe force microscopy (KPFM) experiments [83–85]. The maps extracted from these experiments show how the local contact potential

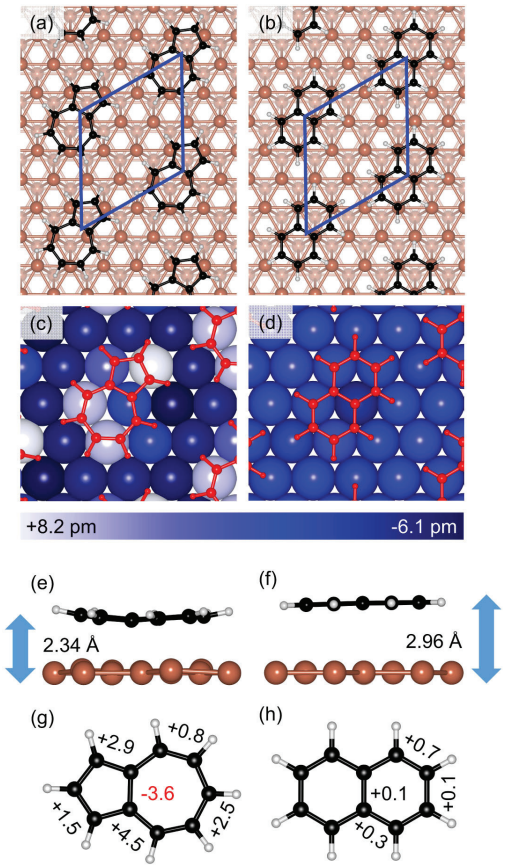

FIG. 8. Structural data for azulene and naphthalene on Cu(111) from dispersion-corrected DFT-D3 calculations. (a,b) Top view of the optimized $(2\sqrt{3}\times 2\sqrt{3})$-R30° structure. The most favorable adsorption site for both molecules is hcp-hcp. (c,d) Vertical displacements (in pm) of the copper atoms in the topmost layer, compared to the relaxed surface without a molecule. Positive values mean a displacement towards the molecule. (e,f) Side view of the molecule in the optimized $(2\sqrt{3}\times 2\sqrt{3})$-R30° structure. Azulene shows a large distortion and is much closer to the surface than naphthalene (average adsorption height 2.34 Å vs 2.96 Å). (g,h) Changes of the in-plane bond lengths relative to the gas phase structure (in pm).

P8

difference varies. This quantity is related to the electrostatic potential above the sample [84]. The KPFM maps presented here are obtained from finding the maximum (V^*) of $\Delta f(V)$ curves extracted from a set of constant-height AFM images at increasing bias [85]. Figure 7(f) presents a V^* map of a single azulene molecule. The V^* for the 5-membered ring is about +0.52 V, while for the 7-membered ring, it is +0.42 V. The value of V^* represents the voltage needed to minimize the electrostatic interaction between the tip and the molecule. Above the 5-membered (7-membered) ring, a larger (smaller) positive voltage is needed to compensate for the presence of the negative (positive) charge. From the V^* data shown in Fig. 7(f), it is evident that the adsorbed molecule has an in-plane dipole along the long molecular axis, pointing from the 5- to the 7-membered ring. The magnitude of the retained dipole moment cannot be extracted from such experiments [86].

F. Theoretical analysis

For additional insight into the surface chemical bond of azulene and naphthalene, dispersion-corrected periodic density functional theory calculations (DFT-D3) [53] were performed for the ordered $(2\sqrt{3}\times 2\sqrt{3})$-R30° structure, which was found in the STM images of azulene/Cu(111) [Fig. 6(a)]. This structure is not observed for naphthalene/Cu(111), but as the $(2\sqrt{3}\times 3)$-Rect structure known in the literature has the same coverage, it is also used here for better comparability [34,36]. For both molecules, the same preferential adsorption site is found. In this geometry, the molecules adsorb with each ring above an hcp hollow site, as shown in Figs. 8(a) and 8(b). This result is in agreement with the nc-AFM data, which show that the molecules are aligned along a principal direction of the surface, which is also the case with this adsorption site.

Closer inspection of the adsorbate geometries reveals that the azulene molecule and the top layer of the surface undergo substantial adsorption-induced deformations. The surface copper atoms in the unit cell differ in height by up to 0.14 Å, as is visualized in Fig. 8(c). For comparison, naphthalene does not cause any significant deformation of the surface [Fig. 8(d)]. Azulene experiences an out-of-plane deformation, which brings the bridging carbon atoms closer to the surface than the apex atoms of the rings [Fig. 8(e)]. This was also observed with nc-AFM [Figs. 7(c) and 7(d)]. In addition, azulene shows extensive changes of the in-plane bond lengths, in particular, a shortening of the bridging bond (−3.6 pm) and elongations of the other bonds (up to +4.5 pm). This can be explained by electron donation into the LUMO [as shown in Fig. 9(a)] because its bonding and antibonding contributions agree with the pattern in the bond length changes. In the case of naphthalene, the adsorption-induced deformations are much smaller [Figs. 8(d), 8(f), and 8(h)].

The adsorption height was calculated as the distance between the average height of the carbon atoms and the relaxed height of the first substrate layer without a molecule. For naphthalene, this approach gives a height of 2.96 Å, which is only slightly smaller than the sum of the van der Waals radii of a carbon and a copper atom (3.10 Å) and thus is consistent with the van der Waals character of the naphthalene-copper interaction. In the case of azulene, the calculated distance of 2.33 Å is closer to the sum of the covalent radii of a carbon and a copper atom (2.20 Å), in line with the much stronger bond of azulene. Both calculated values are in excellent agreement with the NIXSW results of 2.30 Å for azulene and 3.04 Å for naphthalene.

In this comparison, we have considered that the standing x-ray wave is formed by the bulk lattice planes, and therefore, the experimental height value is the distance

between the carbon atoms of the molecule and the ideal, unrelaxed surface layer. For Cu(111), the vertical relaxation of the adsorbate-covered first layer proved to be very small in our calculations (less than 0.01 Å), and thus the relaxation correction is actually negligible.

In the electronic adsorption energies yielded by the DFT-D3 calculations, azulene shows a much higher value than naphthalene, $E_{ads} = -1.79$ eV and -1.40 eV, respectively. When zero-point vibrational energy (ZPVE) corrections are taken into account, the energy for azulene increases to $E_{ads} = -1.87$ eV, while there is no change for naphthalene (because its vibrational frequencies are much less influenced by the adsorption). To compare these DFT results with TPD data, we must use the integral desorption energy at the coverage of the $(2\sqrt{3} \times 2\sqrt{3})$-R30° structure used in the DFT calculations (0.65 ML) and make the (here very reasonable) assumption that the adsorption of azulene and naphthalene has no activation barrier. The corresponding experimental energies are 1.58 eV for azulene and 0.93 eV for naphthalene [see Fig. 3(c), dashed lines]. In comparison, theory overestimates the adsorption energy by 0.29 eV for azulene and by 0.47 eV for naphthalene, which is in the range of expected deviations of current DFT methods [87]. In particular, dispersion-corrected DFT adsorption energies of molecules on metal surfaces are typically overestimated and usually show errors of this magnitude [88,89].

DFT also provides additional insight into the valence electronic structure of the adsorbed molecules. For azulene/Cu(111), the carbon-projected DOS in Fig. 9(e) shows a substantial density of states spread out over a large energy window around E_F, with only small variations in magnitude. In contrast, naphthalene has a clear gap in the carbon-projected DOS between -1.4 and $+0.5$ eV [Fig. 9(f)]. Both findings are in agreement with the UPS data in Fig. 4(c). The reason for this different behavior is related to azulene's low-lying LUMO, which is very close to the Fermi edge of Cu(111), as shown in Fig. 9(e). As a result, the LUMO is pulled below E_F and is partially filled with electrons from the surface, as can be seen in the charge density difference plot [Figs. 9(a) and 9(b)]. Comparison with a related plot for naphthalene using the same isosurface value shows no visible charge transfer [see Figs. 9(c) and 9(d)]. If a much lower isosurface value is chosen, the so-called pillow effect (i.e., the pushback of electron density between the molecule and surface caused by Pauli repulsion [71]) can be seen for both molecules, but it is much larger for azulene. These additional charge density difference plots are shown in Fig. S7 of the Supplemental Material [44].

The participation of the frontier orbitals in the surface chemical bond is illustrated in Figs. 10(a) and 10(b), which show the DOS projected onto the molecular orbitals of the free molecules. Again, drastic differences can be seen between azulene and naphthalene. The frontier orbitals of azulene [Fig. 10(a)] undergo substantial energetic broadening in the adsorbed state. As a result, the LUMO and

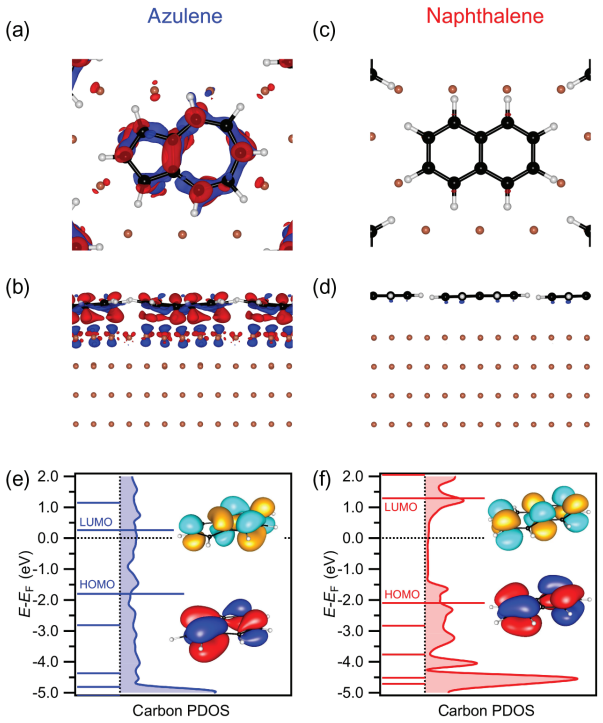

FIG. 9. Electronic structure of azulene and naphthalene on Cu(111) from DFT calculations. (a,b) Charge density difference plots for azulene. (c,d) Charge density difference plots for naphthalene. The isosurface value is 0.003 $e^-/$Å; electrons flow from blue to red. In panel (a), electron enrichment in the shape of the LUMO is clearly visible. (e,f) Carbon partial density of states of the adsorbed species. The horizontal bars represent the energies of the frontier orbitals of the free molecules. These energy levels are shifted to align the lowest valence orbitals for the free and the adsorbed molecules. The figure also shows images of the HOMO and LUMO as calculated by DFT.

LUMO+1 levels show large contributions below the Fermi energy. In the case of naphthalene, the frontier orbitals are much less broadened and the LUMO remains well above the Fermi energy.

The adsorption-induced changes in the valence electronic structure also have important consequences for the NEXAFS spectra, as can be seen in the MO-projected NEXAFS simulations [Figs. 10(c)–10(f)]. The LUMO and LUMO+1 contributions are greatly reduced for azulene, when adsorbed on Cu(111), because these orbitals are now partially occupied and therefore are not fully available for an excitation anymore. For naphthalene, adsorption does not result in substantial spectral changes. Note that the MO contributions do not seem to add up to the total spectrum for azulene on Cu (111) [Fig. 10(e)]. Because of the strong hybridization between the molecular orbitals and the surface, as well as final-state screening effects, the spectral contributions from states with ground-state molecular orbital character are much smaller than for the weakly interacting naphthalene.

The hybridization of the frontier orbitals also has consequences for the charge redistribution between the

P8

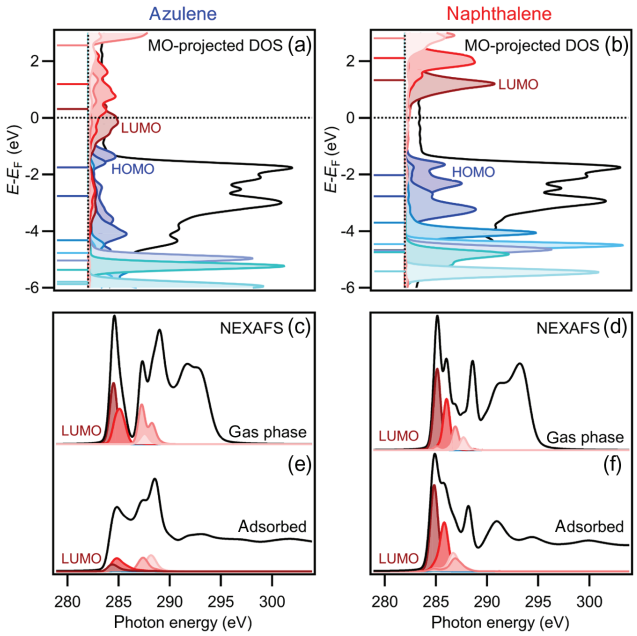

FIG. 10. MO projection analysis, left azulene, right naphthalene. Contributions of the LUMO are shown in dark red and of the HOMO in blue; higher and lower orbitals are shown in incrementally lighter colors. Total DOS and total spectrum are shown in black. (a,b) TDOS and MO-projected density of states of the adsorbed species with the energies of the molecular frontier orbitals. The nonvanishing TDOS around the Fermi energy is caused by the metal substrate. (c,d) MO-projected NEXAFS simulations of the free molecules. (e,f) MO-projected NEXAFS simulations of the adsorbed molecules. The simulated spectra are shifted by −6.1 eV to match the experimental data in Fig. 5.

surface and the molecule. The charge transfer is quantified using two different methods. The Bader analysis method [90] predicts that azulene receives 0.49 negative elementary charges (e^-) from the surface, resulting in a net negative charge at the molecule. In contrast, naphthalene shows only a very small charge transfer of 0.06 e^- from the molecule to the surface, i.e., in the opposite direction. Using an alternative approach, we integrate the MO projection in Figs. 10(a) and 10(b) up to E_F, including the pulled-down contributions of LUMO and LUMO+1. The resulting excess charges (negative charges) on the molecules are 1.39 e^- for azulene and 0.13 e^- for naphthalene, respectively. Both methods thus indicate a significant surface-to-molecule charge transfer. The partial charge is not an observable property, and it is well known that different methods give different absolute values. The chemisorbed character of azulene on Cu(111) means that separation of molecule and surface electronic states is not straightforward, either in real or in orbital space. However, the considerable effects observed in the NEXAFS spectrum of azulene upon adsorption indicate that the magnitude of charge transfer is probably larger than predicted by the Bader analysis method.

IV. DISCUSSION

The combined TPD, NIXSW, PES, NEXAFS, nc-AFM, and DFT results provide a consistent picture of the surface chemical bond of azulene and naphthalene on Cu(111). Azulene, as a prototypical 5-7 system, forms a strong chemical bond to the copper surface, whereas naphthalene as a 6-6 system is only physisorbed. This difference is related to the topology of the π-electron system. In naphthalene, the π system has an alternant topology, which means that all carbon atoms can be divided into two disjoint sets, such that an atom of one set binds only to atoms of the other set [14]. All aromatic systems with 6-membered rings, the benzoid systems, are alternant. In contrast, the 5-7π system of azulene has a nonalternant topology [Fig. 11(a)].

Alternant and nonalternant π systems show fundamental differences in the electronic structure. The Coulson-Rushbrooke theorem, which states that the energy levels of the aromatic π system are symmetrically distributed, is

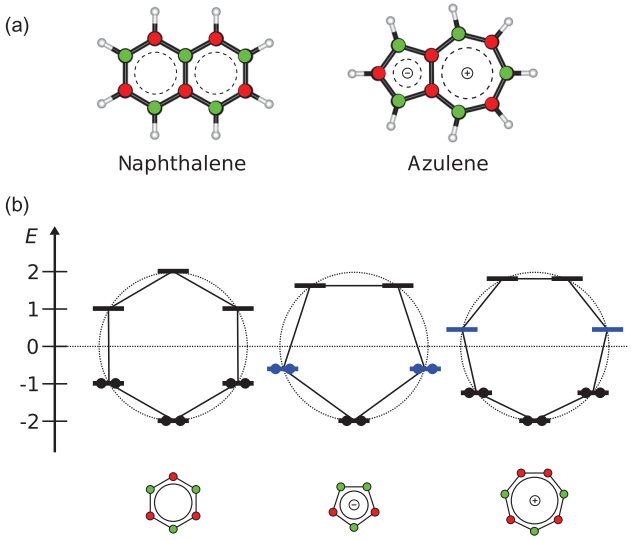

FIG. 11. (a) Alternating labeling of the carbon atoms (red, green), illustrating that the 6-6 system has an alternant and the 5-7 system has a nonalternant π system. The dipole moment of the 5-7 system can also be understood as a consequence of the Hückel $4n+2$ rule for aromatic systems [91], which requires transfer of one electron from the heptagon to the pentagon, such that an aromatic sextet (Clar sextet) can be formed [92]. (b) Frost-Musulin diagrams [93] for 6-, 5-, and 7-membered cyclic π systems. The HOMO level of the 5-membered ring and the LUMO level of the 7-membered ring are highlighted in blue. All π-MO energies lie on a circle, which is centered at the Coulomb integral α and has the radius of 2 times the Hückel exchange integral β. The energy scale is in units of x, with $x \equiv (\alpha - \varepsilon)/\beta$, where ε is the π-MO energy. Only the 6-membered ring is alternant and fulfills the Coulson-Rushbrooke theorem. In the 5-membered system, the HOMO is lifted, and in the 7-membered system, the LUMO is lowered. The hexagon has a neutral closed-shell state, whereas the pentagon and the heptagon form a closed-shell anion and cation, respectively.

violated by nonalternant species [14,94]. While alternant aromatic molecules have highly delocalized π orbitals, these orbitals are more localized in nonalternant molecules.

The concept of alternant and nonalternant cyclic π-conjugated systems is visualized in Fig. 11(b), which compares the Frost-Musulin energy diagrams for 5-, 6-, and 7-membered cyclic π systems [93]. As can be seen, the 6-membered ring is alternant, and its π-orbital energies are paired, such that each occupied bonding orbital with energy $-E$ has an empty antibonding counterpart with energy $+E$. This symmetry is broken for nonalternant 5- and 7-membered π systems. As one of the consequences, the HOMO of the 5-membered ring is lifted, whereas the LUMO of the 7-membered ring is lowered, compared to the 6-membered, alternant system.

Qualitatively, the electronic structure of azulene can be viewed as a combination of 5- and 7-membered π systems. From this consideration, one would expect that the HOMO-LUMO gap of azulene is considerably smaller than that of the corresponding system with two 6-membered rings, naphthalene. The increased HOMO energy should make azulene a better donor, and the reduced LUMO energy a better acceptor, than naphthalene. In addition, the frontier orbitals should be somewhat localized, with increased contributions of the 5-membered ring to the HOMO and of the 7-membered ring to the LUMO.

These anticipated properties are in agreement with the experimental observations. The localization of HOMO and LUMO in azulene causes a molecular dipole moment of 0.8 D [67], which is a very large value for a simple hydrocarbon without heteroatoms. In contrast, naphthalene has no dipole moment. The HOMO-LUMO gap of azulene is 2.1 eV, compared to 3.5 eV for naphthalene, as calculated by DFT.

With respect to the adsorption behavior of azulene, the energetic shift of the frontier orbitals, especially the down-shift of the LUMO, leads to the described accessibility for electron donation from the surface into the LUMO and thus to the much stronger chemical bond to the Cu(111) surface. The partial occupation of the LUMO also explains some of the adsorption-induced deformations, especially the striking shortening of the bridging bond [see Fig. 8(g)] because the LUMO is bonding while the HOMO is antibonding between the two shared C atoms [see Fig. 9(e)].

As pointed out above, the special electronic structure of azulene and the resulting strong surface chemical bond are by no means a coincidence but a consequence of the topology of its π system, which is fundamentally different from that of naphthalene. We expect this to hold true wherever this structural element occurs, whether it be in a molecule, a graphene nanoribbon, or another π-electron system. The limitations of this molecular model system are discussed in the following for a system that is, in many ways, furthest removed from the molecules investigated: defects in an infinite graphene lattice.

The 5-7 defects embedded in the graphene lattice have the same topology as azulene, whereas the regular graphene lattice has the same topology as naphthalene (Fig. 1). Therefore, we expect the 5-7 defects in graphene to have a much stronger and more localized interaction with a metal substrate than the regular graphene. It is also possible that metal atoms deposited onto graphene bind more strongly to 5-7 defects than to regular lattice sites. In addition, electron transfer from the substrate is more likely to occur at the 5-7 defects than at defect-free areas.

Compared to a 5-7 defect in substrate-supported graphene, our molecular system, azulene, differs in two important points. First, the π system in azulene is terminated by hydrogen atoms, and thus the area of π-electron delocalization is spatially confined. In contrast, the 5-7 defect in a graphene layer is embedded in the π system of graphene, making the area of delocalization much larger. However, it is important to keep in mind that the effect of the topological symmetry break caused by the 5-7 defect is a spatial localization and energetic lowering of electronic states. These effects should also occur in the extended structure because the symmetry break is also present there. To verify this assumption, we performed periodic DFT calculations for a 5-7 defect embedded in a freestanding graphene layer. As can be seen in a section through the charge density, the defect interrupts the homogeneous charge distribution present in the defect-free graphene [Fig. 12(a)] and accumulates negative charge at the 5-membered ring and positive charge at the 7-membered ring [Fig. 12(b)]. The local charge accumulation on the embedded 5-7 defect, as quantified by the Hirshfeld charge analysis [95], has a similar magnitude as in the isolated 5-7 system of azulene (see the Supplemental Material [44] for details). The graphene with the embedded defect also shows additional DOS in the vicinity of the Fermi energy [Fig. 12(c)].

Another difference between the molecular nonalternant system and a 5-7 defect in an adsorbed graphene layer will be apparent in the adsorption height. While azulene can always adopt its equilibrium height, the 5-7 defect embedded in the graphene lattice (or in another extended aromatic system) will be pulled closer to the surface, but it will also be held back by the surrounding regular graphene lattice (or other alternant structure), which resides at a larger distance. This competition may further influence the electronic interaction with the substrate and related effects, such as electron transfer. Nevertheless, the molecular nonalternant system of azulene represents a highly valuable model for extended aromatic systems with embedded nonalternant structural elements because reliable quantitative information such as local interaction energies and adsorption heights are very difficult to obtain for defects in extended π-conjugated systems with the presently available experimental and theoretical methods.

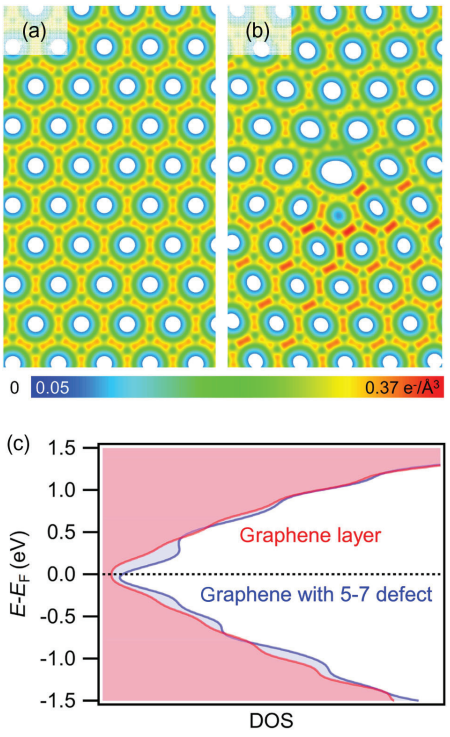

FIG. 12. Results of periodic DFT calculations for a freestanding graphene layer with and without 5-7 defects. (a) The section through the charge density for the planar ideal graphene layer and (b) the section through the charge density for the planar graphene layer with a 5-7 defect. As can be seen, the 5-7 defect accumulates negative charge (red) at the 5-membered ring and positive charge (blue/white) at the 7-membered ring. Only part of the unit cell is shown. For a complete view, see Fig. S9 of the Supplemental Material [44]. (c) Total density of states for both systems. The DOS of the defect structure shows new states around the Fermi energy. The nonzero DOS at E_F for both systems is caused by the employed electronic smearing and is a known artifact of the method [96,97].

V. CONCLUSIONS

Azulene as a nonalternant aromatic hydrocarbon forms a much stronger chemical bond to the Cu(111) surface than naphthalene as its alternant isomer. This result follows from the very different low-coverage TPD peak temperatures (520 K for azulene vs 340 K for naphthalene) and from the resulting zero-coverage desorption energy, which is much higher for azulene (1.86 eV) than for naphthalene (1.07 eV). The same trend is seen in the vertical bonding distances (adsorption heights) as measured by NIXSW and nc-AFM. The NIXSW value of 2.30 Å for azulene is much smaller than the sum of the van der Waals radii and agrees with the formation of a real chemical bond. In contrast, the height of 3.04 Å found for naphthalene is consistent with pure physisorption. The distances calculated by dispersion-corrected DFT agree very well with the measured heights. The calculations also show that both azulene and the surface underneath undergo substantial distortion (as is confirmed by AFM experiments), while naphthalene remains almost undistorted. Repulsive interactions between the adsorbed azulene molecules lead to a strongly coverage-dependent desorption energy, which follows the equation $E_d = (1.86 - 0.67\Theta - 0.40\Theta^2)$ eV. Naphthalene shows less repulsion, and its desorption energy is well described by the equation $E_d = (1.07 - 44\Theta)$ eV. Effects of the intermolecular repulsion are also visible in the submonolayer STM images. The work-function change at monolayer coverage is higher for azulene (−1.07 eV) than for naphthalene (−0.73 eV), indicating that azulene forms the larger surface dipole. The higher intermolecular repulsion seen for azulene is therefore likely related to increased dipole-dipole repulsion.

The differences in the surface chemical bonds of azulene and naphthalene can be rationalized on the basis of the different topologies of the molecular π systems. Because of its violation of the Coulson-Rushbrooke theorem, azulene has a low-lying LUMO, which is close to the Fermi energy of copper. This fact leads to a strong hybridization between the LUMO and electronic states of the surface, as well as electron transfer from the surface into the LUMO. This electron transfer is confirmed by various experimental data: Probing the occupied states, the UP spectra of azulene on Cu(111) show an adsorption-induced, broad feature below the Fermi edge. Complementary NEXAFS studies of the unoccupied states reveal strong changes in the π^* resonance, which is attenuated and broadened. Theoretical analysis shows that the new broad feature in the occupied range is related to the former LUMO and other formerly unoccupied orbitals, while the changes in the NEXAFS are due to the partial occupation of the LUMO and LUMO+1 orbitals. In addition, submolecularly resolved STM images of azulene show the shape of the former LUMO at negative bias, which confirms that this orbital is filled with electrons. This finding is also supported by STM simulations. Theoretical analysis indicates a pronounced redistribution of charge in the case of azulene and a substantial charge transfer from the surface to the molecule. In contrast, the electronic structure of naphthalene is only slightly influenced by the surface, in line with its weaker and longer surface chemical bond.

Our results show that the topology of an aromatic π system greatly influences its interaction with a metal surface. In particular, structural elements with the nonalternant 5-7 topology can form much stronger surface chemical bonds than elements with the regular, alternant 6-6 topology. This may be true not only for aromatic molecules but also for all occurrences of nonalternant topology in carbon-based nanostructures on surfaces, in graphene nanoribbons or, in the form of 5-7 defects, in graphene itself. For all of these structures, we predict a localized surface chemical bond and local electron transfer between the substrate and adsorbate. In addition, our findings may be relevant for the optimization of the

metal-organic interfaces that occur at electrodes in organic electronic devices. They suggest that modifying the topology of the molecular π system represents a possible way to tune performance-related parameters such as wavefunction overlap and energy-level alignment at the electrode-semiconductor interface.

ACKNOWLEDGMENTS

Funded by the Deutsche Forschungsgemeinschaft (DFG, German Research Foundation)-Projektnummer 223848855-SFB 1083. We thank the synchrotron radiation facilities BESSY-II of the Helmholtz-Zentrum für Materialien und Energie, Berlin, for allocation of beam time at the beam lines HE-SGM and PM4/LowDosePES and for financial support. The experimental support by E. Giangrisostomi and R. Ovsyannikov is gratefully acknowledged. Furthermore, we thank Diamond Light Source for access to beam line I09 (Proposal No. SI16259), and the I09 beam-line staff (T.-L. Lee, P. K. Thakur, and D. McCue) for their support during the experiment. We acknowledge computational resources from HLR Stuttgart, CSC-LOEWE Frankfurt, and HRZ Marburg.

[1] J. E. Anthony, *The Larger Acenes: Versatile Organic Semiconductors*, Angew. Chem. Int. Ed. **47**, 452 (2008).
[2] A. Mishra and P. Bäuerle, *Small Molecule Organic Semiconductors on the Move: Promises for Future Solar Energy Technology*, Angew. Chem. **51**, 2020 (2012).
[3] J. H. Burroughes, D. D. C. Bradley, A. R. Brown, R. N. Marks, K. Mackay, R. H. Friend, P. L. Burns, and A. B. Holmes, *Light-Emitting Diodes Based on Conjugated Polymers*, Nature (London) **347**, 539 (1990).
[4] A. Pron and P. Rannou, *Processible Conjugated Polymers: From Organic Semiconductors to Organic Metals and Superconductors*, Prog. Polym. Sci. **27**, 135 (2002).
[5] Z. Chen, Y.-M. Lin, M. J. Rooks, and P. Avouris, *Graphene Nano-ribbon Electronics*, Physica E **40**, 228 (2007).
[6] B. H. Nguyen and V. H. Nguyen, *Promising Applications of Graphene and Graphene-based Nanostructures*, Adv. Nat. Sci. Nanosci. Nanotechnol. **7**, 023002 (2016).
[7] *Concepts in Molecular and Organic Electronics*, MRS Proceedings, edited by N. Koch, E. Zojer, S.-W. Hla, and X. Zhu (Cambridge University Press, Cambridge, England, 2014).
[8] *Organic Electronics: Materials, Manufacturing, and Applications*, edited by H. Klauk (Wiley-VCH, Weinheim, 2006).
[9] *Organic Electronics II: More Materials and Applications*, edited by H. Klauk (Wiley-VCH, Weinheim, 2012).
[10] J. M. Gottfried, *Quantitative Model Studies for Interfaces in Organic Electronic Devices*, New J. Phys. **18**, 111002 (2016).
[11] A. Kahn, N. Koch, and W. Gao, *Electronic Structure and Electrical Properties of Interfaces between Metals and π-conjugated Molecular Films*, J. Polym. Sci. B **41**, 2529 (2003).
[12] N. Koch, *Organic Electronic Devices and Their Functional Interfaces*, Chem. Phys. Chem. **8**, 1438 (2007).
[13] K. Rüdenberg, *Quantum Mechanics of Mobile Electrons in Conjugated Bond Systems. III. Topological Matrix as Generatrix of Bond Orders*, J. Chem. Phys. **34**, 1884 (1961).
[14] R. B. Mallion and D. H. Rouvray, *The Golden Jubilee of the Coulson-Rushbrooke Pairing Theorem*, J. Math. Chem. **5**, 1 (1990).
[15] M. Liu, M. Liu, Z. Zha, J. Pan, X. Qiu, T. Li, J. Wang, Y. Zheng, and D. Zhong, *Thermally Induced Transformation of Nonhexagonal Carbon Rings in Graphene-like Nanoribbons*, J. Phys. Chem. C **122**, 9586 (2018).
[16] J. Hieulle, E. Carbonell-Sanrom, M. Vilas-Varela, A. Garcia-Lekue, E. Guitin, D. Peña, and J. I. Pascual, *On-surface Route for Producing Planar Nanographenes with Azulene Moieties*, Nano Lett. **18**, 418 (2018).
[17] A. Shiotari, T. Nakae, K. Iwata, S. Mori, T. Okujima, H. Uno, H. Sakaguchi, and Y. Sugimoto, *Strain-induced Skeletal Rearrangement of a Polycyclic Aromatic Hydrocarbon on a Copper Surface*, Nat. Commun. **8**, 16089 (2017).
[18] S. Mishra, T. G. Lohr, C. A. Pignedoli, J. Liu, R. Berger, J. I. Urgel, K. Müllen, X. Feng, P. Ruffieux, and R. Fasel, *Tailoring Bond Topologies in Open-Shell Graphene Nanostructures*, ACS Nano, **12**, 11917 (2018).
[19] H. Xin and X. Gao, *Application of Azulene in Constructing Organic Optoelectronic Materials: New Tricks for an Old Dog*, Chem. Plus Chem. **82**, 945 (2017).
[20] Y. Yamaguchi, M. Takubo, K. Ogawa, K.-i. Nakayama, T. Koganezawa, and H. Katagiri, *Terazulene Isomers: Polarity Change of OFETs through Molecular Orbital Distribution Contrast*, J. Am. Chem. Soc. **138**, 11335 (2016).
[21] P. Y. Huang, C. S. Ruiz-Vargas, A. M. van der Zande, W. S. Whitney, M. P. Levendorf, J. W. Kevek, S. Garg, J. S. Alden, C. J. Hustedt, Y. Zhu, J. Park, P. L. McEuen, and D. A. Muller, *Grains and Grain Boundaries in Single-Layer Graphene Atomic Patchwork Quilts*, Nature (London) **469**, 389 (2011).
[22] F. Banhart, J. Kotakoski, and A. V. Krasheninnikov, *Structural Defects in Graphene*, ACS Nano **5**, 26 (2011).
[23] J. Červenka and C. F. J. Flipse, *Structural and Electronic Properties of Grain Boundaries in Graphite: Planes of Periodically Distributed Point Defects*, Phys. Rev. B **79**, 195429 (2009).
[24] N. M. R. Peres, F. Guinea, and A. H. C. Neto, *Electronic Properties of Disordered Two-Dimensional Carbon*, Phys. Rev. B **73**, 125411 (2006).
[25] R. Grantab, V. B. Shenoy, and R. S. Ruoff, *Anomalous Strength Characteristics of Tilt Grain Boundaries in Graphene*, Science **330**, 946 (2010).
[26] Y. Wei, J. Wu, H. Yin, X. Shi, R. Yang, and M. Dresselhaus, *The Nature of Strength Enhancement and Weakening by Pentagon-Heptagon Defects in Graphene*, Nat. Mat. **11**, 759 (2012).
[27] J. Červenka, M. I. Katsnelson, and C. F. J. Flipse, *Room-Temperature Ferromagnetism in Graphite Driven by Two-dimensional Networks of Point Defects*, Nat. Phys. **5**, 840 (2009).

P8

[28] S. Malola, H. Häkkinen, and P. Koskinen, *Structural, Chemical, and Dynamical Trends in Graphene Grain Boundaries*, Phys. Rev. B **81**, 165447 (2010).
[29] K. Müller, A. P. Seitsonen, T. Brugger, J. Westover, T. Greber, T. Jung, and A. Kara, *Electronic Structure of an Organic/Metal Interface: Pentacene/Cu(110)*, J. Phys. Chem. C **116**, 23465 (2012).
[30] F. S. Tautz, *Structure and Bonding of Large Aromatic Molecules on Noble Metal Surfaces: The Example of PTCDA*, Prog. Surf. Sci. **82**, 479 (2007).
[31] E. Umbach, *Characterization of Organic Overlayers on Well-Defined Substrates*, Prog. Surf. Sci. **35**, 113 (1990).
[32] K. Seki, N. Hayashi, H. Oji, E. Ito, Y. Ouchi, and H. Ishii, *Electronic Structure of Organic/Metal Interfaces*, Thin Solid Films **393**, 298 (2001).
[33] *The Molecule-Metal Interface*, edited by N. Koch, N. Ueno, and A. T. S. Wee (Wiley-VCH, New York, 2013).
[34] T. Yamada, M. Shibuta, Y. Ami, Y. Takano, A. Nonaka, K. Miyakubo, and T. Munakata, *Novel Growth of Naphthalene Overlayer on Cu(111) Studied by STM, LEED, and 2PPE*, J. Phys. Chem. C **114**, 13334 (2010).
[35] L.-J. Wan and K. Itaya, *In Situ Scanning Tunneling Microscopy of Benzene, Naphthalene, and Anthracene Adsorbed on Cu(111) in Solution*, Langmuir **13**, 7173 (1997).
[36] R. Forker, J. Peuker, M. Meissner, F. Sojka, T. Ueba, T. Yamada, H. S. Kato, T. Munakata, and T. Fritz, *The Complex Polymorphism and Thermodynamic Behavior of a Seemingly Simple System: Naphthalene on Cu(111)*, Langmuir **30**, 14163 (2014).
[37] S. Lukas, S. Vollmer, G. Witte, and C. Wöll, *Adsorption of Acenes on Flat and Vicinal Cu(111) Surfaces: Step Induced Formation of Lateral Order*, J. Chem. Phys. **114**, 10123 (2001).
[38] H. Wang, G. Dutton, and X. Y. Zhu, *Electronic Structure at Organic/Metal Interfaces: Naphthalene/Cu(111)*, J. Phys. Chem. B **104**, 10332 (2000).
[39] H. Tetlow, J. P. de Boer, I. J. Ford, D. D. Vvedensky, J. Coraux, and L. Kantorovich, *Growth of Epitaxial Graphene: Theory and Experiment*, Phys. Rep. **542**, 195 (2014).
[40] L. Gao, J. R. Guest, and N. P. Guisinger, *Epitaxial Graphene on Cu(111)*, Nano Lett. **10**, 3512 (2010).
[41] X. Li, C. W. Magnuson, A. Venugopal, J. An, J. W. Suk, B. Han, M. Borysiak, W. Cai, A. Velamakanni, Y. Zhu, L. Fu, E. M. Vogel, E. Voelkl, L. Colombo, and R. S. Ruoff, *Graphene Films with Large Domain Size by a Two-Step Chemical Vapor Deposition Process*, Nano Lett. **10**, 4328 (2010).
[42] Q. Fan, J. M. Gottfried, and J. Zhu, *Surface-Catalyzed C–C Covalent Coupling Strategies Toward the Synthesis of Low-Dimensional Carbon-Based Nanostructures*, Acc. Chem. Res. **48**, 2484 (2015).
[43] M. Murai, S. Iba, H. Ota, and K. Takai, *Azulene-fused Linear Polycyclic Aromatic Hydrocarbons with Small Bandgap, High Stability, and Reversible Stimuli Responsiveness*, Org. Lett. **19**, 5585 (2017).
[44] See Supplemental Material at http://link.aps.org/supplemental/10.1103/PhysRevX.9.011030 for details of the coverage determination, the NIXSW, TPD, and NEXAFS data treatment, as well as additional XPS, STM, and nc-AFM data, and further details of the DFT calculations.
[45] F. C. Bocquet, G. Mercurio, M. Franke, G. van Straaten, S. Wei, S. Soubatch, C. Kumpf, and F. S. Tautz, *Torricelli: A Software to Determine Atomic Spatial Distributions from Normal Incidence X-ray Standing Wave Data*, Comput. Phys. Commun. **235**, 502 (2019).
[46] S. G. Hessey and R. G. Jones, *Line-of-Sight Mass Spectrometry: Principles and Practice*, Surf. Interface Anal. **47**, 587 (2015).
[47] I. Horcas, R. Fernandez, J. M. Gomez-Rodriguez, J. Colchero, J. Gomez-Herrero, and A. M. Baro, *WSXM: A Software for Scanning Probe Microscopy and a Tool for Nanotechnology*, Rev. Sci. Instrum. **78**, 013705 (2007).
[48] G. Kresse and J. Hafner, *Ab Initio Molecular Dynamics for Liquid Metals*, Phys. Rev. B **47**, 558 (1993).
[49] G. Kresse and J. Hafner, *Ab Initio Molecular-Dynamics Simulation of the Liquid-Metal-Amorphous-Semiconductor Transition in Germanium*, Phys. Rev. B **49**, 14251 (1994).
[50] G. Kresse and J. Furthmüller, *Efficiency of Ab-Initio Total Energy Calculations for Metals and Semiconductors Using a Plane-Wave Basis Set*, Comput. Mater. Sci. **6**, 15 (1996).
[51] G. Kresse and J. Furthmüller, *Efficient Iterative Schemes for Ab Initio Total-Energy Calculations Using a Plane-Wave Basis Set*, Phys. Rev. B **54**, 11169 (1996).
[52] J. P. Perdew, K. Burke, and M. Ernzerhof, *Generalized Gradient Approximation Made Simple*, Phys. Rev. Lett. **77**, 3865 (1996).
[53] S. Grimme, J. Antony, S. Ehrlich, and H. Krieg, *A Consistent and Accurate Ab Initio Parametrization of Density Functional Dispersion Correction (DFT-D) for the 94 Elements H-Pu*, J. Chem. Phys. **132**, 154104 (2010).
[54] P. E. Blöchl, *Projector Augmented-Wave Method*, Phys. Rev. B **50**, 17953 (1994).
[55] G. Kresse and D. Joubert, *From Ultrasoft Pseudopotentials to the Projector Augmented-Wave Method*, Phys. Rev. B **59**, 1758 (1999).
[56] S. J. Clark, M. D. Segall, C. J. Pickard, P. J. Hasnip, M. I. J. Probert, K. Refson, and M. C. Payne, *First Principles Methods Using CASTEP*, Z. Kristallogr. Cryst. Mater. **220**, 567 (2009).
[57] M. Teruyasu, T. Isao, G. Shang-Peng, and J. P. Chris, *First-Principles Calculation of Spectral Features, Chemical Shift and Absolute Threshold of ELNES and XANES Using a Plane Wave Pseudopotential Method*, J. Phys. Condens. Matter **21**, 104204 (2009).
[58] L. Triguero, L. G. M. Pettersson, and H. Ågren, *Calculations of Near-Edge X-Ray-Absorption Spectra of Gas-Phase and Chemisorbed Molecules by Means of Density-Functional and Transition-Potential Theory*, Phys. Rev. B **58**, 8097 (1998).
[59] M. Klues, K. Hermann, and G. Witte, *Analysis of the Near-Edge X-Ray-Absorption Fine-Structure of Anthracene: A Combined Theoretical and Experimental Study*, J. Chem. Phys. **140**, 014302 (2014).
[60] K. Diller, R. J. Maurer, M. Müller, and K. Reuter, *Interpretation of X-Ray Absorption Spectroscopy in the Presence of Surface Hybridization*, J. Chem. Phys. **146**, 214701 (2017).

P8

[61] R. J. Maurer and K. Reuter, *Excited-State Potential-Energy Surfaces of Metal-Adsorbed Organic Molecules from Linear Expansion Δ-Self-Consistent Field Density-Functional Theory (ΔSCF-DFT)*, J. Chem. Phys. **139**, 014708 (2013).
[62] D. P. Woodruff, *Normal Incidence X-Ray Standing Wave Determination of Adsorbate Structures*, Prog. Surf. Sci. **57**, 1 (1998).
[63] D. P. Woodruff, *Surface Structure Determination Using X-Ray Standing Waves*, Rep. Prog. Phys. **68**, 743 (2005).
[64] J. Zegenhagen, *Surface Structure Determination with X-Ray Standing Waves*, Surf. Sci. Rep. **18**, 202 (1993).
[65] The issue of unrealistically high coherent fractions, recently observed in several measurements performed at the I09 beam line, did not occur in our case. This is possibly due to the moderate maximum count rates we allowed during data acquisition, in order to avoid a possible nonlinearity of the multichannel plate detector.
[66] B. Stadtmüller, S. Schröder, and C. Kumpf, *Heteromolecular Metalorganic Interfaces: Electronic and Structural Fingerprints of Chemical Bonding*, J. Electron Spectrosc. Relat. Phenom. **204**, 80 (2015).
[67] D. R. Lide, *CRC Handbook of Chemistry and Physics*, 90th ed. (CRC Press, Boca Raton, FL, 2010).
[68] K. Christmann, *Introduction to Surface Physical Chemistry* (Steinkopff Verlag, Springer-Verlag, Darmstadt, New York, 1991).
[69] A. M. de Jong and J. W. Niemantsverdriet, *Thermal Desorption Analysis: Comparative Test of Ten Commonly Applied Procedures*, Surf. Sci. **233**, 355 (1990).
[70] D. L. S. Nieskens, A. P. van Bavel, and J. W. Niemantsverdriet, *The Analysis of Temperature Programmed Desorption Experiments of Systems with Lateral Interactions; Implications of the Compensation Effect*, Surf. Sci. **546**, 159 (2003).
[71] G. Witte, S. Lukas, P. S. Bagus, and C. Wöll, *Vacuum Level Alignment at Organic/Metal Junctions: Cushion Effect and the Interface Dipole*, Appl. Phys. Lett. **87**, 263502 (2005).
[72] I. Fernandez-Torrente, S. Monturet, K. J. Franke, J. Fraxedas, N. Lorente, and J. I. Pascual, *Long-Range Repulsive Interaction between Molecules on a Metal Surface Induced by Charge Transfer*, Phys. Rev. Lett. **99**, 176103 (2007).
[73] S. Lukas, G. Witte, and C. Wöll, *Novel Mechanism for Molecular Self-Assembly on Metal Substrates: Unidirectional Rows of Pentacene on Cu(110) Produced by a Substrate-Mediated Repulsion*, Phys. Rev. Lett. **88**, 028301 (2001).
[74] G. Tomba, M. Stengel, W. D. Schneider, A. Baldereschi, and A. De Vita, *Supramolecular Self-Assembly Driven by Electrostatic Repulsion: The 1D Aggregation of Rubrene Pentagons on Au111*, ACS Nano **4**, 7545 (2010).
[75] E. Bauer, F. Bonczek, H. Poppa, and G. Todd, *Thermal Desorption of Metals from Tungsten Single Crystal Surfaces*, Surf. Sci. **53**, 87 (1975).
[76] D. A. King, *Thermal Desorption from Metal Surfaces: A Review*, Surf. Sci. **47**, 384 (1975).
[77] S. L. Tait, Z. Dohnálek, C. T. Campbell, and B. D. Kay, *n-Alkanes on MgO(100). I. Coverage-Dependent Desorption Kinetics of n-Butane*, J. Chem. Phys. **122**, 164707 (2005).
[78] D. P. Chong, *Density Functional Theory Study on the Electron Spectra of Naphthalene and Azulene Vapours*, Can. J. Chem. **88**, 787 (2010).
[79] S. Doniach and M. Šunjić, *Many-Electron Singularity in X-Ray Photoemission and X-Ray Line Spectra from Metals*, J. Phys. C **3**, 285 (1970).
[80] W. Zhao, W. Wei, and J. M. White, *Two-Photon Photoemission Spectroscopy: Naphthalene on Cu(111)*, Surf. Sci. **547**, 374 (2003).
[81] F. Bischoff, K. Seufert, W. Auwärter, S. Joshi, S. Vijayaraghavan, D. Écija, K. Diller, A. C. Papageorgiou, S. Fischer, F. Allegretti, D. A. Duncan, F. Klappenberger, F. Blobner, R. Han, and J. V. Barth, *How Surface Bonding and Repulsive Interactions Cause Phase Transformations: Ordering of a Prototype Macrocyclic Compound on Ag (111)*, ACS Nano **7**, 3139 (2013).
[82] J. Tersoff and D. R. Hamann, *Theory of the Scanning Tunneling Microscope*, Phys. Rev. B **31**, 805 (1985).
[83] B. Schuler, W. Liu, A. Tkatchenko, N. Moll, G. Meyer, A. Mistry, D. Fox, and L. Gross, *Adsorption Geometry Determination of Single Molecules by Atomic Force Microscopy*, Phys. Rev. Lett. **111**, 106103 (2013).
[84] F. Mohn, L. Gross, N. Moll, and G. Meyer, *Imaging the Charge Distribution within a Single Molecule*, Nat. Nanotechnol. **7**, 227 (2012).
[85] L. Gross, F. Mohn, P. Liljeroth, J. Repp, F. J. Giessibl, and G. Meyer, *Measuring the Charge State of an Adatom with Noncontact Atomic Force Microscopy*, Science **324**, 1428 (2009).
[86] B. Schuler, S.-X. Liu, Y. Geng, S. Decurtins, G. Meyer, and L. Gross, *Contrast Formation in Kelvin Probe Force Microscopy of Single p-conjugated Molecules*, Nano Lett. **14**, 3342 (2014).
[87] J. Wellendorff, T. L. Silbaugh, D. Garcia-Pintos, J. K. Nørskov, T. Bligaard, F. Studt, and C. T. Campbell, *A Benchmark Database for Adsorption Bond Energies to Transition Metal Surfaces and Comparison to Selected DFT Functionals*, Surf. Sci. **640**, 36 (2015).
[88] R. J. Maurer, V. G. Ruiz, and A. Tkatchenko, *Many-body Dispersion Effects in the Binding of Adsorbates on Metal Surfaces*, J. Chem. Phys. **143**, 102808 (2015).
[89] R. J. Maurer, W. Liu, I. Poltavsky, T. Stecher, H. Oberhofer, K. Reuter, and A. Tkatchenko, *Thermal and Electronic Fluctuations of Flexible Adsorbed Molecules: Azobenzene on Ag(111)*, Phys. Rev. Lett. **116**, 146101 (2016).
[90] R. F. W. Bader, *Atoms in Molecules—A Quantum Theory* (Oxford University Press, Oxford, 1990).
[91] E. Hückel, *Quantentheoretische Beiträge Zum Problem der Aromatischen und Ungesättigten Verbindungen. III*, Z. Phys. **76**, 628 (1932).
[92] E. Clar, *The Aromatic Sextet*, 2nd ed. (John Wiley & Sons, London, New York, Sydney, Toronto, 1972).
[93] A. A. Frost and B. Musulin, *A Mnemonic Device for Molecular Orbital Energies*, J. Chem. Phys. **21**, 572 (1953).
[94] C. A. Coulson and G. S. Rushbrooke, *Note on the Method of Molecular Orbitals*, J. Phys. Condens. Matter **36**, 193 (1940).

P8

[95] F. L. Hirshfeld, *Bonded-Atom Fragments for Describing Molecular Charge Densities*, Theor. Chim. Acta **44**, 129 (1977).

[96] H. Vita, S. Böttcher, K. Horn, E. N. Voloshina, R. E. Ovcharenko, T. Kampen, A. Thissen, and Y. S. Dedkov, *Understanding the Origin of Band Gap Formation in Graphene on Metals: Graphene on* Cu/Ir(111), Sci. Rep. **4**, 5704 (2014).

[97] H. S. Moon, J. H. Lee, S. Kwon, I. T. Kim, and S. G. Lee, *Mechanisms of Na Adsorption on Graphene and Graphene Oxide: Density Functional Theory Approach*, Carbon Lett. **16**, 116 (2015).

P8

Molecular Topology and the Surface Chemical Bond: Alternant vs. Non-Alternant Aromatic Systems as Functional Structural Elements

SUPPORTING INFORMATION

Benedikt P. Klein[1], Nadine J. van der Heijden[2], Stefan R. Kachel[1], Markus Franke[3], Claudio K. Krug[1], Katharina K. Greulich[1], Lukas Ruppenthal[1], Philipp Müller[1], Phil Rosenow[1], Shayan Parhizkar[3], François C. Bocquet[3], Martin Schmid[1], Wolfgang Hieringer[4], Reinhard J. Maurer[5], Ralf Tonner[1], Christian Kumpf[3], Ingmar Swart[2], and J. Michael Gottfried[1]

[1]Philipps-Universität Marburg, Fachbereich Chemie, Hans-Meerwein-Str. 4, 35032 Marburg, Germany

[2]Condensed Matter and Interfaces, Debye Institute for Nanomaterials Science, Utrecht University, P.O. Box 80000, 3508 TA Utrecht, The Netherlands

[3]Peter Grünberg Institut (PGI-3), Forschungszentrum Jülich, 52425 Jülich, Germany and Jülich Aachen Research Alliance (JARA) Fundamentals of Future Information Technology, 52425 Jülich, Germany

[4]Lehrstuhl für Theoretische Chemie, Universität Erlangen-Nürnberg, Egerlandstr. 3, 91058 Erlangen, Germany and

[5]Department of Chemistry and Centre for Scientific Computing, University of Warwick, Gibbet Hill Road, Coventry, CV4 7AL, United Kingdom

P8

(Dated: November 22, 2018)

I. COVERAGE DETERMINATION

The absolute monolayer coverage (*i.e.* the number of molecules per area) was determined from a large-scale nc-AFM image of a saturated, compressed layer (with partial second layer) prepared by careful dosing at low temperature. For the XPS, UPS and NIXSW measurements, the relative coverage (in ML) was checked by the XPS intensity. The monolayer XPS intensity was beforehand established with an XPS temperature series monitoring peak intensity and position. The thus conceived temperature at which a monolayer is formed by desorption of a multilayer is in accordance with the monolayer trace as measured by TPD. At 300 K a self limiting adsorption of azulene to a coverage of 0.65 ML takes place. This was used as an additional, internal calibration standard.

II. XPS SPECTRA USED FOR THE GENERATION OF NIXSW YIELD CURVES

Examples for the C 1s XP spectra used for the generation of the NIXSW yield curves are shown in Fig. S1. To fully avoid any beam damage, the measurement time was chosen very short, at the expense of increased noise levels. The spectra were fitted using CASA XPS, the resulting yield curves can be found in the main text. The NIXSW analysis was performed with Torricelli [1].

P8

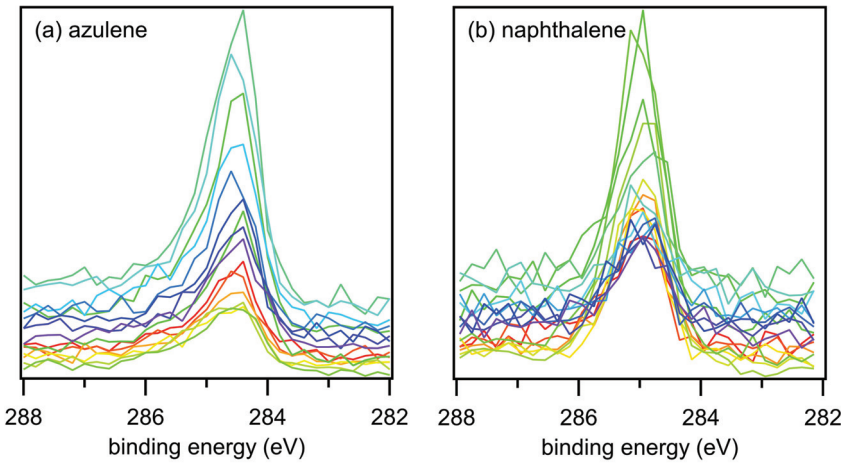

FIG. S1. (a) Examples for the C 1s XP spectra used for the generation of the NIXSW yield curves. (a) 1 ML azulene, (b) 1 ML naphthalene on Cu(111), color scheme from red (lowest photon energy) to blue (highest photon energy) in the order of the visible spectrum.

III. TEMPERATURE PROGRAMMED DESORPTION (TPD)

A. Estimation of desorption activation energies

Quantitative analysis of the TPD spectra based on the Polanyi-Wigner rate equation [2–4], gives access to the desorption activation energy E_d as a measure of the adsorbate-substrate bond energy:

$$\mathrm{rate} = -\frac{\mathrm{d}\Theta}{\mathrm{d}t} = \nu_\mathrm{d}\Theta \exp\left(-E_\mathrm{d}/RT\right) \tag{1}$$

In Eq. (1), Θ is the coverage, ν_d is the desorption prefactor, T is the temperature, and R is the universal gas constant. The most rigorous approach for TPD analysis, the so-called complete methods [5, 6], are not suitable here because of the strong lateral repulsion [4]. Instead, we use an alternative approach as proposed by Nieskens *et al.* [4] and Tait *et al.* [7] and rewrite Eq. (1) as follows:

$$E_\mathrm{d}(\Theta) = -RT \ln\left[\frac{-\mathrm{d}\Theta/\mathrm{d}t}{\nu_\mathrm{d}\Theta}\right] \tag{2}$$

Eq. (2) provides the coverage-dependent desorption energy $E_\mathrm{d}(\Theta)$ from a single TPD trace. The prefactors used in Eq. (2) were determined by heating rate variation (HRV) analysis [2], which is only meaningful for the regular first-order peaks in the low-coverage range. The related data are presented in Fig. S2 and Table SI below. It should be noted that Eq. (2) is strictly applicable only if the prefactor does not change with coverage. However, small changes of ν_d have a negligible effect on the estimate of E_d: Even if ν_d varies by one order of magnitude, E_d changes by only a few percent [4].

P8

B. TPD heating rate variation series

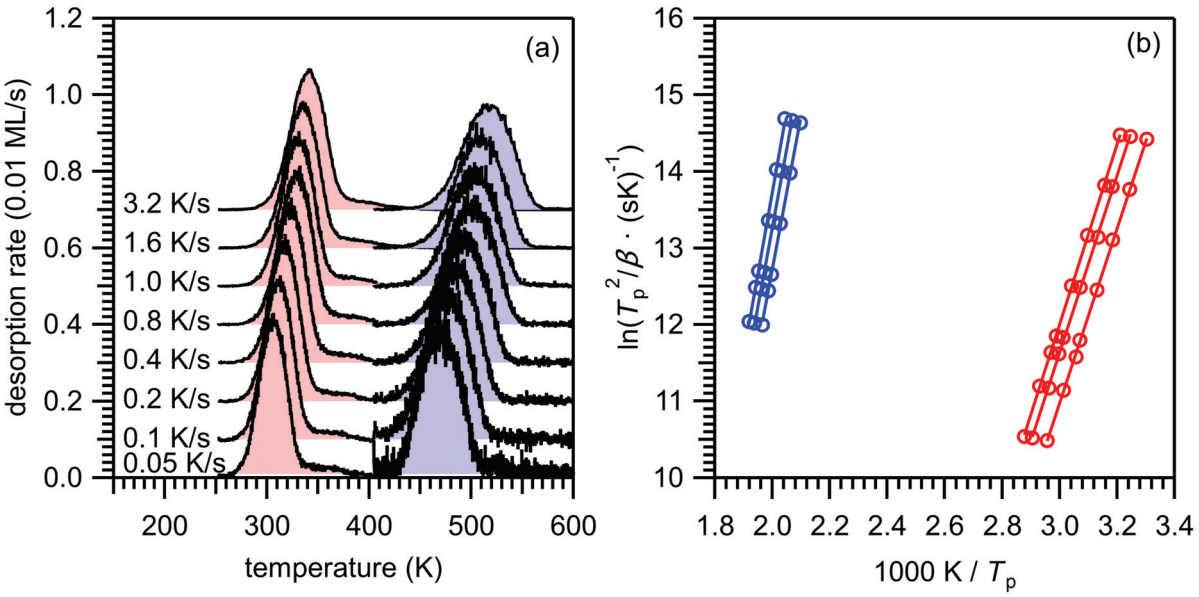

FIG. S 2. (a) Examples for heating rate variation (HRV) series for azulene and naphthalene (both initial coverages 0.16 ML). (b) Analysis of the heating rate variation series for coverages of 0.07, 0.11 and 0.16 ML for azulene and 0.04, 0.08 and 0.16 ML for naphthalene, providing desorption activation energies and pre-exponential factors.

P8

TAB. S I. Desorption energies and prefactors for each heating rate variation series for azulene and naphthalene on Cu(111).

Experiment	ΔE_{des} (eV)	ν_{d} (s^{-1})
Azulene/Cu 0.07 ML	1.83	$7.7 \cdot 10^{16}$
Azulene/Cu 0.11 ML	1.77	$2.6 \cdot 10^{16}$
Azulene/Cu 0.16 ML	1.73	$1.6 \cdot 10^{16}$
Naphthalene/Cu 0.04 ML	1.04	$2.3 \cdot 10^{14}$
Naphthalene/Cu 0.08 ML	1.02	$1.4 \cdot 10^{14}$
Naphthalene/Cu 0.16 ML	0.99	$1.5 \cdot 10^{14}$

C. TPD dosing series coverages

TAB. S II. Initial coverages of the TPD spectra for azulene and naphthalene on Cu(111) (shown in Fig. 3 in the main paper) starting from low coverages to high coverages (from bottom to top).

Azulene (ML)	Naphthalene (ML)
0.015	0.015
0.015	0.015
0.030	0.021
0.044	0.031
0.065	0.037
0.079	0.078
0.12	0.16
0.17	0.20
0.24	0.30
0.29	0.39
0.39	0.49
0.45	0.60
0.56	0.75
0.58	0.78
0.73	1.0
0.76	1.3
0.79	
0.92	
1.0	
1.1	
1.6	

P8

D. Estimation of desorption prefactors from transition state theory

The precise quantitative analysis of TPD data requires careful treatment of the prefactor ν_d . To estimate desorption energies on the basis of single desorption maxima, the prefactor is often assumed to be $1 \cdot 10^{13}\mathrm{s}^{-1}$. For atoms or small molecules, this is a sufficiently accurate approximation in many cases [8]. However, the prefactor can be much higher for larger molecules. It can be derived by various methods from high-quality TPD data using various analysis methods [3], but it can also be estimated using the transition state theory (TST) [9, 10]. Within the framework of TST, the desorption prefactor can be calculated by (3):

$$\nu_\mathrm{d} = \frac{kT}{h} \cdot \frac{q^{\neq}}{q_\mathrm{ad}} \tag{3}$$

(with the Boltzmann constant k, the Planck constant h, and the partition functions $q^{\neq}$ and q_{ad} of the transition state and the adsorbed state, respectively.) An accurate calculation of $q^{\neq}$ and q_{ad} would require detailed knowledge of the interaction potentials of the adsorbed molecule and the transition state [11]. These data are not available. Nevertheless, upper and lower limits for ν_{d} can be estimated on the basis of reasonable assumptions about the degrees of freedom in the adsorbed state and in the transition state. First, we neglect any vibrational partition functions, which are small and mostly cancel in Eq. (3). Second, the transition state is approximated as a free gas-phase molecule with two translational and three rotational degrees of freedom. (The third translational degree of freedom represents the critical coordinate and is therefore omitted in $q^{\neq}$.) The partition function of the transition state is therefore given by:

$$q^{\neq} = q^{\neq}_{\mathrm{tr,2D}} \cdot q^{\neq}_{rot,\mathrm{3D}} \tag{4}$$

The two-dimensional translational partition function per area A is given by [12]:

$$\frac{q^{\neq}_{\mathrm{tr,2D}}}{A} = \frac{2\pi mkT}{h^2} \tag{5}$$

P8

where m is the mass of the molecule. The three-dimensional rotational partition function is [12]:

$$q^{\neq}_{rot,3D} = \frac{\pi^{1/2}}{\sigma}\left(\frac{kT}{hc_0}\right)^{3/2}(B_{\mathrm{A}}B_{\mathrm{B}}B_{\mathrm{C}})^{-1/2} \tag{6}$$

with the symmetry factor σ, the velocity of light c_0, and the rotational constants B_{A}, B_{B} and B_{C} (in m^{-1}).

In the following, we consider the two limiting cases for the degrees of freedom of the adsorbate. In the mobile limit, the adsorbed molecule possesses two translational degrees of freedom parallel to the surface and one rotational degree of freedom around an axis perpendicular to the molecular plane, which is assumed to be parallel to the surface. The partition function for this rotation with the rotational constant B_{A} is given by:

$$q_{rot,1D} = \frac{\pi^{1/2}}{\sigma}\left(\frac{kT}{hc_0B_{\mathrm{A}}}\right)^{1/2} \tag{7}$$

The translational partition function for the mobile adsorbate equals $q^{\neq}_{\mathrm{tr,2D}}$ (Eq. (5)).

TAB. S III. Desorption prefactors in the mobile and immobile limit for azulene and naphthalene, and parameters necessary for the calculation. See the text for further details.

Adsorbate	Azulene on Cu(111)	Naphthalene on Cu(111)
Overlayer Structure	$(2\sqrt{3} \times 2\sqrt{3})$-R30°	$(2\sqrt{3} \times 2\sqrt{3})$-R30°
A (10^{-19} m^{-2})	6.79	6.79
	B_{A}: 0.0948	B_{A}: 0.104
Rotational Constants [14, 15]	B_{B}: 0.0419	B_{B}: 0.0411
(cm^{-1})	B_{C}: 0.0290	B_{C}: 0.0295
$\nu_{\mathrm{d,mobile}}$ (s^{-1})	$1.0 \cdot 10^{16}$	$9.9 \cdot 10^{15}$
$\nu_{\mathrm{d,im}}$ (s^{-1})	$1.3 \cdot 10^{22}$	$6.4 \cdot 10^{21}$

Hence, the translations contributions cancel in Eq. (3) and the prefactor for the mobile limit depends only on the rotational partition functions:

$$\nu_{\mathrm{d,mobile}} = \frac{kT}{h} \cdot \frac{q^{\neq}_{\mathrm{rot,3D}}}{q_{\mathrm{rot,1D}}} \tag{8}$$

In the immobile limit, the adsorbed molecule has no rotational or translational degrees of freedom. The corresponding prefactor $\nu_{\mathrm{d,im}}$ therefore depends only on the partition function of the transition state:

$$\nu_{\mathrm{d,im}} = \frac{kT}{h} \cdot q^{\neq}_{\mathrm{tr,2D}} \cdot q^{\neq}_{\mathrm{rot,3D}} \tag{9}$$

The resulting prefactors are shown in Table SIII. The mass m is $2.13 \cdot 10^{-25}$ kg for both azulene and naphthalene. For A, the area per molecule in the saturated layer is used. (This area is difficult to estimate, because it depends essentially on the lateral mobility of the molecule in the transition state. Some authors use the full area of the crystal here [13].) The symmetry factor σ counts the number of rotational operations ($\mathrm{C_n}$) plus the identity operation. For the free molecules, the values are 4 for naphthalene ($\mathrm{D_{2h}}$) and 2 for azulene ($\mathrm{C_{2v}}$). For the adsorbed molecules, the values are 2 for naphthalene ($\mathrm{C_{2v}}$) and 1 for azulene ($\mathrm{C_s}$). B_{A}, B_{B} and B_{C} are rotational constant for the molecules. The index A denotes the axis perpendicular to the molecule plane. For an exact treatment, the prefactor has to be calculated for each temperature. However, calculating it only for 300 K leads to a small error.

P8

IV. XPS MULTILAYER SPECTRA

Fig. S3 shows the multilayer C 1s XP spectra for azulene and naphthalene in a wider range than depicted in Fig. 3 of the main paper. Here, the shake-up satellites for both molecules are visible. The main satellite for azulene is at lower binding energy and thus closer to the regular C 1s peak.

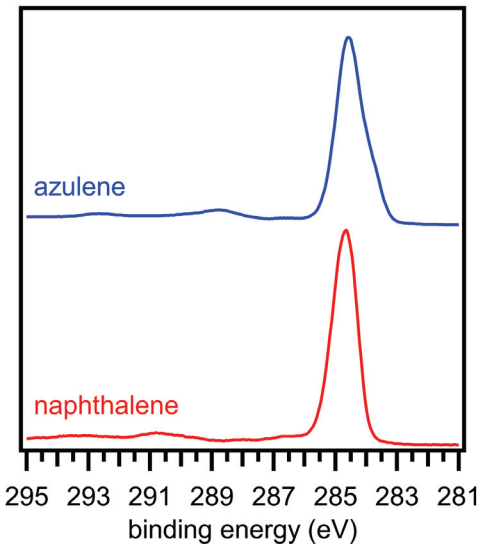

P8

FIG. S3. Multilayer C 1s XP spectra for azulene (top, blue) and naphthalene (bottom, red). The main shake-up satellites are at a binding energy of 289 eV for azulene and 291 eV for naphthalene.

V. SIMULATION OF THE XPS MULTILAYER SPECTRA

The C 1s signal of a azulene multilayer has a broad shape with a distinct shoulder at the low binding energy side (see Fig. 4(a) of the main text and Fig. S3). To understand this shape we calculated the relative peak positions for the different carbon atoms in the free molecule by DFT using the core level shift method described by Chong [16]. The results were found to be in agreement with previously reported values for azulene and naphthalene [17]. The DFT calculations give the relative peak positions for each carbon atom. From these calculations, we derived a fit model by creating a group of pseudo-Voigt peaks linked to each other in accordance with the relative peak positions and the stoichiometry. The resulting model has now six peaks (three for naphthalene), but only four fitted parameters (the position of the combined peak, the total intensity, the peak width and the Gauß-Lorentz ratio). This model was then fitted to the experimental data together with a background function and peaks for the satellites, yielding the good agreement as shown in Fig. 4(a) of the main text.

VI. NEXAFS DATA TREATMENT

This section shortly explains the data treatment used to obtain the shown NEXAFS spectra. The incident photon flux was monitored with a gold grid. Calibration of the photon energy was performed by means of the carbon-related absorption on the gold grid, as previously described [18]. The NEXAFS spectra were treated according to standard procedures [19]. All spectra of the samples and the clean Cu(111) substrate were corrected for a photon energy shift and normalized in the pre-edge region at 282 eV. For background correction, spectra of the clean Cu(111) substrate were fitted and then subtracted from the sample spectra. In a last step, the sample spectra were normalized in the range behind the absorption edge (300 eV).

P8

VII. STM AND NC-AFM IMAGES OF AZULENE ON CU(111) AT LOW COVERAGES

Fig. S4 shows a very low coverage and an intermediate coverage of azulene on Cu(111). It can clearly be seen that no islands are formed. Instead, the molecules tend to avoid each other.

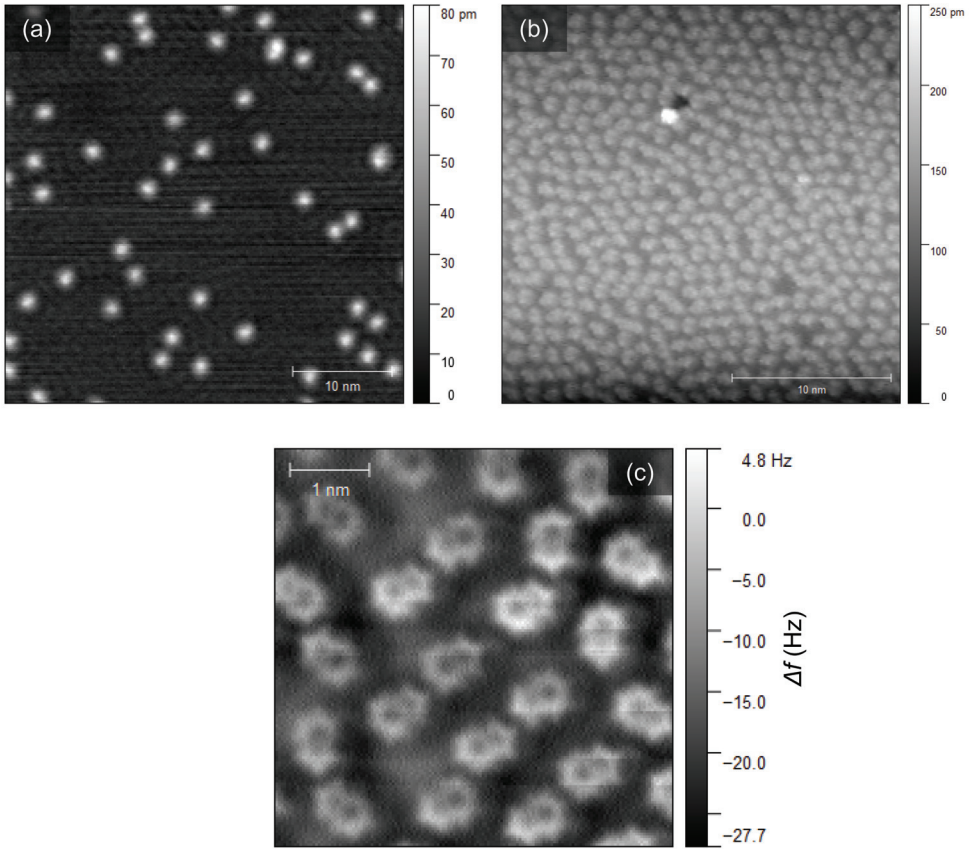

FIG. S4. (a) STM and nc-AFM images of azulene on Cu(111) at various submonolayer coverages. (a) STM image of a very low coverage of 0.01 ML. (b) STM image of an intermediate coverage of 0.4 ML, (c) nc-AFM image of the intermediate coverage of 0.4 ML. The molecules were adsorbed above room temperature, measurements were taken at 4.5 K. The formation of the disordered structure is therefore not caused by limited diffusion. Rather, it likely represents the equilibrium structure.

P8

VIII. NC-AFM IMAGES OF A ROTATION OF AN AZULENE MOLECULE

Fig. S5 shows the tip-induced rotation of an azulene molecule by a 60° angle

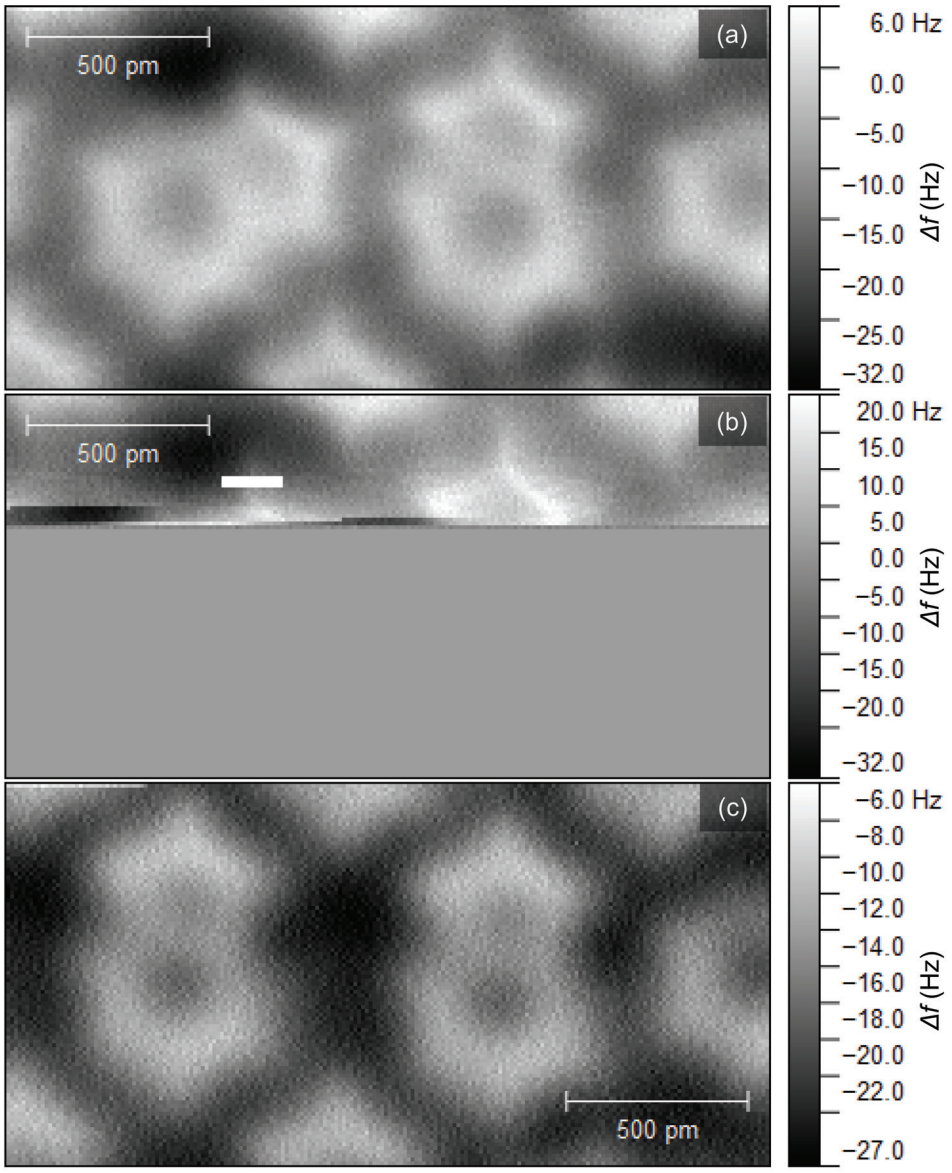

FIG. S 5. nc-AFM images illustrating the tip-induced rotation of an azulene molecule by 60°. (a) nc-AFM image before the rotation. (b) Interrupted nc-AFM scan during which the rotation occurred. (c) nc-AFM image after the rotation.

IX. NC-AFM AND STM IMAGES OF NAPHTHALENE

Fig. S6 shows STM and nc-AFM images of naphthalene adsorbed on Cu(111). In Fig. S6(c), a naphthalene molecule is laterally manipulated by the tip, something that has never been observed for azulene under otherwise identical conditions.

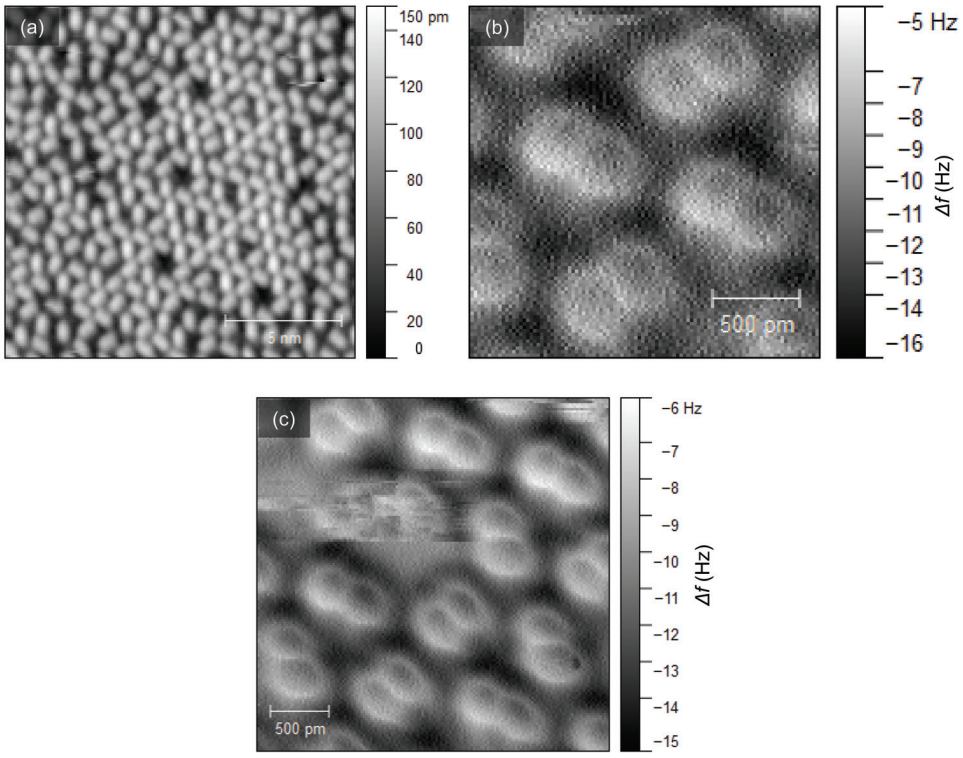

FIG. S 6. STM and nc-AFM images of naphthalene on Cu(111) at a coverage of approximately 0.6 ML: (a) STM image, (b) nc-AFM image, (c) nc-AFM image showing the higher mobility of the naphthalene molecules.

P8

X. CHARGE DENSITY DIFFERENCE PLOTS SHOWING THE PUSH-BACK EFFECT

Fig. S7 shows charge density difference plots for azulene and naphthalene adsorbed on copper. The plots show the same charge density difference calculations as Fig. 9 of the main text, but have a smaller isosurface value, so that the small changes in the case of naphthalene become visible. The images clearly show the operation of the so-called pillow effect, *i.e.*, the push-back of electron density between molecule and surface caused by Pauli repulsion [20]. The effect is more pronounced for azulene (Fig. S7(a,b)) than for naphthalene (Fig. S7(c,d)), in line with the larger work function change and the stronger lateral repulsion in the case of azulene.

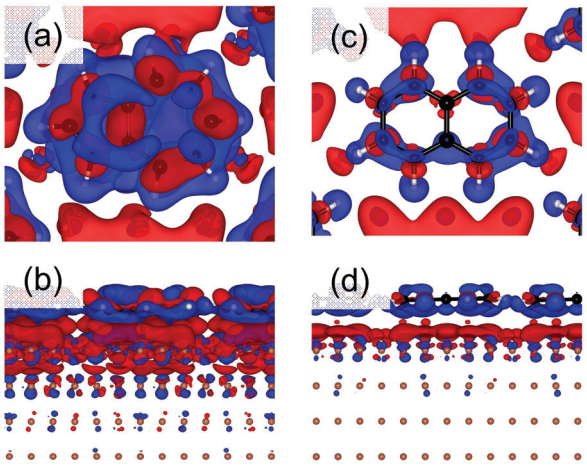

FIG. S 7. (a,b) Charge density difference plots for azulene. (c,d) Charge density difference plots for naphthalene. The isosurface value for all plots is 0.0007. Electrons flow from blue to red.

P8

XI. FURTHER COMPUTATIONAL DETAILS

A. General parameters and optimizations

Periodic density functional theory calculations of azulene and naphthalene on Cu(111) were performed with the Vienna Ab Initio Simulation Package (VASP) [21–24]. The PBE functional [25] was used in combination with the third-generation van der Waals dispersion correction by Grimme (DFT-D3) [26] and the projector-augmented wave (PAW) ansatz [27, 28] for the atomic cores. A plane-wave cutoff energy of 350 eV was employed. The Cu(111) surface was modeled as a 4-layer, $(2\sqrt{3} \times 2\sqrt{3})$-R30° copper atom slab (48 Cu atoms in total) in an hexagonal unit cell. Only the topmost two layers were freely optimized together with the adsorbed molecule, while the bottom two Cu layers were kept frozen at their optimized bulk positions. A vacuum layer of 30 Å was introduced to isolate the repeated slabs from each other. For all calculations, final geometry optimization with a $24 \times 24 \times 1$ Monkhorst-Pack k-point mesh was used, which was adjusted to the unit cell size. Geometries were optimized until the forces on the active atoms dropped below 0.01 eV/Å. Coordinates of the final optimized geometry are attached. STM simulations were visualized with the p4vasp program 0.3.29 based on the Tersoff-Hamann model [29]. The Bader charge analysis [30] was performed in ADF-BAND 2017 [31–35] on the level PBE-D3(BJ)/TZ2P [36–38]. Visualization was done with the program VESTA 3 [39].

P8

B. 7.2 XPS and NEXAFS simulations

All calculations were performed with the PBE functional [25], a plane-wave cutoff of 350 eV, and an $8 \times 8 \times 1$ Monkhorst Pack k-point grid sampling. We calculated the ground-state electronic structure as well as the density of states (DOS) and the molecular-orbital projected DOS [40], which reflects the interaction of the free molecular orbitals (MO) with the metal substrate using standard library ultra-soft pseudopotentials (USPPs) [41]. MO projections and core-level spectra are processed using a self-written post-processing tool for CASTEP [40]. We calculated XPS chemical shifts using the delta self-consistent field (DeltaSCF) method of constraining electronic occupations to resemble full core-hole excitations. NEXAFS simulations were performed using on-the-fly generated USPPs and the CASTEP module ELNES [42] and the transition-potential approach [43, 44], where the occu-

pation of the initial state orbital (here C 1s) is set to 0.5 and the corresponding Kohn-Sham eigen-energies are taken to reflect the NEXAFS spectrum. Atom-wise projected NEXAFS spectra result from XAS calculations for each individual C 1s center in the corresponding molecule. MO-projected spectra have been generated by multiplying XAS intensities with the absolute overlap matrix element of free azulene and naphthalene frontier molecular orbitals and the band structure of the corresponding adsorbed molecules on the surface. For more details on the computational settings and analysis see Diller *et al.* [45]. For more details on the implementation, see Maurer and Reuter [40].

P8

XII. APPROXIMATE C 1S NEXAFS SPECTRA FROM A CORE-LEVEL SHIFTED, SITE- AND ANGULAR MOMENTUM PROJECTED WAVE FUNCTION CHARACTER

In addition to the CASTEP/ELNES transition potential simulations of the NEXAFS (XAS) spectra shown in the main text and the previous section [40], we also used a more approximate way to simulate NEXAFS spectra that resorts to ground-state properties of the system only (*cf.* Bauer *et al.*, J. Phys. Chem. C, in press (2018); DOI: 10.1021/acs.jpcc.8b03746). This scheme employs occupied-unoccupied Kohn-Sham (PBE) orbital energy differences and the site- and angular momentum projected wave function character of each band obtained from standard periodic DFT calculations using the VASP program and the PAW method implemented in VASP. Specifically, excitation energies from a C 1s core level at a specified atom (*i.e.*, all carbon atoms in the present case of naphthalene and azulene) to an unoccupied band $\Phi_{a,k}$ (with band index a and k-point index k) were approximated as the difference $\Delta\varepsilon_{i,a,k}$ between the 1s core level energy $\varepsilon_{1s,i}$ at atom i (ICORELEVEL=1 tag of the VASP program) and the single-particle energy of $\varepsilon_{a,k}$ of the unoccupied band. The obtained $\Delta\varepsilon_{i,a,k}$ are uniformly shifted (by +17.8 eV) such that the onset of the simulated spectrum approximately matches the onset of the experimental spectrum. Approximate intensity information is obtained from the site- and (p_x,p_y,p_z)-projected wave function character of each band at the corresponding carbon atom as provided in the standard VASP PROCAR file. These data (multiplied with appropriate prefactors [46]) are interpreted as approximate dipole intensities for electronic transitions from the C 1s core levels to the unoccupied bands. The resulting line spectra were subsequently convoluted using a standard broadening procedure to obtain the continuous spectrum (*cf.* Fig. 5 of the main text). These simulated spectra, shown in Fig. S8, qualitatively reproduce salient features of the experimental NEXAFS spectra of free and adsorbed naphthalene and azulene, thereby allowing assignment of the dominant features. However, larger uncertainties in relative intensities compared to experiment and those found with the more sophisticated ELNES simulation method (see Fig. 5 of the main paper) are observed.

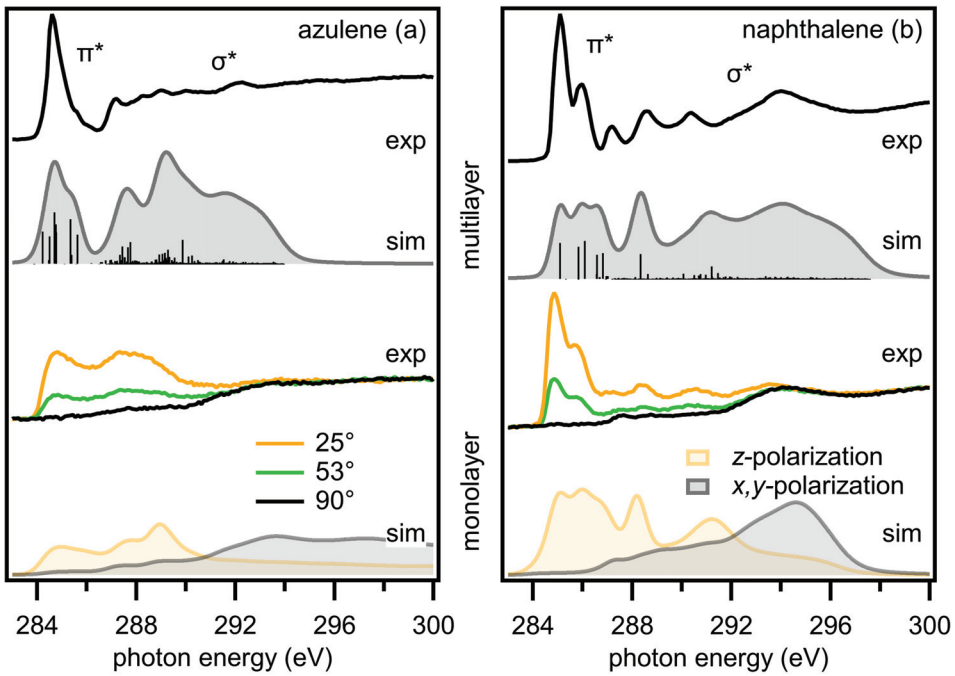

FIG. S 8. Comparison of the approximate NEXAFS with the experimental K-edge spectra of (a) azulene and (b) naphthalene using ground state core orbital energies and local DOS information from the VASP program as described in the text (PBE functional, $8 \times 8 \times 1$ MP k-point mesh, 400 eV plane wave cutoff); upper part: experimental multilayer spectra *vs.* simulated spectra of the isolated molecules; bottom part: experimental and simulated monolayer spectra on Cu(111); simulated spectra for x,y and z-polarization, respectively.

P8

XIII. DFT CALCULATIONS OF THE 5-7 DEFECTS IN GRAPHENE

The calculations for the 5-7 defect in free standing graphene were also performed in VASP on the level PBE-D3(BJ)/PAW with a plane-wave cutoff energy of 350 eV and 30 Å vacuum, the k-grid consisted only of the Γ-Point. The unit cell with 456 carbon atoms was chosen large enough to contain two 5-7 defects isolated by a quite large distance. The size of the cell was optimized for the regular graphene sheet with the same number of carbon atoms. Afterwards the positions of all atoms were allowed to relax. For the sake of simplicity, the local, planar minimum structure was used. In the absolute minimum, the defective graphene sheet distorts out of the plane, but the influence of this on the shown results is negligible. In Figure S9, sections through the charge density are shown for the complete unit cells.

To quantify the charge separation, the partial charges by the Hirshfeld method [47] were calculated using ADF-BAND 2017, PBE-D3(BJ)/TZ2P. In Table SIV, the Hirshfeld charges for all atoms of a 5-7 defect in a free standing graphene layer are compared to the corresponding atoms in a free azulene molecule (H/Cix labels the carbon or hydrogen bonded to the atom i). The higher charges of single carbon atoms in azulene are due to the positive hydrogens bonded to them. The charge separation between 5- and 7-membered ring is approximately the same.

P8

TAB. SIV. Hirshfeld charges for all atoms in the free azulene molecule and the corresponding atoms in a 5-7 defect in a free standing graphene layer. The charges were calculated with ADF-BAND, PBE-D3(BJ)/TZ2P and are given in units of the elementary charge.

	Azulene molecule	5-7 defect in graphene
C1	−0.05	−0.02
C2	−0.08	−0.02
C3	−0.01	−0.01
C4	−0.02	0.01
C5	−0.05	0.01
C6	−0.03	0.02
H/C1x	0.05	0.00
H/C2x	0.04	0.00
H/C4x	0.05	0.00
H/C5x	0.04	0.00
H/C6x	0.05	0.00
5-7 charge difference	−0.13	−0.11

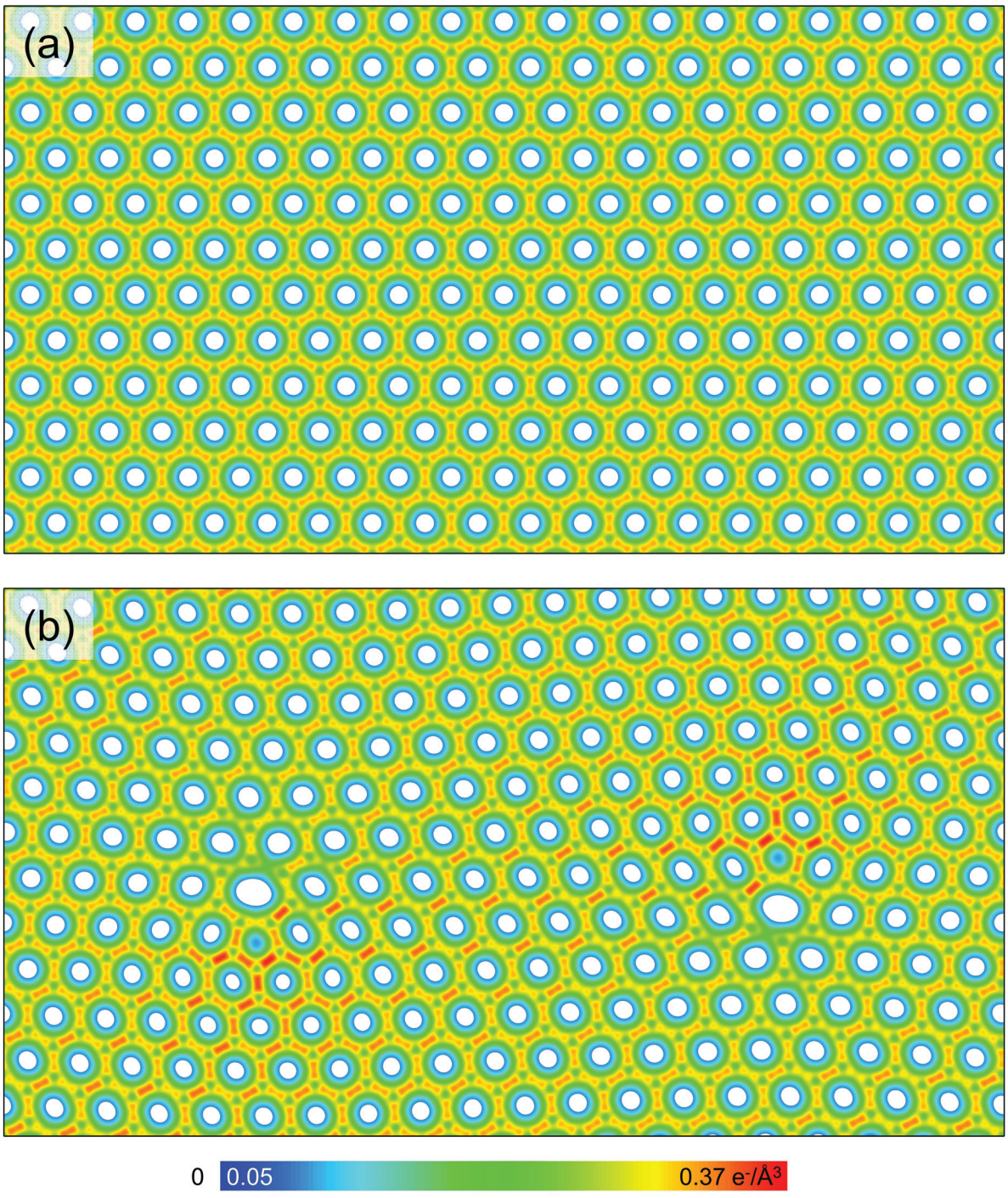

FIG. S 9. Section through the charge density for the pristine graphene layer and (b) Section through the charge density for the graphene layer with two isolated 5-7 defects.

XIV. COORDINATES OF THE OPTIMIZED STRUCTURES

Azulen/Cu(111) 2r3x2r3
1
7.568022460000000 -4.36939980000000 0.000000000000000
0.000000000000000 8.738799610000000 0.000000000000000
0.000000000000000 0.000000000000000 36.17926446000000
Cu C H
48 10 8
Selective dynamics
Direct
0.000000000000000 0.000000000000000 0.000000000000000 F F F
0.000000000000000 0.499999999427843 0.000000000000000 F F F
0.166666667107115 0.833333332599956 0.000000000000000 F F F
0.166666667107115 0.333333333172121 0.000000000000000 F F F
0.333333332892884 0.666666665683557 0.000000000000000 F F F
0.500000000000000 0.999999998855678 0.000000000000000 F F F
0.333333332892884 0.166666666255722 0.000000000000000 F F F
0.500000000000000 0.499999999427843 0.000000000000000 F F F
0.666666667107116 0.833333332599956 0.000000000000000 F F F
0.666666667107116 0.333333333172121 0.000000000000000 F F F
0.833333332892885 0.666666665683557 0.000000000000000 F F F
0.833333332892885 0.166666666255722 0.000000000000000 F F F
0.166666666618220 0.166666666508938 0.056931920279290 F F F
0.166666666618220 0.666666666302959 0.056931920279290 F F F
0.333333333236432 0.999999999413717 0.056931920279290 F F F
0.333333333236432 0.499999999619696 0.056931920279290 F F F
0.499999999841435 0.833333332723853 0.056931920279290 F F F
0.666666666459655 0.166666665834612 0.056931920279290 F F F
0.499999999841435 0.333333332929826 0.056931920279290 F F F
0.666666666459655 0.666666666040584 0.056931920279290 F F F
0.833333333077874 0.999999999151349 0.056931920279290 F F F
0.833333333077874 0.499999999357328 0.056931920279290 F F F
0.999999999696087 0.833333332468087 0.056931920279290 F F F
0.999999999696087 0.333333332674059 0.056931920279290 F F F
0.332848711742287 0.333142756485644 0.115767323384702 T T T
0.333944399347891 0.832252702573379 0.113583903438455 T T T
0.498776372726573 0.166722705301642 0.113970767316169 T T T
0.501236861790010 0.668019641089215 0.115075713986626 T T T
0.667309831488595 0.998890268402075 0.113608791035716 T T T
0.832682011849006 0.333056974937810 0.113025798858840 T T T
0.665866673764026 0.499652492344268 0.113412947856192 T T T
0.832657730001803 0.834493081026438 0.113620190128857 T T T
0.002377596951953 0.168702220403079 0.113641836261603 T T T
0.000648103772099 0.667219879417994 0.112747953509676 T T T
0.168723734918125 0.001553169781761 0.113521702475958 T T T
0.168293010209529 0.500101450888521 0.114192038788208 T T T
0.003542273969833 0.001397470270254 0.169515963191732 T T T
0.995586853201696 0.500229855557409 0.169684726246360 T T T
0.165816383748964 0.831261752870134 0.169641244571653 T T T
0.159907314083559 0.333063839345017 0.172632769537454 T T T
0.331102659512075 0.667935048678675 0.171536118234579 T T T
0.501899698384467 0.998335449466040 0.169684178695577 T T T
0.333157804904178 0.160171403137508 0.172617922787023 T T T
0.507770488664965 0.503244288153981 0.170720991328150 T T T
0.675543946421775 0.839583902330302 0.173041228333131 T T T
0.667931338531516 0.332903474198991 0.170467986700450 T T T
0.839844480335912 0.670092729863831 0.169091286764352 T T T
0.831932316391765 0.168382887005345 0.169447936628823 T T T
0.579150628447997 0.846922841596637 0.238213382312439 T T T
0.661194912187147 0.743196461287479 0.234599557762096 T T T
0.392078272030375 0.732046934184569 0.236339065353324 T T T
0.525374801494527 0.559346948401690 0.231686756385074 T T T
0.355654026144500 0.554099499562656 0.232825407110018 T T T
0.559967827167044 0.415662707310815 0.233959990837919 T T T
0.181098159666244 0.400682195732401 0.234100593555557 T T T
0.436114046979300 0.233542716514849 0.236820659109727 T T T
0.137134919600026 0.222939891065926 0.236042706789866 T T T
0.249081647991366 0.146834949914951 0.236399578945025 T T T
0.646391816086344 0.987768549140986 0.244327445121005 T T T
0.800096080941010 0.787169649528222 0.239706778955689 T T T
0.292568557229814 0.769477232050355 0.241878871827307 T T T
0.698849323161297 0.453851576019774 0.238166120244715 T T T
0.073311283341860 0.427837557284057 0.239074065223796 T T T
0.492486739387064 0.148316813279354 0.241903987723039 T T T
0.996472152732013 0.128599843958274 0.240284084407146 T T T
0.181365811112745 0.004844530493394 0.242065023580986 T T T

Naphthalene 2r3x2r3
1
7.568022460000000 -4.36939980000000 0.000000000000000
0.000000000000000 8.738799610000000 0.000000000000000
0.000000000000000 0.000000000000000 36.17926446000000
Cu C H
48 10 8
Selective dynamics
Direct
0.000000000000000 0.000000000000000 0.000000000000000 F F F
0.000000000000000 0.499999999427843 0.000000000000000 F F F
0.166666667107115 0.833333332599956 0.000000000000000 F F F
0.166666667107115 0.333333333172121 0.000000000000000 F F F
0.333333332892884 0.666666665683557 0.000000000000000 F F F
0.500000000000000 0.999999998855678 0.000000000000000 F F F
0.333333332892884 0.166666666255722 0.000000000000000 F F F
0.500000000000000 0.499999999427843 0.000000000000000 F F F
0.666666667107116 0.833333332599956 0.000000000000000 F F F
0.666666667107116 0.333333333172121 0.000000000000000 F F F
0.833333332892885 0.666666665683557 0.000000000000000 F F F
0.833333332892885 0.166666666255722 0.000000000000000 F F F
0.166666666578578 0.166666666431901 0.056931920279290 F F F
0.166666666578578 0.666666666317468 0.056931920279290 F F F
0.333333333289289 0.999999999405816 0.056931920279290 F F F
0.333333333289289 0.499999999634682 0.056931920279290 F F F
0.499999999867868 0.833333332771396 0.056931920279290 F F F
0.666666666446439 0.166666665793670 0.056931920279290 F F F
0.499999999867868 0.333333332885829 0.056931920279290 F F F
0.666666666446439 0.666666666022536 0.056931920279290 F F F
0.833333333025017 0.999999999159250 0.056931920279290 F F F
0.833333333025017 0.499999999388116 0.056931920279290 F F F
0.999999999735728 0.833333332476464 0.056931920279290 F F F
0.999999999735728 0.333333332705322 0.056931920279290 F F F
0.332853113624547 0.332599895405494 0.114047050022079 T T T
0.333408318363100 0.833226313668926 0.113757018622032 T T T
0.500109256437448 0.166731575001489 0.113745891982721 T T T
0.500098248591397 0.667144598396518 0.113993013851469 T T T
0.666916045222523 -0.000183624304412 0.113726726184362 T T T
0.833638754575209 0.333262306512019 0.113572061878632 T T T
0.667146000612182 0.499890820378755 0.113672170602830 T T T
0.833208673483383 0.833001319905958 0.113722053177966 T T T
0.000072793715471 0.166610771843711 0.113762069106949 T T T
0.000200138767617 0.666530949754057 0.113566733009820 T T T
0.167015983198996 0.000022467842902 0.113762374730593 T T T
0.166669903654652 0.499943185568165 0.113898793080459 T T T
0.000328343677067 -0.000314455216769 0.170612160919380 T T T
-0.001190657166005 0.499807971140068 0.171002959553344 T T T
0.165988803420421 0.832339604467639 0.170853169087652 T T T
0.165424635346845 0.332951872830138 0.170977086515402 T T T
0.332542300071236 0.666711505774503 0.171021337847523 T T T
0.500546866581887 -0.000464614945201 0.170678715040574 T T T
0.334058582206586 0.165116531697342 0.171159078139636 T T T
0.501408422316647 0.500022346982154 0.170098764044209 T T T
0.668461735647842 0.834357243272314 0.171147210280296 T T T
0.667706093225853 0.332900229885767 0.170808810793530 T T T
0.834578403257074 0.666837218162010 0.170871328095671 T T T
0.832974045049519 0.166894125259719 0.170890761074688 T T T
0.165249064813437 0.329305182828500 0.251750690542174 T T T
0.166406854650206 0.171634319065875 0.251004044155810 T T T
0.327953293681096 0.171036611508222 0.251113839613198 T T T
0.486953710800903 0.328505866913074 0.252075202811573 T T T
0.326327528732237 0.493259927387571 0.252978374836590 T T T
0.490624816823994 0.492871090330571 0.253052936363472 T T T
0.329983680861787 0.657604572740771 0.253183523039333 T T T
0.489101908859226 0.814830260278483 0.253858301239660 T T T
0.650726266770028 0.814621051706984 0.253989088229004 T T T
0.651670325338827 0.656894671677769 0.253503904280052 T T T
0.040375533745838 0.329921042325217 0.251374689909797 T T T
0.042582101683431 0.045650639056368 0.249762828573744 T T T
0.325237836556824 0.044818593300200 0.250240623151760 T T T
0.612300883327786 0.328689720265213 0.251744463530555 T T T
0.776540064929746 0.656131959529495 0.253113943341222 T T T
0.774546771255215 0.940584700673086 0.254262293884787 T T T
0.491813036306483 0.941154031429324 0.253812969493004 T T T
0.204767310826226 0.657499944033975 0.252712377762836 T T T

[1] F. C. Bocquet, G. Mercurio, M. Franke, G. van Straaten, S. Wei, S. Soubatch, C. Kumpf, and F. S. Tautz, "Torricelli: A software to determine atomic spatial distributions from normal incidence x-ray standing wave data," Comput. Phys. Commun. **235**, 502–513 (2018).

[2] K. Christmann, *Introduction to Surface Physical Chemistry* (Steinkopff Verlag, Springer-Verlag, Darmstadt, New York, 1991).

[3] A. M. de Jong and J. W. Niemantsverdriet, "Thermal desorption analysis: Comparative test of ten commonly applied procedures," Surf. Sci. **233**, 355–365 (1990).

[4] D. L. S. Nieskens, A. P. van Bavel, and J. W. Niemantsverdriet, "The analysis of temperature programmed desorption experiments of systems with lateral interactions; implications of the compensation effect," Surf. Sci. **546**, 159–169 (2003).

[5] E. Bauer, F. Bonczek, H. Poppa, and G. Todd, "Thermal desorption of metals from tungsten single crystal surfaces," Surf. Sci. **53**, 87–109 (1975).

[6] D. A. King, "Thermal desorption from metal surfaces: A review," Surf. Sci. **47**, 384–402 (1975).

[7] S. L. Tait, Z. Dohnálek, C. T. Campbell, and B. D. Kay, "n-alkanes on mgo(100). i. coverage-dependent desorption kinetics of n-butane," J. Chem. Phys. **122**, 164707 (2005).

[8] P. A. Redhead, "Thermal desorption of gases," Vacuum **12**, 203–211 (1962).

[9] R. I. Masel, *Principles of adsorption and reaction on solid surfaces, Wiley series in chemical engineering* (1996).

[10] H. Eyring, "The activated complex in chemical reactions," J. Chem. Phys. **3**, 107–115 (1935).

[11] J. M. Gottfried, E. K. Vestergaard, P. Bera, and C. T. Campbell, "Heat of adsorption of naphthalene on pt(111) measured by adsorption calorimetry," J. Phys. Chem. B **110**, 17539–17545 (2006).

[12] T. L. Hill, *An Introduction to Statistical Thermodynamics* (Addison-Wesley Publishing Company, Inc., Reading, MA, 1960).

[13] A. Redondo, Y. Zeiri, J. J. Low, and W. A. Goddard, "Application of transition state theory to desorption from solid surfaces: Ammonia on ni(111)," J. Chem. Phys. **79**, 6410–6415 (1983).

[14] M. Goubet and O. Pirali, "The far-infrared spectrum of azulene and isoquinoline and supporting anharmonic density functional theory calculations to high resolution spectroscopy of

polycyclic aromatic hydrocarbons and derivatives," J. Chem. Phys. **140**, 044322 (2014).

[15] O. Pirali, M. Goubet, T. R. Huet, R. Georges, P. Soulard, P. Asselin, J. Courbe, P. Roy, and M. Vervloet, "The far infrared spectrum of naphthalene characterized by high resolution synchrotron ftir spectroscopy and anharmonic dft calculations," Phys. Chem. Chem. Phys. **15**, 10141–50 (2013).

[16] D. P. Chong, "Localized and delocalized 1s core-holes in dft calculations," J. Electron Spectrosc. Rel. Phenom. **159**, 94–96 (2007).

[17] D. P. Chong, "Density functional theory study on the electron spectra of naphthalene and azulene vapours," Can. J. Chem. **88**, 787–796 (2010).

[18] S. Reiß, *Spektroskopische Untersuchungen verschiedener molekularer Adsorbate auf der Titandioxid(110)-Oberfläche*, Thesis (2001).

[19] J. Stöhr, *NEXAFS Spectroscopy* (Springer-Verlag, 1992).

[20] G. Witte, S. Lukas, P. S. Bagus, and C. Wöll, "Vacuum level alignment at organic/metal junctions: cushion effect and the interface dipole," App. Phys. Lett. **87**, 263502 (2005).

[21] G. Kresse and J. Hafner, "Ab initio molecular dynamics for liquid metals," Phys. Rev. B **47**, 558–561 (1993).

P8

[22] G. Kresse and J. Hafner, "Ab initio molecular-dynamics simulation of the liquid-metal-amorphous-semiconductor transition in germanium," Phys. Rev. B **49**, 14251–14269 (1994).

[23] G. Kresse and J. Furthmüller, "Efficiency of ab-initio total energy calculations for metals and semiconductors using a plane-wave basis set," Comput. Mat. Sci. **6**, 15–50 (1996).

[24] G. Kresse and J. Furthmüller, "Efficient iterative schemes for ab initio total-energy calculations using a plane-wave basis set," Phys. Rev. B **54**, 11169–11186 (1996).

[25] J. P. Perdew, K. Burke, and M. Ernzerhof, "Generalized gradient approximation made simple," Phys. Rev. Lett. **77**, 3865–3868 (1996).

[26] S. Grimme, J. Antony, S. Ehrlich, and H. Krieg, "A consistent and accurate ab initio parametrization of density functional dispersion correction (dft-d) for the 94 elements h-pu," J. Chem. Phys. **132**, 154104 (2010).

[27] P. E. Blöchl, "Projector augmented-wave method," Phys. Rev. B **50**, 17953–17979 (1994).

[28] G. Kresse and D. Joubert, "From ultrasoft pseudopotentials to the projector augmented-wave method," Phys. Rev. B **59**, 1758–1775 (1999).

[29] J. Tersoff and D. R. Hamann, "Theory of the scanning tunneling microscope," Phys. Rev. B

31, 805–813 (1985).

[30] R. F. W. Bader, *Atoms in Molecules - A Quantum Theory* (Oxford University Press, Oxford, 1990).

[31] G. te Velde and E. J. Baerends, "Precise density-functional method for periodic structure," Phys. Rev. B **44**, 7888 (1991).

[32] G. Wiesenekker and E. J. Baerends, "Quadratic integration over the three-dimensional brillouin zone," J. Phys.: Condens. Matter **3**, 6721 (1991).

[33] M. Franchini, P. H. T. Philipsen, E. van Lenthe, and L. Visscher, "Accurate coulomb potentials for periodic and molecular systems through density fitting," J. Chem. Theory Comput. **10**, 1994–2004 (2014).

[34] M. Franchini, P. H. T. Philipsen, and L. Visscher, "The becke fuzzy cells integration scheme in the amsterdam density functional program suite," J. Comput. Chem. **34**, 1819–1827 (2013).

[35] BAND2017, SCM, Theoretical Chemistry, Vrije Universiteit, Amsterdam, The Netherlands, http://www.scm.com.

[36] G. te Velde, F. M. Bickelhaupt, S. J. A. van Gisbergen, C. Fonseca Guerra, E. J. Baerends, J. G. Snijders, and T. Ziegler, "Chemistry with adf," J. Comput. Chem. **22**, 931–967 (2001).

[37] C. Fonseca Guerra, J. G. Snijders, G. te Velde, and E. J. Baerends, "Towards an order-n dft method," Theor. Chem. Acc. **99**, 391–403 (1998).

[38] E. van Lenthe and E. J. Baerends, "Optimized slater-type basis sets for the elements 1-118," J. Comput. Chem. **24**, 1142–1156 (2003).

[39] K. Momma and F. Izumi, "Vesta 3 for three-dimensional visualization of crystal, volumentric and morphology data," J. Appl. Cryst. **44**, 1272–1276 (2011).

[40] R. J. Maurer and K. Reuter, "Excited-state potential-energy surfaces of metal-adsorbed organic molecules from linear expansion -self-consistent field density-functional theory (scf-dft)," J. Chem. Phys. **139**, 014708 (2013).

[41] D. Vanderbilt, "Soft self-consistent pseudopotentials in a generalized eigenvalue formalism," Phys. Rev. B **41**, 7892–7895 (1990).

[42] M. Teruyasu, T. Isao, G. Shang-Peng, and J. P. Chris, "First-principles calculation of spectral features, chemical shift and absolute threshold of elnes and xanes using a plane wave pseudopotential method," J. Phys.: Condens. Matter **21**, 104204 (2009).

[43] L. Triguero, L. G. M. Pettersson, and H. Ågren, "Calculations of near-edge x-ray-absorption

spectra of gas-phase and chemisorbed molecules by means of density-functional and transition-potential theory," Phys. Rev. B **58**, 8097–8110 (1998).

[44] M. Klues, K. Hermann, and G. Witte, "Analysis of the near-edge x-ray-absorption fine-structure of anthracene: A combined theoretical and experimental study," J. Chem. Phys. **140**, 014302 (2014).

[45] K. Diller, R. J. Maurer, M. Müller, and K. Reuter, "Interpretation of x-ray absorption spectroscopy in the presence of surface hybridization," J. Chem. Phys. **146**, 214701 (2017).

[46] M. Cohen and R. P. McEachran, "Length and velocity formulae in approximate oscillator strength calculations," Chem. Phys. Lett. **14**, 201–204 (1972).

[47] F. L. Hirshfeld, "Bonded-atom fragments for describing molecular charge densities," Theor. Chim. Acta **44**, 129–138 (1977).

P8

6 Additional Results

Besides the data that have already been published in scientific journals and are included in the cumulative part of this dissertation, some further research projects have been conducted. However, the data of these projects are currently incomplete or not relevant enough for publication in a journal. Nevertheless, the results shall be mentioned and discussed in this chapter. The first project is the investigation of the 1,3-dibromoazulene (DBAz) precursor on the Ag(111) surface. The second one is concerned with the initial operation of a commercially available atomic layer injection (ALI) device, which can be used to deposit molecules from solution.

6.1 Investigations of 1,3-Dibromoazulene on the Ag(111) Surface

The 1,3-dibromoazulene (DBAz) precursor has been intensively studied on the Cu(111) surface and the results investigating the ring/chain ratio are published in the articles P1 and P2. To further expand these investigations and to study the influence of the substrate, experiments on the Ag(111) surface were conducted. Later on, Cu atoms were co-deposited with the DBAz precursor because the reactivity of the Ag(111) surface was not sufficient to trigger the complete debromination of the precursor molecules.

6.1.1 DBAz on Bare Ag(111)

The deposition of DBAz on Ag(111) was performed in the same way as on Cu(111) (*cf.* P1 and P2) using the line-of-sight evaporator described in Section 4.3. Deposition of a monolayer on Ag(111) leads to the formation of an ordered structure of small molecular features, which extends over large areas of the surface (Figure 6.1a). A closer inspection of these repetitive features reveals that they are azulene dimers connected by C−Ag−C bonds (Figure 6.1b). This observation is in line with a partial cleavage of the C−Br bond after deposition

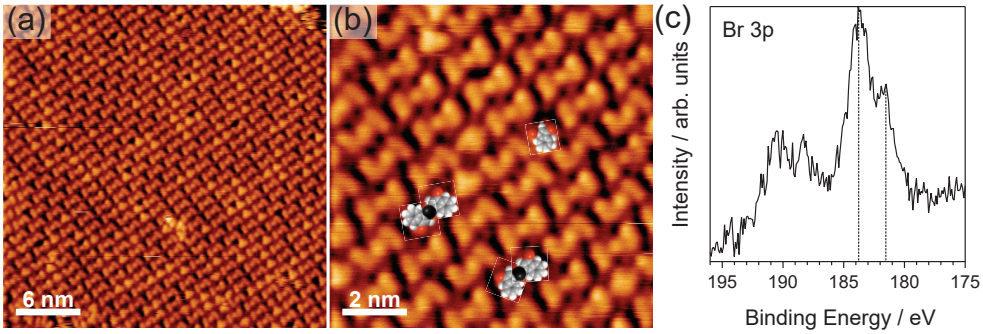

Figure 6.1: DBAz on Ag(111) after deposition at 300 K. (a) Large-scale STM image showing a regular structure formed on a large terrace. (b) Close-up STM image showing the formation of azulene dimers connected by C−Ag−C bonds. Molecular models indicating *cis* and *trans* dimers and an intact molecule are superimposed. Color code: white, hydrogen; gray, carbon; red, bromine; black, silver. (c) Br 3p XP spectrum indicating the partial debromination of the DBAz precursor. The peaks of the Br $3p_{3/2}$ components corresponding to C-bonded and chemisorbed Br are indicted by dashed lines. Tunneling parameters: (a) $U_t = -0.49$ V, $I_t = -0.15$ nA; (b) $U_t = -0.49$ V, $I_t = -0.17$ nA.

at 300 K reported for other precursor molecules on Ag(111).[43,246] The Ag atoms connecting the two azulene monomers can clearly be seen in the close-up STM image (Figure 6.1b) as round features between the two azulene monomers. As has already been discussed in P1 the two azulene monomers can either be connected *cis* or *trans*. Indeed, both connection motifs are observed as indicated by the molecular models superimposed to the STM image in Figure 6.1b. Besides these *cis*- and *trans*-connected organometallic dimers, features with a triangular shape are observed, which appear smaller than the dimers. These are tentatively assigned to intact DBAz molecules. This is in accordance with the Br 3p XP spectrum (Figure 6.1c), which shows two doublets. The doublet with the Br $3p_{3/2}$ peak located at a binding energy of 183.8 eV corresponds to C-bonded Br, while that with the Br $3p_{3/2}$ peak located at a binding energy of 181.5 eV is associated with chemisorbed Br. Although the quality of the spectrum does not allow meaningful fitting to determine the exact ratio of the two Br species, it can be stated that less than half of the C−Br bonds are cleaved. A similar behavior has been reported for the 1,3-bis(*p*-bromophenyl)-5-(*p*-iodophenyl)benzene (BIB) precursor on Ag(111), where 38% of the C−Br bonds are broken after deposition at 300 K.[43]

In order to cleave the remaining intact C−Br bonds, the sample was stepwise annealed (Figure 6.2). After annealing to 360 K the coverage seems to be reduced compared to the situation after deposition at 300 K (Figure 6.2a,b). Furthermore, streaky features appear in the STM images, which can be caused by mobile molecules. These findings can be explained by the weaker interaction of the DBAz precursor with the Ag(111) surface compared to Cu(111).[247] Ap-

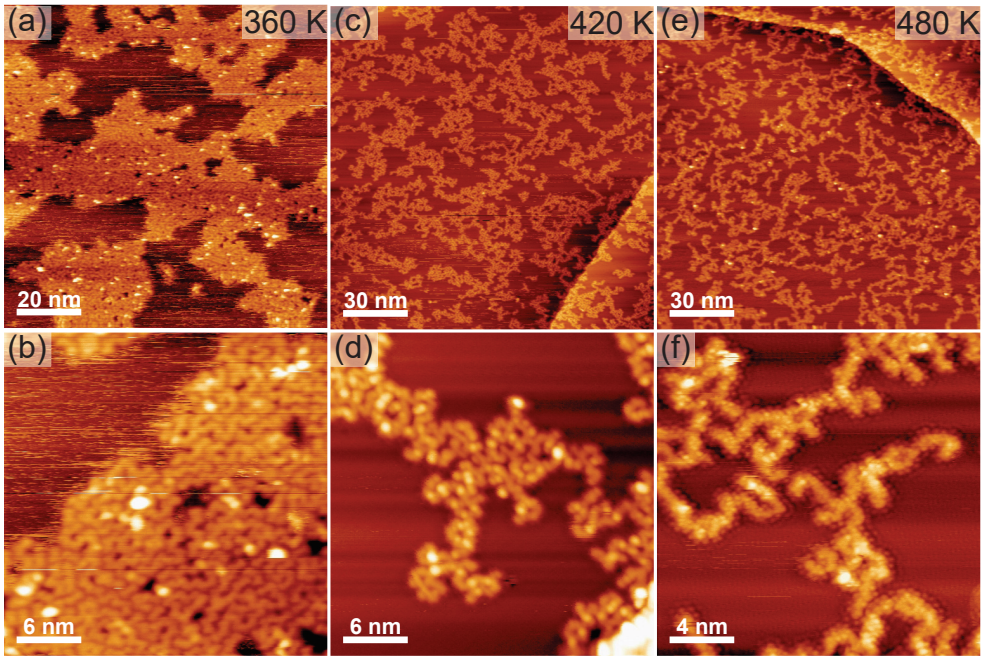

Figure 6.2: Annealing series of DBAz on Ag(111). (a), (b) Large-scale and close-up STM images after annealing the sample from Figure 6.1 to 360 K. (c), (d) Large-scale and close-up STM images after annealing the same sample to 420 K. (e), (f) Large-scale and close-up STM images after annealing the same sample to 480 K. Tunneling parameters: (a) $U_t = -3.63$ V, $I_t = -0.08$ nA; (b) $U_t = -3.63$ V, $I_t = -0.10$ nA; (c) $U_t = -3.63$ V, $I_t = -0.09$ nA; (d) $U_t = -3.02$ V, $I_t = -0.11$ nA; (e) $U_t = -3.63$ V, $I_t = -0.07$ nA; (f) $U_t = 1.96$ V, $I_t = 0.09$ nA.

parently, some of the molecules desorb from the surface before cleavage of both C−Br bonds takes place, which is required to obtain organometallic oligomers. Whether these molecules desorb as monomers or as the dimers observed in Figure 6.1 cannot be stated. Dimers are no longer observed and the molecules seem to have formed short oligomeric chains, which aggregate into islands, but no cyclic hexamers are present.

If the sample is further annealed to 420 K, the situation changes again (Figure 6.2c,d). This temperature should still be too low to initiate covalent C−C bond formation and thus a completely organometallic network is expected. In analogy to the experiments on Cu(111) (*cf.* P1 and P2) and to the case of 4,4''-dibromo-1,1':3',1''-terphenyl (DMTP) on Ag(111)[45] this should result in a mixture of rings and chains. However, the situation is different for DBAz on Ag(111). The streaky features observed after annealing to 360 K are less and the size of the islands, into which the molecules aggregate, seems to be decreased. Some ring-shaped features are observed but these cannot clearly be assigned to cyclic hexamers. The structure of the chains cannot be further elucidated by the close-up STM image in Figure 6.2d but it seems as if they were branched. This could have happened due to dehydrogenative coupling reactions between different chains.

In a third step the sample was annealed to 480 K (Figure 6.2e,f). This temperature should be high enough to enable covalent C−C bond formation.[45] Such a reaction could not be observed for DBAz on Cu(111), which was attributed to the strong steric hindrance between the H atoms in the 2-positions of the azulene molecule. The large-scale STM image in Figure 6.2e shows chains, which appear longer than those observed after annealing to 420 K (*cf.* Figure 6.2c). However, again these chains seem to be branched and no obvious structure can be deduced. This is not possible from the close-up STM image shown in Figure 6.2f either. What can be stated is that the chains seem to be comparably uniform in height, which would support the hypothesis of a covalent C−C bond formation. Furthermore, small round features are visible around the chains, which are attributed to the split-off Br atoms, an observation regularly made in surface-confined Ullmann coupling reactions.[39,55]

6.1.2 Co-Deposition of DBAz and Cu on Ag(111)

Apparently the interaction of the DBAz precursor with the Ag(111) surface is too weak to cleave all C−Br bonds before desorption of the molecules starts. However, cleavage of all these bonds is necessary to obtain a completely organometallic network, which is required to maximize the ring yield by applying the principle of thermodynamic reaction control (for details, *cf.* the discussion in P1 and P2). Thus, an alternative approach was chosen to investigate the influence of the Ag(111) surface on the ring/chain ratio compared with Cu(111). In this approach, Cu atoms were co-deposited to DBAz on Ag(111) in order to cleave the remaining intact C−Br bonds and to obtain a completely organometallic network by the formation of C−Cu−C bonds in addition to the already present C−Ag−C bonds.

In a first attempt, the applicability of the chosen approach was tested. For this purpose, a saturation coverage of DBAz was deposited at 300 K on Ag(111) (defined as 1.0 ML). Cu atoms were co-deposited on this sample with an electron beam evaporator. The exact amount of co-deposited Cu is unknown and this topic will be addressed later. The sample was stepwise annealed for 30 min and the influence of the co-deposited Cu atoms was investigated with STM and XPS (Figure 6.3). After deposition at 300 K (Figure 6.3a) the situation resembles that on bare Ag(111) (*cf.* Figure 6.1). Mostly organometallic dimers and even some intact molecules are present. This is supported by the Br 3p XP spectrum (Figure 6.3f). After deposition at 300 K two doublets with approximately equal intensities are observed. As discussed for the sample without Cu (*cf.* Figure 6.1c)

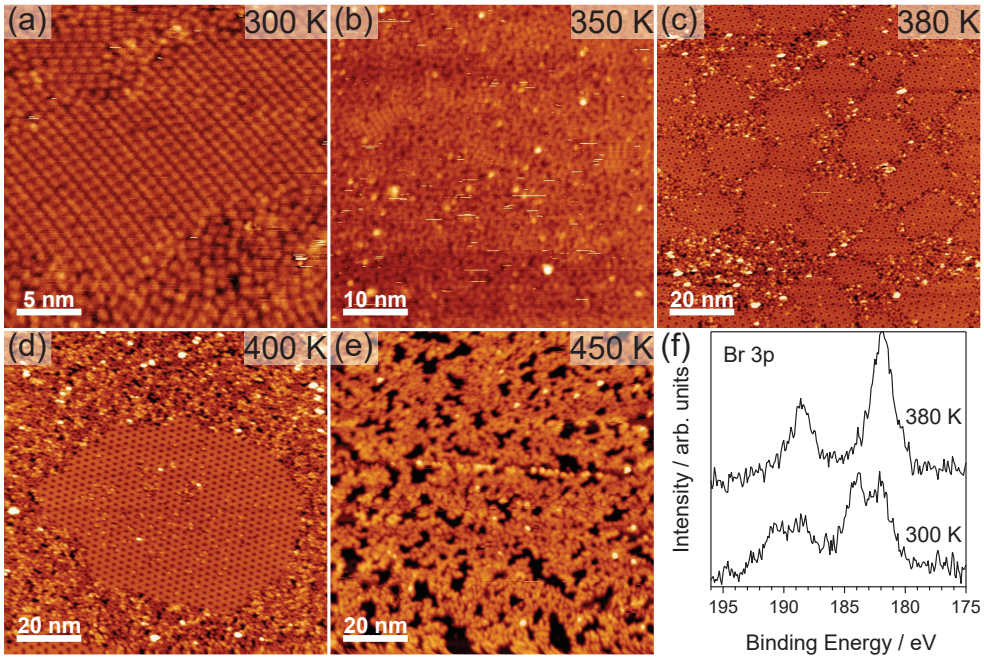

Figure 6.3: Annealing series of DBAz on Ag(111) with co-deposited Cu. (a) to (e) STM images of a sample with saturation coverage (defined as 1.0 ML) after deposition at 300 K and annealing to the indicated temperatures. (f) Br 3p XP spectra after deposition at 300 K and annealing to 380 K, indicating the partial and complete debromination, respectively. Tunneling parameters: (a) $U_t = 0.88$ V, $I_t = 0.06$ nA; (b) $U_t = 1.28$ V, $I_t = 0.12$ nA; (c) $U_t = -2.59$ V, $I_t = -0.12$ nA; (d) $U_t = 2.43$ V, $I_t = 0.05$ nA; (e) $U_t = 2.43$ V, $I_t = 0.05$ nA.

the doublets with the Br $3p_{3/2}$ peaks located at a binding energy of 183.8 eV and 182.1 eV correspond to C-bonded and chemisorbed Br, respectively.

After annealing the sample to 350 K, a different situation than on bare Ag(111) is observed (Figure 6.3b). The coverage is not decreased compared to deposition at 300 K and no streaky features associated with mobile molecules are present in the STM image. Instead, the molecules have mostly formed chains and also some cyclic hexamers are found. The ring yield is 4% and was determined in the same way as in P1 and P2, *i.e.*, the number of rings was counted manually and the area occupied by the monomers incorporated in cyclic hexamers was referenced to the total area occupied by all monomers. In addition to the organometallic species, still some small islands of dimers are present. Accordingly, the temperature was sufficiently high to cleave most of the C−Br bonds and the situation resembles that after deposition at 300 K on Cu(111). Most of the species are organometallic oligomers but it cannot be stated whether Cu, Ag, or a mixture of both is present in the C−M−C bonds. However, the temperature was still too low to make the formation of these C−M−C bonds reversible and thus enter the regime of thermodynamic reaction control.

In order achieve thermodynamic reaction control, the sample was annealed to 380 K (Figure 6.3c), leading to a high yield of cyclic hexamers of 54%. This yield is higher than that observed for a coverage of 1.0 ML of DBAz on Cu(111) (*cf.* P1 and P2). The cyclic hexamers form many small islands, which are separated by small areas of short chains. The Br 3p XP spectrum in Figure 6.3f shows only one doublet with the peak of the Br $3p_{3/2}$ component located at a binding energy of 181.9 eV. This peak corresponds to chemisorbed Br and shows that all C−Br bonds are cleaved at this annealing temperature.

According to P2, an optimum temperature to maximize the ring yield is expected. To test this expectation, the sample was further annealed to 400 K (Figure 6.3d). The rings now form larger islands (center and bottom left of Figure 6.3d), which are surrounded by larger areas of chains and the ring yield is decreased to 34%. Thus, the optimum temperature for ring formation is exceeded at 400 K.

On Cu(111) no covalently bonded hexamers could be observed. In order to test this on Ag(111) with co-deposited Cu atoms, the sample was annealed to 450 K (Figure 6.3e). After this annealing step, no hexamers are present anymore. Furthermore, the coverage is decreased to 0.9 ML compared to the previous temperature steps. Nevertheless, the observed short, branched chains appear very uniform in height. Thus, covalent C−C bond formation might have happened, also *via* dehydrogenative coupling reactions. However, covalent hexamers cannot be realized on Ag(111) with co-deposited Cu atoms either.

The expected optimum temperature to maximize the ring yield has been confirmed and was determined to be 380 K. Interestingly, this temperature is lower than for DBAz on Cu(111) (430 K, *cf.* P2). The reason might again be the weaker interaction of the azulene moiety with Ag(111). As a consequence, the molecules might be mobile enough to diffuse and form the energetically more stable rings already at lower temperature. Another reason might be the weaker C−Ag−C bonds in comparison with C−Cu−C bonds.[36,45] However, this conclusion remains speculative since it cannot be stated whether Ag or Cu atoms or a mixture of both are present in the organometallic C−M−C bonds. Furthermore, the influence of the excess co-deposited Cu atoms, which remain on the surface, cannot be satisfactorily determined. As already mentioned, this topic will be addressed later.

As a next point, the influence of the DBAz coverage on the ring/chain ratio on Ag(111) with co-deposited Cu atoms is investigated. For this purpose, samples with different coverages of DBAz were prepared. Afterwards, different amounts of Cu were co-deposited and the samples were annealed at the optimum temper-

ature for ring formation of 380 K for 30 min. STM images of samples with four different coverages after annealing to 380 K are shown in Figure 6.4. Deposition of a low coverage of 0.04 ML (referenced to the saturation coverage shown in Figure 6.4d, which is defined as 1.0 ML) leads to a mixture of rings and chains (Figure 6.4a). The situation is different to a low-coverage sample on Cu(111). The rings do not appear isolated, but rather aggregate into islands. A larger island can be seen on the bottom of Figure 6.4a. Furthermore, the ring yield of 38% is lower than for a low-coverage sample on Cu(111) (*cf.* P1 and P2).

Annealing a medium-coverage sample (0.5 ML) of DBAz on Ag(111) with co-deposited Cu leads to a similar situation (Figure 6.4b). Here, a large island of rings is observed. Those monomers, which are not incorporated in this island, mostly form rather short zigzag chains and some larger rings than the cyclic hexamer. In between the chains, a few additional cyclic hexamers are present. The ring yield is strongly increased to 81%, which is much higher than for a medium-coverage sample on Cu(111) (*cf.* P2).

A high-coverage sample (0.9 ML) of DBAz on Ag(111) with co-deposited Cu atoms is shown in Figure 6.4c. The situation resembles that of the medium-coverage sample. A large island of rings is observed, while the structures around that island are mostly short zigzag chains. The ring yield is decreased to 59%.

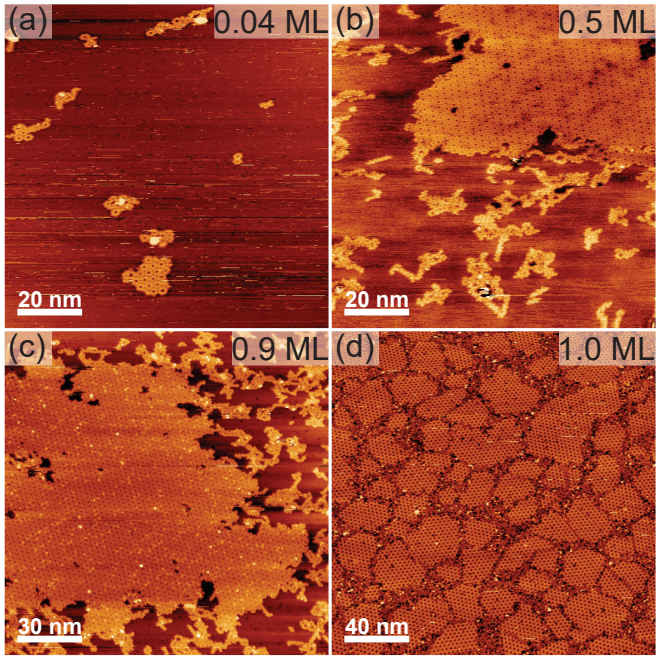

Figure 6.4: Coverage series of DBAz on Ag(111) with co-deposited Cu. (a) to (d) STM images of samples with the indicated coverages after annealing at 380 K for 30 min. Tunneling parameters: (a) $U_t = -3.52$ V, $I_t = -0.14$ nA; (b) $U_t = 1.44$ V, $I_t = 0.06$ nA; (c) $U_t = 1.96$ V, $I_t = 0.04$ nA; (d) $U_t = 2.51$ V, $I_t = 0.06$ nA.

At last, a sample with saturation coverage (defined as 1.0 ML) was investigated (Figure 6.4d). This sample shows a different behavior. The rings form many small islands, which are surrounded by short chains. This situation has already been described after annealing the sample in the annealing series to 380 K (*cf.* Figure 6.3c). The ring yield is only slightly decreased to 58% compared to the sample with a coverage of 0.9 ML.

The trends in the coverage series differ from those observed for DBAz on Cu(111) (*cf.* P2). In these studies the highest ring yield was obtained for the lowest coverage and it decreased with increasing coverage. This finding is explained by the competition between ring closure and chain growth as first- and second-order reactions, respectively. For DBAz on Ag(111) with co-deposited Cu the ring yield shows a maximum for an intermediate coverage of 0.5 ML and the ring yield is lowest for the sample with the lowest coverage. These observations cannot be explained exclusively by the competition between first- and second-order reactions. Thus, it seems likely that the differences are caused by the co-deposited Cu atoms. At this point, the problem of the amount of co-deposited Cu arises.

For the different samples shown in Figure 6.4 the amount of Cu was not kept constant. This amount along with the DBAz coverage Θ_{DBAz} and the resulting ring yield is shown in Table 6.1. Furthermore, the amount of co-deposited Cu is referenced to the DBAz coverage (Cu / Θ_{DBAz}). The amount of co-deposited Cu is given as the ion flux of the electron beam evaporator used for the deposition multiplied by the time. No clear statements concerning the influence of the amount of Cu can be made. However, some considerations are possible. First of all, it can be stated that all monomers are incorporated in organometallic rings or chains and no monomers or dimers are observed in the presented STM images (*cf.* Figures 6.3c and 6.4). This observation indicates

Table 6.1: Ring yield, amount of co-deposited Cu and amount of Cu referenced to the DBAz coverage (Cu / Θ_{DBAz}) for the samples with different coverages of DBAz Θ_{DBAz} on Ag(111) shown in Figures 6.3c and 6.4.

Θ_{DBAz} / ML	Ring yield / %	Cu / nA min	Cu / Θ_{DBAz} / $\frac{\mathrm{nA\,min}}{\mathrm{ML}}$
0.04	38	37.8	945
0.5	81	35.0	70
0.9	59	105	117
1.0	58	125	125
1.0[a]	54	270	270

[a] Sample from the annealing series shown in Figure 6.3c.

that the amount of co-deposited Cu was always (over-)stoichiometric, *i.e.*, it was sufficient to cleave all (remaining) intact C−Br bonds. The lowest amount of Cu referenced to the DBAz coverage was deposited on the sample with a coverage of 0.5 ML (70 nA min/ML). For all other samples, the amount of Cu was significantly higher. Interestingly, this is the sample with the highest ring yield. The lowest ring yield was observed for the sample with the highest amount of Cu referenced to the DBAz coverage (0.04 ML, 38%, 945 nA min/ML). This observation suggests that a low amount of Cu per DBAz monomer is beneficial for a high ring yield. This hypothesis is further supported by the fact that the two samples with a similar amount of Cu per DBAz precursor (0.9 and 1.0 ML, 117 nA min/ML and 125 nA min/ML, Figure 6.4c and d, respectively) show a similar ring yield. Furthermore, a comparison of the two samples with saturation coverage (Figures 6.3c and 6.4d) shows that the higher ring yield is observed for the sample with the lower amount of Cu.

It would be desirable to quantify the exact amount of co-deposited Cu. For this purpose, XPS seems to be the method of choice. The Ag 3d and Cu 2p XP spectra and a plot of the Cu/Ag intensity ratio of the samples with DBAz coverages of 0.5, 0.9, and 1.0 ML from the coverage series (*cf.* Figure 6.4b to d) are shown in Figure 6.5. For the sample with a coverage of 0.04 ML (Figure 6.4a) no Cu 2p XP spectrum was measured. The samples show an increasing Cu/Ag ratio with increasing coverage. This is in accordance with the data of the flux monitor of the electron beam evaporator (*cf.* Table 6.1). However, the exact amount of Cu cannot be determined from the XPS data because a sample with a known amount of Cu would be needed as a reference. Furthermore, for the analysis of the data it needs to be considered that the amount of organics on top of the Ag(111) substrate is different. This leads to a different damping of the Ag 3d signal and thus has an influence on the Cu/Ag ratio.

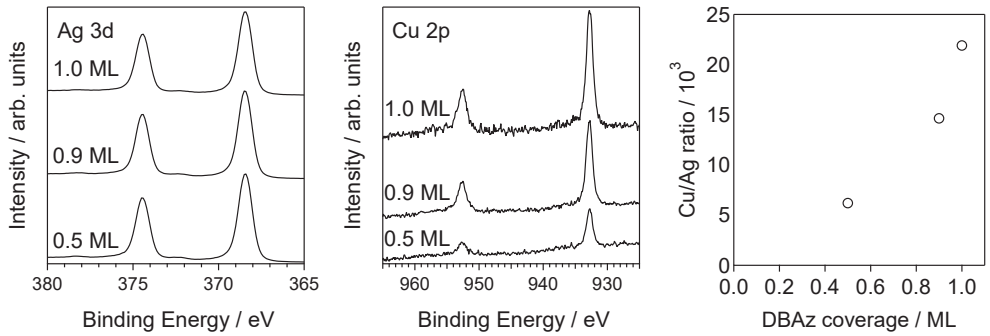

Figure 6.5: Ag 3d and Cu 2p XP spectra and Cu/Ag ratio of DBAz on Ag(111) with co-deposited Cu for the samples with DBAz coverages of 0.5, 0.9, and 1.0 ML (Figures 6.4b to d).

Based on these qualitative observations, it can be speculated that the amount of Cu should be as low as possible to cleave all the remaining intact C−Br bonds and form C−Cu−C bonds. In that case, the organometallic rings and chains would be adsorbed on a pure Ag(111) surface and the influence of the Cu would be minimized. If higher amounts of Cu are deposited, the excess Cu atoms remain adsorbed on the Ag(111) surface as adatoms, Cu clusters, or even closed Cu layers, which influence the interaction between the DBAz precursors and the Ag(111) substrate. Because of the high ring yield observed for the sample with the lowest amount of co-deposited Cu it seems possible that the ring yield on Ag(111) can be increased compared to the case of DBAz on Cu(111). A possible explanation for this is the weaker interaction of the azulene monomers with Ag(111) already mentioned before.[247] Due to the weaker interaction, diffusion of the monomers might be increased, which gives access to thermodynamic reaction control at lower temperatures. Another reason might be the weaker C−Ag−C bond compared with the C−Cu−C bond, which becomes reversible at lower temperatures. These effects could, in turn, increase the ring yield, because the entropically favored chains are formed with a lower probability at lower temperature. However, based on the available data, these suggestions cannot be proven and further experiments would be required.

In summary, it can be said that the formation of organometallic oligomers based on the DBAz precursor on Ag(111) can be achieved with co-deposited Cu atoms, which is not possible without Cu. Yet, it cannot be shown whether Cu, Ag, or a mixture of both is present in the C−M−C bonds. The presented results suggest that the ring yield could be significantly increased compared to DBAz on Cu(111) (*cf.* P1 and P2). However, in order to confirm these suggestions and to show general trends, the influence of the co-deposited Cu atoms would need to be investigated further. Possible additional experiments should consider the following two aspects. First, the necessary amount of Cu should be determined and substantiated by XPS. For this purpose, the amount of Cu could be varied on samples with the same coverage of DBAz. If the optimum amount of Cu per DBAz monomer is known, a coverage series with precisely that amount of Cu for the respective samples could be investigated. Second, the amount of Cu could be kept constant while the coverage of DBAz is varied. By this means, general trends for the influence of the DBAz coverage on the ring yield could be obtained and compared to the results on Cu(111) presented in P2, while a maximization of the ring yield and the direct comparison of the influence of the substrate between Cu(111) and Ag(111) would not be possible.

6.2 Atomic Layer Injection

The atomic layer injection (ALI) device provided by BihurCrystal S.L. is a commercially available device that can be used for the deposition of molecules on surfaces from solution under UHV conditions. This might be required for large or unstable molecules that cannot be deposited intact by thermal evaporation. In the ALI device the solution is inserted into the pre-injection system, which can be loaded using an inert driving gas. The deposition is performed by a magnetic pulse valve, which is opened for a short time so that the solution is drawn into the deposition chamber, which has a lower pressure. Small droplets of the solution land on the surface, the solvent evaporates and the molecules remain adsorbed on the surface. The whole deposition process is controlled by a software, which also records the pressure in the deposition chamber.

In order to test the ALI device, it was mounted to the load lock of the preparation chamber of the combined STM and XPS setup of the Gottfried group in Marburg (*cf.* Section 3.4.1). *meso*-tetraphenylporphyrin (2HTPP, *cf.* Figure 1.3b) was chosen for the test measurements because it is well characterized on surfaces.[159] For this purpose, a solution with a concentration of $c = 1 \cdot 10^{-5}$ mol/l in dichloromethane (DCM) was prepared and inserted into the pre-injection system. The deposition with the ALI device was performed on Ag(111) with Ar as the driving gas. The parameters used for the deposition are given in Table 6.2 and will be explained briefly. t_{log} is the logging time used by the software, *i.e.*, the time interval, in which the pressure in the deposition chamber is recorded. The actuation pressure p_{act} and the locking pressure p_{lock} give the pressure range in the deposition chamber, in which the pulsing valve can be opened. Only if the pressure is below p_{act}, the pulsing valve will be opened. If it exceeds p_{lock} it will be closed. t_{on} is the maximum duration of a pulse. If p_{lock} is not exceeded after this time, the pulse valve will be closed anyway. t_{off} is the minimum time between two pulses. The pulse valve will only be opened after this time, although the pressure might be below p_{act} earlier. However, if the pressure is still above p_{act} after t_{off}, the pulse valve will not be opened. p_{inj} is the pressure in the pre-injection system. This pressure can be adjusted by the driving gas and the higher it is, the more solution will be pulsed into the deposition chamber.

Table 6.2: Parameters used for the deposition of 2HTPP on Ag(111) with the ALI device.

t_{log} / s	p_{act} / mbar	p_{lock} / mbar	t_{on} / s	t_{off} / min	p_{inj} / mbar
0.10	$5 \cdot 10^{-7}$	0.01	0.01	2	1040

To test the deposition, a series of several pulsing sequences was performed. After each sequence, the sample was checked with XPS to see whether molecules were deposited and to get an estimation of the coverage. The C 1s, N 1s, Ag 3d, and Cl 2p XP spectra are shown in Figure 6.6. The XP spectra recorded before deposition show that the Ag(111) surface was clean (Figure 6.6i). After the first sequence with 10 pulses (Figure 6.6ii) the presence of C-containing species can be seen in the C 1s spectrum. However, due to the background caused by the Ag 3d signal in the N 1s region, it is difficult to tell whether there is also N present on the surface. Furthermore, the Cl 2p spectrum shows that the sample contains Cl contaminations, which most likely originate from the solvent DCM.

To deposit more 2HTPP on the sample, another sequence with 10 pulses (Figure 6.6iii) was performed. As expected, the intensity of the C 1s signal is increased. Moreover, the intensity of the Cl 2p signal is decreased and only a small amount of Cl remains on the sample. Perhaps the DCM solvent molecules are replaced by 2HTPP. After the deposition of a total of 30 pulses (Figure 6.6iv) the Cl 2p signal is completely gone and the intensity of the C 1s signal is further increased. However, the N 1s spectrum still does not allow a clear statement whether N is present on the sample.

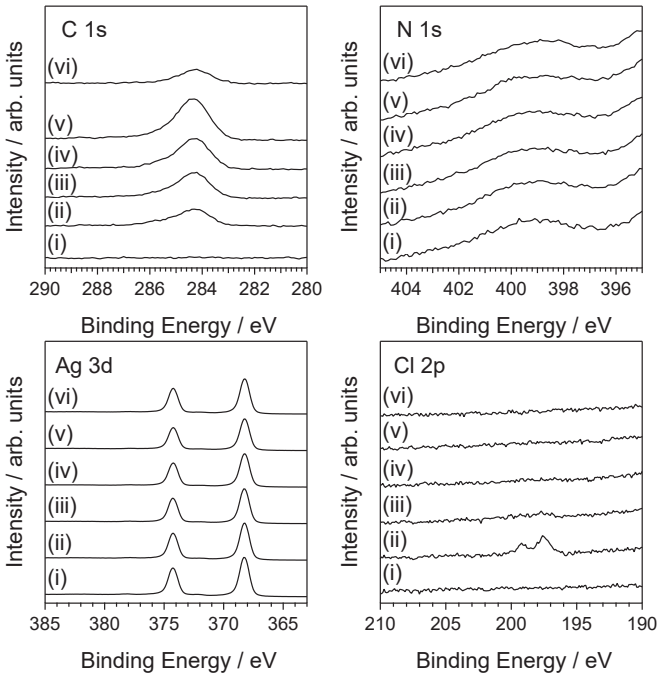

Figure 6.6: C 1s, N 1s, Ag 3d, and Cl 2p XP spectra after deposition of 2HTPP on Ag(111) with the ALI device recorded (i) before the deposition, after the deposition of (ii) 10 pulses, (iii) 20 pulses, (iv) 30 pulses, (v) 60 pulses, and (vi) after annealing the sample to 540 K for 5 min.

To get a thicker layer of 2HTPP, another sequence of 30 pulses was performed (Figure 6.6v). After this sequence changes in the N 1s region around a binding energy of 398 eV are clearly visible compared with the spectrum of the clean Ag(111) surface (Figure 6.6i). Thus, it seems likely that 2HTPP was successfully deposited on the sample. The intensity of the C 1s signal is further increased, so that a thin multilayer of 2HTPP on Ag(111) was expected.

To desorb the multilayer and obtain a monolayer of 2HTPP on Ag(111), the sample was annealed to 540 K (Figure 6.6vi). Indeed, the intensity of the C 1s signal is decreased and the N 1s spectrum resembles those after deposition of a lower number of pulses. Accordingly, the sample was investigated with STM (Figure 6.7) to check the coverage of the 2HTPP molecules. The large-scale STM image (Figure 6.7a) shows square features, which can clearly be assigned to 2HTPP molecules.[248] However, the coverage is lower than the expected monolayer. To determine the coverage, the number of 2HTPP molecules per area is compared with data reported in the literature. While in the STM image in Figure 6.7a the density of the 2HTPP molecules is 0.10 nm^{-2}, this value was calculated to be 0.51 nm^{-2} from an STM image of a monolayer of 2HTPP on Ag(111) reported by Di Santo *et al.*[249] Thus, a coverage of 0.20 ML results after annealing the sample to 540 K.

The close-up STM image in Figure 6.7b shows the structure of the 2HTPP molecules more clearly. Most of the molecules appear as two bright lobes. This appearance has been reported for 2HTPP on Cu(111).[250,251] Interestingly, a lot of small dots appear around the molecules. Since all the Cl is desorbed from the surface as shown by the XP spectra in Figure 6.6, these dots cannot be Cl atoms. However, as indicated by the Br 3p XP spectrum (Figure 6.7c), a lot of Br is present on the sample. This cannot originate from the molecule itself or the solvent. Yet, a number of brominated precursor molecules had been investigated

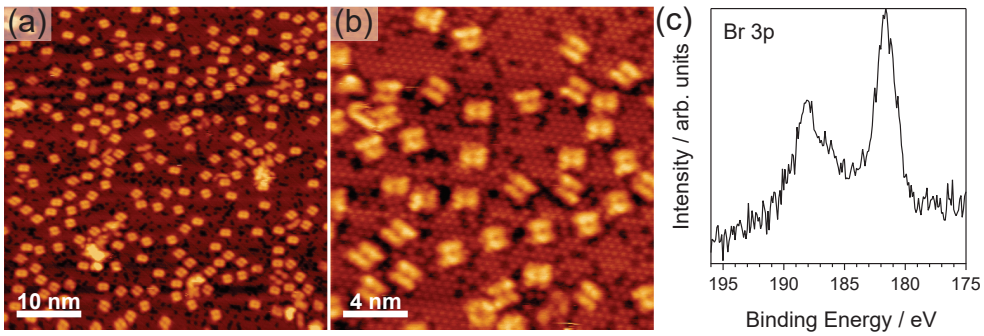

Figure 6.7: (a) Large-scale, (b) close-up STM images, and (c) Br 3p XP spectrum of 2HTPP on Ag(111) after annealing the sample to 540 K for 5 min. Tunneling parameters: (a), (b) $U_t = 1.49$ V, $I_t = 0.02$ nA.

in the UHV chambers prior to the shown measurements. It seems likely that these precursor molecules are the source of the Br contaminations.

The Br contaminations also help to explain the lower coverage than expected. Because the Br layer decouples the 2HTPP molecules from the Ag(111) substrate the interaction is weaker and a large fraction of the monolayer has already desorbed at a lower temperature than expected. Such a decoupling by halogen atoms has been reported for an organic layer by I atoms.[252] Nevertheless, based on the coverage of 0.20 ML and the intensity ratios of the C 1s and Ag 3d XP spectra (Figure 6.6) the coverages after the other pulsing sequences can be estimated. For this purpose, the C/Ag ratios are referenced to the value of the sample after annealing to 540 K. The results are given in Table 6.3.

The question for future uses of the ALI device is, how reproducible the amount of deposited molecules per pulse is. It can be seen that with the first 10 pulses 0.26 ML of 2HTPP were deposited. With the second and third 10 pulses, this amount decreased to 0.10 ML per 10 pulses. However, as was shown in the Cl 2p XP spectrum after the first pulsing sequence (Figure 6.6ii) there were Cl contaminations present on the sample. These were most likely caused by the solvent DCM. If the solvent molecules were replaced by 2HTPP and desorbed intact, this explains why the amount of C-containing species was higher for the first 10 pulses and decreased for the following sequences. The lower increase of only 0.15 ML with the 30 pulses of the fourth pulsing sequence could be explained by the Br contaminations on the sample. These weaken the interaction of 2HTPP with the substrate and perhaps not all molecules stay adsorbed on the surface. Thus, the presented results help to give an estimation of how many molecules are deposited with 1 pulse under the settings given in Table 6.2.

In summary, the successful initial operation of the ALI device on the combined STM and XPS setup of the Gottfried group was shown using a solution of 2HTPP in DCM. The deposition of intact 2HTPP molecules was demonstrated by STM and the amount of molecules per pulse was estimated by XPS. This knowledge can be used as a starting point for further preparations using the ALI device.

Table 6.3: Coverages of the different samples of 2HTPP on Ag(111) shown in Figure 6.6 prepared with the ALI device. The coverages are calculated by the C/Ag ratio and referenced to the monolayer coverage reported in ref. [249].

Sample	C/Ag ratio	Coverage / ML
(ii)	0.0048	0.26
(iii)	0.0069	0.36
(iv)	0.0088	0.46
(v)	0.0126	0.61
(vi)	0.0035	0.20

7 Summary

This thesis deals with several aspects of surface and interface chemistry. In this context the presented studies aim at a fundamental understanding of the processes that occur in on-surface synthesis, as well as the interactions of organic molecules with metal substrates and co-deposited metal atoms. For this purpose, a number of microscopic and spectroscopic techniques have been applied, which allow to study the relevant questions of the different projects.

The main topic of this thesis is concerned with the on-surface synthesis of carbon-based nanostructures on metal single-crystal surfaces. Here, different brominated molecules were used as precursors for the surface-confined Ullmann coupling reaction. The investigations especially focus on the organometallic or covalent ring and chain structures formed as reaction products. Different strategies were applied to steer the reaction outcome to the desired direction and to understand how the ring/chain ratio can be influenced by parameters such as temperature or coverage.

1,3-Dibromoazulene (DBAz) on Cu(111) was chosen as a model system for the investigation of the ring/chain competition and the product structures were studied by scanning tunneling microscopy (STM). The connection pattern of the Br substituents in this molecule is chosen in a way that it enables the formation of rings as well as chains. It was demonstrated that upon deposition at 300 K an organometallic intermediate of the surface-confined Ullmann coupling is formed. Analysis of the data showed the preferential formation of oligomeric chains. Annealing of the samples to higher temperatures ($\geq$ 430 K) led to an increase of cyclic organometallic hexamers. In order to explain this finding the principles of kinetic and thermodynamic reaction control were applied. At 300 K the thermal energy is sufficient to cleave the C−Br bonds and to form organometallic oligomers connected by C−Cu−C bonds. However, these organometallic bonds, which can be considered reversible in general, are irreversible on the time scale of the experiment at this temperature. These non-equilibrium conditions are associated with kinetic reaction control. Under these conditions the connection pattern of the oligomer products is determined by statistics, which makes the formation of rings unlikely because all six monomers in a hexamer would have to

be connected with the same orientation. At elevated temperatures, the C−Cu−C bonds become reversible, *i.e.*, they are broken and reformed again quickly. This leads to equilibrium conditions and thermodynamic reaction control. Under these conditions the single monomer units can rearrange their connection pattern until an energetically more stable product is formed. This energetically more stable product is the cyclic hexamer because it possesses one more C−Cu−C bond compared with the open-chain hexamer. The situation becomes more difficult if the coverage as a second parameter is taken into account. An analysis of the ring/chain ratio of samples with different coverages showed a decreasing ring yield with increasing coverage. To explain this finding, reaction kinetics have to be considered. Whereas chain growth is a second-order reaction because two molecules (monomers or already existing chains) need to react intermolecularly, ring closure is a first-order reaction, in which the two ends of an existing chain react intramolecularly. While first-order reactions are preferred at low concentrations, *i.e.*, low coverages, second-order reactions compete more strongly with increasing concentration. In this way, the decreasing ring yield with increasing coverage can be explained. Furthermore, the existence of an optimal temperature to maximize the ring yield of 430 K was found. This observation can be understood based on thermodynamic considerations. Since the rings are formed at all they must be the energetically favored product. However, this means that the chains are the entropically favored product and an increased temperature should again lead to preferred chain formation. Thus, the optimal temperature for ring formation is just high enough to reach the regime of thermodynamic reaction control, *i.e.*, reversible C−Cu−C bonds. All these fundamental considerations have been applied to Monte Carlo (MC) simulations, in which the DBAz precursor was represented by a simple model. A good qualitative agreement between simulation and experiment supports the conclusions made and additionally suggests their general applicability to on-surface synthesis.

In order to investigate the influence of the substrate on the ring/chain ratio, the studies using the DBAz precursor were expanded to the Ag(111) surface. The reactivity of this substrate towards debromination is not sufficient to obtain a completely organometallic network before desorption of the molecules starts. Thus, Cu atoms were co-deposited to the DBAz molecules and it was shown that a completely organometallic network could be obtained in this way. A decreased optimal temperature for the maximization of the ring yield of 380 K compared with Cu(111) was found. This observation is explained by the weaker interaction of the azulene precursor with the Ag(111) surface and the weaker C−Ag−C

bonds compared to C−Cu−C bonds. Both these aspects enable thermodynamic reaction control at a lower temperature. However, the amount of co-deposited Cu atoms was not kept constant for samples with different DBAz coverages and thus no obvious statements concerning the dependence of the ring yield on the coverage can be made. Yet, the data suggest that a lower amount of Cu is beneficial for a higher ring yield, because the highest ring yield was observed for the sample with the lowest amount of Cu in relation to the DBAz coverage.

A different approach to control the ring/chain ratio was chosen by applying a surface template. In this study a vicinal Ag surface with small terraces of equal size was used to favor chain growth of the 4,4''-dibromo-1,1':3',1''-terphenyl (DMTP) precursor. The kinked steps of the curved Ag(645) crystal are oriented in a way that they can reconstruct in order to perfectly match the structure of the covalent DMTP polymer chains. The formation of chains in a very high yield and their alignment in the direction of the steps was proven by STM and low-energy electron diffraction (LEED). The structural quality of the polymer chains was high enough to study them with the space-averaging angle-resolved photoemission spectroscopy (ARPES) technique. The ARPES measurements showed a band dispersion in the direction of the chains, whereas no dispersion was observed in the perpendicular direction. Furthermore, a comparison with poly-(*para*-phenylene) chains showed the influence of the *meta* junctions on the electronic structure of organic polymer chains. These results were substantiated by scanning tunneling spectroscopy (STS) experiments and density functional theory (DFT) calculations.

Exclusive chain formation can, of course, also be achieved by an appropriate design of the precursor molecule. This was demonstrated by using 2,6-dibromoazulene (2,6-DBAz), a structural isomer of DBAz, on the Au(111) surface. In this precursor molecule the Br substituents are located on both ends of the azulene backbone and thus only allow a linear connection. The exclusive formation of chains was shown by STM, while this technique could not reveal the connection pattern of the single azulene monomer units within the oligomers. For this purpose, non-contact atomic force microscopy (nc-AFM) with submolecular resolution was applied and a random connection pattern was observed. In an additional reaction step the fusion of single oligomer chains by dehydrogenative coupling was demonstrated. Again, the formed structures were elucidated by nc-AFM. Depending on the connection pattern of the individual chains and their relative orientation nanoribbons of two new carbon allotropes with non-alternant π topology were found. Namely, these are phagraphene and

tetra-penta-hepta-graphene, which had been theoretically predicted but not experimentally observed before.

The presented studies investigate ring and chain structures formed as reaction products in on-surface synthesis. They provide different ways how to produce one of the two reaction products with high yield. Based on fundamental considerations and a clever design of the reaction parameters, samples with high structural homogeneity can be prepared. These findings help to better understand the fundamental processes that determine the products of on-surface synthesis. Thus, they might be applied in the precise fabrication of carbon-based nanodevices.

In addition to the investigations of on-surface synthesis, a number of studies concerned with surface and interface chemistry have been presented. These investigate the interactions between organic molecules and metal substrates or co-deposited metal atoms in general. In this connection the polymorphism of 1,1':3',1'':4'',1'''-quaterphenyl-4,4'''-dicarbonitrile (*m*-4PDN) on Ag(111) was studied. It was shown that this molecule forms different adsorbate structures depending on the coverage. While at saturation coverage a densely-packed layer is formed, at a low coverage of 0.1 ML two different ordered phases are observed. One of these phases consists of both flat-lying and upright-standing molecules, which had not been reported before. The direct metalation of tetrapyrrole macrocycles was investigated for *meso*-tetraphenylporphyrin (2HTPP) and 2,3,8,12,17,18-hexaethyl-7,13-dimethylcorrole (3HHEDMC). For the metalation of thin films of 2HTPP with Co the reaction depth was determined and the formation of a diffuse interphase rather than an abrupt interface was observed. For 3HHEDMC the stabilization of a metal trication was shown, whereas for porphyrins usually dications are observed. The influence of the molecular π topology on the adsorption and desorption was studied for the non-alternant model molecule azulene and compared with its alternant counterpart naphthalene. It was shown that the non-alternant azulene interacts much more strongly with the Cu(111) surface than naphthalene.

As an additional result the successful initial operation of a commercially available atomic layer injection (ALI) device on the combined STM and XPS setup of the Gottfried group in Marburg was shown. For this purpose, 2HTPP was deposited on Ag(111) from a dichloromethane (DCM) solution. The intact deposition of 2HTPP molecules was shown by STM and X-ray photoelectron spectroscopy (XPS) was applied to estimate the amount of molecules deposited per pulse of the ALI device.

The experimental part of this thesis is completed by the design and construction of technical equipment for the combined STM and XPS setup in the laboratory of the Gottfried group. Redesign of the sputtering and annealing stage in the STM chamber and the sample stage of the manipulator of the preparation chamber facilitated several aspects of the daily working routine. Furthermore, a new designed line-of-sight evaporator was used to deposit the medium-vapor pressure molecules DBAz and 2,6-DBAz investigated in this thesis.

8 Zusammenfassung

Diese Dissertation behandelt verschiedene Aspekte der Oberflächen- und Grenzflächenchemie. In diesem Zusammenhang untersuchen die vorgestellten Studien das grundlegende Verständnis der Prozesse der oberflächengestützten Synthese sowie die Wechselwirkungen von organischen Molekülen mit Metallsubstraten und zusätzlich abgeschiedenen Metallatomen. Zu diesem Zweck wurde eine Vielzahl an mikroskopischen und spektroskopischen Methoden angewandt, die es erlauben, die relevanten Fragestellungen der entsprechenden Projekte zu beantworten.

Der Hauptteil dieser Arbeit behandelt die oberflächengestützte Synthese von kohlenstoffbasierten Nanostrukturen auf Metall-Einkristalloberflächen. Hierbei wurden verschiedene bromierte Moleküle als Präkursoren für die oberflächengestützte Ullmann-Kupplung genutzt. Die Untersuchungen konzentrieren sich besonders auf die kovalenten oder organometallischen Ring- und Kettenstrukturen, die als Reaktionsprodukte gebildet werden. Es wurden verschiedene Strategien verwendet, um das Ergebnis der Reaktion in die gewünschte Richtung zu steuern und um zu verstehen, wie das Ring/Ketten-Verhältnis durch Parameter wie Temperatur oder Bedeckungsgrad beeinflusst werden kann.

1,3-Dibromazulen (DBAz) auf Cu(111) wurde als Modellsystem gewählt, um die Konkurrenz zwischen Ring- und Kettenbildung zu untersuchen und die Produktstrukturen wurden mit Rastertunnelmikroskopie (engl. *scanning tunneling microscopy*, STM) charakterisiert. Das Verknüpfungsmuster der Br-Substituenten in diesem Molekül ist so gewählt, dass es sowohl Ring- als auch Kettenbildung erlaubt. Es wurde gezeigt, dass nach Abscheiden bei 300 K eine organometallische Zwischenstufe der oberflächengestützten Ullmann-Kupplung gebildet wird. Die Analyse der Daten zeigte eine bevorzugte Bildung von Oligomerketten. Tempern bei höheren Temperaturen ($\geq$ 430 K) führte zu einem Anstieg von zyklischen organometallischen Hexameren. Um diese Beobachtung zu erklären, wurden die Prinzipien der kinetischen und thermodynamischen Reaktionskontrolle angewandt. Bei 300 K ist die thermische Energie ausreichend, um die C−Br-Bindung zu spalten und organometallische Oligomere zu bilden, die durch C−Cu−C-Bindungen verknüpft sind. Allerdings sind diese organometallischen Bindungen,

die grundsätzlich als reversibel betrachtet werden können, bei dieser Temperatur auf der Zeitskala des Experiments irreversibel. Diese Bedingungen, bei denen sich die Bildung und Spaltung der C−Cu−C-Bindungen nicht im Gleichgewicht befindet, werden als kinetische Kontrolle bezeichnet. Das Verknüpfungsmuster der Oligomere wird durch eine statistische Verteilung bestimmt. Diese macht die Bildung von Ringen unwahrscheinlich, da alle sechs Monomere in einem Hexamer mit der gleichen Ausrichtung verknüpft sein müssten. Bei erhöhten Temperaturen werden die C−Cu−C-Bindungen reversibel, das heißt, sie werden schnell gebrochen und erneut gebildet. Dies führt zu Gleichgewichtsbedingungen und thermodynamischer Reaktionskontrolle. Unter diesen Bedingungen können die einzelnen Monomere ihr Verknüpfungsmuster ändern, bis ein energetisch stabileres Produkt gebildet wird. Dieses energetisch stabilere Produkt ist das zyklische Hexamer, da es eine C−Cu−C-Bindung mehr besitzt als ein offenkettiges Hexamer. Die Situation wird komplizierter, wenn der Bedeckungsgrad als zweiter Parameter berücksichtigt wird. Eine Analyse des Ring/Ketten-Verhältnisses von Proben mit verschiedenem Bedeckungsgrad zeigte eine abnehmende Ringausbeute mit zunehmender Bedeckung. Um diese Beobachtung zu erklären, muss die Reaktionskinetik betrachtet werden. Das Kettenwachstum ist eine Reaktion zweiter Ordnung, da zwei Moleküle (Monomere oder bereits existierende Ketten) intermolekular miteinander reagieren müssen. Im Gegensatz dazu ist der Ringschluss eine Reaktion erster Ordnung, bei der die zwei Enden einer Kette intramolekular miteinander reagieren. Während Reaktionen erster Ordnung bei niedrigen Konzentrationen (Bedeckungen) bevorzugt ablaufen, werden Reaktionen zweiter Ordnung bei höherer Konzentration wahrscheinlicher. Auf diese Weise kann die abnehmende Ringausbeute mit steigender Bedeckung erklärt werden. Des Weiteren wurde eine optimale Temperatur von 430 K beobachtet, bei der die Ringausbeute maximal ist. Diese Beobachtung kann anhand von thermodynamischen Überlegungen erklärt werden. Da die Ringe überhaupt gebildet werden, müssen sie das thermodynamisch stabilere Produkt sein. Dies bedeutet allerdings, dass die Ketten das entropisch bevorzugte Produkt sind und eine Erhöhung der Temperatur wiederum die Kettenbildung begünstigen sollte. Daher ist die optimale Temperatur für die Ringbildung gerade hoch genug, um den Zustand der thermodynamischen Reaktionskontrolle, also reversible C−Cu−C-Bindungen, zu erreichen. All diese grundlegenden Überlegungen wurden in Monte-Carlo-Simulationen (MC) angewandt, in denen das DBAz-Molekül durch ein einfaches Modell repräsentiert wird. Eine gute qualitative Übereinstimmung zwischen Experiment und Simulation untermauert die getroffenen Schlussfolgerun-

gen und deutet zusätzlich darauf hin, dass sie generell in der oberflächengestützten Synthese anwendbar sind.

Um den Einfluss des Substrats auf das Ring/Ketten-Verhältnis zu untersuchen, wurden die Experimente mit dem DBAz-Molekül auf die Ag(111)-Oberfläche erweitert. Die Reaktivität dieses Substrats gegenüber der Debromierung ist allerdings nicht ausreichend, um ein vollständig organometallisches Netzwerk zu erhalten, bevor die Desorption der Moleküle beginnt. Daher wurden zusätzlich zu den DBAz-Molekülen Cu-Atome abgeschieden und es wurde gezeigt, dass auf diese Weise ein vollständig organometallisches Netzwerk erhalten werden kann. Die optimale Temperatur, um die Ringausbeute zu maximieren, verringerte sich im Vergleich zu Cu(111) auf 380 K. Diese Beobachtung wird durch die schwächere Wechselwirkung des Azulene-Moleküls mit der Ag(111)-Oberfläche und die C−Ag−C-Bindungen erklärt, die schwächer sind als die C−Cu−C-Bindungen. Allerdings wurde die Menge der abgeschiedenen Cu-Atome für Proben mit verschiedenen DBAz-Bedeckungen nicht konstant gehalten, sodass keine eindeutigen Aussagen über den Einfluss der Bedeckung auf die Ringausbeute getroffen werden können. Dennoch legen die Daten nahe, dass eine geringere Menge an Cu vorteilhaft für eine höhere Ringausbeute ist, da die höchste Ringausbeute bei der Probe mit der niedrigsten Cu-Menge im Verhältnis zur DBAz-Bedeckung erhalten wurde.

Ein anderer Ansatz, um das Ring/Ketten-Verhältnis zu kontrollieren, wurde durch die Verwendung eines Oberflächentemplats gewählt. In dieser Studie wurde eine vicinale Ag-Oberfläche mit kleinen Terrassen gleicher Größe verwendet, um das Kettenwachstum von 4,4''-Dibrom-1,1':3',1''-terphenyl (DMTP) zu fördern. Die geknickten Stufenkanten des gekrümmten Ag(645)-Kristalls sind so ausgerichtet, dass sie auf eine Weise rekonstruieren können, die perfekt zur Struktur der kovalenten DMTP-Polymerketten passt. Die Bildung der Ketten in sehr hoher Ausbeute und ihre perfekte Ausrichtung entlang der Stufenkanten wurde mit STM und der Beugung niederenergetischer Elektronen (engl. *low-energy electron diffraction*, LEED) bewiesen. Die strukturelle Qualität der Polymerketten war hoch genug, um sie mit winkelaufgelöster Ultraviolettphotoelektronenspektroskopie (engl. *angle-resolved photoemission spectroscopy*, ARPES) zu untersuchen. Die ARPES-Messungen zeigten eine Banddispersion entlang der Richtung der Ketten, während senkrecht zu dieser keine Dispersion beobachtet wurde. Des Weiteren zeigte ein Vergleich mit Poly-(*para*-phenylen)-Ketten den Einfluss der *meta*-Verknüpfungen auf die elektronische Struktur der organischen Polymerketten. Die Ergebnisse wurden durch Rastertunnelspektroskopie (engl. *scanning tunneling spectroscopy*, STS) und Dichtefunktionaltheorie (DFT) bewiesen.

Die ausschließliche Bildung von Ketten lässt sich auch durch einen geeigneten Präkursor erreichen. Dies wurde gezeigt, indem 2,6-Dibromazulen (2,6-DBAz), ein Strukturisomer von DBAz, auf der Au(111)-Oberfläche verwendet wurde. In diesem Molekül befinden sich die Br-Substituenten an beiden Enden des Azulen-Gerüsts, wodurch nur eine lineare Verknüpfung möglich ist. Die ausschließliche Bildung von Ketten wurde mit STM gezeigt. Allerdings konnte diese Methode nicht das genaue Verknüpfungsmuster der Monomere in den Oligomeren aufklären. Zu diesem Zweck wurde *non-contact* Rasterkraftmikriskopie (engl. *atomic force microscopy*, nc-AFM) mit submolekularer Auflösung verwendet und es wurde ein zufälliges Verknüpfungsmuster gefunden. In einem zusätzlichen Reaktionsschritt wurde der Zusammenschluss einzelner Ketten durch eine dehydrierende Kupplung gezeigt. Auch die auf diese Weise gebildeten Strukturen wurden mittels nc-AFM aufgeklärt. Abhängig vom Verknüpfungsmuster der einzelnen Ketten und deren relativer Ausrichtung wurden Nanobänder von zwei neuen Kohlenstoff-Allotropen mit alternierender π-Topologie beobachtet. Hierbei handelt es sich um Phagraphen und Tetra-Penta-Hepta-Graphen, die zuvor zwar bereits theoretisch vorhergesagt aber noch nicht experimentell beobachtet worden waren.

Die vorgestellten Untersuchungen behandeln Ring- und Kettenstrukturen, die als Reaktionsprodukte in der oberflächengestützten Synthese gebildet werden. Sie beschreiben verschieden Wege, wie sich eines der beiden Produkte mit hoher Ausbeute herstellen lässt. Basierend auf grundlegenden Überlegungen und einer geschickten Wahl der Reaktionsparameter können Proben mit hoher struktureller Homogenität hergestellt werden. Diese Ergebnisse helfen dabei, die grundlegenden Prozesse, die die Reaktionsprodukte einer oberflächengestützten Synthese beeinflussen, besser zu verstehen. Daher können sie Anwendung in der Herstellung von kohlenstoffbasierten Nanobauteilen finden.

Zusätzlich zu den Ergebnissen zur oberflächengestützten Synthese wurde eine Reihe von Studien vorgestellt, die sich mit der Oberflächen- und Grenzflächenchemie im Allgemeinen beschäftigen. In ihnen werden die Wechselwirkungen zwischen organischen Molekülen und Metallsubstraten oder zusätzlich abgeschiedenen Metallatomen untersucht. In diesem Zusammenhang wurde der Polymorphismus von 1,1':3',1'':4'',1'''-Quaterphenyl-4,4'''-dicarbonitril (*m*-4PDN) auf Ag(111) untersucht. Es wurde gezeigt, dass dieses Molekül in Abhängigkeit der Bedeckung verschiedene Adsorbatstrukturen ausbildet. Während bei Sättigungsbedeckung eine dichtest gepackte Lage gebildet wird, wurden bei einer niedrigen Bedeckung von 0.1 ML zwei verschiedene geordnete Phasen be-

obachtet. Eine dieser Phasen besteht sowohl aus flach liegenden als auch aus aufrecht stehenden Molekülen. Eine solche Phase wurde zuvor noch nicht beobachtet. Die direkte Metallierung von Tetrapyrrol-Makrocyclen wurde für *meso*-Tetraphenylporphyrin (2HTPP) und 2,3,8,12,17,18-Hexaethyl-7,13-dimethylcorrol (3HHEDMC) untersucht. Bei der Metallierung von 2HTPP mit Co wurde die Reaktionstiefe bestimmt und die Bildung einer diffusen Interphase anstelle einer abrupten Grenzfläche beobachtet. Für 3HHEDMC konnte die Stabilisierung eines Metall-Trikations gezeigt werden, während für Porphyrine in der Regel Dikationen beobachtet werden. Der Einfluss der π-Topologie eines Moleküls auf die Adsorption und Desorption wurde für den nichtalternierenden Aromaten Azulen untersucht und mit seinem alternierenden Gegenstück Naphthalin verglichen. Es wurde gezeigt, dass das nichtalternierende Azulen deutlich stärker mit der Cu(111)-Oberfläche wechselwirkt als Naphthalin.

Als zusätzliches Ergebnis wurde die erfolgreiche Inbetriebnahme eines kommerziell erhältlichen *atomic layer injection*-Geräts (ALI) an der kombinierten STM- und XPS-Apparatur der AG Gottfried in Marburg gezeigt. Zu diesem Zweck wurde 2HTPP aus einer Dichlormethan-Lösung auf Ag(111) abgeschieden. Die Abscheidung von intakten 2HTPP-Molekülen wurde mittels STM gezeigt und Röntgenphotoelektronenspektroskopie (engl. *X-ray photoelectron spectroscopy*, XPS) wurde verwendet, um die Menge an abgeschiedenen Molekülen pro Puls des ALI-Geräts abzuschätzen.

Der experimentelle Teil dieser Arbeit wird durch die Entwicklung von technischen Gerätschaften für die kombinierte STM- und XPS-Apparatur im Labor der AG Gottfried in Marburg vervollständigt. Überarbeitete Konstruktionen der Probenaufnahme zum *Sputtern* und *Annealen* in der STM-Kammer und des Manipulators in der Präparationskammer vereinfachten viele Aspekte des täglichen Arbeitens. Des Weiteren wurde ein neu entwickelter *line-of-sight*-Verdampfer genutzt, um Moleküle mit mittlerem Dampfdruck wie DBAz und 2,6-DBAz abzuscheiden, die in dieser Arbeit untersucht wurden.

Appendix

A Bibliography

[1] R. Otero, A. V. de Parga, J. Gallego, "Electronic, structural and chemical effects of charge-transfer at organic/inorganic interfaces", *Surf. Sci. Rep.* **2017**, *72*(3), 105–145, DOI 10.1016/j.surfrep.2017.03.001.

[2] C. W. Tang, S. A. VanSlyke, "Organic electroluminescent diodes", *Appl. Phys. Lett.* **1987**, *51*(12), 913–915, DOI 10.1063/1.98799@apl.2019.APLCLASS2019.issue-1.

[3] J. H. Burroughes, D. D. C. Bradley, A. R. Brown, R. N. Marks, K. Mackay, R. H. Friend, P. L. Burns, A. B. Holmes, "Light-emitting diodes based on conjugated polymers", *Nature* **1990**, *347*(6293), 539–541, DOI 10.1038/347539a0.

[4] C. W. Tang, "Two-layer organic photovoltaic cell", *Appl. Phys. Lett.* **1986**, *48*(2), 183–185, DOI 10.1063/1.96937.

[5] C. Dimitrakopoulos, P. Malenfant, "Organic Thin Film Transistors for Large Area Electronics", *Adv. Mater.* **2002**, *14*(2), 99–117, DOI 10.1002/1521-4095(20020116)14:2<99::aid-adma99>3.0.co;2-9.

[6] S. R. Forrest, M. E. Thompson, "Introduction: Organic Electronics and Optoelectronics", *Chem. Rev.* **2007**, *107*(4), 923–925, DOI 10.1021/cr0501590.

[7] A. Kahn, N. Koch, W. Gao, "Electronic structure and electrical properties of interfaces between metals and π-conjugated molecular films", *J. Polym. Sci. Part B: Polym. Phys.* **2003**, *41*(21), 2529–2548, DOI 10.1002/polb.10642.

[8] L. Bartels, "Tailoring molecular layers at metal surfaces", *Nat. Chem.* **2010**, *2*(2), 87–95, DOI 10.1038/nchem.517.

[9] J. V. Barth, G. Costantini, K. Kern, "Engineering atomic and molecular nanostructures at surfaces.", *Nature* **2005**, *437*(7059), 671–679, DOI 10.1038/nature04166.

[10] N. Koch, "Organic Electronic Devices and Their Functional Interfaces", *ChemPhysChem* **2007**, *8*(10), 1438–1455, DOI 10.1002/cphc.200700177.

[11] J. M. Gottfried, "Quantitative model studies for interfaces in organic electronic devices", *New J. Phys.* **2016**, *18*(11), 111002, DOI 10.1088/1367-2630/18/11/111002.

[12] *On-Surface Synthesis, Proceedings of the International Workshop On-Surface Synthesis, École des Houches, Les Houches 25–30 May 2014*, (Ed.: A. Gourdon), Springer International Publishing, Cham, **2016**, DOI 10.1007/978-3-319-26600-8.

[13] *On-Surface Synthesis II, Proceedings of the International Workshop On-Surface Synthesis, San Sebastián, 27-30 June 2016*, (Eds.: D. G. de Oteyza, C. Rogero), Springer, Cham, **2018**, DOI 10.1007/978-3-319-75810-7.

[14] A. Gourdon, D. G. de Oteyza, J. Zhu, "On-Surface Synthesis", *ChemPhysChem* **2019**, *20*(18), 2249–2250, DOI 10.1002/cphc.201900847.

[15] F. Ullmann, J. Bielecki, "Ueber Synthesen in der Biphenylreihe", *Ber. Dtsch. Chem. Ges.* **1901**, *34*(2), 2174–2185, DOI 10.1002/cber.190103402141.

[16] F. Ullmann, "Ueber symmetrische Biphenylderivate", *Justus Liebigs Ann. Chem.* **1904**, *332*(1-2), 38–81, DOI 10.1002/jlac.19043320104.

[17] C. Sambiagio, S. P. Marsden, A. J. Blacker, P. C. McGowan, "Copper catalysed Ullmann type chemistry: from mechanistic aspects to modern development", *Chem. Soc. Rev.* **2014**, *43*(10), 3525–3550, DOI 10.1039/c3cs60289c.

[18] X.-L. Zhou, M. Castro, J. White, "Interactions of UV photons and low energy electrons with chemisorbed benzene on Ag (111)", *Surf. Sci.* **1990**, *238*(1-3), 215–225, DOI 10.1016/0039-6028(90)90079-N.

[19] M. Xi, B. E. Bent, "Iodobenzene on Cu (111): formation and coupling of adsorbed phenyl groups", *Surf. Sci.* **1992**, *278*(1-2), 19–32, DOI 10.1016/0039-6028(92)90580-Y.

[20] P. S. Weiss, M. M. Kamna, T. M. Graham, S. J. Stranick, "Imaging Benzene Molecules and Phenyl Radicals on Cu{111}", *Langmuir* **1998**, *14*(6), 1284–1289, DOI 10.1021/la970736i.

[21] S.-W. Hla, L. Bartels, G. Meyer, K.-H. Rieder, "Inducing All Steps of a Chemical Reaction with the Scanning Tunneling Microscope Tip: Towards Single Molecule Engineering", *Phys. Rev. Lett.* **2000**, *85*(13), 2777–2780, DOI 10.1103/physrevlett.85.2777.

[22] G. S. McCarty, P. S. Weiss, "Footprints of a Surface Chemical Reaction: Dissociative Chemisorption of *p*-Diiodobenzene on Cu{111}", *J. Phys. Chem. B* **2002**, *106*(33), 8005–8008, DOI 10.1021/jp025874h.

[23] G. S. McCarty, P. S. Weiss, "Formation and Manipulation of Protopolymer Chains", *J. Am. Chem. Soc.* **2004**, *126*(51), 16772–16776, DOI 10.1021/ja038930g.

[24] L. Grill, M. Dyer, L. Lafferentz, M. Persson, M. V. Peters, S. Hecht, "Nano-architectures by covalent assembly of molecular building blocks", *Nat. Nanotechnol.* **2007**, *2*(11), 687–691, DOI 10.1038/nnano.2007.346.

[25] J. Eichhorn, D. Nieckarz, O. Ochs, D. Samanta, M. Schmittel, P. J. Szabelski, M. Lackinger, "On-surface Ullmann coupling: the influence of kinetic reaction parameters on the morphology and quality of covalent networks", *ACS Nano* **2014**, *8*(8), 7880–7889, DOI 10.1021/nn501567p.

[26] M. Lackinger, "Surface-assisted Ullmann coupling", *Chem. Commun.* **2017**, *53*(56), 7872–7885, DOI 10.1039/c7cc03402d.

[27] A. Rastgoo Lahrood, J. Björk, W. M. Heckl, M. Lackinger, "1,3-Diiodobenzene on Cu(111) – an exceptional case of on-surface Ullmann coupling", *Chem. Commun.* **2015**, *51*(68), 13301–13304, DOI 10.1039/c5cc04453g.

[28] A. Rastgoo-Lahrood, M. Lischka, J. Eichhorn, D. Samanta, M. Schmittel, W. M. Heckl, M. Lackinger, "Reversible intercalation of iodine monolayers between on-surface synthesised covalent polyphenylene networks and Au(111)", *Nanoscale* **2017**, *9*(15), 4995–5001, DOI 10.1039/c7nr00705a.

[29] D. Barton, H.-Y. Gao, P. A. Held, A. Studer, H. Fuchs, N. L. Doltsinis, J. Neugebauer, "Formation of Organometallic Intermediate States in On-Surface Ullmann Couplings", *Chem. Eur. J.* **2017**, *23*(25), 6190–6197, DOI 10.1002/chem.201605802.

[30] C. J. Judd, S. L. Haddow, N. R. Champness, A. Saywell, "Ullmann Coupling Reactions on Ag(111) and Ag(110); Substrate Influence on the Formation of Covalently Coupled Products and Intermediate Metal-Organic Structures", *Sci. Rep.* **2017**, *7*, 14541, DOI 10.1038/s41598-017-13315-1.

[31] H. Zhang, J.-H. Franke, D. Zhong, Y. Li, A. Timmer, O. D. Arado, H. Mönig, H. Wang, L. Chi, Z. Wang, K. Müllen, H. Fuchs, "Surface supported gold-organic hybrids: on-surface synthesis and surface directed orientation", *Small* **2014**, *10*(7), 1361–1368, DOI 10.1002/smll.201303011.

[32] K. J. Shi, X. Zhang, C. H. Shu, D. Y. Li, X. Y. Wu, P. N. Liu, "Ullmann coupling reaction of aryl chlorides on Au(111) using dosed Cu as a catalyst and the programmed growth of 2D covalent organic frameworks", *Chem. Commun.* **2016**, *52*(56), 8726–8729, DOI 10.1039/c6cc03137d.

[33] K. J. Shi, D. W. Yuan, C. X. Wang, C. H. Shu, D. Y. Li, Z. L. Shi, X. Y. Wu, P. N. Liu, "Ullmann Reaction of Aryl Chlorides on Various Surfaces and the Application in Stepwise Growth of 2D Covalent Organic Frameworks", *Org. Lett.* **2016**, *18*(6), 1282–1285, DOI 10.1021/acs.orglett.6b00172.

[34] J. Dai, W. Zhao, L. Xing, J. Shang, H. Ju, X. Zhou, J. Liu, Q. Chen, Y. Wang, J. Zhu, K. Wu, "Dechlorinated Ullmann Coupling Reaction of Aryl Chlorides on Ag(111): A Combined STM and XPS Study", *ChemPhysChem* **2019**, *20*(18), 2367–2375, DOI 10.1002/cphc.201900264.

[35] C.-X. Wang, J.-L. Chen, C.-H. Shu, K.-J. Shi, P.-N. Liu, "On-surface synthesis of 2D COFs on Cu(111) via the formation of thermodynamically stable organometallic networks as the template", *Phys. Chem. Chem. Phys.* **2019**, *21*(24), 13222–13229, DOI 10.1039/c9cp01843c.

[36] Q. Fan, C. Wang, Y. Han, J. Zhu, W. Hieringer, J. Kuttner, G. Hilt, J. M. Gottfried, „Oberflächengestützte Synthese von Hyperbenzol-Nanogehegen", *Angew. Chem.* **2013**, *125*(17), 4766–4770, DOI 10.1002/ange.201300610; „Surface-Assisted Organic Synthesis of Hyperbenzene Nanotroughs", *Angew. Chem. Int. Ed.* **2013**, *52*(17), 4668–4672, DOI 10.1002/anie.201300610.

[37] M. Chen, J. Xiao, H.-P. Steinrück, S. Wang, W. Wang, N. Lin, W. Hieringer, J. M. Gottfried, "Combined Photoemission and Scanning Tunneling Microscopy Study of the Surface-Assisted Ullmann Coupling Re-

action", *J. Phys. Chem. C* **2014**, *118*(13), 6820–6830, DOI 10.1021/jp4121468.

[38] Q. Fan, C. Wang, L. Liu, Y. Han, J. Zhao, J. Zhu, J. Kuttner, G. Hilt, J. M. Gottfried, "Covalent, Organometallic, and Halogen-Bonded Nanomeshes from Tetrabromo-Terphenyl by Surface-Assisted Synthesis on Cu(111)", *J. Phys. Chem. C* **2014**, *118*(24), 13018–13025, DOI 10.1021/jp5037475.

[39] Q. Fan, C. Wang, Y. Han, J. Zhu, J. Kuttner, G. Hilt, J. M. Gottfried, "Surface-Assisted Formation, Assembly, and Dynamics of Planar Organometallic Macrocycles and Zigzag Shaped Polymer Chains with C–Cu–C Bonds", *ACS Nano* **2014**, *8*(1), 709–718, DOI 10.1021/nn405370s.

[40] Q. Fan, T. Wang, L. Liu, J. Zhao, J. Zhu, J. M. Gottfried, "Tribromobenzene on Cu(111): Temperature-dependent formation of halogen-bonded, organometallic, and covalent nanostructures", *J. Chem. Phys.* **2015**, *142*(10), 101906, DOI 10.1063/1.4906214.

[41] Q. Fan, J. M. Gottfried, J. Zhu, "Surface-Catalyzed C–C Covalent Coupling Strategies toward the Synthesis of Low-Dimensional Carbon-Based Nanostructures", *Acc. Chem. Res.* **2015**, *48*(8), 2484–2494, DOI 10.1021/acs.accounts.5b00168.

[42] Q. Fan, J. Dai, T. Wang, J. Kuttner, G. Hilt, J. M. Gottfried, J. Zhu, "Confined Synthesis of Organometallic Chains and Macrocycles by Cu–O Surface Templating", *ACS Nano* **2016**, *10*(3), 3747–3754, DOI 10.1021/acsnano.6b00366.

[43] J. Eichhorn, T. Strunskus, A. Rastgoo-Lahrood, D. Samanta, M. Schmittel, M. Lackinger, "On-surface Ullmann polymerization via intermediate organometallic networks on Ag(111)", *Chem. Commun.* **2014**, *50*(57), 7680–1682, DOI 10.1039/c4cc02757d.

[44] M. Ammon, T. Sander, S. Maier, "On-Surface Synthesis of Porous Carbon Nanoribbons from Polymer Chains", *J. Am. Chem. Soc.* **2017**, *139*(37), 12976–12984, DOI 10.1021/jacs.7b04783.

[45] Q. Fan, T. Wang, J. Dai, J. Kuttner, G. Hilt, J. M. Gottfried, J. Zhu, "On-Surface Pseudo-High-Dilution Synthesis of Macrocycles: Principle and Mechanism", *ACS Nano* **2017**, *11*(5), 5070–5079, DOI 10.1021/acsnano.7b01870.

[46] X. Zhou, C. Wang, Y. Zhang, F. Cheng, Y. He, Q. Shen, J. Shang, X. Shao, W. Ji, W. Chen, G. Xu, K. Wu, "Steering Surface Reaction Dynamics with a Self-Assembly Strategy: Ullmann Coupling on Metal Surfaces", *Angew. Chem.* **2017**, *129*(42), 13032–13036, DOI 10.1002/ange.201705018; *Angew. Chem. Int. Ed.* **2017**, *56*(42), 12852–12856, DOI 10.1002/anie.201705018.

[47] K. A. Simonov, A. V. Generalov, A. S. Vinogradov, G. I. Svirskiy, A. A. Cafolla, C. McGuinness, T. Taketsugu, A. Lyalin, N. Mårtensson, A. B. Preobrajenski, "Synthesis of armchair graphene nanoribbons from the 10,10'-dibromo-9,9'-bianthracene molecules on Ag(111): the role of organometallic intermediates.", *Sci. Rep.* **2018**, *8*, 3506, DOI 10.1038/s41598-018-21704-3.

[48] Q. Fan, L. Liu, J. Dai, T. Wang, H. Ju, J. Zhao, J. Kuttner, G. Hilt, J. M. Gottfried, J. Zhu, "Surface Adatom Mediated Structural Transformation in Bromoarene Monolayers: Precursor Phases in Surface Ullmann Reaction", *ACS Nano* **2018**, *12*(3), 2267–2274, DOI 10.1021/acsnano.7b06787.

[49] T. A. Pham, F. Song, M.-T. Nguyen, Z. Li, F. Studener, M. Stöhr, "Comparing Ullmann Coupling on Noble Metal Surfaces: On-Surface Polymerization of 1,3,6,8-Tetrabromopyrene on Cu(111) and Au(111)", *Chem. Eur. J* **2016**, *22*(17), 5937–5944, DOI 10.1002/chem.201504946.

[50] T. A. Pham, B. V. Tran, M.-T. Nguyen, M. Stöhr, "Chiral-Selective Formation of 1D Polymers Based on Ullmann-Type Coupling: The Role of the Metallic Substrate", *Small* **2017**, *13*(13), 1603675, DOI 10.1002/smll.201603675.

[51] J. Li, K. Martin, N. Avarvari, C. Wäckerlin, K.-H. Ernst, "Spontaneous separation of on-surface synthesized tris-helicenes into two-dimensional homochiral domains", *Chem. Commun.* **2018**, *54*(57), 7948–7951, DOI 10.1039/c8cc04235g.

[52] M. Fritton, D. A. Duncan, P. S. Deimel, A. Rastgoo-Lahrood, F. Allegretti, J. V. Barth, W. M. Heckl, J. Björk, M. Lackinger, "The Role of Kinetics versus Thermodynamics in Surface-Assisted Ullmann Coupling on Gold and Silver Surfaces", *J. Am. Chem. Soc.* **2019**, *141*(12), 4824–4832, DOI 10.1021/jacs.8b11473.

[53] W. Wang, X. Shi, S. Wang, M. A. V. Hove, N. Lin, "Single-Molecule Resolution of an Organometallic Intermediate in a Surface-Supported Ullmann Coupling Reaction", *J. Am. Chem. Soc.* **2011**, *133*(34), 13264–13267, DOI 10.1021/ja204956b.

[54] M. Di Giovannantonio, M. E. Garah, J. Lipton-Duffin, V. Meunier, L. Cardenas, Y. Fagot Revurat, A. Cossaro, A. Verdini, D. F. Perepichka, F. Rosei, G. Contini, "Insight into Organometallic Intermediate and Its Evolution to Covalent Bonding in Surface-Confined Ullmann Polymerization", *ACS Nano* **2013**, *7*(9), 8190–8198, DOI 10.1021/nn4035684.

[55] J. Dai, Q. Fan, T. Wang, J. Kuttner, G. Hilt, J. M. Gottfried, J. Zhu, "The role of the substrate structure in the on-surface synthesis of organometallic and covalent oligophenylene chains", *Phys. Chem. Chem. Phys.* **2016**, *18*(30), 20627–20634, DOI 10.1039/c6cp03551e.

[56] S. Kawai, A. Sadeghi, T. Okamoto, C. Mitsui, R. Pawlak, T. Meier, J. Takeya, S. Goedecker, E. Meyer, "Organometallic Bonding in an Ullmann-Type On-Surface Chemical Reaction Studied by High-Resolution Atomic Force Microscopy", *Small* **2016**, *12*(38), 5303–5311, DOI 10.1002/smll.201601216.

[57] M. Di Giovannantonio, M. Tomellini, J. Lipton-Duffin, G. Galeotti, M. Ebrahimi, A. Cossaro, A. Verdini, N. Kharche, V. Meunier, G. Vasseur, Y. Fagot-Revurat, D. F. Perepichka, F. Rosei, G. Contini, "Mechanistic Picture and Kinetic Analysis of Surface-Confined Ullmann Polymerization", *J. Am. Chem. Soc.* **2016**, *138*(51), 16696–16702, DOI 10.1021/jacs.6b09728.

[58] X. Zhou, F. Bebensee, Q. Shen, R. Bebensee, F. Cheng, Y. He, H. Su, W. Chen, G. Q. Xu, F. Besenbacher, T. R. Linderoth, K. Wu, "On-surface synthesis approach to preparing one-dimensional organometallic and poly-*p*-phenylene chains", *Mater. Chem. Front.* **2017**, *1*(1), 119–127, DOI 10.1039/c6qm00142d.

[59] S. Zint, D. Ebeling, T. Schlöder, S. Ahles, D. Mollenhauer, H. A. Wegner, A. Schirmeisen, "Imaging Successive Intermediate States of the On-Surface Ullmann Reaction on Cu(111): Role of the Metal Coordination", *ACS Nano* **2017**, *11*(4), 4183–4190, DOI 10.1021/acsnano.7b01109.

[60] E. A. Lewis, M. D. Marcinkowski, C. J. Murphy, M. L. Liriano, A. J. Therrien, A. Pronschinske, E. C. H. Sykes, "Controlling selectivity in the

Ullmann reaction on Cu(111)", *Chem. Commun.* **2017**, *53*(55), 7816–7819, DOI 10.1039/c7cc02901b.

[61] M. Lischka, G. S. Michelitsch, N. Martsinovich, J. Eichhorn, A. Rastgoo-Lahrood, T. Strunskus, R. Breuer, K. Reuter, M. Schmittel, M. Lackinger, "Remote functionalization in surface-assisted dehalogenation by conformational mechanics: organometallic self-assembly of 3,3',5,5'-tetrabromo-2,2',4,4',6,6'-hexafluorobiphenyl on Ag(111)", *Nanoscale* **2018**, *10*(25), 12035–12044, DOI 10.1039/c8nr01987h.

[62] M. Fritton, K. Otte, J. Björk, P. K. Biswas, W. M. Heckl, M. Schmittel, M. Lackinger, "The influence of *ortho*-methyl substitution in organometallic self-assembly – a comparative study on Cu(111) *vs.* Ag(111)", *Chem. Commun.* **2018**, *54*(70), 9745–9748, DOI 10.1039/c8cc04854a.

[63] G. Galeotti, M. Di Giovannantonio, A. Cupo, S. Xing, J. Lipton-Duffin, M. Ebrahimi, G. Vasseur, B. Kierren, Y. Fagot-Revurat, D. Tristant, V. Meunier, D. F. Perepichka, F. Rosei, G. Contini, "An unexpected organometallic intermediate in surface-confined Ullmann coupling", *Nanoscale* **2019**, *11*(16), 7682–7689, DOI 10.1039/c9nr00672a.

[64] C. Zhang, E. Kazuma, Y. Kim, "Atomic-Scale Visualization of the Stepwise Metal-Mediated Dehalogenative Cycloaddition Reaction Pathways: Competition between Radicals and Organometallic Intermediates", *Angew. Chem.* **2019**, *131*(49), 17900–17908, DOI 10.1002/ange.201909111; *Angew. Chem. Int. Ed.* **2019**, *58*(49), 17736–17744, DOI 10.1002/anie.201909111.

[65] A. Saywell, W. Greń, G. Franc, A. Gourdon, X. Bouju, L. Grill, "Manipulating the Conformation of Single Organometallic Chains on Au(111)", *J. Phys. Chem. C* **2014**, *118*(3), 1719–1728, DOI 10.1021/jp409323g.

[66] H. Zhang, L. Chi, "Gold-Organic Hybrids: On-Surface Synthesis and Perspectives", *Adv. Mater.* **2016**, *28*(47), 10492–10498, DOI 10.1002/adma.201602131.

[67] M. Liu, S. Li, J. Zhou, Z. Zha, J. Pan, X. Li, J. Zhang, Z. Liu, Y. Li, X. Qiu, "High-Yield Formation of Graphdiyne Macrocycles through On-Surface Assembling and Coupling Reaction", *ACS Nano* **2018**, *12*(12), 12612–12618, DOI 10.1021/acsnano.8b07349.

[68] M. Bieri, S. Blankenburg, M. Kivala, C. A. Pignedoli, P. Ruffieux, K. Müllen, R. Fasel, "Surface-supported 2D heterotriangulene polymers", *Chem. Commun.* **2011**, *47*(37), 10239–10241, DOI 10.1039/c1cc12490k.

[69] C. Steiner, J. Gebhardt, M. Ammon, Z. Yang, A. Heidenreich, N. Hammer, A. Görling, M. Kivala, S. Maier, "Hierarchical on-surface synthesis and electronic structure of carbonyl-functionalized one- and two-dimensional covalent nanoarchitectures", *Nat. Commun.* **2017**, *8*, 14765, DOI 10.1038/ncomms14765.

[70] G. Franc, A. Gourdon, "Covalent networks through on-surface chemistry in ultra-high vacuum: state-of-the-art and recent developments", *Phys. Chem. Chem. Phys.* **2011**, *13*(32), 14283–14292, DOI 10.1039/c1cp20700h.

[71] L. Dong, P. N. Liu, N. Lin, "Surface-Activated Coupling Reactions Confined on a Surface", *Acc. Chem. Res.* **2015**, *48*(10), 2765–2774, DOI 10.1021/acs.accounts.5b00160.

[72] P. A. Held, H. Fuchs, A. Studer, "Covalent-Bond Formation via On-Surface Chemistry", *Chem. Eur. J.* **2017**, *23*(25), 5874–5892, DOI 10.1002/chem.201604047.

[73] M. Chen, J. Shang, Y. Wang, K. Wu, J. Kuttner, G. Hilt, W. Hieringer, J. M. Gottfried, "On-Surface Synthesis and Characterization of Honeycombene Oligophenylene Macrocycles", *ACS Nano* **2017**, *11*(1), 134–143, DOI 10.1021/acsnano.6b05709.

[74] J. Kröger, N. Néel, H. Jensen, R. Berndt, R. Rurali, N. Lorente, "Molecules on vicinal Au surfaces studied by scanning tunnelling microscopy", *J. Phys.: Condens. Matter* **2006**, *18*(13), S51–S66, DOI 10.1088/0953-8984/18/13/s04.

[75] A. Basagni, G. Vasseur, C. A. Pignedoli, M. Vilas-Varela, D. Peña, L. Nicolas, L. Vitali, J. Lobo-Checa, D. G. de Oteyza, F. Sedona, M. Casarin, J. E. Ortega, M. Sambi, "Tunable Band Alignment with Unperturbed Carrier Mobility of On-Surface Synthesized Organic Semiconducting Wires", *ACS Nano* **2016**, *10*(2), 2644–2651, DOI 10.1021/acsnano.5b07683.

[76] G. Vasseur, Y. Fagot-Revurat, M. Sicot, B. Kierren, L. Moreau, D. Malterre, L. Cardenas, G. Galeotti, J. Lipton-Duffin, F. Rosei, M. Di Giovannantonio, G. Contini, P. Le Fèvre, F. Bertran, L. Liang, V. Meunier, D. F. Perepichka, "Quasi one-dimensional band dispersion and surface metallization in long-range ordered polymeric wires", *Nat. Commun.* **2016**, *7*, 10235, DOI 10.1038/ncomms10235.

[77] N. Merino-Díez, J. Lobo-Checa, P. Nita, A. García-Lekue, A. Basagni, G. Vasseur, F. Tiso, F. Sedona, P. K. Das, J. Fujii, I. Vobornik, M. Sambi, J. I. Pascual, J. E. Ortega, D. G. de Oteyza, "Switching from Reactant to Substrate Engineering in the Selective Synthesis of Graphene Nanoribbons", *J. Phys. Chem. Lett.* **2018**, *9*(10), 2510–2517, DOI 10.1021/acs.jpclett.8b00796.

[78] K. S. Novoselov, A. K. Geim, S. V. Morozov, D. Jiang, Y. Zhang, S. V. Dubonos, I. V. Grigorieva, A. A. Firsov, "Electric field effect in atomically thin carbon films", *Science* **2004**, *306*(5696), 666–669, DOI 10.1126/science.1102896.

[79] Y. Wu, Y.-m. Lin, A. A. Bol, K. A. Jenkins, F. Xia, D. B. Farmer, Y. Zhu, P. Avouris, "High-frequency, scaled graphene transistors on diamond-like carbon", *Nature* **2011**, *472*(7341), 74–78, DOI 10.1038/nature09979.

[80] M. F. El-Kady, V. Strong, S. Dubin, R. B. Kaner, "Laser scribing of high-performance and flexible graphene-based electrochemical capacitors", *Science* **2012**, *335*(6074), 1326–1330, DOI 10.1126/science.1216744.

[81] V. Skrypnychuk, N. Boulanger, V. Yu, M. Hilke, S. C. B. Mannsfeld, M. F. Toney, D. R. Barbero, "Enhanced Vertical Charge Transport in a Semiconducting P3HT Thin Film on Single Layer Graphene", *Adv. Funct. Mater.* **2014**, *25*(5), 664–670, DOI 10.1002/adfm.201403418.

[82] X. Yang, X. Dou, A. Rouhanipour, L. Zhi, H. J. Räder, K. Müllen, "Two-Dimensional Graphene Nanoribbons", *J. Am. Chem. Soc.* **2008**, *130*(13), 4216–4217, DOI 10.1021/ja710234t.

[83] J. Cai, P. Ruffieux, R. Jaafar, M. Bieri, T. Braun, S. Blankenburg, M. Muoth, A. P. Seitsonen, M. Saleh, X. Feng, K. Müllen, R. Fasel, "Atomically precise bottom-up fabrication of graphene nanoribbons", *Nature* **2010**, *466*(7305), 470–473, DOI 10.1038/nature09211.

[84] Z. Chen, Y.-M. Lin, M. J. Rooks, P. Avouris, "Graphene nano-ribbon electronics", *Physica E* **2007**, *40*(2), 228–232, DOI 10.1016/j.physe.2007.06.020.

[85] M. Y. Han, B. Ozyilmaz, Y. Zhang, P. Kim, "Energy band-gap engineering of graphene nanoribbons", *Phys. Rev. Lett.* **2007**, *98*(20), 206805, DOI 10.1103/PhysRevLett.98.206805.

[86] Y.-C. Chen, D. G. de Oteyza, Z. Pedramrazi, C. Chen, F. R. Fischer, M. F. Crommie, "Tuning the band gap of graphene nanoribbons synthesized from molecular precursors", *ACS Nano* **2013**, *7*(6074), 6123–6128, DOI 10.1021/nn401948e.

[87] J. Cai, C. A. Pignedoli, L. Talirz, P. Ruffieux, H. Söde, L. Liang, V. Meunier, R. Berger, R. Li, X. Feng, K. Müllen, R. Fasel, "Graphene nanoribbon heterojunctions", *Nat. Nanotechnol.* **2014**, *9*(11), 896–900, DOI 10.1038/nnano.2014.184.

[88] A. Kimouche, M. M. Ervasti, R. Drost, S. Halonen, A. Harju, P. M. Joensuu, J. Sainio, P. Liljeroth, "Ultra-narrow metallic armchair graphene nanoribbons", *Nat. Commun.* **2015**, *6*, 10177, DOI 10.1038/ncomms10177.

[89] H. Zhang, H. Lin, K. Sun, L. Chen, Y. Zagranyarski, N. Aghdassi, S. Duhm, Q. Li, D. Zhong, Y. Li, K. Müllen, H. Fuchs, L. Chi, "On-surface synthesis of rylene-type graphene nanoribbons", *J. Am. Chem. Soc.* **2015**, *137*(12), 4022–4025, DOI 10.1021/ja511995r.

[90] R. R. Cloke, T. Marangoni, G. D. Nguyen, T. Joshi, D. J. Rizzo, C. Bronner, T. Cao, S. G. Louie, M. F. Crommie, F. R. Fischer, "Site-Specific Substitutional Boron Doping of Semiconducting Armchair Graphene Nanoribbons", *J. Am. Chem. Soc.* **2015**, *137*(28), 8872–8875, DOI 10.1021/jacs.5b02523.

[91] S. Kawai, S. Saito, S. Osumi, S. Yamaguchi, A. S. Foster, P. Spijker, E. Meyer, "Atomically controlled substitutional boron-doping of graphene nanoribbons", *Nat. Commun.* **2015**, *6*, 8098.

[92] D. G. de Oteyza, A. García-Lekue, M. Vilas-Varela, N. Merino-Díez, E. Carbonell-Sanromà, M. Corso, G. Vasseur, C. Rogero, E. Guitián, J. I. Pascual, J. E. Ortega, Y. Wakayama, D. Peña, "Substrate-Independent Growth of Atomically Precise Chiral Graphene Nanoribbons", *ACS Nano* **2016**, *10*(9), 9000–9008, DOI 10.1021/acsnano.6b05269.

[93] L. Talirz, P. Ruffieux, R. Fasel, "On-Surface Synthesis of Atomically Precise Graphene Nanoribbons", *Adv. Mater.* **2016**, *28*(29), 6222–6231, DOI 10.1002/adma.201505738.

[94] Z. Chen, W. Zhang, C.-A. Palma, A. Lodi Rizzini, B. Liu, A. Abbas, N. Richter, L. Martini, X.-Y. Wang, N. Cavani, H. Lu, N. Mishra, C. Coletti, R. Berger, F. Klappenberger, M. Kläui, A. Candini, M. Affronte, C. Zhou, V. De Renzi, U. Del Pennino, J. V. Barth, H. J. Räder, A. Narita,

X. Feng, K. Müllen, "Synthesis of Graphene Nanoribbons by Ambient-Pressure Chemical Vapor Deposition and Device Integration", *J. Am. Chem. Soc.* **2016**, *138*(47), 15488–15496, DOI 10.1021/jacs.6b10374.

[95] E. Carbonell-Sanromà, J. Hieulle, M. Vilas-Varela, P. Brandimarte, M. Iraola, A. Barragán, J. Li, M. Abadia, M. Corso, D. Sánchez-Portal, D. Peña, J. I. Pascual, "Doping of Graphene Nanoribbons via Functional Group Edge Modification", *ACS Nano* **2017**, *11*(7), 7355–7361, DOI 10.1021/acsnano.7b03522.

[96] Z. Chen, H. I. Wang, J. Teyssandier, K. S. Mali, T. Dumslaff, I. Ivanov, W. Zhang, P. Ruffieux, R. Fasel, H. J. Räder, D. Turchinovich, S. De Feyter, X. Feng, M. Kläui, A. Narita, M. Bonn, K. Müllen, "Chemical Vapor Deposition Synthesis and Terahertz Photoconductivity of Low-Band-Gap N = 9 Armchair Graphene Nanoribbons", *J. Am. Chem. Soc.* **2017**, *139*(10), 3635–3638, DOI 10.1021/jacs.7b00776.

[97] Z. Chen, H. I. Wang, N. Bilbao, J. Teyssandier, T. Prechtl, N. Cavani, A. Tries, R. Biagi, V. De Renzi, X. Feng, M. Kläui, S. De Feyter, M. Bonn, A. Narita, K. Müllen, "Lateral Fusion of Chemical Vapor Deposited N = 5 Armchair Graphene Nanoribbons", *J. Am. Chem. Soc.* **2017**, *139*(28), 9483–9486, DOI 10.1021/jacs.7b05055.

[98] M. Di Giovannantonio, O. Deniz, J. I. Urgel, R. Widmer, T. Dienel, S. Stolz, C. Sánchez-Sánchez, M. Muntwiler, T. Dumslaff, R. Berger, A. Narita, X. Feng, K. Müllen, P. Ruffieux, R. Fasel, "On-Surface Growth Dynamics of Graphene Nanoribbons: The Role of Halogen Functionalization", *ACS Nano* **2017**, *12*(1), 74–81, DOI 10.1021/acsnano.7b07077.

[99] H. Hayashi, J. Yamaguchi, H. Jippo, R. Hayashi, N. Aratani, M. Ohfuchi, S. Sato, H. Yamada, "Experimental and Theoretical Investigations of Surface-Assisted Graphene Nanoribbon Synthesis Featuring Carbon-Fluorine Bond Cleavage", *ACS Nano* **2017**, *11*(6), 6204–6210, DOI 10.1021/acsnano.7b02316.

[100] F. Schulz, P. H. Jacobse, F. F. Canova, J. van der Lit, D. Z. Gao, A. van den Hoogenband, P. Han, R. J. M. Klein Gebbink, M.-E. Moret, P. M. Joensuu, I. Swart, P. Liljeroth, "Precursor Geometry Determines the Growth Mechanism in Graphene Nanoribbons", *J. Phys. Chem. C* **2017**, *121*(5), 2896–2904, DOI 10.1021/acs.jpcc.6b12428.

[101] L. Talirz, H. Söde, T. Dumslaff, S. Wang, J. R. Sanchez-Valencia, J. Liu, P. Shinde, C. A. Pignedoli, L. Liang, V. Meunier, N. C. Plumb, M. Shi, X. Feng, A. Narita, K. Müllen, R. Fasel, P. Ruffieux, "On-Surface Synthesis and Characterization of 9-Atom Wide Armchair Graphene Nanoribbons", *ACS Nano* **2017**, *11*(2), 1380–1388, DOI 10.1021/acsnano.6b06405.

[102] J. D. Teeter, P. S. Costa, M. Mehdi Pour, D. P. Miller, E. Zurek, A. Enders, A. Sinitskii, "Epitaxial growth of aligned atomically precise chevron graphene nanoribbons on Cu(111)", *Chem. Commun.* **2017**, *53*(60), 8463–8466, DOI 10.1039/c6cc08006e.

[103] O. Gröning, S. Wang, X. Yao, C. A. Pignedoli, G. Borin Barin, C. Daniels, A. Cupo, V. Meunier, X. Feng, A. Narita, K. Müllen, P. Ruffieux, R. Fasel, "Engineering of robust topological quantum phases in graphene nanoribbons", *Nature* **2018**, *560*(7717), 209–213, DOI 10.1038/s41586-018-0375-9.

[104] J. Li, N. Merino-Díez, E. Carbonell-Sanromà, M. Vilas-Varela, D. G. de Oteyza, D. Peña, M. Corso, J. I. Pascual, "Survival of spin state in magnetic porphyrins contacted by graphene nanoribbons", *Sci. Adv.* **2018**, *4*(2), eaaq0582, DOI 10.1126/sciadv.aaq0582.

[105] J. Liu, B. Xia, H. Xu, N. Lin, "Controlling the Reaction Steps of Bi-Functional Molecules 1,5-Dibromo-2,6-Dimethylnaphthalene on Different Substrates", *J. Phys. Chem. C* **2018**, *122*(24), 13001–13008, DOI 10.1021/acs.jpcc.8b04651.

[106] C. Moreno, M. Paradinas, M. Vilas-Varela, M. Panighel, G. Ceballos, D. Peña, A. Mugarza, "On-surface synthesis of superlattice arrays of ultralong graphene nanoribbons", *Chem. Commun.* **2018**, *54*(68), 9402–9405, DOI 10.1039/c8cc04830d.

[107] Z. Pedramrazi, C. Chen, F. Zhao, T. Cao, G. D. Nguyen, A. A. Omrani, H.-Z. Tsai, R. R. Cloke, T. Marangoni, D. J. Rizzo, T. Joshi, C. Bronner, W.-W. Choi, F. R. Fischer, S. G. Louie, M. F. Crommie, "Concentration Dependence of Dopant Electronic Structure in Bottom-up Graphene Nanoribbons", *Nano Lett.* **2018**, *18*(6), 3550–3556, DOI 10.1021/acs.nanolett.8b00651.

[108] M. Shekhirev, P. Zahl, A. Sinitskii, "Phenyl Functionalization of Atomically Precise Graphene Nanoribbons for Engineering Inter-ribbon Interactions and Graphene Nanopores", *ACS Nano* **2018**, *12*(8), 8662–8669, DOI 10.1021/acsnano.8b04489.

[109] Q. Sun, R. Zhang, J. Qiu, R. Liu, W. Xu, "On-Surface Synthesis of Carbon Nanostructures", *Adv. Mater.* **2018**, *30*(17), 1705630, DOI 10.1002/adma.201705630.

[110] X.-Y. Wang, J. I. Urgel, G. Borin Barin, K. Eimre, M. Di Giovannantonio, A. Milani, M. Tommasini, C. A. Pignedoli, P. Ruffieux, X. Feng, R. Fasel, K. Müllen, A. Narita, "Bottom-Up Synthesis of Heteroatom-Doped Chiral Graphene Nanoribbons", *J. Am. Chem. Soc.* **2018**, *140*(29), 9104–9107, DOI 10.1021/jacs.8b06210.

[111] D. Beyer, S. Wang, C. A. Pignedoli, J. Melidonie, B. Yuan, C. Li, J. Wilhelm, P. Ruffieux, R. Berger, K. Müllen, R. Fasel, X. Feng, "Graphene Nanoribbons Derived from Zigzag Edge-Encased Poly(*para*-2,9-dibenzo[*bc*,*kl*]coronenylene) Polymer Chains", *J. Am. Chem. Soc.* **2019**, *141*(7), 2843–2846, DOI 10.1021/jacs.8b10407.

[112] P. H. Jacobse, K. A. Simonov, M. J. J. Mangnus, G. I. Svirskiy, A. V. Generalov, A. S. Vinogradov, A. Sandell, N. Mårtensson, A. B. Preobrajenski, I. Swart, "One Precursor but Two Types of Graphene Nanoribbons: On-Surface Transformations of 10,10'-Dichloro-9,9'-bianthryl on Ag(111)", *J. Phys. Chem. C* **2019**, *123*(14), 8892–8901, DOI 10.1021/acs.jpcc.8b12209.

[113] A. Narita, Z. Chen, Q. Chen, K. Müllen, "Solution and on-surface synthesis of structurally defined graphene nanoribbons as a new family of semiconductors", *Chem. Sci.* **2019**, *10*(4), 964–975, DOI 10.1039/c8sc03780a.

[114] X. Zhou, G. Yu, "Modified Engineering of Graphene Nanoribbons Prepared via On-Surface Synthesis", *Adv. Mater.* **2020**, *32*(6), 1905957, DOI 10.1002/adma.201905957.

[115] J. van der Lit, M. P. Boneschanscher, D. Vanmaekelbergh, M. Ijäs, A. Uppstu, M. Ervasti, A. Harju, P. Liljeroth, I. Swart, "Suppression of electron–vibron coupling in graphene nanoribbons contacted via a single atom", *Nat. Commun.* **2013**, *4*, 2023, DOI 10.1038/ncomms3023.

[116] C. Rogers, C. Chen, Z. Pedramrazi, A. A. Omrani, H.-Z. Tsai, H. S. Jung, S. Lin, M. F. Crommie, F. R. Fischer, "Closing the Nanographene Gap: Surface-Assisted Synthesis of Peripentacene from 6,6'-Bipentacene Precursors", *Angew. Chem.* **2015**, *127*(50), 15358–15361, DOI 10.1002/ange.201507104; *Angew. Chem. Int. Ed.* **2015**, *54*(50), 15143–15146, DOI 10.1002/anie.201507104.

[117] K. A. Simonov, N. A. Vinogradov, A. S. Vinogradov, A. V. Generalov, E. M. Zagrebina, G. I. Svirskiy, A. A. Cafolla, T. Carpy, J. P. Cunniffe, T. Taketsugu, A. Lyalin, N. Mårtensson, A. B. Preobrajenski, "From Graphene Nanoribbons on Cu(111) to Nanographene on Cu(110): Critical Role of Substrate Structure in the Bottom-Up Fabrication Strategy", *ACS Nano* **2015**, *9*(9), 8997–9011, DOI 10.1021/acsnano.5b03280.

[118] P. H. Jacobse, A. van den Hoogenband, M.-E. Moret, R. J. M. Klein Gebbink, I. Swart, "Aryl Radical Geometry Determines Nanographene Formation on Au(111)", *Angew. Chem.* **2016**, *128*(42), 13246–13249, DOI 10.1002/ange.201606440; *Angew. Chem. Int. Ed.* **2016**, *55*(42), 13052–13055, DOI 10.1002/anie.201606440.

[119] J. Hieulle, E. Carbonell-Sanromà, M. Vilas-Varela, A. García-Lekue, E. Guitián, D. Peña, J. I. Pascual, "On-Surface Route for Producing Planar Nanographenes with Azulene Moieties", *Nano Lett.* **2018**, *18*(1), 418–423, DOI 10.1021/acs.nanolett.7b04309.

[120] R. Zuzak, J. Castro-Esteban, P. Brandimarte, M. Engelund, A. Cobas, P. Piątkowski, M. Kolmer, D. Pérez, E. Guitián, M. Szymonski, D. Sánchez-Portal, S. Godlewski, D. Peña, "Building a 22-ring nanographene by combining in-solution and on-surface syntheses", *Chem. Commun.* **2018**, *54*(73), 10256–10259, DOI 10.1039/c8cc05353g.

[121] J. Liu, S. Mishra, C. A. Pignedoli, D. Passerone, J. I. Urgel, A. Fabrizio, T. G. Lohr, J. Ma, H. Komber, M. Baumgarten, C. Corminboeuf, R. Berger, P. Ruffieux, K. Müllen, R. Fasel, X. Feng, "Open-Shell Nonbenzenoid Nanographenes Containing Two Pairs of Pentagonal and Heptagonal Rings", *J. Am. Chem. Soc.* **2019**, *141*(30), 12011–12020, DOI 10.1021/jacs.9b04718.

[122] D. Skidin, F. Eisenhut, M. Richter, S. Nikipar, J. Krüger, D. A. Ryndyk, R. Berger, G. Cuniberti, X. Feng, F. Moresco, "On-surface synthesis of nitrogen-doped nanographenes with 5–7 membered rings", *Chem. Commun.* **2019**, *55*(32), 4731–4734, DOI 10.1039/c9cc00276f.

[123] X.-Y. Wang, X. Yao, A. Narita, K. Müllen, "Heteroatom-Doped Nanographenes with Structural Precision", *Acc. Chem. Res.* **2019**, *52*(9), 2491–2505, DOI 10.1021/acs.accounts.9b00322.

[124] K. Xu, J. I. Urgel, K. Eimre, M. Di Giovannantonio, A. Keerthi, H. Komber, S. Wang, A. Narita, R. Berger, P. Ruffieux, C. A. Pignedoli, J. Liu, K. Müllen, R. Fasel, X. Feng, "On-Surface Synthesis of a Non-

planar Porous Nanographene", *J. Am. Chem. Soc.* **2019**, *141*(19), 7726–7730, DOI 10.1021/jacs.9b03554.

[125] R. Zuzak, I. Pozo, M. Engelund, A. García-Lekue, M. Vilas-Varela, J. M. Alonso, M. Szymonski, E. Guitián, D. Pérez, S. Godlewski, D. Peña, "Synthesis and reactivity of a trigonal porous nanographene on a gold surface", *Chem. Sci.* **2019**, *10*(43), 10143–10148, DOI 10.1039/c9sc03404h.

[126] A. Gourdon, „Kovalente Kupplung auf Oberflächen im Ultrahochvakuum", *Angew. Chem.* **2008**, *120*(37), 7056–7059, DOI 10.1002/ange.200802229; „On-Surface Covalent Coupling in Ultrahigh Vacuum", *Angew. Chem. Int. Ed.* **2008**, *47*(37), 6950–6953, DOI 10.1002/anie.200802229.

[127] M. Lackinger, W. M. Heckl, "A STM perspective on covalent intermolecular coupling reactions on surfaces", *J. Phys. D: Appl. Phys.* **2011**, *44*(46), 464011, DOI 10.1088/0022-3727/44/46/464011.

[128] F. Klappenberger, Y.-Q. Zhang, J. Björk, S. Klyatskaya, M. Ruben, J. V. Barth, "On-Surface Synthesis of Carbon-Based Scaffolds and Nanomaterials Using Terminal Alkynes", *Acc. Chem. Res.* **2015**, *48*(7), 2140–2150, DOI 10.1021/acs.accounts.5b00174.

[129] Q. Shen, H.-Y. Gao, H. Fuchs, "Frontiers of on-surface synthesis: From principles to applications", *Nano Today* **2017**, *13*, 77–96, DOI 10.1016/j.nantod.2017.02.007.

[130] S. Clair, D. G. de Oteyza, "Controlling a Chemical Coupling Reaction on a Surface: Tools and Strategies for On-Surface Synthesis", *Chem. Rev.* **2019**, *119*(7), 4717–4776, DOI 10.1021/acs.chemrev.8b00601.

[131] T. Wang, J. Zhu, "Confined on-surface organic synthesis: Strategies and mechanisms", *Surf. Sci. Rep.* **2019**, *74*(2), 97–140, DOI 10.1016/j.surfrep.2019.05.001.

[132] V. K. Kanuru, G. Kyriakou, S. K. Beaumont, A. C. Papageorgiou, D. J. Watson, R. M. Lambert, "Sonogashira Coupling on an Extended Gold Surface in Vacuo: Reaction of Phenylacetylene with Iodobenzene on Au(111)", *J. Am. Chem. Soc.* **2010**, *132*(23), 8081–8086, DOI 10.1021/ja1011542.

[133] Q. Sun, L. Cai, H. Ma, C. Yuan, W. Xu, "Dehalogenative Homocoupling of Terminal Alkynyl Bromides on Au(111): Incorporation of Acetylenic Scaffolding into Surface Nanostructures", *ACS Nano* **2016**, *10*(7), 7023–7030, DOI 10.1021/acsnano.6b03048.

[134] T. Wang, J. Huang, H. Lv, Q. Fan, L. Feng, Z. Tao, H. Ju, X. Wu, S. L. Tait, J. Zhu, "Kinetic Strategies for the Formation of Graphyne Nanowires via Sonogashira Coupling on Ag(111)", *J. Am. Chem. Soc.* **2018**, *140*(41), 13421–13428, DOI 10.1021/jacs.8b08477.

[135] Z. Yang, J. Gebhardt, T. A. Schaub, T. Sander, J. Schönamsgruber, H. Soni, A. Görling, M. Kivala, S. Maier, "Two-dimensional delocalized states in organometallic bis-acetylide networks on Ag(111)", *Nanoscale* **2018**, *10*(8), 3769–3776, DOI 10.1039/c7nr08238j.

[136] A. Rabia, F. Tumino, A. Milani, V. Russo, A. L. Bassi, S. Achilli, G. Fratesi, G. Onida, N. Manini, Q. Sun, W. Xu, C. S. Casari, "Scanning tunneling microscopy and Raman spectroscopy of polymeric sp–sp^2 carbon atomic wires synthesized on the Au(111) surface", *Nanoscale* **2019**, *11*(39), 18191–18200, DOI 10.1039/c9nr06552k.

[137] Q. Sun, X. Yu, M. Bao, M. Liu, J. Pan, Z. Zha, L. Cai, H. Ma, C. Yuan, X. Qiu, W. Xu, "Direct Formation of C–C Triple-Bonded Structural Motifs by On-Surface Dehalogenative Homocouplings of Tribromomethyl-Substituted Arenes", *Angew. Chem.* **2018**, *130*(15), 4099–4102, DOI 10.1002/ange.201801056; *Angew. Chem. Int. Ed.* **2018**, *57*(15), 4035–4038, DOI 10.1002/anie.201801056.

[138] X. Yu, L. Cai, M. Bao, Q. Sun, H. Ma, C. Yuan, W. Xu, "On-surface synthesis of graphyne nanowires through stepwise reactions", *Chem. Commun.* **2020**, *56*(11), 1685–1688, DOI 10.1039/c9cc07421j.

[139] C.-H. Shu, M.-X. Liu, Z.-Q. Zha, J.-L. Pan, S.-Z. Zhang, Y.-L. Xie, J.-L. Chen, D.-W. Yuan, X.-H. Qiu, P.-N. Liu, "On-surface synthesis of poly(*p*-phenylene ethynylene) molecular wires via in situ formation of carbon-carbon triple bond", *Nat. Commun.* **2018**, *9*, 2322, DOI 10.1038/s41467-018-04681-z.

[140] L. Cai, X. Yu, M. Liu, Q. Sun, M. Bao, Z. Zha, J. Pan, H. Ma, H. Ju, S. Hu, L. Xu, J. Zou, C. Yuan, T. Jacob, J. Björk, J. Zhu, X. Qiu, W. Xu, "Direct Formation of C–C Double-Bonded Structural Motifs by On-Surface Dehalogenative Homocoupling of *gem*-Dibromomethyl Molecules", *ACS Nano* **2018**, *12*(8), 7959–7966, DOI 10.1021/acsnano.8b02459.

[141] Q. Sun, B. V. Tran, L. Cai, H. Ma, X. Yu, C. Yuan, M. Stöhr, W. Xu, "On-Surface Formation of Cumulene by Dehalogenative Homocoupling of Alkenyl *gem*-Dibromides", *Angew. Chem.* **2017**, *129*(40), 12333–12337, DOI 10.1002/ange.201706104; *Angew. Chem. Int. Ed.* **2017**, *56*(40), 12165–12169, DOI 10.1002/anie.201706104.

[142] L. Cai, F. Kang, Q. Sun, W. Gao, X. Yu, H. Ma, C. Yuan, W. Xu, "The Stereoselective Formation of *trans*-Cumulene through Dehalogenative Homocoupling of Alkenyl *gem*-Dibromides on Cu(110)", *ChemCatChem* **2019**, *11*(22), 5417–5420, DOI 10.1002/cctc.201901300.

[143] A. Sánchez-Grande, B. de la Torre, J. Santos, B. Cirera, K. Lauwaet, T. Chutora, S. Edalatmanesh, P. Mutombo, J. Rosen, R. Zbořil, R. Miranda, J. Björk, P. Jelínek, N. Martín, D. Écija, "On-Surface Synthesis of Ethynylene-Bridged Anthracene Polymers", *Angew. Chem.* **2019**, *131*(20), 6631–6635, DOI 10.1002/ange.201814154; *Angew. Chem. Int. Ed.* **2019**, *58*(20), 6559–6563, DOI 10.1002/anie.201814154.

[144] Q. Sun, L. Cai, H. Ma, C. Yuan, W. Xu, "The stereoselective synthesis of dienes through dehalogenative homocoupling of terminal alkenyl bromides on Cu(110)", *Chem. Commun.* **2016**, *52*(35), 6009–6012, DOI 10.1039/c6cc01059h.

[145] Q. Sun, L. Cai, Y. Ding, H. Ma, C. Yuan, W. Xu, "Single-molecule insight into Wurtz reactions on metal surfaces", *Phys. Chem. Chem. Phys.* **2016**, *18*(4), 2730–2735, DOI 10.1039/c5cp06459g.

[146] B. V. Tran, T. A. Pham, M. Grunst, M. Kivala, M. Stöhr, "Surface-confined [2 + 2] cycloaddition towards one-dimensional polymers featuring cyclobutadiene units", *Nanoscale* **2017**, *9*(46), 18305–18310, DOI 10.1039/c7nr06187k.

[147] Y.-Q. Zhang, N. Kepčija, M. Kleinschrodt, K. Diller, S. Fischer, A. C. Papageorgiou, F. Allegretti, J. Björk, S. Klyatskaya, F. Klappenberger, M. Ruben, J. V. Barth, "Homo-coupling of terminal alkynes on a noble metal surface", *Nat. Commun.* **2012**, *3*, 1286, DOI 10.1038/ncomms2291.

[148] J. Eichhorn, W. M. Heckl, M. Lackinger, "On-surface polymerization of 1,4-diethynylbenzene on Cu(111)", *Chem. Commun.* **2013**, *49*(28), 2900–2902, DOI 10.1039/c3cc40444g.

[149] L. Colazzo, F. Sedona, A. Moretto, M. Casarin, M. Sambi, "Metal-Free on-Surface Photochemical Homocoupling of Terminal Alkynes", *J. Am. Chem. Soc.* **2016**, *138*(32), 10151–10156, DOI 10.1021/jacs.6b03589.

[150] T. Wang, H. Lv, L. Feng, Z. Tao, J. Huang, Q. Fan, X. Wu, J. Zhu, "Unravelling the Mechanism of Glaser Coupling Reaction on Ag(111) and Cu(111) Surfaces: a Case for Halogen Substituted Terminal Alkyne", *J. Phys. Chem. C* **2018**, *122*(26), 14537–14545, DOI 10.1021/acs.jpcc.8b02893.

[151] J. Liu, P. Ruffieux, X. Feng, K. Müllen, R. Fasel, "Cyclotrimerization of arylalkynes on Au(111)", *Chem. Commun.* **2014**, *50*(76), 11200–11203, DOI 10.1039/c4cc02859g.

[152] H. Zhou, J. Liu, S. Du, L. Zhang, G. Li, Y. Zhang, B. Z. Tang, H.-J. Gao, "Direct Visualization of Surface-Assisted Two-Dimensional Diyne Polycyclotrimerization", *J. Am. Chem. Soc.* **2014**, *136*(15), 5567–5570, DOI 10.1021/ja501308s.

[153] B. Schuler, S. Fatayer, F. Mohn, N. Moll, N. Pavliček, G. Meyer, D. Peña, L. Gross, "Reversible Bergman cyclization by atomic manipulation", *Nat. Chem.* **2016**, *8*(3), 220–224, DOI 10.1038/nchem.2438.

[154] D. Zhong, J.-H. Franke, S. K. Podiyanachari, T. Blomker, H. Zhang, G. Kehr, G. Erker, H. Fuchs, L. Chi, "Linear Alkane Polymerization on a Gold Surface", *Science* **2011**, *334*(6053), 213–216, DOI 10.1126/science.1211836.

[155] S. Wang, Q. Sun, O. Gröning, R. Widmer, C. A. Pignedoli, L. Cai, X. Yu, B. Yuan, C. Li, H. Ju, J. Zhu, P. Ruffieux, R. Fasel, W. Xu, "On-surface synthesis and characterization of individual polyacetylene chains", *Nat. Chem.* **2019**, *11*(10), 924–930, DOI 10.1038/s41557-019-0316-8.

[156] M. Kittelmann, P. Rahe, M. Nimmrich, C. M. Hauke, A. Gourdon, A. Kühnle, "On-surface covalent linking of organic building blocks on a bulk insulator", *ACS Nano* **2011**, *5*(10), 8420–8425, DOI 10.1021/nn2033192.

[157] R. Lindner, A. Kühnle, "On-surface reactions", *ChemPhysChem* **2015**, *16*(8), 1582–1592, DOI 10.1002/cphc.201500161.

[158] A. Richter, A. Floris, R. Bechstein, L. Kantorovich, A. Kühnle, "On-surface synthesis on a bulk insulator surface", *J. Phys.: Condens. Matter* **2018**, *30*(13), 133001, DOI 10.1088/1361-648X/aab0b9.

[159] J. M. Gottfried, "Surface chemistry of porphyrins and phthalocyanines", *Surf. Sci. Rep.* **2015**, *70*(3), 259–379, DOI 10.1016/j.surfrep.2015.04.001.

[160] J. M. Gottfried, K. Flechtner, A. Kretschmann, T. Lukasczyk, H.-P. Steinrück, "Direct Synthesis of a Metalloporphyrin Complex on a Surface", *J. Am. Chem. Soc.* **2006**, *128*(17), 5644–5645, DOI 10.1021/ja0610333.

[161] T. E. Shubina, H. Marbach, K. Flechtner, A. Kretschmann, N. Jux, F. Buchner, H.-P. Steinrück, T. Clark, J. M. Gottfried, "Principle and Mechanism of Direct Porphyrin Metalation: Joint Experimental and Theoretical Investigation", *J. Am. Chem. Soc.* **2007**, *129*(30), 9476–9483, DOI 10.1021/ja072360t.

[162] K. Flechtner, A. Kretschmann, L. R. Bradshaw, M.-M. Walz, H.-P. Steinrück, J. M. Gottfried, "Surface-Confined Two-Step Synthesis of the Complex (Ammine)(meso-tetraphenylporphyrinato)-zinc(II) on Ag(111)", *J. Phys. Chem. C* **2007**, *111*(16), 5821–5824, DOI 10.1021/jp071531d.

[163] F. Buchner, V. Schwald, K. Comanici, H.-P. Steinrück, H. Marbach, "Microscopic Evidence of the Metalation of a Free-Base Porphyrin Monolayer with Iron", *ChemPhysChem* **2007**, *8*(2), 241–243, DOI 10.1002/cphc.200600698.

[164] I. Aviv, Z. Gross, "Corrole-based applications", *Chem. Commun.* **2007**, (20), 1987–1999, DOI 10.1039/b618482k.

[165] S. Nardis, F. Mandoj, M. Stefanelli, R. Paolesse, "Metal complexes of corrole", *Coord. Chem. Rev.* **2019**, *388*, 360–405, DOI 10.1016/j.ccr.2019.02.034.

[166] A. W. Johnson, I. T. Kay, "306. Corroles. Part I. Synthesis", *J. Chem. Soc.* **1965**, 1620–1629, DOI 10.1039/jr9650001620.

[167] S. Kuck, G. Hoffmann, M. Bröring, M. Fechtel, M. Funk, R. Wiesendanger, ""Naked" Iron-5,10,15-triphenylcorrole on Cu(111): Observation of Chirality on a Surface and Manipulation of Multiple Conformational States by STM", *J. Am. Chem. Soc.* **2008**, *130*(43), 14072–14073, DOI 10.1021/ja8059478.

[168] M. Rashidi, S. Müllegger, M. Roithner, W. Schöfberger, R. Koch, "Spectroscopic Scanning Tunneling Microscopy Studies of Single Surface-Supported Free-Base Corroles", *J. Am. Chem. Soc.* **2012**, *134*(1), 91–94, DOI 10.1021/ja209225f.

[169] S. Tebi, H. Aldahhak, G. Serrano, W. Schöfberger, E. Rauls, W. G. Schmidt, R. Koch, S. Müllegger, "Manipulation resolves non-trivial structure of corrole monolayer on Ag(111)", *Nanotechnology* **2016**, *27*(2), 025704, DOI 10.1088/0957-4484/27/2/025704.

[170] H. Aldahhak, M. Paszkiewicz, F. Allegretti, D. A. Duncan, S. Tebi, P. S. Deimel, P. C. Aguilar, Y.-Q. Zhang, A. C. Papageorgiou, R. Koch, J. V. Barth, W. G. Schmidt, S. Müllegger, W. Schöfberger, F. Klappenberger, E. Rauls, U. Gerstmann, "X-ray Spectroscopy of Thin Film Free-Base Corroles: A Combined Theoretical and Experimental Characterization", *J. Phys. Chem. C* **2017**, *121*(4), 2192–2200, DOI 10.1021/acs.jpcc.6b09935.

[171] S. Tebi, M. Paszkiewicz, H. Aldahhak, F. Allegretti, S. Gonglach, M. Haas, M. Waser, P. S. Deimel, P. C. Aguilar, Y.-Q. Zhang, A. C. Papageorgiou, D. A. Duncan, J. V. Barth, W. G. Schmidt, R. Koch, U. Gerstmann, E. Rauls, F. Klappenberger, W. Schöfberger, S. Müllegger, "On-Surface Site-Selective Cyclization of Corrole Radicals", *ACS Nano* **2017**, *11*(3), 3383–3391, DOI 10.1021/acsnano.7b00766.

[172] H. Aldahhak, M. Paszkiewicz, E. Rauls, F. Allegretti, S. Tebi, A. C. Papageorgiou, Y.-Q. Zhang, L. Zhang, T. Lin, T. Paintner, R. Koch, W. G. Schmidt, J. V. Barth, W. Schöfberger, S. Müllegger, F. Klappenberger, U. Gerstmann, "Identifying On-Surface Site-Selective Chemical Conversions by Theory-Aided NEXAFS Spectroscopy: The Case of Free-Base Corroles on Ag(111)", *Chem. Eur. J.* **2018**, *24*(26), 6787–6797, DOI 10.1002/chem.201705921.

[173] D. J. Gundlach, Y.-Y. Lin, T. N. Jackson, D. G. Schlom, "Oligophenyl-based organic thin film transistors", *Appl. Phys. Lett.* **1997**, *71*(26), 3853–3855, DOI 10.1063/1.120524.

[174] S. Tasch, C. Brandstätter, F. Meghdadi, G. Froyer, L. Athouel, "Red-Green-Blue Light Emission from a Thin Film Electroluminescence Device Based on Parahexaphenyl", *Adv. Mater.* **1997**, *9*(1), 33–36, DOI 10.1002/adma.19970090105.

[175] H. Yanagi, S. Okamoto, T. Mikami, "Organic electroluminescent device with epitaxial *p*-sexiphenyl films", *Synth. Met.* **1997**, *91*(1-3), 91–93, DOI 10.1016/s0379-6779(97)03984-2.

[176] U. Schlickum, R. Decker, F. Klappenberger, G. Zoppellaro, S. Klyatskaya, W. Auwärter, S. Neppl, K. Kern, H. Brune, M. Ruben, J. V. Barth, "Chiral kagomé lattice from simple ditopic molecular bricks", *J. Am. Chem. Soc.* **2008**, *130*(35), 11778–11782, DOI 10.1021/ja8028119.

[177] F. Klappenberger, D. Kühne, W. Krenner, I. Silanes, A. Arnau, F. J. García de Abajo, S. Klyatskaya, M. Ruben, J. V. Barth, "Dichotomous array of chiral quantum corrals by a self-assembled nanoporous kagomé network", *Nano Lett.* **2009**, *9*(10), 3509–3514, DOI 10.1021/nl901700b.

[178] D. Kühne, F. Klappenberger, R. Decker, U. Schlickum, H. Brune, S. Klyatskaya, M. Ruben, J. V. Barth, "Self-assembly of nanoporous chiral networks with varying symmetry from sexiphenyl-dicarbonitrile on Ag (111)", *J. Phys. Chem. C* **2009**, *113*(41), 17851–17859, DOI 10.1021/jp9041217.

[179] F. Klappenberger, D. Kühne, M. Marschall, S. Neppl, W. Krenner, A. Nefedov, T. Strunskus, K. Fink, C. Wöll, S. Klyatskaya, O. Fuhr, M. Ruben, J. V. Barth, "Uniform π-System Alignment in Thin Films of Template-Grown Dicarbonitrile-Oligophenyls", *Adv. Funct. Mater.* **2011**, *21*(9), 1631–1642, DOI 10.1002/adfm.201001940.

[180] S. Klyatskaya, F. Klappenberger, U. Schlickum, D. Kühne, M. Marschall, J. Reichert, R. Decker, W. Krenner, G. Zoppellaro, H. Brune, J. V. Barth, M. Ruben, "Surface-Confined Self-Assembly of Di-carbonitrile Polyphenyls", *Adv. Funct. Mater.* **2011**, *21*(7), 1230–1240, DOI 10.1002/adfm.201001437.

[181] M. Marschall, J. Reichert, K. Seufert, W. Auwärter, F. Klappenberger, A. Weber-Bargioni, S. Klyatskaya, G. Zoppellaro, A. Nefedov, T. Strunskus, C. Wöll, M. Ruben, J. V. Barth, "Supramolecular organization and chiral resolution of *p*-terphenyl-*m*-dicarbonitrile on the Ag(111) surface", *ChemPhysChem* **2010**, *11*(7), 1446–1451, DOI 10.1002/cphc.200900938.

[182] D. Abbasi-Pérez, J. M. Recio, L. Kantorovich, "Building Motifs during Self-Assembly of *para*-Terphenyl-*meta*-dicarbonitrile on a Metal Surface: A Gas-Phase Study", *J. Phys. Chem. C* **2014**, *118*(19), 10358–10365, DOI 10.1021/jp4122672.

[183] M. Marschall, J. Reichert, K. Diller, S. Klyatskaya, M. Ruben, A. Nefedov, C. Wöll, L. N. Kantorovich, F. Klappenberger, J. V. Barth, "Meta-Positioning of Carbonitrile Functional Groups Induces Interfacial Edge-

On Phase of Oligophenyl Derivatives", *J. Phys. Chem. C* **2014**, *118*(5), 2622–2633, DOI 10.1021/jp4118584.

[184] D. Abbasi-Pérez, J. Manuel Recio, L. Kantorovich, "The role of isomerization in the kinetics of self-assembly: *p*-terphenyl-*m*-dicarbonitrile on the Ag(111) surface", *Phys. Chem. Chem. Phys.* **2015**, *17*(17), 11182–11192, DOI 10.1039/c5cp00220f.

[185] L. Cai, Q. Sun, M. Bao, H. Ma, C. Yuan, W. Xu, "Competition between Hydrogen Bonds and Coordination Bonds Steered by the Surface Molecular Coverage", *ACS Nano* **2017**, *11*(4), 3727–3732, DOI 10.1021/acsnano.6b08374.

[186] U. Schlickum, R. Decker, F. Klappenberger, G. Zoppellaro, S. Klyatskaya, M. Ruben, I. Silanes, A. Arnau, K. Kern, H. Brune, J. V. Barth, "Metal-Organic Honeycomb Nanomeshes with Tunable Cavity Size", *Nano Lett.* **2007**, *7*(12), 3813–3817, DOI 10.1021/nl072466m.

[187] U. Schlickum, F. Klappenberger, R. Decker, G. Zoppellaro, S. Klyatskaya, M. Ruben, K. Kern, H. Brune, J. V. Barth, "Surface-Confined Metal-Organic Nanostructures from Co-Directed Assembly of Linear Terphenyl-dicarbonitrile Linkers on Ag(111)", *J. Phys. Chem. C* **2010**, *114*(37), 15602–15606, DOI 10.1021/jp104518h.

[188] J. Reichert, M. Marschall, K. Seufert, D. Ecija, W. Auwärter, E. Arras, S. Klyatskaya, M. Ruben, J. V. Barth, "Competing Interactions in Surface Reticulation with a Prochiral Dicarbonitrile Linker", *J. Phys. Chem. C* **2013**, *117*(24), 12858–12863, DOI 10.1021/jp4021273.

[189] G. E. Pacchioni, M. Pivetta, H. Brune, "Competing Interactions in the Self-Assembly of NC-Ph_3-CN Molecules on Cu(111)", *J. Phys. Chem. C* **2015**, *119*(45), 25442–25448, DOI 10.1021/acs.jpcc.5b08644.

[190] M. Pivetta, G. E. Pacchioni, E. Fernandes, H. Brune, "Temperature-dependent self-assembly of NC-Ph_5-CN molecules on Cu(111)", *J. Chem. Phys.* **2015**, *142*(10), 101928, DOI 10.1063/1.4909518.

[191] D. Écija, J. I. Urgel, A. C. Papageorgiou, S. Joshi, W. Auwärter, A. P. Seitsonen, S. Klyatskaya, M. Ruben, S. Fischer, S. Vijayaraghavan, J. Reichert, J. V. Barth, "Five-vertex Archimedean surface tessellation by lanthanide-directed molecular self-assembly", *Proc. Natl. Acad. Sci. U.S.A.* **2013**, *110*(17), 6678–6681, DOI 10.1073/pnas.1222713110.

[192] J. I. Urgel, D. Écija, G. Lyu, R. Zhang, C.-A. Palma, W. Auwärter, N. Lin, J. V. Barth, "Quasicrystallinity expressed in two-dimensional coordination networks", *Nat. Chem.* **2016**, *8*(7), 657–662, DOI 10.1038/nchem.2507.

[193] Q. Sun, L. Cai, H. Ma, C. Yuan, W. Xu, "On-surface construction of a metal–organic Sierpiński triangle", *Chem. Commun.* **2015**, *51*(75), 14164–14166, DOI 10.1039/c5cc05554g.

[194] N. Li, X. Zhang, G.-C. Gu, H. Wang, D. Nieckarz, P. Szabelski, Y. He, Y. Wang, J.-T. Lü, H. Tang, L.-M. Peng, S.-M. Hou, K. Wu, Y.-F. Wang, "Sierpiński-triangle fractal crystals with the C_{3v} point group", *Chin. Chem. Lett.* **2015**, *26*(10), 1198–1202, DOI 10.1016/j.cclet.2015.08.006.

[195] D. G. de Oteyza, P. Gorman, Y.-C. Chen, S. Wickenburg, A. Riss, D. J. Mowbray, G. Etkin, Z. Pedramrazi, H.-Z. Tsai, A. Rubio, M. F. Crommie, F. R. Fischer, "Direct Imaging of Covalent Bond Structure in Single-Molecule Chemical Reactions", *Science* **2013**, *340*(6139), 1434–1437, DOI 10.1126/science.1238187.

[196] D. G. de Oteyza, A. Pérez Paz, Y.-C. Chen, Z. Pedramrazi, A. Riss, S. Wickenburg, H.-Z. Tsai, F. R. Fischer, M. F. Crommie, A. Rubio, "Noncovalent Dimerization after Enediyne Cyclization on Au(111)", *J. Am. Chem. Soc.* **2016**, *138*(34), 10963–10967, DOI 10.1021/jacs.6b05203.

[197] S. Kawai, V. Haapasilta, B. D. Lindner, K. Tahara, P. Spijker, J. A. Buitendijk, R. Pawlak, T. Meier, Y. Tobe, A. S. Foster, E. Meyer, "Thermal control of sequential on-surface transformation of a hydrocarbon molecule on a copper surface", *Nat. Commun.* **2016**, *7*, 12711, DOI 10.1038/ncomms12711.

[198] F. Eisenhut, T. Lehmann, A. Viertel, D. Skidin, J. Krüger, S. Nikipar, D. A. Ryndyk, C. Joachim, S. Hecht, F. Moresco, G. Cuniberti, "On-Surface Annulation Reaction Cascade for the Selective Synthesis of Diindenopyrene", *ACS Nano* **2017**, *11*(12), 12419–12425, DOI 10.1021/acsnano.7b06459.

[199] S. Mishra, M. Krzeszewski, C. A. Pignedoli, P. Ruffieux, R. Fasel, D. T. Gryko, "On-surface synthesis of a nitrogen-embedded buckybowl with inverse Stone-Thrower-Wales topology", *Nat. Commun.* **2018**, *9*, 1714, DOI 10.1038/s41467-018-04144-5.

[200] S. Mishra, T. G. Lohr, C. A. Pignedoli, J. Liu, R. Berger, J. I. Urgel, K. Müllen, X. Feng, P. Ruffieux, R. Fasel, "Tailoring Bond Topologies in Open-Shell Graphene Nanostructures", *ACS Nano* **2018**, *13*(12), 11917-11927, DOI 10.1021/acsnano.8b07225.

[201] *CRC Handbook of Chemistry and Physics*, 87th ed., (Ed.: D. R. Lide), CRC Press/Taylor and Francis Group, Boca Raton, FL, **2006**, DOI 10.1021/ja069813z.

[202] Y. Yamaguchi, M. Takubo, K. Ogawa, K.-I. Nakayama, T. Koganezawa, H. Katagiri, "Terazulene Isomers: Polarity Change of OFETs through Molecular Orbital Distribution Contrast", *J. Am. Chem. Soc.* **2016**, *138*(35), 11335–11343, DOI 10.1021/jacs.6b06877.

[203] H. Xin, X. Gao, "Application of Azulene in Constructing Organic Optoelectronic Materials: New Tricks for an Old Dog", *ChemPlusChem* **2017**, *82*(7), 945–956, DOI 10.1002/cplu.201700039.

[204] F. Banhart, J. Kotakoski, A. V. Krasheninnikov, "Structural defects in graphene", *ACS Nano* **2011**, *5*(1), 26–41, DOI 10.1021/nn102598m.

[205] P. Y. Huang, C. S. Ruiz-Vargas, A. M. van der Zande, W. S. Whitney, M. P. Levendorf, J. W. Kevek, S. Garg, J. S. Alden, C. J. Hustedt, Y. Zhu, J. Park, P. L. McEuen, D. A. Muller, "Grains and grain boundaries in single-layer graphene atomic patchwork quilts", *Nature* **2011**, *469*(7330), 389–392, DOI 10.1038/nature09718.

[206] *Surface Science Techniques*, (Eds.: G. Bracco, P. Holst), Springer-Verlag, Berlin, Heidelberg, **2013**, DOI 10.1007/978-3-642-34243-1.

[207] *Surface Analysis: The Principal Techniques*, 2nd ed., (Eds.: J. C. Vickerman, I. S. Gilmore), John Wiley & Sons Ltd, Chichester, West Sussex, **2009**, DOI 10.1002/9780470721582.

[208] P. van der Heide, *X-ray Photoelectron Spectroscopy*, John Wiley & Sons, Inc., Hoboken, New Jersey, **2012**.

[209] S. Hüfner, *Photoelectron Spectroscopy: Principles and Applications*, 2nd ed., Springer-Verlag, Berlin, Heidelberg, **1996**, DOI 10.1007/978-3-662-03209-1.

[210] G. A. Somorjai, *Chemistry in two Dimensions: Surfaces*, Cornell University Press, Ithaca, London, **1981**.

[211] K. Christmann, *Introduction to Surface Physical Chemistry*, Steinkopff, Heidelberg, **1991**, DOI 10.1007/978-3-662-08009-2.

[212] G. Binnig, H. Rohrer, C. Gerber, E. Weibel, "Surface Studies by Scanning Tunneling Microscopy", *Phys. Rev. Lett.* **1982**, *49*(1), 57–61, DOI 10.1103/physrevlett.49.57.

[213] G. Binnig, H. Rohrer, C. Gerber, E. Weibel, "Tunneling through a controllable vacuum gap", *Appl. Phys. Lett.* **1982**, *40*(2), 178–180, DOI 10.1063/1.92999.

[214] G. Binnig, H. Rohrer, "Scanning tunneling microscopy", *IBM J. Res. Develop.* **1986**, *30*(4), 356–369.

[215] E. Laegsgaard, F. Besenbacher, K. Mortensen, I. Stensgaard, "A fully automated, 'thimble-size' scanning tunnelling microscope", *J. Microsc.* **1988**, *152*(3), 663–669, DOI 10.1111/j.1365-2818.1988.tb01435.x.

[216] M. Schunack, "Scanning Tunneling Microscopy Studies of Organic Molecules on Metal Surfaces", dissertation, University of Aarhus, **2002**.

[217] E. K. Vestergaard, "Scanning Tunneling Microscopy Studies of Model Systems Relevant to Catalysis", dissertation, University of Aarhus, **2002**.

[218] M. S. A. Zugermeier, "Reactive Aromatic Molecules on Metal Surfaces: Syntheses, Reactions and Structures", dissertation, Philipps-Universität Marburg, **2018**, DOI 10.17192/z2018.0239.

[219] R. J. Hamers, R. M. Tromp, J. E. Demuth, "Surface Electronic Structure of Si (111)-(7×7) Resolved in Real Space", *Phys. Rev. Lett.* **1986**, *56*(18), 1972–1975, DOI 10.1103/physrevlett.56.1972.

[220] G. Binnig, C. F. Quate, C. Gerber, "Atomic Force Microscope", *Phys. Rev. Lett.* **1986**, *56*(9), 930–933, DOI 10.1103/physrevlett.56.930.

[221] T. R. Albrecht, P. Grütter, D. Horne, D. Rugar, "Frequency modulation detection using high-Q cantilevers for enhanced force microscope sensitivity", *J. Appl. Phys.* **1991**, *69*(2), 668–673, DOI 10.1063/1.347347.

[222] F. J. Giessibl, "High-speed force sensor for force microscopy and profilometry utilizing a quartz tuning fork", *Appl. Phys. Lett.* **1998**, *73*(26), 3956–3958, DOI 10.1063/1.122948.

[223] L. Bartels, G. Meyer, K.-H. Rieder, "Controlled vertical manipulation of single CO molecules with the scanning tunneling microscope: A route to chemical contrast", *Appl. Phys. Lett.* **1997**, *71*(2), 213–215, DOI 10.1063/1.119503.

[224] L. Gross, F. Mohn, N. Moll, P. Liljeroth, G. Meyer, "The Chemical Structure of a Molecule Resolved by Atomic Force Microscopy", *Science* **2009**, *325*(5944), 1110–1114, DOI 10.1126/science.1176210.

[225] L. Gross, B. Schuler, N. Pavliček, S. Fatayer, Z. Majzik, N. Moll, D. Peña, G. Meyer, „Rasterkraftmikroskopie für die molekulare Strukturaufklärung", *Angew. Chem.* **2018**, *130*(15), 3950–3972, DOI 10.1002/ange.201703509; „Atomic Force Microscopy for Molecular Structure Elucidation", *Angew. Chem. Int. Ed.* **2018**, *57*(15), 3888–3908, DOI 10.1002/anie.201703509.

[226] H. Hertz, „Ueber einen Einfluss des ultravioletten Lichtes auf die electrische Entladung", *Ann. Physik* **1887**, *267*(8), 983–1000, DOI 10.1002/andp.18872670827.

[227] A. Einstein, „Über einen die Erzeugung und Verwandlung des Lichtes betreffenden heuristischen Gesichtspunkt", *Ann. Physik* **1905**, *322*(6), 132–148, DOI 10.1002/andp.19053220607.

[228] T. Koopmans, „Über die Zuordnung von Wellenfunktionen und Eigenwerten zu den Einzelnen Elektronen Eines Atoms", *Physica* **1934**, *1*(1-6), 104–113, DOI 10.1016/s0031-8914(34)90011-2.

[229] K. Wille, *Physik der Teilchenbeschleuniger und Synchrotronstrahlungsquellen*, 2. Aufl., Vieweg+Teubner Verlag, Stuttgart, **1996**, DOI 10.1007/978-3-663-11039-2.

[230] J. Stöhr, *NEXAFS Spectroscopy*, 1st ed., Springer-Verlag, Berlin, Heidelberg, **1992**.

[231] T. Breuer, M. Klues, G. Witte, "Characterization of orientational order in π-conjugated molecular thin films by NEXAFS", *J. Electron Spectrosc. Relat. Phenom.* **2015**, *204*, 102–115, DOI 10.1016/j.elspec.2015.07.011.

[232] A. Nefedov, C. Wöll in *Surface Science Techniques*, (Eds.: G. Bracco, B. Holst), Springer-Verlag, Berlin, Heidelberg, **2013**, pp. 277–303, DOI 10.1007/978-3-642-34243-1_10.

[233] C. K. Krug, „Untersuchungen adsorbierter aromatischer Dicarbonitrile auf der Ag(111)-Oberfläche mittels Rastertunnelmikroskopie", master's thesis, Philipps-Universität Marburg, **2015**.

[234] B. P. Klein, "The Surface Chemical Bond of Non-alternant Aromatic Molecules on Metal Surfaces", dissertation, Philipps-Universität Marburg, **2019**.

[235] N. A. Wollscheid, „Konstruktion und Inbetriebnahme einer Probenpräparationskammer für Oberflächenexperimente im UHV", master's thesis, Philipps-Universität Marburg, **2016**.

[236] F. Schaefers, M. Mertin, M. Gorgoi, "KMC-1: A high resolution and high flux soft x-ray beamline at BESSY", *Rev. Sci. Instrum.* **2007**, *78*(12), 123102, DOI 10.1063/1.2808334.

[237] H. Zhou, "Reactive Metal-Organic Interfaces Studied with Adsorption Calorimetry and Photoelectron Spectroscopy", dissertation, Philipps-Universität Marburg, **2018**, DOI 10.17192/z2018.0513.

[238] C. K. Krug, Q. Fan, F. Fillsack, J. Glowatzki, N. Trebel, L. J. Heuplick, T. Koehler, J. M. Gottfried, "Organometallic ring *vs.* chain formation beyond kinetic control: steering their equilibrium in two-dimensional confinement", *Chem. Commun.* **2018**, *54*(70), 9741–9744, DOI 10.1039/c8cc05357j.

[239] C. K. Krug, D. Nieckarz, Q. Fan, P. Szabelski, M. Gottfried, "The Macrocycle versus Chain Competition in On-Surface Polymerization: Insights from Reactions of 1,3-Dibromoazulene on Cu(111)", *Chem. Eur. J.* **2020**, *26*(34), 7647–7656, DOI 10.1002/chem.202000486.

[240] I. Piquero-Zulaica, A. García-Lekue, L. Colazzo, C. K. Krug, M. S. G. Mohammed, Z. M. Abd El-Fattah, J. M. Gottfried, D. G. de Oteyza, J. E. Ortega, J. Lobo-Checa, "Electronic Structure Tunability by Periodic *meta*-Ligand Spacing in One-Dimensional Organic Semiconductors", *ACS Nano* **2018**, *12*(10), 10537–10544, DOI 10.1021/acsnano.8b06536.

[241] Q. Fan, D. Martin-Jimenez, D. Ebeling, C. K. Krug, L. Brechmann, C. Kohlmeyer, G. Hilt, W. Hieringer, A. Schirmeisen, J. M. Gottfried, "Nanoribbons with Nonalternant Topology from Fusion of Polyazulene: Carbon Allotropes beyond Graphene", *J. Am. Chem. Soc.* **2019**, *141*(44), 17713–17720, DOI 10.1021/jacs.9b08060.

[242] C. K. Krug, M. Zugermeier, J. Kuttner, M. Schmid, G. Hilt, J. M. Gottfried, "Polymorphism at the Metal/Organic Interface: Hybrid Phase with Alternating Coplanar and Vertical Adsorption Geometry", *J. Phys. Chem. C* **2020**, *124*(29), 15928–15934, DOI 10.1021/acs.jpcc.0c03601.

[243] M. Chen, H. Zhou, B. P. Klein, M. Zugermeier, C. K. Krug, H.-J. Drescher, M. Gorgoi, M. Schmid, J. M. Gottfried, "Formation of an interphase layer during deposition of cobalt onto tetraphenylporphyrin: a hard X-ray photoelectron spectroscopy (HAXPES) study", *Phys. Chem. Chem. Phys.* **2016**, *18*(44), 30643–30651, DOI 10.1039/c6cp05894a.

[244] M. Schmid, M. Zugermeier, J. Herritsch, B. P. Klein, C. K. Krug, L. Ruppenthal, P. Müller, M. Kothe, P. Schweyen, M. Bröring, J. M. Gottfried, "On-Surface Synthesis and Characterization of an Iron Corrole", *J. Phys. Chem. C* **2018**, *122*(19), 10392–10399, DOI 10.1021/acs.jpcc.8b00067.

[245] B. P. Klein, N. J. van der Heijden, S. R. Kachel, M. Franke, C. K. Krug, K. K. Greulich, L. Ruppenthal, P. Müller, P. Rosenow, S. Parhizkar, F. C. Bocquet, M. Schmid, W. Hieringer, R. J. Maurer, R. Tonner, C. Kumpf, I. Swart, J. M. Gottfried, "Molecular Topology and the Surface Chemical Bond: Alternant Versus Nonalternant Aromatic Systems as Functional Structural Elements", *Phys. Rev. X* **2019**, *9*(1), 011030, DOI 10.1103/physrevx.9.011030.

[246] R. Gutzler, L. Cardenas, J. Lipton-Duffin, M. E. Garah, L. E. Dinca, C. E. Szakacs, C. Fu, M. Gallagher, M. Vondráček, M. Rybachuk, D. F. Perepichka, F. Rosei, "Ullmann-type coupling of brominated tetrathienoanthracene on copper and silver", *Nanoscale* **2014**, *6*(5), 2660–2668, DOI 10.1039/c3nr05710k.

[247] S. R. Kachel, B. P. Klein, J. M. Morbec, M. Schöniger, M. Hutter, M. Schmid, P. Kratzer, B. Meyer, R. Tonner, J. M. Gottfried, "Chemisorption and Physisorption at the Metal/Organic Interface: Bond Energies of Naphthalene and Azulene on Coinage Metal Surfaces", *J. Phys. Chem. C* **2020**, *124*(15), 8257–8268, DOI 10.1021/acs.jpcc.0c00915.

[248] G. Rojas, S. Simpson, X. Chen, D. A. Kunkel, J. Nitz, J. Xiao, P. A. Dowben, E. Zurek, A. Enders, "Surface state engineering of molecule–molecule interactions", *Phys. Chem. Chem. Phys.* **2012**, *14*(14), 4971, DOI 10.1039/c2cp40254h.

[249] G. Di Santo, S. Blankenburg, C. Castellarin-Cudia, M. Fanetti, P. Borghetti, L. Sangaletti, L. Floreano, A. Verdini, E. Magnano, F. Bondino, C. A. Pignedoli, M.-T. Nguyen, R. Gaspari, D. Passerone, A. Goldoni, "Supramolecular Engineering through Temperature-Induced Chemical Modification of 2H-Tetraphenylporphyrin on Ag(111): Flat

Phenyl Conformation and Possible Dehydrogenation Reactions", *Chem. Eur. J.* **2011**, *17*(51), 14354–14359, DOI 10.1002/chem.201102268.

[250] F. Buchner, J. Xiao, E. Zillner, M. Chen, M. Röckert, S. Ditze, M. Stark, H.-P. Steinrück, J. M. Gottfried, H. Marbach, "Diffusion, Rotation, and Surface Chemical Bond of Individual 2H-Tetraphenylporphyrin Molecules on Cu(111)", *J. Phys. Chem. C* **2011**, *115*(49), 24172–24177, DOI 10.1021/jp206675u.

[251] M. Röckert, S. Ditze, M. Stark, J. Xiao, H.-P. Steinrück, H. Marbach, O. Lytken, "Abrupt Coverage-Induced Enhancement of the Self-Metalation of Tetraphenylporphyrin with Cu(111)", *J. Phys. Chem. C* **2014**, *118*(3), 1661–1667, DOI 10.1021/jp412121b.

[252] A. Rastgoo-Lahrood, J. Björk, M. Lischka, J. Eichhorn, S. Kloft, M. Fritton, T. Strunskus, D. Samanta, M. Schmittel, W. M. Heckl, M. Lackinger, „Postsynthetische Entkopplung oberflächensynthetisierter kovalenter Nanostrukturen von Ag(111)", *Angew. Chem.* **2016**, *128*(27), 7780–7784, DOI 10.1002/ange.201600684; „Post-Synthetic Decoupling of On-Surface-Synthesized Covalent Nanostructures from Ag(111)", *Angew. Chem. Int. Ed.* **2016**, *55*(27), 7650–7654, DOI 10.1002/anie.201600684.

B Permissions of Use for the Included Publications

In the following list the copyright status of all articles that are part of this thesis is given. For those publications, where it applies, the permission of use is appended on the following pages.

P1 Reproduced by permission of The Royal Society of Chemistry. As author of the article no further permission needs to be obtained. [238]

P2 Available under the terms of the Creative Commons Attribution License (CC BY). Reproduction is permitted if the article is properly cited. [239]

P3 Reprinted with permission from ref. [240]. © 2018 American Chemical Society.

P4 Reprinted with permission from ref. [241]. © 2019 American Chemical Society.

P5 Reprinted with permission from ref. [242]. © 2020 American Chemical Society.

P6 Reproduced by permission of the PCCP Owner Societies. As author of the article no further permission needs to be obtained. [243]

P7 Reprinted with permission from ref. [244]. © 2018 American Chemical Society.

P8 Published by the American Physical Society under the terms of the Creative Commons Attribution 4.0 International license. This license permits unrestricted reproduction if the article is properly cited. [245]

Electronic Structure Tunability by Periodic meta-Ligand Spacing in One-Dimensional Organic Semiconductors

Author: Ignacio Piquero-Zulaica, Aran Garcia-Lekue, Luciano Colazzo, et al

Publication: ACS Nano

Publisher: American Chemical Society

Date: Oct 1, 2018

PERMISSION/LICENSE IS GRANTED FOR YOUR ORDER AT NO CHARGE

This type of permission/license, instead of the standard Terms & Conditions, is sent to you because no fee is being charged for your order. Please note the following:

- Permission is granted for your request in both print and electronic formats, and translations.
- If figures and/or tables were requested, they may be adapted or used in part.
- Please print this page for your records and send a copy of it to your publisher/graduate school.
- Appropriate credit for the requested material should be given as follows: "Reprinted (adapted) with permission from (COMPLETE REFERENCE CITATION). Copyright (YEAR) American Chemical Society." Insert appropriate information in place of the capitalized words.
- One-time permission is granted only for the use specified in your request. No additional uses are granted (such as derivative works or other editions). For any other uses, please submit a new request.

BACK CLOSE WINDOW

ACS Publications
Most Trusted. Most Cited. Most Read.

Polymorphism at the Metal/Organic Interface: Hybrid Phase with Alternating Coplanar and Vertical Adsorption Geometry

Author: Claudio K. Krug, Malte Zugermeier, Julian Kuttner, et al

Publication: The Journal of Physical Chemistry C

Publisher: American Chemical Society

Date: Jul 1, 2020

PERMISSION/LICENSE IS GRANTED FOR YOUR ORDER AT NO CHARGE

This type of permission/license, instead of the standard Terms & Conditions, is sent to you because no fee is being charged for your order. Please note the following:

- Permission is granted for your request in both print and electronic formats, and translations.
- If figures and/or tables were requested, they may be adapted or used in part.
- Please print this page for your records and send a copy of it to your publisher/graduate school.
- Appropriate credit for the requested material should be given as follows: "Reprinted (adapted) with permission from (COMPLETE REFERENCE CITATION). Copyright (YEAR) American Chemical Society." Insert appropriate information in place of the capitalized words.
- One-time permission is granted only for the use specified in your request. No additional uses are granted (such as derivative works or other editions). For any other uses, please submit a new request.

BACK CLOSE WINDOW

Nanoribbons with Nonalternant Topology from Fusion of Polyazulene: Carbon Allotropes beyond Graphene

Author: Qitang Fan, Daniel Martin-Jimenez, Daniel Ebeling, et al

Publication: Journal of the American Chemical Society

Publisher: American Chemical Society

Date: Nov 1, 2019

PERMISSION/LICENSE IS GRANTED FOR YOUR ORDER AT NO CHARGE

This type of permission/license, instead of the standard Terms & Conditions, is sent to you because no fee is being charged for your order. Please note the following:

- Permission is granted for your request in both print and electronic formats, and translations.
- If figures and/or tables were requested, they may be adapted or used in part.
- Please print this page for your records and send a copy of it to your publisher/graduate school.
- Appropriate credit for the requested material should be given as follows: "Reprinted (adapted) with permission from (COMPLETE REFERENCE CITATION). Copyright (YEAR) American Chemical Society." Insert appropriate information in place of the capitalized words.
- One-time permission is granted only for the use specified in your request. No additional uses are granted (such as derivative works or other editions). For any other uses, please submit a new request.

BACK CLOSE WINDOW

On-Surface Synthesis and Characterization of an Iron Corrole

Author: Martin Schmid, Malte Zugermeier, Jan Herritsch, et al

Publication: The Journal of Physical Chemistry C

Publisher: American Chemical Society

Date: May 1, 2018

PERMISSION/LICENSE IS GRANTED FOR YOUR ORDER AT NO CHARGE

This type of permission/license, instead of the standard Terms & Conditions, is sent to you because no fee is being charged for your order. Please note the following:

- Permission is granted for your request in both print and electronic formats, and translations.
- If figures and/or tables were requested, they may be adapted or used in part.
- Please print this page for your records and send a copy of it to your publisher/graduate school.
- Appropriate credit for the requested material should be given as follows: "Reprinted (adapted) with permission from (COMPLETE REFERENCE CITATION). Copyright (YEAR) American Chemical Society." Insert appropriate information in place of the capitalized words.
- One-time permission is granted only for the use specified in your request. No additional uses are granted (such as derivative works or other editions). For any other uses, please submit a new request.

BACK CLOSE WINDOW

Erklärung zur kumulativen Dissertation

Ich versichere, dass die im kumulativen Teil der Dissertation mit dem Titel

Structure and Reactivity of Aromatic Molecules on Metal Single-Crystal Surfaces and at Metal/Organic Interfaces

aufgeführten Anteile der Autoren an den verfassten Publikationen und Manuskripten korrekt und vollständig dargelegt sind.

Der kumulative Teil umfasst das Kapitel 5.

Marburg, _____

Unterschrift Doktorand Claudio K. Krug	Unterschrift Betreuer Prof. Dr. J. Michael Gottfried

C Constructional Drawings

In this chapter all the constructional drawings used to manufacture the designed parts described in Chapter 4 are given. The drawings were created with the 3D CAD software Autodesk Inventor, which was used to design the parts. They specify the dimensions and precisions needed and were given to the department's mechanical workshop or external companies. The constructional drawings of the different parts and the pages, on which they are found, are listed in the following table.

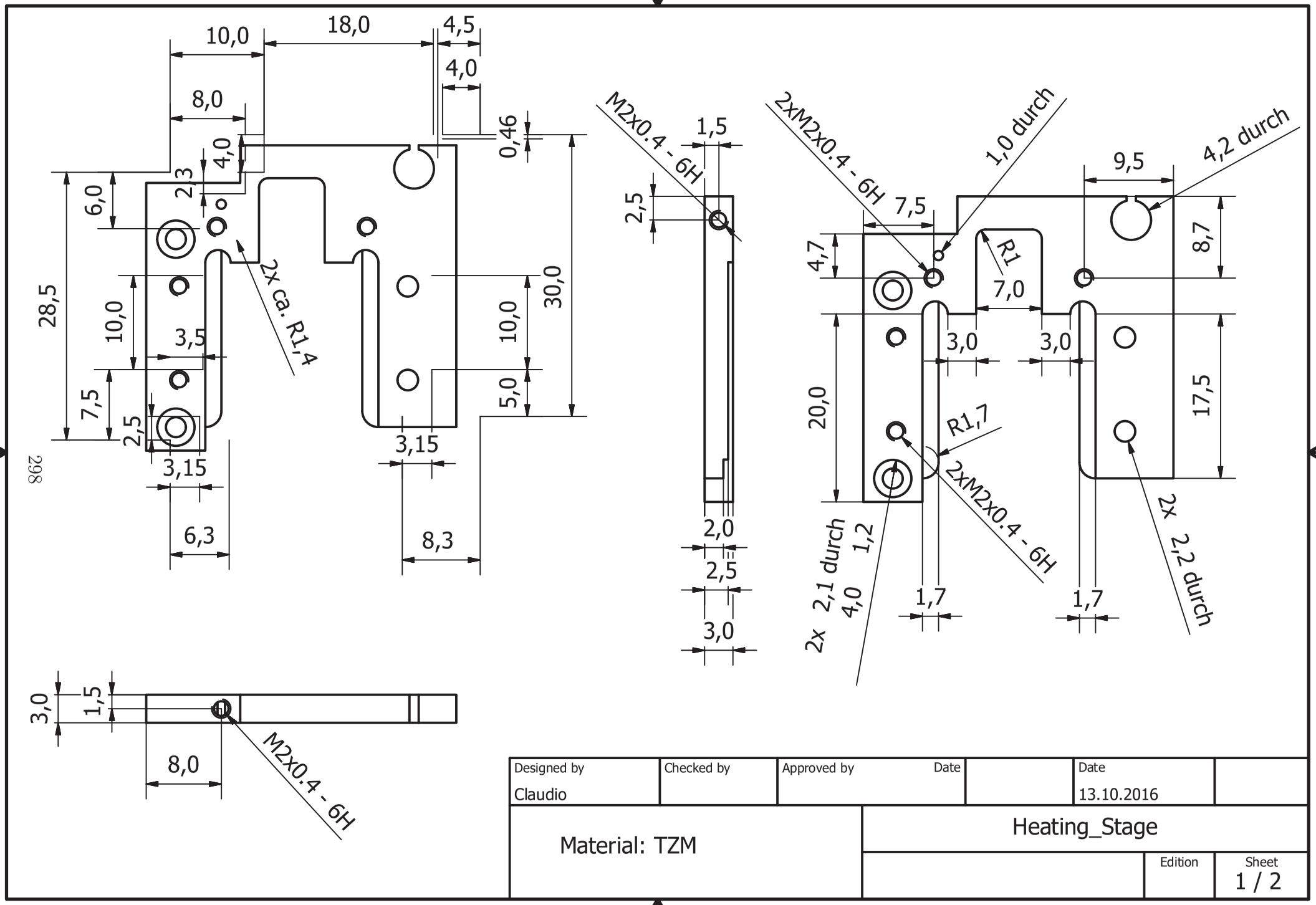
10,0
18,0
4,5
4,0
8,0
4,0
2,3
6,0
28,5
10,0
3,5
7,5
2,5
3,15
6,3
2x ca. R1,4
0,46
30,0
10,0
5,0
3,15
8,3
M2x0.4 - 6H
1,5
2,5
2,0
2,5
3,0
2xM2x0.4 - 6H
7,5
1,0 durch
4,2 durch
9,5
8,7
4,7
R1
7,0
3,0
3,0
20,0
17,5
R1,7
2xM2x0.4 - 6H
2x 2,1 durch
4,0
1,2
1,7
1,7
2x 2,2 durch
3,0
1,5
8,0
M2x0.4 - 6H
298
Designed by
Claudio
Checked by
Approved by
Date
Date
13.10.2016
Material: TZM
Heating_Stage
Edition
Sheet
1 / 2

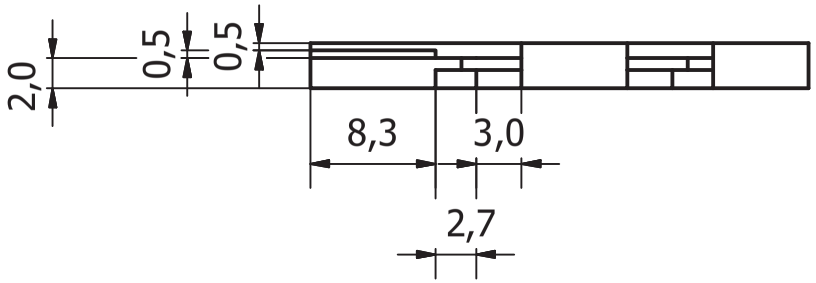

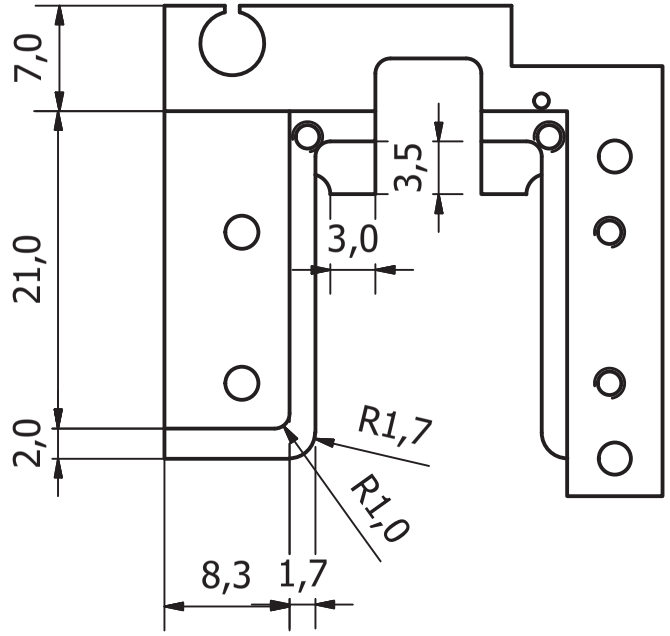

299

Designed by	Checked by	Approved by	Date		Date	
Claudio					13.10.2016	

Material: TZM	Heating_Stage		
		Edition	Sheet 2 / 2

Maßstab 2:1

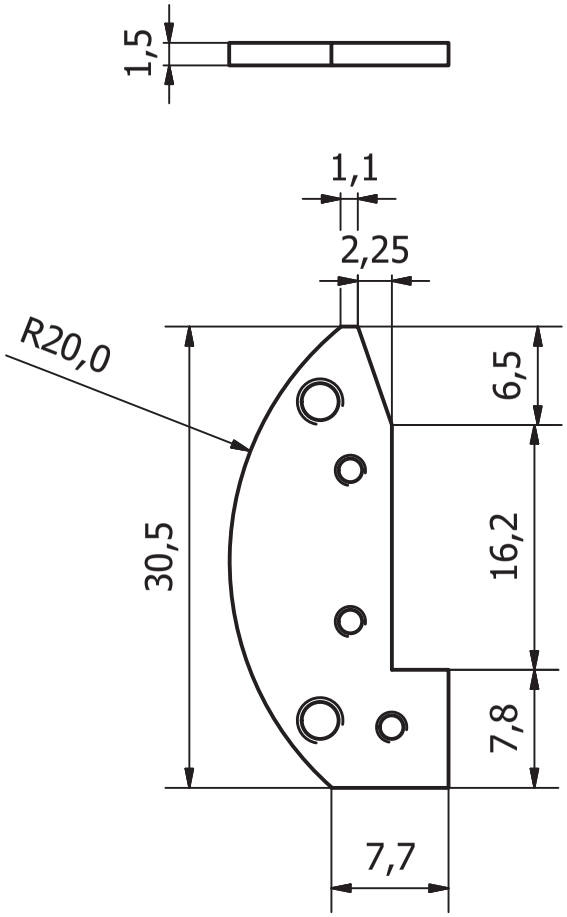

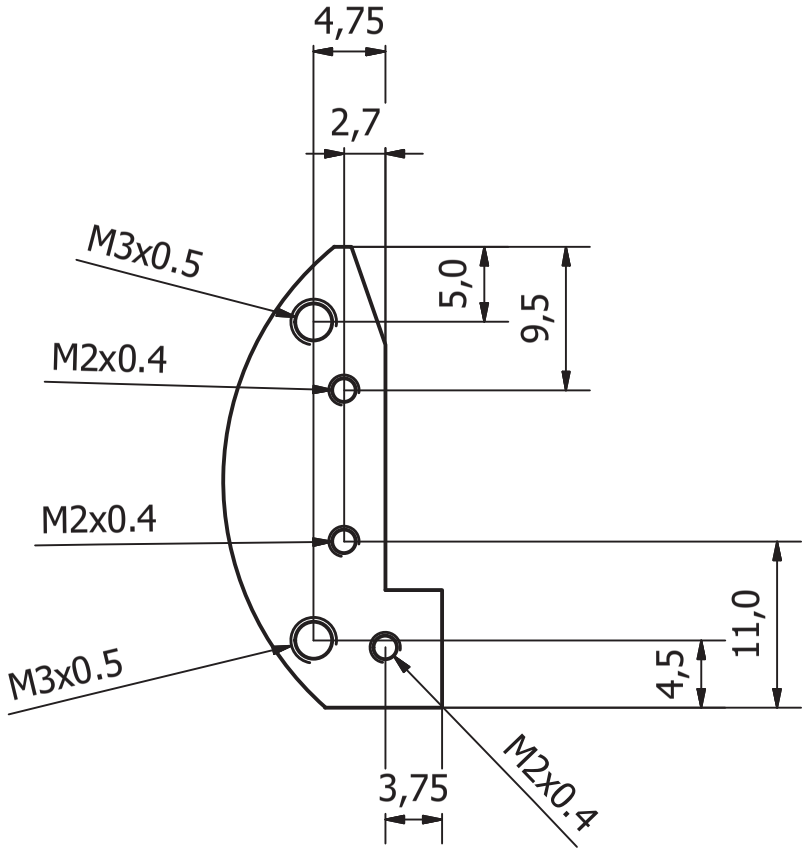

300

Designed by	Checked by	Approved by	Date		Date	
Claudio					05.09.2017	

Material: TZM

TZM-Plättchen links

Edition	Sheet
	1 / 1

Maßstab 2:1

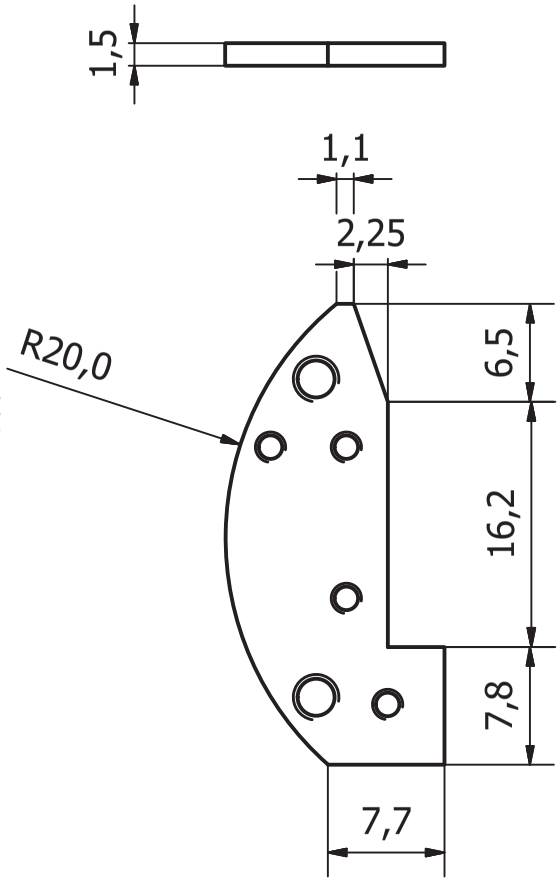

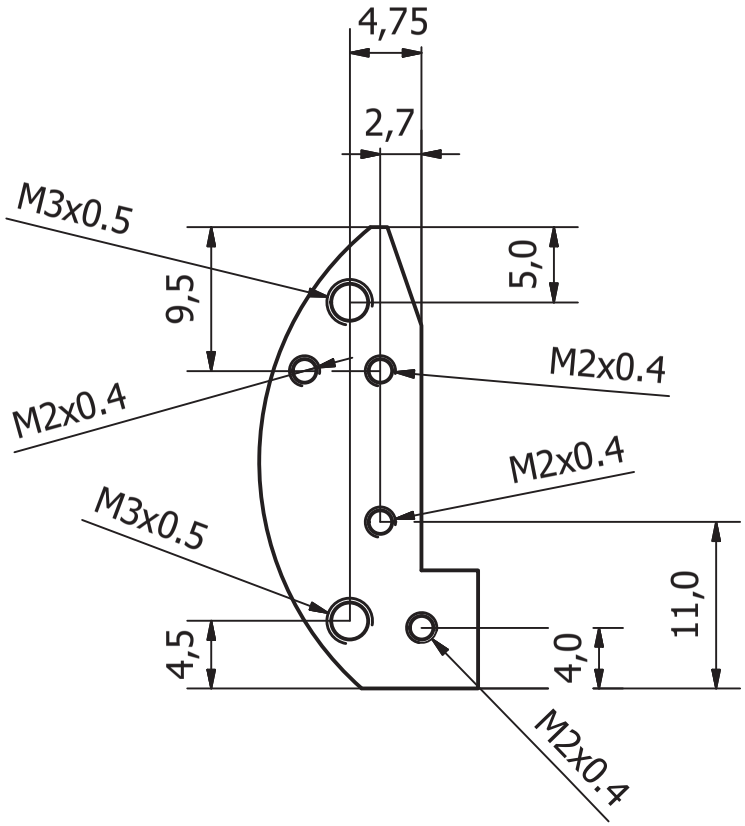

Designed by	Checked by	Approved by	Date		Date	
Claudio					05.09.2017	

Material: TZM	TZM-Plättchen rechts	Edition	Sheet 1 / 1

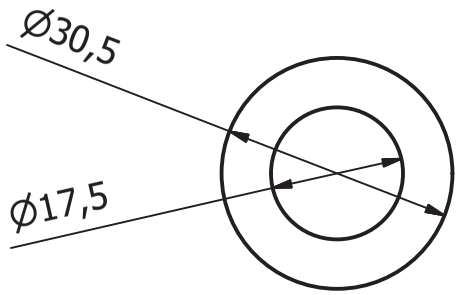

302

Designed by	Checked by	Approved by	Date		Date	
Claudio					05.09.2017	

Prep_Manip_Sapphire_Disc	Edition	Sheet 1 / 1	

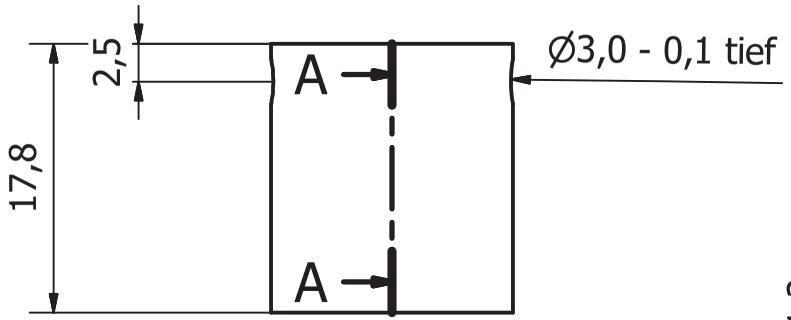

A-A (2 : 1)

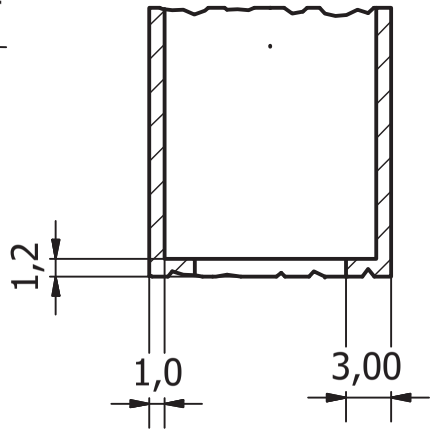

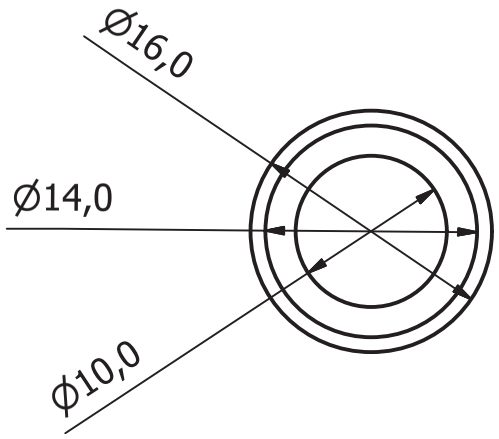

Maßstab: 2:1

303

Designed by	Checked by	Approved by	Date		Date	
Claudio					05.09.2017	

Material: TZM			
	TZM-Zylinder	Edition	Sheet 1 / 1

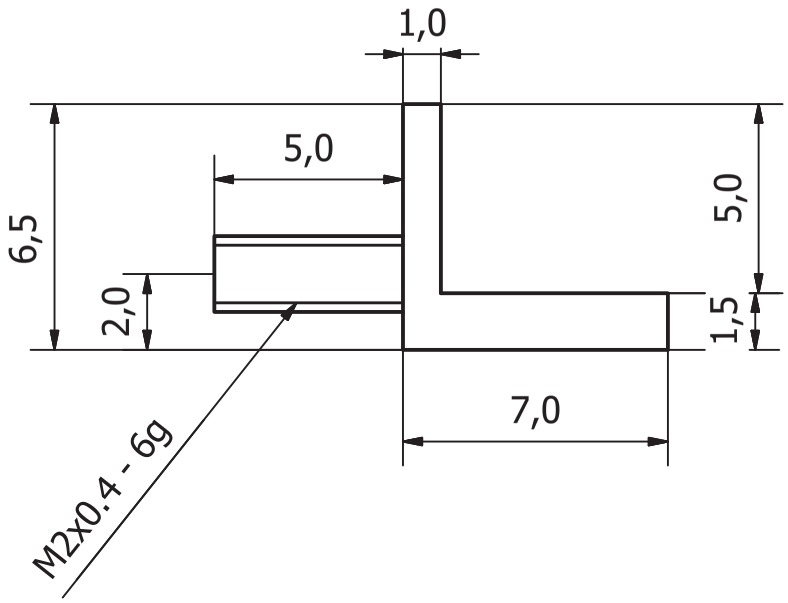

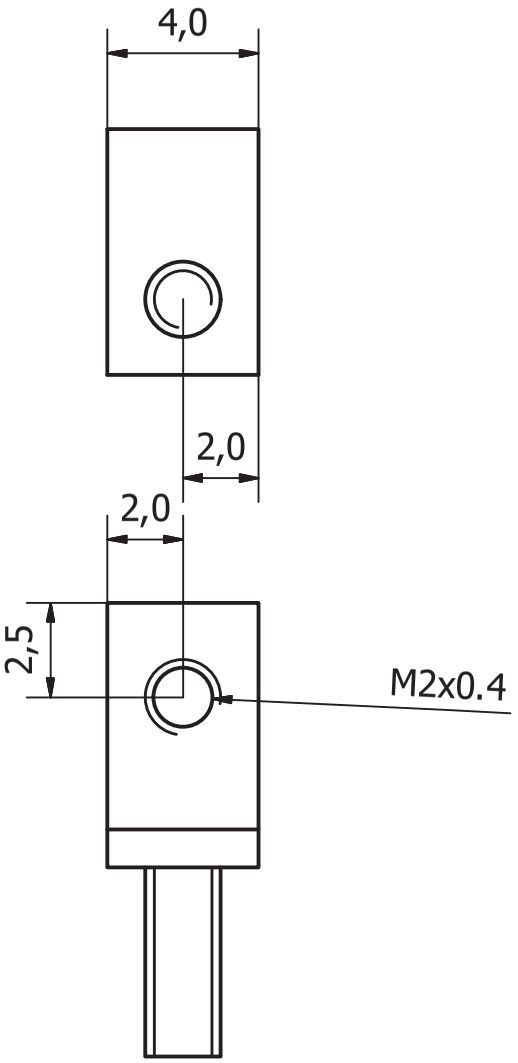

Maßstab 5:1

304

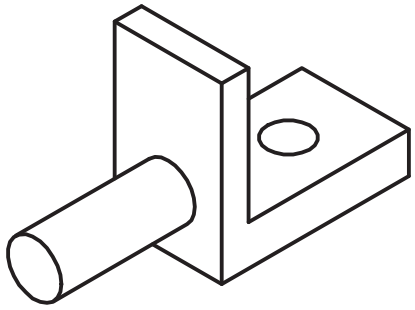

Designed by	Checked by	Approved by	Date		Date	
Claudio					05.09.2017	

Material: Edelstahl 1.4404	Keramikhalterungs-Fuß	Edition	Sheet
			1 / 1

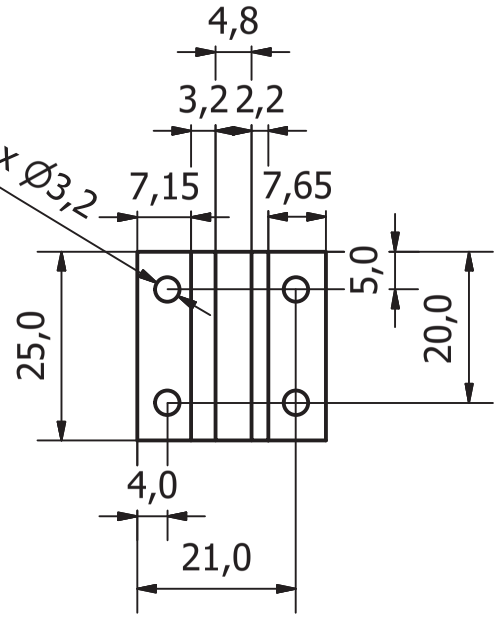

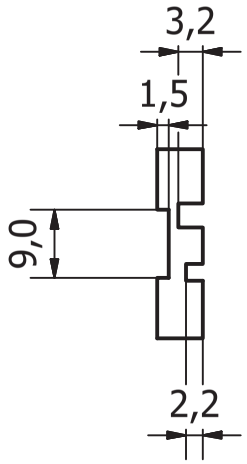

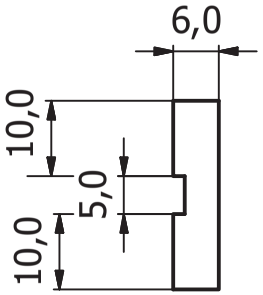

Maßstab 1:1

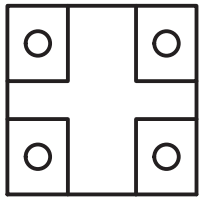

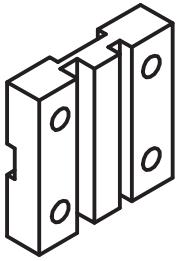

Designed by	Checked by	Approved by	Date		Date	
Claudio					05.09.2017	

Material: OFHC Kupfer	Cu-Halterung	Edition	Sheet 1 / 1

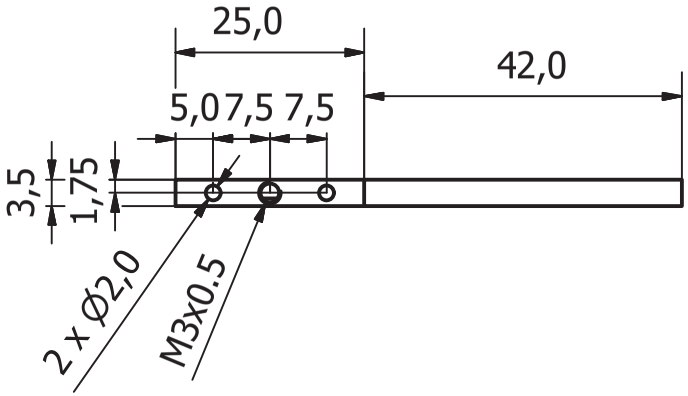

Maßstab 1:1

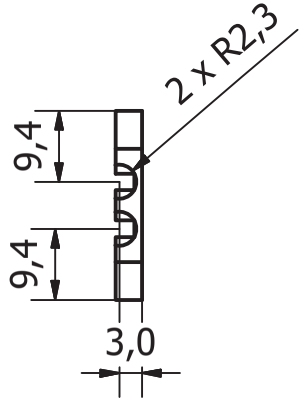

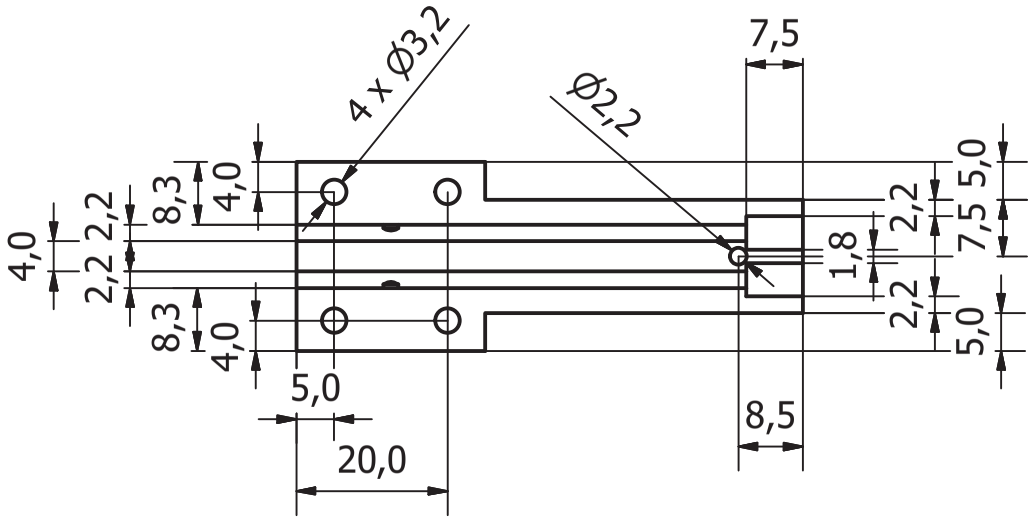

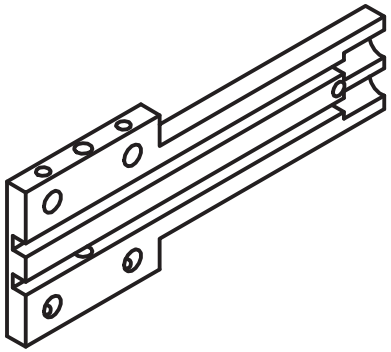

Designed by	Checked by	Approved by	Date		Date	
Claudio					05.09.2017	

Material: Edelstahl 1.4404	Bodenhalterung	Edition	Sheet
			1 / 1

306

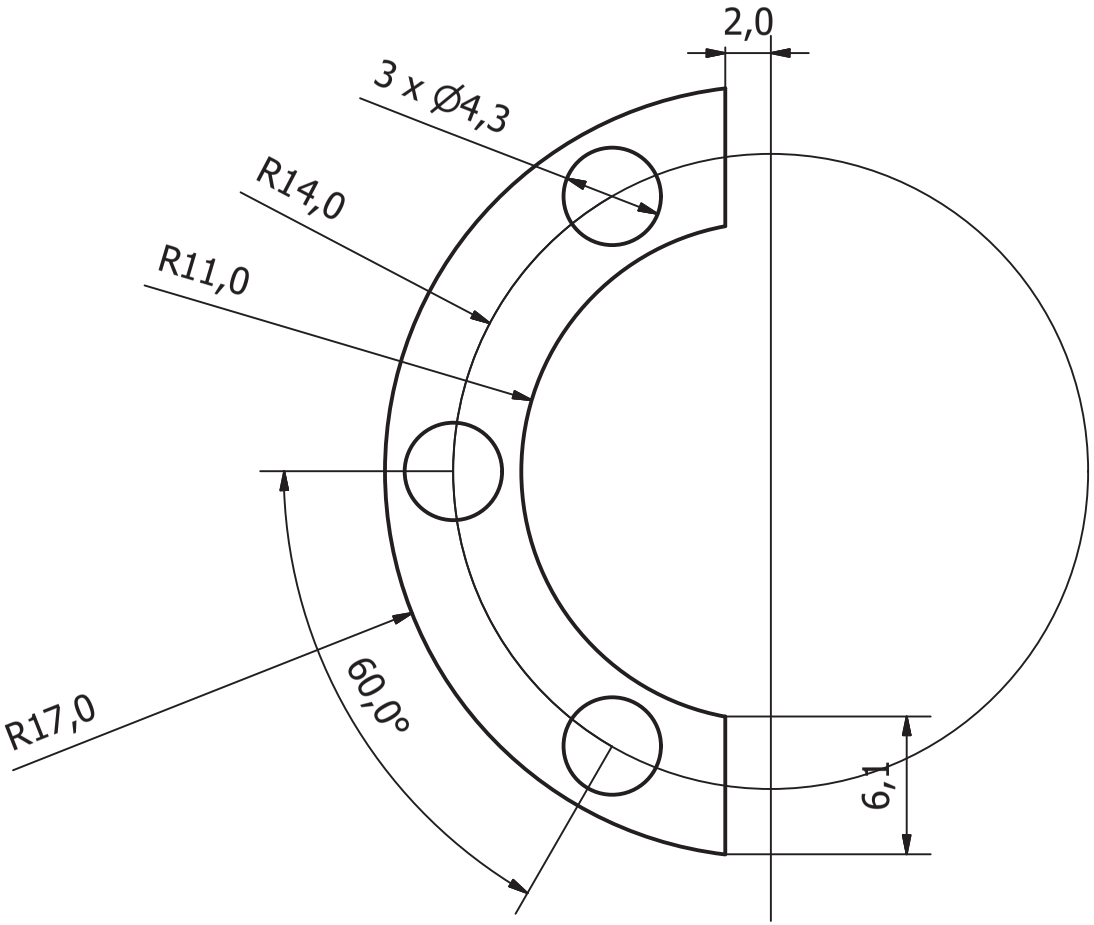

Maßstab 3:1

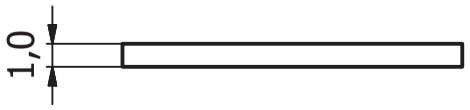

307

Designed by	Checked by	Approved by	Date		Date	
Claudio					05.09.2017	

Material: Edelstahl 1.4404
2 Stück

Dreifachmutter

Edition	Sheet
	1 / 1

Maßstab 1:3

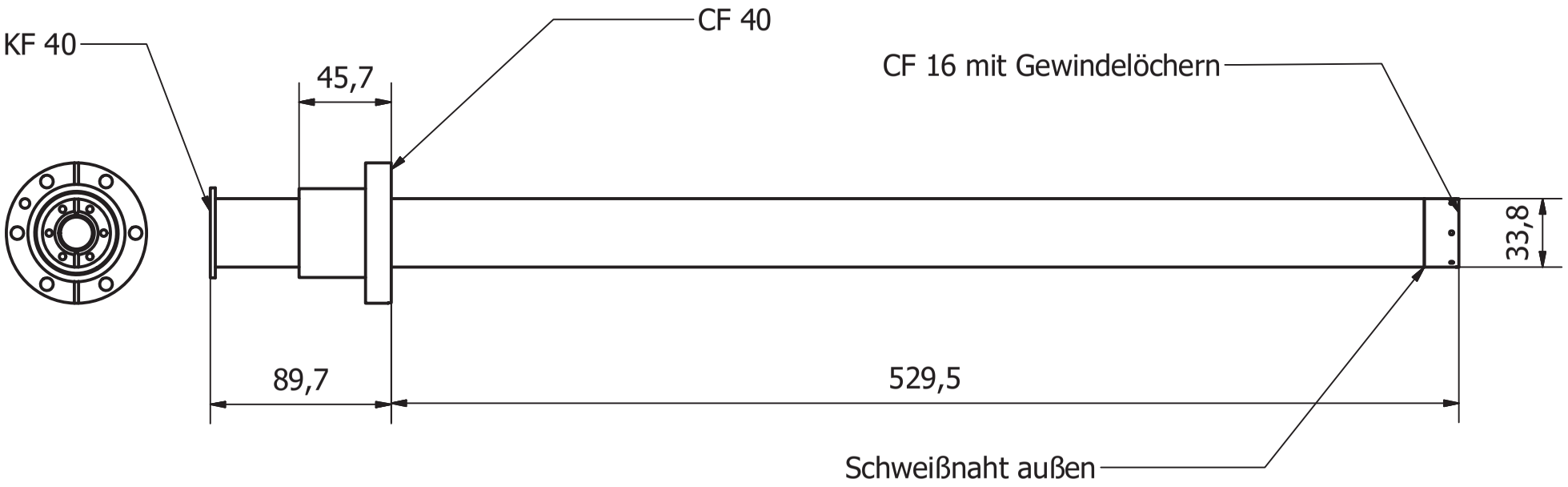

Designed by	Checked by	Approved by	Date		Date	
Claudio					15.11.2017	

Material: Edelstahl 1.4404	Kühlfinger_Manipulator	Edition	Sheet 1 / 1

B-B (1 : 1)

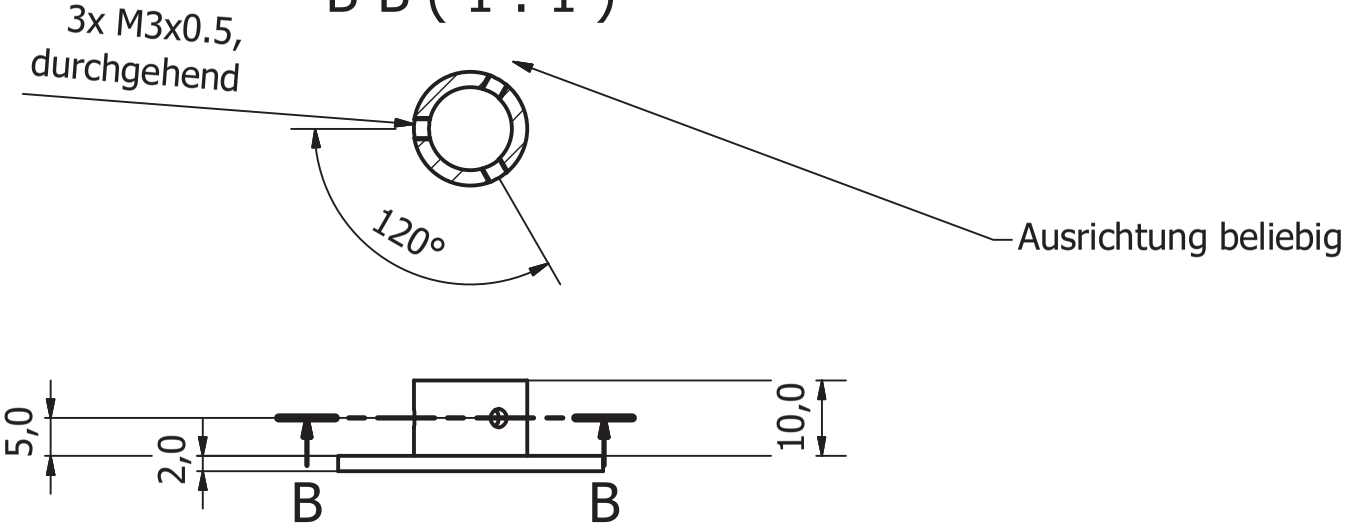

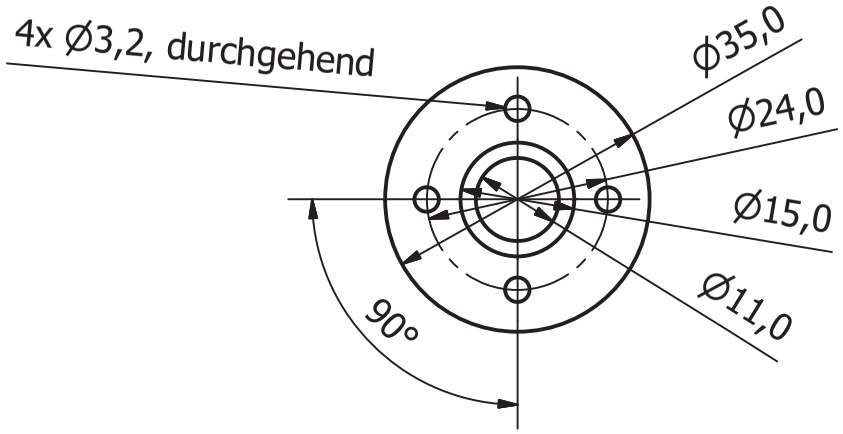

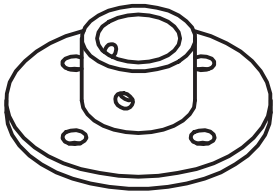

309

Designed by	Checked by	Approved by	Date		Date	
Claudio					19.04.2017	

Material: Edelstahl 1.4404	Halterung_Glasrohr	Edition	Sheet
			1 / 1

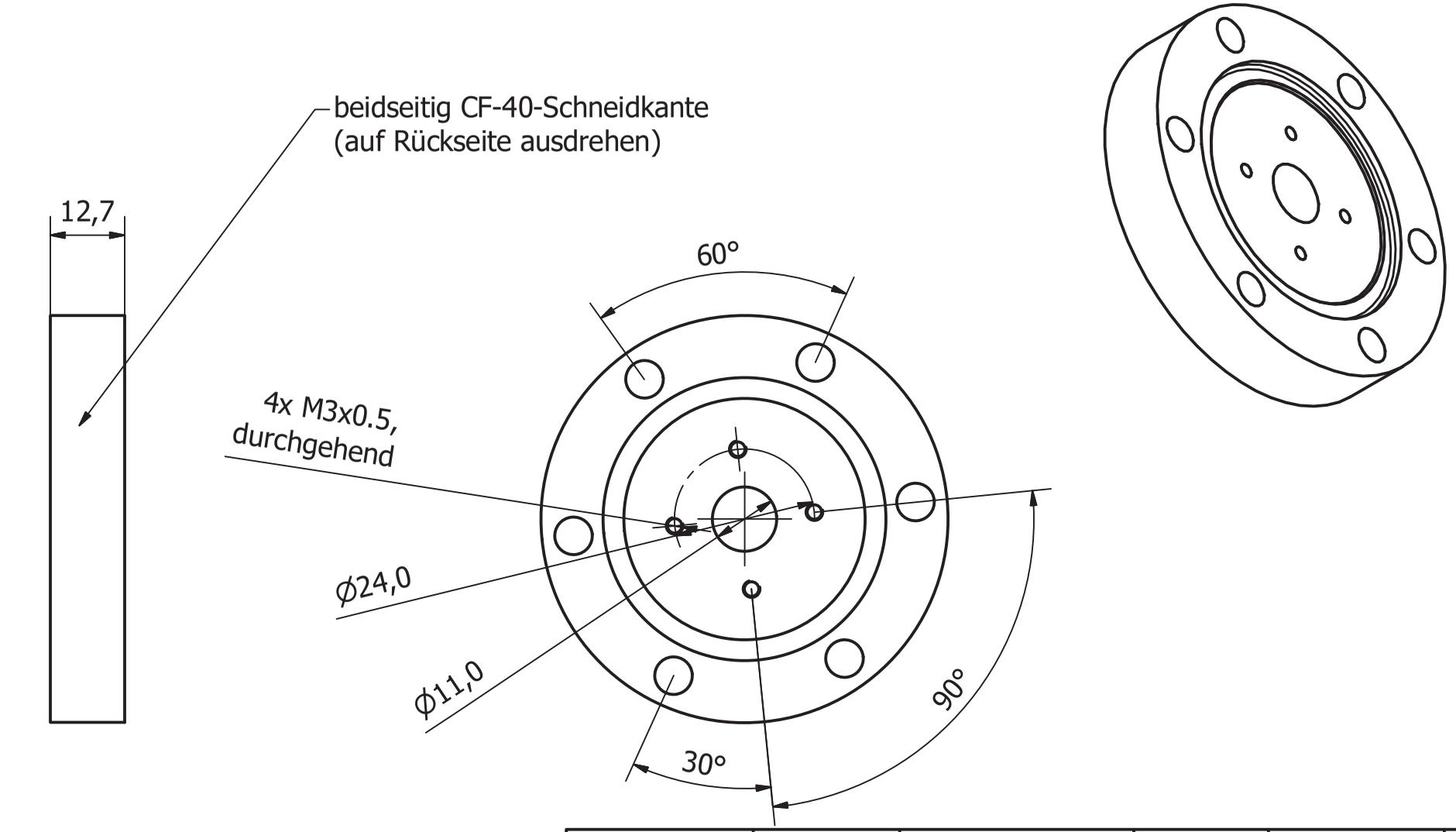

310

Designed by	Checked by	Approved by	Date		Date	
Claudio					19.04.2017	

Material: Mitgelieferter Blindflansch (Edelstahl 1.4404)	LOSE_Doppelflansch_CF40	Edition	Sheet 1 / 1

Maßstab: 1:2

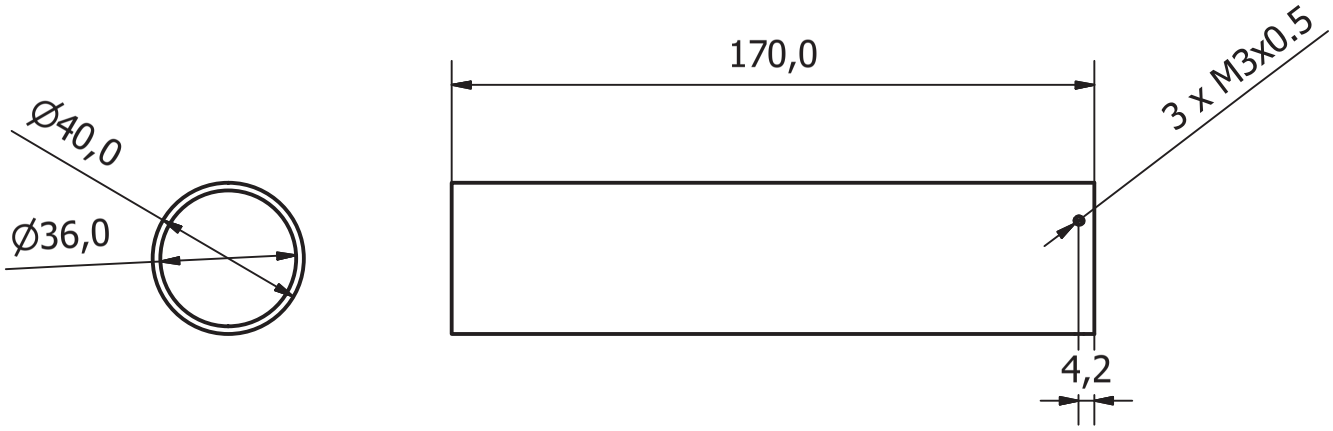

311

Designed by	Checked by	Approved by	Date		Date	
Claudio					03.05.2018	

Material: Edelstahl

LOSE_Cap_CF16_Tube	Edition	Sheet
		1 / 1

D List of Figures

E List of Schemes

F List of Tables

Curriculum Vitae

Der Lebenslauf wurde aus Datenschutzgründen aus der elektronisch publizierten Version entfernt.

Scientific Contributions

Journal Articles

The following list contains all articles published in scientific journals and manuscripts prepared in the course of the present PhD studies.

P1 **C. K. Krug**, Q. Fan, F. Fillsack, J. Glowatzki, N. Trebel, L. J. Heuplick, T. Koehler, J. M. Gottfried, "Organometallic ring *vs.* chain formation beyond kinetic control: steering their equilibrium in two-dimensional confinement", *Chem. Commun.* **2018**, *54*(70), 9741–9744, DOI 10.1039/c8cc05357j.

P2 **C. K. Krug**, D. Nieckarz, Q. Fan, P. Szabelski, J. M. Gottfried, "The Macrocycle versus Chain Competition in On-Surface Polymerization: Insights from Reactions of 1,3-Dibromoazulene on Cu(111)", *Chem. Eur. J.* **2020**, *26*(34), 7647–7656, DOI 10.1002/chem.202000486.

P3 I. Piquero-Zulaica, A. Garcia-Lekue, L. Colazzo, **C. K. Krug**, M. S. G. Mohammed, Z. M. Abd El-Fattah, J. M. Gottfried, D. G. de Oteyza, J. E. Ortega, J. Lobo-Checa, "Electronic Structure Tunability by Periodic *meta*-Ligand Spacing in One-Dimensional Organic Semiconductors", *ACS Nano* **2018**, *12*(10), 10537–10544, DOI 10.1021/acsnano.8b06536.

P4 Q. Fan, D. Martin-Jimenez, D. Ebeling, **C. K. Krug**, L. Brechmann, C. Kohlmeyer, G. Hilt, W. Hieringer, A. Schirmeisen, J. M. Gottfried, "Nanoribbons with Nonalternant Topology from Fusion of Polyazulene: Carbon Allotropes beyond Graphene", *J. Am. Chem. Soc.* **2019**, *141*(44), 17713–17720, DOI 10.1021/jacs.9b08060.

P5 **C. K. Krug**, M. Zugermeier, J. Kuttner, M. Schmid, G. Hilt, J. M. Gottfried, "Polymorphism at the Metal/Organic Interface: Hybrid Phase with Alternating Coplanar and Vertical Adsorption Geometry", *J. Phys. Chem. C* **2020**, *124*(29), 15928–15934, DOI 10.1021/acs.jpcc.0c03601.

P6 M. Chen, H. Zhou, B. P. Klein, M. Zugermeier, **C. K. Krug**, H.-J. Drescher, M. Gorgoi, M. Schmid, J. M. Gottfried, "Formation of an interphase layer during deposition of cobalt onto tetraphenylporphyrin: a hard X-ray photoelectron spectroscopy (HAXPES) study", *Phys. Chem. Chem. Phys.* **2016**, *18*(44), 30643–30651, DOI 10.1039/c6cp05894a.

P7 M. Schmid, M. Zugermeier, J. Herritsch, B. P. Klein, **C. K. Krug**, L. Ruppenthal, P. Müller, M. Kothe, P. Schweyen, M. Bröring, J. M. Gottfried, "On-Surface Synthesis and Characterization of an Iron Corrole", *J. Phys. Chem. C* **2018**, *122*(19), 10392–10399 DOI 10.1021/acs.jpcc.8b00067.

P8 B. P. Klein, N. J. van der Heijden, S. R. Kachel, M. Franke, **C. K. Krug**, K. K. Greulich, L. Ruppenthal, P. Müller, P. Rosenow, S. Parhizkar, F. C. Bocquet, M. Schmid, W. Hieringer, R. J. Maurer, R. Tonner, C. Kumpf, I. Swart, J. M. Gottfried, "Molecular Topology and the Surface Chemical Bond: Alternant Versus Nonalternant Aromatic Systems as Functional Structural Elements", *Phys. Rev. X* **2019**, *9*(1), 011030, DOI 10.1103/physrevx.9.011030.

P9 M. Schmid, K. Ishioka, A. Beyer, B. P. Klein, **C. K. Krug**, M. Sachs, H. Petek, C. J. Stanton, W. Stolz, K. Volz, J. M. Gottfried, U. Höfer, "Direct Characterization of Band Bending in GaP/Si(001) Heterostructures with Hard X-ray Photoelectron Spectroscopy", **2016**, arXiv: 1611.03785[cond-mat.mes-hall].

P10 M. Sachs, K. Bohnen, M. Conrad, B. P. Klein, **C. K. Krug**, C. Pietzonka, M. Schmid, S. Zörb, J. M. Gottfried, B. Harbrecht, "Forcing substitution of tantalum by copper in 1T-TaS_2: synthesis, structure and electronic properties of 1T-$Cu_xTa_{1-x}S_2$", *J. Phys.: Condens. Matter* **2018**, *30*(38), 385501, DOI 10.1088/1361-648X/aad9c6.

P11 H. L. Deubner, M. Sachs, J. Bandemehr, S. I. Ivlev, A. J. Karttunen, S. R. Kachel, B. P. Klein, L. Ruppenthal, M. Schöniger, **C. K. Krug**, J. Herritsch, J. M. Gottfried, J. N. M. Aman, J. Schmedt auf der Günne, F. Kraus, "Binary Lead Fluoride Pb_3F_8", *Chem. Eur. J.* **2019**, *25*(68), 15656–15661, DOI 10.1002/chem.201903954.

Conference Contributions

The following list contains all conference contributions made during the course of the present PhD studies. The respective presenting author is underlined.

1. **C. K. Krug**, M. Chen, Q. Fan, I. Piquero-Zulaica, M. Kroll, J. Kuttner, M. Schmid, J. Lobo-Checa, J. E. Ortega, G. Hilt, J. Zhu, J. M. Gottfried, "Ullmann Coupling on Coinage Metal Surfaces", 116$^{\text{th}}$ General Assembly of the German Bunsen Society for Physical Chemistry (DBG), Kaiserslautern, May 25$^{\text{th}}$ – 27$^{\text{th}}$, 2017. (Poster)

2. **C. K. Krug**, Q. Fan, F. Fillsack, J. Glowatzki, N. Trebel, M. Schmid, J. M. Gottfried, "Towards Ullmann Coupling of 1,3-Dibromoazulene", Spring Meeting of the German Physical Society (DPG) and Meeting of the Condensed Matter Section of the European Physical Society (EPS), Berlin, March 11$^{\text{th}}$ – 16$^{\text{th}}$, 2018. (Poster)

3. **C. K. Krug**, Q. Fan, D. Nieckarz, F. Fillsack, J. Glowatzki, N. Trebel, L. J. Heuplick, T. Koehler, P. Szabelski, J. M. Gottfried, "Ring/Chain Competition in Organometallic Oligomers", Spring Meeting of the German Physical Society (DPG), Regensburg, March 31$^{\text{st}}$ – April 5$^{\text{th}}$, 2019. (Talk)

4. Q. Fan, C. Wang, T. Wang, J. Zhu, M. Chen, M. Zugermeier, **C. K. Krug**, J. Kuttner, G. Hilt, W. Hieringer, J. M. Gottfried, "Controlled on-surface synthesis of organic and organometallic macrocycles", Spring Meeting of the German Physical Society (DPG), Dresden, March 19$^{\text{th}}$ – 24$^{\text{th}}$, 2017. (Talk)

5. K. K. Greulich, B. P. Klein, N. van der Heijden, **C. K. Krug**, S. R. Kachel, M. Schöniger, P. Rosenow, M. Schmid, R. Tonner, I. Swart, J. M. Gottfried, "Topologically Different Aromatic Isomers on Metal Surfaces: A Molecular Model System for 5-7 Defects in Graphene", Spring Meeting of the German Physical Society (DPG), Dresden, March 19$^{\text{th}}$ – 24$^{\text{th}}$, 2017. (Poster)

6. B. P. Klein, N. van der Heijden, **C. K. Krug**, M. Schöniger, P. Rosenow, M. Schmid, R. Tonner, I. Swart, J. M. Gottfried, "Molecular Topology and Surface Chemical Bond: Alternant vs. Non-Alternant Aromatic Molecules", Spring Meeting of the German Physical Society (DPG), Dresden, March 19$^{\text{th}}$ – 24$^{\text{th}}$, 2017. (Talk)

7. M. Schmid, M. Chen, K. Ishioka, A. Beyer, B. P. Klein, **C. K. Krug**, M. Sachs, W. Stolz, K. Volz, U. Höfer, J. M. Gottfried, "Interphase Formation and Band Bending in Organic and Inorganic Semiconductor Films Examined with Hard X-ray Photoelectron Spectroscopy", Spring Meeting of the German Physical Society (DPG), Dresden, March 19th – 24th, 2017. (Talk)

8. Q. Fan, C. Wang, T. Wang, J. Zhu, M. Chen, M. Zugermeier, **C. K. Krug**, J. Kuttner, G. Hilt, W. Hieringer, J. M. Gottfried, "On-surface synthesis of macrocycles", Spring Meeting of the German Physical Society (DPG), Dresden, March 19th – 24th, 2017. (Talk)

9. Q. Fan, C. Wang, T. Wang, J. Zhu, M. Chen, **C. K. Krug**, M. Zugermeier, J. Kuttner, G. Hilt, W. Hieringer, J. M. Gottfried, "On-surface synthesis of low-dimensional nanostructures from haloarenes", Spring Meeting of the German Physical Society (DPG), Dresden, March 19th – 24th, 2017. (Poster)

10. Q. Fan, C. Wang, T. Wang, J. Zhu, M. Chen, M. Zugermeier, **C. K. Krug**, J. Kuttner, G. Hilt, W. Hieringer, J. M. Gottfried, "Template-Controlled On-Surface Synthesis of Macrocycles", 116th General Assembly of the German Bunsen Society for Physical Chemistry (DBG), Kaiserslautern, May 25th – 27th, 2017. (Poster)

11. B. P. Klein, N. van der Heijden, **C. K. Krug**, M. Schöniger, P. Rosenow, M. Schmid, R. Tonner, I. Swart, J. M. Gottfried, "Molecular Topology and Metal/Organic Interfaces", 116th General Assembly of the German Bunsen Society for Physical Chemistry (DBG), Kaiserslautern, May 25th – 27th, 2017. (Talk)

12. M. Zugermeier, M. Chen, H.-J. Drescher, L. Heuplick, B. P. Klein, **C. K. Krug**, M. Liebold, F. Niefind, L. Ruppenthal, M. Schmid, P. Schweyen, H. Zhou, M. Bröring, J. Sundermeyer, J. M. Gottfried, "Synthesis, Metalation and Structures of Tetrapyrroles at Interfaces", 116th General Assembly of the German Bunsen Society for Physical Chemistry (DBG), Kaiserslautern, May 25th – 27th, 2017. (Poster)

13. M. Schmid, M. Zugermeier, B. P. Klein, **C. K. Krug**, S. R. Kachel, J. M. Gottfried, "Examination of Buried Interfaces Between Transition

Metal Layers and Tetrapyrrole Films with Hard X-ray Photoelectron Spectroscopy", 116th General Assembly of the German Bunsen Society for Physical Chemistry (DBG), Kaiserslautern, May 25th – 27th, 2017. (Talk)

14. B. P. Klein, N. van der Heijden, **C. K. Krug**, M. Schöniger, P. Rosenow, M. Schmid, R. Tonner, I. Swart, J. M. Gottfried, "Molecular Topology and Metal/Organic Interfaces", 33rd European Conference on Surface Science (ECOSS-33), Szeged, Hungary, August 27th – September 1st, 2017. (Talk)

15. M. Zugermeier, M. Chen, H.-J. Drescher, L. Heuplick, B. P. Klein, **C. K. Krug**, M. Liebold, F. Niefind, L. Ruppenthal, M. Schmid, P. Schweyen, H. Zhou, M. Bröring, J. Sundermeyer, J. M. Gottfried, "Synthesis, Metalation and Structures of Tetrapyrroles at Interfaces", 33rd European Conference on Surface Science (ECOSS-33), Szeged, Hungary, August 27th – September 1st, 2017. (Poster)

16. M. Schmid, B. P. Klein, **C. K. Krug**, S. R. Kachel, J. M. Gottfried, "Examination of Metal-Organic Interphases with Hard X-Ray Photoelectron Spectroscopy (HAXPES)", 655. WE-Heraeus-Seminar: Surfaces and Interfaces of Ionic Liquids, Ban Honnef, December 3rd – 6th, 2017. (Poster)

17. J. M. Gottfried, Q. Fan, J. Zhu, **C. K. Krug**, K. K. Greulich, "On-Surface Synthesis of Polymers and Macrocycles", 255th ACS National Meeting & Exposition, New Orleans, Louisiana, USA, March 18th – 22nd, 2018. (Talk)

18. B. P. Klein, N. van der Heijden, M. Franke, **C. K. Krug**, S. R. Kachel, P. Rosenow, M. Schmid, R. Tonner, I. Swart, C. Kumpf, J. M. Gottfried, "Molecular Topology and Surface Chemical Bond: Alternant vs. Non-Alternant Aromatic Molecules", 255th ACS National Meeting & Exposition, New Orleans, Louisiana, USA, March 18th – 22nd, 2018. (Talk)

19. B. P. Klein, N. van der Heijden, M. Franke, **C. K. Krug**, S. R. Kachel, P. Rosenow, M. Schmid, R. Tonner, I. Swart, C. Kumpf, J. M. Gottfried, "A Molecular Model System for 5-7 Defects in Graphene", 255th ACS National Meeting & Exposition, New Orleans, Louisiana, USA, March 18th – 22nd, 2018. (Poster)

20. B. P. Klein, M. Franke, **C. K. Krug**, S. R. Kachel, P. Rosenow, F. Posseik, M. Schmid, R. J. Maurer, R. Tonner, C. Kumpf, J. M. Gottfried, "A Molecular Model System for 5-7 Defects in Graphene", Spring Meeting

of the German Physical Society (DPG), Berlin, March 11th – 16th, 2018. (Talk)

21. I. Piquero-Zulaica, A. García-Lekue, **C. K. Krug**, J. E. Ortega, J. M. Gottfried, J. Lobo-Checa, "Electronic band structure of poly (*meta*-phenylene) zigzag chains", Spring Meeting of the German Physical Society (DPG), Berlin, March 11th – 16th, 2018. (Talk)

22. L. Ruppenthal, B. P. Klein, N. J. van der Heijden, M. Franke, **C. K. Krug**, S. R. Kachel, P. Rosenow, F. Posseik, M. Schmid, R. Tonner, I. Swart, C. Kumpf, J. M. Gottfried, "Surface Chemical Bond of a Non-Alternant Aromatic Molecule on Metal Substrates", Spring Meeting of the German Physical Society (DPG), Berlin, March 11th – 16th, 2018. (Poster)

23. M. Schmid, M. Zugermeier, J. Herritsch, B. P. Klein, **C. K. Krug**, L. Ruppenthal, P. Müller, M. Bröring, J. M. Gottfried, "On-Surface Synthesis and Characterization of an Iron Corrole", Spring Meeting of the German Physical Society (DPG), Berlin, March 11th – 16th, 2018. (Talk)

24. M. Schmid, M. Zugermeier, J. Herritsch, B. P. Klein, **C. K. Krug**, L. Ruppenthal, P. Müller, M. Kothe, P. Schweyen, M. Bröring, J. M. Gottfried, "Comparing Interfacial Interactions in Tetrapyrrole Monolayers: Fe(II)porphyrin/Ag(111) vs. Fe(III)corrole/Ag(111)", 34th European Conference on Surface Science (ECOSS-34), Aarhus, Denmark, August 25th – 31st, 2018. (Talk)

25. S. R. Kachel, **C. K. Krug**, M. Schmid, J. M. Gottfried "HAXPES on Metal/Organic Interfaces", Joint Seminar SFB 1083 "Structure and Dynamics of Internal Interfaces" and GRK "Functionalization of Semiconductor Interfaces", Volkenroda, September 2nd – 6th, 2018. (Talk)

26. M. Schöniger, S. R. Kachel, **C. K. Krug**, T. Koehler, M. Schmid, J. M. Gottfried, "Reaction of Calcium with Tetraphenylporphyrin Thin Films: Reaction Energies and Reaction Depths", Spring Meeting of the German Physical Society (DPG), Regensburg, March 31st – April 5th, 2019. (Talk)

27. J. M. Gottfried, Q. Fan, **C. K. Krug**, J.-N. Luy, R. Tonner, D. Ebeling, A. Schirmeisen, W. Hieringer, "Carbon-Based Functional Nanomaterials in 2D Confinement: On-Surface Synthesis, Aromaticity, and Molecular Topology", 118th General Assembly of the German Bunsen Society for Physical Chemistry (DBG), Jena, May 30th – June 1st, 2019. (Talk)

28. S. R. Kachel, B. P. Klein, M. Franke, **C. K. Krug**, L. Ruppenthal, F. C. Bocquet, W. Hieringer, R. J. Maurer, R. Tonner, C. Kumpf, J. M. Gottfried, "Functional Structural Elements in Carbon-Based Nanomaterials: Alternant vs. Non-Alternant Topology and Interface Chemical Bond", 118$^{\text{th}}$ General Assembly of the German Bunsen Society for Physical Chemistry (DBG), Jena, May 30$^{\text{th}}$ – June 1$^{\text{st}}$, 2019. (Poster)

Acknowledgment

At this point I want to thank all those people, who have contributed to the success of this thesis.

First of all, I want to thank my supervisor Prof. Dr. J. Michael Gottfried for providing me with the opportunity to pursue my PhD studies in the fascinating field of on-surface synthesis and his continuous support throughout all the times.

I thank Prof. Dr. Ralf Tonner for acting as the second referee and also for the collaboration before and during my PhD studies.

I also thank Prof. Dr. Carsten von Hänisch for acting as the third member of the examination committee.

A big thank you goes to the whole Gottfried group for providing an excellent working atmosphere during all these years and also for the fun times we had outside of the university during our various parties and trips. Especially I want to mention Dr. Qitang Fan, Jan Herritsch, Stefan Kachel, Maik Schöniger, and Dr. Malte Zugermeier. It was very nice to share the office and the lab with you! Dr. Martin Schmid has told me a lot and the scientific discussions were always very helpful. Furthermore, Marco Hill and Rigo Donner have helped me a lot with all the technical and administrative things they have taken care of.

A lot of the work presented in this thesis originated from collaboration projects, which would not have been possible without excellent collaboration partners. First, I want to thank Dr. Ignacio Piquero-Zulaica and Dr. Jorge Lobo-Checa for the great time I had during my stay in Donostia-San Sebastián. Although we really worked a lot, you managed to show me the nice cultural life of the Basque Country and I really enjoyed *pintxo-pote*! Thank you also to Prof. Dr. J. Enrique Ortega for giving me the opportunity to work in his lab. Furthermore, I want to mention Dr. Damian Nieckarz and Dr. Paweł Szabelski, who supplemented our experimental findings with their MC simulations and Lea Brechmann, Corinna Kohlmeyer, Dr. Julian Kuttner, and Dr. Robert Möckel for the precursor synthesis they performed under the supervision of Prof. Dr. Gerhard Hilt.

I had the pleasure to instruct a number of students during their bachelor's thesis and internship projects for their M.Sc. studies. It was always nice to

have company in the lab and I learned a lot myself. Thank you to Florian Fillsack, Melanie Förster, Johannes Glowatzki, Lukas Heuplick, Tabea Köhler, Oliver Kreuz, Moritz Kroll, Benedict Paulus, Philipp Schröder, Yohan Song, and Nicole Trebel for contributing to this work!

The mechanical and electronic workshop and the glassblowers of the department have realized a number of parts that were designed and used during my PhD studies. Thank you very much for your excellent work!

Many of the things I was able to do in the past years would not have been possible without financial support. This was mainly granted by the *Sonderforschungsbereich 1083*, which did not only pay for my trip to Donostia-San Sebastián but also for several conference participations and synchrotron beamtimes at BESSY II. The latter were also funded by the *Helmholtz-Zentrum Berlin*.

I want to thank Jan Herritsch, Stefan Kachel, Matthias Kilian, Lola-Sophia and Dr. Tim Lichtenberg, Maik Schöniger as well as Lukas Uhde for carefully proofreading this thesis.

A big thanks, of course, goes to all my friends, who always provided the necessary distraction, when I needed it!

At last, and most of all, I want to thank my family for all the support they gave me during my studies. Mama, Lola, and Tim, without you this work would not have been possible!

Danksagung

An dieser Stelle möchte ich all den Menschen danken, die zum Gelingen dieser Arbeit beigetragen haben.

Zunächst möchte ich meinem Doktorvater Prof. Dr. J. Michael Gottfried dafür danken, dass er es mir ermöglicht hat, meine Doktorarbeit auf dem faszinierenden Gebiet der oberflächengestützten Synthese anzufertigen und für seine durchgehende Unterstützung während der gesamten Zeit.

Prof. Dr. Ralf Tonner danke ich für die Übernahme des Zweitgutachtens sowie die Kooperation vor und während meiner Doktorarbeit.

Ebenfalls möchte ich Prof. Dr. Carsten von Hänisch dafür danken, dass er bereit war, als drittes Mitglied der Prüfungskommission zur Verfügung zu stehen.

Ein großes Dankeschön geht an die gesamte AG Gottfried für die exzellente Arbeitsatmosphäre in all diesen Jahren und auch für die schönen Feiern und Exkursionen außerhalb der Universität. Besonders möchte ich hierbei Dr. Qitang Fan, Jan Herritsch, Stefan Kachel, Maik Schöniger und Dr. Malte Zugermeier erwähnen. Es war immer schön, mit euch das Büro und das Labor zu teilen! Dr. Martin Schmid hat mir sehr viel beigebracht und die wissenschaftlichen Diskussionen waren immer sehr hilfreich. Des Weiteren haben mir Marco Hill und Rigo Donner sehr mit all den technischen und administrativen Aufgaben geholfen, die sie übernommen haben.

Ein Großteil der Arbeit in dieser Dissertation stammt aus Kooperationsprojekten, die ohne exzellente Kooperationspartner nicht möglich gewesen wären. Zunächst möchte ich Dr. Ignacio Piquero-Zulaica und Dr. Jorge Lobo-Checa für die tolle Zeit danken, die ich während meines Aufenthalts in Donostia-San Sebastián hatte. Auch wenn wir wirklich viel gearbeitet haben, habt ihr es geschafft, mir das kulturelle Leben des Baskenlandes zu zeigen und *pintxo-pote* hat mir sehr gut gefallen! Danke auch an Prof. Dr. J. Enrique Ortega für die Möglichkeit, in seinem Labor zu arbeiten. Außerdem möchte ich Dr. Damian Nieckarz und Dr. Paweł Szabelski erwähnen, die unsere experimentellen Daten mit ihren MC-Simulationen untermauert haben. Dank gebührt ebenfalls Lea Brechmann, Corinna Kohlmeyer, Dr. Julian Kuttner und Dr. Robert Möckel für die Synthese von Molekülen, die sie unter der Anleitung von Prof. Dr. Gerhard Hilt durchgeführt haben.

Ich hatte das Vergnügen, eine Vielzahl von Studierenden während ihrer Bachelorarbeit oder Vertiefungspraktika zu betreuen. Es war immer schön, Gesellschaft im Labor zu haben und ich habe selber viel dabei gelernt. Vielen Dank an Florian Fillsack, Melanie Förster, Johannes Glowatzki, Lukas Heuplick, Tabea Köhler, Oliver Kreuz, Moritz Kroll, Benedict Paulus, Philipp Schröder, Yohan Song und Nicole Trebel für ihren Beitrag zu dieser Arbeit!

Die feinmechanische und elektronische Werkstatt und die Glasbläser des Fachbereichs haben eine Vielzahl an Bauteilen hergestellt, die im Zuge meiner Doktorarbeit entwickelt und verwendet wurden. Vielen Dank für die exzellente Arbeit!

Viele der Dinge, die ich in den letzten Jahren machen durfte, wären ohne finanzielle Unterstützung nicht möglich gewesen. Diese wurde vor allem durch den Sonderforschungsbereich 1083 gewährt, der nicht nur meine Reise nach Donostia-San Sebastián bezahlt hat, sondern auch viele Konferenzteilnahmen und Synchrotron-Strahlzeiten. Letztere wurden ebenfalls vom Helmholtz-Zentrum Berlin unterstützt.

Ich möchte Jan Herritsch, Stefan Kachel, Matthias Kilian, Lola-Sophia und Dr. Tim Lichtenberg, Maik Schöniger sowie Lukas Uhde für das sorgfältige Korrekturlesen dieser Arbeit danken.

Ein großes Dankeschön geht natürlich an all meine Freunde, die immer für die notwendige Ablenkung gesorgt haben, wenn ich sie einmal brauchte!

Zuletzt und am allermeisten möchte ich meiner Familie für all die Unterstützung während meines Studiums danken. Mama, Lola und Tim, ohne euch wäre diese Arbeit nicht möglich gewesen!